CO_2 Electroreduction on Silver Catalysts Under Controlled Mass Transport Conditions

Inaugural dissertation
of the Faculty of Science,
University of Bern

presented by

María de Jesús Gálvez-Vázquez
from Mexico

Supervisor of the doctoral thesis:

Prof. Dr. Peter Broekmann

Department of Chemistry, Biochemistry and Pharmaceutical Sciences

CO_2 Electroreduction on Silver Catalysts Under Controlled Mass Transport Conditions

Inaugural dissertation
of the Faculty of Science,
University of Bern

presented by

María de Jesús Gálvez-Vázquez
from Mexico

Supervisor of the doctoral thesis:
Prof. Dr. Peter Broekmann
Department of Chemistry, Biochemistry and Pharmaceutical Sciences

Accepted by the Faculty of Science

Bern, October 1st, 2021

The Dean
Prof. Dr. Zoltan Balogh

Abstract

The electrochemical reduction of carbon dioxide (CO_2RR) to value-added chemicals using excess intermittent electric power from renewable energy sources is considered a promising approach to mitigate global warming caused by anthropogenic CO_2 emissions.

The product selectivity of the CO_2RR can be controlled by the chemical nature and the morphology of the catalyst material. Among the various products of the CO_2RR, the production of carbon monoxide (CO) is highly desirable because it can be used as feedstock in the Fischer–Tropsch synthesis to produce higher long-chain hydrocarbons and alcohols. Silver is well known as a promising catalyst material for CO production.

Most of the screening experiments to test the activity, selectivity, and stability of an electrocatalyst have been carried out in H-type cell configurations using aqueous electrolytes. However, the low solubility of CO_2 in aqueous electrolytes under ambient conditions imposes severe mass transport limitations. This PhD thesis has addressed this challenge, by carrying out classical half-cell measurements in aqueous environments extended to a zero-gap gas-fed electrolyzer. The catalytic properties of two colloidal silver nanomaterials with different morphologies were studied (nanocubes and nanowires).

The electrocatalysts studied herein present high selectivity and activity towards CO formation, e.g., in the case of silver nanocubes, a partial current density of ~625 mA cm^{-2} and a faradaic efficiency of ~85% for CO were attained. Besides, it is particularly pointed out that the reaction environment plays an essential role in the product distribution of the reaction; formate is generated with higher selectivities and activities in a highly alkaline environment than in a weak one.

Furthermore, identical location scanning electron microscopy (IL-SEM) is herein demonstrated as a powerful technique to study the structural degradation of the electrocatalysts. By imaging the same spot on the catalyst before and after the CO_2RR, it is possible to directly visualize changes of the catalyst morphology on a nm-length scale attributed to the electrolysis reaction. Limitations of this analysis technique are discussed based on surfactant-protected nanocatalysts.

Additionally, a new electrochemical surfactant removal method based on potentiostatic CO_2RR electrolysis was developed to remove polyvinylpyrrolidone or PVP (the capping agent) from Ag nanowire and nanocube surfaces, resulting in a substantially improved selectivity towards CO formation.

Overall, the studies presented herein clearly demonstrate the importance of performing CO_2RR under more realistic conditions to bring this process closer to what is needed for the scale-up of this reaction, which means that high faradaic efficiencies, partial current densities, and long stability are pursued.

Table of Contents

List of figures

List of tables

List of abbreviations

AEM	Anion exchange membrane
Ag NCs	Silver nanocubes
Ag NWs	Silver nanowires
BPM	Bipolar membrane
BSD	Backscattered electron detector
CE	Counter electrode
CEM	Cation exchange membrane
CO_2RR	Electrochemical CO_2 reduction reaction
ec-l	Electrochemical looping
ECSA	Electrochemically active surface area
EDX	Energy dispersive X-ray analysis
FE_i or FE(i)	Faradaic efficiency or current efficiency of the product i
GC	Gas chromatography
GDE	Gas diffusion electrode
GDL	Gas diffusion layer
HER	Hydrogen evolution reaction
IEM	Ion exchange membrane
IL-SEM	Identical location scanning electron microscopy
InLens	InLens secondary electron detector
j	Current density
j_i or PCD_i	Partial current density of the product i
MEA	Membrane electrode assembly
MPL	Microporous layer
MPS	Macroporous substrate
n	Number of electrons
OER	Oxygen evolution reaction
PTFE	Polytetrafluoroethylene
PVP	Polyvinylpyrrolidone
Q	Charge
RE	Reference electrode
RHE	Reversible hydrogen electrode
SEM	Scanning electron microscopy
SHE	Standard hydrogen electrode
WE	Working electrode
XPS	X-ray photoelectron spectroscopy

1. Theoretical background

1.1 Climate system

Climate is a statistical description of the state of the climate system, and it is defined as the average condition of the weather over a long period of time. The Earth's climate system is complex and dynamic. Its components are the atmosphere, hydrosphere, cryosphere, terrestrial surface and biosphere (Figure 1.1). All are interactive, interrelated, and driven by the energy coming from the Sun.[1, 2]

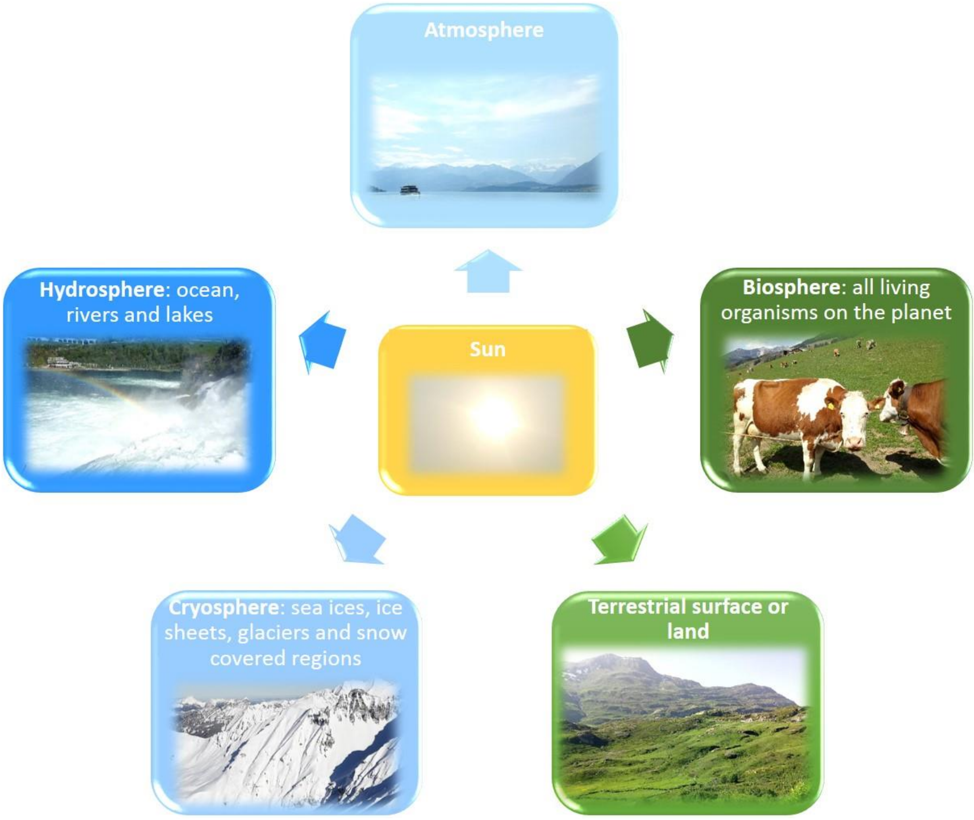

Figure 1.1. Components of the climate system.

To understand better how the climate system works, it is essential to know about the flow of solar energy into and out of the Earth, also defined as the Earth energy budget (Figure 1.2). The average solar radiation that reached the Earth per year is 342 W m^{-2} (energy delivered per unit time per unit area). About 22.5% (77 W m^{-2}) of that energy is reflected by clouds, aerosols, and the atmosphere, and 8.8 % (30 Wm^{-2}) is reflected by the white and bright surfaces of the Earth (like ice, snow and sand, which are also known as albedo). The Earth's surface absorbs 49.1% (168 W m^{-2}) and 19.6% (67 W m^{-2}) is absorbed by the atmosphere. The energy absorbed by the Earth's surface and atmosphere (235 W m^{-2}) should be radiated back into space to maintain an energy balance.

The radiation absorbed by the Earth's surface is transferred to the atmosphere through sensible heat (24 W m^{-2} are transferred in the form of heat from a warmed surface to the air), latent heat

(78 W m^{-2} are involved in the process of evaporation and condensation of water molecules) and thermal infrared radiation (66 W m^{-2}).

The atmosphere is composed mainly of 78.08% nitrogen, 20.95% oxygen, and 0.934% argon (volume percentage), and all of these gases are transparent to the incoming sunlight and the outgoing infrared radiation. If the atmosphere were composed only of these constituents, the energy emitted by the Earth (235 W m^{-2}) could leave it directly. However, the other gaseous components of the atmosphere, gases with a less than 0.05% concentration, absorb and re-emit infrared (IR) radiation. These gases are denoted as greenhouse gases.

The most important greenhouse gases are water vapor (H_2O), carbon dioxide (CO_2), methane (CH_4), nitrous oxide (N_2O), ozone (O_3), and chlorofluorocarbons (CFC). The two with the most significant effect are H_2O vapor and CO_2. Greenhouse gases absorb infrared radiation emitted by the Earth's surface, atmosphere and clouds, and then re-emit infrared radiation in all directions. Some of this energy can be back-radiated to the surface resulting in trapped heat that warms the Earth's surface. This cycle is known as the natural greenhouse effect and is responsible for raising the Earth's temperature to an average of 15 °C. Without the greenhouse effect, the temperature of the Earth would be around −18 °C.

Due to the greenhouse gases, 324 W m^{-2} are back-radiated to the Earth's surface, adding this amount of energy to the infrared radiation coming from the incoming solar energy (66 W m^{-2}), resulting in a total of 390 W m^{-2} emitted by the surface of the Earth. Of this amount, 235 W m^{-2} goes to space (40 W m^{-2} passes directly to space from the surface through the atmospheric infrared window, and 195 W m^{-2} are part of the upward infrared emission), and 155 Wm^{-2} are retained by the greenhouse gases, leaving a system in a steady-state.[1, 3-5]

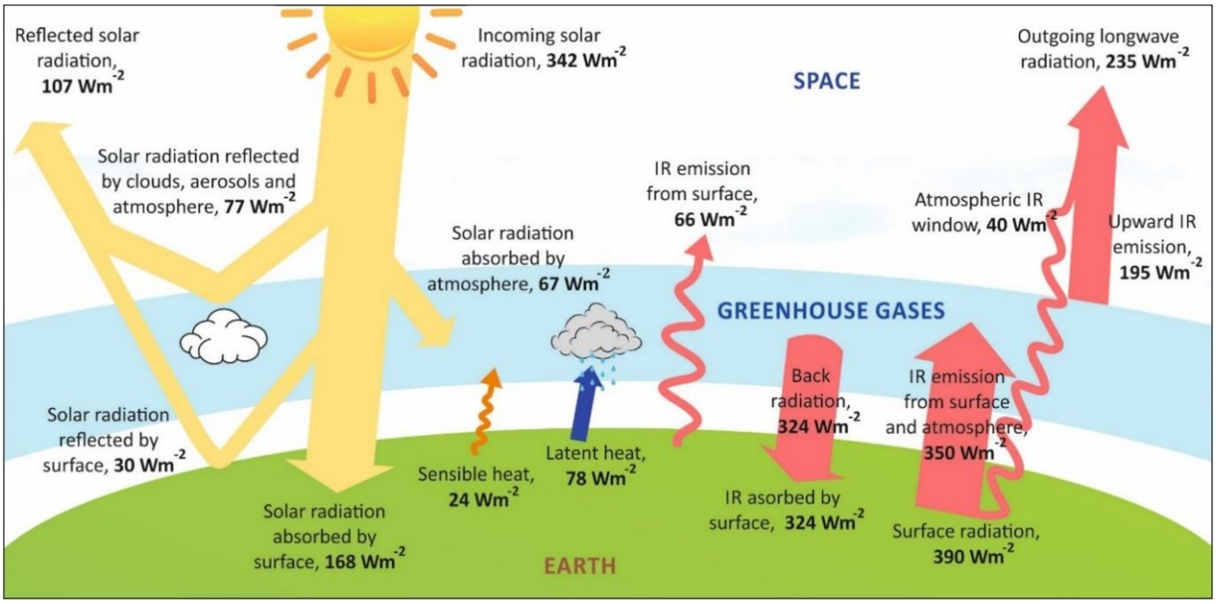

Figure 1.2. Energy budget of the Earth. Adapted from References 2–4.

1.1.1 Climate change

Any disturbance in the “steady-state” of the Earth’s energy budget that affects how much energy enters or leaves the system will produce climate change. Variations in the solar processes, changes in the Earth’s orbit, and large volumes of reflecting-light particles ejected in volcanic eruptions are examples of natural effects that can disturb the climate system.

Climate change has occurred naturally since the formation of the planet, and it typically happens over long time scales of thousands of years. However, anthropogenic activities like aerosol production, change in land use (caused by urbanization, deforestation, and agriculture), and the increase of greenhouse gas concentration (Table 1.1) have dominated and accelerated this process since the middle of the 19th century.

Even though water is the most abundant greenhouse gas, it is not considered in Table 1 because its atmospheric lifetime is short (in terms of days), and it can be removed from the atmosphere through the hydrologic cycle. However, the situation related to the increase of CO_2 in the atmosphere is different from that of water.[6, 7]

Table 1.1. Atmospheric concentration of greenhouse gases before 1750 and in 2018[2, 7]

Greenhouse gas	Atmospheric concentration before 1750, ppm	Atmospheric concentration in June 2018, ppm	Increase, %	Lifetime, years
CO_2	280	410	46	1-hundreds
CH_4	0.70	1.86	166	12
N_2O	0.27	0.33	22	114

1.1.2 Carbon cycle

Carbon dioxide is part of the planet’s carbon cycle, which describes its (natural) formation and consumption and, most importantly, how human activities affect this cycle (Figure 1.3). Carbon is the 17th most abundant element on the Earth’s crust,[8] and all living organisms contain carbon. The carbon in the Earth is contained in different reservoirs. The three largest ones are the deep ocean that contains about 37,100 gigatons of carbon (GtC), vegetation and soil that contain 2,300 GtC, and the atmosphere with 597 GtC.

Using photosynthesis, plants on land remove atmospheric CO_2 (fixation) and form part of their structures with it. When the plants die, they transport carbon back to the soil. Animals and microbes gain energy from the breakdown of organic carbon and respiration, releasing CO_2 back to the atmosphere (or CH_4 under anaerobic conditions).

At the ocean surface, CO_2 from the atmosphere dissolves in seawater (forming bicarbonate and carbonate ions), and marine phytoplankton use that CO_2 for photosynthesis. When animals consume the phytoplankton, they breathe out the carbon or pass it through the food chain. When the animals and plants die in the ocean, they decompose. Parts of their bodies can sink onto the ocean floor, forming sediments that consist of another reservoir of 150 GtC. Ocean currents bring carbon from the deep ocean up to the surface, where it can be released as a gas into the atmosphere. By recirculating vast amounts of carbon, the oceans help to regulate the climate.

The movement of carbon from the atmosphere to rocks starts when carbonic acid, resulting from the dissolution of CO_2 in raining water, dissolves the rock through chemical weathering that releases calcium, magnesium, potassium, and sodium ions that are transported by rivers to the ocean. Calcium ions react with carbonates dissolved in the water to produce calcium carbonate that is then deposited onto the ocean floor. Over time, layers of sediments and shells (from marine organisms like corals) are cemented together and turn to rock, storing carbon in stoles such as limestone and its derivatives. Volcanoes are also part of the carbon cycle because they release millions of metric tons of CO_2 during their eruptions.[9]

The continuous movement of carbon between the atmosphere, ocean, and land constitutes the natural carbon cycle. These processes occur at different rates going from short periods of time, like days or seasons, until very long periods that can take millions of years.[6, 10]

According to the analysis of ice cores in Antarctica, the concentration of carbon dioxide in the atmosphere has remained constant for thousands of years before the industrial revolution, at a value of 280 ± 10 ppm (Figure 1.4a). After 1750, the carbon cycle has been altered by the release of large amounts of CO_2 into the atmosphere originating from the burning of fossil fuels (coal, petroleum oil, and natural gas, which form another carbon reservoir of the Earth), cement manufacturing, deforestation and changes in land use.[1]

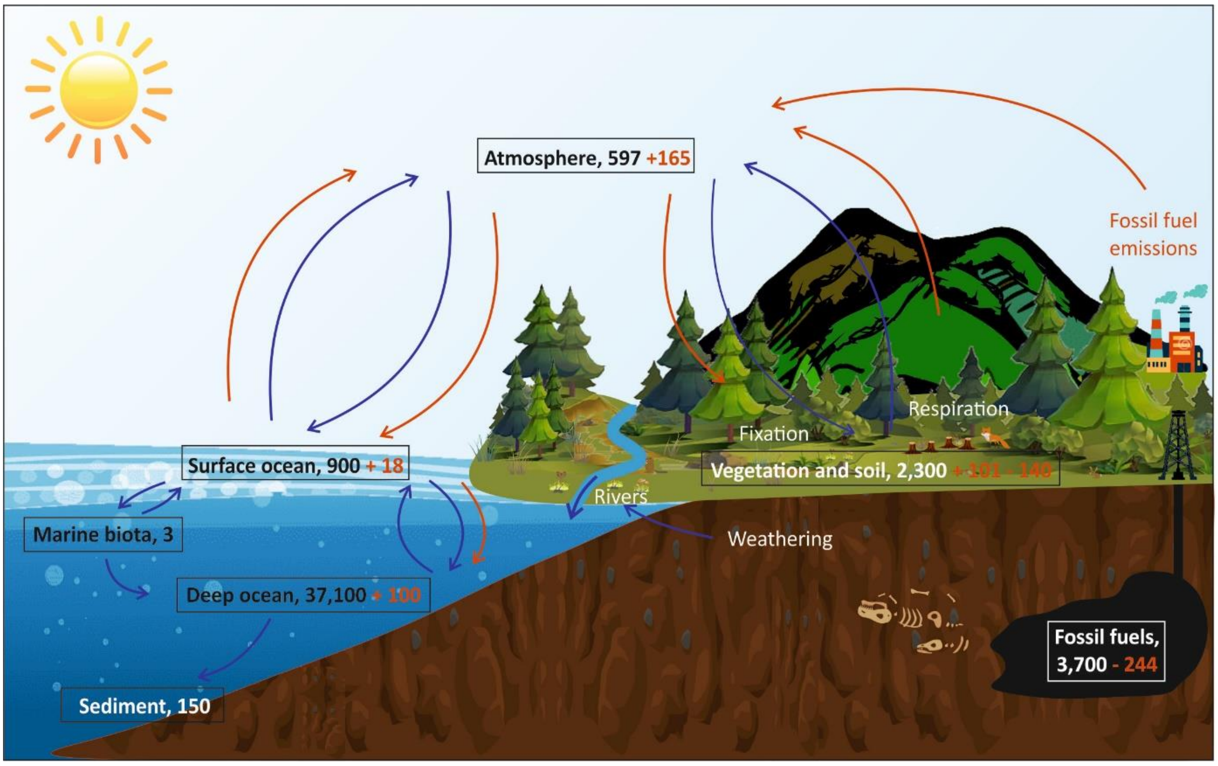

Figure 1.3. The carbon cycle showing reservoirs in GtC yr^{-1} (in black font, inside boxes) and changes caused by anthropogenic activities (red font), natural fluxes (blue arrows), and fluxes altered by human activities (red arrows). Adapted from References 2 and 6.

1.1.3 Keeling curve

In 1958, Charles David Keeling began to measure the CO_2 concentration in the atmosphere at the Mauna Loa Observatory, Hawaii, performing direct, accurate, and continuous quantification of CO_2 amount in dry air. Keeling's measurements of CO_2 concentration are presented in a plot known as the Keeling curve (Figure 1.4b).[11, 12]

Keeling's observations showed for the first time that the CO_2 concentration in the atmosphere is lower in the day than in the night because CO_2 is taken up by vegetation during the day. In the course of the night, CO_2 is released from the soil and by respiration.

Keeling also identified oscillations in the concentration of CO_2 in the atmosphere because of different seasons in the year. During spring and summer in the northern hemisphere, CO_2 levels decrease because of plants growing and photosynthesis. Throughout autumn and winter, CO_2 levels increase because carbon is released when the plants and trees lose their leaves. This process is known as the Earth's breathing cycle.[13, 14]

The greatest importance of the Keeling curve is that it was the first experimental proof that the CO_2 levels tend to increase every year as a result of anthropogenic activities. The atmospheric CO_2 increase as a fraction of the total anthropogenic CO_2 emissions is defined as the airborne fraction, and knowing this value is very important because an increase in the amount of CO_2 in the atmosphere means more heat is trapped, warming the Earth and, consequently, changing the climate system.

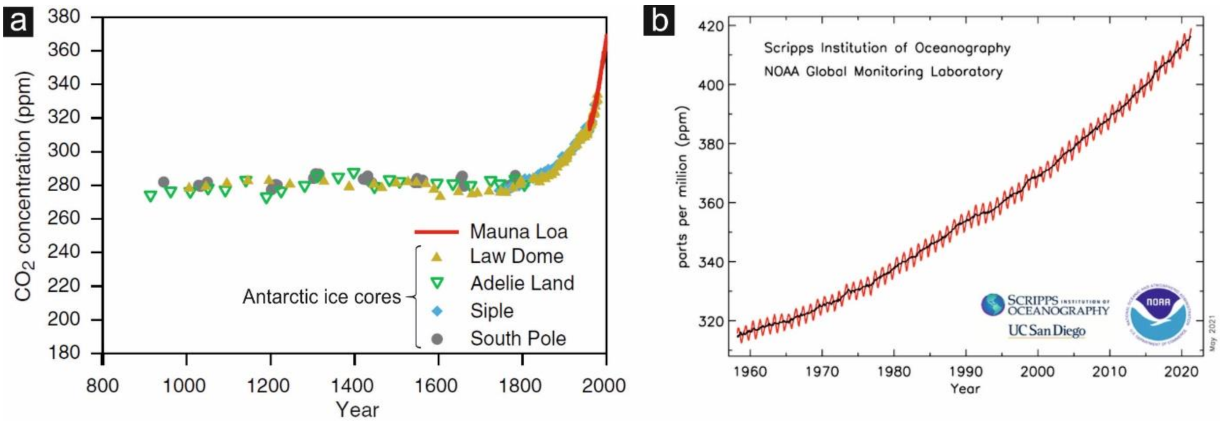

Figure 1.4. a) Atmospheric CO_2 concentration data from Antarctic ice cores analysis (adapted from Reference 1) and b) Keeling curve: atmospheric CO_2 concentration at the Mauna Loa Observatory.[11]

1.1.4 Further evidence for climate change

One of the consequences of the enhanced greenhouse effect is global warming, which consists of increasing the planet's average surface temperature (land and oceans) by almost 1 °C in the last 40 years (Figure 1.5a); 2016 and 2020 were the warmest registered years.[15] With the increase of the Earth's temperature, other consequences appear: snow cover and mountain glaciers are decreasing in area and thickness, the Arctic sea ice has declined over the last decades (Figure 1.5b)[16], the mass of ice sheets (in Greenland and Antarctica) is shrinking (Figure

1.5c)[17], and the melted water in the sea has increased. Therefore, the sea level has risen around 200 mm in the last century (Figure 1.5d).[18]

Other impacts of the Earth's temperature increase are that the oceans are removing atmospheric CO_2 less effectively because this gas is less soluble in warmer water. At the same time, oceans experience more acidification resulting from higher CO_2 concentrations in the atmosphere. As a consequence of a lower ocean pH, marine animals have reduced their ability to build skeletons and shells.[19, 20]

Extreme weather events such as heatwaves, droughts, changes in precipitation amounts, stronger hurricanes, and species extinction are also likely attributable to climate change.[2]

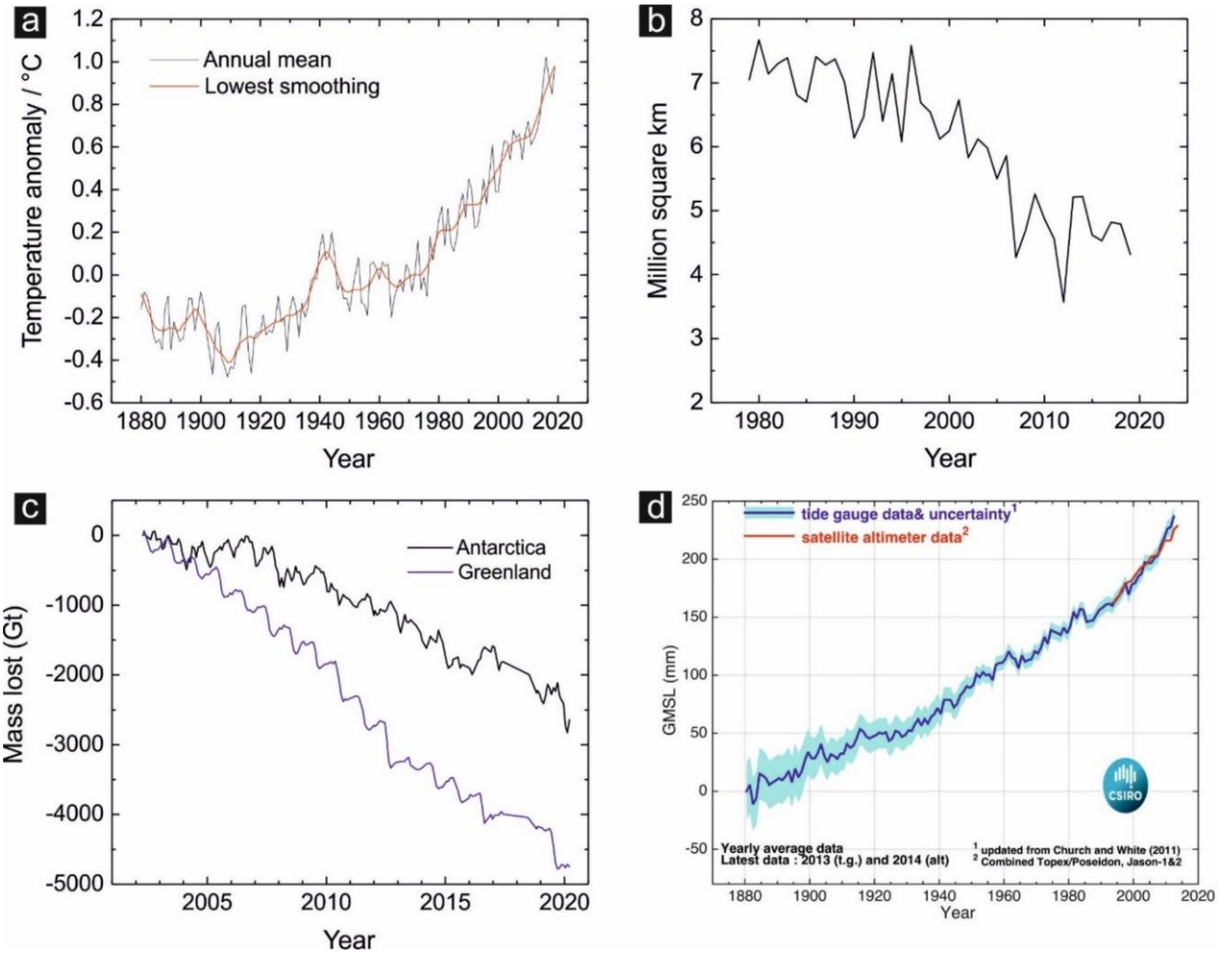

Figure 1.5. a) Temperature anomaly of the Earth (change in global surface temperature relative to 1951–1980 average temperatures).[15] b) Average monthly Arctic sea ice extent each September since 1979, derived from satellite observations.[16] c) Antarctica and Greenland mass variations since 2002, derived from satellite observations.[17] d) Global mean sea level (GMSL) from 1880 to 2014.[18]

1.1.5 International agreements on climate change

The United Nations and the World Meteorological Organization (WMO) created the Intergovernmental Panel on Climate Change (IPCC) in 1988 to prepare assessments reports (ARs) of the state of knowledge of human-induced climate change and its causes, impacts, and responses. Five assessment reports have been issued from 1990 to 2014.

The ARs are an invaluable resource for scientific information and improved understanding of climate change. The ARs play an essential role in the United Nations Framework Convention on Climate Change (UNFCCC) because they set the scientific input for diplomatic decisions.

The ultimate objective of the UNFCCC is the "'stabilization of greenhouse gas concentrations in the atmosphere at a level that would prevent dangerous anthropogenic interference with the climate system" through the provisions of the Kyoto protocol (which commits 192 Parties to reduce their anthropogenic greenhouse gas emissions: CO_2, CH_4, N_2O, hydrofluorocarbons, perfluorocarbons, and sulfur hexafluoride) and the Paris Agreement (adopted by 196 member countries that commit to hold the increase of global average temperature to well below 2 °C above pre-industrial levels and pursue efforts to limit it to 1.5 °C).[5, 19, 21]

1.2 Strategies for reducing CO_2 emissions

Given the problems caused by high CO_2 emissions, the scientific community has conducted intensive research on different approaches to tackle this problem.

In the early 2000s, some strategies were proposed to keep CO_2 emissions stable and eventually reduce them. These actions involve the increase of the energy efficiency of vehicles and their reduced use; insulation of buildings (so they will require less heating or air conditioning); fuel shift from coal to gas or oil (because coal emits 1 kg CO_2 per kWh of electric energy generated while oil and gas produce 0.75 kg and 0.5 kg, respectively); capturing CO_2 from industrial powered plants and its storage (CO_2 capture and storage); increasing use of renewable energy sources such as wind, solar, hydro and geothermal, nuclear and biofuels in the electricity grid and transportation sector; reducing deforestation; reforestation and conservation tillage.[22 23]

1.2.1 CO_2 conversion and utilization

Carbon dioxide is used as a feedstock in various industrially important chemical reactions, such as the synthesis of urea, salicylic acid (precursor of aspirin), carboxylic acids, organic carbamates, pigments, inorganic and organic carbonates, formic acid or used as an additive in the synthesis of methanol.[24-26]

Different approaches for CO_2 conversion and utilization include technological utilization (physical process), enzymatic conversion (biological/biochemical process), and chemical/catalytic conversion (chemical process).[27, 28]

Technological utilization refers to changing the physical nature or state of CO_2. It includes compressing, recycling, or phase transition. It is important because, in this way, CO_2 can be used directly in many applications, for example, in the production of carbonated beverages, dry ice, and fire extinguishers. CO_2 can be applied as a solvent (e.g., in organic and polymerization reactions and for the extraction of caffeine and fragrances), a refrigerant (for food preservation and controlling reactors temperatures), an inert agent, a process fluid, and a welding medium. Additionally, CO_2 is used in large-scale industries to indirectly boost a process as in the enhanced fuel recovery and enhanced geothermal systems (EGS). In the previous applications, CO_2 is not converted and can be recovered at the end of the application or released to the atmosphere. Therefore, these applications are not suited to reducing CO_2 content in the atmosphere.[23, 24, 28, 29]

Enzymatic conversion of CO_2 involves using enzymes or microorganisms to convert CO_2 into other chemicals through bioreactions. One advantage of this process is that it usually occurs at low temperature and pressure; however, it is generally a slow process. The most critical strategy to bioconversion technologies is to find enzymes or microorganisms to convert CO_2 into the desired product with high selectivity, yield, and a fast conversion rate.[30, 31] One example is the Rheticus project that aims to convert carbon monoxide and hydrogen (produced using electrochemical reduction of CO_2) into alcohols by fermentation utilizing two different species of *Clostridium* bacteria.[30]

Chemical conversion of CO_2 comprises thermochemical, mineralization, photochemical, electrochemical, and photoelectrochemical approaches.[9, 27]

1.3 Electrochemical reduction of CO_2

The industry uses approximately 120 Mt CO_2 per year, excluding the use for enhanced oil recovery. However, this amount of CO_2 represents only 0.5% of the total anthropogenic CO_2 emissions, or about 24 Gt CO_2 annually.[26] Therefore, converting carbon dioxide into useful chemicals is a very attractive route that not only considers CO_2 as a new source of fuels and raw materials but also represents a method to mitigate the effects of rising atmospheric CO_2 concentration.[32]

Of the different CO_2 conversion approaches, of particular interest is the electrochemical CO_2 reduction reaction (denoted as CO_2RR hereinafter). This approach uses the surplus of renewable electric power from solar, wind, and hydro sources to convert CO_2 into value-added chemical feedstocks. This concept is also known as “Power to X” because it evolves around converting power (electricity) to chemicals (X), as shown in Figure 1.6.[33] This approach allows CO_2 to be seen as a valuable raw material instead of an environmentally dangerous waste and may also provide a solution for the storage of excess renewable (hydro-, solar or wind) energy.[34, 35]

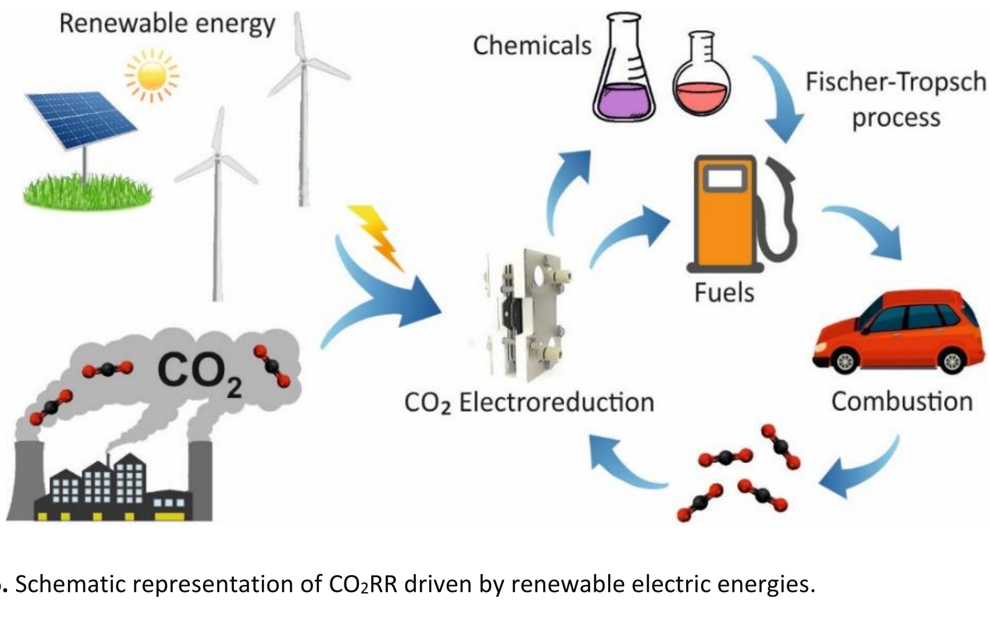

Figure 1.6. Schematic representation of CO_2RR driven by renewable electric energies.

The research conducted for this PhD project focuses on the half-reaction that involves CO_2RR. The catalytic properties, in terms of CO_2RR activity, product selectivity, and catalyst durability, of two different kinds of silver-based nanomaterial were studied using two different types of electrochemical cell configurations. In the following sections, the most relevant aspects required to discuss the main results of this project are presented.

1.3.1 Chemical and physical properties of CO_2

Carbon dioxide is a triatomic molecule with two oxygen atoms, each covalently double bonded to a single carbon atom. It has a linear structure in which each C and O bond has a length of 116.3 pm. The bond energy of C=O in CO_2 is 803 kJ mol^{-1}, which is much higher than the oxygen and hydrogen bond in water molecules (463 kJ mol^{-1}). This molecule has two σ bonds and two π bonds (orthogonal to one another). The carbon-oxygen bonds are polarized due to the higher electronegativity of O compared to C, such that the C atom has a partial positive charge, and the O atoms have a partial negative charge.

CO_2 is a symmetrical molecule with one inversion center, a circular axial symmetry, and one horizontal plane of symmetry. The combination of high bond energy and symmetry and low polarity are the main reasons for the high stability of the CO_2 molecule. Another feature is that CO_2 can coordinate with metals, and this coordination modifies the electron distribution and molecular geometry, which results in changes in its chemical reactivity.

CO_2 is the ultimate product of the oxidation of carbon and hydrocarbons. It has high thermodynamic stability as illustrated by its standard Gibbs free energy of formation, ΔG_f^θ, equal to −394.4 kJ mol^{-1} (the superscript θ refers to standard conditions of temperature and pressure, 298.15 K and 10^5 Pa or 1 bar, respectively). This means that CO_2 conversion is highly endergonic from a thermodynamic point of view.[27, 36]

1.3.2 Thermodynamic considerations

Electrochemistry is the branch of chemical sciences that deals with electrical and chemical phenomena and studies two kinds of processes: galvanic and electrolytic. A galvanic reaction is a spontaneous process that involves the generation of electric energy utilizing chemical transformations. A non-spontaneous transformation of a chemical compound is achieved in an electrolytic process by applying an electric potential or passing an electric current through the electrolysis cell. CO_2RR is one example of this type of a “forced” electrolysis processes.[37]

An electrochemical cell is a device where an electrochemical reaction occurs. A complete electrochemical reaction consists of two independent half-reactions: an oxidizing reaction (loss of one or more electrons by an atom, molecule or ion) and a reduction reaction (gain of one or more electrons by an atom, molecule or ion). Each of the two half-reactions happens simultaneously at separate parts of an electrochemical cell, called a half-cell. Each half-cell comprises an electrode (electron conductor named anode or cathode) in contact with an electrolyte (an ionic conductor). The electrode at which oxidation occurs is called the anode, and the electrode at which reduction occurs is called the cathode.

The electrodes in an electrochemical cell may need to be placed in different electrolytes. Then, an electrolytic conductor, such as an ion-exchange membrane or a salt-bridge, is employed to ensure electrical contact between them. A conducting polymer or a solid electrolyte might be used in an electrochemical cell instead of a liquid electrolyte.

Each half-reaction has a specific standard reduction potential, which is reported as the potential difference of the reduction reaction with respect to the standard hydrogen electrode (SHE) (under standard conditions, 298.15 K, 1 bar and a hydrogen ion activity of 1).[38] In practice, experimental results are stated as being obtained vs. a specific reference electrode (RE) or converted to potentials vs. SHE. Silver/silver chloride electrode (Ag/AgCl) and mercury/mercurous sulfate (Hg/Hg_2SO_4) are examples of commonly used REs.

Most of the time, only one of the half-reactions in an electrochemical cell is of particular interest, and the electrode at which it occurs is called the working electrode (WE). The other one is referred to as the counter electrode (CE). Within the study of the electrochemical reduction of CO_2, the WE is the cathode because the reduction process takes place at the surface of this electrode. The oxidation reaction that occurs on the CE surface when an aqueous electrolyte is used is typically the oxygen evolution reaction (OER).[39-41]

Depending on the electrode material, electrolyte, temperature, or pressure, CO_2RR can generate more than 16 different products.[42, 43] Table 2 provides a list of some of the half-reactions related to CO_2RR, the number of required electrons (n), and their standard potentials.

The electrode potential of the half-reactions in an electrochemical cell can be combined to calculate the cell potential (ΔE):

$$\Delta E = E_{cathode} - E_{anode} \tag{1}$$

The maximum amount of electrical work obtainable from a reversible reaction produced in an electrochemical cell is defined by the Gibbs free energy change (ΔG) through Equation (2):

$$\Delta G = -nF\Delta E \tag{2}$$

where n is the number of electrons involved in the reaction, F is the Faraday's constant (electric charge per mol of electrons, 96485.33 C mol^{-1}), and ΔE is the cell potential. The importance of Equation 2 is that it indicates the quantitative relationship between the chemical and electrical energy in cell reactions.

As the reaction Gibbs energy is related to the composition of the reaction mixture by Equation 3,

$$\Delta G = \Delta G^{\theta} + RT \ln Q_r \tag{3}$$

where ΔG^{θ} is the standard reaction Gibbs free energy, R is the universal gas constant, and Q_r is the reaction quotient $\left(\prod_J a_J^{\nu_J}\right)$, then the cell potential (ΔE) can be rewritten as:

$$\Delta E = -\frac{\Delta G^{\theta}}{nF} - \frac{RT}{nF}\ln Q_r = \Delta E^{\theta} - \frac{RT}{nF}\ln Q_r, \tag{4}$$

Equation 4 is known as the Nernst equation, and ΔE^{θ} is denoted as the standard cell potential. [39-41]

An electrochemical reaction will not be spontaneous if ΔE is negative. However, with Equation (2) and knowing that $\Delta G = \Delta H(T) - T\,\Delta S(T)$ (where ΔH is the enthalpy change, T the temperature, and ΔS the entropy change), it is possible to calculate the minimum potential that an electrochemical reaction requires to start to proceed forward using Equation (5).[44] In Table 1.3, ΔE values at standard conditions are given for several CO_2 reactions.

$$\Delta E = -\frac{\Delta H(T) - T\,\Delta S(T)}{nF}, \tag{5}$$

Table 1.2 Reduction potential of possible CO_2RR products and of the anode reaction[43, 45]

Product	Half-cell reaction	n	Standard potential vs. SHE, V	Reduction potential vs. Ag/AgCl†, V
Formic acid	$CO_2 + 2H^+ + 2e^- \rightarrow HCOOH$	2	−0.25	−0.46
Formate	$CO_2 + H_2O + 2e^- \rightarrow HCOO^- + OH^-$	2	−1.078	−1.288
Carbon monoxide	$CO_2 + 2H^+ + 2e^- \rightarrow CO + H_2O$	2	−0.106	−0.316
	$CO_2 + H_2O + 2e^- \rightarrow CO + 2OH^-$	2	−0.934	−1.144
Oxalic acid	$2CO_2 + 2H^+ + 2e^- \rightarrow H_2C_2O_4$	2	−0.500	−0.71
Oxalate	$2CO_2 + 2e^- \rightarrow C_2O_4^{2-}$	2	−0.590	−0.8
Formaldehyde	$CO_2 + 4H^+ + 4e^- \rightarrow CH_2O + H_2O$	4	−0.070	−0.28
	$CO_2 + 3H_2O + 4e^- \rightarrow CH_2O + 4OH^-$	4	−0.898	−1.108
Methanol	$CO_2 + 6H^+ + 6e^- \rightarrow CH_3OH + H_2O$	6	−0.016	−0.226
	$CO_2 + 5H_2O + 6e^- \rightarrow CH_3OH + 6OH^-$	6	−0.812	−1.022
Methane	$CO_2 + 8H^+ + 8e^- \rightarrow CH_4 + 2H_2O$	8	0.169	−0.041
	$CO_2 + 6H_2O + 8e^- \rightarrow CH_4 + 8OH^-$	8	−0.659	−0.869
Ethylene	$2CO_2 + 12H^+ + 12e^- \rightarrow C_2H_4 + 4H_2O$	12	0.064	−0.146
	$2CO_2 + 8H_2O + 12e^- \rightarrow C_2H_4 + 12OH^-$	12	−0.764	−0.974
Ethanol	$2CO_2 + 12H^+ + 12e^- \rightarrow C_2H_5OH + 3H_2O$	12	0.084	−0.126
	$2CO_2 + 9H_2O + 12e^- \rightarrow C_2H_5OH + 12OH^-$	12	−0.744	−0.954
CO_2 anion radical	$CO_2 + e^- \rightarrow CO_2^{\cdot-}$	1	−1.90	−2.11
Hydrogen	$2H^+ + 2e^- \rightarrow H_2$	2	0.0	−0.21
Oxygen (anode reaction)	$2H_2O \rightarrow O_2 + 4H^+ + 4e^-$	4	1.23	1.02

† For the sake of comparability of the results, the standard reduction potentials were converted to the Ag/AgCl (3M KCl) reference electrode scale, considering that the electrode potential of the reference electrode used is 0.210 V vs. SHE.

The conversion of CO_2 to several products is an endergonic process at standard conditions ($\Delta G^\theta > 0$), which means that it will require a certain amount of energy to proceed depending on the target product.[27] Moreover, ΔE in Table 3 are negative values, and this further confirms that CO_2RR is a non-spontaneous process (independently of the generated product); a cell potential must be applied to proceed forward.

Table 1.3 Cell reactions and corresponding Gibbs free energy, enthalpy, entropy and cell potential values of some CO_2 conversions processes (considering OER as the counter-reaction) at standard conditions[34, 46, 47]

Product (cathode)	Overall reaction	ΔG^θ, kJ mol^{-1}	ΔH^θ, kJ mol^{-1}	ΔS^θ, J mol^{-1} K^{-1}	ΔE, V
Hydrogen	$H_2O \leftrightarrows H_2 + ½O_2$	237.3	286	163.30	−1.23
Carbon monoxide	$CO_2 \leftrightarrows CO + ½O_2$	257.2	283.1	86.55	−1.33
Formic acid	$CO_2 + H_2O \leftrightarrows HCOOH + ½O_2$	285.5	270.3	−52.15	−1.48
Formaldehyde	$CO_2 + H_2O \leftrightarrows HCHO + O_2$	522	563	140.25	−1.35
Methanol	$CO_2 + 2H_2O \leftrightarrows CH_3OH + 1.5O_2$	703	727	80.85	−1.21
Ethanol	$2CO_2 + 3H_2O \leftrightarrows C_2H_5OH + 3O_2$	1325.56	1366.90	138.75	−1.14
Methane	$CO_2 + 2H_2O \leftrightarrows CH_4 + 2O_2$	818.4	890.8	242.90	−1.06
Ethane	$2CO_2 + 3H_2O \leftrightarrows C_2H_6 + 3.5O_2$	1468.18	1560.51	309.80	−1.09
Ethylene	$2CO_2 + 2H_2O \leftrightarrows C_2H_4 + 3O_2$	1331.2	1411.2	267.30	−1.15
Propanol	$3CO_2 + 4H_2O \leftrightarrows C_3H_7OH + 4.5O_2$	1962.94	2021.24	195.65	−1.13

1.3.3 Kinetics of CO_2RR

Experimentally, higher cell potentials than the thermodynamic minimum must be applied to accelerate the reaction. Considering the thermodynamic standard potential alone does not allow a conclusion about the potentials that must be applied to obtain a reasonable current density or reaction rate. Thermodynamics deals only with the equilibrium and related potential differences, whereas kinetics starts when the system abandons the equilibrium, and a certain current density is attained.

In CO_2RR, the energy barriers or resistances (R_{total}, Equation 6) that must be overcome include activation energies of the electrochemical reactions occurring on the surfaces of the cathode ($R_{cathode}$) and anode (R_{anode}), ohmic losses from conduction of ions (R_{ions}) in the bulk electrolytes, ion transport across the membrane ($R_{membrane}$), loss of active area due to partial coverage by gas bubbles formed on the cathode and anode surfaces ($R_{bubble,\ cathode}$ and $R_{bubble,\ anode}$, respectively) and the sum (R) of electrical resistances in other cell components and contact resistances between components.[48, 49]

$$R_{total} = R_{cathode} + R_{anode} + R_{ions} + R_{membrane} + R_{bubble,\ cathode} + R_{bubble,\ anode} + R \tag{6}$$

The difference between the thermodynamic potential needed for a half-reaction to occur and the applied potential that is needed for the reaction to occur experimentally is referred to as the overpotential ($\eta_{cathode}$ or η_{anode} for the different electrode half-reaction, respectively).[50]

Under mild experimental conditions, this means when gas bubble formation and concentration differences can be neglected, the cell potential (ΔE) of a CO_2RR process can be expressed as:

$$\Delta E = \Delta E^0_{cell} + \eta_{cathode} + \eta_{anode} + iR_{ohmic} \quad (7)$$

where ΔE^0_{cell} is the equilibrium cell potential, and the term iR_{ohmic} represents voltage losses caused by the finite ionic conductivity of the electrolyte solution, the form of the electrodes, and the cell design.[34, 49]

The object of study of electrode kinetics involves determining the dependence of the current ($\rightarrow$ scales with the reaction rate) on the applied potential. As outlined above, an overpotential must be applied for a non-spontaneous electrochemical reaction to occur. This overpotential is defined as the difference between the applied potential and the equilibrium potential of a specific electrode reaction (this is when no current flows).[51, 52] Large overpotentials and low selectivity at industrially relevant current densities are the main kinetic obstacles for the CO_2RR.[53]

The total reaction rate or current density depends on the kinetics of the system (charge transfer) and on mass transport, and those aspects must be treated separately. The slowest process will be the rate-determining step. At low reaction rates, the rate-determining step is the charge transfer (electron transfer), and at higher reaction rates, mass transport is the rate-determining step.

CO_2RR kinetics is influenced mainly by the concentration of reactants and by the use of electrocatalysts. The most important aspects of CO_2RR kinetics relevant to this PhD project will be reviewed in the following sections.

1.3.3.1 Electrocatalysts for the CO_2RR

The activation barrier associated with CO_2RR is high. One method of decreasing this activation barrier and reduce the applied overpotential (to achieve a certain current density) involves the use of electrocatalysts (Figure 1.7).[54]

The function of an electrocatalyst in an electrochemical reaction is to provide alternative pathways with a lower energy of activation and hence to permit such electrode reactions to occur at high current density close to the equilibrium potential, in other words, accelerating the target reaction.[36, 55] For example, in the electrochemical reduction of CO_2 to produce CO, HCOOH, or $HCOO^-$ (a two e^- process), the rate-determining step is the formation of the radical anion $CO_2^{\cdot-}$, which has a standard potential of −1.9 V vs. SHE. This step significantly increases the energy requirement. Figure 1.7 shows a qualitative reaction scheme for CO_2 conversion to CO with and without a catalyst. It is evident that the activation energy to form the $CO_2^{\cdot-}$

intermediate without a catalyst is too high. Electrocatalysts and electrolytes acting as co-catalyst can decrease the activation energy of the intermediate $CO_2^{\cdot-}$.[56]

One major goal of applied electrocatalysis research is the development of electrode materials that are selective, active, inexpensive, and stable towards the production of desired products.[57]

To determine the catalytic activity of different electrocatalysts, one can compare the current density at a constant overpotential or measure the overpotential at a constant current density. A more active electrocatalyst shows a given partial current density at a lower overpotential or provides a larger partial current density at a given overpotential.[57]

During the electrochemical conversion process, the provided overpotential is relatively high to activate carbon-oxygen bonds in CO_2 molecules, thus improving the rate constant of the electrode reaction, which increases the faradaic current. The most direct indication for the electrocatalytic effect is the shift of the electrode reaction to lower overpotentials at a given current density.[27, 61]

Hydrogen evolution reaction (HER) occurs at similar potentials than the CO_2RR. Therefore, if aqueous electrolytes are used, the parasitic HER tends to compete with CO_2RR for catalytic sites. The adsorbed *H intermediate is more stable than adsorbed *CO or *COOH intermediates, making the HER dominant at more negative potentials.[56, 58, 59]

An effective electrocatalyst for CO_2RR needs to have different active sites for CO_2RR and HER, and it should be sluggish toward HER while exhibiting a low overpotential for CO_2RR.[60]

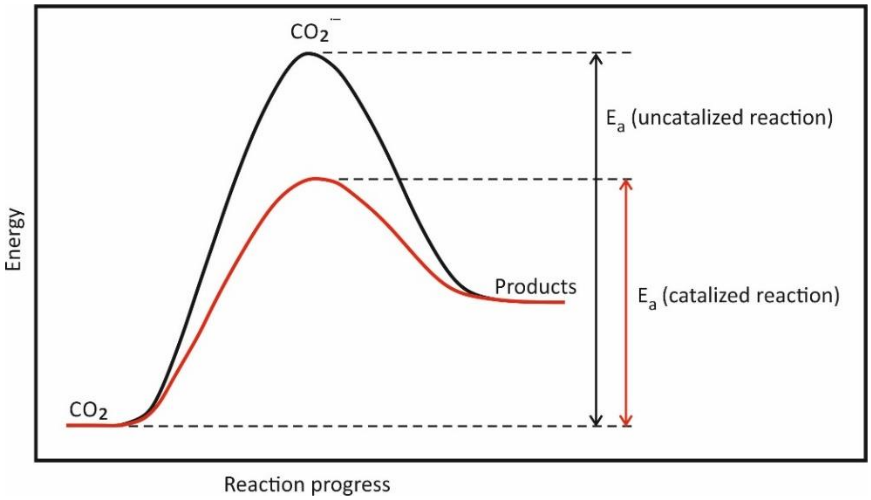

Figure 1.7. Schematic reaction pathway energy diagram for CO_2RR showing energy profiles in the absence and presence of an electrocatalyst represented by the black and red lines, respectively. The activation energy of the reaction (E_a) is decreased when a catalyst is used.

1.3.3.2 Performance metrics of CO_2RR

The performance of a CO_2RR catalyst and the complete process can be described with the following figures of merit:

1. Cathode potential ($E_{cathode}$ in V vs. RE) scales with the energy required to carry out the CO_2 electroreduction reaction at the cathode.

2. Cathode overpotential ($\eta_{cathode}$ in V) indicates the difference between the cathode potential ($E_{cathode}$) at which the reaction is experimentally observed and the thermodynamic minimum cathode reduction potential ($E^0_{cathode}$, assuming that the CO_2RR experiments were conducted under standard conditions):

$$\eta_{cathode} = E_{cathode} - E^0_{cathode} \tag{8}$$

3. Faradaic efficiency or current efficiency (FE_i in %) is a measure of the selectivity of the CO_2RR towards a product i. It is defined by the ratio of the amount of charge used to form a product calculated from Faraday's law to the total charge supplied:

$$FE_i = \frac{nm_iF}{Q} \times 100 \tag{9}$$

   where n represents the number of electrons exchanged to form the product i, m_i is the number of moles of the product i, F is the Faraday's constant, and Q is the amount of charge passed. The sum of FEs of all products of CO_2RR should be close to 100%. If this is not the case, other non-identified faradaic processes are occurring (e.g., reduction of surface oxides), or there are leaks in the electrolyzer.[62, 63]

4. Current density (j in mA cm^{-2}) represents the electrochemical reaction rate at a specific applied potential. It is obtained by normalizing the total electric current with the surface area of the electrode. In some cases, the total electric current is normalized according to the electrochemically active surface area (ECSA).

5. Partial current density (j_i or PCD_i in mA cm^{-2}) is the activity of CO_2RR to the formation of the product i (if it is normalized to the ECSA). It is calculated as follows:

$$j_i = j \times FE_i \tag{10}$$

6. Catalyst durability or stability (in hours) denotes the durability of the catalyst under investigation, or it expresses for how long the catalyst is active.

7. Cell potential (ΔE in V) denotes the potential difference required to drive the reduction of CO_2 at the cathode and the oxygen evolution at the anode (if the reaction is performed in an aqueous electrolyte). It is defined by the Equation (11):

$$\Delta E = E_{cathode} - E_{anode} \tag{11}$$

8. Cell overpotential (η_{cell} in V) points out the difference between the value of the cell potential experimentally observed (ΔE) and the equilibrium cell potential (ΔE^0_{cell}, at standard conditions). It is defined by:

$$\eta_{cell} = \Delta E_{cell} - \Delta E^0_{cell} \tag{12}$$

9. Energetic or energy efficiency for the product i (EE_i in %) is a measure of the net energy consumption toward a specific product. It is expressed by Equation (13) as a ratio of the amount of energy used to produce a specific product to the net electric energy supplied

to the system, assuming that the CO_2RR experiments were conducted under standard conditions.

$$EE_i = \frac{\Delta E^0_{cell} \times FE_i}{\Delta E_{cell}} = \frac{\Delta E^0_{cell} \times FE_i}{\Delta E^0_{cell} + \eta_{cell}} \tag{13}$$

When the experiments are conducted at nonstandard conditions (pressure, temperature, and activity), the equilibrium potential is estimated based on the Nernst equation (Equation 4). That value should be used in Equations (8), (12), and (13). [56, 64]

It is important to mention that the figures of merit described in the points list 1–6 are essential to describe the metrics of the interested half-reaction, the electrochemical reduction of CO_2. The figures of merit 7–9 are used to analyze the complete cell reaction, which is out of scope in this project.

1.3.3.3 Classification of electrocatalysts for the CO_2RR

In the 1980s and 1990s, Hori and co-workers at Chiba University in Japan screened different metals for CO_2RR. They classified them according to their selectivity towards different products when a $KHCO_3$ solution was used as the electrolyte, and four groups were identified (Figure 1.8). The first group includes Pb, Hg, In, Sn, Cd, Tl, and Bi; they hardly bind the $CO_2^{\cdot-}$ intermediate and therefore transform CO_2 to formate or formic acid. The second group includes Au, Ag, Zn, Pd, and Ga; they can bind the $CO_2^{\cdot-}$ intermediate and form CO as the main CO_2RR product. Cu is the only catalyst in the third group, and it produces hydrocarbons and oxygenates. The fourth group includes Ni, Fe, Pt, and Ti; these metals have strong CO adsorption properties; consequently, they might become poisoned by adsorbed CO, and in this way, H_2 is the major generated product.[65-68]

Although CO_2RR was first described by the pioneering work of Royer in 1870,[35, 69] more than 150 years ago, the research performed by Hori and his colleagues represented the starting point of intensive investigations by several research groups that have focused on the design and development of CO_2RR catalysts with better activity, selectivity, and stability towards different products.[70]

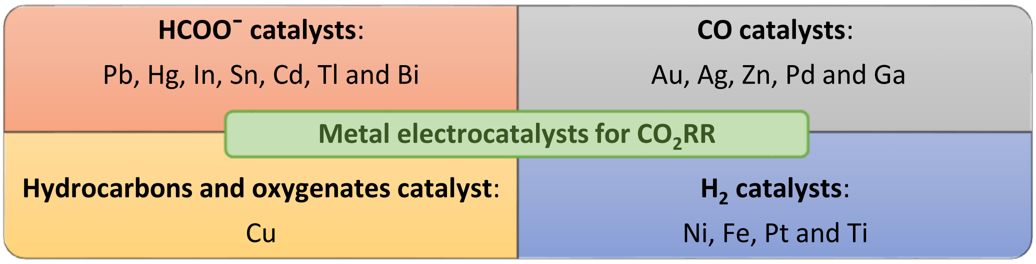

Figure 1.8. Classification of metal electrocatalysts for CO_2RR according to Hori et al. Adapted from References 65 and 67.

Hori's classification of metal electrocatalysts for CO_2RR is meant only for monometallic catalysts. Today, other types of catalysts have been developed that do not fit in that classification scheme. Consequently, Larrazábal et al.[71] proposed an extended classification of the different catalyst materials for CO_2RR that consists of six families of materials (Figure 1.9): transition metals, p-block metals/oxides, chalcogenides, carbon-based materials, and molecular catalysts and enzymes.[72-75]

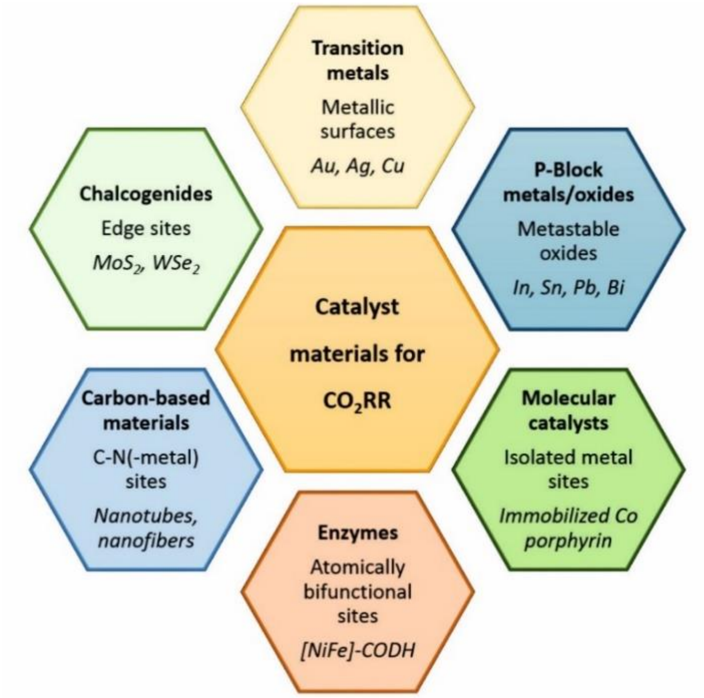

Figure 1.9. a) Classification of catalyst materials for CO_2RR (in bold), kind of active sites and some examples (in italic). Adapted from Reference 71.

At the same time, the electrocatalysts for CO_2RR can be non-supported or supported. The non-supported electrocatalysts work as the WE itself (e.g., metal foils). The supported ones need to be deposited on a carbon substrate, such as glassy carbon or carbon fibers that work as the WE. Metal nanoparticles, like the silver-based nanoparticles used in this project, are examples of supported electrocatalysts.

1.3.3.4 Sabatier principle and volcano plots

According to the Sabatier principle, a good catalyst should bind the reaction intermediates sufficiently strongly to activate the reactants but weakly enough to allow for the easy release of the product. If the binding between the catalyst and the reactants is not strong enough, no interaction will occur. If the binding is too strong, the reaction intermediates or the products will tend to stick to the active sites, thereby irreversibly poisoning the catalyst.

This fundamental principle in catalysis can be expressed in the form of a so-called "volcano" plot correlating the activity of a catalyst material (measured quantity) with one or more key kinetic descriptors of the system of interest (often derived from modeling/theory).

These volcano plots rationalize variations in the activity (or selectivity) for a series of catalyst materials.[52, 76, 77] This is exemplified in Figure 1.10a for various monometallic CO_2RR catalysts relating the partial current density ($\rightarrow$ selectivity towards CO_2RR) for a constant electrolysis potential to the binding strength of chemisorbed CO (denoted *CO), which is considered as the key CO_2RR intermediate, at least for those CO_2RR pathways proceeding via a metal-carbon bonding. Catalysts found on the right side of the volcano maximum (e.g., Au, Ag, and Ag → weak *CO binding) demonstrate a facile CO(g) desorption, thus rationalizing why CO is the main CO_2RR product in these cases. Catalyst materials located on the left side of the volcano maximum (e.g., Pt, Ni → extremely strong *CO binding) tend to become poisoned by the formed CO intermediate, thus resulting into a catalyst degradation. Only Cu demonstrates a metal-CO binding that is sufficiently low to prevent such poisoning but high enough to allow for further consecutive reactions of the *CO intermediate as a mechanistic prerequisite for the production of hydrocarbons or oxygenates. Such right balance in the metal-CO binding might even allow for C-C coupling reactions on the Cu, which is particularly appealing when liquid CO_2RR products of high energy density are targeted (e.g., ethanol, n-propanol).[57, 78, 79]

A volcano plot that shows similar trends can be derived when the binding strength of the *COOH intermediate is considered as a descriptor for the CO_2RR and related to the experimentally derived partial current densities towards CO (Figure 1.10b).[80]

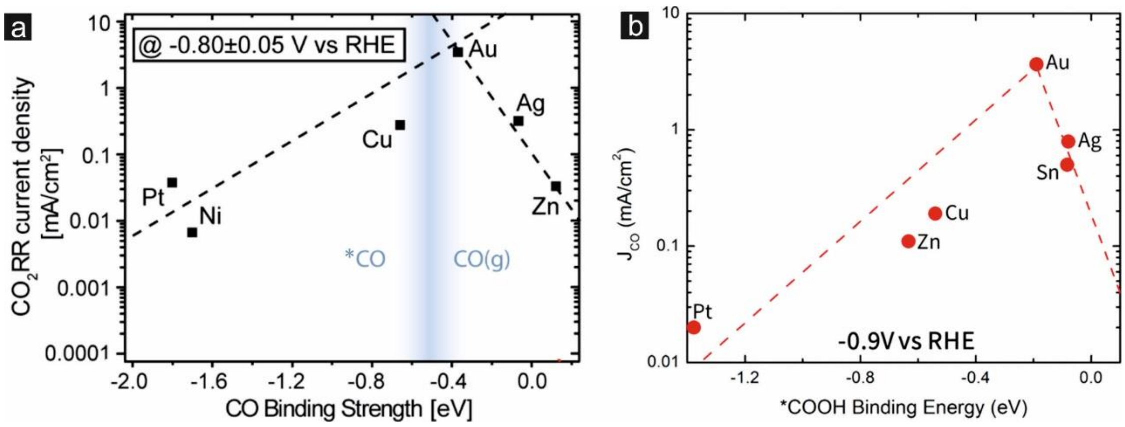

Figure 1.10. a) Volcano plot of CO_2RR partial current density at −0.8 V vs. RHE vs. CO binding strength (Reprinted with permission from *J. Am. Chem. Soc.* 2014, 136, 40, 14107–14113. Copyright 2014 American Chemical Society);[78] b) Volcano plot of CO partial current density at −0.9 V vs. RHE vs. *COOH binding energy (Reprinted with permission from *ACS Catal.* 2017, 7, 7, 4822–4827. Copyright 2017 American Chemical Society).[80]

1.3.3.5 CO_2RR mechanisms

The CO_2RR is of catalytic nature, and therefore takes place at the interface between a solid catalyst surface and the electrolyte. The latter can be a liquid electrolyte solution or an ion-conducting polymer (see below).

The overall reaction can be subdivided into three individual steps: 1) the chemisorption of the CO_2 reactant on the surface of the electrocatalyst, 2) the electron transfer and proton migration leading to the dissociation of C=O bond(s) and/or the formation of new C-O and C-H bonds, and 3) the desorption of the formed products from the catalyst surface.[81]

Simpler reaction mechanisms involving only two electron transfer steps, e.g., leading to CO_2RR products like formate and carbon monoxide, are much better understood than those involving multiple electron transfer steps or more complex C-C coupling reactions (→ C_{2+} products). Figure 1.11 depicts the reaction mechanism proposed for the formation of CO, e.g., on Ag catalysts. The first reaction step consists of forming the $*CO_2^{\cdot-}$ radical anion (*denotes an adsorption state) by a single electron transfer followed by a proton transfer that leads to the formation of the chemisorbed carboxyl intermediate (denoted *COOH). A second coupled proton-electron transfer to the *COOH intermediate yields water and *CO that desorbs from the active site as the CO_2RR product due to the reasons detailed above. The formation of the $*CO_2^{\cdot-}$ radical anion is suggested as the rate-determining step for the conversion of CO_2 into CO. An alternative mechanism assumes the coupled proton-electron transfer to the CO_2 directly yield the carboxyl intermediate *COOH.[82, 83] If there is a strong CO binding to the surface, the CO desorption could become the rate-limiting step.[80, 81]

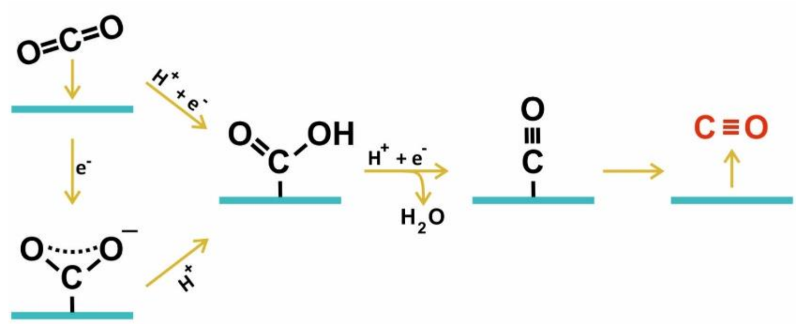

Figure 1.11. Mechanistic pathway of CO formation. Adapted from References 82 and 83.

Different reaction pathways are discussed in the literature for the formation of formate and are depicted in Figure 1.12. Particularly on oxophilic catalysts (e.g., Sn), CO_2 is assumed to bind through the oxygen atoms to the active sites (met-O pathway). The reaction likely proceeds through (individual) consecutive electron/proton/electron transfer reactions.

An alternative reaction pathway assumes binding through the carbon of the CO_2 (similar to the CO pathway), also involving the formation of $*CO_2^{\cdot-}$ or *COOH intermediates (Figure 1.12). A third possible pathway involves the hydrogenation of the CO_2 through adsorbed H (or metal hydrides). A prime example of this reaction pathway is Pd which forms hydrides even under mild HER conditions that allows for the hydrogenation of the CO_2 at particularly low overpotentials.[82, 83]

Recently a new pathway of formate formation, a “sub-carbonate” pathway, has been discovered for oxidic Bi_2O_3 catalysts involving the embedment of CO_2 into the oxide catalyst matrix prior to the CO_2 reduction into formate.[84]

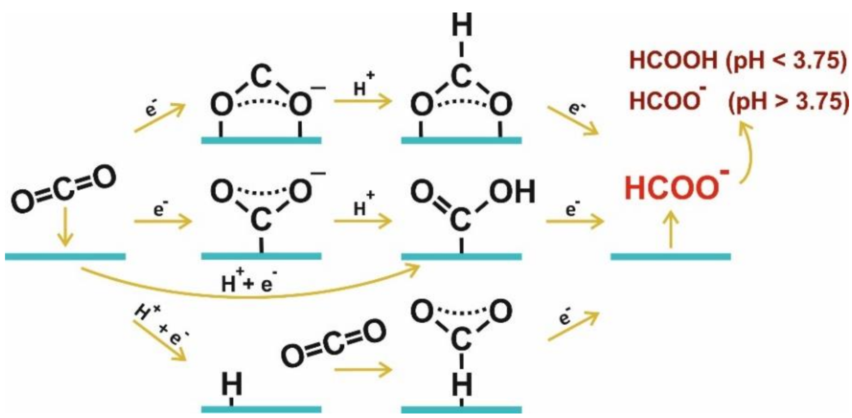

Figure 1.12. Mechanistic pathways towards formate formation. Adapted from References 82, 83 and 85.

The formation of C_1 products like CH_4 and CH_3OH is more complex because, as shown in Figure 1.13, it requires eight or six electrons and protons, respectively, and involves the formation of multiple intermediates. Due to their complexity, the C_{2+} pathways are less well understood.[83] Still, as outlined above, the binding energy of adsorbed CO is the crucial descriptor for products that require more than two electrons/protons.[57]

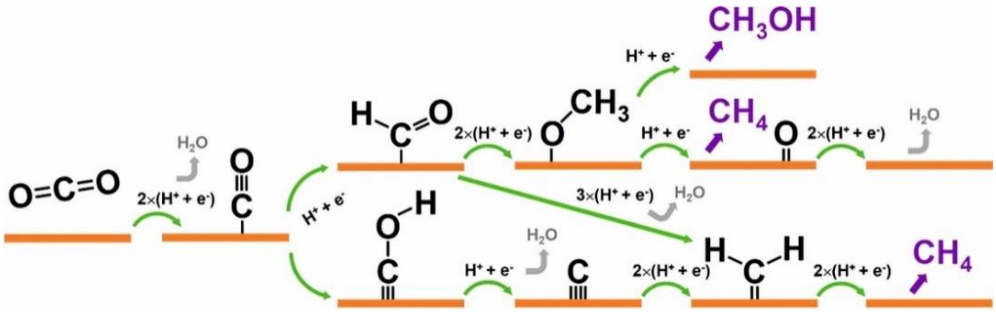

Figure 1.13. Mechanistic pathway of methane and methanol formation (Reprinted with permission from *Chem. Rev.* 2020, 120, 2, 1184–1249. Copyright 2020 American Chemical Society).[83]

1.3.3.6 Electrolytes for the CO_2RR

The main function of an electrolyte is to provide ionic current flow between the electrodes. The type and concentration of the electrolyte will affect the selectivity and activity of the catalysts.[82] The most frequently used electrolytes for CO_2RR are CO_2-saturated aqueous solutions, which commonly comprise alkali cations (e.g., Na^+ and K^+) and anions such as Cl^-, SO_4^{2-}, and HCO_3^-. Furthermore, water itself serves in the aqueous electrolytes as a proton source for the coupled electron/proton transfer reactions.[64]

The pH of the electrolyte is a key parameter for the selectivity and overpotentials for the CO_2RR. It is important to distinguish between bulk electrolyte pH and local pH at the interface. A high local pH can be generated due to the CO_2 electroreduction reaction itself because either H^+ are consumed, or OH^- are generated (depending on the pH of the electrolyte) and also due to the HER (hydrogen evolution reaction) associated with the reductive water splitting, which is superimposed on the CO_2RR.[62] A decrease of the proton concentration leads to an increase in the local pH and therefore to a decrease in the local CO_2 concentration.[58, 85]

In general, lower pH electrolytes favor the undesirable HER; therefore, weakly acidic or alkaline aqueous electrolytes are preferred for the CO_2RR.[82] Bicarbonate solutions are one of the most frequently applied electrolytes as the bicarbonate anions act as a buffer for the local pH at the electrode surface during CO_2RR.[48] On the other hand, it has been found that highly concentrated potassium hydroxide (KOH) solutions suppress the parasitic HER and reduce the activation energy barriers for CO_2RR. Moreover, OH^- anions exhibit excellent ionic conductivity, which improves the reaction performance.[62, 86-90]

In addition to electrolyte pH and cations and anions effects, it is crucial to consider some aspects of the solvents, such as their conductivity, electrochemical stability (potential window), viscosity, cost, ease of handling, storage, and safety and mainly their solubility for the reactant (CO_2).[48, 91] One of the disadvantages of using water as a solvent of the electrolyte for CO_2RR is the low solubility of CO_2 in water: 33 mM at 25 °C and ambient pressure.[40]

Organic solvents have been used as electrolytes for CO_2RR as they have a broader potential window for electrolysis and a higher solubility for CO_2 than water. For example, acetonitrile (AN), dimethylformamide (DMF), dimethyl sulfoxide (DMSO), and methanol have a solubility for CO_2 of 314, 194, 131, and 151 mM, respectively.[62, 91, 92]

Room temperature ionic liquids (RTILs) are organic salts that consist of ionic species in the liquid state at room temperature. They represent another alternative for CO_2RR electrolytes, exhibiting high CO_2 solubility, thermal stability, a broad potential window, high ionic conductivity, and low vapor pressure.[93] Furthermore, some RTILs can form a complex with the intermediates during CO_2RR, thus lowering the energy barrier of the reaction. In other words, they act as a co-catalyst for CO_2RR, lowering the required overpotential.[48, 58]

Although organic solvents electrolytes offer another alternative as electrolytes for CO_2RR, they have some disadvantages, as their high cost, volatility, flammability, and possible toxicity have narrowed their use. At the same time, RTILs are also expensive, and their viscosity is high, which limits the CO_2 diffusion and their current densities, and those aspects have limited their direct application in the CO_2RR.[48, 62]

1.3.4 Mass transport in CO_2RR

Previously, it was pointed out that the total reaction rate or current density of the CO_2RR depends on charge transfer and mass transport. The aspects related to the first process were discussed in the previous section. The important aspects of mass transport will be discussed in the following paragraphs.

Several steps are needed for an electrochemical reaction to happen: 1) mass transfer or transport of reactants from the bulk electrolyte to the electrode surface, 2) charge or electron transfer to the reactant in the interface of the electrode and electrolyte, 3) mass transfer of the products away from the electrode surface into the bulk of the electrolyte.

The steps for CO_2RR are shown in Figure 1.14. First, CO_2 is dissolved in the electrolyte, then transported and adsorbed on the electrode surface, and then it is reduced. The adsorption of CO_2 on the electrode surface presumably takes place simultaneously with the first electron and/or proton transfer due to the high energy requited to bend the CO_2 molecule. [94]

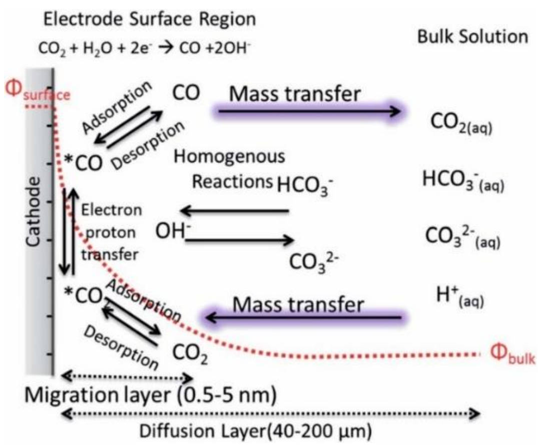

Figure 1.14. Schematic representation of CO_2RR consisting of an electrode surface region, mass transport layer, and bulk solution.[94]

Mass transport and charge transfer are two consecutive processes, and the slowest step will be the rate-determining step. The reaction rate of the CO_2RR is usually limited by charge transfer at lower applied overpotentials because it is slow, and mass transport limitations can be ignored. At high applied overpotentials, charge transfer becomes the faster process and stops influencing the overall rate. A further increase of the overpotential will increase the rate of charge transfer, but this will not affect the overall rate, which is now limited by mass transport of CO_2 to the electrode surface. The rate of consumption of the reactants is linearly dependent on the current density. Therefore, the reactant concentrations at the cathode decrease with increasing current density and can eventually reach a negligible value. The result is a current that is independent of potential and referred to as the mass transport limited current density. It represents the maximum current density at which the electrochemical reaction can occur.[51, 52, 85]

Mass transport to the interphase of the electrode can occur through three independent mechanisms: migration, convection, and diffusion. Migration refers to the movement of charged particles due to the electrical field. Convective mass transport denotes the bulk movement of a fluid, and the driving force is an external energy, like stirring, rotating the electrode, or pumping a liquid or gas close to the electrode. Mass transport by diffusion consists of the transport of particles due to the local difference in the chemical potential caused by a gradient in concentration.[37, 51, 52]

The concentration and environment of the reactants and the cell design can influence the mass transport in the CO_2RR. Before describing those aspects, it is important to consider the following reactions to have a better understanding of the processes that affect the CO_2RR reaction rate under a mass transport regime (especially when CO is the main product of CO_2RR):

$$CO_2 + 2e^- + H_2O \rightarrow CO + 2\,OH^- \tag{14}$$

$$2\,H_2O + 2\,e^- \rightarrow H_2 + 2\,OH^- \tag{15}$$

$$CO_2 + H_2O \rightleftharpoons H_2CO_3 \tag{16}$$

$$CO_2 + OH^- \rightleftharpoons HCO_3^- \tag{17}$$

$$HCO_3^- + OH^- \rightleftharpoons CO_3^{2-} + H_2O \tag{18}$$

Reactions 14 and 15 represent the reduction of CO_2 to CO and HER (from water splitting), respectively. Reactions 16–18 exemplify homogeneous reactions. Reaction 16 is thermodynamically uphill and kinetically slow. At high current densities (relevant for practical application), reactions 17 and 18 play a critical role in carbon-mass balance that must be considered.[57]

The general trend for FE and PCD in the function of the applied overpotential for an electrocatalyst selective for CO (for instance, Ag-based catalysts) in an H-type cell and a gas flow cell (with a GDE)[1] is shown in Figure 1.15, where three regimes are observed: I, II and III.

The regime I of CO_2RR performed in an H-type cell occurs at low overpotential and is characterized by low activity for CO_2 reduction and HER. The CO faradaic efficiency (FE(CO) or

[1] H-type cell and gas-flow cell are electrochemical devices to carry out the CO_2RR and will be described in further detail in Section 1.3.4.1.

FE_{CO}) starts to increase with the onset of CO production while HER activity remains low. As the PCD_{CO} is low, mass transport and Reactions 16 and 17 do not affect CO production. When a high overpotential is applied, regime II is reached, the FE_{CO} rises, and a maximum value is reached (with some catalysts, this value can reach almost 100%); however, the PCD_{CO} is still too low for practical applications. Regime III occurs at higher overpotentials, and its main feature is a decrease in FE_{CO} due to mass transport limitations caused by the low solubility and slow diffusion of CO_2 in aqueous solutions. Moreover, in this regime, the homogeneous reactions become relevant because as the PCD_{CO} and PCD_{H_2} increase (Reactions 14 and 15), more OH^- is produced at the electrode surface (leading to a higher local pH), and OH^- reacts with CO_2 to generate bicarbonate ions (Reaction 17) that decrease the CO_2 concentration near the electrode surface. Additionally, the production of bicarbonate enhances HER because this is a viable substrate for the reaction. In other words, high-rate CO_2RR results in substantial CO_2 consumption via a local pH effect (high local pH).[95]

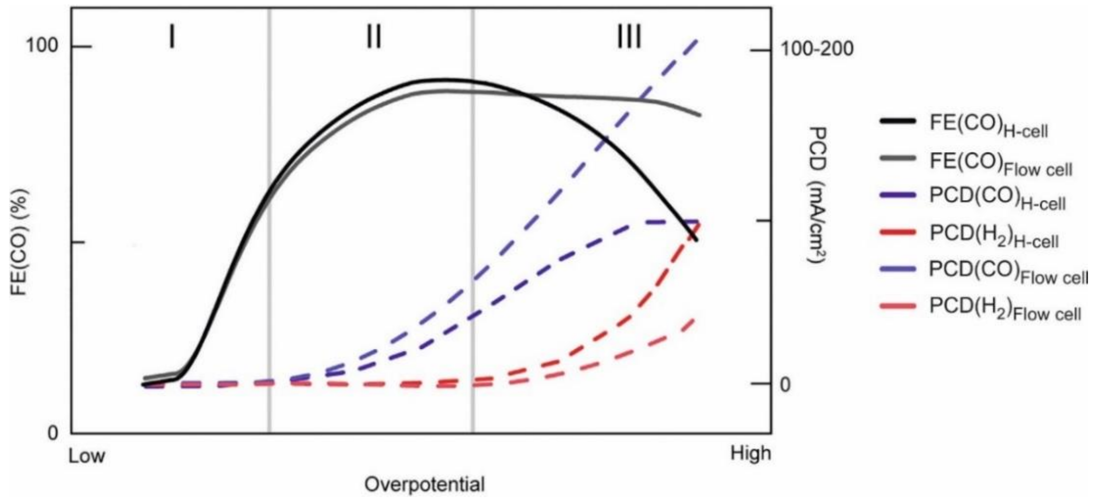

Figure 1.15. Faradaic efficiencies and partial current densities for CO_2RR and HER in an H-cell and a gas-flow cell. Adapted from Reference 95.

An option to circumvent the mass transport limitations of CO_2RR in aqueous electrolytes implies using gas-flow cells equipped with GDEs, where CO_2 is fed in a gaseous phase. In a gas-flow cell, CO_2 is continuously and rapidly delivered in the GDE, which prevents the gaseous porous agglomeration and blocking of the catalyst surface and, in the process, facilitates the adsorption of incoming CO_2.[96-98]

Figure 1.15 also shows the FE_{CO} and PCD_{CO} when a GDE in a flow cell is used. As seen with this configuration, higher FE_{CO} is attained with higher PCD in regime III due to increased mass transport, reaching what is needed for industrial applications.[95] Highly basic electrolytes have been shown to increase FE_{CO} and decrease HER in flow cells. However, at high current densities, CO_2 is rapidly consumed by OH^- to produce bicarbonate and carbonate (Reactions 17 and 18), limiting the conversion efficiency of CO_2.[57] For that reason, it is also necessary to address the loss of CO_2 to bicarbonate and carbonate (analysis of the mass balance of carbon) in flow cells, as CO_2 acts as a reactant and a buffer.[99, 100]

1.3.4.1 CO_2RR cell designs

Several CO_2RR reactor concepts have been proposed through the last decades. In general, they work when either a constant electric current or an electric potential difference is applied in either galvanostatic or potentiostatic mode, respectively.[101] When the electrolytic cell is working in a potentiostatic mode, a third electrode is necessary, a reference electrode or RE (with a known electrode potential value) that allows measuring the electric potential difference applied on the working electrode (WE) and simultaneously the electric current between the WE and CE is measured.[102] Additionally, the surface of the CE should be at least ten times larger than the surface of the WE.[103] As the mass transport in CO_2RR is affected by the cell design, the main features of the different kinds of CO_2RR cell designs found in the literature are described in the following paragraphs.

1.3.4.1.1 H-type cell

More than 95% of CO_2RR studies have been performed in an electrolytic cell called an H-type cell.[94, 104] As shown in Figure 1.16, the H-type cell consists of two compartments: one for the cathode or WE (negative electrode) where the CO_2RR takes place and another for the anode or CE (positive electrode) where an oxidation reaction occurs (oxygen evolution in the case of an aqueous electrolyte being used) both immersed in the electrolyte and separated by a membrane (cation or anion exchange membrane).

The WE and RE are held by air-tight caps and located in the cathode compartment. An ion-exchange membrane (usually a Nafion membrane, a cation exchange membrane) separates it from the anode compartment. The function of the membrane is to prevent an undesired cross-over of reduction products from the catholyte to the anolyte, followed by their re-oxidation on the anode. This type of cell receives its name because it shows a typical “H” form.

During the electrolysis experiments, CO_2 is dissolved and continuously purged through the catholyte (with a flow rate of 10–20 mL min^{-1}, controlled by a flow meter). The CO_2 bubbling further transports the formed gaseous products from the liquid electrolyte phase into the gas chromatograph (GC), where they are analyzed. H-type cells are gas-tight so that the faradaic efficiencies of the products can be determined accurately.

Non-volatile reaction products are detected and quantified directly from the liquid catholyte using ion-exchange chromatography, high-performance liquid chromatography (HPLC), or nuclear magnetic resonance (NMR) spectroscopy.

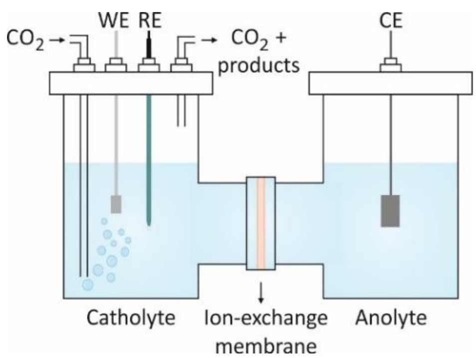

Figure 1.16. H-type electrolysis cell. Adapted from Reference 101.

H-type cells are commonly used for lab-scale CO_2RR experiments because this configuration is simple and low cost, and they offer a rapid catalyst and electrolyte screening.[105-107]

One of the limitations of H-type cells is the slow diffusional transport and the low CO_2 solubility in aqueous electrolytes (0.0016 mm^2/s and 33 mM, respectively), which limits the CO_2RR partial current density typically to values below 100 mA cm^{-2}.[104, 108]

To bring the CO_2RR technology close to industrial-scale implementation and to be economically viable, it is necessary to develop systems that reach high current densities (> 200 mA cm^{-2}), with operation times longer than 8000 h or one year, and with high selectivity and low overpotential.[63, 108, 109] Therefore, inspired by the technology of water electrolyzers and proton-exchange membrane fuel cells (PEMFC) (systems with efficient mass transfer efficiency that fulfill high current densities), similar electrolyzers have been designed for the CO_2RR application, where the reactants and products are continuously circulating to and away from the electrodes, and this flow surmount mass transfer limitations.[89, 105] These devices are denoted as flow cells[108, 110], gas-flow cells, flow reactors[106, 111, 112] or continuous-flow electrolyzers.[104]

1.3.4.1.2 Gas diffusion electrodes (GDE)

Most of the flow cell electrolyzers rely on the use of gas diffusion electrodes (GDE), where CO_2 can be fed to the cell in the gas phase.[113, 114] A conventional GDE comprises a gas diffusion layer (GDL) coated by a catalyst layer (Figure 1.17).[98, 106]

A GDL is a hydrophobic, porous, and conductive structure consisting of two layers: a macroporous substrate (MPS) and a microporous layer (MPL). The MPS or macroporous layer consists of an array of hydrophobic carbon fibers that form a so-called carbon cloth or carbon paper. On top of the MPS, a smooth microporous layer is located to improve the water management, electrical conductivity (reduce the contact resistance between the catalyst layer and the MPS) and provide better structural integrity to the GDE.[48, 115] The MPL is a thinner and denser layer that contains carbon powder or nanofibers held together by a wet-proof binder such as PTFE. [56, 111, 116]

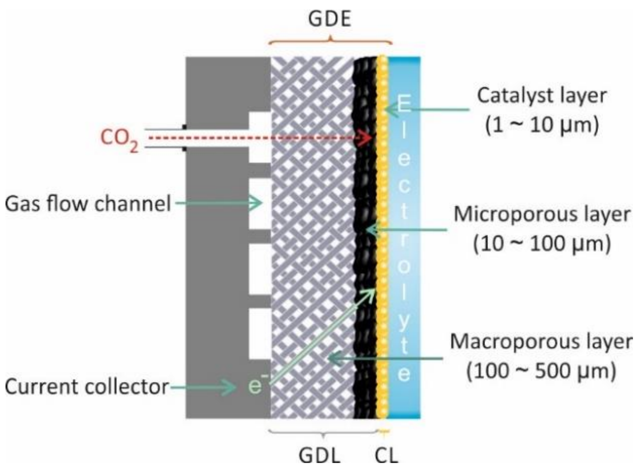

Figure 1.17. Schematic diagram of GDE, its components, and typical thickness range for micro and macroporous and catalyst layers. Adapted from References 95 and 106.

The functions of the GDL are to support the catalyst layer mechanically; allow easy diffusion of CO_2 and products between the gas flow channel and the catalyst layer while providing electric conductivity between the current collector, the external circuit and the catalyst layer; and separate the electrolyte from the gas channel.[98, 117] The catalyst layer is frequently prepared by depositing an ink that contains the catalyst, an ionic polymer binder, and sometimes, a carbon support on top of the MPL. The binder holds the catalyst particles together and may provide ionic conductivity within the catalyst layer. The most common methods to immobilize the catalyst layer on the GDL are drop-casting, hand-painting, air-brushing, electrodeposition, sputtering, or incorporating a catalyst into the material of the GDL itself.[89, 104]

The immobilization of catalysts on the GDL creates a high density of active sites per geometric electrode area, promoting an efficient conversion of CO_2 to desired products. The GDE with the catalyst layer for CO_2RR is located over a gas flow channel or field in the flow cell. Additionally, a continuous supply of electrolyte and CO_2 is needed to ensure that the cell functions in a kinetically limited regime rather than in a mass transport-limited regime.[108, 109, 111, 118]

Nowadays, three main flow cell architectures have been presented in the literature (Figure 1.18): zero-gap membrane reactor, hybrid reactor, and microfluidic reactor. CO_2RR takes place on the cathode side of every reactor, and an oxygen evolution reaction occurs on the anode side. The main feature of those kinds of cells is that the local CO_2 concentration is not limited by the CO_2 solubility in an aqueous electrolyte.[111]

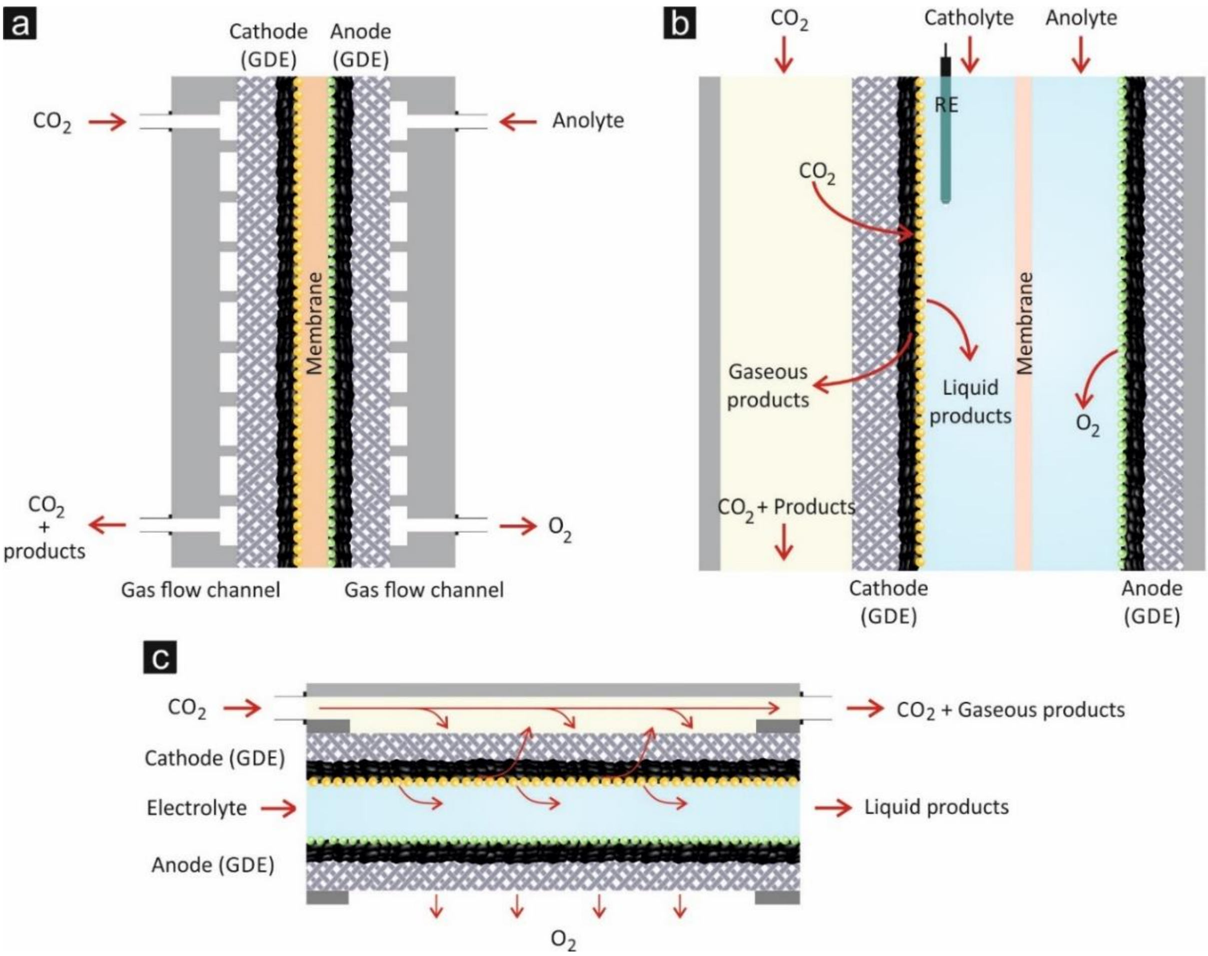

Figure 1.18. Schematic representations of the different types of CO_2RR flow cell: a) zero-gap membrane reactor, b) hybrid reactor, and c) microfluidic reactor. Adapted from References 106 and 110.

1.3.4.1.3 Zero-gap membrane reactor

The zero-gap membrane reactor, membrane electrode assembly electrolyzer, or gas-phase electrolyzer (Figure 1.18a) resemble a proton-exchange membrane water electrolyzer and a polymer exchange membrane fuel cell. This electrolyzer comprises a cathode GDE and an anode (that can also be a GDE) separated by a solid polymer electrolyte (ion-exchange membrane, IEM) to form a membrane electrode assembly (MEA) that is fit in between two flow plates or gas flow channels, where gaseous reactants and products flow in and out of the reactor. This configuration leaves no space between the membrane and the catalysts on the electrode; the cathode is directly pressed against the ion exchange membrane leading to a zero-gap configuration. The proximity of the electrodes decreases the cell resistance. The membrane transports ionic species and circumvents the crossover of CO_2 and electrochemical products between the electrodes.[105]

Because there is no liquid electrolyte present in the zero-gap gas-flow cell, the CO_2 gas inlet stream must be humidified, or the water required for CO_2RR should be provided by using an aqueous anolyte; this would also keep the membrane hydrated during operation. The elimination of the aqueous catholyte reduces the risk of GDE flooding and catalyst poisoning from impurities in the catholyte (which can potentially deactivate the catalyst), thereby improving the system's stability.[89]

One drawback of the zero-gap electrolyzers is that the generated liquid products from CO_2RR can accumulate in the GDE and obstruct CO_2 diffusion to the active catalyst sites.

Due to the configuration of this reactor, it is hard to place a reference electrode in the cathode compartment. Hence, CO_2RR is carried out by controlling current or cell voltage, and this makes the study of the CO_2RR process difficult to separate from the corresponding anodic process.[106]

The ion-exchange membrane is a critical component in the performance of a gas-phase electrolyzer because it allows the transport of ions to produce either acidic or basic conditions at the electrodes. Three main classes of membranes are used in CO_2 flow reactors. They are classified by the type of ion they conduct: anion exchange membranes (AEMs) transport anions from a basic cathode to the anode, cation exchange membranes (CEMs) mediate cations transport from an acidic anode to the cathode, and bipolar membranes (BPMs) enable the dissociation of H_2O under an applied potential and transport H^+ to the cathode and OH^- to the anode.

In the absence of a catholyte, the type of membrane provides the local environment, and therefore it enormously affects the CO_2RR. Hence, the selection of the membrane is based on the target products and the reaction environment.[111]

The majority of CO_2RR studies in gas-phase electrolyzer have been performed using CEMs, but over operational time, the acidification of the cathode side (caused by the transport of H^+ from the anode to the cathode) accelerates HER at the expense of CO_2RR, especially at high current densities. The use of a buffer layer between the catalyst and the membrane could circumvent the acidification of the cathode side.[89]

Currently, AEMs are receiving more attention because they can be used efficiently in both neutral and alkaline media, which work best for CO_2RR. When AEMs are used instead of CEMs, humidification of the CO_2 gas stream is very important because water dissociation provides the protons for CO_2RR. Usually, there is less HER in AEM reactors because of lower proton availability at the catalyst surface. Another advantage of working in an alkaline environment is that non-precious metals can be used as a catalyst for the oxygen evolution reaction.

BPMs are formed when an AEM and a CEM are laminated. Recently they have been applied for CO_2RR electrolyzers because the dissociation of water at the interface of the CEM-AEM interface under applied potential keeps a constant pH at both sides of the reactor as protons migrate towards the cathode and OH^- ions move to the anode. This enables the operation of cathode and anode at different pH, which means that in the anode alkaline environment, inexpensive catalyst materials can be used as a catalyst for oxygen evolution instead of rare earth metal catalysts.[119] However, the H^+ migrating to the cathode side lowers the pH and affects the CO_2RR selectivity. [111, 117] Consequently, BPMs require a buffer layer, such as a solid-supported aqueous $NaHCO_3$ or $KHCO_3$ layer, on the surface of the catalyst to be efficient for CO_2RR.[120]

1.3.4.1.4 Hybrid reactor

The hybrid reactor or liquid-phase electrolyzer design consists of three flow channels, one for the CO_2 gas, one for the catholyte and one for the anolyte, as is shown in Figure 1.18b. A GDE separates the catholyte and CO_2 channel; the catalyst layer of the GDE faces the electrolyte, while CO_2 is continuously delivered to the catalyst through the backside of the GDE. The gaseous products are diffused back to the CO_2 gas phase while the liquid products enter the liquid electrolyte. In this type of electrolyzer, it is possible to place a reference electrode in the catholyte compartment next to the cathode to study and control the cathode's potential.[104] The catholyte and anolyte streams are separated by an IEM and are continuously circulated via a peristaltic pump. The membrane prevents the CO_2RR products from reaching the anode (where they are oxidized), and it also restricts evolved oxygen to be reduced back to water in the cathode.

The choice of the IEM depends on the products of interest and the pH of the used electrolytes. This configuration allows for precise control and optimization of the reaction environment to achieve high CO_2 conversion efficiency.[106]

The use of alkaline electrolytes (high KOH concentration) in liquid-phase electrolyzers results in reduced overpotentials and higher selectivity for CO on Ag catalysts[121-124] and also slows the kinetics of water reduction. Strongly adsorbed OH^- blocks hydrogen evolution sites on the catalyst.[125] Moreover, the high ionic conductivity of the hydroxide electrolytes (KOH and NaOH) compared to that of the pH neutral electrolytes ($KHCO_3$) reduces ohmic losses and increases the overall energy efficiency of the system.[117]

The presence of an electrolyte can promote impurity depositions on the catalyst and the potential penetration of electrolyte in the GDE, also called flooding or perspiration,[126, 127] which is a common source of instability that reduces CO_2 diffusion to the catalyst and decreases the performance in the system. The presence of electrolytes can also increase ohmic resistance through bubble production. CO_2 reacts with alkaline electrolytes, leading to bicarbonate and carbonate formation, which reduce electrolyte conductivity because of their lower mobilities. Additionally, the formation of bicarbonate and carbonate modifies electrolyte pH and salt precipitation blocks GDE and membrane pores, hindering the CO_2RR.[48, 118]

1.3.4.1.5 Microfluidic reactor

The microfluidic reactor resembles a hybrid reactor without membrane, but instead, a thin (< 1 mm) electrolyte flow field channel separates the electrodes, CO_2 is supplied from the gaseous channel to the catalyst layer on a GDE, while oxygen is released directly into the air on the anode side. See Figure 1.18c.

The crossover of reactants and products is controlled by laminar flow conditions. Also, the electrolyte flow can be adjusted to control operation conditions, including pH and water management. A reference electrode can be placed in the outlet of the electrolyte, which allows the measurements of electrode potentials.[105]

This kind of design was first proposed by Kenis et al. for formate production,[128] and later it was also used to produce CO.[90, 129] In particular, an AEM was inserted in between the electrolyte flow field channel, to separate the catholyte and anolyte chamber, when a mixture of liquid and gaseous products was generated (ethanol and ethylene),[130, 131] this resembled an architecture like the hybrid reactor.

Microfluidic reactors are appropriate to work with strong alkaline electrolytes. However, the scale-up is challenging due to the pressure of the microfluidic architecture, which limits their potential industrialization.[106]

1.3.5 Economically viable products: CO and $HCOO^-$ and their importance

From the economic point of view, it is crucial to identify which products from CO_2RR are economically viable to generate. Durst et al.[34] estimated the production costs of different CO_2RR products, compared them with the current processes used to generate them and determined that CO and $HCOO^-$/HCOOH are the most promising and profitable target products for CO_2RR. However, it is known that the global market for $HCOO^-$/HCOOH is much smaller than the one for CO.[34] This hypothesis was further confirmed by other analyses performed by Verma et al.,[132] Kibria et al.,[89] and Jouny et al.[133] In Table 4, we can see that the generation of CO employing CO_2RR costs from 0.27–0.54 \$ kg^{-1}, which is below the current market price of 0.65 \$ kg^{-1}. Additionally, the global market for CO is extremely large (210000 Mt y^{-1}).

CO production by means of CO_2RR is promising because it is utilized as a precursor for several industrial processes. For example, when combined with H_2 (denoted as synthesis gas or syngas), liquid fuels can be produced via the Fischer–Tropsch synthesis.[64, 100] CO is also used to produce methanol, the Monsanto/Cativa acetic acid synthesis, and the hydroformylation of olefins to aldehydes and alcohols.[97, 134] To further note the importance of CO produced electrochemically, it is worth mentioning that in 2018, Siemens and Evonik launched the Rheticus project, which aims at coupling the production of CO via CO_2RR (Siemens) with a biotechnological fermentation process (Evonik) to produce alcohols such as butanol and hexanol as intermediates for the production of specialty plastics or food supplements.[30, 116, 135] On the other hand, silver-based materials have been identified as some of the best electrocatalysts toward CO formation due to their excellent selectivity and activity in the CO2RR process.[121, 124, 136-138]

The production of $HCOO^-$/HCOOH from CO_2RR appears to be also promising as the production price is 2–4 times cheaper than the current market price, see Table 1.4. Formic acid is used as a preservative and an antibacterial agent in animal feeds, and its demand keeps rising in pharmaceutical and biotechnological synthesis and paper and pulp production.[139] It can also be used as chemical fuel for direct formic acid (or formate) fuel cells and hydrogen storage.[140]

Table 1.4. Current and estimated costs of production of several CO_2RR products[34]

Product	Produced by	Current market price, $ kg^{-1}	Current production volume, Mt y^{-1}	Production price by electrolysis, $ kg^{-1}
H_2	Steam reforming, partial oxidation of methane or gasification of coal	2–4	65	4
CH_4	Methanogenesis or hydrogenation of CO_2	< 0.08	2400	2–4
C_2H_4	Pyrolysis or vapocracking	0.8–105	141	1.6–3.2
CO	Boudouard reaction	0.65	210000	0.27–0.54
$HCOO^-$ / HCOOH	Hydrolysis from methyl formate and formamide or by-product of acetic acid production	0.8–1.2	0.8	0.17–0.34
CH_3OH	From natural gas, coal biomass, waste	0.4–0.6	100	0.70–1.4

1.4 Thesis outline

The electrochemical conversion of CO_2 to value-added chemicals by using the surplus of renewable electric power is considered a promising approach to mitigate anthropogenic CO_2 emissions, which at the same time offers a solution for the storage of excess renewable energy. Among the various products of the CO_2RR, carbon monoxide is particularly valuable due to its high demand in the chemical industry as a platform chemical for the large-scale production of long-chain hydrocarbons and alcohols via the Fischer–Tropsch synthesis, and silver is well known as a promising catalyst material for CO production.

Two methods are used to fabricate silver-based electrocatalysts in our research group: a classical colloidal synthesis approach and electrodeposition. The object of study of this PhD project are two different types of silver-based nanomaterials with different morphologies (prepared through the first-mentioned method) applied as electrocatalysts for the CO_2RR: silver nanowires and silver nanocubes, Ag NWs and Ag NCs, respectively.

The main goal of this PhD thesis consists of achieving the transition of CO_2RR catalyst screening from H-type cells to gas-flow cells. For this purpose, a methodology was designed to test electrocatalysts under controlled mass transport conditions using a novel gas/liquid flow setup.

As a first step, the selectivity, activity, and stability of these catalysts were studied in a classical H-type cell. A systematic study determined that the removal of capping agents (employed in the synthesis process of nanomaterials) is essential to observe the “real” performance of Ag NWs and NCs towards CO formation. Scanning electron microscopy analysis (SEM) was used to identify that corrosion (appearance of smaller nanoparticles) is observed after the CO_2RR process when Ag NCs are used as electrocatalysts. On the other hand, identical location SEM (IL-SEM) is a technique that shows some limitations when used to characterize the morphological changes of surfactant-capped Ag nanoparticles after CO_2RR.

Due to the low solubility and diffusion of CO_2 in aqueous electrolytes under ambient conditions, which impose severe CO_2 mass transport limitations, the classical half-cell measurements carried out in aqueous environments using Ag NWs and NCs as electrocatalysts were extended to a zero-gap gas flow cell, where CO_2RR current densities are realized that are more relevant for future industrial applications.

Remarkably, it was observed that when changing the environment of the reaction to neutral or to basic (by using two electrolytes with different pH) with Ag NCs as electrocatalyst, the activity and product distribution of the CO_2RR vary. Furthermore, bicarbonate and carbonate precipitation, loss of hydrophobicity and flooding of the electrode during CO_2RR were the main reasons for failure when high current densities were reached (more than 300 mA/cm^2). The changes in the morphology of the electrocatalysts when performing experiments in the zero-gap electrolyzer were monitored by SEM and IL-SEM. Similar observations obtained from the experiments carried out in H-type cell were detected with the last technique.

The strategy followed in carrying out the CO_2RR catalyst testing in the Interfacial Electrochemistry Group is presented in the following scheme, Figure 1.19, where the main achievements and findings are also summarized. Green bullets denote the topics related to this PhD project.

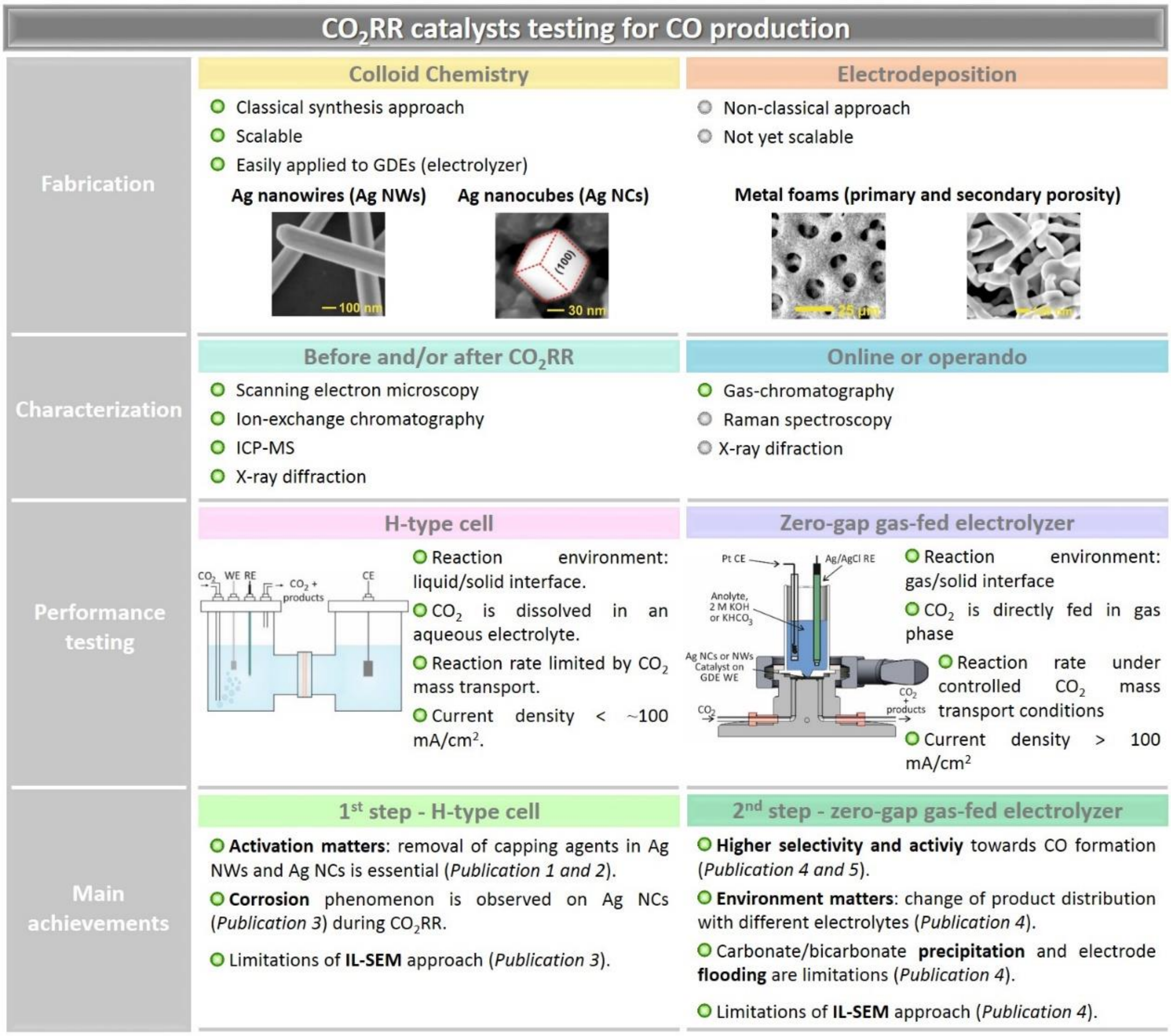

Figure 1.19. Outline of the strategy developed for CO_2RR catalyst testing for CO production in the Interfacial Electrochemistry Group. Green bullets show the topics related to this PhD project and its main achievements.

2. Results and discussion

Carbon monoxide is one of the most promising and profitable products from CO_2RR (Section 1.3.5), and silver-based catalysts show excellent catalytic properties towards CO formation (Section 1.3.3.3–1.3.3.4). The results of this PhD thesis encompass diverse investigations about CO_2RR using silver nanomaterials with two different morphologies as electrocatalysts: Ag NWs and Ag NCs. The former can form networks, and the latter are distributed as single particles or clusters with more than one particle on the electrode surface.

The main findings will be presented in two sections, according to the device employed to test their catalytic properties. In the first section, the results of experiments performed in an H-type cell are presented, emphasizing the main findings of those experiments in two subsections: the development of an electrochemical method to remove organic capping agents (surfactants) from silver nanoparticles and the limitations of IL-SEM as a method to monitor the morphological changes of silver nanomaterial-based electrocatalysts.

The second section will show the results of experiments performed under mass-transport-controlled conditions. Ag NCs and NWs were tested for CO_2RR using a zero-gap flow cell setup.

Further details of this section can be found in the peer-reviewed publications listed in Chapter 5 of this thesis, and the respective numbers of those publications are indicated through the text.

1.5 CO_2RR using Ag nanomaterials as catalysts in an H-type cell

1.5.1 Electrochemical looping as an effective method for surfactant removal

Surfactants or capping agents are commonly used in colloidal electrocatalyst synthesis because they control the size distribution and shape of the resulting nanoparticles and prevent them from agglomeration during and after the synthesis. However, the presence of surfactants on the nanoparticle surface after the synthesis is highly detrimental for their application as electrocatalysts because the capping agents sterically block the access of reactants to the active catalyst sites during the electrocatalyzed reaction of interest. Several methods, such as thermal annealing, chemical washing, or electrochemical treatments, have been established to remove surfactants from the surface of the electrocatalyst.

An electrochemical method was applied in this study to remove surfactants from Ag-NWs produced via polyvinylpirrolydone (PVP)-assisted polyol synthesis. The Ag-NWs mean thickness was approximately 162 nm with a length range from ca. one to several µm, see Figure 2.1. This method, called electrochemical looping (ec-l), uses the CO_2RR itself to achieve the desired catalyst deprotection in an H-type cell configuration. This method consists of applying a forward run of a defined sequence of potentiostatic electrolysis experiments in a stepwise manner from a less cathodic potential (E_{start}) to a more cathodic potential (E_{vertex}). The electrolysis loop is closed through the corresponding backward run of electrolysis experiments from the E_{vertex} and ends at the initial starting potential ($E_{start} = E_{end}$).

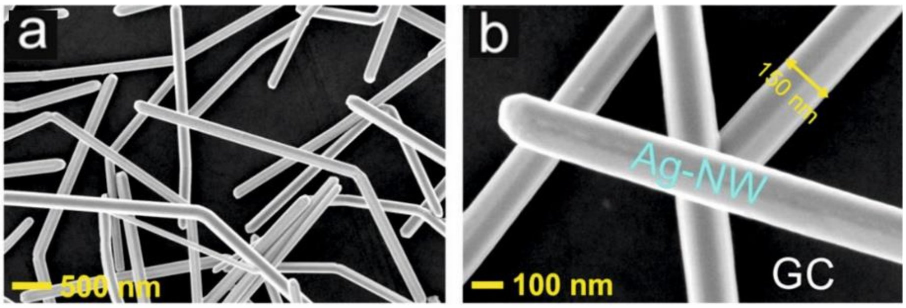

Figure 2.1. a-b) SEM images of the Ag-NWs drop cast on a glassy carbon (GC) support electrode. Readapted with permission from *ACS Catal* 2020, 10, 15, 8503–8514. Copyright 2020 American Chemical Society.

In a single catalyst approach (the use of one electrode to carry out all the ec-l steps), an electrolysis time of 40 min and an E_{start} and E_{vertex} of −0.6 V and −1.3V vs. RHE, respectively, in CO_2-saturated 0.5 M $KHCO_3$, were the conditions that provide better results in terms of product distribution, where a profound hysteresis in the forward and corresponding backward run of the ec-l was observed. See Figure 2.2a. In the forward run, it is possible to see that the FE_{CO} is lower than in the backward run, and an anti-correlated effect is observed for H_2, where the backward run presents lower FE than the forward run. CO efficiencies of > 80% were achieved in the corresponding backward scan; this means that an efficient catalyst activation towards CO formation was achieved by the ec-l.

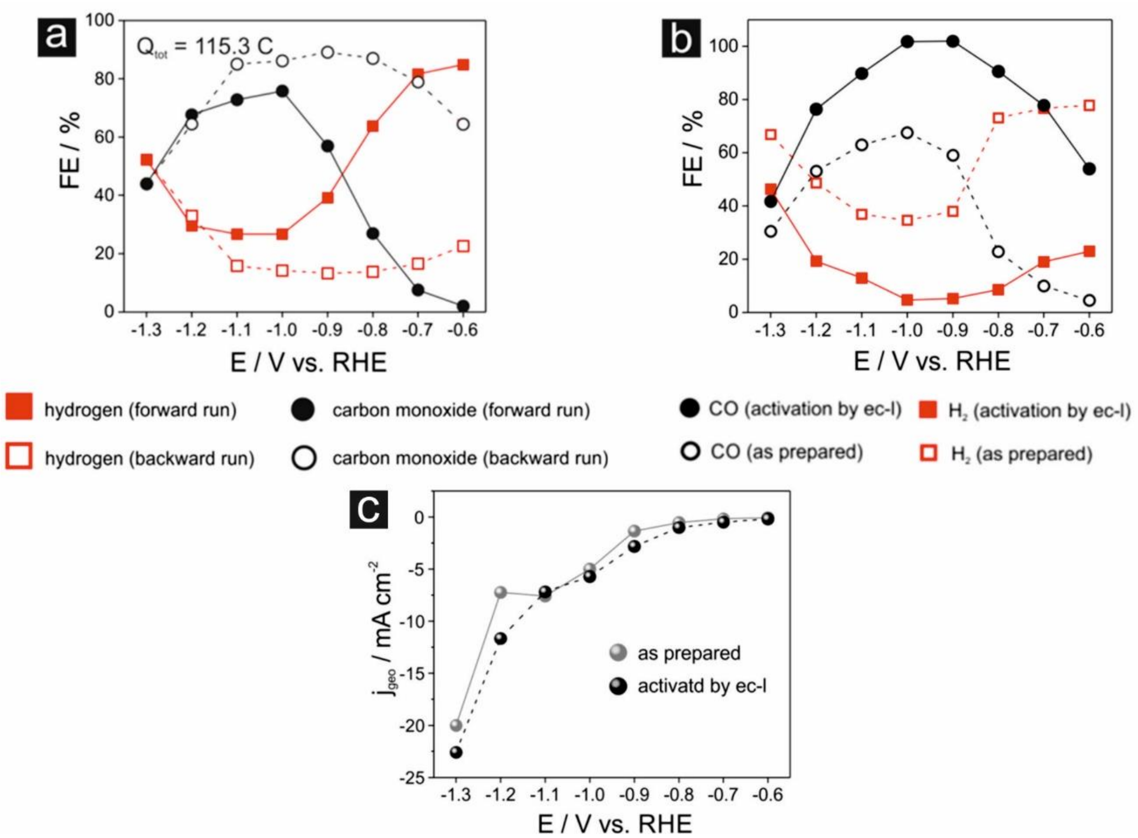

Figure 2.2. a) Hysteresis effects appearing in the forward and backward runs of the electrochemical looping experiments (40 min duration at each potential) carried out over Ag-NW catalysts in CO_2-saturated 0.5 M$KHCO_3$ (single catalyst approach), the total cathodic charge transferred during the “electrochemical looping” is indicated. b) CO_2RR product distribution of 1 h duration electrolysis experiments comparing the as-prepared Ag-NW catalysts and those pretreated by electrochemical looping. c) Steady-state total current densities of the

electrolysis experiments correspond to the data in panel b. Readapted with permission from *ACS Catal* 2020, 10, 15, 8503–8514. Copyright 2020 American Chemical Society.

A multicatalyst approach was applied to check the “real” product distribution (after the surfactant removal) when using Ag-NWs as the catalyst for CO_2RR, which means that several electrodes were treated with the ec-l and were further used for each applied potential. The results are shown in Figure 2.2b. The FE of the as-prepared Ag NWs catalyst is also plotted for comparison. It is evident that due to the efficient surfactant removal, FE_{CO} ~100% were obtained in the potential range between −0.9 and −1.0 V vs. RHE. Moreover, the observed total current densities are slightly higher after the ec-l than with the as-prepared electrodes; see Figure 2.2c.

This catalyst deprotection protocol was transferred to a carbon-supported Ag-NWs catalyst system and it was demonstrated that the ec-l also works when the NWs are embedded into a technical carbon matrix. An improvement of FE_{CO} values in the corresponding backward run of the electrochemical looping was observed.

In addition, X-ray photoelectron (XPS) analysis was used to confirm that the PVP (and its removal) is the main origin of the observed hysteresis effects in the product distribution. A more detailed description of these findings is provided in ***Publication 1***.

To deepen our research and bring it closer to the conditions applied in flow cell electrolyzers, Ag NCs embedded in a carbon support matrix on a porous gas diffusion layer (consisting of a MPS and a MPL, Section 1.3.4.1.2) were subjected to ec-l. The results are shown in Figure 2.3. As in the case of Ag NWs, higher CO selectivity in the backward run is observed, and even at lower applied cathodic potentials, ~85% FE_{CO} is reached in the potential range between −0.7 and −0.85 vs. RHE. In contrast to what was observed in the ec-l of the Ag-NWs, the CO PCDs (and therefore charges) are not the same in the forward and backward scans. This might indicate that besides the PVP removal from the Ag NCs, other changes are taking place.

A post-ec-l SEM analysis of the electrodes was carried out and showed the appearance of smaller nanoparticles around the Ag NCs (Figure 2.4). This might explain that higher partial current densities are reached in the backward scan (Figure 2.3b) because a larger catalyst surface is available. Further details of these studies are shown in ***Publication 2.***

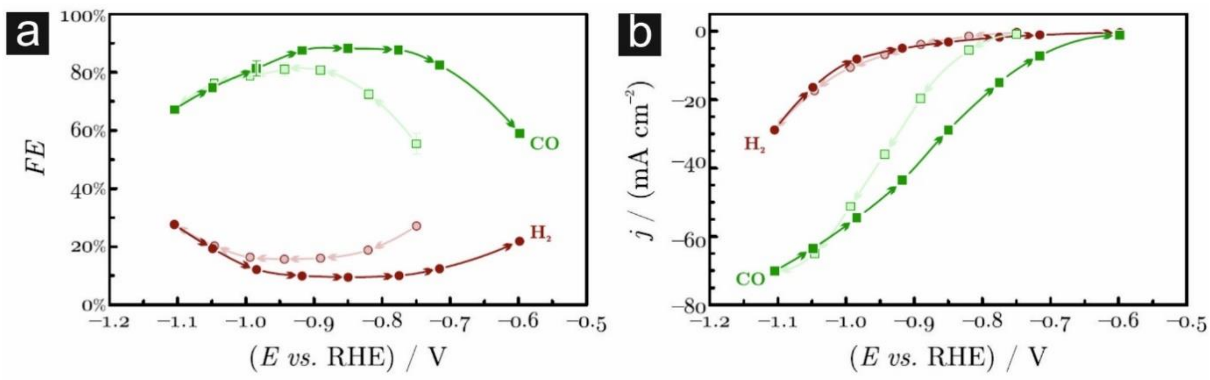

Figure 2.3. Potentiostatic electrolyses were carried out using PVP-coated Ag NCs drop cast on a GDE, used as electrocatalysts of CO_2RR in a CO_2-saturated 0.5 M $KHCO_3$ solution. a) Faradaic efficiencies and b) partial current densities of CO (green) and H_2 (red) are shown as a function of the IR-drop corrected electrode

potential. Data (dots) were recorded by gas chromatography; trends (curves) were created by spline interpolation. Arrows show the direction of the potential excursion.

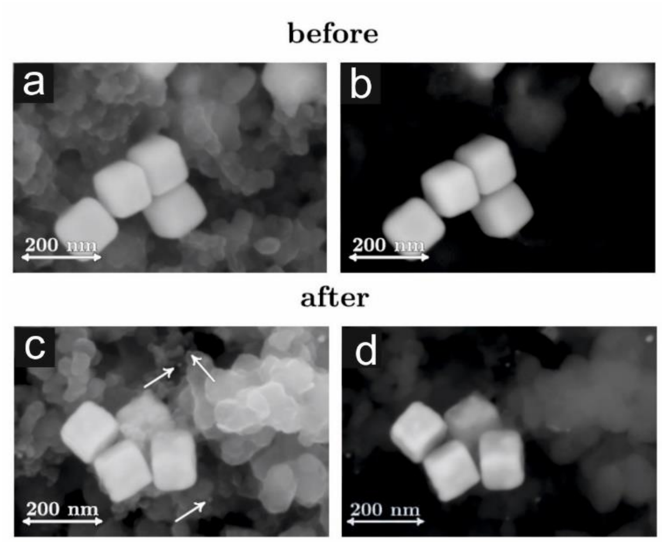

Figure 2.4. Ag NCs drop cast on a GDE, observed before and after applying the electrochemical treatment shown in Figure 2.3. Panels a) and c) show the secondary electron, b) and d) the back-scattered electron images of the NCs. The arrows point to smaller Ag particles formed by the degradation of the NCs during the potential-induced activation.

1.5.2 Identical location scanning electron microscopy (IL-SEM) as a method to characterize Ag nanomaterial based electrocatalysts for CO_2RR

IL-SEM is a prominent method to study catalyst degradation in the field of CO_2RR, mainly because it is a non-destructive method. IL-SEM analysis consists of imaging identical sample positions of the electrode before and after it is subjected to an electrochemical reaction.[141, 142] A catalyst is presumed to be stable if it does not present structural changes after long periods of electrolysis, which makes it to be considered as a potential candidate for up-scaled experiments. However, special attention must be paid when surfactant capped nanoparticles are used as electrocatalyst for CO_2RR experiments.

Ag NCs are synthesized using PVP as a capping agent because PVP is strongly bound to the (100) facets of Ag, which facilitates the formation of nanocubes. A systematic IL-SEM study on the morphological changes of PVP functionalized Ag nanocubes (like those described in the previous section with a side length of about 100 nm) under CO_2RR conditions was carried out. A glassy carbon electrode was used as support of the Ag NCs (with and without carbon support) to better observe the changes on the nanocubes.

The IL-SEM micrographs in Figure 2.5a-b show that after the CO_2RR experiments at −1.0 V vs. RHE, no significant changes are observed. However, when a random spot was imaged, a significant number of smaller nanoparticles were observed. Therefore, it is clear that during the pre-electrolysis scan, the electron beam of the SEM induces changes on the catalyst surface (the formation of a carbonaceous layer most probably made of by the remnant PVP capping agent used in the synthesis procedure), which might become partially deactivated for the catalyzed process. Consequently, after the CO_2RR, the pre-scanned area of the sample may show little or no changes at all. In the meantime, the Ag NCs that were not affected by the pre-electrolysis SEM scanning preserve their activity and show the effects of degradation, Figure 2.5c.

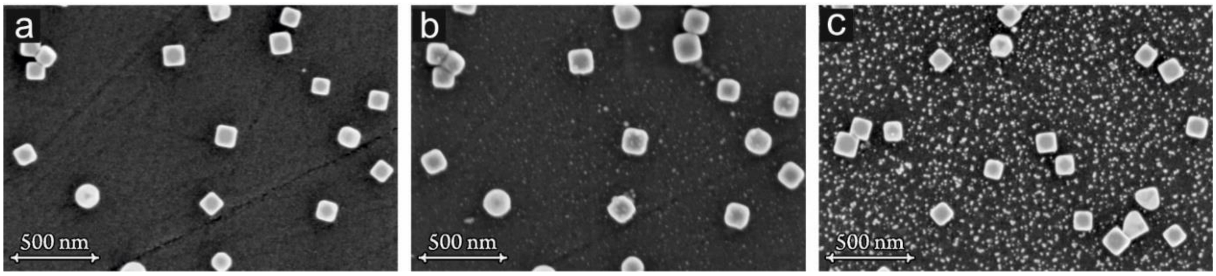

Figure 2.5. Secondary electron - SEM investigation of the degradation of non-supported Ag NCs used as catalysts of CO_2RR. The same spot of the WE surface is shown before a) and right after b) the electrode was used for a 20-hour electrolysis of a CO_2-saturated 0.5 M $KHCO_3$ solution at −1.0 V vs. RHE. A different spot of the same sample is shown after electrolysis in c).

IL-SEM turned out to be unsuitable for the characterization of colloidal catalyst because the remaining surfactants on the Ag NCs (from the synthesis method) suffer alterations with the SEM beam, leading to the formation of a shell that hides the changes of the catalyst after the CO_2RR reaction. The passive carbonaceous layer on the Ag NCs formed after the SEM scanning is better observed when the sample is exposed to longer times under the beam of the SEM and when the images are recorded with higher acceleration voltages, Figure 2.6.

Special attention must be paid when nanoparticles with surface-adsorbed capping agents are used as an electrocatalyst for CO_2RR because, as was shown before, the pre-electrolysis scanning can contaminate (and subsequently disable) the catalyst sample in a way that the post-electrolysis scan would unrepresentative show no degradation. Accordingly, it is very important to consider that the non-destructiveness of IL-SEM cannot be granted for all types of catalysts. A more detailed description of these observations is given in ***Publication 3***.

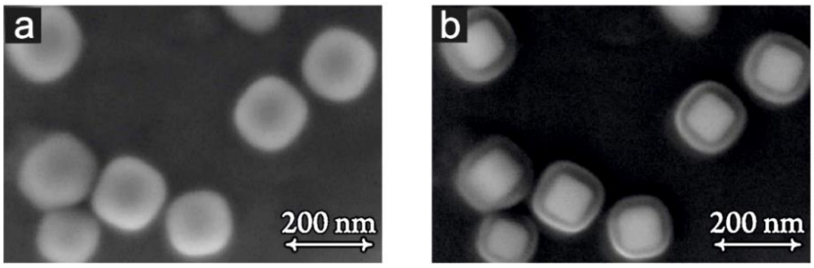

Figure 2.6. SEM images of Ag NCs after electron beam irradiation was carried out for 10 min. a) Secondary electron SEM image taken at 1.5 kV acceleration voltage. b) Secondary electron SEM image obtained at 20 kV.

1.6 CO_2RR using Ag nanomaterials as catalysts in a zero-gap flow cell

1.6.1 Ag nanocubes

Among the various types of CO_2 electrolyzers under development, zero-gap flow cells seem to be one of the best options because they present reduced ohmic losses and attenuate complications that arise from poor membrane hydration and electrode flooding at high current densities. However, their long-term operation (needed for the commercial deployment of these technologies) has not been achieved. One reason may be related to the deterioration of the catalyst material, but unfortunately, this issue has been insufficiently studied. Motivated by this, morphologically tailored Ag nanomaterial, Ag nanocubes (Ag NCs) assembled in a GDE (Ag NCs – GDE), were chosen to establish correlations between structure, environment, electrocatalytic performance, and degradation mechanism under highly alkaline conditions.

The catalyst activity, selectivity, and the evolution over time of the electrochemical performance and the nanostructure of the Ag NCs (Figure 2.7a-b) were studied in a zero-gap flow cell[143-148] resembling the one shown in Figure 2.7c-d. It is important to mention that this cell was initially designed to benchmark oxygen reduction reaction electrocatalysts under realistic mass transport conditions. Similar to a real fuel cell, in this setup, the gaseous reactant is guided to the catalyst layer through a GDL, avoiding mass transport limitations. The catalyst layer is not in contact with any liquid electrolyte. Instead, a membrane electrolyte separates the working electrode compartment from an electrochemical cell housing the liquid electrolyte, the CE, and the RE. Thus, a realistic condition for the WE environment is combined with the advantages offered by a three-electrode setup. Through some modifications, it was possible to employ this flow cell setup for CO_2RR experiments.

The two main products when using Ag NCs as electrocatalyst and 2 M KOH as anolyte were CO and H_2. Their FE and PCD are shown in Figure 2.8a-b. As seen in these figures, the system exhibits a remarkable and competitive CO_2 to CO conversion with a FE_{CO} ~85% and a PCD_{CO} ~625 mA cm^{-2}. Two regimes were identified with the temporal system stability (in terms of FE and PCD values). From −1.5 V to −1.8 V vs. Ag/AgCl, the CO_2RR process improved or remained stable over time, reaching PCD_{CO}s >300 mA cm^{-2} and FE_{CO} ~85% (Figure 2.8c,e). However, at more cathodic potentials, the selectivity and activity towards CO increased, but after ~30 min, there was an abrupt decrease in both the FE_{CO} and PCD_{CO} with increasing applied overpotentials (Figure 2.8d,f).

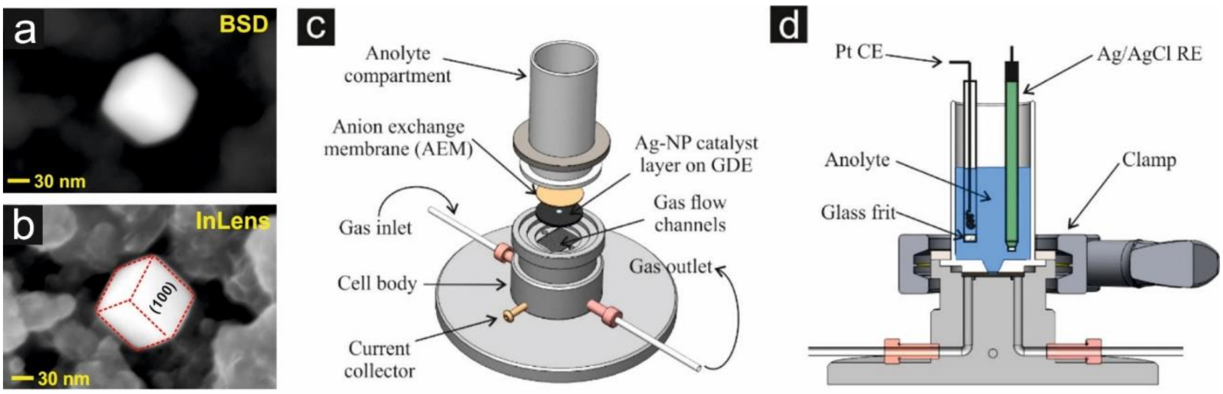

Figure 2.7. SEM images showing an Ag NC on the surface of an Ag NCs – GDE: a) image acquired with BSD detector and b) image acquired with InLens detector. c) Depiction and assembly of the zero-gap flow cell used in this work for the CO_2RR. d) Cross-sectional view of the assembled cell with RE and CE immersed in the anolyte compartment. Reprinted with permission from *ACS Catal*. 2020, 10, 21, 13096–13108. Copyright 2020 American Chemical Society.

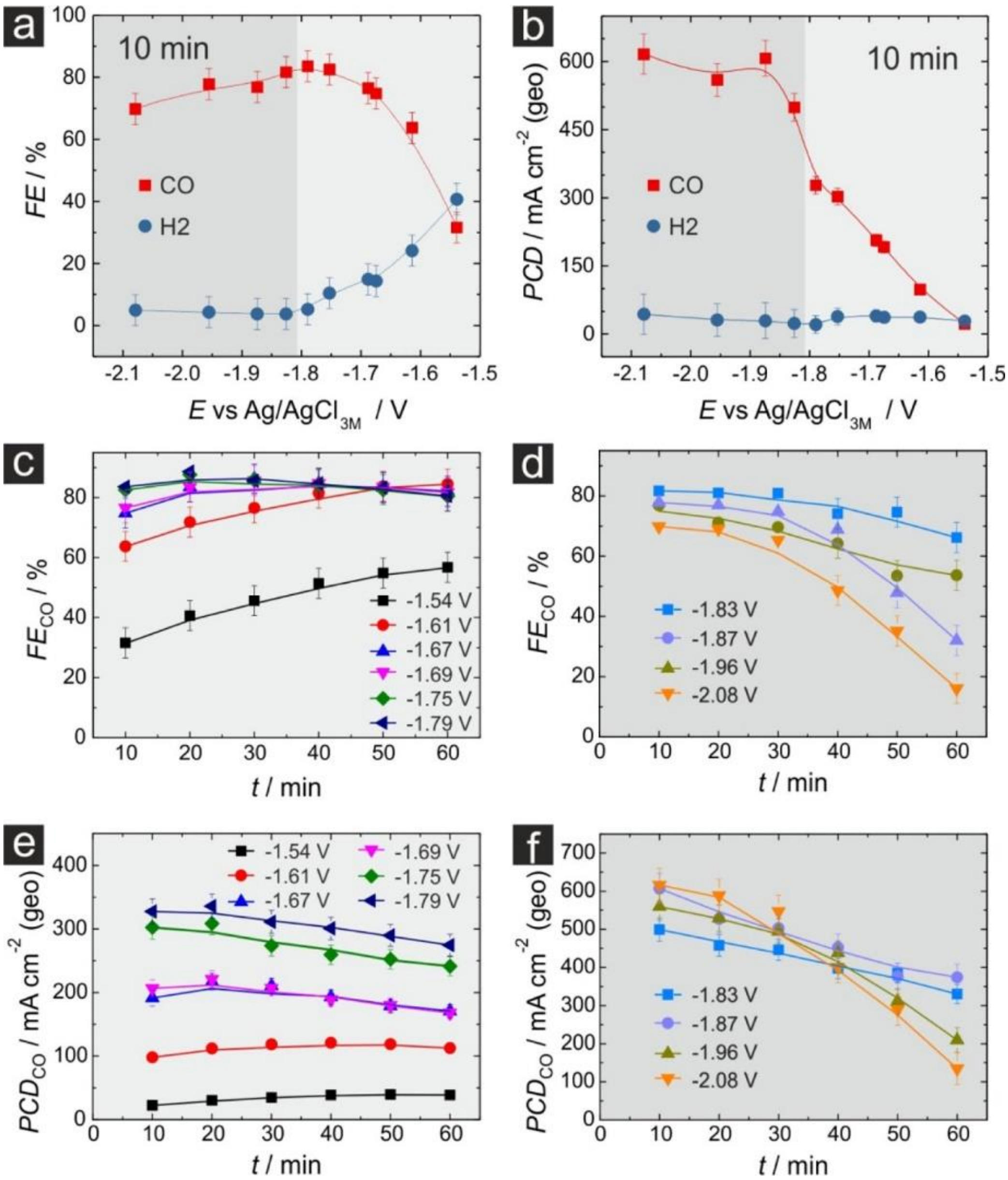

Figure 2.8. Potential-dependent FEs a) and PCDs b) of the gaseous products obtained from CO_2RR on the gas-fed Ag NCs – GDEs 10 min after beginning CO_2 electrolysis. Time evolution of the FE_{CO} at c) mild (−1.5 V > E > −1.8 V) and d) high applied potentials (−1.83 V > E > −2.1 V). Corresponding time evolution of the PCD_{CO} at mild e) and high f) applied potentials. All experiments were carried out using 2 M KOH in the anolyte compartment. The solid lines in all panels are visual guides to show the trends. The experimental error was accounted for using ±5% error bars. Reprinted with permission from *ACS Catal.* 2020, 10, 21, 13096–13108. Copyright 2020 American Chemical Society.

IL-SEM was employed to characterize the morphological changes of the Ag NCs before and after the CO_2RR experiments; see Figure 2.9a-d. Independently of the applied overpotential, no detachment of the Ag NCs was observed. Effects similar to those observed with Ag-NCs in an aqueous environment (H-type cell) with glassy carbon as support were detected; see Figure 2.5a-b. The nanocubes are also deactivated after the pre-electrolysis SEM imaging when they are supported on a GDL. EDX mapping of the Ag NCs after the CO_2RR, shown in Figure 2.9e-f, further confirms no changes on the Ag NCs after the electrochemical process.

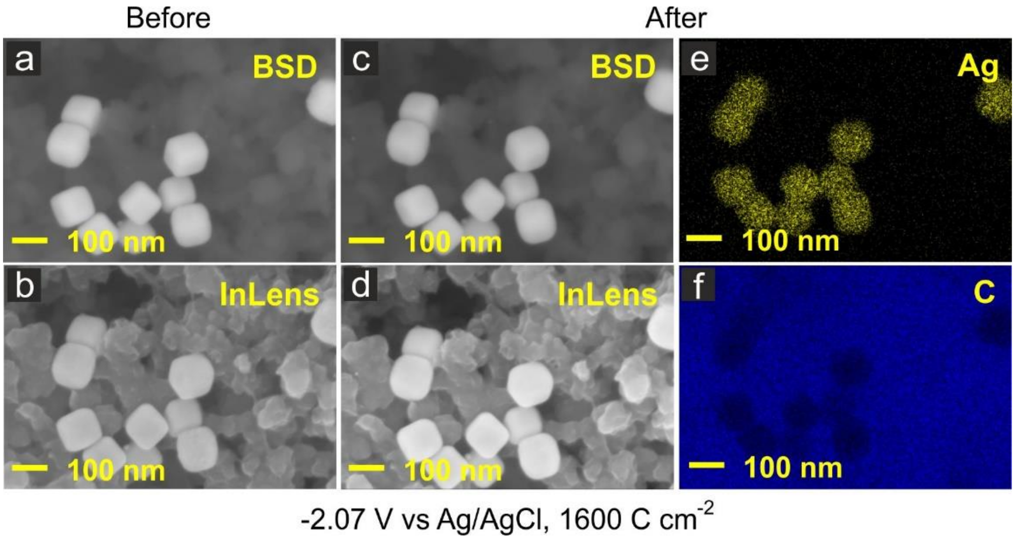

Figure 2.9. Representative IL–SEM images of Ag NCs – GDEs cathode surfaces before and after having conducted dedicated gas-fed CO_2RR experiments at −2.07 V for 32 min (1600 C cm^{-2}) captured using both BSD and InLens SE detectors. e-f) Elemental EDX mappings showing the spatial distribution of C (dark blue) and Ag (yellow) corresponding to the same sample location of c-d. CO_2RR experiments were carried out using 2 M KOH in the anolyte compartment. Readapted with permission from *ACS Catal.* 2020, 10, 21, 13096–13108. Copyright 2020 American Chemical Society.

Accordingly, the morphological changes of the Ag NCs were analyzed using post-electrolysis SEM and EDX mapping investigations. At low and mild applied overpotentials, no significant changes in the morphology of the Ag NCs were observed. However, at harsher cathodic conditions, the catalyst corrosion leads to the appearance of smaller Ag nanoparticles close to the Ag NCs (Figure 2.10).

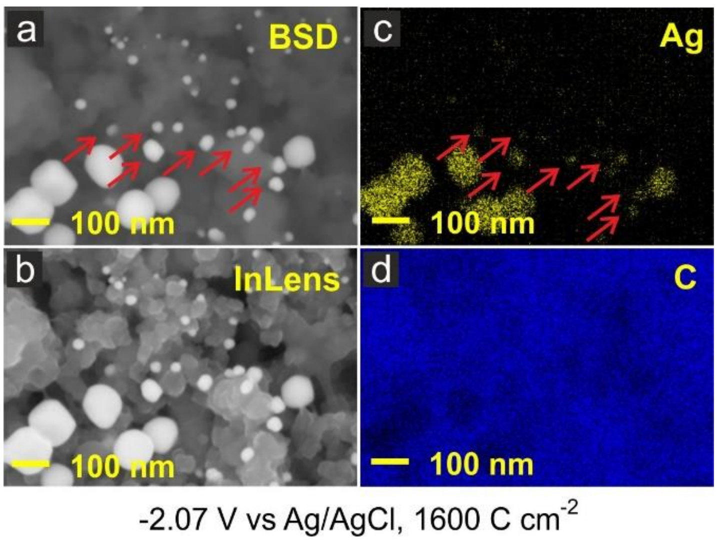

Figure 2.10. a-b) Representative SEM images of Ag NCs – GDEs cathode surfaces after conducting dedicated gas-fed CO_2RR experiments at −2.07 V for 32 min (1600 C cm^{-2}) captured using both BSD and InLens SE detectors. c-d) Elemental EDX mappings showing the spatial distribution of C (dark blue) and Ag (yellow), red arrows identify Ag nanoparticles formed upon cathodic corrosion of the Ag NCs catalyst. CO_2RR experiments were carried out using 2 M KOH in the anolyte compartment. Readapted with permission from *ACS Catal.* 2020, 10, 21, 13096–13108. Copyright 2020 American Chemical Society.

Complementary experiments were performed using a neutral environment (2 M $KHCO_3$) to determine whether the highly alkaline conditions were responsible for those changes. Results similar to those obtained from the more alkaline electrolyte were observed, except that with a less alkaline electrolyte, lower PCD_{CO}s were reached. This outcome would suggest that the system's failure could be attributed more to other factors, for example, electrode flooding (due to the degradation of the hydrophobic PTFE coating of the MPL) and salt precipitation on the GDE (confirmed using changes in the contact angle images for water droplets on the as-prepared Ag NCs – GDEs and after CO_2RR and by EDX-analysis), than to the catalyst morphological degradation. Reactions (17) and (18) indicate that the neutralization of CO_2 by OH^- leads to the formation of bicarbonate and carbonate salts that form the precipitate observed on the Ag – GDE after the CO_2RR.

Figure 2.11a presents optical images showing the typical appearance of the employed Ag NCs – GDEs at different experimental stages (as-received GDE, as prepared Ag NCs – GDE and Ag NCs – GDE after having sustained CO_2RR at −2.07 V for 32 min (1600 C cm^{-2}). The EDX spectra and mapping displayed in Figure 2.11b-c further support that potassium carbonate and bicarbonate precipitation on the catalyst-modified GDE surface and its periphery takes place under these drastic cathodic conditions.

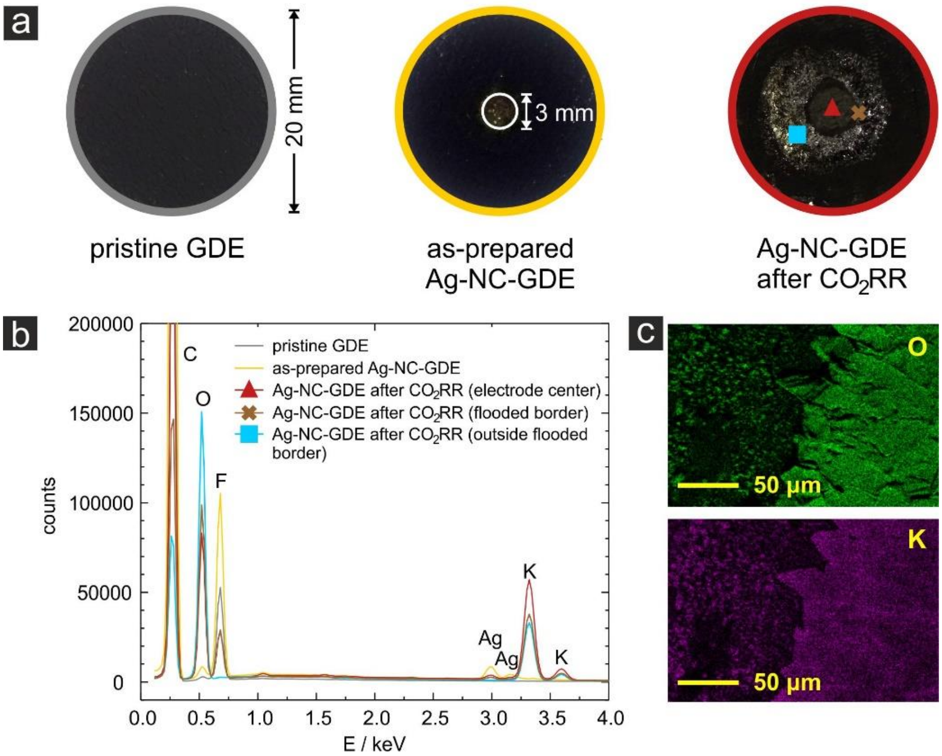

Figure 2.11. a) Representative optical micrographs of GDEs at different experimental stages. The white circle in the central part of the as-prepared Ag NCs – GDE shows the catalyst-modified area of the GDE that is in direct contact with the anion exchange membrane. The Ag NCs – GDE on the right was subjected to gas-fed CO_2RR at −2.07 V for 32 min (1600 C cm^{-2}) with 2 M KOH in the anolyte compartment. b) EDX spectra acquired on indicated locations along the sample surface of the Ag NCs – GDE after having been subjected to CO_2 electrolysis. c) EDX mapping of the flooded border region showing O and K intensities in green and magenta, respectively. Reprinted with permission from *ACS Catal.* 2020, 10, 21, 13096–13108. Copyright 2020 American Chemical Society.

Interesting results were observed regarding the spectrum of the products yielded in different kinds of electrolyzers. In the zero-gap flow cell, formate was detected post-electrolysis by ion-exchange chromatography over a large potential window when 2 M KOH and $KHCO_3$ were used as electrolytes; see Figure 2.12. Specifically, with the most alkaline electrolyte, a FE_{HCOO^-} of ~20.1% and a PCD_{HCOO^-} of ~148 mA cm^{-2} at −1.87 V vs. Ag/AgCl were quantified. A FE_{HCOO^-} of ~12.6% and a PCD_{HCOO^-} of ~72.7 mA at −2.14 V vs. Ag/AgCl were obtained with the weakly alkaline electrolyte. However, when the H-cell was used, formate was only detected at the highest applied overpotential with a FE_{HCOO^-} and PCD_{HCOO^-} of ~2.6% and 7.5 mA cm^{-2}, respectively. This result highlights that the acquired knowledge from experiments performed in H-type cells cannot be translated directly to more practical approaches (gas-flow cells) because the reaction environment plays an essential role in the product distribution of the CO_2RR.

As stated by some other recent works,[96, 149] CO_2RR investigations must be carried out using technical approaches that allow reaching conditions close to those needed for industrial applications. Further details of this research can be found in ***Publication 4***.

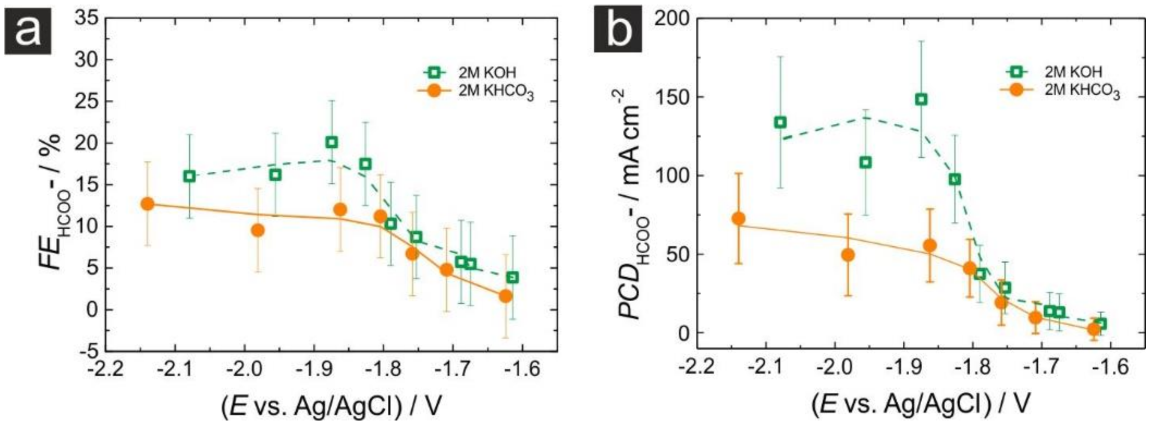

Figure 2.12. Potential dependence of a) FE_{HCOO^-} and b) PCD_{HCOO^-} on the gas-fed Ag NCs – GDEs after 60 min CO_2RR in highly (green) and weakly alkaline (yellow) anolytes, obtained by post-electrolysis ion chromatography analysis. The solid lines in all panels are visual guides to show the trends. The experimental error was accounted for using ± 5% error bars. Reprinted with permission from *ACS Catal*. 2020, 10, 21, 13096–13108. Copyright 2020 American Chemical Society.

1.6.2 Ag nanowires

The approach used to study the Ag NCs under controlled CO_2 mass transport conditions was extended to study other silver nanomaterials with a different shape, Ag nanowires (Ag NWs). Carbon monoxide and hydrogen were the only products detected by online gas chromatography (GC), and formate was detected post-electrolysis by ion-exchange chromatography. The FE and PCD of the products detected when using Ag NWs as a catalyst material for CO_2RR are shown in Figure 2.13.

The FE vs. applied overpotential can be subdivided into three regimes. H_2 is the main product at potentials > −1.55 V vs. Ag/Cl with FE values not lower than 40%, while the FE_{CO} does not exceed 35%. In the second regime, from −1.55 to −1.9 V vs. Ag/AgCl, the FE_{H_2} starts to decrease, and the CO selectivity reaches a maximum of ~70% at −1.75 V vs. Ag/AgCl. Formate appears as a by-product at potentials of <−1.6 V vs. Ag/AgCl and reaches a maximum of ~25% at −1.9 V vs. Ag/AgCl. In the third characteristic regime, the parasitic HER becomes dominant at potentials <−1.9 V vs. Ag/AgCl, and the FE_{CO} decays abruptly at the two most cathodic overpotentials.

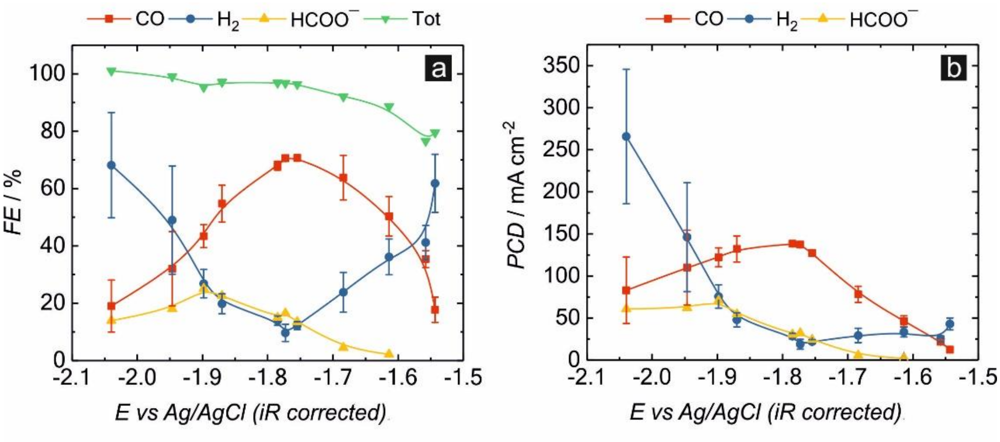

Figure 2.13. a) Product distribution of the CO_2RR carried out in the gas-fed flow cell using Ag NW-based electrocatalysts (85% wt.% Ag NW and 15% wt.% of C) at different applied potentials (2 M KOH electrolyte); each value for FE_{CO} and FE_{H_2} is the average from six measurements taken every 10 min for a total of 1 h of electrolysis. The error bars indicate the standard deviation; b) corresponding partial current densities (PCDs).

The corresponding PCDs at different applied overpotentials are displayed in Figure 2.13b. It is seen that by using GDE, a PCD_{CO} of ~130 mA cm^{-2} with a FE_{CO} of 70% was determined at ~−1.78 V vs. Ag/AgCl. Pre-screening experiments on the same catalyst, carried out in an H-cell arrangement, resulted in higher selectivity for CO, reaching more than 95% of FE. However, the corresponding PCD_{CO} did not reach more than ~16 mA cm^{-2} at ~−1.73 V vs. Ag/AgCl. CO_2RR current densities can be achieved by using gas diffusion electrodes that are ~1 order of magnitude higher than the ones typically observed in classical half-cell electrolysis measurements carried out in unstirred aqueous electrolytes.

The stability of the Ag NWs was analyzed employing IL-SEM and post-electrolysis SEM analysis after the CO_2RR at −1.88 V vs. Ag/AgCl (after 133 min, with an applied charge of 2,453C cm^{-2}), and neither severe morphological changes nor particle detachment were observed; see Figure 2.14. More specific information about these results is shown in ***Publication 5***.

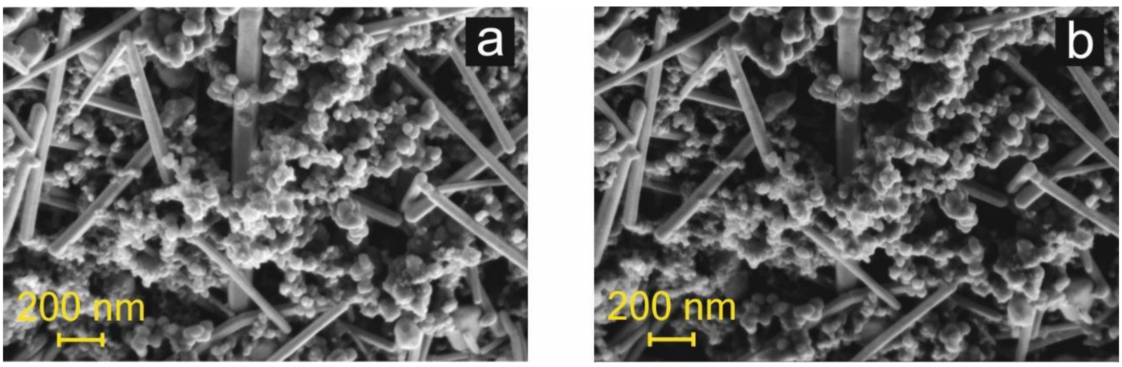

Figure 2.14. IL-SEM analysis of the Ag NW before (a) and after (b) performing the CO_2 electrolysis at −1.88 V vs. Ag/AgCl for 133 min (total charge density applied = 2,453C cm^{-2}).

3. Concluding remarks and future directions

The work presented in this PhD thesis was motivated by the urge to transfer the CO_2RR electrocatalyst screening from H-type cells where there are mass transport limitations due to low solubility and diffusivity of CO_2 in aqueous electrolytes to systems without those problems and where technical current densities can be reached. A successful method of overcoming CO_2 mass transport limitation during CO_2RR was proposed to tackle this situation. This method consists of using a zero-gap flow cell as a fast approach to investigate the electrocatalytic properties of silver nanomaterials under technical conditions. Two silver nanomaterials, nanocubes and nanowires, were identified as excellent catalysts for the electrochemical reduction of CO_2 in terms of selectivity and activity for CO production.

Especially, the system formed by the Ag NCs as electrocatalyst in the zero-gap flow cell exhibited remarkable CO_2 to CO conversion figures in terms of FE and PCD (FE_{CO} ~ 85% and PCD_{CO} ~ 625 mA cm^{-2}). Through a systematic study, it was possible to deconvolute the catalyst structural stability from the system performance stability. The system remains stable over time at mild applied potentials. The system stability fails at large cathodic potentials because of flooding of the electrode and salt precipitation rather than by catalyst degradation.

In addition, IL-SEM is a very useful technique to study the degradation of electrocatalysts upon CO_2RR; however, it should be used carefully when capped nanomaterials are used as an electrocatalyst because pre-electrolysis exposure to the electron beam can modify the catalyst surface and hide the actual catalyst changes after the electrochemical reaction.

The presence of surfactants on the electrocatalyst surface negatively affects the CO_2RR. Consequently, electrochemical looping was introduced as a surfactant removal method, which allowed us to observe the authentic response of unprotected Ag nanowires. This methodology was efficiently transferred to carbon-supported Ag nanowires and nanocubes and used with different electrode material supports.

CO_2RR performed in gas-flow cell reactors is one of the best options to bring CO_2RR closer to realistic operation conditions; however, many challenges must still be addressed.

First of all, it has been demonstrated that the catalyst knowledge acquired in H-type cells cannot be immediately transferred to gas-flow cells; even though some electrocatalysts have been identified as a scalable option through experiments with H-type cells, their performance must be verified in flow cells before scaling because the product distribution changes with different reaction environment.

The election of the gas-flow cell design and operation conditions has to be made according to the electrocatalyst and the different products that can be generated. Additionally, it is vital to investigate the interrelation of all the reactor components and operation parameters to achieve not just excellent selectivities and activities towards a specific product but also to maintain the system operation for long periods.

Flooding, loss of hydrophobicity and salt precipitation on the gas diffusion electrodes are common problems that hinder the system's stability. One possible solution is developing new gas diffusion electrodes and a better understanding through more advanced techniques like focused ion beam or X-ray tomography. Another solution may involve developing models that could explain and describe the effects happening there during and after the CO_2RR.

The anode-side reaction must also be studied because it plays a significant role when the energy efficiencies are calculated.

Because CO_2 reacts as a reactant and buffer in aqueous systems, it is fundamental to study the carbon balance in both the cathode and anode compartments of the reactor.

Last but not least, mass transport is the main factor determining the amount of product that can be produced in a specific reactor per unit of time. Hence, once an excellent electrocatalyst has been identified, electrolyzers with high rates of mass transport must be designed to take full advantage of the improvement of the catalytic activity.

4. References

1. J. T. Houghton, Y. Ding, D. J. Griggs, M. Noguer, P. J. van der Linden, X. Dai, K. Maskell, C. Johnson, *Climate change 2001: the scientific basis* (The Press Syndicate of the University of Cambridge, 2001).
2. S. Solomon, M. Manning, M. Marquis, D. Qin, *Climate change 2007-the physical science basis: Working group I contribution to the fourth assessment report of the IPCC* (Cambridge university press, 2007), vol. 4.
3. J. T. Kiehl, K. E. Trenberth, Earth's Annual Global Mean Energy Budget. *Bulletin of the American Meteorological Society* 78, 197-208 (1997).
4. I. Strangeways, The greenhouse effect: a closer look. *Weather* 66, 44-48 (2011).
5. G. R. North, J. A. Pyle, F. Zhang, *Encyclopedia of atmospheric sciences* (Elsevier, 2014), vol. 1.
6. A. Gettelman, R. B. Rood, Demystifying climate models. *A Users Guide to Earth System Models*, (2016).
7. J. S. Gaffney, N. A. Marley, *Chemistry of Environmental Systems: Fundamental Principles and Analytical Methods* (Wiley, 2019).
8. D. R. Lide, *CRC Handbook of Chemistry and Physics, 89th Edition* (Taylor & Francis, 2008).
9. M. A. Scibioh, B. Viswanathan, "Chapter 1 - CO_2 Conversion—Relevance and Importance" in *Carbon Dioxide to Chemicals and Fuels,* M. A. Scibioh, B. Viswanathan, Eds. (Elsevier, 2018), pp. 1-22.
10. J. T. Hardy, *Climate change: causes, effects, and solutions* (John Wiley & Sons, 2003).
11. D. P. Tans Trends in Atmospheric Carbon Dioxide. www.esrl.noaa.gov/gmd/ccgg/trends/ (accessed May 12, 2021)
12. D. R. Keeling Scripps CO_2 Program. https://scrippsco2.ucsd.edu/ (accessed July 1, 2020)
13. D. C. Harris, Charles David Keeling and the Story of Atmospheric CO_2 Measurements. *Analytical Chemistry* 82, 7865-7870 (2010).
14. K. Lindblom The Keeling Curve. https://www.acs.org/content/dam/acsorg/education/whatischemistry/landmarks/keeling-curve/2015-keeling-curve-landmark-booklet.pdf (accessed July 1, 2020)
15. NASA/GISS Global Temperature. https://climate.nasa.gov/vital-signs/global-temperature/ (accessed June 1, 2020)
16. NASA/GISS Arctic Sea Ice Minimum. https://climate.nasa.gov/vital-signs/arctic-sea-ice/ (accessed June 1, 2020)
17. D.-N. Y. D. N. Wiese, C. Boening, F. W. Landerer, M. M. Watkins. JPL GRACE and GRACE-FO Mascon Ocean, Ice, and Hydrology Equivalent Water Height JPL RL06 Version 02. Ver. 2. PO.DAAC, CA, USA. https://doi.org/10.5067/TEMSC-3MJ62. (accessed June 1, 2020)
18. B. Legresy Sea Level. https://research.csiro.au/slrwavescoast/sea-level/ (accessed June 1, 2020)
19. C. F. Ropelewski, P. A. Arkin, *Climate Analysis* (Cambridge University Press, 2019).
20. T. F. Stocker, I. P. o. C. C. W. G. I., *Climate Change 2013: The Physical Science Basis : Frequently Asked Questions* (Intergovernmental Panel on Climate Change, 2013).
21. V. Masson-Delmotte, P. Zhai, H.-O. Pörtner, D. Roberts, J. Skea, P.R. Shukla, A. Pirani, W. Moufouma-Okia, C. Péan, R. Pidcock, S. Connors, J.B.R. Matthews, Y. Chen, X. Zhou, M.I. Gomis, E. Lonnoy, T. Maycock, M. Tignor, and T. Waterfield, "Global Warming of 1.5°C" (2018).
22. S. Pacala, R. Socolow, Stabilization Wedges: Solving the Climate Problem for the Next 50 Years with Current Technologies. *Science* 305, 968-972 (2004).
23. M. Aresta, *Carbon Dioxide as Chemical Feedstock* (Wiley, 2010).
24. A. Rafiee, K. Rajab Khalilpour, D. Milani, M. Panahi, Trends in CO_2 conversion and utilization: A review from process systems perspective. *Journal of Environmental Chemical Engineering* 6, 5771-5794 (2018).
25. M. Aresta, A. Dibenedetto, A. Angelini, Catalysis for the Valorization of Exhaust Carbon: from CO_2 to Chemicals, Materials, and Fuels. Technological Use of CO_2. *Chemical Reviews* 114, 1709-1742 (2014).
26. M. Mikkelsen, M. Jørgensen, F. C. Krebs, The teraton challenge. A review of fixation and transformation of carbon dioxide. *Energy & Environmental Science* 3, 43-81 (2010).

27. Y. Zheng, B. Yu, J. Wang, J. Zhang, *Carbon Dioxide Reduction Through Advanced Conversion and Utilization Technologies* (CRC Press, 2019).
28. A. Rafiee, K. R. Khalilpour, D. Milani, "Chapter 8 - CO_2 Conversion and Utilization Pathways" in *Polygeneration with Polystorage for Chemical and Energy Hubs,* K. R. Khalilpour, Ed. (Academic Press, 2019), pp. 213-245.
29. C. Song, Global challenges and strategies for control, conversion and utilization of CO_2 for sustainable development involving energy, catalysis, adsorption and chemical processing. *Catalysis Today* 115, 2-32 (2006).
30. T. Haas, R. Krause, R. Weber, M. Demler, G. Schmid, Technical photosynthesis involving CO_2 electrolysis and fermentation. *Nature Catalysis* 1, 32-39 (2018).
31. Q. Zhu, Developments on CO_2-utilization technologies. *Clean Energy* 3, 85-100 (2019).
32. Change is in the air. *Nature Catalysis* 1, 93-93 (2018).
33. B. Rego de Vasconcelos, J.-M. Lavoie, Recent Advances in Power-to-X Technology for the Production of Fuels and Chemicals. *Frontiers in Chemistry* 7, (2019).
34. J. Durst, A. Rudnev, A. Dutta, Y. Fu, J. Herranz, V. Kaliginedi, A. Kuzume, A. A. Permyakova, Y. Paratcha, P. Broekmann, T. J. Schmidt, Electrochemical CO_2 Reduction; A Critical View on Fundamentals, Materials and Applications. *CHIMIA International Journal for Chemistry* 69, 769-776 (2015).
35. A. Dutta, A. Kuzume, M. Rahaman, S. Vesztergom, P. Broekmann, Monitoring the Chemical State of Catalysts for CO_2 Electroreduction: An In Operando Study. *ACS Catal.* 5, 7498-7502 (2015).
36. M. North, "Chapter 1 - What is CO_2? Thermodynamics, Basic Reactions and Physical Chemistry" in *Carbon Dioxide Utilisation,* P. Styring, E. A. Quadrelli, K. Armstrong, Eds. (Elsevier, Amsterdam, 2015), pp. 3-17.
37. A. J. Bard, G. Inzelt, F. Scholz, *Electrochemical dictionary* (Springer Science & Business Media, 2008).
38. A. J. Bard, L. R. Faulkner, *Electrochemical Methods: Fundamentals and Applications* (Wiley, 2000).
39. P. Atkins, J. d. Paula, *Physical Chemistry Thermodynamics, Structure, and Change* (WH Freeman and Company New York, 2014).
40. J. Qiao, Y. Liu, J. Zhang, *Electrochemical Reduction of Carbon Dioxide: Fundamentals and Technologies* (CRC Press, 2016).
41. M. Ciobanu, J. P. Wilburn, M. L. Krim, D. E. Cliffel, "1 - Fundamentals" in *Handbook of Electrochemistry,* C. G. Zoski, Ed. (Elsevier, Amsterdam, 2007), pp. 3-29.
42. K. P. Kuhl, E. R. Cave, D. N. Abram, T. F. Jaramillo, New insights into the electrochemical reduction of carbon dioxide on metallic copper surfaces. *Energy & Environmental Science* 5, 7050-7059 (2012).
43. J. Qiao, Y. Liu, F. Hong, J. Zhang, A review of catalysts for the electroreduction of carbon dioxide to produce low-carbon fuels. *Chemical Society Reviews* 43, 631-675 (2014).
44. I. Dincer, C. Zamfirescu, "Chapter 3 - Hydrogen Production by Electrical Energy" in *Sustainable Hydrogen Production,* I. Dincer, C. Zamfirescu, Eds. (Elsevier, 2016), pp. 99-161.
45. A. J. Bard, *Standard Potentials in Aqueous Solution* (CRC Press, 2017).
46. J. R. Bolton, Solar Fuels. *Science* 202, 705 (1978).
47. Y. Zheng, W. Zhang, Y. Li, J. Chen, B. Yu, J. Wang, L. Zhang, J. Zhang, Energy related CO_2 conversion and utilization: Advanced materials/nanomaterials, reaction mechanisms and technologies. *Nano Energy* 40, 512-539 (2017).
48. S. Garg, M. Li, A. Z. Weber, L. Ge, L. Li, V. Rudolph, G. Wang, T. E. Rufford, Advances and challenges in electrochemical CO_2 reduction processes: an engineering and design perspective looking beyond new catalyst materials. *Journal of Materials Chemistry A* 8, 1511-1544 (2020).
49. K. Zeng, D. Zhang, Recent progress in alkaline water electrolysis for hydrogen production and applications. *Progress in Energy and Combustion Science* 36, 307-326 (2010).
50. H. Guzmán, M. A. Farkhondehfal, K. R. Tolod, S. Hernández, N. Russo, "Chapter 11 - Photo/electrocatalytic hydrogen exploitation for CO_2 reduction toward solar fuels production" in *Solar Hydrogen Production,* F. Calise, M. D. D'Accadia, M. Santarelli, A. Lanzini, D. Ferrero, Eds. (Academic Press, 2019), pp. 365-418.
51. E. Gileadi, *Electrode Kinetics for Chemists, Chemical Engineers, and Materials Scientists* (VCH, 1993).
52. N. Eliaz, E. Gileadi, *Physical Electrochemistry: Fundamentals, Techniques, and Applications* (Wiley, 2018).

53. A. J. Martín, G. O. Larrazábal, J. Pérez-Ramírez, Towards sustainable fuels and chemicals through the electrochemical reduction of CO_2: lessons from water electrolysis. *Green Chemistry* 17, 5114-5130 (2015).
54. C. Costentin, K. Daasbjerg, M. Robert, "Chapter 2 Homogeneous Electrochemical Reduction of CO_2. From Homogeneous to Supported Systems" in *Carbon Dioxide Electrochemistry: Homogeneous and Heterogeneous Catalysis* (The Royal Society of Chemistry, 2021), pp. 67-97.
55. D. Pletcher, R. Greff, R. Peat, L. M. Peter, J. Robinson, "7 - Electrocatalysis" in *Instrumental Methods in Electrochemistry,* D. Pletcher, R. Greff, R. Peat, L. M. Peter, J. Robinson, Eds. (Woodhead Publishing, 2010), pp. 229-250.
56. S. Verma, U. O. Nwabara, P. J. A. Kenis, "Carbon-Based Electrodes and Catalysts for the Electroreduction of Carbon Dioxide (CO_2) to Value-Added Chemicals" in *Nanocarbons for Energy Conversion: Supramolecular Approaches,* N. Nakashima, Ed. (Springer International Publishing, Cham, 2019), pp. 219-251.
57. S. Nitopi, E. Bertheussen, S. B. Scott, X. Liu, A. K. Engstfeld, S. Horch, B. Seger, I. E. L. Stephens, K. Chan, C. Hahn, J. K. Nørskov, T. F. Jaramillo, I. Chorkendorff, Progress and Perspectives of Electrochemical CO_2 Reduction on Copper in Aqueous Electrolyte. *Chemical Reviews* 119, 7610-7672 (2019).
58. T. Ma, Q. Fan, H. Tao, Z. Han, M. Jia, Y. Gao, W. Ma, Z. Sun, Heterogeneous electrochemical CO_2 reduction using nonmetallic carbon-based catalysts: current status and future challenges. *Nanotechnology* 28, 472001 (2017).
59. T. Ma, Q. Fan, X. Li, J. Qiu, T. Wu, Z. Sun, Graphene-based materials for electrochemical CO_2 reduction. *Journal of CO2 Utilization* 30, 168-182 (2019).
60. J. Wu, T. Sharifi, Y. Gao, T. Zhang, P. M. Ajayan, Emerging Carbon-Based Heterogeneous Catalysts for Electrochemical Reduction of Carbon Dioxide into Value-Added Chemicals. *Advanced Materials* 31, 1804257 (2019).
61. D. T. Whipple, P. J. A. Kenis, Prospects of CO_2 Utilization via Direct Heterogeneous Electrochemical Reduction. *The Journal of Physical Chemistry Letters* 1, 3451-3458 (2010).
62. Q. Fan, M. Zhang, M. Jia, S. Liu, J. Qiu, Z. Sun, Electrochemical CO_2 reduction to C_{2+} species: Heterogeneous electrocatalysts, reaction pathways, and optimization strategies. *Materials Today Energy* 10, 280-301 (2018).
63. R. Küngas, Review—Electrochemical CO_2 Reduction for CO Production: Comparison of Low- and High-Temperature Electrolysis Technologies. *Journal of The Electrochemical Society* 167, 044508 (2020).
64. H.-R. M. Jhong, S. Ma, P. J. A. Kenis, Electrochemical conversion of CO_2 to useful chemicals: current status, remaining challenges, and future opportunities. *Current Opinion in Chemical Engineering* 2, 191-199 (2013).
65. Y. Hori, H. Wakebe, T. Tsukamoto, O. Koga, Electrocatalytic process of CO selectivity in electrochemical reduction of CO_2 at metal electrodes in aqueous media. *Electrochimica Acta* 39, 1833-1839 (1994).
66. H. Yoshio, K. Katsuhei, S. Shin, Production of CO and CH_4 in electrochemical reduction of CO_2 at metal electrodes in aqueous hydrogencarbonate solution. *Chemistry Letters* 14, 1695-1698 (1985).
67. Y. Hori, "CO_2 Reduction Using Electrochemical Approach" in *Solar to Chemical Energy Conversion: Theory and Application,* M. Sugiyama, K. Fujii, S. Nakamura, Eds. (Springer International Publishing, Cham, 2016), pp. 191-211.
68. H. Yoshio, K. Katsuhei, M. Akira, S. Shin, Production of methane and ethylene in electrochemical reduction of carbon dioxide at copper electrode in aqueous hydrogencarbonate solution. *Chemistry Letters* 15, 897-898 (1986).
69. M. Jitaru, D. A. Lowy, M. Toma, B. C. Toma, L. Oniciu, Electrochemical reduction of carbon dioxide on flat metallic cathodes. *Journal of Applied Electrochemistry* 27, 875-889 (1997).
70. M. B. Ross, P. De Luna, Y. Li, C.-T. Dinh, D. Kim, P. Yang, E. H. Sargent, Designing materials for electrochemical carbon dioxide recycling. *Nature Catalysis* 2, 648-658 (2019).
71. G. O. Larrazábal, A. J. Martín, J. Pérez-Ramírez, Building Blocks for High Performance in Electrocatalytic CO_2 Reduction: Materials, Optimization Strategies, and Device Engineering. *The Journal of Physical Chemistry Letters* 8, 3933-3944 (2017).

72. D. D. Zhu, J. L. Liu, S. Z. Qiao, Recent Advances in Inorganic Heterogeneous Electrocatalysts for Reduction of Carbon Dioxide. *Advanced Materials* 28, 3423-3452 (2016).
73. F. Yu, P. Wei, Y. Yang, Y. Chen, L. Guo, Z. Peng, Material design at nano and atomic scale for electrocatalytic CO_2 reduction. *Nano Materials Science* 1, 60-69 (2019).
74. Z. W. Seh, J. Kibsgaard, C. F. Dickens, I. Chorkendorff, J. K. Nørskov, T. F. Jaramillo, Combining theory and experiment in electrocatalysis: Insights into materials design. *Science* 355, eaad4998 (2017).
75. B. Khezri, A. C. Fisher, M. Pumera, CO_2 reduction: the quest for electrocatalytic materials. *Journal of Materials Chemistry A* 5, 8230-8246 (2017).
76. S. Kattel, W. Yu, X. Yang, B. Yan, Y. Huang, W. Wan, P. Liu, J. G. Chen, CO_2 Hydrogenation over Oxide-Supported PtCo Catalysts: The Role of the Oxide Support in Determining the Product Selectivity. *Angew. Chem. Int. Ed.* 55, 7968-7973 (2016).
77. K. S. Exner, Activity-Stability Volcano Plots for Material Optimization in Electrocatalysis. *ChemCatChem* 11, 3234-3241 (2019).
78. K. P. Kuhl, T. Hatsukade, E. R. Cave, D. N. Abram, J. Kibsgaard, T. F. Jaramillo, Electrocatalytic Conversion of Carbon Dioxide to Methane and Methanol on Transition Metal Surfaces. *Journal of the American Chemical Society* 136, 14107-14113 (2014).
79. E. L. Clark, A. T. Bell, "Chapter 3 Heterogeneous Electrochemical CO_2 Reduction" in *Carbon Dioxide Electrochemistry: Homogeneous and Heterogeneous Catalysis* (The Royal Society of Chemistry, 2021), pp. 98-150.
80. J. T. Feaster, C. Shi, E. R. Cave, T. Hatsukade, D. N. Abram, K. P. Kuhl, C. Hahn, J. K. Nørskov, T. F. Jaramillo, Understanding Selectivity for the Electrochemical Reduction of Carbon Dioxide to Formic Acid and Carbon Monoxide on Metal Electrodes. *ACS Catal.* 7, 4822-4827 (2017).
81. L. Zhang, Z.-J. Zhao, J. Gong, Nanostructured Materials for Heterogeneous Electrocatalytic CO_2 Reduction and their Related Reaction Mechanisms. *Angew. Chem. Int. Ed.* 56, 11326-11353 (2017).
82. Z. Sun, T. Ma, H. Tao, Q. Fan, B. Han, Fundamentals and Challenges of Electrochemical CO_2 Reduction Using Two-Dimensional Materials. *Chem* 3, 560-587 (2017).
83. C. Xie, Z. Niu, D. Kim, M. Li, P. Yang, Surface and Interface Control in Nanoparticle Catalysis. *Chemical Reviews* 120, 1184-1249 (2020).
84. A. Dutta, I. Zelocualtecatl Montiel, K. Kiran, A. Rieder, V. Grozovski, L. Gut, P. Broekmann, A Tandem ($Bi_2O_3 \rightarrow Bi_{met}$) Catalyst for Highly Efficient ec-CO_2 Conversion into Formate: Operando Raman Spectroscopic Evidence for a Reaction Pathway Change. *ACS Catal.* 11, 4988-5003 (2021).
85. M. R. Singh, E. L. Clark, A. T. Bell, Effects of electrolyte, catalyst, and membrane composition and operating conditions on the performance of solar-driven electrochemical reduction of carbon dioxide. *Physical Chemistry Chemical Physics* 17, 18924-18936 (2015).
86. C.-T. Dinh, T. Burdyny, M. G. Kibria, A. Seifitokaldani, C. M. Gabardo, F. P. García de Arquer, A. Kiani, J. P. Edwards, P. De Luna, O. S. Bushuyev, C. Zou, R. Quintero-Bermudez, Y. Pang, D. Sinton, E. H. Sargent, CO_2 electroreduction to ethylene via hydroxide-mediated copper catalysis at an abrupt interface. *Science* 360, 783-787 (2018).
87. M. Liu, Y. Pang, B. Zhang, P. De Luna, O. Voznyy, J. Xu, X. Zheng, C. T. Dinh, F. Fan, C. Cao, F. P. G. de Arquer, T. S. Safaei, A. Mepham, A. Klinkova, E. Kumacheva, T. Filleter, D. Sinton, S. O. Kelley, E. H. Sargent, Enhanced electrocatalytic CO_2 reduction via field-induced reagent concentration. *Nature* 537, 382-386 (2016).
88. M. Jouny, W. Luc, F. Jiao, High-rate electroreduction of carbon monoxide to multi-carbon products. *Nature Catalysis* 1, 748-755 (2018).
89. M. G. Kibria, J. P. Edwards, C. M. Gabardo, C.-T. Dinh, A. Seifitokaldani, D. Sinton, E. H. Sargent, Electrochemical CO_2 Reduction into Chemical Feedstocks: From Mechanistic Electrocatalysis Models to System Design. *Advanced Materials* 31, 1807166 (2019).
90. S. Verma, X. Lu, S. Ma, R. I. Masel, P. J. A. Kenis, The effect of electrolyte composition on the electroreduction of CO_2 to CO on Ag based gas diffusion electrodes. *Physical Chemistry Chemical Physics* 18, 7075-7084 (2016).
91. M. König, J. Vaes, E. Klemm, D. Pant, Solvents and Supporting Electrolytes in the Electrocatalytic Reduction of CO_2. *iScience* 19, 135-160 (2019).
92. M. Moura de Salles Pupo, R. Kortlever, Electrolyte Effects on the Electrochemical Reduction of CO_2. *ChemPhysChem* 20, 2926-2935 (2019).

93. A. V. Rudnev, Y.-C. Fu, I. Gjuroski, F. Stricker, J. Furrer, N. Kovács, S. Vesztergom, P. Broekmann, Transport Matters: Boosting CO_2 Electroreduction in Mixtures of [BMIm][BF_4]/Water by Enhanced Diffusion. *ChemPhysChem* 18, 3153-3162 (2017).
94. R. Kas, K. Yang, D. Bohra, R. Kortlever, T. Burdyny, W. A. Smith, Electrochemical CO_2 reduction on nanostructured metal electrodes: fact or defect? *Chemical Science* 11, 1738-1749 (2020).
95. B. A. Zhang, C. Costentin, D. G. Nocera, On the Conversion Efficiency of CO_2 Electroreduction on Gold. *Joule* 3, 1565-1568 (2019).
96. T. Burdyny, W. A. Smith, CO_2 reduction on gas-diffusion electrodes and why catalytic performance must be assessed at commercially-relevant conditions. *Energy & Environmental Science* 12, 1442-1453 (2019).
97. J. Resasco, A. T. Bell, Electrocatalytic CO_2 Reduction to Fuels: Progress and Opportunities. *Trends in Chemistry* 2, 825-836 (2020).
98. L.-C. Weng, A. T. Bell, A. Z. Weber, Modeling gas-diffusion electrodes for CO_2 reduction. *Physical Chemistry Chemical Physics* 20, 16973-16984 (2018).
99. M. Ma, E. L. Clark, K. T. Therkildsen, S. Dalsgaard, I. Chorkendorff, B. Seger, Insights into the carbon balance for CO_2 electroreduction on Cu using gas diffusion electrode reactor designs. *Energy & Environmental Science* 13, 977-985 (2020).
100. S. Hernández, M. Amin Farkhondehfal, F. Sastre, M. Makkee, G. Saracco, N. Russo, Syngas production from electrochemical reduction of CO_2: current status and prospective implementation. *Green Chemistry* 19, 2326-2346 (2017).
101. A. V. Rudnev, "Online Chromatographic Detection" in *Encyclopedia of Interfacial Chemistry,* K. Wandelt, Ed. (Elsevier, Oxford, 2018), pp. 321-325.
102. G. Hilt, Basic Strategies and Types of Applications in Organic Electrochemistry. *ChemElectroChem* 7, 395-405 (2020).
103. P. Westbroek, "1 - Fundamentals of electrochemistry" in *Analytical Electrochemistry in Textiles,* P. Westbroek, G. Priniotakis, P. Kiekens, Eds. (Woodhead Publishing, 2005), pp. 3-36.
104. B. Endrődi, G. Bencsik, F. Darvas, R. Jones, K. Rajeshwar, C. Janáky, Continuous-flow electroreduction of carbon dioxide. *Progress in Energy and Combustion Science* 62, 133-154 (2017).
105. S. Liang, N. Altaf, L. Huang, Y. Gao, Q. Wang, Electrolytic cell design for electrochemical CO_2 reduction. *Journal of CO2 Utilization* 35, 90-105 (2020).
106. S. Hernandez-Aldave, E. Andreoli, Fundamentals of Gas Diffusion Electrodes and Electrolysers for Carbon Dioxide Utilisation: Challenges and Opportunities. *Catalysts* 10, (2020).
107. H. Ju, G. Kaur, A. P. Kulkarni, S. Giddey, Challenges and trends in developing technology for electrochemically reducing CO_2 in solid polymer electrolyte membrane reactors. *Journal of CO2 Utilization* 32, 178-186 (2019).
108. D. M. Weekes, D. A. Salvatore, A. Reyes, A. Huang, C. P. Berlinguette, Electrolytic CO_2 Reduction in a Flow Cell. *Accounts of Chemical Research* 51, 910-918 (2018).
109. K. Liu, W. A. Smith, T. Burdyny, Introductory Guide to Assembling and Operating Gas Diffusion Electrodes for Electrochemical CO_2 Reduction. *ACS Energy Letters* 4, 639-643 (2019).
110. R. Lin, J. Guo, X. Li, P. Patel, A. Seifitokaldani, Electrochemical Reactors for CO_2 Conversion. *Catalysts* 10, 473 (2020).
111. M. Goldman, E. W. Lees, P. L. Prieto, B. A. W. Mowbray, D. M. Weekes, A. Reyes, T. Li, D. A. Salvatore, W. A. Smith, C. P. Berlinguette, "Chapter 10 Electrochemical Reactors" in *Carbon Dioxide Electrochemistry: Homogeneous and Heterogeneous Catalysis* (The Royal Society of Chemistry, 2021), pp. 408-432.
112. L. Fan, C. Xia, F. Yang, J. Wang, H. Wang, Y. Lu, Strategies in catalysts and electrolyzer design for electrochemical CO_2 reduction toward C_{2+} products. *Science Advances* 6, eaay3111 (2020).
113. D. Higgins, C. Hahn, C. Xiang, T. F. Jaramillo, A. Z. Weber, Gas-Diffusion Electrodes for Carbon Dioxide Reduction: A New Paradigm. *ACS Energy Letters* 4, 317-324 (2019).
114. S. Malkhandi, B. S. Yeo, Electrochemical conversion of carbon dioxide to high value chemicals using gas-diffusion electrodes. *Current Opinion in Chemical Engineering* 26, 112-121 (2019).
115. H. Rabiee, L. Ge, X. Zhang, S. Hu, M. Li, Z. Yuan, Gas diffusion electrodes (GDEs) for electrochemical reduction of carbon dioxide, carbon monoxide, and dinitrogen to value-added products: a review. *Energy & Environmental Science* 14, 1959-2008 (2021).

116. O. G. Sánchez, Y. Y. Birdja, M. Bulut, J. Vaes, T. Breugelmans, D. Pant, Recent advances in industrial CO_2 electroreduction. *Current Opinion in Green and Sustainable Chemistry* 16, 47-56 (2019).
117. T. N. Nguyen, C.-T. Dinh, Gas diffusion electrode design for electrochemical carbon dioxide reduction. *Chemical Society Reviews* 49, 7488-7504 (2020).
118. U. O. Nwabara, E. R. Cofell, S. Verma, E. Negro, P. J. A. Kenis, Durable Cathodes and Electrolyzers for the Efficient Aqueous Electrochemical Reduction of CO_2. *ChemSusChem* 13, 855-875 (2020).
119. Y. C. Li, D. Zhou, Z. Yan, R. H. Gonçalves, D. A. Salvatore, C. P. Berlinguette, T. E. Mallouk, Electrolysis of CO_2 to Syngas in Bipolar Membrane-Based Electrochemical Cells. *ACS Energy Letters* 1, 1149-1153 (2016).
120. D. A. Salvatore, D. M. Weekes, J. He, K. E. Dettelbach, Y. C. Li, T. E. Mallouk, C. P. Berlinguette, Electrolysis of Gaseous CO_2 to CO in a Flow Cell with a Bipolar Membrane. *ACS Energy Letters* 3, 149-154 (2018).
121. C. M. Gabardo, A. Seifitokaldani, J. P. Edwards, C.-T. Dinh, T. Burdyny, M. G. Kibria, C. P. O'Brien, E. H. Sargent, D. Sinton, Combined high alkalinity and pressurization enable efficient CO_2 electroreduction to CO. *Energy & Environmental Science* 11, 2531-2539 (2018).
122. B. Kim, S. Ma, H.-R. Molly Jhong, P. J. A. Kenis, Influence of dilute feed and pH on electrochemical reduction of CO_2 to CO on Ag in a continuous flow electrolyzer. *Electrochimica Acta* 166, 271-276 (2015).
123. A. S. Varela, The importance of pH in controlling the selectivity of the electrochemical CO_2 reduction. *Current Opinion in Green and Sustainable Chemistry* 26, 100371 (2020).
124. C.-T. Dinh, F. P. García de Arquer, D. Sinton, E. H. Sargent, High Rate, Selective, and Stable Electroreduction of CO_2 to CO in Basic and Neutral Media. *ACS Energy Letters* 3, 2835-2840 (2018).
125. S. C. Perry, P.-k. Leung, L. Wang, C. Ponce de León, Developments on carbon dioxide reduction: Their promise, achievements, and challenges. *Current Opinion in Electrochemistry* 20, 88-98 (2020).
126. M. E. Leonard, L. E. Clarke, A. Forner-Cuenca, S. M. Brown, F. R. Brushett, Investigating Electrode Flooding in a Flowing Electrolyte, Gas-Fed Carbon Dioxide Electrolyzer. *ChemSusChem* 13, 400-411 (2020).
127. P. Jeanty, C. Scherer, E. Magori, K. Wiesner-Fleischer, O. Hinrichsen, M. Fleischer, Upscaling and continuous operation of electrochemical CO_2 to CO conversion in aqueous solutions on silver gas diffusion electrodes. *Journal of CO2 Utilization* 24, 454-462 (2018).
128. D. T. Whipple, E. C. Finke, P. J. A. Kenis, Microfluidic Reactor for the Electrochemical Reduction of Carbon Dioxide: The Effect of pH. *Electrochemical and Solid-State Letters* 13, B109 (2010).
129. S. Ma , Y. Lan , G. M. J. Perez, S. Moniri, P. J. A. Kenis Silver Supported on Titania as an Active Catalyst for Electrochemical Carbon Dioxide Reduction. *ChemSusChem* 7, 866-874 (2014).
130. S. Ma, M. Sadakiyo, R. Luo, M. Heima, M. Yamauchi, P. J. A. Kenis, One-step electrosynthesis of ethylene and ethanol from CO_2 in an alkaline electrolyzer. *Journal of Power Sources* 301, 219-228 (2016).
131. T. T. H. Hoang, S. Verma, S. Ma, T. T. Fister, J. Timoshenko, A. I. Frenkel, P. J. A. Kenis, A. A. Gewirth, Nanoporous Copper–Silver Alloys by Additive-Controlled Electrodeposition for the Selective Electroreduction of CO_2 to Ethylene and Ethanol. *Journal of the American Chemical Society* 140, 5791-5797 (2018).
132. S. Verma, B. Kim, H.-R. M. Jhong, S. Ma, P. J. A. Kenis, A Gross-Margin Model for Defining Technoeconomic Benchmarks in the Electroreduction of CO_2. *ChemSusChem* 9, 1972-1979 (2016).
133. M. Jouny, W. Luc, F. Jiao, General Techno-Economic Analysis of CO_2 Electrolysis Systems. *Industrial & Engineering Chemistry Research* 57, 2165-2177 (2018).
134. B. R. C. Marc Koper "Electrochemical CO_2 reduction" in Research needs towards sustainable production of fuels and chemicals (Energy X). https://www.energy-x.eu/research-needs-report/ (accessed July 1, 2020)
135. R. Krause, D. Reinisch, C. Reller, H. Eckert, D. Hartmann, D. Taroata, K. Wiesner-Fleischer, A. Bulan, A. Lueken, G. Schmid, Industrial Application Aspects of the Electrochemical Reduction of CO_2 to CO in Aqueous Electrolyte. *Chemie Ingenieur Technik* 92, 53-61 (2020).
136. A. Senocrate, C. Battaglia, Electrochemical CO_2 reduction at room temperature: Status and perspectives. *Journal of Energy Storage* 36, 102373 (2021).

137. S. Ma, R. Luo, J. I. Gold, A. Z. Yu, B. Kim, P. J. A. Kenis, Carbon nanotube containing Ag catalyst layers for efficient and selective reduction of carbon dioxide. *Journal of Materials Chemistry A* 4, 8573-8578 (2016).
138. S. S. Bhargava, F. Proietto, D. Azmoodeh, E. R. Cofell, D. A. Henckel, S. Verma, C. J. Brooks, A. A. Gewirth, P. J. A. Kenis, System Design Rules for Intensifying the Electrochemical Reduction of CO_2 to CO on Ag Nanoparticles. *ChemElectroChem* 7, 2001-2011 (2020).
139. M. d. J. Gálvez-Vázquez, P. Moreno-García, H. Guo, Y. Hou, A. Dutta, S. R. Waldvogel, P. Broekmann, Leaded Bronze Alloy as a Catalyst for the Electroreduction of CO_2. *ChemElectroChem* 6, 2324-2330 (2019).
140. N. Han, P. Ding, L. He, Y. Li, Y. Li, Promises of Main Group Metal–Based Nanostructured Materials for Electrochemical CO_2 Reduction to Formate. *Advanced Energy Materials* 10, 1902338 (2020).
141. M. Arenz, A. Zana, Fuel cell catalyst degradation: Identical location electron microscopy and related methods. *Nano Energy* 29, 299-313 (2016).
142. K. J. J. Mayrhofer, J. C. Meier, S. J. Ashton, G. K. H. Wiberg, F. Kraus, M. Hanzlik, M. Arenz, Fuel cell catalyst degradation on the nanoscale. *Electrochemistry Communications* 10, 1144-1147 (2008).
143. M. Inaba, A. W. Jensen, G. W. Sievers, M. Escudero-Escribano, A. Zana, M. Arenz, Benchmarking high surface area electrocatalysts in a gas diffusion electrode: measurement of oxygen reduction activities under realistic conditions. *Energy & Environmental Science* 11, 988-994 (2018).
144. G. K. H. Wiberg, M. Fleige, M. Arenz, Gas diffusion electrode setup for catalyst testing in concentrated phosphoric acid at elevated temperatures. *Review of Scientific Instruments* 86, 024102 (2015).
145. G. W. Sievers, A. W. Jensen, V. Brüser, M. Arenz, M. Escudero-Escribano, Sputtered Platinum Thin-films for Oxygen Reduction in Gas Diffusion Electrodes: A Model System for Studies under Realistic Reaction Conditions. *Surfaces* 2, 336-348 (2019).
146. A. Zana, G. K. H. Wiberg, Y.-J. Deng, T. Østergaard, J. Rossmeisl, M. Arenz, Accessing the Inaccessible: Analyzing the Oxygen Reduction Reaction in the Diffusion Limit. *ACS Applied Materials & Interfaces* 9, 38176-38180 (2017).
147. S. Alinejad, J. Quinson, J. Schröder, J. J. K. Kirkensgaard, M. Arenz, Carbon-Supported Platinum Electrocatalysts Probed in a Gas Diffusion Setup with Alkaline Environment: How Particle Size and Mesoscopic Environment Influence the Degradation Mechanism. *ACS Catal.* 10, 13040-13049 (2020).
148. S. Alinejad, M. Inaba, J. Schröder, J. Du, J. Quinson, A. Zana, M. Arenz, Testing fuel cell catalysts under more realistic reaction conditions: accelerated stress tests in a gas diffusion electrode setup. *Journal of Physics: Energy* 2, 024003 (2020).
149. F. P. García de Arquer, C.-T. Dinh, A. Ozden, J. Wicks, C. McCallum, A. R. Kirmani, D.-H. Nam, C. Gabardo, A. Seifitokaldani, X. Wang, Y. C. Li, F. Li, J. Edwards, L. J. Richter, S. J. Thorpe, D. Sinton, E. H. Sargent, CO_2 electrolysis to multicarbon products at activities greater than 1 A cm^{-2}. *Science* 367, 661-666 (2020).

5. Publications

The following sections present the research works in which I participated during my PhD. The first five publications are the core of this project. The subsequent five publications consist of additional research works that I undertook concurrently.

1.1 Activation Matters: Hysteresis Effects During Electrochemical Looping of Colloidal Ag Nanowire (Ag-NW) Catalysts

Authors: Huifang Hu, Menglong Liu, Ying Kong, Nisarga Mysuru, Changzhe Sun, María de Jesús Gálvez-Vázquez, Ulrich Müller, Rolf Erni, Vitali Grozovski, Yuhui Hou, and Peter Broekmann

ACS Catal. **10** (15), 8503–8514 (2020), DOI: 10.1021/acscatal.0c02026

Highlights: In this work, Ag nanowires (produced via PVP-assisted polyol synthesis) are presented as an excellent catalyst for CO_2RR after being subjected to a surfactant removal electrochemical pre-treatment. The electrochemical pre-treatment is called electrochemical looping and consists of a sequence of potentiostatic CO_2 electrolysis experiments with defined starting, vertex, and ending potentials. The resulting product distribution undergoes a profound hysteresis in the forward and corresponding backward run of the electrochemical looping experiment, pointing to an effective PVP removal of the catalyst, which was further confirmed utilizing post-electrolysis XPS inspection.

Contributions: I was involved in the design of the experiments and the scientific discussion of the results.

ACS Catalysis

pubs.acs.org/acscatalysis Research Article

Activation Matters: Hysteresis Effects during Electrochemical Looping of Colloidal Ag Nanowire Catalysts

Huifang Hu, Menglong Liu, Ying Kong, Nisarga Mysuru, Changzhe Sun, María de Jesús Gálvez-Vázquez, Ulrich Müller, Rolf Erni, Vitali Grozovski, Yuhui Hou,* and Peter Broekmann*

Cite This: *ACS Catal.* 2020, 10, 8503–8514 Read Online

ACCESS | Metrics & More | Article Recommendations | Supporting Information

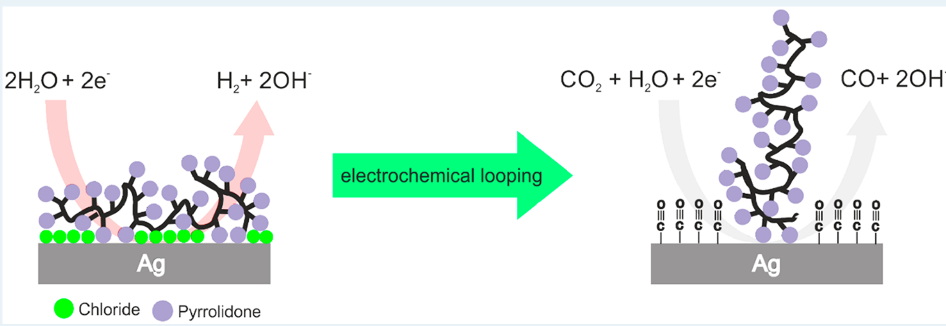

ABSTRACT: Colloidal electrocatalysts are commonly synthesized using organic capping agents (surfactants), which control the size distribution and shape of the resulting nano-objects and prevent them from agglomerating during and after synthesis. However, the presence of a surfactant shell on the catalyst is detrimental, as the resulting performance of the electrocatalyst depends crucially on the ability of reactants to access active surface sites. Techniques for postsynthesis deprotection are therefore mandatory for removing the capping agents from the otherwise blocked reactions sites without compromising the structural integrity of the nanocatalysts. Herein, we present silver nanowires (Ag-NWs)—produced via PVP-assisted polyol synthesis (PVP, polyvinylpyrrolidone)—as effective catalysts for the electrochemical CO_2 reduction reaction (*ec*-CO_2RR), which reach Faradaic efficiencies close to 100% for CO formation after deprotection by a so-called "electrochemical looping" (ec-l) pretreatment. Electrochemical looping refers to a sequence of potentiostatic CO_2 electrolysis experiments that exhibit well-defined starting (E_{start}), vertex (E_{vertex}), and end (E_{end}) potentials. The resulting product distribution undergoes a profound hysteresis in the forward and corresponding backward run of the electrochemical looping experiment, thus pointing to an effective deprotection of the catalyst as made evident by postelectrolysis XPS inspection. These results can be considered as a prime example demonstrating the importance of the catalyst's "history" for the resulting *ec*-CO_2RR performance. These transient (non-steady-state) effects are crucial in particular for the initial stage of the CO_2 electrolysis reaction and for catalyst screening approaches carried out on the time scale of hours.

KEYWORDS: *CO_2 reduction reaction, silver nanowires, surfactant removal, catalyst deprotection, electrochemical looping*

INTRODUCTION

The conversion of environmentally harmful carbon dioxide (CO_2) into value-added products is one of the major intersectoral challenges that we currently face.[1] In this context, electrochemical approaches of CO_2 valorization deserve particular attention as they can utilize the "green" electric power—generated by renewables such as solar or wind energy—as energy input for the highly endergonic process of CO_2 electrolysis, thereby rendering the overall process more sustainable.[2−4] One of the main target products of the electrochemical CO_2 reduction reaction (hereafter referred to as *ec*-CO_2RR) is carbon monoxide (CO), which is currently produced on an industrial scale via the "Boudouard" reaction and reaches a yearly production volume of approximately 210 000 Mt.[5] CO is considered to be a valuable intermediate (current market price: ≈0.65 \$ kg^{-1})[5] and has the potential to be used as a reactant on a large scale (e.g., in the Fischer–Tropsch synthesis of aliphatic hydrocarbons [synthetic fuels] or alcohols).[6] Cost estimates suggest that the electrochemical coelectrolysis of water/CO_2 might indeed become competitive with more well-established routes of CO production.[5] The electrochemical production of CO via the coelectrolysis of water/CO_2 can be considered to be a versatile "synthesis module", which also can be coupled to other process units for

Received: May 6, 2020
Revised: June 26, 2020
Published: July 6, 2020

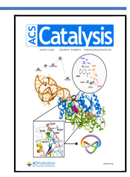

https://dx.doi.org/10.1021/acscatal.0c02026
ACS Catal. 2020, 10, 8503–8514

the production of valuable end products. A promising alternative to interlinking this process to the heterogeneous gas-phase Fischer−Tropsch reaction has recently been proposed by the Siemens/Evonik consortium[1,7] and couples the *ec*-CO_2RR (CO production; Siemens) to a biotechnological fermentation process (Evonik), thereby yielding fine chemicals such as butanol and hexanol as key intermediates for the production of specialty plastics.[7] The first test plant is expected to become operative in 2021[1] and thus demonstrates the enormous efforts that are currently underway to bring the *ec*-CO_2RR process from the lab to the market.[1]

Catalysts are essential for *ec*-CO_2RR, as they direct the electrolytic reaction toward the desired target product (e.g., CO). The pioneering work by Hori et al.[8−10] identified silver (Ag) as one of best (electro)catalysts, in addition to Au and Zn, which yielded CO with Faradaic efficiencies (FEs) that reached 81.5% (E = −1.14 V vs NHE).[8] In these early studies, catalyst screening was mainly based on the use of polycrystalline electrode materials as active catalysts (e.g., metal foils). However, substantial progress has been made during the last two decades in the development of tailored nanomaterials with an improved surface-to-volume ratio and well-defined shapes, the latter being important for the rational design of active surface sites.[11,12] In future, these nanomaterials have the potential to be used in gas diffusion electrodes (GDEs) as a key component of advanced gas-flow electrolyzer systems.[7,13−16] From a technical point of view, it is mandatory to use a gas-flow approach to reach the current densities that are targeted by industry (100 to 1000 mA cm^{-2}) to cover the capital and operating costs of these systems.[13,17,18] Typically, these nanomaterials are produced via colloidal synthesis, which also allows the process to be easily scaled up and which is considered to be a key perquisite for any industrial application. A wide range of particle morphologies can be obtained using this colloidal approach, ranging from spheres,[19] cubic shapes,[20] and triangular platelets (confined 2-D systems)[21] to 1-D nano-objects such as rods[19] and wires.[22−26] To rationally design these nano-objects, a multiparameter space needs to be considered, which includes but is not limited to (i) the reaction temperature, (ii) the convective transport of reactants (e.g., stirring speed), (iii) the ratio of reactants (e.g., metal ion precursor, reducing agent, etc.), (iv) reaction times, and (v) the injection speed of chemicals.[27−29] However, the most important aspect to consider is the action of the so-called surfactants and capping agents.[19,25,30] Their presence in the reaction medium crucially affects the nucleation and growth kinetics of the nano-objects and could even cause crystal growth to be anisotropic, which is required for the synthesis of metallic nanowires (NWs).[31] The physical origin of this anisotropic growth behavior is the preferential surfactant adsorption on certain surface facets (e.g., [100] textured), which reduces their growth rate relative to surfaces with different surface orientations (e.g., [111]).[30,32−35] In this sense, the role of the surfactants is a result of the steric blocking of surface sites that are active for the (e-less) metal deposition by selectively limiting the access of precursor metal ions in the liquid reaction medium to the emerging surface of the nanocrystals (NCs).[36] Note that not only the monomeric[11,37] or polymeric (e.g., polyvinylpyrrolidone, PVP[38]) organic surfactants need to be considered, but also anionic species (e.g., halides) that are added to the reaction media along with the metal precursors. These counteranions usually play a crucial role in the initial nucleation process of the nano-objects (concept of self-seeded growth[25,35]) and further tend to chemisorb on the emerging facets in an advanced stage of NC growth.[31]

While this facet-specific blocking by adsorbed surfactants is a mechanistic prerequisite for any anisotropic growth mode, it is highly detrimental to the desired (electro)catalytic performance of the nanocatalysts. As capping agents sterically block the access of reactants to the active catalyst sites during the electrocatalyzed reaction of interest,[37−40] various "soft" postsynthesis methods have been proposed to deprotect the "capped" nano-objects without compromising their structural integrity (e.g., loss of the shape, changes in size distribution, NP agglomeration, etc.). These deprotection techniques range from purely physical (e.g., thermal annealing[41,42] or exposure to light of particular wavelength and intensity[43,44]) to chemical treatments under nonreactive (e.g., "chemical" washing[38]) or reactive conditions (e.g., plasma treatment, the use of oxidizing or reducing agents, etc.).[37,38,44−51] Note that, under extremely drastic experimental conditions (e.g., thermal treatment at elevated temperatures), this type of catalyst pretreatment could lead to the loss of surface texture or to the agglomeration of nanoparticles.[52]

Also, electrochemical treatments (anodic or cathodic polarization) have successfully been applied to deprotect colloidal catalysts.[53−56] For example, Oezaslan et al.[54] reported on the efficient removal of a PVP capping shell from Pt nanocubes by applying an oxidative stressing protocol (electrochemical cycling up to +0.8 V vs reversible hydrogen electrode [RHE] in 0.1 M $HClO_4$), whereas the electrochemical deprotection failed under alkaline conditions. Also, the chemical nature of the capping agent (PVP versus oleylamine) has been shown to play a crucial role in the structural integrity of the nanocatalysts after electrochemical deprotection.[54]

So far, most studies on catalyst activation have considered only one single electrocatalytic reaction, (e.g., the oxygen reduction reaction [ORR],[53,54] the oxygen evolution reaction [OER], or the hydrogen evolution reaction [HER][37] etc.). For these single reactions, there are straightforward electrochemical descriptors and measuring approaches available to monitor the effectiveness of the applied deprotection technique (e.g., via the electrochemically active surface area [ECSA]), which is probed either by Faradaic or non-Faradaic processes. Their increase is directly proportional to the increase in the ECSA and is related to an overall improvement in the reaction rate.[37,40,49,53,54]

However, the situation is more complex when considering the *ec*-CO_2RR owing to the fact that the CO_2 electroreduction is necessarily superimposed on the parasitic HER when carried out in an aqueous reaction environment, which leads to a less-than-unity Faradaic efficiency of the *ec*-CO_2RR. Thus, the presence of the capping agents and the applied deprotection treatment affect not only the overall reaction rate (current density normalized to the geometric surface area) but also the resulting product distribution.

Herein, we present a comprehensive study on an approach to electrochemical catalyst activation (surfactant removal) that utilizes the *ec*-CO_2RR itself to achieve the desired catalyst deprotection. As the catalyst of choice, we applied silver nanowires (Ag-NWs) that were synthesized by a self-seeding polyol process using high-molecular-weight PVP as the capping agent.[24,27,32,57,58] The coelectrolysis of water/CO_2 that is performed over Ag catalysts yields only H_2 and CO as the reaction products.[8−10,59] In the present study, we sought to demonstrate that the formed CO acts as an excellent surfactant removal agent that is capable of deprotecting the Ag-NWs, thereby further self-accelerating the *ec*-CO_2RR at the expense of the parasitic HER and leading to CO efficiencies of nearly 100%. This PVP removal by "cathodic" electrode polarization complements the "oxidative" approach that was proposed by Oezaslan et al.[54]

■ EXPERIMENTAL SECTION

Catalyst Synthesis. Ag nanowires (Ag-NWs) were synthesized in a three-necked flask according to a modified protocol introduced by Jiu et al. and others.[24,27,32,57,58] For this purpose, 0.2 g of PVP (M_w = 1 300 000 g mol^{-1}, Sigma-Aldrich; see Figure 1) was dissolved at room temperature under magnetic agitation in 25 mL of ethylene glycol (EG, Sigma-Aldrich, 99.8%). Subsequently, 0.25 g of silver nitrate ($AgNO_3$, Sigma-Aldrich, ACS reagent, ≥99.8%) was added to the PVP containing EG, followed by the addition of a solution of 1.95 mg of $FeCl_3$ (Sigma-Aldrich, 97%) predissolved in 2 mL of EG, which serves as a solvent and reducing agent.[24,32,57,58] This mixture was then stirred for an additional 2 min before the three-necked flask containing the transparent EG solution was transferred to a preheated oil bath. This solution was kept at 130 °C for a total of 5 h. During the first hour, the solution was continuously stirred, while no magnetic agitation was applied during the last 4 h of the thermal treatment. The resulting Ag-NW precipitate was separated from the EG solvent by centrifugation at 4000 rpm for 10 min, followed by three repetitive washing/centrifugation treatments using a mixture of Milli-Q water and acetone (V_{water}:V_{aceton} = 2:1), ultimately yielding 24 mg of the Ag-NW catalyst (denoted "as-synthesized"). The Ag-NW powder was finally redispersed in 8 mL of isopropanol (BASF SE, assay ≥99.0%).

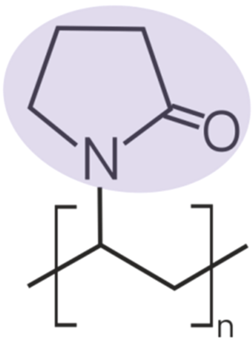

Figure 1. Polyvinylpyrrolidone (PVP) used as the capping agent for the Ag-NW synthesis. The pyrrolidone functionality attached to the linear aliphatic backbone is highlighted purple.

Electrode Preparation. After 30 min of sonication, 50 μL of the Ag-NW suspension was drop-cast onto a glassy carbon support electrode (A = 0.8 cm^{-2}, Alfa Aesar, 2 mm thickness).

For the sake of comparison, Ag-NW catalysts were also dispersed onto a technical carbon support. For this purpose, 12 mg of the as-prepared Ag-NWs was suspended in 15 mL of isopropanol, followed by 1 h of sonication. Technical carbon powder (12 mg, Vulcan XC 72R, Cabot) was dispersed in 15 mL of isopropanol, and this was also followed by 1 h of sonication. Both suspensions were subsequently mixed and homogenized by sonicating for 30 min. The resulting suspension was dried under vacuum conditions and yielded a carbon-supported (C-supported) Ag-NW catalyst powder. This powder was redispersed in 4 mL of isopropanol containing 400 μL of Nafion solution (Aldrich, 5 wt % dissolved in a mixture of lower aliphatic alcohols and water) and subjected to 30 min of sonication. Subsequently, 50 μL of the resulting ink was drop-cast onto the glassy carbon support electrode (see the aforementioned protocol).

Electrode Characterization. The morphologies of the Ag-NW films (nonsupported, C-supported) that were deposited on the glassy carbon support electrodes were characterized by means of scanning electron microscopy (Zeiss Gemini SEM450). Complementary white-light interferometry (ContourGT profilometer, Bruker) was applied to determine the thickness and roughness of the Ag-NW films. For the transmission electron microscopy (TEM) imaging and selective area electron diffraction, an FEI Titan Themis instrument was used with an accelerating voltage of 300 kV.

An X-ray photoelectron (XPS) inspection was performed on a Physical Electronics (PHI) Quantum 2000 scanning ESCA microprobe system using monochromated Al Kα radiation ($h\nu$ = 1486.7 eV). A hemispherical capacitor electron-energy analyzer, equipped with a channel plate and a position-sensitive detector, was operated under an electron takeoff angle of 45°. For the acquisition of the high-resolution Ag3*d*, Cl2*p* and N1*s* photoemission data, the analyzer was operated with a constant pass energy mode at 23.5 eV and an energy step width of 0.20 eV. The X-ray beam diameter was around 150 μm. The binding energy was calibrated using the Cu$2p_{3/2}$, Ag$3d_{5/2}$, and Au$4f_{7/2}$ emissions at 932.62, 368.21, and 83.96 eV, respectively, to within ±0.1 eV [see ISO 15472; 2010-05]. Built-in electron and argon ion neutralizers were applied in order to compensate for eventual surface charging effects. The base pressure of the XPS system was below 5 × 10^{-7} Pa. The XPS spectra were analyzed using the MultiPak 8.2B software package and were subjected to a Shirley background subtraction. The atomic concentrations were determined based on the corrected relative sensitivity factors that were provided by the manufacturer and normalized to 100 atom %. The uncertainty was estimated to be ca. 10%.

Electrochemical Experiments. For all electrochemical experiments, a potentiostat/galvanostat (Metrohm Autolab 302N) was used to control the potential, current density, and transferred charge. The electrolysis experiments were carried out using a custom-built, airtight glass-cell (H-type) as previously described (see Figure S1).[60−62] For the *iR* compensation, cell resistance was determined by means of impedance spectroscopy (FRA module, Autolab Nova). Hence, all potentials provided herein are *iR*-compensated to ~85% of the measured cell resistance.

The three-electrode arrangement used here consisted of a leakless Ag/$AgCl_{3M}$ electrode (Pine), a bright Pt-foil (15 mm × 5 mm), and the Ag-NW catalyst film (nonsupported, C-supported) serving as the reference, counter, and working electrodes, respectively.

For the sake of comparability, all potentials measured versus Ag/$AgCl_{3M}$ are referenced herein with respect to the reversible hydrogen electrode (RHE). The applied potentials (vs Ag/$AgCl_{3M}$) were converted to the RHE scale using the following equation:

$$E_{RHE}\,(V) = E_{Ag/AgCl(3M)}\,(V) + 0.210\ V + (0.059\ V \times pH)$$

Note that the anolyte and the catholyte were separated by a Nafion 117 membrane (Figure S1). This cell design also prevents the transfer of trace amounts of Pt ions from the anolyte to the catholyte when using Pt as the material for the counter electrode (see reference measurements presented in Figures S2−S5) as made evident by ICP-MS measurements

https://dx.doi.org/10.1021/acscatal.0c02026
ACS Catal. 2020, 10, 8503−8514

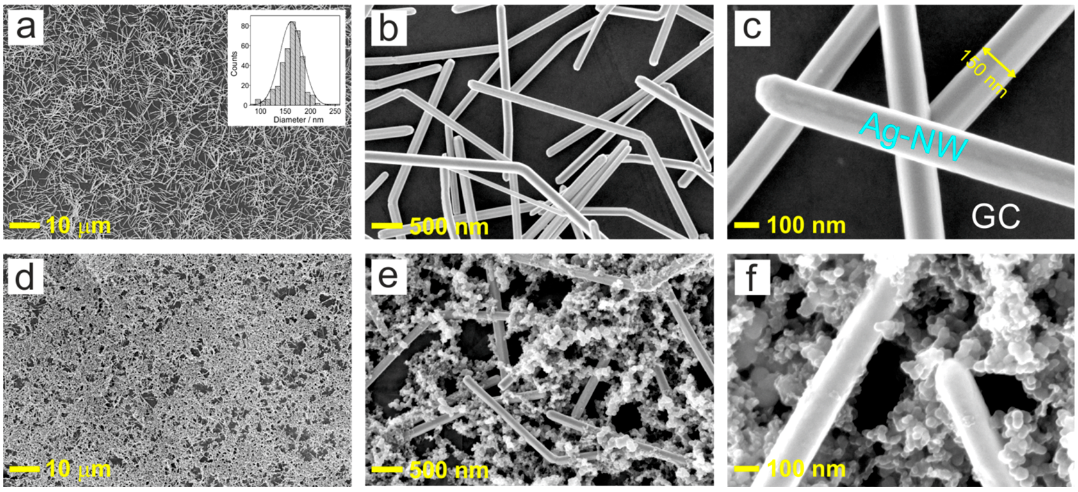

Figure 2. (a−c) Top-down SEM images of the Ag-NW film drop-cast on the glassy carbon (GC) support electrode; the inset in panel a shows a histogram representing the thickness distribution of the Ag-NWs. (d−f) Corresponding SEM images of the C-supported (Vulcan XC 72R) Ag-NWs drop-cast on the GC support electrode (for details, see the Experimental Section).

(NexION 2000 ICP-MS instrument, PerkinElmer). Also note that no change of the *ec*-CO_2RR product distribution is observed when exchanging the Pt counter electrode by Ir (see Figure S5).

Electrolysis experiments were carried out in 0.5 M $KHCO_3$ (ACS grade, Sigma-Aldrich) electrolyte solutions that were saturated with either Ar (blank) or CO_2 gas (99.999%, Carbagas). The pH of the CO_2- and Ar-saturated 0.5 M $KHCO_3$ was 7.5 and 8.9, respectively.

Technical details of the CO_2RR product analysis based on online gas-chromatography have been previously described.[60−62] A so-called single-catalyst approach was applied in order to demonstrate the pronounced hysteresis effects on the potential-dependent CO_2RR product distribution.[63] The same electrode was used for a defined sequence of potentiostatic electrolysis experiments, which differed in both the electrolysis time and the width of the potential window applied to the catalyst. In a further step a multicatalyst approach was applied,[63] in which a newly prepared (preconditioned) catalyst was used for each applied electrolysis potential to demonstrate the performance of the deprotected Ag-NW catalysts.

RESULTS AND DISCUSSION

Structural Characterization. Figure 2 displays top-down SEM images of the two types of Ag-NW catalysts used in this study. A three-dimensional network of randomly distributed and loosely packed Ag-NWs is formed after drop-casting the Ag-NW suspension on the glassy carbon support electrode (Figure 2a−c). Complementary white light interferometry reveals a homogeneous layer of Ag-NWs on the glassy carbon electrode with a root-mean-square (RMS) roughness and film thickness of 76 and 885 nm, respectively (Figure S6a−c). On the nm length scale the network of Ag-NWs shows a more inhomogeneous appearance. Note that the surface of the glassy carbon support remains visible in the top-down SEM inspection (Figure 2c). Therefore, the entirety of the Ag-NW film is, when exposed to the aqueous environment, likely to be wetted by the electrolyte down to the glassy carbon electrode. A statistical analysis of the SEM images reveals that the mean thickness of the Ag-NWs is approximately 162 nm (inset of Figure 2a), whereas they range in length from ca. 1 to several microns. According to the literature,[22,64,65] the Ag-NWs exhibit a 5-fold twinned face-centered cubic (fcc) structure with a preferential orientation along the (110) crystallographic direction. The sidewalls of the Ag-NWs consist of five (100) textured facets, whereas the pentagonal apex of the Ag-NW is (111) terminated. These hexagonal facets represent the actual growth front in the Ag-NW synthesis in which the monovalent Ag^+ precursor ions are reduced and added to the developing nanowire. The origin of this highly anisotropic metal growth is the chemisorption of additives/surfactants (e.g., chloride and PVP), which is supposed to be weaker on the (111) facets, thereby rendering them more active for the e-less metal deposition than the (100) facets.[58] The latter experience a steric blocking by the more strongly chemisorbed surfactants.[22,66]

One drawback of the Ag-NW model catalyst drop-cast on the glassy carbon support is the potential loss of catalyst material during extended electrolysis, in particular when the electrolysis reaction involves massive gas evolution, e.g., by the parasitic HER that is inevitably superimposed on the CO_2RR in an aqueous environment.[43] This loss of catalyst material is a result of the weak adhesion of the NW layer to the glassy carbon support electrode and the loose packing of the Ag-NWs inside the catalyst film. One possible approach to circumventing this structural degradation is based on the mechanical stabilization of the NW film. This stabilization can be achieved by the use of a technical carbon support (e.g., Vulcan) in combination with a Nafion binder, thereby substantially improving both the adhesion of the catalyst film to the glassy carbon support and the cohesion inside the film.[67] Figure 2d−f depicts the corresponding top-down SEM images of the C-supported Ag-NW catalysts that were drop-cast on the glassy carbon electrode, demonstrating that individual Ag-NWs were embedded in the highly porous carbon support. However, one possible drawback of this approach could be an increase in the contribution of the porous carbon material to the resulting product distribution in the form of an increase in the parasitic HER (see the discussion of Figure 6 below). An alternative approach to catalyst stabilization, which is based on a so-called photonic curing, has recently been introduced by Hou et al.[43] This treatment induces a local melting and subsequent solidifying of the NWs at their points of contact. Photonically

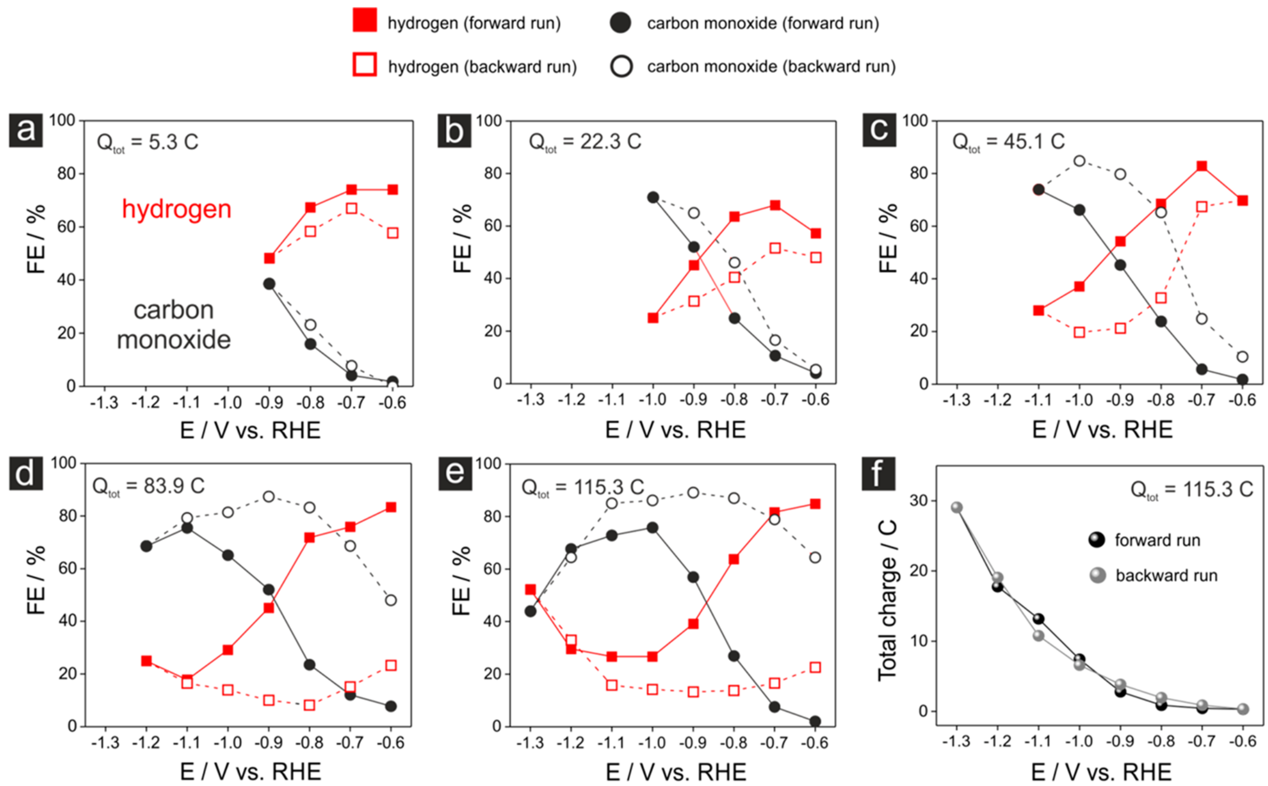

Figure 3. (a−e) Hysteresis effects appearing in the forward and backward runs of the electrochemical looping experiments (40 min duration at each potential) carried out over Ag-NW catalysts (see Figure 2a−c) in CO_2-saturated 0.5 M $KHCO_3$ (single catalyst approach); the total cathodic charges transferred during the "electrochemical looping" are indicated. (f) Graph showing the total integrated charge corresponding to the electrolysis experiments shown in panel e.

cured freestanding films of metallic nanowires were demonstrated to resist even massive gas-evolution reactions without any indication of structural degradation.[43]

Electrochemical Activation of Ag-NW Catalysts by Electrochemical Looping. The working hypothesis, which was to be verified in the following experiments, is that the surfactants (i.e., chloride and PVP) on the Ag surface of the deposited nanowires severely affect the product distribution of *ec*-CO_2RR and undergo substantial alterations over the course of the performed coelectrolysis reaction. An efficient catalyst activation that is induced by the electrolysis reaction itself can be deduced from the pronounced hysteresis characteristics observed in the potential-dependent product distribution, which is displayed in Figure 3 as Faradaic efficiency versus applied potential (FE versus E) plots (Table S1). These dedicated electrolysis experiments are referred to as "electrochemical looping" (ec-l), in which the applied electrolysis potentials of the individual 40 min long electrolyses were changed in a stepwise manner from a fixed starting point of E_{start} = −0.6 V vs RHE to a variable "lower" vertex potential (E_{vertex}) that ranged from −0.9 V vs RHE to −1.3 V vs RHE (Figure 3a−e). The electrolysis loop is closed through the corresponding backward run of electrolysis experiments and ends at the initial starting potential (E_{start} = E_{end}). The main products of the electrolysis in the CO_2-saturated 0.5 M $KHCO_3$ aqueous solution are CO (black circles, Figure 3) and H_2 (red squares, Figure 3). The filled and nonfilled circles/squares refer to FE values, which correspond to the forward and the corresponding backward runs of the electrochemical looping campaigns. As long as the lower vertex potential remains larger than or equal to −0.9 V vs RHE (Figure 3a), only a marginal deviation is observed in the product distributions of the forward and the corresponding backward electrolysis runs (see also Figure S7). However, a minor trend toward increased CO efficiencies (decreased H_2 efficiencies) can be observed in the backward run. This positive trend of catalyst activation is continued by further shifting the lower vertex potential to more negative applied electrolysis potentials (Figure 3b−e). When extending the potential window of electrolysis to a vertex potential of E_{vertex} = −1.3 V vs RHE, CO efficiencies of >80% were achieved in the corresponding backward electrolysis run (Table S1e). In general, the shape of the product distribution in the FE versus E plot in Figure 3e displays an anticorrelated change in the FE values for CO and H_2, which exceed the maximum in CO efficiency (minimum in H_2 efficiency) at potentials between −1.0 and −1.1 V vs RHE (forward run). Interestingly, a more extended plateau of approximately 300 mV develops in the corresponding backward run in the potential range from −1.1 V to −0.8 V vs RHE, ultimately reaching CO efficiencies of >80%.

The FE_{CO} and FE_{H_2} values were the most substantially impacted by electrochemical looping at medium and low overpotentials (>−1.1 V vs RHE), whereas only minor differences were observed in the forward and backward runs for applied electrolysis potentials of < −1.2 V vs RHE (Figure 3e). In Figure 3e, the differences in potentials between the backward and the respective forward runs were ΔFE_{CO} = +10.3% at −1.0 V vs RHE, ΔFE_{CO} = +32.2% at −0.9 V vs RHE, ΔFE_{CO} = +60.0% at −0.8 V vs RHE, ΔFE_{CO} = +71.4% at −0.7 V vs RHE, and ΔFE_{CO} = +62.3% at −0.6 V vs RHE (see also Figure S7).

The absence of any substantial improvement in the FE_{CO} values at the lowest applied electrolysis potentials (<−1.2 V vs

https://dx.doi.org/10.1021/acscatal.0c02026
ACS Catal. 2020, 10, 8503−8514

RHE) can be rationalized by the onset of CO_2 mass transfer limitations, where the CO_2 concentration in the diffusion boundary layer is expected to drop down to zero as a result of increased CO_2RR rates (partial current densities). Therefore, the continuous activation of the catalyst material under CO_2 mass transport conditions does not lead to a further shift in the product distribution toward CO. The characteristics of pronounced hysteresis that can be seen at medium and low overpotentials (Figure 3a−e, Figure S7) are clearly indicative of the "activation" of the Ag-NW catalyst toward CO formation, which is mediated by the applied electrochemical looping. This is demonstrated in the first experiment, as the coelectrolysis of water/CO_2 resulted in the desired deprotection (chemical cleaning) of the catalyst surface. It can be hypothesized that changes in the composition of the surface are responsible for the observed changes in the potential-dependent product distribution (see discussion on the XPS analysis below). A first control experiment proving that the improved FE values (Figure 3) indeed originate from an effective removal of the surfactants from the catalyst surface during the ec-l treatment is shown in Figure S8. It compares the CO efficiencies of a Ag-NW catalyst before and after the ec-l treatment with the ones of a Ag-foil (GoodFellow, 99.95%, 0.25 mm thickness) which serves as a model system for a surfactant-free Ag catalyst. As expected, the CO efficiencies do not change by the ec-l treatment in the case of the Ag-foil catalyst. Further, we exclude severe structural or morphological changes of the Ag-NW catalyst in the course of the ec-l treatment as origin of the observed catalyst activation (see combined SEM and TEM analysis in Figure S9). It should be noted that, based on our experimental results, it cannot be concluded on which active sites of the Ag-NWs the HER and the *ec*-CO_2RR take place. Both experimental and theoretical studies on Ag single crystals strongly suggest, however, that defects, in particular steps and kink sites, are substantially more active toward CO formation than the planar (100) and (111) facets.[10,68]

One important aspect of this activation effect, discussed herein, is displayed in Figure 3f. In principle, the total (integrated) charge that is transferred at each electrolysis potential—derived from the respective j versus t (40 min) plots—exponentially increases with the applied overpotential (Table S2a). However, when comparing the forward and backward runs, it becomes obvious that the total transferred charge for a given electrolysis potential does not substantially change during electrochemical looping. This implies that only the product distribution (ratio of FE_{CO} and FE_{H_2} values) is altered by this treatment, whereas the total current density normalized to the geometric surface area (total transferred charge) remains unaffected. This is an important distinction between the current study and previous studies on catalyst activation processes in which only a single electrocatalytic reaction needs to be considered (e.g., ORR,[40,49,55] OER,[49] or HER[37]) and where increased reaction rates directly correlate with an increase of the electrochemically active surface area (ECSA).[53,54]

In order to elaborate on which experimental factors contribute to the observed change in the product distribution (e.g., nature of the formed CO_2RR reaction product, applied vertex potential [E_{vertex}], current density [j], electrolysis time, total transferred charge [Q], etc.), an extra electrochemical looping experiment was carried out in an Ar-saturated (CO_2-free) 0.5 M $KHCO_3$ electrolyte (pH = 8.9) while applying the full range of electrolysis potentials (E_{vertex} = −1.3 V vs RHE). This approach excludes CO as a reaction product and exclusively produces H_2 during electrolysis. Note that bicarbonate can be neglected as a reactant when Ag is used as the catalyst.[63] Figure 4a compares the total transferred

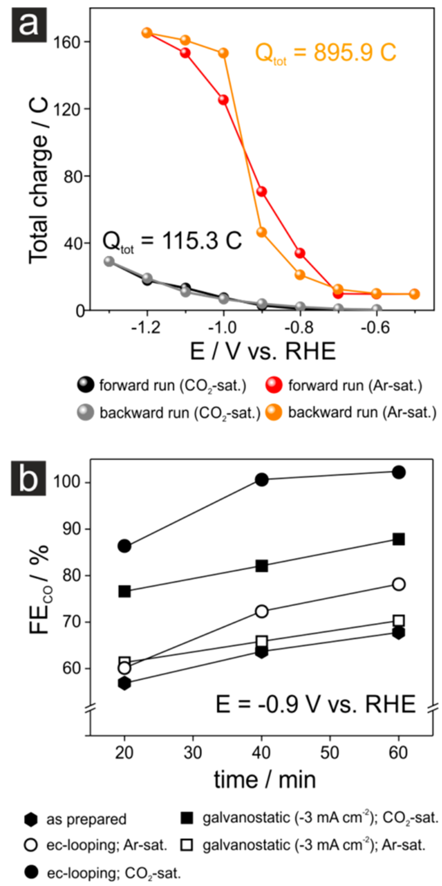

Figure 4. (a) Integrated cathodic charges of potentiostatic electrolysis reactions carried out in Ar- and CO_2-saturated 0.5 M $KHCO_3$ electrolytes (electrochemical looping). (b) Time-resolved FE_{CO} values derived from electrolysis reactions carried out at −0.9 V vs RHE after applying various activation protocols (for details, see the text).

charges of the chemical looping experiments carried out in the Ar- and the CO_2-saturated electrolyte (Table S2a). The most obvious difference is in the total amount of transferred charges, which is substantially higher for the CO_2-free case in which the HER is the only electrolytic reaction. These results suggest that the HER is not effectively hindered by the presence of the surfactants (chloride and PVP). Note that the expected exponential increase in the total transferred charge passes into a plateau regime at applied potentials that are more negative than −1.1 V vs RHE (Figure 4a). This particular feature originates from the partial blocking of the electrode surface by hydrogen bubbles, which appear at elevated current densities (surface area change under massive gas evolution; see Figure S10).

It becomes obvious from Figure 4a that the total transferred charges are substantially lower when CO is formed as one of the reaction products. This is likely owing to a high surface concentration of formed and temporarily adsorbed *CO (the asterisk represents an adsorption state), which therefore effectively sterically blocks those surface sites on the Ag-NW that are active toward the competing HER. It is clear that the chemisorbed *CO acts as an efficient "suppressor" with regard to the HER.[63] The binding strength of *CO to the Ag catalyst is generally considered to be relatively low (i.e., in comparison to Cu),[69−71] thereby rationalizing the easy release of the formed *CO from the catalyst surface into the electrolyte phase (Figure 5). However, the *CO binding to the Ag-NW surface seems

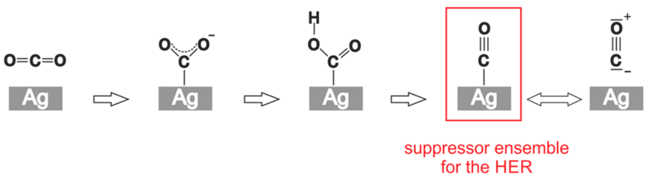

Figure 5. Reaction pathway of CO_2 conversion into CO on Ag catalysts; the strong suppressing action of the chemisorbed CO with regard to the HER is highlighted.

sufficiently high to remove surfactants from the surface during the water/CO_2 coelectrolysis reaction, which can be considered to be the origin of the profound hysteresis effects observed in the FE vs E plots (Figure 3). It can be hypothesized that the observed Ag-NW deprotection is based on the "chemisorptive displacement" of the surfactants by the *CO. The temporary presence of chemisorbed *CO on the Ag-catalyst surface has been previously demonstrated by operando vibrational (IR or Raman) spectroscopy.[72−74] The massive gas evolution (by H_2 and CO)—which is in agreement with the water/CO_2 coelectrolysis at high current densities (Figure S10)—can be considered to be an additional beneficial effect and facilitates the convectional transport of the released PVP from the catalyst surface into the bulk of the electrolyte phase. This process therefore prevents the readsorption of the PVP on the catalyst surface. Possible surfactant readsorption phenomena have been identified by Oezaslan et al.[54] as one possible drawback of the oxidative approach to PVP removal.

The chemical nature of the electrolysis product (H_2 or CO) that is formed during the electrochemical looping clearly plays a vital role in the deprotection of the desired catalyst. This effect can be denoted as surfactant removal by "chemical" cleaning. This has been demonstrated by additional experiments for CO_2 electrolysis, which were performed at a constant electrolysis potential of $E = -0.9$ V vs RHE using Ag-NW catalysts that had been subjected to a full chemical looping pretreatment ($E_{vertex} = -1.3$ V vs RHE) in either the CO_2-saturated or the CO_2-free (Ar-saturated) electrolyte. Figure 4b illustrates the time-dependent evolution of the FE_{CO} values of the electrolyses that were carried out in the CO_2-saturated electrolyte following the ec-l treatments.

For the purpose of comparison, the resulting FE_{CO} values of the as-prepared samples are also provided. It is clear that maximal CO efficiency (close to 100%) is most rapidly attained when preconditioning in the CO_2-saturated electrolyte, whereas the one subjected to the chemical looping in the Ar-saturated electrolyte demonstrates only marginally improved CO efficiencies. This finding is striking, as substantially higher charges were transferred, and higher current densities were applied during chemical looping in the Ar-saturated electrolyte ($Q_{tot} = 895.9$ C, $j_{max} = -85.6$ mA cm^{-2} at $E = -1.3$ V vs RHE, see Table S2a) in comparison to the CO_2-saturated electrolyte ($Q_{tot} = 115.3$ C, $j_{max} = -15.1$ mA cm^{-2} at $E = -1.3$ V vs RHE). The total charge is obviously not the key parameter for the activation of the catalyst. Furthermore, the massive gas evolution alone does not seem to be sufficient for the deprotection of the Ag-NW catalyst (see also Figure S11).

As the total transferred charges were different in both electrochemical looping treatments (Ar- and CO_2-saturated electrolytes, Figure 4a) it is hard to compare them directly. We therefore applied two addition pretreatment techniques on the Ag-NW catalysts—based on galvanostatic electrolyses at $j = -3$ mA cm^{-2}—in both CO_2-saturated and CO_2-free electrolytes. In these cases, the total transferred charge was normalized to $Q_{tot} = 115.3$ C, which allowed for a direct comparison to the electrochemical looping experiment performed in the CO_2-containing electrolyte (Figure 4a). The corresponding FE_{CO} data for the subsequent CO_2 electrolysis reactions at -0.9 V vs RHE are included in the plot in Figure 4b. Again, pretreatment in the CO_2-free electrolyte yields poor FE_{CO} values in the actual CO_2 electrolysis experiment. Interestingly, the electrochemical looping in the CO_2-saturated electrolyte is superior to the galvanostatic pretreatment at $j = -3$ mA cm^{-2} that was carried out in the same electrolyte. Obviously, the applied electrolysis potential and the electrolysis time are important factors for the efficiency of surfactant removal (see also Figures S12 and S13, and discussion of the XPS data below). It can be assumed that, due to the increased CO partial current densities, the CO surface coverage is higher at lower vertex potentials thus also rationalizing the observed potential dependence of the hysteresis characteristics (Figure 3).

An extra electrolysis experiment was carried out using C-supported Ag-NWs as the catalyst in order to demonstrate that the electrochemical looping works when the NWs are embedded into a technical carbon matrix. The result of this ec-l experiment exhibits the desired trend of improved FE_{CO} values in the corresponding backward run of the electrochemical looping (Figure 6), in which values of $FE_{CO} = 90.7\%$

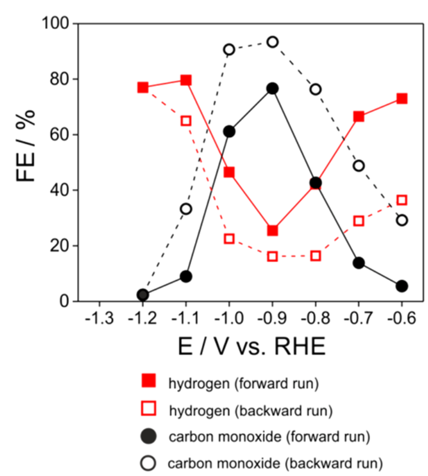

Figure 6. Activation of C-supported Ag-NW catalysts (see Figure 2d–f).

and $FE_{CO} = 93.4\%$ at $E = -1.0$ V and -0.9 V vs RHE were achieved. However, the HER is still dominating the product distribution at lower applied overpotentials in contrast to the nonsupported Ag-NWs (see Figure 3e). This observation can be rationalized by an effect that is mediated by the high surface area of the C-support, which is active toward the HER but not toward the CO_2RR. The increased FE_{H_2} values at the lowest overpotentials (Figure 6) are therefore the result of a surface

https://dx.doi.org/10.1021/acscatal.0c02026
ACS Catal. 2020, 10, 8503−8514

area effect of the component in the catalyst film, which is selective toward the HER (Vulcan and glassy carbon support electrode, see Figure S6d–f).

As the extended electrochemical looping (E_{vertex} = −1.3 V) was identified as the most effective pretreatment for the deprotection of the catalyst, a full set of additional electrolysis experiments were performed using a single catalyst approach[63] in which newly prepared and preconditioned catalyst (see Figures 2a–c and 3e) were used for 1 h long electrolysis experiments and applied potential. This approach guaranteed identical starting conditions for CO_2 electrolysis and minimized time-dependent changes on the selectivity of the CO_2RR products. Figure 7a represents the "true" potential-dependent

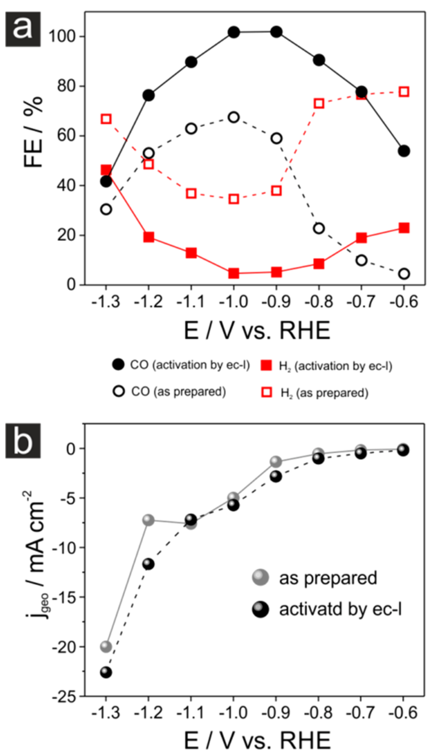

Figure 7. (a) *ec*-CO_2RR product distribution of 1 h lasting electrolysis experiments comparing the as prepared Ag-NW catalysts and those pretreated by an electrochemical looping (E_{vertex} = −1.3 V vs RHE, see Figure 3e). (b) Steady-state total current densities of the electrolysis experiments which correspond to the data in panel a.

product distribution of the Ag-NW catalyst after the successful deprotection of the Ag-NWs. For comparison purposes, the corresponding 1 h lasting *ec*-CO_2RR experiments of the as-prepared Ag-NW catalysts are also provided. CO efficiencies of ∼100% are obtained after the ec-l preconditioning (E_{vertex} = −1.3 V vs RHE) in the potential range between −1.0 and −1.1 V. These efficiencies are competitive in comparison to previously published data.[20,21,63,75] Table S6 provides a comprehensive overview of the relevant benchmark studies that have used Ag as the *ec*-CO_2RR catalyst material, while Figure 7b demonstrates again that only the product selectivity is changed by the ec-l treatment, and not the overall reaction rate. The total (steady-state) current densities remain largely unaffected by electrochemical looping.

XPS Analysis. Our analysis of the *ec*-CO_2RR product distribution (Figures 3 and 7a) clearly demonstrates an activation of the Ag-NW catalyst by the chemical looping but lacks deeper mechanistic insights into the chemical origin of the observed improved CO selectivity. Therefore, complementary XPS experiments were performed to provide information on the compositional changes of the catalyst surface. Figure 8a–c depicts spectra of the Ag3*d*, Cl2*p*, and N1*s* photoemissions that are representative of the as-prepared Ag-NW catalyst prior to its deprotection. These results demonstrate that both chloride and PVP are present on the surface of the as-prepared Ag-NWs, as indicated in the schematics of Figure 9. The performed electrolysis experiments clearly show that the HER does not effectively contribute to the deprotection of the desired catalyst (Figure 4b).

Figure 8d,e displays the integrated intensities of the N1*s* and Cl2*p* emissions normalized to the one of the respective Ag3*d* emissions. These data can be used to assess the effectiveness of the surfactant removal depending on the particular pretreatment protocol that is applied. Note that the (I_{Cl2p}:I_{Ag3d}) ratios are generally lower than the corresponding (I_{N1s}:I_{Ag3d}) values, irrespective of the applied pretreatment. One possible reason for this observation is that a layered structure of the surfactant shell was covering the Ag-NWs. Chloride is likely to be chemisorbed and would therefore be in direct contact with the Ag-NW surface.

These halide anions are considered to play a crucial role in the initial nucleation stage of Ag-NW formation (self-seeding via AgCl nuclei).[32] Furthermore, the (100) textured sidewalls of the Ag-NWs in particular exhibit a strong tendency toward specific chloride adsorption, which can result in a maximum (saturation) surface coverage of Θ = 0.5 ML (normalized to the number of surface atoms on the [100] surface) when a Ag(100)-c(2 × 2)-Cl surface ad-layer is formed.[76−78] The high-molecular-mass PVP polymer (M_w = 1 300 000 g mol^{-1}) presumably constitutes the outermost shell of the as deposited Ag-NW. A "coiling" of the linear PVP around the Ag-NW is discussed in the literature, where the pyrrolidone acts as the anchor group of the polymer backbone to free metallic sites on the surface (Ag–O or Ag–N coordination).[32] Considering the high molecular mass of the PVP, it is likely that hydrophobic effects lead to an enhanced PVP agglomeration on the Ag-NWs beyond monolayer coverages. This layered configuration of surfactants, as depicted in Figure 9 (left panel), could also contribute to the reduced intensity observed in the Cl2*p* emission of the chloride that accumulated at the "buried" interface.

The electrochemical activation treatments applied to the Ag-NW catalysts exhibit strong variations in the PVP removal efficiency. The treatments in which H_2 was the exclusive electrolysis product (protocols 2 and 3 in Figure 8d) were less effective, while those using postsynthesis deprotection approaches involving the formation of CO (protocol 4 and 5 in Figure 8d) were more effective. The optimal PVP removal characteristics that were observed for the electrochemical looping approach (E_{vertex} = −1.3 V vs RHE) are in full agreement with our electrolysis data (Figures 4b and 7a). The XPS results also confirm that the PVP (and its removal) is the main origin for the observed hysteresis effects in the product distribution (Figure 3).

Interestingly, all pretreatments that were applied herein led to the near-complete removal of the chemisorbed chloride (Figure 8e). The origin of the chloride removal is the potential-dependent electrostatic repulsion of the chloride anions at the negatively polarized electrode surface.

https://dx.doi.org/10.1021/acscatal.0c02026
ACS Catal. 2020, 10, 8503−8514

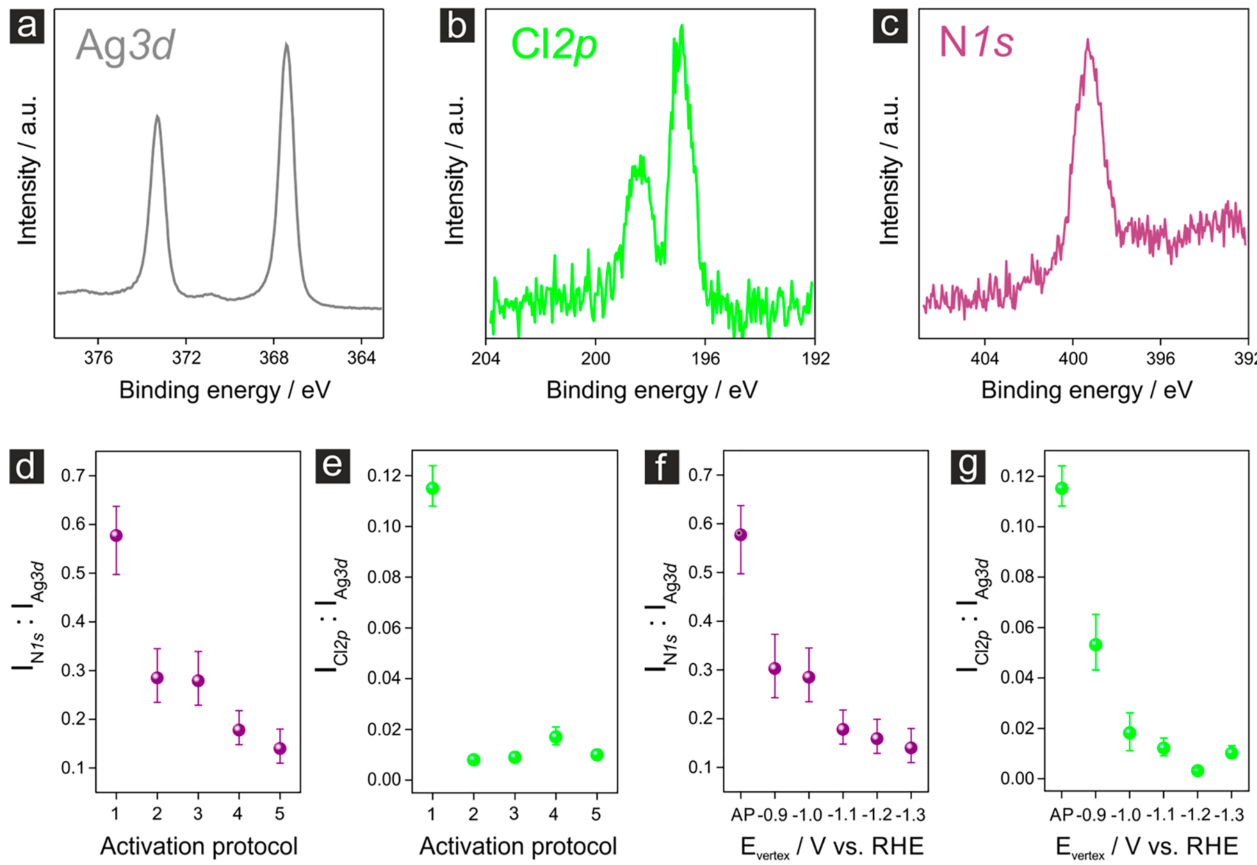

Figure 8. (a−c) Representative XPS spectra of the Ag3*d*, Cl2*p*, and N1*s* emissions derived from the Ag-NW catalyst on the GC support electrode (see Figure 2a−c). (d, e) Integrated intensities of the N1*s* and Cl2*p* emissions normalized to the corresponding integrated intensity of the Ag 3d emission; the digits on the *x*-axis indicate the respective catalyst activation protocols. **1**, as prepared; **2**, galvanostatic electrolysis in Ar-saturated (CO_2-free) 0.5 M $KHCO_3$ solution at $j = -3$ mA cm^{-2}, the total transferred charge was $Q = 115.3$ C; **3**, electrochemical looping (ec-l) in Ar-saturated 0.5 M $KHCO_3$ solution, the vertex potential was $E_{vertex} = -1.3$ V vs RHE, the total transferred charge was $Q = 895.9$ C; **4**, galvanostatic electrolysis in CO_2-saturated 0.5 M $KHCO_3$ solution at $j = -3$ mA cm^{-2}, the total transferred charge was $Q = 115.3$ C; **5**, electrochemical looping (ec-l) in CO_2-saturated 0.5 M $KHCO_3$ solution, the vertex potential was $E_{vertex} = -1.3$ V vs RHE, the total transferred charge was $Q = 115.3$ C (the activation conditions correspond to those in Figure 2b). (f, g) Integrated intensities of the N1*s* and Cl2*p* emissions normalized to the corresponding integrated intensity of the Ag3*d* emission measured after the electrochemical looping (ec-l) treatment; the respective vertex potentials are indicated on the *x*-axis (the activation conditions correspond to those in Figure 3).

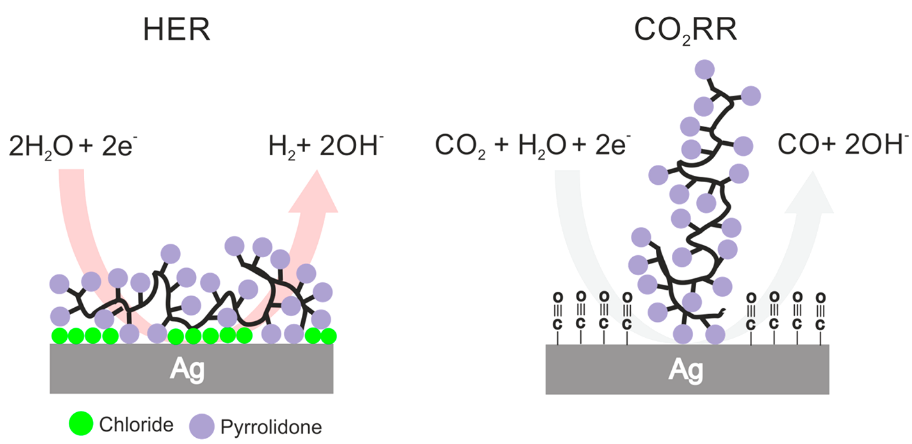

Figure 9. Schematics demonstrating the PVP and Cl terminated Ag surface which is still active for the HER (left panel) and the Ag surface which is activated upon CO production through PVP and Cl removal (right panel).

From these observations it can safely be concluded that it is the remaining PVP that disturbs the *ec*-CO_2RR rather than the chemisorbed chloride. Our analyses were further complemented by an extra XPS inspection of the catalyst films subjected to the systematic electrochemical looping experiments presented in Figure 3a−d. The results of this analysis are depicted in Figure 8f,g and clearly demonstrate that the vertex potential E_{vertex} and the width of the potential window that were applied to the catalysts in the electrochemical looping are necessary for the effectiveness of the surfactant removal. The

https://dx.doi.org/10.1021/acscatal.0c02026
ACS Catal. 2020, 10, 8503−8514

surface concentration of adsorbed chloride could be reduced to the minimum possible quantity when vertex potentials of E_{vertex} = −1.1 V vs RHE were applied, whereas the PVP surface coverage continued to decrease to an applied vertex potential of E_{vertex} = −1.3 V vs RHE. Our XPS results are also in full agreement with the working hypothesis made on the basis of the electrolysis data presented in Figure 3 and confirm that compositional changes at the catalyst surface are the origin of the hysteresis features observed in the electrochemical analysis (see also Figure S15). Complementary ^{1}H NMR measurements suggest that the PVP is removed structurally intact from the Ag surface. There are no PVP degradation products observed in the electrolyte after the electrolysis.

■ CONCLUSIONS AND OUTLOOK

Here, we demonstrate that the presence of surfactants (e.g., chloride and in particular PVP) on the surface of the colloidal silver catalyst negatively impacts the *ec*-CO_2RR selectivity and instead favors the HER in electrolysis reactions carried out in CO_2-saturated aqueous 0.5 M bicarbonate electrolytes.

The present work clearly demonstrates the importance of complete surfactant removal for the catalyst performance evaluation which might otherwise be superimposed by "transient artifacts", in particular in the initial stage of electrolysis (time scale of hours).

Electrochemical looping—a sequence of potentiostatic electrolysis experiments with defined starting, vertex, and ending potentials—has been demonstrated to be highly effective in the deprotection of catalysts, provided that CO is formed as the main electrolysis product. The chemical nature of the reaction product formed during electrolysis is found to be vital to the effectiveness of the activation of the catalysts via surfactant removal. An extended potential window in the electrochemical looping pretreatment, spanning from E_{start} = −0.6 V vs RHE to E_{vertex} = −1.3 V vs RHE, yields substantially improved CO efficiencies, which attained FE_{CO} = 100% at −1.0 V (j_{CO} = −5.8 mA cm^{-2}) and −1.1 V vs RHE (j_{CO} = −6.5 mA cm^{-2}). This improvement in the product selectivity relative to the as-prepared Ag-NWs is in agreement with the observed decrease in the normalized PVP surface concentration. This catalyst deprotection protocol is also transferable to C-supported Ag-NW catalyst systems.

Our future research will address the application of these electrochemically activated Ag-NW catalysts in flow-cell electrolyzer systems in detail in order to demonstrate the importance of the environment (gaseous versus aqueous/liquid) for surfactant removal under *operando* experimental conditions.

■ ASSOCIATED CONTENT

Supporting Information

The Supporting Information is available free of charge at https://pubs.acs.org/doi/10.1021/acscatal.0c02026.

> Additional data and figures including a photograph, calibration curve, XPS spectrum, product distributions, white-light interferometric characterization, hysteresis characteristics, CO efficiencies, SEM images, TEM images, optical photographs, electrochemical looping, and ^{1}H NMR analysis (PDF)

■ AUTHOR INFORMATION

Corresponding Authors

Yuhui Hou − *Department of Chemistry and Biochemistry, University of Bern, Bern 3012, Switzerland;* orcid.org/0000-0003-1616-562X; Email: yuhui.hou@dcb.unibe.ch

Peter Broekmann − *Department of Chemistry and Biochemistry, University of Bern, Bern 3012, Switzerland;* orcid.org/0000-0002-6287-1042; Email: peter.broekmann@dcb.unibe.ch

Authors

Huifang Hu − *Department of Chemistry and Biochemistry, University of Bern, Bern 3012, Switzerland*

Menglong Liu − *Department of Chemistry and Biochemistry, University of Bern, Bern 3012, Switzerland*

Ying Kong − *Department of Chemistry and Biochemistry, University of Bern, Bern 3012, Switzerland*

Nisarga Mysuru − *Department of Chemistry and Biochemistry, University of Bern, Bern 3012, Switzerland*

Changzhe Sun − *Department of Chemistry and Biochemistry, University of Bern, Bern 3012, Switzerland*

María de Jesús Gálvez-Vázquez − *Department of Chemistry and Biochemistry, University of Bern, Bern 3012, Switzerland*

Ulrich Müller − *Surface Science and Coating Technology, Empa, Swiss Federal Laboratories for Materials Science and Technology, Dübendorf 8600, Switzerland*

Rolf Erni − *Electron Microscopy Center, Empa, Swiss Federal Laboratories for Materials Science and Technology, Dübendorf 8600, Switzerland;* orcid.org/0000-0003-2391-5943

Vitali Grozovski − *Department of Chemistry and Biochemistry, University of Bern, Bern 3012, Switzerland*

Complete contact information is available at: https://pubs.acs.org/10.1021/acscatal.0c02026

Notes

The authors declare no competing financial interest.

■ ACKNOWLEDGMENTS

The financial support by the CTI Swiss Competence Center for Energy Research (SCCER Heat and Electricity Storage) is gratefully acknowledged. P.B. acknowledges the financial support by the Swiss National Science Foundation (SNSF) via Project 200020_172507. H.H., M.L., Y.K., and C.S. acknowledge the financial support by the Chinese Scholarship Council (CSC). Y.H. acknowledges the financial support by the University of Bern.

■ REFERENCES

(1) Change is in the air. *Nat. Catal.* **2018**, *1* (2), 93−93.

(2) Jhong, H.-R. M.; Ma, S.; Kenis, P. J. A. Electrochemical Conversion of CO_2 to Useful Chemicals: Current Status, Remaining Challenges, and Future Opportunities. *Curr. Opin. Chem. Eng.* **2013**, *2* (2), 191−199.

(3) Jones, J.-P.; Prakash, G. K. S.; Olah, G. A. Electrochemical CO_2 Reduction: Recent Advances and Current Trends. *Isr. J. Chem.* **2014**, *54* (10), 1451−1466.

(4) Whipple, D. T.; Kenis, P. J. A. Prospects of CO_2 Utilization via Direct Heterogeneous Electrochemical Reduction. *J. Phys. Chem. Lett.* **2010**, *1* (24), 3451−3458.

(5) Durst, J.; Rudnev, A.; Dutta, A.; Fu, Y.; Herranz, J.; Kaliginedi, V.; Kuzume, A.; Permyakova, A. A.; Paratcha, Y.; Broekmann, P.; Schmidt, T. J. Electrochemical CO_2 Reduction - A Critical View on Fundamentals, Materials and Applications. *Chimia* **2015**, *69* (12), 769−776.

(6) Samavati, M.; Santarelli, M.; Martin, A.; Nemanova, V. Production of Synthetic Fischer−Tropsch Diesel from Renewables: Thermoeconomic and Environmental Analysis. *Energy Fuels* **2018**, *32* (2), 1744−1753.
(7) Haas, T.; Krause, R.; Weber, R.; Demler, M.; Schmid, G. Technical photosynthesis involving CO_2 electrolysis and fermentation. *Nat. Catal.* **2018**, *1* (1), 32−39.
(8) Hori, Y.; Wakebe, H.; Tsukamoto, T.; Koga, O. Electrocatalytic Process of CO Selectivity in Electrochemical Reduction of CO_2 at Metal Electrodes in Aqueous Media. *Electrochim. Acta* **1994**, *39* (11−12), 1833−1839.
(9) Hori, Y.; Kikuchi, K.; Suzuki, S. Production of CO and CH_4 in Electrochemical Reduction of CO_2 at Metal-Electrodes in Aqueous Hydrogencarbonate Solution. *Chem. Lett.* **1985**, *14*, 1695−1698.
(10) Hoshi, N.; Kato, M.; Hori, Y. Electrochemical reduction of CO_2 on single crystal electrodes of silver Ag(111), Ag(100) and Ag(110). *J. Electroanal. Chem.* **1997**, *440* (1−2), 283−286.
(11) Boles, M. A.; Ling, D.; Hyeon, T.; Talapin, D. V. The surface science of nanocrystals. *Nat. Mater.* **2016**, *15* (2), 141−153.
(12) Back, S.; Yeom, M. S.; Jung, Y. Active Sites of Au and Ag Nanoparticle Catalysts for CO_2Electroreduction to CO. *ACS Catal.* **2015**, *5* (9), 5089−5096.
(13) Gabardo, C. M.; Seifitokaldani, A.; Edwards, J. P.; Dinh, C.-T.; Burdyny, T.; Kibria, M. G.; O'Brien, C. P.; Sargent, E. H.; Sinton, D. Combined high alkalinity and pressurization enable efficient CO_2 electroreduction to CO. *Energy Environ. Sci.* **2018**, *11* (9), 2531−2539.
(14) Salvatore, D. A.; Weekes, D. M.; He, J.; Dettelbach, K. E.; Li, Y. C.; Mallouk, T. E.; Berlinguette, C. P. Electrolysis of Gaseous CO_2 to CO in a Flow Cell with a Bipolar Membrane. *ACS Energy Lett.* **2018**, *3* (1), 149−154.
(15) Larrazábal, G. O.; Strøm-Hansen, P.; Heli, J. P.; Zeiter, K.; Therkildsen, K. T.; Chorkendorff, I.; Seger, B. Analysis of Mass Flows and Membrane Cross-over in CO_2 Reduction at High Current Densities in an MEA-Type Electrolyzer. *ACS Appl. Mater. Interfaces* **2019**, *11* (44), 41281−41288.
(16) Liu, Z.; Yang, H.; Kutz, R.; Masel, R. I. CO_2 Electrolysis to CO and O_2 at High Selectivity, Stability and Efficiency Using Sustainion Membranes. *J. Electrochem. Soc.* **2018**, *165* (15), J3371−J3377.
(17) Verma, S.; Kim, B.; Jhong, H.-R. M.; Ma, S.; Kenis, P. J. A. A Gross-Margin Model for Defining Technoeconomic Benchmarks in the Electroreduction of CO_2. *ChemSusChem* **2016**, *9* (15), 1972−1979.
(18) Martín, A. J.; Larrazábal, G. O.; Pérez-Ramírez, J. Towards sustainable fuels and chemicals through the electrochemical reduction of CO_2: lessons from water electrolysis. *Green Chem.* **2015**, *17* (12), 5114−5130.
(19) Kan, C. X.; Zhu, J. J.; Zhu, X. G. Silver nanostructures with well-controlled shapes: synthesis, characterization and growth mechanisms. *J. Phys. D: Appl. Phys.* **2008**, *41* (15), 155304.
(20) Liu, S.; Sun, C.; Xiao, J.; Luo, J.-L. Unraveling Structure Sensitivity in CO_2 Electroreduction to Near-Unity CO on Silver Nanocubes. *ACS Catal.* **2020**, *10*, 3158−3163.
(21) Liu, S.; Tao, H.; Zeng, L.; Liu, Q.; Xu, Z.; Liu, Q.; Luo, J.-L. Shape-Dependent Electrocatalytic Reduction of CO_2 to CO on Triangular Silver Nanoplates. *J. Am. Chem. Soc.* **2017**, *139* (6), 2160−2163.
(22) Zhang, S. H.; Jiang, Z. Y.; Xie, Z. X.; Xu, X.; Huang, R. B.; Zheng, L. S. Growth of silver nanowires from solutions: A cyclic penta-twinned-crystal growth mechanism. *J. Phys. Chem. B* **2005**, *109* (19), 9416−9421.
(23) Xi, W.; Ma, R.; Wang, H.; Gao, Z.; Zhang, W.; Zhao, Y. Ultrathin Ag Nanowires Electrode for Electrochemical Syngas Production from Carbon Dioxide. *ACS Sustainable Chem. Eng.* **2018**, *6* (6), 7687−7694.
(24) Sun, Y. G.; Yin, Y. D.; Mayers, B. T.; Herricks, T.; Xia, Y. N. Uniform silver nanowires synthesis by reducing $AgNO_3$ with ethylene glycol in the presence of seeds and poly(vinyl pyrrolidone). *Chem. Mater.* **2002**, *14* (11), 4736−4745.
(25) Li, X.; Wang, L.; Yan, G. Review: Recent research progress on preparation of silver nanowires by soft solution method and their applications. *Cryst. Res. Technol.* **2011**, *46* (5), 427−438.
(26) Li, B.; Ye, S.; Stewart, I. E.; Alvarez, S.; Wiley, B. J. Synthesis and Purification of Silver Nanowires To Make Conducting Films with a Transmittance of 99%. *Nano Lett.* **2015**, *15* (10), 6722−6726.
(27) Jiu, J.; Araki, T.; Wang, J.; Nogi, M.; Sugahara, T.; Nagao, S.; Koga, H.; Suganuma, K.; Nakazawa, E.; Hara, M.; Uchida, H.; Shinozaki, K. Facile synthesis of very-long silver nanowires for transparent electrodes. *J. Mater. Chem. A* **2014**, *2* (18), 6326−6330.
(28) Xia, Y.; Xiong, Y.; Lim, B.; Skrabalak, S. E. Shape-Controlled Synthesis of Metal Nanocrystals: Simple Chemistry Meets Complex Physics? *Angew. Chem., Int. Ed.* **2009**, *48* (1), 60−103.
(29) Coskun, S.; Aksoy, B.; Unalan, H. E. Polyol Synthesis of Silver Nanowires: An Extensive Parametric Study. *Cryst. Growth Des.* **2011**, *11* (11), 4963−4969.
(30) Gao, Y.; Jiang, P.; Song, L.; Liu, L. F.; Yan, X. Q.; Zhou, Z. Q.; Liu, D. F.; Wang, J. X.; Yuan, H. J.; Zhang, Z. X.; Zhao, X. W.; Dou, X. Y.; Zhou, W. Y.; Wang, G.; Xie, S. S. Growth mechanism of silver nanowires synthesized by polyvinylpyrrolidone-assisted polyol reduction. *J. Phys. D: Appl. Phys.* **2005**, *38* (7), 1061−1067.
(31) Kim, M. J.; Alvarez, S.; Chen, Z.; Fichthorn, K. A.; Wiley, B. J. Single-Crystal Electrochemistry Reveals Why Metal Nanowires Grow. *J. Am. Chem. Soc.* **2018**, *140* (44), 14740−14746.
(32) Sun, Y.; Xia, Y. Large-Scale Synthesis of Uniform Silver Nanowires Through a Soft, Self-Seeding, Polyol Process. *Adv. Mater.* **2002**, *14* (11), 833−837.
(33) Sun, D.; Xu, X.; Qin, Y.; Jiang, S. P.; Shao, Z. Rational Design of Ag-Based Catalysts for the Electrochemical CO_2 Reduction to CO: A Review. *ChemSusChem* **2020**, *13* (1), 39−58.
(34) Mourdikoudis, S.; Liz-Marzán, L. M. Oleylamine in Nanoparticle Synthesis. *Chem. Mater.* **2013**, *25* (9), 1465−1476.
(35) Yang, H.-J.; He, S.-Y.; Tuan, H.-Y. Self-Seeded Growth of Five-Fold Twinned Copper Nanowires: Mechanistic Study, Characterization, and SERS Applications. *Langmuir* **2014**, *30* (2), 602−610.
(36) Jin, M.; He, G.; Zhang, H.; Zeng, J.; Xie, Z.; Xia, Y. Shape-Controlled Synthesis of Copper Nanocrystals in an Aqueous Solution with Glucose as a Reducing Agent and Hexadecylamine as a Capping Agent. *Angew. Chem., Int. Ed.* **2011**, *50* (45), 10560−10564.
(37) Ung, D.; Cossairt, B. M. Effect of Surface Ligands on CoP for the Hydrogen Evolution Reaction. *ACS Appl. Energy Mater.* **2019**, *2* (3), 1642−1645.
(38) Luo, M.; Hong, Y.; Yao, W.; Huang, C.; Xu, Q.; Wu, Q. Facile removal of polyvinylpyrrolidone (PVP) adsorbates from Pt alloy nanoparticles. *J. Mater. Chem. A* **2015**, *3* (6), 2770−2775.
(39) Lopez-Sanchez, J. A.; Dimitratos, N.; Hammond, C.; Brett, G. L.; Kesavan, L.; White, S.; Miedziak, P.; Tiruvalam, R.; Jenkins, R. L.; Carley, A. F.; Knight, D.; Kiely, C. J.; Hutchings, G. J. Facile removal of stabilizer-ligands from supported gold nanoparticles. *Nat. Chem.* **2011**, *3* (7), 551−556.
(40) Naresh, N.; Wasim, F. G. S.; Ladewig, B. P.; Neergat, M. Removal of surfactant and capping agent from Pd nanocubes (Pd-NCs) using tert-butylamine: its effect on electrochemical characteristics. *J. Mater. Chem. A* **2013**, *1* (30), 8553−8559.
(41) Cargnello, M.; Chen, C.; Diroll, B. T.; Doan-Nguyen, V. V. T.; Gorte, R. J.; Murray, C. B. Efficient Removal of Organic Ligands from Supported Nanocrystals by Fast Thermal Annealing Enables Catalytic Studies on Well-Defined Active Phases. *J. Am. Chem. Soc.* **2015**, *137* (21), 6906−6911.
(42) Rioux, R. M.; Song, H.; Grass, M.; Habas, S.; Niesz, K.; Hoefelmeyer, J. D.; Yang, P.; Somorjai, G. A. Monodisperse platinum nanoparticles of well-defined shape: synthesise characterization, catalytic properties and future prospects. *Top. Catal.* **2006**, *39* (3−4), 167−174.
(43) Hou, Y.; Bolat, S.; Bornet, A.; Romanyuk, Y. E.; Guo, H.; Moreno-García, P.; Zelocualtecatl Montiel, I.; Lai, Z.; Müller, U.; Grozovski, V.; Broekmann, P. Photonic Curing: Activation and Stabilization of Metal Membrane Catalysts (MMCs) for the

Electrochemical Reduction of CO_2. *ACS Catal.* **2019**, *9* (10), 9518−9529.
(44) Bartholomew, C. H. Mechanisms of catalyst deactivation. *Appl. Catal., A* **2001**, *212* (1−2), 17−60.
(45) Shaw, S.; Tian, X. C.; Silva, T. F.; Bobbitt, J. M.; Naab, F.; Rodrigues, C. L.; Smith, E. A.; Cademartiri, L. Selective Removal of Ligands from Colloidal Nanocrystal Assemblies with Non-Oxidizing He Plasmas. *Chem. Mater.* **2018**, *30* (17), 5961−5967.
(46) Aliaga, C.; Park, J. Y.; Yamada, Y.; Lee, H. S.; Tsung, C.-K.; Yang, P.; Somorjai, G. A. Sum Frequency Generation and Catalytic Reaction Studies of the Removal of Organic Capping Agents from Pt Nanoparticles by UV−Ozone Treatment. *J. Phys. Chem. C* **2009**, *113* (15), 6150−6155.
(47) Rosen, E. L.; Buonsanti, R.; Llordes, A.; Sawvel, A. M.; Milliron, D. J.; Helms, B. A. Exceptionally Mild Reactive Stripping of Native Ligands from Nanocrystal Surfaces by Using Meerwein's Salt. *Angew. Chem., Int. Ed.* **2012**, *51* (3), 684−689.
(48) Doris, S. E.; Lynch, J. J.; Li, C. Y.; Wills, A. W.; Urban, J. J.; Helms, B. A. Mechanistic Insight into the Formation of Cationic Naked Nanocrystals Generated under Equilibrium Control. *J. Am. Chem. Soc.* **2014**, *136* (44), 15702−15710.
(49) Nelson, A.; Zong, Y.; Fritz, K. E.; Suntivich, J.; Robinson, R. D. Assessment of Soft Ligand Removal Strategies: Alkylation as a Promising Alternative to High-Temperature Treatments for Colloidal Nanoparticle Surfaces. *ACS Mater. Lett.* **2019**, *1* (1), 177−184.
(50) Menard, L. D.; Xu, F. T.; Nuzzo, R. G.; Yang, J. C. Preparation of TiO_2-supported Au nanoparticle catalysts from a Au-13 cluster precursor: Ligand removal using ozone exposure versus a rapid thermal treatment. *J. Catal.* **2006**, *243* (1), 64−73.
(51) Ansar, S. M.; Perera, G. S.; Ameer, F. S.; Zou, S. L.; Pittman, C. U.; Zhang, D. M. Desulfurization of Mercaptobenzimidazole and Thioguanine on Gold Nanoparticles Using Sodium Borohydride in Water at Room Temperature. *J. Phys. Chem. C* **2013**, *117* (26), 13722−13729.
(52) Hasché, F.; Oezaslan, M.; Strasser, P. In Situ Observation of the Thermally Induced Growth of Platinum-Nanoparticle Catalysts Using High-Temperature X-ray Diffraction. *ChemPhysChem* **2012**, *13* (3), 828−834.
(53) Li, D. G.; Wang, C.; Tripkovic, D.; Sun, S. H.; Markovic, N. M.; Stamenkovic, V. R. Surfactant Removal for Colloidal Nanoparticles from Solution Synthesis: The Effect on Catalytic Performance. *ACS Catal.* **2012**, *2* (7), 1358−1362.
(54) Safo, I. A.; Oezaslan, M. Electrochemical Cleaning of Polyvinylpyrrolidone-capped Pt Nanocubes for the Oxygen Reduction Reaction. *Electrochim. Acta* **2017**, *241*, 544−552.
(55) Safo, I. A.; Dosche, C.; Özaslan, M. Effects of Capping Agents on the Oxygen Reduction Reaction Activity and Shape Stability of Pt Nanocubes. *ChemPhysChem* **2019**, *20* (22), 3010−3023.
(56) Bong, S.; Jang, B.; Han, D.; Piao, Y. Effective Electrochemical Activation of Oleate-Residue-Fouled Pt Nanoparticle Catalysts for Methanol and Formic Acid Oxidation. *ACS Omega* **2019**, *4* (23), 20330−20334.
(57) Sun, Y. G.; Gates, B.; Mayers, B.; Xia, Y. N. Crystalline silver nanowires by soft solution processing. *Nano Lett.* **2002**, *2* (2), 165−168.
(58) Sun, Y. G.; Mayers, B.; Herricks, T.; Xia, Y. N. Polyol synthesis of uniform silver nanowires: A plausible growth mechanism and the supporting evidence. *Nano Lett.* **2003**, *3* (7), 955−960.
(59) Hori, Y. Electrochemical CO_2 Reduction on Metal Electrodes. In *Modern Aspects of Electrochemistry*; Springer: New York, 2008; pp 89−189.
(60) Dutta, A.; Rahaman, M.; Luedi, N. C.; Mohos, M.; Broekmann, P. Morphology Matters: Tuning the Product Distribution of CO_2 Electroreduction on Oxide-Derived Cu Foam Catalysts. *ACS Catal.* **2016**, *6* (6), 3804−3814.
(61) Dutta, A.; Rahaman, M.; Mohos, M.; Zanetti, A.; Broekmann, P. Electrochemical CO_2 Conversion Using Skeleton (Sponge) Type of Cu Catalysts. *ACS Catal.* **2017**, *7* (8), 5431−5437.
(62) Rahaman, M.; Dutta, A.; Broekmann, P. Size-Dependent Activity of Palladium Nanoparticles: Efficient Conversion of CO_2 into Formate at Low Overpotentials. *ChemSusChem* **2017**, *10* (8), 1733−1741.
(63) Dutta, A.; Morstein, C. E.; Rahaman, M.; Cedeño López, A.; Broekmann, P. Beyond Copper in CO_2 Electrolysis: Effective Hydrocarbon Production on Silver-Nanofoam Catalysts. *ACS Catal.* **2018**, *8*, 8357−8368.
(64) da Silva, R. R.; Yang, M.; Choi, S.-I.; Chi, M.; Luo, M.; Zhang, C.; Li, Z.-Y.; Camargo, P. H. C.; Ribeiro, S. J. L.; Xia, Y. Facile Synthesis of Sub-20 nm Silver Nanowires through a Bromide-Mediated Polyol Method. *ACS Nano* **2016**, *10* (8), 7892−7900.
(65) Niu, Z.; Cui, F.; Kuttner, E.; Xie, C.; Chen, H.; Sun, Y.; Dehestani, A.; Schierle-Arndt, K.; Yang, P. Synthesis of Silver Nanowires with Reduced Diameters Using Benzoin-Derived Radicals to Make Transparent Conductors with High Transparency and Low Haze. *Nano Lett.* **2018**, *18* (8), 5329−5334.
(66) Jiang, P.; Li, S.-Y.; Xie, S.-S.; Gao, Y.; Song, L. Machinable Long PVP-Stabilized Silver Nanowires. *Chem. - Eur. J.* **2004**, *10* (19), 4817−4821.
(67) Li, Y.; Cui, F.; Ross, M. B.; Kim, D.; Sun, Y.; Yang, P. Structure-Sensitive CO_2 Electroreduction to Hydrocarbons on Ultrathin 5-fold Twinned Copper Nanowires. *Nano Lett.* **2017**, *17* (2), 1312−1317.
(68) Clark, E. L.; Ringe, S.; Tang, M.; Walton, A.; Hahn, C.; Jaramillo, T. F.; Chan, K.; Bell, A. T. Influence of Atomic Surface Structure on the Activity of Ag for the Electrochemical Reduction of CO_2 to CO. *ACS Catal.* **2019**, *9* (5), 4006−4014.
(69) Kuhl, K. P.; Hatsukade, T.; Cave, E. R.; Abram, D. N.; Kibsgaard, J.; Jaramillo, T. F. Electrocatalytic Conversion of Carbon Dioxide to Methane and Methanol on Transition Metal Surfaces. *J. Am. Chem. Soc.* **2014**, *136* (40), 14107−14113.
(70) Liu, X. Y.; Xiao, J. P.; Peng, H. J.; Hong, X.; Chan, K.; Norskov, J. K. Understanding trends in electrochemical carbon dioxide reduction rates. *Nat. Commun.* **2017**, *8*, 15438.
(71) Hammer, B.; Morikawa, Y.; Nørskov, J. K. CO Chemisorption at Metal Surfaces and Overlayers. *Phys. Rev. Lett.* **1996**, *76* (12), 2141−2144.
(72) Zhu, S.; Li, T.; Cai, W.-B.; Shao, M. CO_2 Electrochemical Reduction As Probed through Infrared Spectroscopy. *ACS Energy Lett.* **2019**, *4* (3), 682−689.
(73) Schmitt, K. G.; Gewirth, A. A. In Situ Surface-Enhanced Raman Spectroscopy of the Electrochemical Reduction of Carbon Dioxide on Silver with 3,5-Diamino-1,2,4-Triazole. *J. Phys. Chem. C* **2014**, *118* (31), 17567−17576.
(74) Ichinohe, Y.; Wadayama, T.; Hatta, A. Electrochemical reduction of CO_2 on silver as probed by surface-enhanced Raman scattering. *J. Raman Spectrosc.* **1995**, *26* (5), 335−340.
(75) Liu, S.; Wang, X.-Z.; Tao, H.; Li, T.; Liu, Q.; Xu, Z.; Fu, X.-Z.; Luo, J.-L. Ultrathin 5-Fold Twinned Sub-25 nm Silver Nanowires Enable Highly Selective Electroreduction of CO_2 to CO. *Nano Energy* **2018**, *45*, 456.
(76) Fu, H.; Jia, L. L.; Wang, W. N.; Fan, K. N. The first-principle study on chlorine-modified silver surfaces. *Surf. Sci.* **2005**, *584* (2−3), 187−198.
(77) Bowker, M.; Waugh, K. C.; Wolfindale, B.; Lamble, G.; King, D. A. THE ADSORPTION OF CHLORINE AND CHLORIDATION OF AG(100). *Surf. Sci.* **1987**, *179* (2−3), 254−266.
(78) Lamble, G. M.; Brooks, R. S.; Campuzano, J. C.; King, D. A.; Norman, D. STRUCTURE OF THE C(2 × 2) COVERAGE OF CL ON AG(100) - A CONTROVERSY RESOLVED BY SURFACE EXTENDED X-RAY-ABSORPTION FINE-STRUCTURE SPECTROSCOPY. *Phys. Rev. B: Condens. Matter Mater. Phys.* **1987**, *36* (3), 1796−1798.

Supporting information

Activation matters: hysteresis effects during electrochemical looping of colloidal Ag nanowire (Ag-NW) catalysts

Huifang Hu[†], *Menglong Liu*[†], *Ying Kong*[†], *Nisarga Mysuru*[†], *Changzhe Sun*[†], *María de Jesús Gálvez-Vázquez*[†], *Ulrich Müller*[‡], *Rolf Erni*[‖], *Vitali Grozovski*[†], *Yuhui Hou*[†]*, *and Peter Broekmann*[†]*

[†]Department of Chemistry and Biochemistry, University of Bern, Freiestrasse 3, Bern 3012 Switzerland

[‡]Surface Science and Coating Technology, Empa – Swiss Federal Laboratories for Materials Science and Technology, 8600 Dübendorf, Switzerland

[‖]Electron Microscopy Center, Empa, Swiss Federal Laboratories for Materials Science and Technology, Überlandstrasse 129, 8600 Dübendorf, Switzerland

Content

Figures

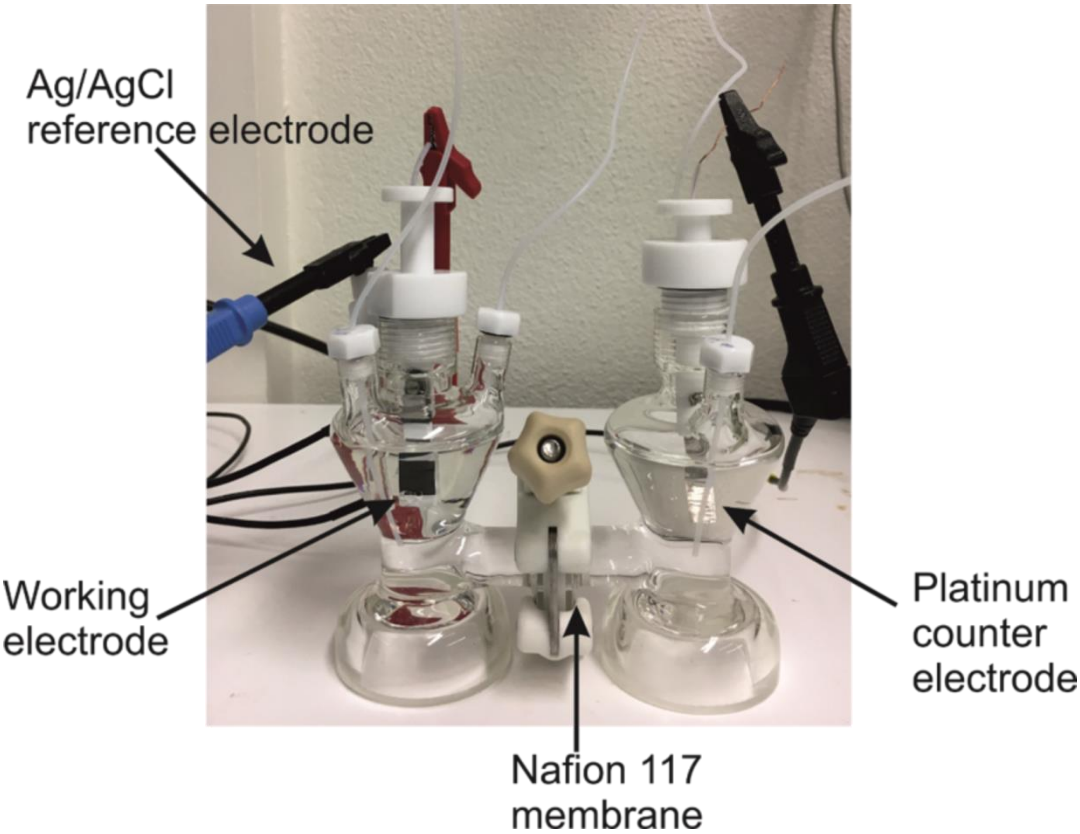

Figure S1. Custom-made H-type electrolysis cell used in this study for the catalyst performance testing. Anolyte and catholyte were separated by a Nafion membrane thus preventing any transfer of Pt contaminations from the anolyte to the catholyte when using a Pt foil as counter electrode.

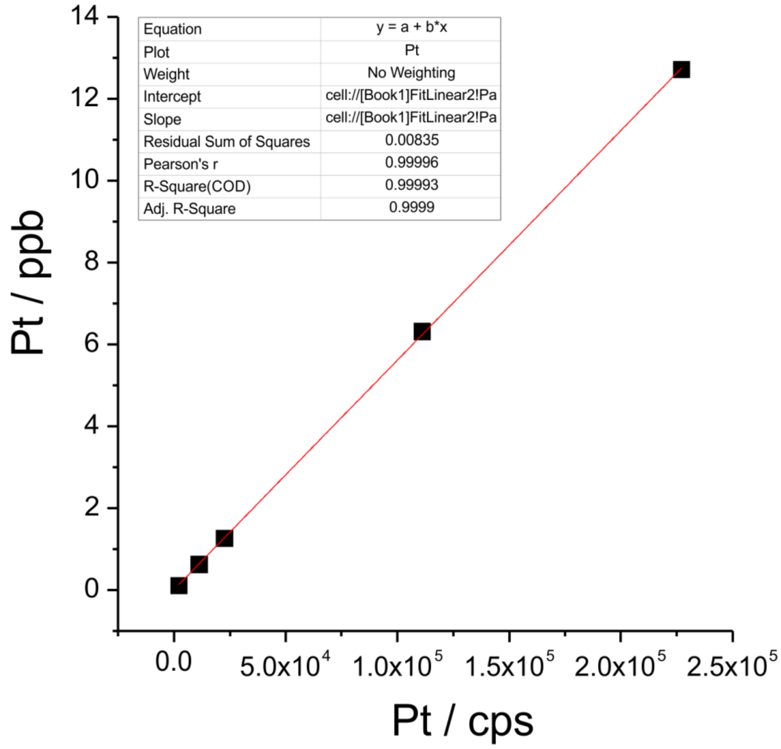

Reference measurement: 0.5 M $KHCO_3$ solution prior to the electrolysis.	**0.4 ppb** (noise level)
Exp. 1: After electrochemical looping in CO_2-saturated 0.5M $KHCO_3$ (-0.6 to -1.3 V to -0.6 V) using Pt as the counter electrode according to Figure 3e	**0 ppb (catholyte)**
	5 ppb (anolyte)
Exp. 2: After electrochemical looping in CO_2-saturated 0.5M $KHCO_3$ (-0.6 to -1.3 V to -0.6 V) using Pt as the counter electrode according to Figure 3e	**0 ppb (catholyte)**
	9.7 ppb (anolyte)
Exp. 3: After electrochemical looping in CO_2-saturated 0.5M $KHCO_3$ (-0.6 to -1.3 V to -0.6 V) using Pt as the counter electrode according to Figure 3e	**0 ppb (catholyte)**
	6.1 ppb (anolyte)

Figure S2. Calibration curve used for the quantification of the Pt content in the electrolyte by means of ICP-MS; the results of the Pt detection are given in the table below the graph proving that there is no Pt contamination in the catholyte even after extended electrolysis (full *ec* looping according to Figure 3e in the main text). The Pt content in the anolyte is marginally increased after the extended electrolysis. Two repetitions of the experiment (Exp. 2 and 3) confirm these conclusions.

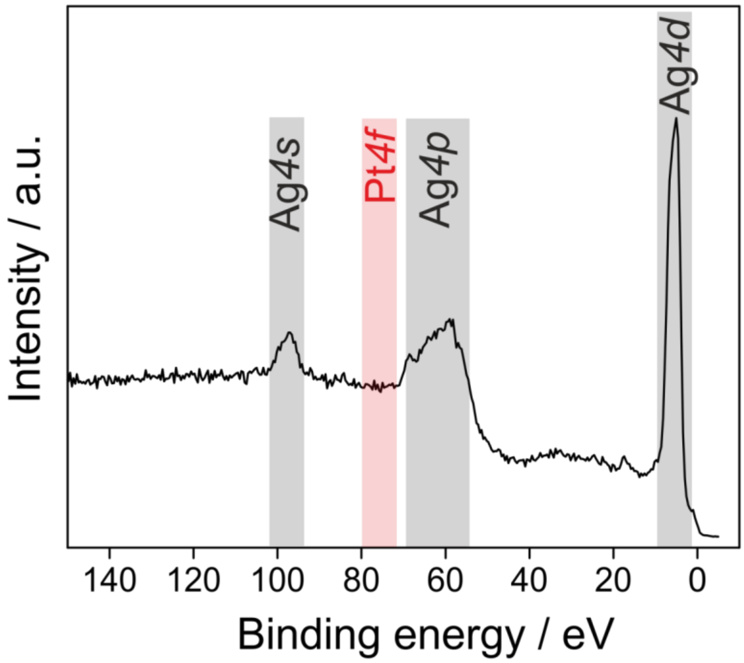

Figure S3. XPS spectrum of the Ag-NW catalyst recorded after the full electrochemical looping experiment in CO_2-saturated 0.5M $KHCO_3$ (-0.6 to -1.3 V to -0.6 V) according to Figure 3e using Pt as the counter electrode. There is no indication for any Pt contamination on the electrode after the extended electrolysis reaction. This result agrees well with the ICP-MS analysis of the catholyte after the electrolysis (see Figure S2).

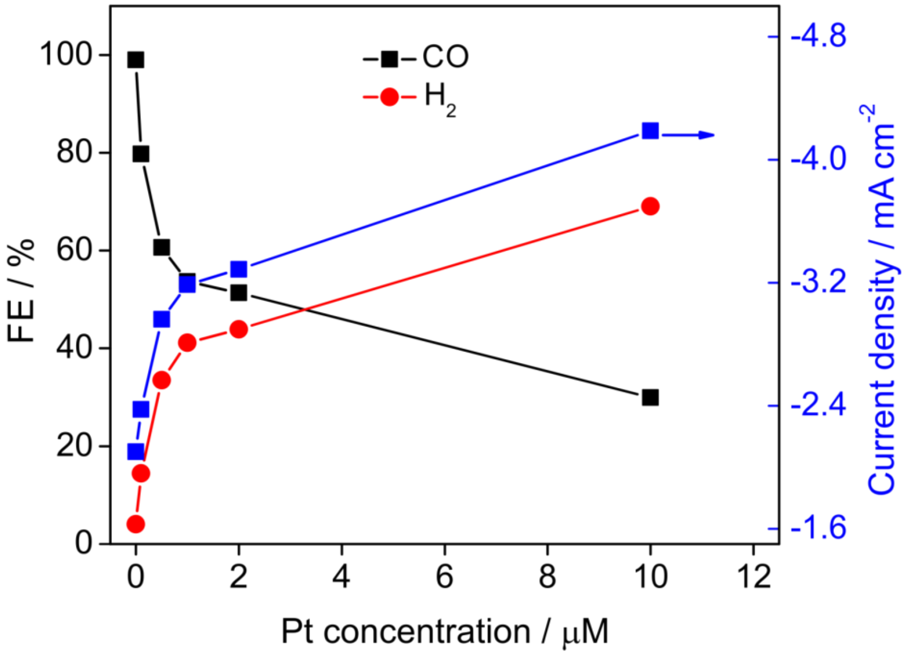

Figure S4. Changes of the CO_2RR product distribution (CO_2-saturated 0.5 M $KHCO_3$ solution, 1 h electrolysis at -0.9 V vs. RHE) caused by the intentional addition of Pt (hexachloro-platinate source) to the catholyte compartment during electrolysis. As expected, trace amounts of Pt contaminations lead to a drastic increase of the FE_{H2} values on the expense of the respective CO efficiency. Note that, under the cathodic conditions applied, Pt ions are expected to rapidly deposit on the cathode surface thereby altering the catalytic behavior of the electrode.
In addition to the Faradaic efficiencies, also the total current density substantially increases upon the Pt addition due to the high catalytic activity of Pt towards the HER.

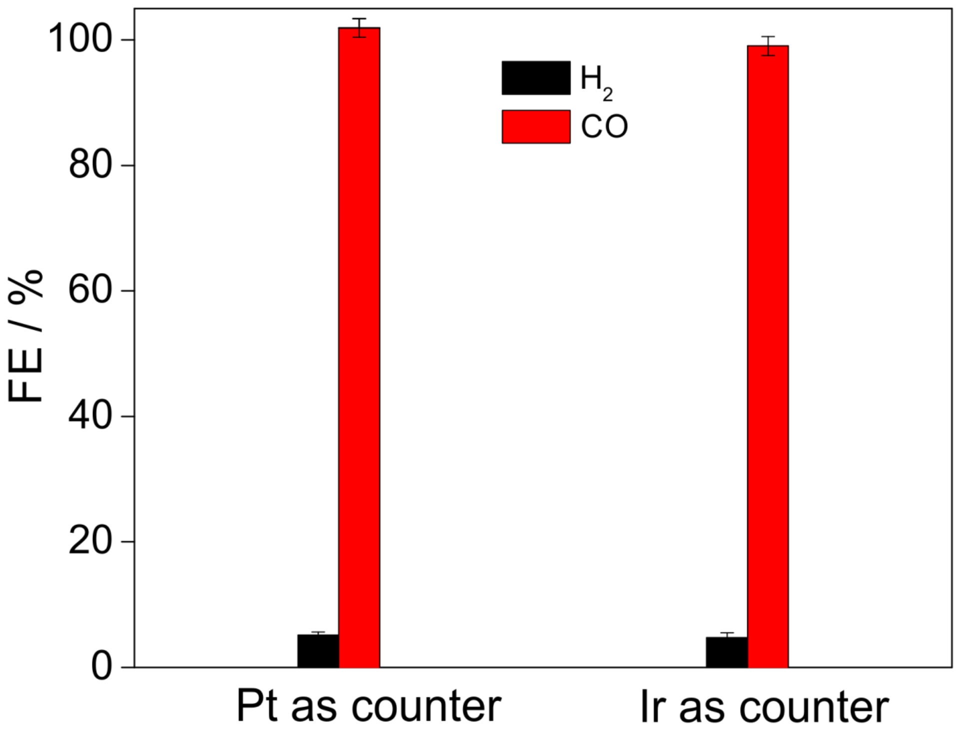

Figure S5. CO_2RR product distribution after catalyst activation by electrochemical looping (ec-l) in CO_2-saturated 0.5M $KHCO_3$ (-0.6 to -1.3 V to -0.6 V) according to Figure 3e. The resulting product distributions are, within the error margins, identical no matter whether Pt or Ir was used as the counter electrode material for both the initial ec-l and the subsequent CO_2RR screening experiment (analogue to the approach presented in Figure 7).

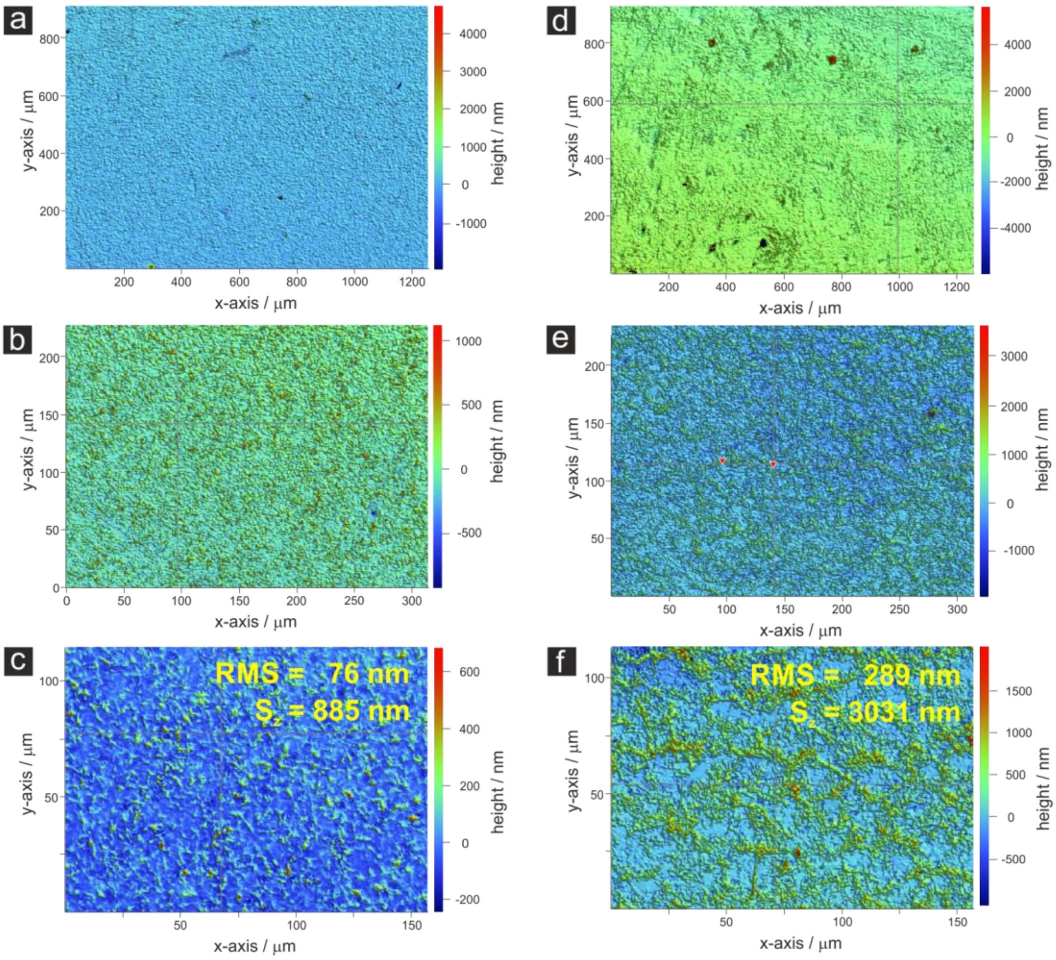

Figure S6. a) – c) White-light interferometric characterization of the Ag-NW catalyst deposited on the glassy carbon support electrode. The interferometry data correspond to Figure 2a-c; d) – f) White-light interferometric characterization of the C-supported Ag-NW catalyst deposited on the glassy carbon support electrode. The interferometry data correspond to Figure 2d-f.

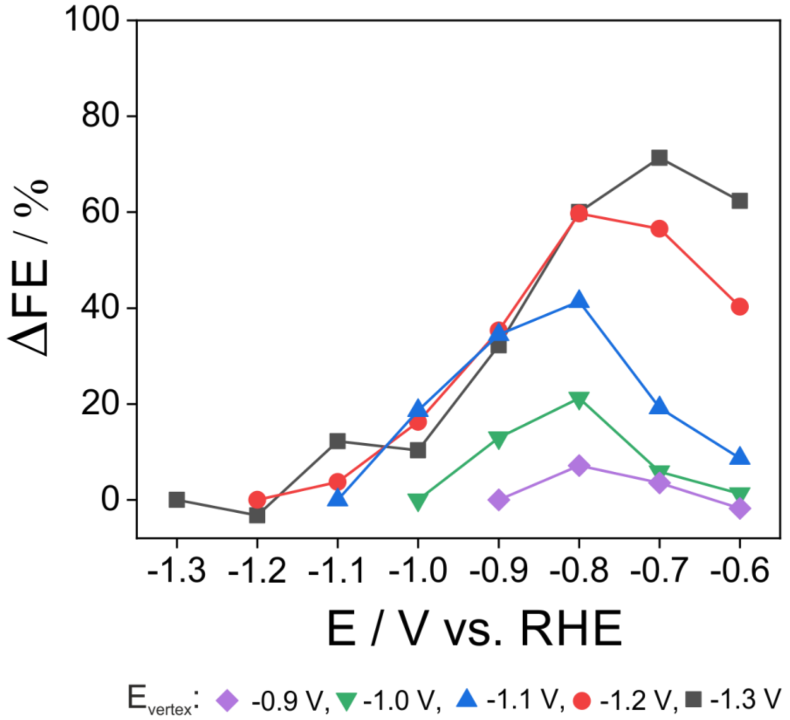

Figure S7. This graph shows the hysteresis characteristics of the electrochemical looping experiment (derived from Figure 3). The hysteresis is represented as the difference between the FE values of the forward and the ones of the respective backward scan.

As discussed in the manuscript, the hysteresis effect is largest for the most negative vertex potential of -1.3 V vs. RHE.

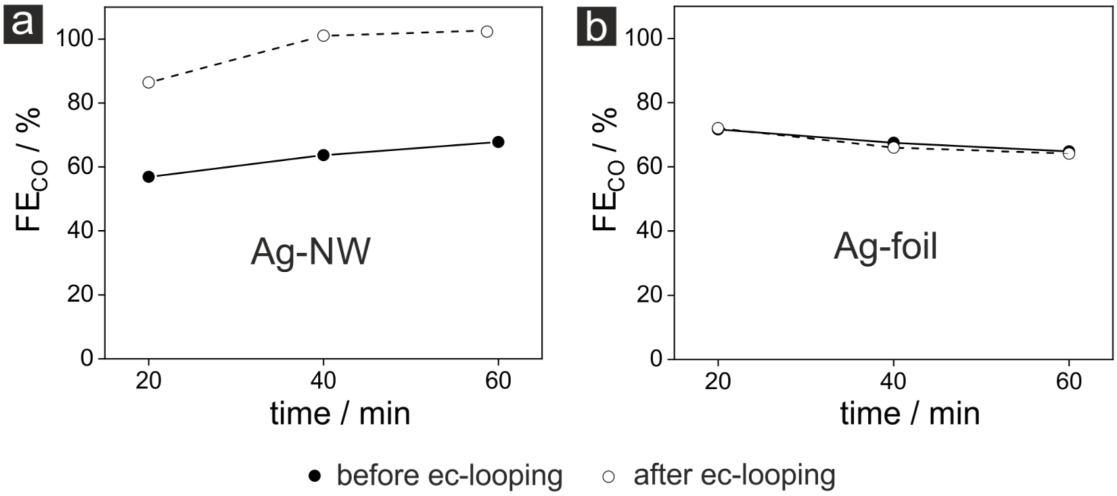

Figure S8. a) Comparison of the time-dependent CO efficiencies obtained for as-deposited Ag-NW catalysts (denoted before ec-looping) and Ag-NW catalysts activated by a full ec-l treatment (vertex potential: -1,3 V vs. RHE); the constant electrolysis potential was -0.9 V vs. RHE; the electrolyte used was CO_2-saturated 0.5M $KHCO_3$, these results demonstrate the activation of the catalyst by surfactant removal; b) Analogue experiments carried out using an Ag-foil as the catalyst. There is no effect of the ec-l on the resulting catalyst performance as there was no capping layer present which could be removed by the ec-l treatment.

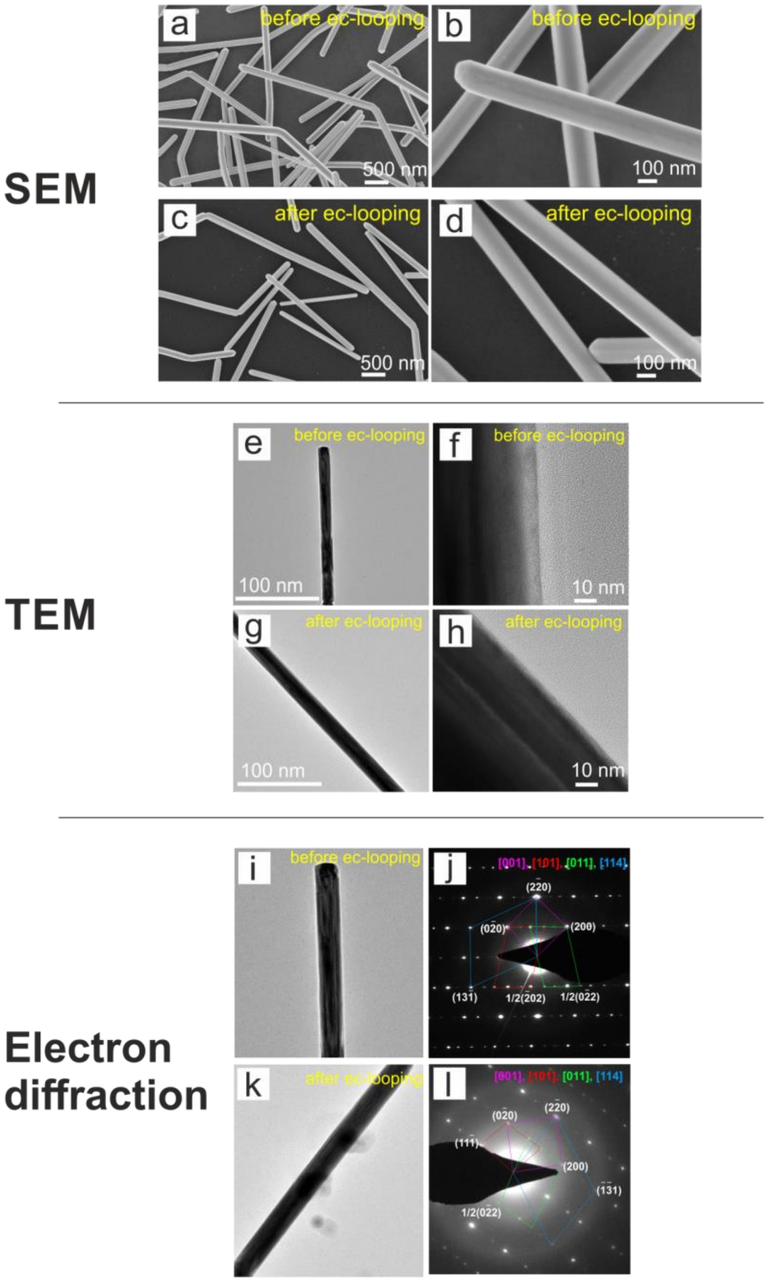

Figure S9. a) –d) SEM inspection of Ag-NWs on glassy carbon support before (panel a and b) and after the electrochemical looping (ec-l) in CO_2-saturated 0.5 M $KHCO_3$ (vertex potential: -1.3 V vs. RHE); e) – h) Corresponding TEM inspection; i) – l) Corresponding selective area electron diffraction analysis of individual Ag-NWs carried out in a TEM configuration.

All experiments presented demonstrate that there are no severe structural alterations of the Ag-NWs induced by the applied ec-l treatment. We note however, that the resolution of the TEM experiment used herein is not sufficient to probe eventual alterations of the (100) surface on an atomic scale.

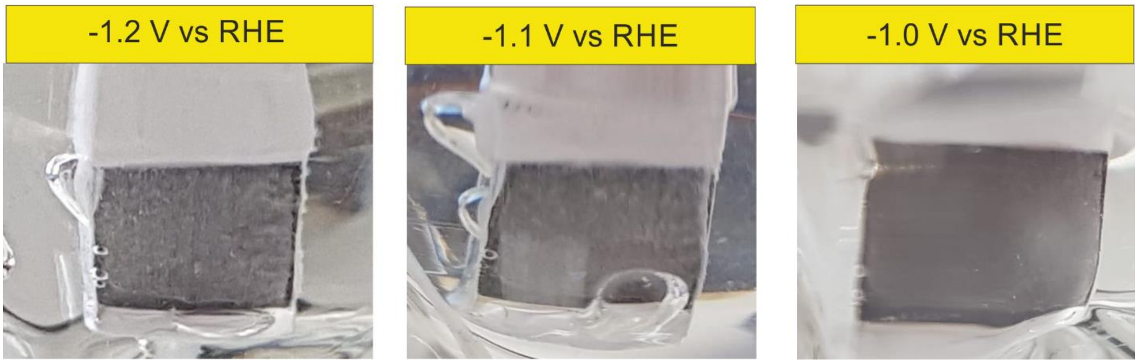

Figure S10. Optical photographs of the electrode (Ag-NWs on glassy carbon) during the electrolysis reaction at various applied potentials. At -1.2 V vs. RHE there is clearly massive hydrogen bubble formation taking place, thus partially blocking the electrode surface area.

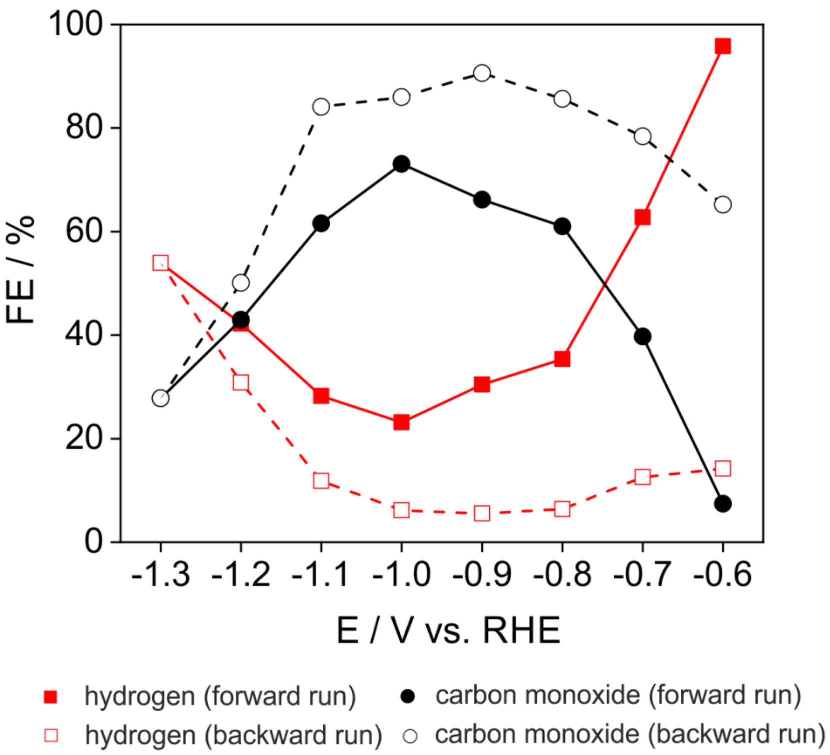

Figure S11. Electrochemical looping of the Ag-NW catalysts (glassy carbon support) carried out in CO_2-saturated 0.5M $KHCO_3$ (vertex potential: -1.3 V vs. RHE; 40 min. electrolysis time at each potential applied) after an initial full electrochemical looping in Ar-saturated 0.5M $KHCO_3$. The product distribution is similar to the one of the single ec-l experiment shown in Figure 3e.

This further demonstrates that the HER (ec-l in Ar-saturated electrolyte) is ineffective with regard to the surfactant removal.

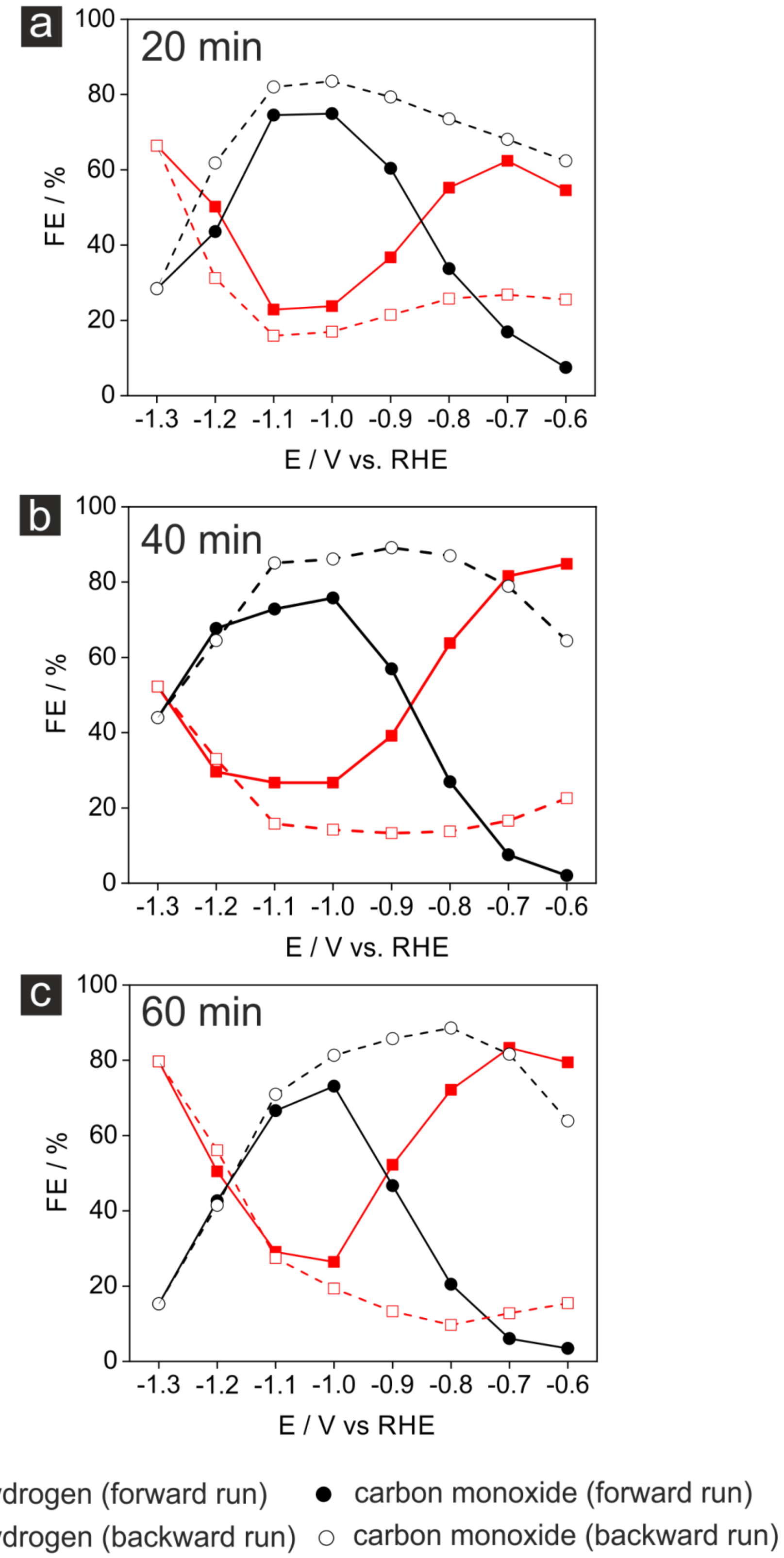

Figure S12. Electrochemical looping of the Ag-NW catalysts (glassy carbon support) carried out in CO_2-saturated 0.5 M $KHCO_3$ (vertex potential: -1.3 V vs. RHE); a) 20 min electrolysis time (each applied potential); 40 min electrolysis time (each applied potential); 60 min electrolysis time (each applied potential).

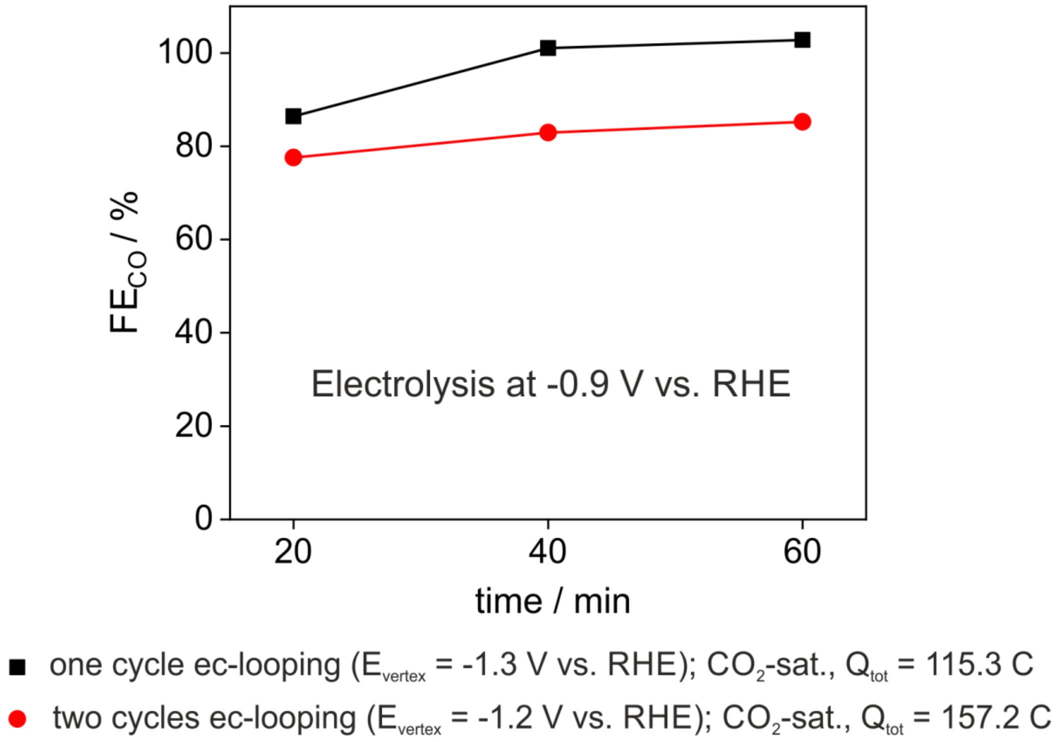

Figure S13. Comparison of the time-dependent CO efficiencies obtained after one single ec-l treatment (vertex potential: -1.3 V vs. RHE) and a double ec-l pretreatment (vertex potential: -1.2 V vs. RHE).

This comparison demonstrates that, for the surfactant removal, the applied vertex potential is even more important than the total transferred charge.

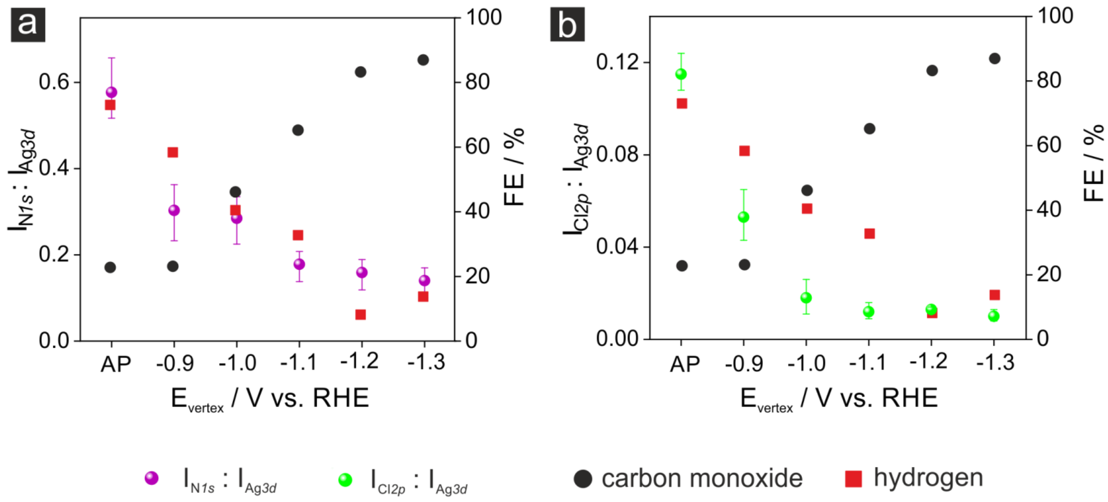

Figure S14. a) Correlation between the surfactant removal (ec-l treatments applying different vertex potentials) and the resulting product distribution at -0.8 V vs. RHE; b) Correlation between the chloride removal (ec-l treatments applying different vertex potentials) and the resulting product distribution at -0.8 V vs. RHE.

These results clearly demonstrate that the CO efficiency increases with decreasing surface concentrations of PVP and Cl.

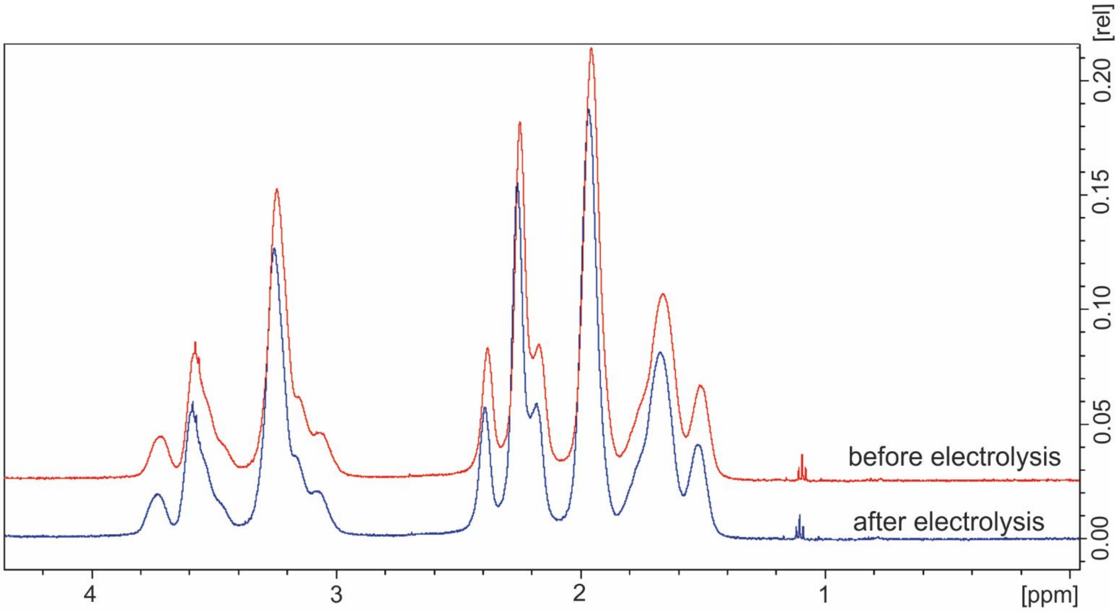

Figure S15. ^{1}H-NMR analysis of the PVP containing electrolyte before and after electrolysis.

Samples were prepared from 10 mM PVP containing 0.5 M $KHCO_3$ electrolyte using the following procedure: Two sample aliquots (0.5ml) were isolated before and after the electrolysis (the electrolysis was performed at -0.9 V vs. RHE for 1 hour using an Ag foil as a catalyst). 0.2 mL of D_2O (Cambridge Isotope Laboratories, Inc, USA, 99.9%) were added to each sample. NMR data were recorded using a Bruker AVANCE IIHD spectrometer operating at the nominal proton frequency of 500 MHz, equipped with a dual inverse broadband 5 ‐ mm probe head with an additional z ‐ gradient coil. The ^{1}H-NMR spectra were recorded at room temperature (298 K) using a standard pulse experiment (*noesygppr1d* pulse sequence from the Bruker pulse ‐ program library). Typically, 512 transients were acquired over a spectral width of 14.7 ppm, with a data size of 64 k points, and a relaxation delay of 6 s. The spectra were processed using Bruker TopSpin 4.0.2 and SpinWorks 4.2.0 software.[12]

Tables

Table S1a: Faradaic efficiency (FE) and partial current density (j) values as function of the applied electrolysis potentials; the data correspond to Figure 3a. The partial current densities indicate the values reached at the end of the 40 min. lasting electrolysis (non-steady-state conditions!). The subscripts 'f' and 'b' refer to the forward and backward scan of the electrochemical looping, respectively.

E / V vs RHE	FE_{H2_f} (j_{H2_f})	FE_{CO_f} (j_{CO_f})	FE_{H2_b} (j_{H2_b})	FE_{CO_b} (j_{CO_b})
	% (mA cm^{-2})			
-0.6	74.0 (0.10)	1.8 (0.003)	57.7 (0.046)	0.0 (0.0)
-0.7	74.0 (0.22)	4.1 (0.012)	67.0 (0.10)	7.7 (0.012)
-0.8	67.4 (0.30)	15.9 (0.070)	58.4 (0.21)	23.1 (0.083)
-0.9	48.2 (0.57)	38.6 (0.46)	48.2 (0.57)	38.6 (0.46)

Table S1b: Faradaic efficiency (FE) and partial current density (j) values as function of the applied electrolysis potentials; the data correspond to Figure 3b.

E / V vs RHE	FE_{H2_f} (j_{H2_f})	FE_{CO_f} (j_{CO_f})	FE_{H2_b} (j_{H2_b})	FE_{CO_b} (j_{CO_b})
	% (mA cm^{-2})			
-0.6	57.3 (0.052)	4.0 (0.004)	48.1 (0.030)	5.4 (0.003)
-0.7	68.0 (0.16)	10.7 (0.026)	51.6 (0.072)	16.6 (0.023)
-0.8	63.6 (0.31)	24.9 (0.12)	40.5 (0.15)	46.1 (0.17)
-0.9	45.1 (0.68)	52.1 (0.78)	31.4 (0.47)	65.0 (0.98)
-1	25.1 (0.95)	71.0 (2.7)	25.1 (0.95)	71.0 (2.7)

Table S1c: Faradaic efficiency (FE) and partial current density (j) values as function of the applied electrolysis potentials; the data correspond to Figure 3c.

E / V vs RHE	FE_{H2_f} (j_{H2_f})	FE_{CO_f} (j_{CO_f})	FE_{H2_b} (j_{H2_b})	FE_{CO_b} (j_{CO_b})
	% (mA cm^{-2})			
-0.6	69.7 (0.077)	1.7 (0.002)	69.8 (0.13)	10.4 (0.02)
-0.7	82.8 (0.22)	5.7 (0.015)	67.5 (0.23)	24.9 (0.08)
-0.8	68.5 (0.35)	23.8 (0.12)	32.8 (0.17)	65.3 (0.33)
-0.9	54.3 (0.81)	45.3 (0.68)	21.2 (0.28)	79.8 (1.0)
-1	37.2 (1.5)	66.2 (2.6)	19.7 (0.59)	84.8 (2.5)
-1.1	28.1 (2.1)	73.9 (5.5)	28.1 (2.1)	73.9 (5.5)

Table S1d: Faradaic efficiency (FE) and partial current density (j) values as function of the applied electrolysis potentials; the data correspond to Figure 3d.

E / V vs RHE	FE_{H2_f} (j_{H2_f})	FE_{CO_f} (j_{CO_f})	FE_{H2_b} (j_{H2_b})	FE_{CO_b} (j_{CO_b})
	% (mA cm^{-2})			
-0.6	83.4 (0.075)	7.8 (0.007)	23.3 (0.023)	48.1 (0.048)
-0.7	75.9 (0.12)	12.1 (0.019)	15.1 (0.030)	68.6 (0.14)
-0.8	71.8 (0.34)	23.5 (0.11)	8.1 (0.043)	83.2 (0.44)
-0.9	45.1 (0.63)	52.1 (0.73)	10.0 (0.15)	87.4 (1.3)
-1	29.1 (1.2)	65.1 (2.6)	14.0 (0.55)	81.4 (3.2)
-1.1	17.8 (1.2)	75.6 (5.3)	16.5 (1.3)	79.3 (6.2)
-1.2	25.0 (2.4)	68.6 (6.6)	25.0 (2.4)	68.6 (6.6)

Table S1e: Faradaic efficiency (FE) and partial current density (j) values as function of the applied electrolysis potentials; the data correspond to Figure 3e.

E / V vs RHE	FE_{H2_f} (j_{H2_f})	FE_{CO_f} (j_{CO_f})	FE_{H2_b} (j_{H2_b})	FE_{CO_b} (j_{CO_b})
	% (mA cm^{-2})			
-0.6	84.8 (0.13)	2.1 (0.003)	22.6 (0.043)	64.4 (0.12)
-0.7	81.6 (0.19)	7.5 (0.017)	16.6 (0.076)	78.9 (0.36)
-0.8	63.8 (0.29)	27.0 (0.12)	13.8 (0.14)	87.0 (0.87)
-0.9	39.2 (0.59)	56.9 (0.85)	13.3 (0.27)	89.1 (1.8)
-1	26.7 (1.0)	75.8 (3.0)	14.2 (0.48)	86.1 (2.9)
-1.1	26.7 (1.8)	72.8 (5.0)	15.8 (0.88)	85.1 (4.8)
-1.2	29.6 (2.8)	67.7 (6.3)	33.0 (3.3)	64.5 (6.5)
-1.3	52.2 (7.9)	44.0 (6.6)	52.2 (7.9)	44.0 (6.6)

Table S2a: Transferred charge and current density (j) as function of the applied electrolysis potential during the electrochemical looping in Ar- and CO_2-saturated electrolyte; the data correspond to Figure 3f and 4a. The subscripts 'f' and 'b' refer to the forward and backward scan of the electrochemical looping, respectively.

E / V vs RHE CO_2-sat.	Charge_f (j_f)	Charge_b (j_b)	E / V vs RHE Ar-sat.	Charge_f (j_f)	Charge_b (j_b)
	/ C (mA cm^{-2}) CO_2-sat.			C / (mA cm^{-2}) Ar-sat.	
-0.6	0.3 (0.15)	0.4 (0.19)	-0.5	0.2 (0.094)	0.09 (0.045)
-0.7	0.4 (0.23)	0.9 (0.46)	-0.6	0.2 (0.078)	0.5 (0.27)
-0.8	0.9 (0.46)	2.0 (1.0)	-0.7	0.4 (0.22)	3.2 (1.7)
-0.9	2.8 (1.5)	3.9 (2.0)	-0.8	25.9 (13.5)	12.2 (6.4)
-1	7.4 (3.9)	6.6 (3.4)	-0.9	64.6 (33.7)	39.0 (20.3)
-1.1	13.2 (6.9)	10.8 (5.6)	-1.0	122.2 (63.7)	151.6 (79.0)
-1.2	17.8 (9.3)	19.1 (10.0)	-1.1	151.7 (79.0)	159.7 (83.2)
-1.3	29.1 (15.1)	29.1 (15.1)	-1.2	164.4 (85.6)	164.4 (85.6)

Table S2b: Time evolution of the FE_{CO} values depending on the applied pre-treatment protocol; the data correspond to Figure 4b.

Electrolysis time /min	ap	Gal (Ar)	Gal(CO_2)	El-looping (Ar)	El-looping (CO_2)
	/ %				
20	56.9	61.3	76.6	60.1	86.4
40	63.7	65.8	82.1	72.3	101.0
60	67.8	70.3	87.8	78.1	102.8

Table S3: Faradaic efficiency (FE) and partial current density (j) values as function of the applied electrolysis potentials; the data correspond to Figure 6.

Potential / V vs RHE	FE_{H2_f} (j_{H2_f})	FE_{CO_f} (j_{CO_f})	FE_{H2_b} (j_{H2_b})	FE_{CO_b} (j_{CO_b})
	% (mA cm^{-2})			
-0.6	73.0 (0.11)	5.5 (0.008)	36.5 (0.058)	29.2 (0.047)
-0.7	66.6 (0.17)	13.9 (0.035)	29.0 (0.096)	48.9 (0.16)
-0.8	42.2 (0.24)	42.7 (0.24)	16.4 (0.11)	76.3 (0.52)
-0.9	25.5 (0.41)	76.7 (1.2)	16.2 (0.21)	93.4 (1.2)
-1	46.6 (1.68)	61.2 (2.2)	22.6 (0.86)	90.7 (3.4)

-1.1	79.7 (24.7)	9.0 (2.8)	65.0 (16.3)	33.3 (8.3)
-1.2	77.0 (75.5)	2.4 (2.4)	77.0 (75.5)	2.4 (2.4)

Table S4: Faradaic efficiency (FE) and partial current density (j) values as function of the applied electrolysis potentials; the data correspond to Figure 7.

Potential / V vs RHE	FE_{H2}_ap	FE_{CO}_ap	FE_{H2}_ec-l	FE_{CO}_ec-l
		/ %		
-0.6	77.8 (0.058)	4.5 (0.003)	23.0 (0.046)	54.0 (0.11)
-0.7	76.7 (0.14)	9.9 (0.018)	19.0 (0.095)	77.8 (0.39)
-0.8	73.1 (0.39)	22.8 (0.12)	8.5 (0.085)	90.6 (0.91)
-0.9	38.0 (0.53)	59.0 (0.83)	5.1 (0.14)	101.9 (2.85)
-1	34.6 (1.73)	67.5 (3.38)	4.7 (0.27)	101.7 (5.80)
-1.1	36.9 (2.80)	63.0 (4.79)	12.9 (0.93)	89.8 (6.47)
-1.2	48.6 (3.55)	53.1 (3.88)	19.2 (2.25)	76.4 (8.94)
-1.3	66.9 (13.4)	30.5 (6.1)	46.3 (10.46)	41.7 (9.42)

Table S5a. (I_{N1s} : I_{Ag3d}) ratio and total charge as function of surfactant removal protocols presented in Figure 8d

Catalyst	N/Ag	Error (-)	Error (+)	Total charge
as prepared	0.577	0.06	0.08	0
gal-Ar (3 mA cm^{-2})	0.285	0.05	0.06	115.3
ec-l: (Ar)	0.279	0.05	0.06	895.9
gal-CO_2(3 mA cm^{-2})	0.178	0.03	0.04	115.3
ec-l: (CO_2)	0.14	0.03	0.03	115.3

Table S5b. (I_{Cl2p} : I_{Ag3d}) ratio and total charge as function of surfactant removal protocols in Figure 8e

Catalyst	Cl/Ag	Error (-)	Error (+)	Total charge / C
as prepared	0.115	0.007	0.009	0
gal-Ar (3 mA cm^{-2})	0.008	0.001	0.002	115.3
ec-l: (Ar)	0.009	0.002	0.002	895.9
gal-CO_2(3 mA cm^{-2})	0.017	0.003	0.004	115.3
ec-l: (CO_2)	0.01	0.002	0.002	115.3

Table S5c. (I_{N1s} : I_{Ag3d}) ratio and total charge as function of surfactant removal protocols presented in Figure 8f

Catalyst	N/Ag	Error (-)	Error (+)	Total charge
as prepared	0.577	0.06	0.08	0
ec-l: -0.9	0.303	0.06	0.07	5.3
ec-l: -1.0	0.290	0.05	0.06	22.3
ec-l: -1.1	0.17	0.03	0.04	45.1
ec-l: -1.2	0.159	0.03	0.04	83.9
ec-l: -1.3	0.14	0.03	0.03	115.3

Table S5d. (I_{Cl2p} : I_{Ag3d}) ratio and total charge as function of electro-looping window in Figure 8g

Catalyst	Cl/Ag	Error (-)	Error (+)	Total charge
as prepared	0.115	0.007	0.009	0
ec-l: -0.9	0.053	0.01	0.012	5.3
ec-l: -1.0	0.018	0.007	0.008	22.3
ec-l: -1.1	0.012	0.003	0.004	45.1
ec-l: -1.2	0.003	0.001	0.001	83.9
ec-l: -1.3	0.01	0.002	0.003	115.3

Table S6: Overview on the performance of Ag catalysts for *ec*-CO_2RR applications

Ag catalysts	Maximum FEco (%)	Potential / V vs RHE	reference	Title
Nanocubes (NCs)	99	−0.856	Subiao Liu[1]	Unraveling Structure Sensitivity in CO_2 Electroreduction to Near Unity CO on Silver Nanocubes
Nanofoam	97	-0.9	Li Wei [2]	Thiocyanate Modified Silver Nanofoam for Efficient CO_2 Reduction to CO
Hollow Porous Ag Spherical	94	-0.8446	Shao-Qing Liu[3]	Hollow Porous Ag Spherical Catalysts for Highly Efficient and Selective Electrocatalytic Reduction of CO_2 to CO
Deposited Ag NPs on GDE	92	-0.95 to -1.1	Sang Youn Chae[4]	Directly synthesized silver nanoparticles on gas diffusion layers by electrospray pyrolysis for electrochemical CO_2 reduction
Ultrathin 5-fold twinned NWs	99	−0.956	Subiao Liu[5]	Ultrathin 5-fold twinned sub-25 nm silver nanowires enable highly selective electroreduction of CO_2 to CO
Triangular Silver Nanoplates	96.8	0.746	Subiao Liu[6]	Shape-Dependent Electrocatalytic Reduction of CO_2 to CO on Triangular Silver Nanoplates
NPs	94.2	−0.75	Cheonghee Kim[7]	Insight into Electrochemical CO_2 Reduction on Surface-Molecule Mediated Ag Nanoparticles
nano-coral	95	−0.60	Yu-Chi Hsieh[8]	The Effect of Chloride Anions on the Synthesis and Enhanced Catalytic Activity of Silver Nano-Coral Electrodes for CO_2 Electroreduction
nanoporous	92	-0.60	Qi Lu[9]	A selective and efficient electrocatalyst for carbon dioxide reduction
nanofoam	99	-0.30	Dutta[10]	Beyond Copper in CO_2 Electrolysis: Effective Hydrocarbon Production on Silver-Nanofoam Catalysts
Ag	96	-1.0	Riming Wang[11]	Maximizing Ag Utilization in High-Rate CO_2 Electrochemical Reduction with a Coordination Polymer-Mediated Gas Diffusion Electrode

References

1. Liu, S., Sun, C., Xiao, J.,Luo, J.-L., Unraveling Structure Sensitivity in CO_2 Electroreduction to Near-Unity CO on Silver Nanocubes. ACS Catal. 2020, 3158-3163.
2. Ung, D.,Cossairt, B. M., Effect of Surface Ligands on CoP for the Hydrogen Evolution Reaction. ACS Appl. Energy Mater. 2019, 2, 1642-1645.
3. Liu, S.-Q., Wu, S.-W., Gao, M.-R., Li, M.-S., Fu, X.-Z.,Luo, J.-L., Hollow Porous Ag Spherical Catalysts for Highly Efficient and Selective Electrocatalytic Reduction of CO_2 to CO. ACS Sustainable Chem. Eng. 2019, 7, 14443-14450.
4. Chae, S. Y., Lee, S. Y.,Joo, O.-S., Directly synthesized silver nanoparticles on gas diffusion layers by electrospray pyrolysis for electrochemical CO2 reduction. Electrochim. Acta 2019, 303, 118-124.
5. Liu, S., Wang, X.-Z., Tao, H., Li, T., Liu, Q., Xu, Z., Fu, X.-Z.,Luo, J.-L., Ultrathin 5-fold twinned sub-25 nm silver nanowires enable highly selective electroreduction of CO_2 to CO. Nano Energy 2018, 45, 456-462.
6. Liu, S., Tao, H., Zeng, L., Liu, Q., Xu, Z., Liu, Q.,Luo, J.-L., Shape-Dependent Electrocatalytic Reduction of CO_2 to CO on Triangular Silver Nanoplates. J. Am. Chem. Soc. 2017, 139, 2160-2163.
7. Cao, Z., Kim, D., Hong, D., Yu, Y., Xu, J., Lin, S., Wen, X., Nichols, E. M., Jeong, K., Reimer, J. A., Yang, P.,Chang, C. J., A Molecular Surface Functionalization Approach to Tuning Nanoparticle Electrocatalysts for Carbon Dioxide Reduction. J. Am. Chem. Soc. 2016, 138, 8120-8125.
8. Hsieh, Y.-C., Senanayake, S. D., Zhang, Y., Xu, W.,Polyansky, D. E., Effect of Chloride Anions on the Synthesis and Enhanced Catalytic Activity of Silver Nanocoral Electrodes for CO_2 Electroreduction. ACS Catal. 2015, 5, 5349-5356.
9. Lu, Q., Rosen, J., Zhou, Y., Hutchings, G. S., Kimmel, Y. C., Chen, J. G.,Jiao, F., A selective and efficient electrocatalyst for carbon dioxide reduction. Nat. Commun. 2014, 5, 3242.
10. Dutta, A., Morstein, C. E., Rahaman, M., Cedeño López, A.,Broekmann, P., Beyond Copper in CO_2 Electrolysis: Effective Hydrocarbon Production on Silver-Nanofoam Catalysts. ACS Catal. 2018, 8, 8357-8368.
11. Wang, R., Haspel, H., Pustovarenko, A., Dikhtiarenko, A., Russkikh, A., Shterk, G., Osadchii, D., Ould-Chikh, S., Ma, M., Smith, W. A., Takanabe, K., Kapteijn, F.,Gascon, J., Maximizing Ag Utilization in High-Rate CO_2 Electrochemical Reduction with a Coordination Polymer-Mediated Gas Diffusion Electrode. ACS Energy Lett. 2019, 4, 2024-2031.
12. ftp://davinci.chem.umanitoba.ca/pub/marat/SpinWorks/

1.2 Unwrap Them First: Operando Potential-Induced Activation Is Required When Using PVP-Capped Ag Nanocubes as Catalysts of CO_2 Electroreduction

Authors: María de Jesús Gálvez-Vázquez, Heng Xu, Pavel Moreno-García, Yuhui Hou, Huifang Hu, Benjamin J. Wiley, Soma Vesztergom, and Peter Broekmann

CHIMIA International Journal for Chemistry **75** (3), 163-168(6) (2021), DOI: 10.2533/chimia.2021.163

Highlights: A potential-induced activation method was used to effectively remove PVP from the surface of Ag nanocubes. The method requires that the working electrode be polarized to harsh negative potentials. After this step, the catalyst improves its activity during subsequent normal operation at mild (not so negative electrode) potentials. SEM imaging of the electrodes pre- and post-electrolysis reveals that the method causes only minor degradation to the catalyst surface. The method can be fine-tuned by selecting proper electrolyte compositions.

Contributions: I executed all the electrochemical measurements and SEM characterization of the electrodes before and after the electrochemical reactions. Moreover, I analyzed the results and contributed to the manuscript writing.

doi:10.2533/chimia.2021.163 Chimia 75 (2021) 163–168

Unwrap Them First: *Operando* Potential-induced Activation Is Required when Using PVP-Capped Ag Nanocubes as Catalysts of CO_2 Electroreduction

María de Jesús Gálvez-Vázquez[a], Heng Xu[b], Pavel Moreno-García[a], Yuhui Hou[a], Huifang Hu[a], Benjamin J. Wiley[b], Soma Vesztergom*[c], and Peter Broekmann*[a]

Abstract: Metallic nanoparticles of different shape can be used as efficient electrocatalysts for many technologically and environmentally relevant processes, like the electroreduction of CO_2. Intense research is thus targeted at finding the morphology of nanosized features that best suits catalytic needs. In order to control the shape and size distribution of the designed nanoobjects, and to prevent their aggregation, synthesis routes often rely on the use of organic capping agents (surfactants). It is known, however, that these agents tend to remain adsorbed on the surface of the synthesized nanoparticles and may significantly impair their catalytic performance, both in terms of overall yield and of product selectivity. It thus became a standard procedure to apply certain methods (*e.g.* involving UV-ozone or plasma treatments) for the removal of capping agents from the surface of nanoparticles, before they are used as catalysts. Proper design of the operating procedure of the electrocatalysis process may, however, render such cleaning steps unnecessary. In this paper we use poly-vinylpyrrolidone (PVP) capped Ag nanocubes to demonstrate a mere electrochemical, *operando* activation method. The proposed method is based on an observed hysteresis of the catalytic yield of CO (the desired product of CO_2 electroreduction) as a function of the applied potential. When as-synthesized nanocubes were directly used for CO_2 electroreduction, the CO yield was rather low at moderate overpotentials. However, following a potential excursion to more negative potentials, most of the (blocking) PVP was irreversibly removed from the catalyst surface, allowing a significantly higher catalytic yield even under less harsh operating conditions. The described hysteresis of the product distribution is shown to be of transient nature, and following *operando* activation by a single 'break-in' cycle, a truly efficient catalyst was obtained that retained its stability during long hours of operation.

Keywords: Catalyst activation · CO_2 reduction · Electrocatalysis · Nanoparticles · Polyvinylpyrrolidone (PVP)

María de Jesús Gálvez-Vázquez studied chemistry and received her MSc specialization in materials science at the Benemérita Universidad Autónoma de Puebla in Mexico. In 2017 she started her PhD project in the group of Prof. Dr. Peter Broekmann at the University of Bern. Her main focus is the study of different catalyst materials applied for the electrochemical reduction of carbon dioxide under controlled mass transport conditions.

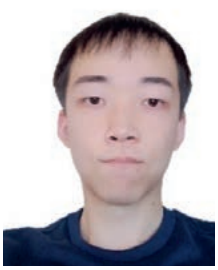

Heng Xu is a PhD student in the Department of Chemistry at Duke University. He received his BSc in chemistry from Jilin University in 2018 and then joined Prof. Dr. Benjamin J. Wiley's group in the same year. His research interests include the shape-controlled synthesis of metal nanocrystals and understanding of the anisotropic growth of metal nanocrystals with electrochemistry.

Dr. Pavel Moreno-García obtained a PhD in chemistry and molecular science at the University of Bern in 2013, under supervision of Prof. Dr. Thomas Wandlowski. At that time, his work was devoted to the study of electronic transport through nanoobjects at electrified interfaces by *in situ* STM. In 2013, he joined the group of Prof. Dr. Peter Broekmann, where he is involved in electrocatalysis research on the direct electrochemical conversion of carbon dioxide to more valuable products, instrumental development, and studies using laser ablation/ ionization mass spectrometry.

Dr. Yuhui Hou received her PhD in physical chemistry from Xiamen University, China in 2015. Before joining Prof. Dr. Peter Broekmann's group at the University of Bern, she worked as a post-doctoral fellow in Hokkaido University (Japan), where she mainly focused on methane conversion. Her current research interest is to develop

*Correspondence: Prof. Dr. P. Broekmann[a], E-mail: peter.broekmann@dcb.unibe.ch; Dr. S. Vesztergom[c], E-mail: vesztergom@chem.elte.hu
[a]University of Bern, Department of Chemistry, Biochemistry and Pharmaceutical Sciences; [b]Duke University, Department of Chemistry, USA ;[c]Eötvös Loránd University, Department of Physical Chemistry, H-1107 Budapest, Pázmány Péter sétány 1/A, Hungary

electrocatalysts *via* colloidal synthesis for electrochemical CO_2 reduction. She is also interested in investigating catalyst degradation under electrochemical CO_2 reduction conditions by identical-location scanning electron microscopy.

Huifang Hu obtained her MSc in materials science and engineering from Fuzhou University (China). After a short experience in technical college, she joined the Interfacial Electrochemistry Group of Prof. Dr. Peter Broekmann as a PhD student in 2019. Her PhD project focuses on the electrochemical conversion of CO_2 into value-added products.

Prof. Dr. Benjamin J. Wiley is a professor in the Department of Chemistry at Duke University. He received his BSc in chemical engineering from the University of Minnesota in 2003, and his PhD in chemical engineering from the University of Washington, Seattle in 2007. Prof. Dr. Wiley is the recipient of the Beilby Medal from the Royal Society of Chemistry and has been recognized as a Highly Cited Researcher by Thomson Reuters in 2014 and 2018. His current research focuses on understanding the processes that drive anisotropic growth of nanostructures and understanding the structure–property relationship of nanostructures and for applications in electronics, medicine, and electrochemistry.

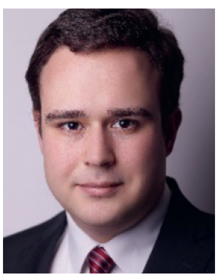

Dr. Soma Vesztergom obtained his MSc (2010) and PhD (2014) degrees in chemistry, working with Prof. Dr. Győző G. Láng at Eötvös Loránd University, Hungary. He was a post-doctoral researcher in Prof. Dr. Peter Broekmann's group at the University of Bern for a year (2014) and is a regular collaborator of this group since then. His research primarily focuses on instrumental developments in electrochemistry and on the modelling of electrocatalytic processes. Currently, he is an assistant professor at Eötvös Loránd University in Budapest.

Prof. Dr. Peter Broekmann obtained his MSc in chemistry (1998) and a PhD (2000) from the University of Bonn. After a post-doctoral stay at the University of Twente (The Netherlands) in 2001, he became project leader at the Institute of Physical Chemistry in Bonn. Since 2008 he holds a lecturer position for electrochemistry at the University of Bern. His research focuses on metal deposition processes for semiconductor and electrocatalysis applications.

1. Introduction

As a result of the ever-increasing consumption of fossil fuels, gigatons of CO_2 are released to the atmosphere every year, expediting global warming.[1] A possible way of mitigating the effects of rising CO_2 concentrations in the atmosphere is to reduce it electrochemically. This approach does not only allow CO_2 to be regarded as a valuable raw material instead of an environmentally dangerous waste, but it may also provide a solution for the storage of excess renewable (hydro-, solar or wind) energy.[1] It is probably for this reason that the topic of electrochemical CO_2 reduction – an otherwise more than 150 years old idea[2] – has recently become the forefront of electrochemical research.[3] Today, a tremendous amount of research is invested in the design of new electrocatalyst materials for CO_2 electroreduction, and researchers seem to agree that apart from their chemical composition it is the nanoscale structure of electrocatalysts that mostly affect their performance.[4,5]

In order to create nanosized catalyst particles with a well-defined size and structure distribution, and to avoid the agglomeration of such particles, the synthesis route of colloidal catalyst nanoparticles (NPs) very often involves the use of surfactants (capping agents). When the aim is to synthesize metallic (*e.g.* Ag[6,7]) NPs, a very often used agent is poly-(vinylpyrrolidone), PVP. PVP owes its popularity to a four-fold synergistic effect, *i.e.* depending on the conditions of synthesis, it may act as a stabilizer, a shape control, a dispersant and/or a reducing agent.[8] Although PVP can be used for the design of a variety of Ag nanostructures (such as nanocubes[6,9] or nanowires[10]), the application of such agents has one significant drawback. That is, surfactants used for the synthesis tend to remain adsorbed on the surface of the nanoparticles, hindering or even impairing their catalytic activity.

As a result, capping agent removal steps must be applied before the NPs can effectively be used as catalysts in a CO_2 electroreduction process. Removal steps often imply the use of additional solvents,[11] or they rely on high temperature plasma[12] or UV–ozone treatments.[13] These require precise optimization in order to remove most of the capping agents while keeping effects detrimental to the catalyst structure at a minimum. Of course, in order to keep the catalyst particles as intact as possible, evading any forms of thermal treatments would be highly desirable, and in this respect the application of electrochemical activation methods seem to provide a viable alternative. That the application of harsh reductive potentials in an electrochemical cell can successfully activate a catalyst (that may afterwards be used more effectively, even under milder conditions) was recently shown by our group for Ag nanowires,[10] and by the group of Buonsanti[14] for Cu nanocrystal catalysts.

In this short communication we aim to investigate this effect further, and show that by applying PVP-capped (untreated) Ag nanocubes for the electroreduction of CO_2, a positive hysteresis effect can be observed when determining the catalytic selectivity towards CO formation as a function of the applied (cathodic) potential. Based on these findings we infer that instead of using thermal methods, surface-pinned capping agents could also be removed and metallic NP catalysts can be activated *operando*, by the application of a 'break-in' cycle in the electrolysis cell.

Effective 'break in', in the case of PVP-capped Ag nanocubes (Ag NCs) applied for the electroreduction of CO_2, requires the setting of harsh cathodic potentials. Under such conditions, although the CO:H_2 yield ratio is far from ideal, most of the capping agents are irreversibly desorbed from the surface of the NCs. While during the time of 'break-in', some catalyst degradation does occur, at the end we obtain a catalyst that works better even under normal (not so harsh) operating conditions. Improvement can be seen both in the achievable current and in the higher selectivity for CO production.

2. Experimental

2.1 *Synthesis of Ag NCs*

Ag NCs were synthesized using a previously reported method with minor modification.[6] 5 cm³ of ethylene glycol (J. T. Baker) was added to a 250 cm³ two-neck flask preheated to 160 °C. A light N_2 flow was introduced just above the ethylene glycol for the first 10 min, followed by heating the solvent for another 50 min. Next, 3 cm³ ethylene glycol solution of $AgNO_3$ (94 mmol dm^{-3}) and 3 cm^3 ethylene glycol solution containing polyvinylpyrrolidone (M_w = 55000 g mol^{-1}, 144 mmol dm^{-3}) and NaCl (0.22 mmol dm^{-3}) were simultaneously injected into the flask at a rate of 45 cm^3 h^{-1}, with the solution observed to turn yellow during this process. Under continuous stirring at 160 °C, the solution exhibited a color transition series from yellow to clear yellow, brown, greenish, and finally ochre and opaque. The whole process required 16 to 24 h for completion. After the solution had turned opaque, the reaction was quenched by adding 22 cm^3 acetone to the hot solution, followed by cooling in an ice-water bath. To purify the NCs, the solution was first centrifuged at 2000 *g* for 30 min, then the precipitate was dispersed and centrifuged, three times, in 10 cm^3 of deionized water at 9000 *g* for 10 min per run.[15]

2.2 *Preparation of Ag NCs catalyst ink*

For the preparation of the carbon-supported Ag NCs ink, 1.5 mg of the Ag NCs and 0.26 mg of carbon black (Vulcan XC 72R, Cabot) were separately dispersed in 10 cm^3 of isopropanol (VLSI Selectipur, BASF) by 1 h sonication. Both suspensions were intermixed, sonicated for 1 h and dried using a rotary evaporator. The obtained carbon-supported Ag NCs were then re-dispersed in 1 cm^3 of isopropanol containing 50 µl of Nafion (5 wt.%, 15–20% water, Sigma-Aldrich). The resulting suspension was subjected to sonication for 1 h, yielding a homogeneous catalyst ink (85% Ag NCs and 15% carbon black).

2.3 *Preparation of the Gas Diffusion Electrodes*

Ag NCs containing gas diffusion electrodes (Ag NC GDEs) for all electrochemical and characterization experiments were prepared as follows: a 0.8 cm × 3 cm carbon paper (Sigracet 39 BC, Fuel Cell Store) was cut and placed over a nylon membrane filter (pore size 0.22 µm, Fischerbrand) on top of the funnel of a vacuum filtrating system. The GDE was then covered by a rectangular mask, leaving 0.2 cm^2 uncovered and 141.5 µl of the carbon supported Ag NCs ink was drop-cast on top of it. The resulting Ag NC GDEs were dried at ambient conditions for at least 30 min and then their backside and edges were masked with Teflon tape, to leave only the Ag NCs ink-modified surface uncovered (0.2 cm^2). Analysis by inductively coupled plasma-mass spectrometry (ICP–MS) of the freshly prepared samples was used to determine the catalyst mass loading, which amounted to ~71 µg cm^{-2} Ag.

2.4 *Electrochemical Measurements and Product Analysis*

Electrochemical experiments were performed using a PGSTAT128N potentiostat/galvanostat (Metrohm Autolab) and a custom-made, airtight H-type cell with a Nafion membrane (Nafion 117, Sigma Aldrich) separating the cathode and anode compartments. The three-electrode arrangement consisted of the Ag-NC-GDE working, a Pt foil (1 cm × 1 cm) counter and a single junction (Pine Research) Ag | AgCl | KCl (sat.) reference electrode. Reported current densities were obtained by normalizing the current to the geometric surface area of the working electrode, 0.2 cm^2. Prior to the electrolysis experiments, both cell compartments were filled with 32 cm^3 of either 0.5 mol dm^{-3} or 2 mol dm^{-3} $KHCO_3$ solution (ACS grade, Sigma-Aldrich) and then saturated by CO_2 gas (99.999%, Carbagas, Switzerland) for at least 30 min. For the sake of comparability, electrode potentials in the paper are referred to the reversible hydrogen electrode (RHE), calculated as:

$$E_{vs.\,\mathrm{RHE}} = E_{vs.\,\mathrm{Ag\,|\,AgCl}} + 210\ \mathrm{mV} + 59\ \mathrm{mV} \cdot p\mathrm{H} \qquad (1)$$

For all potentiostatic experiments, the measured electrode potential was *IR*-corrected post-experimentally, for which the solution resistance was determined impedimetrically at the beginning of electrolysis. The *p*H values of the CO_2-saturated 0.5 mol dm^{-3} and 2 mol dm^{-3} $KHCO_3$ solutions were 7.4 and 7.9, respectively. Electrolyses were run for 60 min and online gas chromatography was applied (every 20 min) to quantify the formed products.

Gaseous products generated in the cell were detected by connecting the purging gas outlet to a GC analyzer (SRI Instruments Multigas Analyzer). The continuous flow of the carrier CO_2 gas through the electrolysis cell carried volatile reaction products from the head-space into the sampling loops of the gas chromatograph. The partial current I_i, corresponding to the formation of a gaseous product i, can be calculated[16] as

$$I_i = x_i\, n_i\, F\, \nu_\mathrm{m}, \qquad (2)$$

where x_i denotes the mole fraction of the products, determined by GC using an independent calibration standard gas (Carbagas); n_i is the number of electrons involved in the reduction reaction to form a particular product (n = 2 for both CO and H_2 formation); F = 96485.3 C mol^{-1} is Faraday's constant; and ν_m is the molar CO_2 gas flow rate measured by a universal flowmeter (7000 GC flowmeter, Ellutia) at the exit of the electrochemical cell. The Faradaic efficiency (FE) of a given reaction product can be determined by dividing the respective partial current, determined from Eqn. (2), by the total current measured electrochemically. A thermal conductivity detector (TCD, for the detection of H_2) and a flame ionization detector (FID, for the detection of CO) were equipped to our gas chromatograph.

The electrolyte was analyzed after the electrolysis experiment to quantify the amount of formate produced by means of ion exchange chromatography (Metrohm Ltd., Switzerland). This chromatograph was coupled to an L–7100 pump, a separation and an ion exclusion column (Metrosep A Supp 7-250) and a conductivity detector.

2.5 *Scanning Electron Microscopy (SEM) and Energy-dispersive X-ray Spectroscopy (EDX) Characterization*

The morphological characterization of the prepared Ag NC GDEs by SEM imaging experiments was performed before (for the as-prepared electrodes) and after electrochemical treatment. Analysis was conducted using a Zeiss Gemini 450 SEM equipped with an InLens secondary electron and a back-scattered electron detector. An accelerating voltage of 5 kV and a beam current of 200 pA were applied at a working distance of 4.5 mm. The AZtec 4.2 software (Oxford Instruments) was used to acquire EDX surface mappings of selected Ag NC GDEs. An acceleration voltage of 10 kV and a beam current of 1.2 nA were applied at a working distance of 8.5 mm.

2.6 *Determination of Catalyst Loading by Inductively Coupled Plasma-Mass Spectrometry (ICP–MS)*

Freshly prepared Ag NC GDEs were immersed in 3 cm^3 of concentrated HNO_3 (BASF) to dissolve the Ag NCs embedded on their surfaces for 24 h. The resulting solutions were diluted with 3% HNO_3 solution by a factor of 500 and were then fed into a NExION 2000 ICP–MS instrument (Perkin Elmer) to obtain the Ag mass loading of the electrodes.

3. Results and Discussion

A peculiar hysteresis effect (Fig. 1) was observed when conducting electrolysis experiments coupled to chromatographic product detection using PVP-capped Ag NCs in a CO_2-saturated, 2.0 mol dm^{-3} $KHCO_3$ solution. Here we carried out potentiostatic electrolyses, all lasting for one hour, and recorded a relatively stationary current that was later averaged and compared to the amounts of CO and H_2, determined by gas chromatography. It is important to note that the determined total amounts of CO and H_2 did not account for a 100% of Faradaic efficiency, and some 5% of formate ($HCOO^-$) was found in the solution by post-electrolysis liquid chromatography analysis after each electrolysis, practically independently from the applied potential.

The first electrolysis experiment was carried out at an applied potential of –0.75 V *vs.* RHE, where the Faradaic efficiency of CO production was relatively low, ~55%. By gradually stepping the potential in the cathodic direction, the FE of CO production first increased, reaching a maximum of ~82% at around –0.9 V, as shown in Fig. 1(a). At potentials even more negative, CO_2 reduction (CO production) became disfavored compared to the competing hydrogen evolution reaction (HER).

In our experiments, –1.1 V was the most extreme potential reached, following which we began to gradually apply lower voltages. As shown in Fig. 1(a), after a first excursion to –1.1 V, the measured FE of CO production remained higher even at potentials just mildly cathodic, and the FE of CO production did not drop below 70% at potentials as positive as –0.6 V *vs.* RHE.

It is interesting to note in Fig. 1(b), showing plots of partial current densities of CO and H_2 formation as a function of potential, that the partial current of HER follows – within range of error – the same track during the negative and the positive going scans of the potential excursion. For CO, however, a significant enhancement of currents can be observed during the latter, positive going scan, which allows us to conclude that the first potential excursion to extremely negative potentials indeed served as a 'break-in' of the catalyst. Although it is obvious that –1.1 V, in the current system, is not an ideal operating potential, it seems that applying this value for a short time allows the catalyst to be operated, later on, at milder potentials, where it can then still produce CO with a good yield.

The described activation method has its origins in the potential-induced removal of PVP from the surface of the Ag NCs, occurring at negative potentials that can overcome the

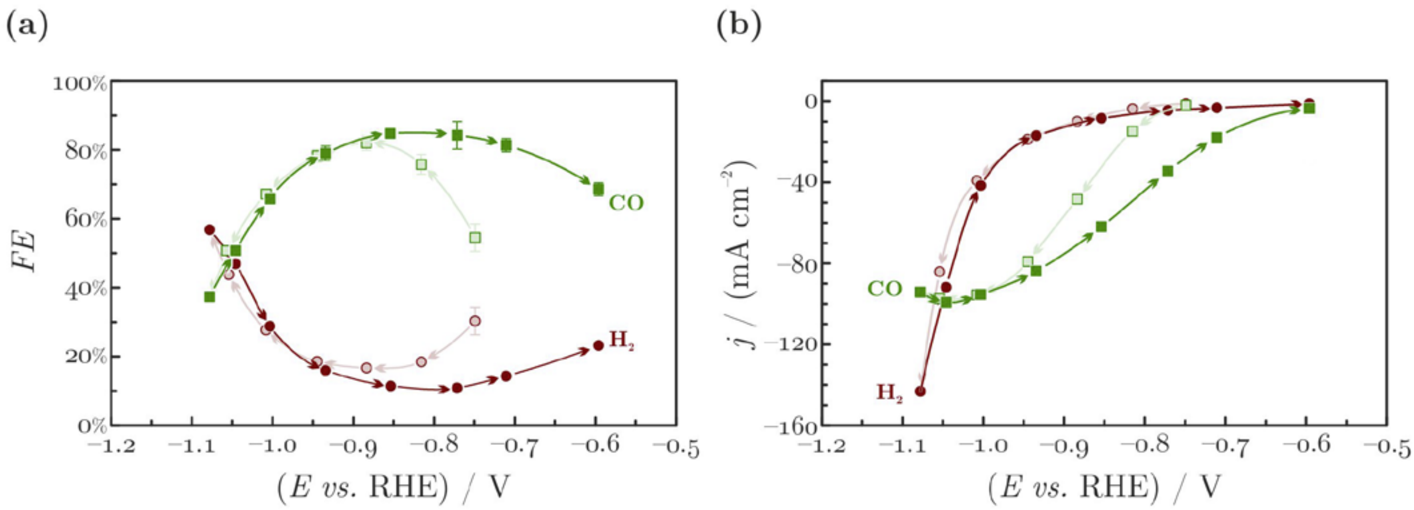

Fig. 1. Potentiostatic electrolyses were carried out using PVP-coated Ag NCs dropcast on a GDE, used as electrocatalysts of CO_2-reduction in a CO_2-saturated 2.0 mol dm^{-3} $KHCO_3$ solution. Faradaic efficiencies (a) and partial current densities (b) of CO (green) and H_2 (red) are shown as a function of the *IR*-drop corrected electrode potential. Data (dots) were recorded by gas chromatography; trends (curves) were created by spline interpolation. Arrows show the direction of the potential excursion.

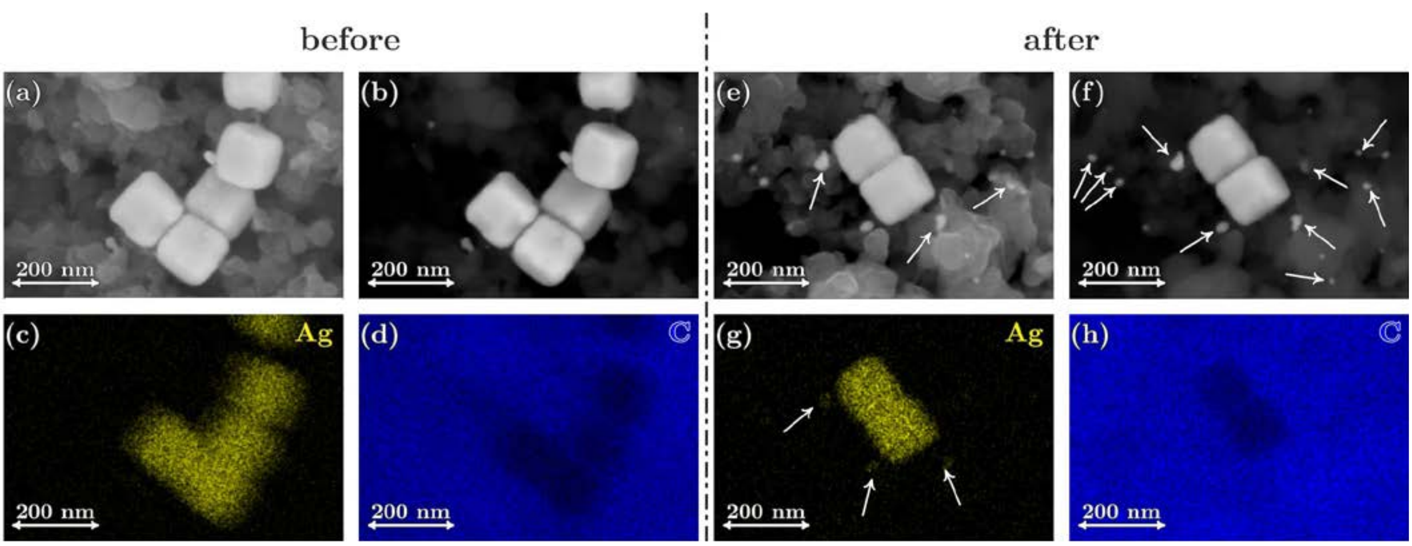

Fig. 2. Ag NCs drop-cast on a GDE, as observed before and after applying the electrochemical treatment shown in Fig. 1, in a CO_2-saturated 2.0 mol dm^{-3} $KHCO_3$ solution. Panels (a) and (e) show the secondary electron, (b) and (f) the back-scattered electron images of the NCs, with a side length of ~100 nm. Elemental composition maps, recorded by EDX, are shown in panels (c) and (g) for silver and in panels (d) and (h) for carbon. The arrows point to smaller Ag particles, formed by the degradation of the NCs during the potential-induced activation.

binding strength between the Ag NCs and their PVP coating.[14] The method can be called *operando*, since it can directly be realized within an electrochemical cell, rendering the use of other (solvent[11] or thermal annealing-based[12,13]) capping agent removal techniques unnecessary.

In order to apply *operando* activation, only a single 'break-in' electrolysis cycle (at suitably negative potentials) is required to gain a catalyst that can later work stably and highly active, even at less reductive potentials. The increase of activity is, as seen in Fig. 1, very significant, and following *operando* activation the catalyst does not lose its activity for hours of electrolyses.

The method has only one, minor flaw: that is, as seen in Fig. 2, during the initial activation step the Ag NCs tend to degrade. As a result, some newly formed, small Ag particles appear on the catalyst surface. These, however, seem not to disturb the electrocatalysis process, and when the electrolysis is continued at milder potentials, degradation stops and no such particles will further be formed.

The degradation effects described above can be sufficiently overcome if we make sure that during the 'break-in' cycle only lower currents (creating less mechanical strain) flow through the catalyst. This can be achieved by supplying less reactants to the surface; *e.g.* by lowering the concentration of the $KHCO_3$ electrolyte from 2 to 0.5 mol dm^{-3}. By conducting electrolyses in such a system, we observe a hysteresis (Fig. 3) that is similar to the one seen in the previous case, although the measured partial currents (both for CO and for H_2) are significantly lower. Yet, this does not seem change the PVP-to-metal binding strength and the value of the cathodic potential that has to be reached in order to break these bonds. Thus the activity increases observed in Fig. 3 compare well with those seen in Fig. 1, while significantly less degradation is observed (compare Figs 4 and 2).

4. Conclusion

Silver nanoparticles with well-defined shapes can be fabricated by a variety of synthesis methods, and the thus prepared particles can potentially be used as efficient catalysts in CO_2

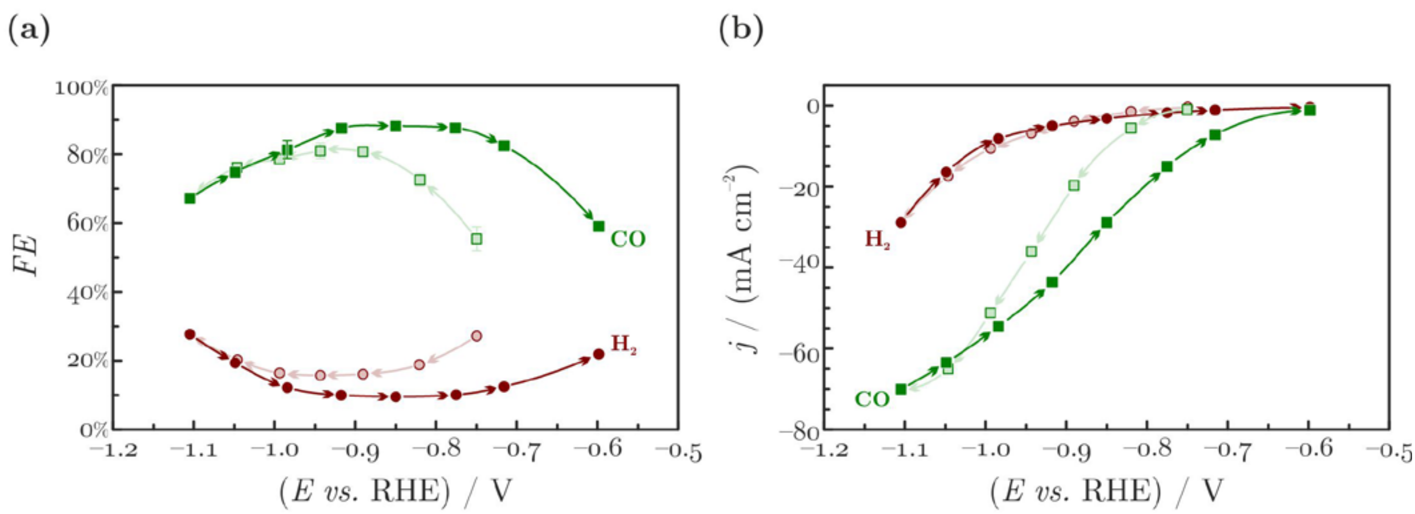

Fig. 3. Potentiostatic electrolyses were carried out using PVP-coated Ag NCs dropcast on a GDE, used as electrocatalysts of CO_2-reduction in a CO_2-saturated 0.5 mol dm^{-3} $KHCO_3$ solution. Faradaic efficiencies (a) and partial current densities (b) of CO (green) and H_2 (red) are shown as a function of the *IR*-drop corrected electrode potential. Data (dots) were recorded by gas chromatography; trends (curves) were created by spline interpolation. Arrows show the direction of the potential excursion.

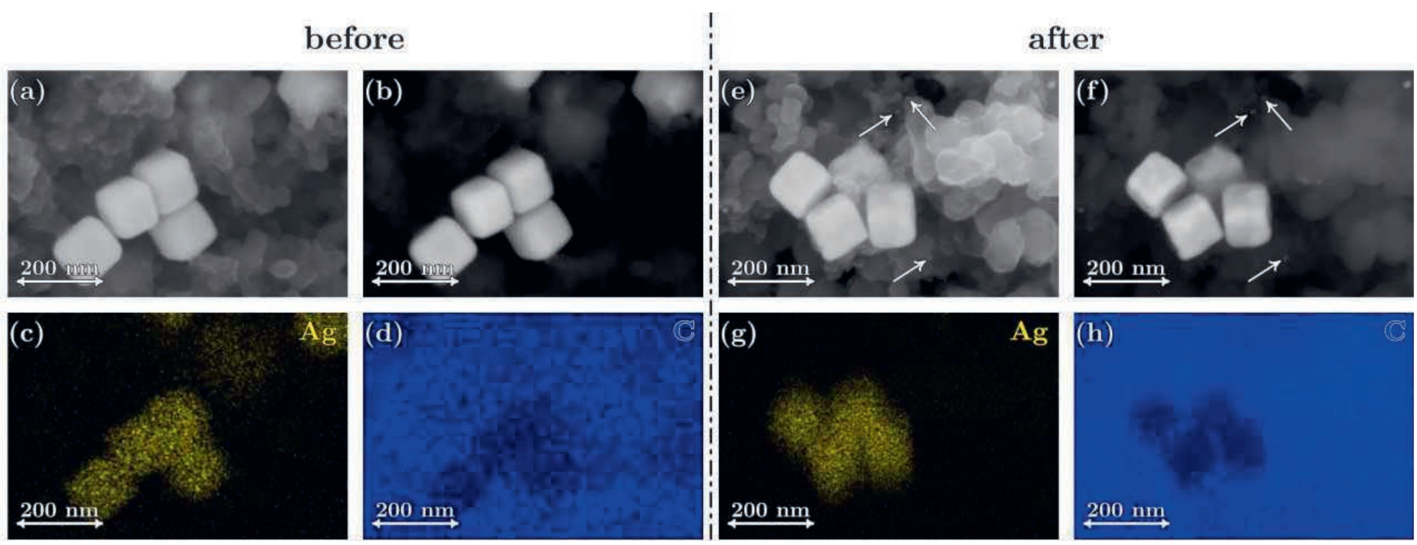

Fig. 4. Ag NCs drop-cast on a GDE, as observed before and after applying the electrochemical treatment shown in Fig. 3, in a CO_2-saturated 0.5 mol dm^{-3} $KHCO_3$ solution. Panels (a) and (e) show the secondary electron, (b) and (f) the back-scattered electron images of the NCs, with a side length of ~100 nm. Elemental composition maps, recorded by EDX, are shown in panels (c) and (g) for silver and in panels (d) and (h) for carbon. The arrows point to smaller Ag particles, formed by the degradation of the NCs during the potential-induced activation.

electroreduction. It is a major problem of catalyst design, however, that PVP – a capping agent used for the shape control of the catalyst particles – can remain adsorbed on the surface of the nanostructures, significantly decreasing the catalytic activity. Although some methods (solvent or thermal annealing based ones) are available for PVP removal, these can potentially damage the catalyst by exhibiting it to contaminations or to thermal shock.

In this short communication we described an alternative, potential-induced activation method that can be used to effectively remove PVP from the surface of Ag nanocubes. The method works *operando* in the electrochemical cell, and requires that before use, the working electrode is polarized to harsh negative potentials. By applying a single ‘break-in’ cycle, we gain a catalyst that shows higher activity and good stability during subsequent normal operation at mild (not so negative) electrode potentials. The described activation method, as was studied by pre- and post-electrolysis SEM imaging, causes only little degradation to the catalyst surface, and the method can be fine-tuned by selecting proper electrolyte compositions.

Acknowledgements

P. B. acknowledges financial support by NCCR Catalysis and from the Swiss National Foundation (grant 200020–172507). S. V. acknowledges support from the National Research, Development and Innovation Office of Hungary (NKFIH grant FK135375). M. de J. G.-V. acknowledges the financial support by the Swiss Government Excellence Scholarships for Foreign Scholars (ESKAS). H. H. acknowledges the financial support by the Chinese Scholarship Council (CSC).

Received: January 21, 2021

[1] D. R. Feldman, W. D. Collins, P. J. Gero, M. S. Torn, E. J. Mlawer, T. R. Shippert, *Nature* **2015**, *519*, 339, https://doi.org/10.1038/nature14240
[2] E. Royer, *Compt. Rend. Hebd. Séances Acad. Sci.* **1870**, *70*, 731.
[3] H.-R. M. Jhong, S. Ma, P. J. A. Kenis, *Curr. Opin. Chem. Eng.* **2013**, *2*, 191, https://doi.org/10.1016/j.coche.2013.03.005
[4] F. Yu, P. Wei, Y. Yang, Y. Chen, L. Guo, Z. Peng, *Nano Mater. Sci.* **2019**, *1*, 60, https://doi.org/10.1016/j.nanoms.2019.03.006
[5] D. Sun, X. Xu, Y. Qin, S. P. Jiang, Z. Shao, *ChemSusChem* **2019**, *13*, 39, https://doi.org/10.1002/cssc.201902061
[6] S. H. Im, Y. T. Lee, B. Wiley, Y. Xia, *Angew. Chem.* **2005**, *117*, 2192, https://doi.org/10.1002/anie.200462208
[7] J. Zhang, Q. Wang, X. Zhang, J. Wang, M. Guo, B. J. Wiley, C. Li, C. Hu, *Inorg. Chem. Front.* **2016**, *3*, 547, https://doi.org/10.1039/C5QI00256G
[8] K. M. Koczkur, S. Mourdikoudis, L. Polavarapu, S. E. Skrabalak, *Dalton Trans.* **2015**, *44*, 17883, https://doi.org/10.1039/C5DT02964C
[9] Y. Hou, N. Kovács, H. Xu, C. Sun, R. Erni, M. d. J. Gálvez-Vázquez, A. Rieder, H. Hu, Y. Kong, M. Liu, B. J. Wiley, S. Vesztergom, P. Broekmann, *J. Catal.* **2020**, *394*, 58, https://doi.org/10.1016/j.jcat.2020.12.006
[10] H. Hu, M. Liu, Y. Kong, N. Mysuru, C. Sun, M. d. J. Gálvez-Vázquez, U. Müller, R. Erni, V. Grozovski, Y. Hou, P. Broekmann, *ACS Catal.* **2020**, *10*, 8503, https://doi.org/10.1021/acscatal.0c02026
[11] N. Naresh, F. G. S. Wasim, B. P. Ladewig, M. Neergat, *J. Mater. Chem. A* **2013**, *1*, 8553, https://doi.org/10.1039/C3TA11183K
[12] I. Puspitasari, E. Skupien, F. Kapteijn, P. Kooyman, *Catalysts* **2016**, *6*, 179, https://doi.org/10.3390/catal6110179
[13] Z. Niu, Y. Li, *Chem. Mater.* **2014**, *26*, 72, https://doi.org/10.1021/cm4022479
[14] J. R. Pankhurst, P. Iyengar, A. Loiudice, M. Mensi, R. Buonsanti, *Chem. Sci.* **2020**, *11*, 9296, https://doi.org/10.1039/D0SC03061A
[15] S. E. Skrabalak, L. Au, X. Li, Y. Xia, *Nat. Protoc.* **2007**, *2*, 2182, https://doi.org/10.1038/nprot.2007.326
[16] A. V. Rudnev, in ‘Encyclopedia of Interfacial Chemistry’, Ed.: K. Wandelt, Elsevier, Amsterdam, **2018**, pp. 321–325.

1.3 Limitations of Identical Location SEM as a Method of Degradation Studies on Surfactant Capped Nanoparticle Electrocatalysts

Authors: Yuhui Hou, Noémi Kovács, Heng Xu, Changzhe Sun, Rolf Erni, María de Jesús Gálvez-Vázquez, Alain Rieder, Huifang Hu, Ying Kong, Menglong Liu, Benjamin J. Wiley, Soma Vesztergom, and Peter Broekmann

Journal of Catalysis, **394**, 58-66 (2021), DOI: 10.1016/j.jcat.2020.12.006

Highlights: In this report, identical-location scanning electron microscopy (IL-SEM) studies on polyvinylpyrrolidone-capped silver nanocubes revealed that the pre-electrolysis exposure of the nanoparticles to the electron beam deactivates their catalytic activity due to the formation of a passive carbonaceous layer formed on the surface of the nanoparticles. Even though the entirety of the catalyst degrades, the spot mapped by IL–SEM reflects no or little changes during electrolysis. Therefore, special attention must be paid when the IL-SEM technique is used to characterize catalyst changes of surfactant-capped nanoparticles.

Contributions: I conducted some of the SEM studies when a glassy carbon electrode was used to support the Ag nanoparticles. Also, I prepared and performed the electrochemical experiments using gas diffusion electrodes and carried out their IL-SEM studies. Furthermore, I participated in the manuscript writing process.

Journal of Catalysis 394 (2021) 58–66

Contents lists available at ScienceDirect

Journal of Catalysis

journal homepage: www.elsevier.com/locate/jcat

Limitations of identical location SEM as a method of degradation studies on surfactant capped nanoparticle electrocatalysts

Yuhui Hou [a,1,*], Noémi Kovács [a,b,1], Heng Xu [c], Changzhe Sun [a], Rolf Erni [d], María de Jesús Gálvez-Vázquez [a], Alain Rieder [a], Huifang Hu [a], Ying Kong [a], Menglong Liu [a], Benjamin J. Wiley [c], Soma Vesztergom [a,b,*], Peter Broekmann [a]

[a] University of Bern, Department of Chemistry and Biochemistry, Freiestrasse 3, 3012 Bern, Switzerland
[b] Eötvös Loránd University, Department of Physical Chemistry, Pázmány Péter sétány 1/A, 1117 Budapest, Hungary
[c] Duke University, Department of Chemistry, French Family Science Cen 2214, NC–27708 Durham, NC, USA
[d] Swiss Federal Laboratories for Materials Science and Technology (EMPA), Electron Microscopy Center, Überlandstrasse 129, CH–8600 Dübendorf, Switzerland

A R T I C L E I N F O

Article history:
Received 14 October 2020
Revised 11 December 2020
Accepted 12 December 2020
Available online 23 December 2020

Keywords:
Electrocatalysis
CO_2 reduction
Electron microscopy
Under-beam contamination
Carbon
Polyvinylpyrrolidone (PVP)

A B S T R A C T

Identical location scanning electron microscopy (IL–SEM) has become an important tool for electrocatalysis research in the past few years. The method allows for the observation of the same site of an electrode, often down to the same nanoparticle, before and after electrochemical treatment. It is presumed that by IL–SEM, alterations in the surface morphology (the growth, shrinkage, or the disappearance of nanosized features) can be detected, and the thus visualized degradation can be linked to changes of the catalytic performance, observed during prolonged electrolyses. In the rare cases where no degradation is seen, IL–SEM may provide comfort that the studied catalyst is ready for up-scaling and can be moved towards industrial applications. However, although it is usually considered a non-invasive technique, the interpretation of IL–SEM measurements may get more complicated. When, for example, IL–SEM is used to study the degradation of surfactant-capped Ag nanocubes employed as electrocatalysts of CO_2 electroreduction, nanoparticles subjected to the electron beam during pre-electrolysis imaging may lose some of their catalytic activity due to the under-beam formation of a passive organic contamination layer. Although the entirety of the catalyst obviously degrades, the spot mapped by IL–SEM reflects no or little changes during electrolysis. The aim of this paper is to shed light on an important limitation of IL–SEM: extreme care is necessary when applying this method for catalyst degradation studies, especially in case of nanoparticles with surface-adsorbed capping agents.

1. Introduction

Due to the ever-increasing consumption of fossil fuels, gigatons of CO_2 are released yearly to the atmosphere, expediting global warming [1]. A possible way of mitigating the effects of atmospheric CO_2 is to reduce it electrochemically. Electrochemical reduction does not only allow CO_2 to be regarded as a valuable raw material instead of an environmentally dangerous waste, but it may also provide a solution for the storage of excess renewable (hydro-, solar or wind) energy [2].

Mostly due to this, electrochemical CO_2 reduction —a process that was first described more than 150 years ago [3]— has recently become the forefront of electrochemical research [4]. Searching for the term “electrochemical CO_2 reduction” on the website of ACS Publications yields 3334 research papers about this topic, only from the past year; Google Scholar, when searched for the same term and for the same period of time, gives $>$ 17000 matches. A majority of these publications are original research papers that describe new catalyst materials, which —somewhat remarkably— all exhibit excellent qualities when applied for CO_2 reduction. This means that by covering electrodes with the newly invented catalysts, and carrying out electrolyses of solutions that contain CO_2 dissolved in some form, high current densities of CO_2 reduction can be achieved at relatively low overpotentials, and the process may in an ideal case yield only one or just a few desired products [4].

* Corresponding authors at: University of Bern, Department of Chemistry and Biochemistry, Freiestrasse 3, 3012 Bern, Switzerland (Y. Hou); Eötvös Loránd University, Department of Physical Chemistry, Pázmány Péter sétány 1/A, 1117 Budapest, Hungary (S. Vesztergom).

E-mail addresses: yuhui.hou@dcb.unibe.ch (Y. Hou), vesztergom@chem.elte.hu (S. Vesztergom), peter.broekmann@dcb.unibe.ch (P. Broekmann).

[1] These authors contributed equally.

https://doi.org/10.1016/j.jcat.2020.12.006
0021-9517/

Compared to the tremendous amount of research invested in the design of new electrocatalyst materials for CO_2 electroreduction, technologies that operate on an industrial scale are still rare. Undoubtedly, the most important obstacle that hinders the application of newly developed catalysts on an industrial level is an issue of stability: catalysts that may show remarkable features in lab experiments tend to degrade and lose their performance over prolonged use. This may especially be true for catalysts owing their activity to a fine structure, such as colloidally synthesized nanoparticles that are especially prone to degradation over long-time operation. In case of these catalysts, studying (electro-)mechanical degradation and its effects on the catalytic performance has to be the first step of technological up-scaling.

Although many *operando* techniques (*e.g.*, X-ray diffraction, scattering or absorption, as well as Raman spectroscopies [5,6]) can provide an insight to nanoparticle transformations occurring during CO_2 reduction, it is still more common to use *ex situ* electron microscopic (EM) techniques to observe, in particular, the structural changes that electrocatalysts suffer during CO_2 reduction.

In order to apply EM in an electrocatalysis study, the catalyst has to be sampled before and after it is made subject to electrochemical treatment. When comparing images taken before and after electrolysis, we usually work under two implicit assumptions: *(i.)* that the areas scanned before and after the electrolysis are either physically the same, or are both representative of the sample as a whole; and *(ii.)* that any changes we observe are indeed caused by the electrochemical treatment and not by other operations, *e.g.,* the pre-electrolysis scanning of the sample, careless sample transportation, exposition to air or to chemicals, etc.

The former of the above two assumptions can readily be made explicit, for example, if identical location scanning or transmission electron microscopies (IL–SEM or IL–TEM) are employed. IL–TEM was first described by a work of Mayrhofer et al. in 2008 [7], and the first report on the application of IL–SEM by Hodnik et al. [8] followed not much later, in 2012. In early studies, the catalyst material was loaded on a TEM finder grid (made of gold) to facilitate identical location imaging [7]. Later it was found that it is enough to apply a small incision (a cross-like scratch) on other (*e.g.*, graphite) holders to relocate the scanned site after electrolysis, which rendered the use of finder grids unnecessary. Due to the fact that IL–EM is able to visualize changes of a catalyst surface, often down to the details of individual nanoparticles, IL–EM found immediate application in catalyst degradation studies on a variety of target reactions [9,10].

In the field of CO_2 electrolysis, IL–EM became a prominent method of studying catalyst degradation [11–21], mainly because it is considered (and, starting from its discovery, often advertised as) a non-destructive method. It is usually assumed that if a given catalyst preserves good performance characteristics over longer periods of electrolysis, and neither IL–SEM nor IL–TEM reveal any structural degradation, the catalyst is stable and can be considered a potential candidate for up-scaled (*e.g.*, flow cell) studies [15].

Unfortunately, however, the situation is not this simple, especially because, in some cases, the pre-electrolysis EM imaging does affect the future catalytic performance of the sampled catalyst areas. For example, in the literature of IL–TEM studies of electrocatalysts, there are reports on the electron beam induced shrinkage (as well as some ripening) of Pt nanoparticles used in fuel cells [22]. Based on these results, Arenz and Zana strongly recommend that in order to check if the electron beam changes the sample, TEM analysis following the electrochemical measurements should also be performed at pristine locations; *i.e.*, locations which have not been previously exposed to the electron beam [23].

For IL–SEM, probably based on the assumption that the electron dose is much lower than in the case of TEM, no such warning was given, and it is indeed not likely that the beam used under SEM conditions could induce similar sintering effects observed in TEM. The sintering of nanoparticles may however not be the only way an electron beam can alter a catalyst surface: another, equally important phenomenon —namely, the under-beam formation of a passive layer— should also deserve attention.

That electron bombardment of a conducting sample *in vacuo*, where only slightest traces of organic vapours occur, can result in the coverage of the sample with a non-conducting layer of polymerized carbon compounds was first noticed by Lariviere Stewart [24] in 1934 — that is, four years before von Ardenne built the first SEM [25]. That electron bombardment, especially during focusing, can also cause changes to the surface of a sample inside an SEM was first noticed as early as 1946 by Marton et al. [26]. Recently, two reviews from Postek et al. [27,28] discussed some issues of interpreting SEM images: the second part [28] was entirely devoted to the issue of electron beam-induced specimen contamination.

Postek et al. [28] pointed out that the origin of beam-induced contaminations can both be the sample itself and the vacuum system of the SEM. While the cleanliness of the latter can be significantly improved (for example, by the replacement of diffusion pumps with turbomolecular ones backed by dry backing pumps in modern instruments), the history of the specimen prior to entering the vacuum system still remains important [28]. In case of samples with significant organic content, organic molecules remaining on the sample surface can break, undergo polymerization, and get "pinned" to the sample by the beam during scanning [28]. Depending on the electron dose, the formed carbonaceous layer can grow at a rate of a few nanometers/seconds over the sample surface, even if only low accelerating voltages are used.

It is interesting to note that although under-beam contamination is a well-studied subject in the literature of SEM (see [27,28], as well as the references cited therein), studies on the effect of under-beam contamination/passivation on the future electrochemical behaviour of the sample are scarce, and are mostly focused on corrosion and not on electrocatalytic properties [29]. Yet, as we are going to demonstrate in this paper, under-beam passivation can practically disable the sampled part of a catalyst, especially if it contains organic remnants (capping agents) from the synthesis process. While other parts of the catalyst (not affected by the electron beam before electrolysis) remain active and very often degrade significantly during the catalysed process, the part of the sample affected by pre-electrolysis scanning remains intact, and probably entirely passive, due to the carbonaceous film formed on it under the beam.

Here we demonstrate, by IL–SEM studies on polyvinylpyrrolidone (PVP) functionalized Ag nanocubes used as electrocatalysts for CO_2 reduction, a catalytic activity disabling effect of a passive carbonaceous layer that is known to be formed under the electron beam during pre-electrolysis SEM scans [30]. The aim of this paper is to emphasize the necessity of extreme care being taken not to misinterpret IL–SEM studies that seemingly demonstrate excellent catalyst stability.

2. Experimental

Catalyst preparation. Ag nanocubes (Ag NCs) were prepared by an upscaled synthesis route described elsewhere [31]. As support, a glassy carbon plate (2 mm thickness, Alfa Aesar, type 1) was mirror-polished (0.5 μm alumina suspension, Buehler), was thoroughly rinsed with ultrapure water and ethanol, dried, and masked with an inert PTFE tape to leave an 0.8 cm × 1 cm geometric surface area open for catalyst coating.

In order to form a carbon-supported Ag NC catalyst, 5.6 mg of the as-prepared Ag nanocubes [31] (in the form of powder) was dispersed in 6 cm^3 isopropanol (VLSI Selectipur, BASF) by a 1-hour sonication. 1.5 mg of technical carbon powder (Vulcan XC 72R, Cabot, USA) was also dispersed in 3 cm^3 isopropanol by 1-hour of sonication, and the two suspensions were subsequently mixed by sonicating for 30 min. The resulting suspension was dried overnight under vacuum conditions, yielding a C-supported Ag NC catalyst powder. This powder was re-dispersed in 1.5 cm^3 of isopropanol containing 75 $\mu\ell$ of a Nafion solution (Aldrich, 5 wt% dissolved in a mixture of lower aliphatic alcohols and water). The obtained dispersion was subjected to sonication for 30 min, and for each electrode, 25 $\mu\ell$ of the resulted ink was drop-cast onto the glassy carbon plate and dried in a vacuum oven.

An Ag NC catalyst without carbon support was prepared by dispersing 22 mg of the as-prepared Ag NCs in 6 cm^3 isopropanol by 1-hour sonication and spin-coating 75 $\mu\ell$ of this suspension onto a glassy carbon support in three steps over 1 minute, using 1000 min^{-1} rotation rate on an Ossila spin coater.

Both the C-supported and the unsupported Ag NC catalysts were exposed to a UV-ozone atmosphere (PSD Series, Novascan, operated with air at atmospheric pressure) for 12 min.

For studies on a gas diffusion electrode (GDE, experimental details were described elsewhere [15]) the suspension of carbon-supported Ag NCs was drop-cast on the hydrophobic surface of a Sigracet 39 BC (Fuel Cell Store) GDE, and the nanocubes were percolated through the porous body of the GDE by a vacuum filtration system placed on the rear side of the electrode, followed by air-drying at ambient conditions lasting 30 min. No UV-ozone treatment was applied to the thus prepared, Ag NC-modified GDE. The GDE was used as part of the gas flow cell described in [15], combined with a Sustainion alkaline membrane (X37-50 RT, Dioxide materials) and an anode compartment containing 2 mol dm^{-3} KOH solution.

XPS Characterization. X-ray photoelectron spectroscopy (XPS) studies were carried out using a Thermo ESCALAB 250 XI instrument at a pass energy of 30 eV using monochromated Al K-α line ($h\nu = 1486.7$ eV). Charge correction was based on the position of the C*1s* peak (284.8 eV). The XPS spectra were subjected to a Shirley background subtraction and were analysed using the CasaXPS software.

Electrocatalysis studies. For all electrochemical experiments, a potentiostat/galvanostat (Metrohm Autolab 302N, The Netherlands) was used to control the potential, current density, and transferred charge. The electrolysis experiments were carried out using a custom-built, air-tight, H-type glass cell. Apart from the working electrode that was prepared as described above, the three-electrode arrangement consisted of a "leakless" Ag|AgCl|3 mol dm^{-3}KCl reference (Pine) and a Pt-foil (1.5 cm × 0.5 cm, Goodfellow) counter electrode. For electrolyses, 0.5 mol dm^{-3} $KHCO_3$ (ACS grade, Sigma-Aldrich) electrolyte solutions were prepared with ultrapure water (Milli-Q by Merck Millipore) and were saturated with CO_2 (99.999%, Carbagas, Switzerland). During the experiments, continuous gas flow was maintained through the electrolyte solution. To avoid possible fluctuations in CO_2 solubility caused by a change in the ambient temperature, all electrochemical experiments were performed at 20 °C, by immersing the H-type cell into a thermostated water bath. Automatic *IR* compensation was applied following the determination of the cell resistance by positive feedback. For the sake of comparability, all potentials given herein were converted to the reversible hydrogen electrode (RHE) scale. The reported current densities were normalized to the geometric surface area.

Gaseous products generated in the cell were detected by connecting the purging gas outlet to a GC analyzer (SRI Instruments Multigas Analyzer Nº3). The continuous flow of the carrier CO_2 gas through the electrolysis cell carried volatile reaction products from the head-space into the sampling loops of the gas chromatograph. The partial current I_i, corresponding to the formation of a gaseous product i, can be calculated [32] as

$$I_i = x_i n_i F \nu_m, \tag{1}$$

where x_i denotes the mole fraction of the products, determined by GC using an independent calibration standard gas (Carbagas); n_i is the number of electrons involved in the reduction reaction to form a particular product ($n = 2$ for both CO and H_2 formation); $F = 96485.3$ C mol^{-1} is Faraday's constant; and ν_m is the molar CO_2 gas flow rate measured by a universal flowmeter (7000 GC flowmeter, Ellutia) at the exit of the electrochemical cell.

The Faradaic efficiency (*FE*) of a given reaction product can be determined by dividing the respective partial current, determined from Eq. (1), by the total current measured electrochemically. A thermal conductivity detector (TCD, for the detection of H_2) and a flame ionization detector (FID, for the detection of CO) were applied in our studies. We found that in the studied system H_2 and CO are the only two detectable products, accounting for $100\% \pm 5\%$ of the current density that was electrochemically measurable. The electrochemically measured current densities were thus subdivided into partial current densities by taking into account the chromatographically determined concentration ratios, as will be shown later in Fig. 2. During operation, aliquots were analysed in intervals of 20 min during steady state electrolyses.

EM Measurements. EM analysis was conducted with a Zeiss Gemini 450 SEM with an InLens secondary electron (SE) and a backscatter electron detector (BSD). An accelerating voltage of 1.5 kV (probe current of 20 pA) and 5.0 kV (probe current of 120 pA) were applied for SE and BSD imaging, respectively. For high-angle annular dark-field scanning transmission electron microscopy (HAADF–STEM) combined with energy-dispersive X-ray spectroscopy (EDX) and TEM imaging, an FEI Titan Themis (equipped with a SuperEDX detector) was used with an acceleration voltage of 300 kV.

3. Results and discussion

In colloidal nanoparticle synthesis, PVP is a widely applied shape-control agent that promotes the growth of specific crystal faces while hindering others [33,34]. In the synthesis of Ag NCs used in this study, PVP —by strongly binding to the (100) facets of Ag—, facilitated the formation of almost perfect nanocubes of side lengths of about 100 nm, as shown in Fig. 1a. The XPS spectrum (Fig. 1b) of a catalyst prepared without carbon support clearly exhibits a strong Ag*3d* signal, as well as a small peak that can be assigned to the N*1s* excitation of the PVP molecules adsorbed on the surface of the nanocubes. As shown in Fig. 1b, the applied UV-ozone treatment resulted in a significantly decreased N*1s* peak intensity. The peak has not disappeared, however, which hints that some PVP still remained on the surface despite the UV-ozone treatment.

Although the adsorbed PVP could, in principle, inhibit the catalytic activity of the nanocubes [35,36], the UV-ozone treated, C-supported Ag NCs showed good performance when applied for the electroreduction of CO_2. This is demonstrated by Fig. 2a, showing the current density and the product distribution as a function of the applied electrode potential. The current densities shown in Fig. 2a were averaged for 1-hour electrolyses carried out in CO_2 saturated 0.5 mol dm^{-3} $KHCO_3$ solutions: for the electrolyses at different potentials, fresh solutions and newly prepared catalysts were applied.

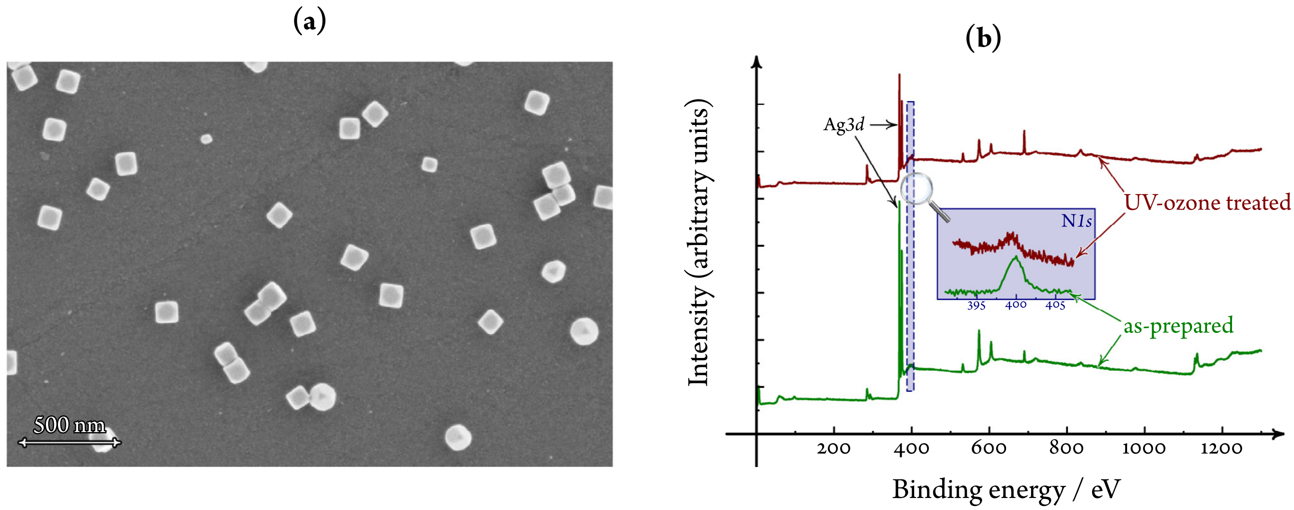

Fig. 1. Scanning electron micrograph **(a)** and X-ray photoelectron survey **(b)** of the unsupported Ag NC catalyst. XPS spectra are shown in **(b)** for the as-prepared catalyst (green curve) and for the catalyst made subject to UV-ozone treatment (red curve) as well. (For interpretation of the references to colour in this figure legend, the reader is referred to the web version of this article.)

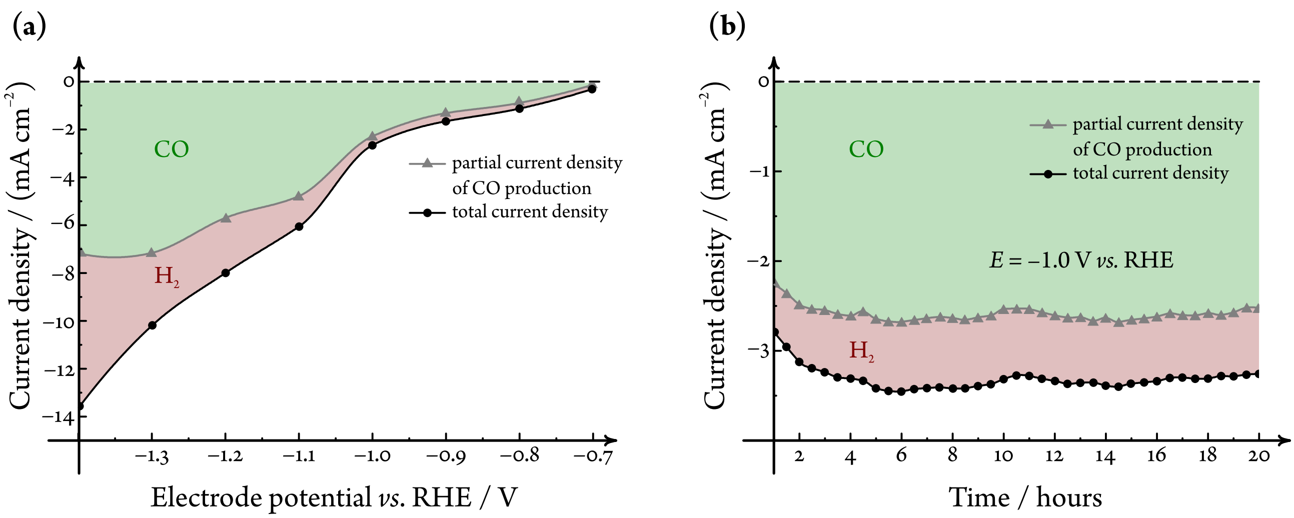

Fig. 2. The electrocatalytic performance of carbon-supported Ag nanocubes, used as catalysts of CO_2 electroreduction in a CO_2-saturated 0.5 mol dm^{-3} $KHCO_3$ solution. **(a)** Potential dependence of the current density and the product distribution, as determined by means of online gas chromatography in an H-type cell for 1-hour electrolyses. Each electrolysis (data points) were carried out using a freshly prepared catalyst and a fresh solution. Curves were created by interpolation. **(b)** Time dependence of the catalytic performance, as determined by a single electrolysis experiment lasting 20 hours, with subsequent chromatographic head-space analysis (data points). The curve was created by interpolation.

It is known that on Ag, the primary product of CO_2 reduction is CO [37]. The same is true for the carbon-supported Ag NCs, with the addition that compared to plain silver —*e.g.*, a silver foil [14]— the Ag nanocubes exhibit a broader overpotential range for CO production. That is, only a little amount of H_2 is formed at potentials less negative than −1.1 V *vs.* RHE, and CO_2 reduction generally prevails over hydrogen evolution in the entirety of the studied potential range ($-1.3\ \mathrm{V} < E < -0.7\ \mathrm{V}$). This observation is in agreement with other reports on nanoparticulate silver catalysts of CO_2 electroreduction [38].

In order to check the stability of the catalyst, we chose the moderate potential value of −1.0 V *vs.* RHE for a prolonged operation study. As shown in Fig. 2b, the catalyst preserved both its overall activity and its relative selectivity towards the production of CO (the Faradaic efficiency of CO formation was about 80%) for an electrolysis lasting 20 hours.

Nevertheless, since catalysts can maintain their macroscopic activity even as they undergo partial deactivation or decomposition [39], we carried out IL–SEM investigations of the working electrode surface, which —although the overall activity remained unchanged— indeed revealed some degradation.

In Fig. 3 we compare two scanning electron micrographs of the same spot of a working electrode surface; one recorded before (Fig. 3a) and one after (Fig. 3b) a 20-hours electrolysis treatment at −1.0 V *vs.* RHE, similar to the one used to obtain the data of Fig. 2b. Fig. 3a shows highly isotropic Ag NCs of a side length of about 100 nanometers, distributed evenly on the supporting carbon matrix. As revealed by Fig. 3b, the nanocubes undergo some slight deformation and shrinkage during electrolysis, and, more prominently, some subnanometer sized particles appear on the surface. EDX mapping (Fig. 3c) confirmed that these small particles consist of silver, and are most probably formed as a debris of nanoparticle degradation due to the mechanical impact of gas evolution [16].

In order to get a clearer view of the degradation process of Ag NCs, the above SEM experiment was repeated with a working elec-

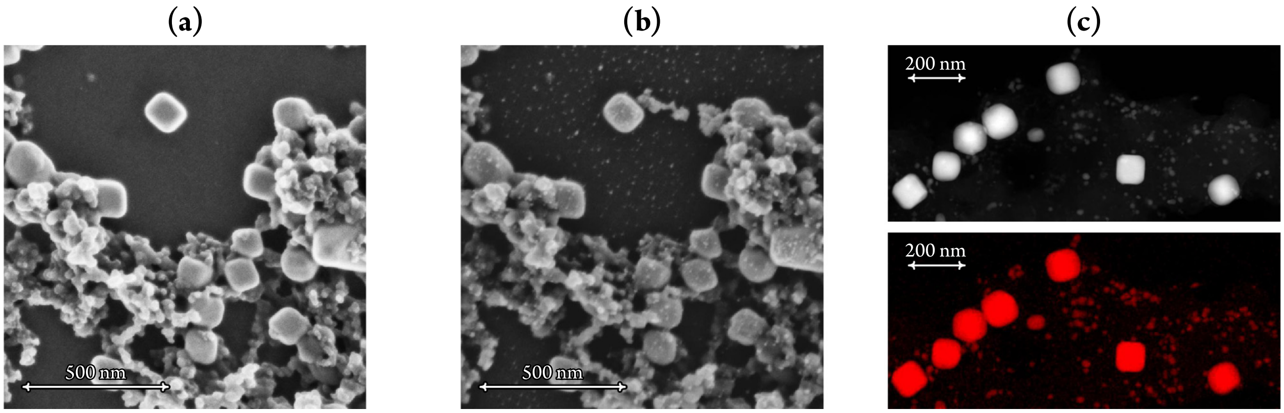

Fig. 3. IL–SEM investigation of the degradation of carbon-supported Ag nanocubes, used as catalysts of CO_2 electroreduction. The same spot of the working electrode surface is shown just before **(a)** and right after **(b)** the electrode was used for a 20-hours electrolysis of a CO_2-saturated 0.5 mol dm^{-3} $KHCO_3$ solution at an electrode potential of −1.0 V *vs.* RHE. The formation of subnanometer sized Ag particles during electrolysis is revealed by the HAADF–STEM (gray-scale) and EDX scans (red-scale) in **(c)**, recorded post-electrolysis at a pristine location that has not been subjected to an electron beam before.

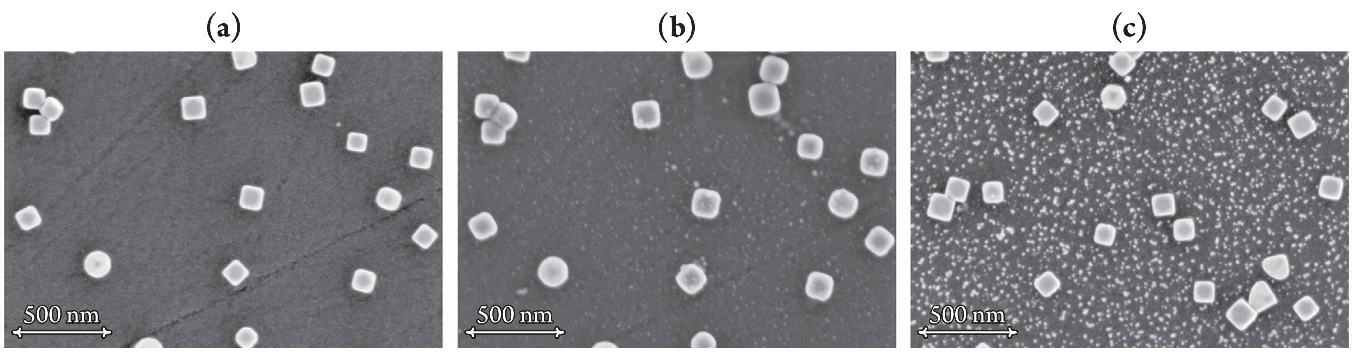

Fig. 4. SEM investigation of the degradation of non-supported Ag nanocubes, used as catalysts of CO_2 electroreduction. The same spot of the working electrode surface is shown just before **(a)** and right after **(b)** the electrode was used for a 20-hours electrolysis of a CO_2-saturated 0.5 mol dm^{-3} $KHCO_3$ solution. A different spot of the same sample is shown after electrolysis in **(c)**.

trode prepared without the supporting carbon matrix (see the Experimental section for details).

The as-prepared electrode surface is shown in Fig. 4a, exhibiting cubic shaped Ag nanoparticles distributed on the glassy carbon electrode substrate. Somewhat surprisingly, the SEM image of the same spot, recorded after a 20-hours electrolysis, shows practically no degradation and the appearance of just a little amount of the subnanometer sized particles, as shown in Fig. 4b. What is even more surprising is that if we record an SEM micrograph with the same configuration, just of a different spot of the sample —that was not scanned before electrolysis—, the picture gets quite different. Fig. 4c clearly shows slightly deformed Ag nanocubes, along with a significant amount of Ag debris formed during electrolysis.

The micrographs of Fig. 4 very clearly reveal an important pitfall of IL–SEM analysis; namely, that due to electron beam-induced changes of the catalyst surface during the pre-electrolysis scan, the sample may get at least partially deactivated for the catalysed process. Due to its decreased electrocatalytic activity, the pre-scanned area of the sample may show no or little changes during the electrolytic process, while other spots (that were not affected by pre-electrolysis SEM scanning) preserve their activity and, in turn, exhibit significant degradation. In other words, the often advertised nondestructiveness of IL–SEM [8,9] should not be taken as granted — at least, not for all catalyst types.

That the effect shown in Fig. 4 can indeed be explained by pre-electrolysis electron beam–sample interactions is further demonstrated by Fig. 5, showing an SEM micrograph of a working electrode surface obtained after electrolysis. Only a part (a rectangular segment) of this sample was scanned by SEM before electrolysis took place, and despite that the sample was exposed

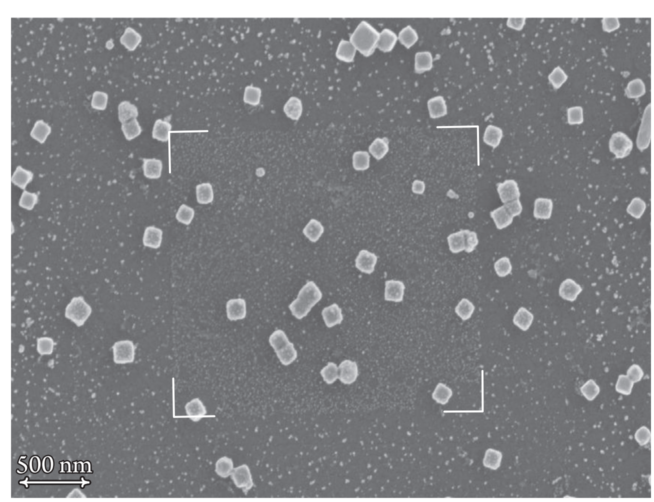

Fig. 5. SEM micrograph of a sample of non-supported Ag NC catalyst taken after a 40-hours electrolysis at −1 V *vs.* RHE in a CO_2-saturated 0.5 mol dm^{-3} $KHCO_3$ solution. A rectangular segment of the sample —shown in the image by its corners— was also scanned before electrolysis. This pre-scanned area exhibits different degradation features compared to the rest of the surface.

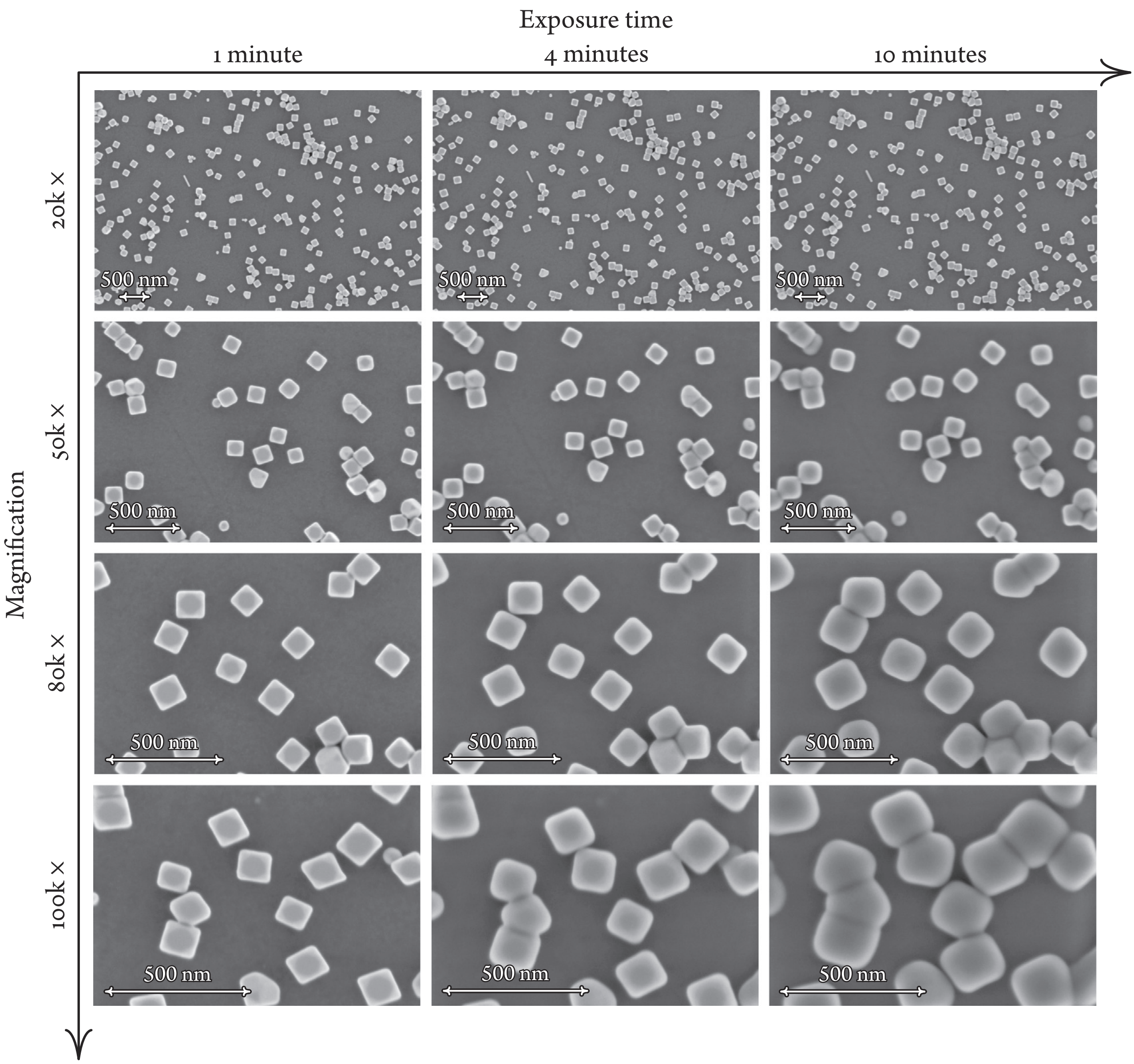

Fig. 6. SEM micrographs of a catalyst surface, obtained using different magnifications and after different scanning times. The applied accelerating voltage was 1.5 kV.

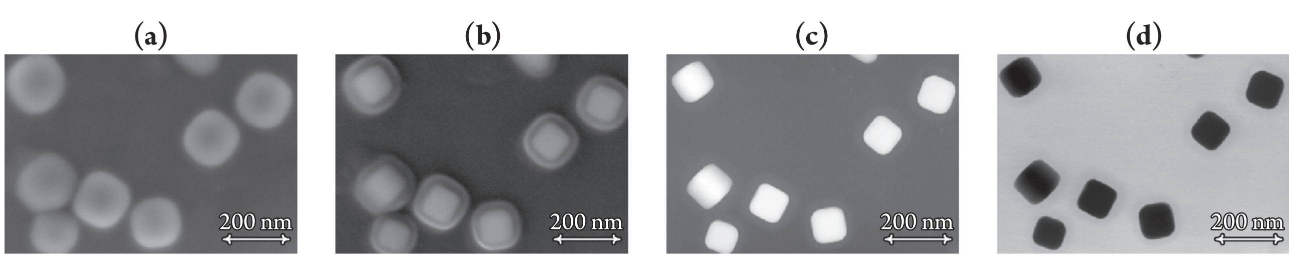

Fig. 7. Electron microscopic images of Ag NCs after electron beam irradiation was carried out for 10 min with a scanning electron beam of 1.5 kV accelerating voltage. **(a)** Secondary electron SEM image taken at 1.5 kV acceleration voltage. **(b)** Secondary electron SEM image obtained at 20 kV. **(c)** HAADF–STEM image taken at 300 kV. **(d)** TEM bright field image taken at 300 kV.

to the electron beam only for a short time, a marked difference can be observed between the degradation features of the pre-scanned segment and the rest of the surface area. Most notably, the coverage of the pre-scanned area with the subnanometer sized Ag particles is less pronounced, compared to other sites. This hints that the electron beam exerts an effect not only on the Ag nanoparticles but also on the underlying glassy carbon substrate.

Note that provided we refrain from long-time exposure of the sample to the electron beam, the above-described electron beam irradiation effect is hardly noticeable *per se*. Yet, as shown by Fig. 5, even the irradiation damages that remained undetected dur-

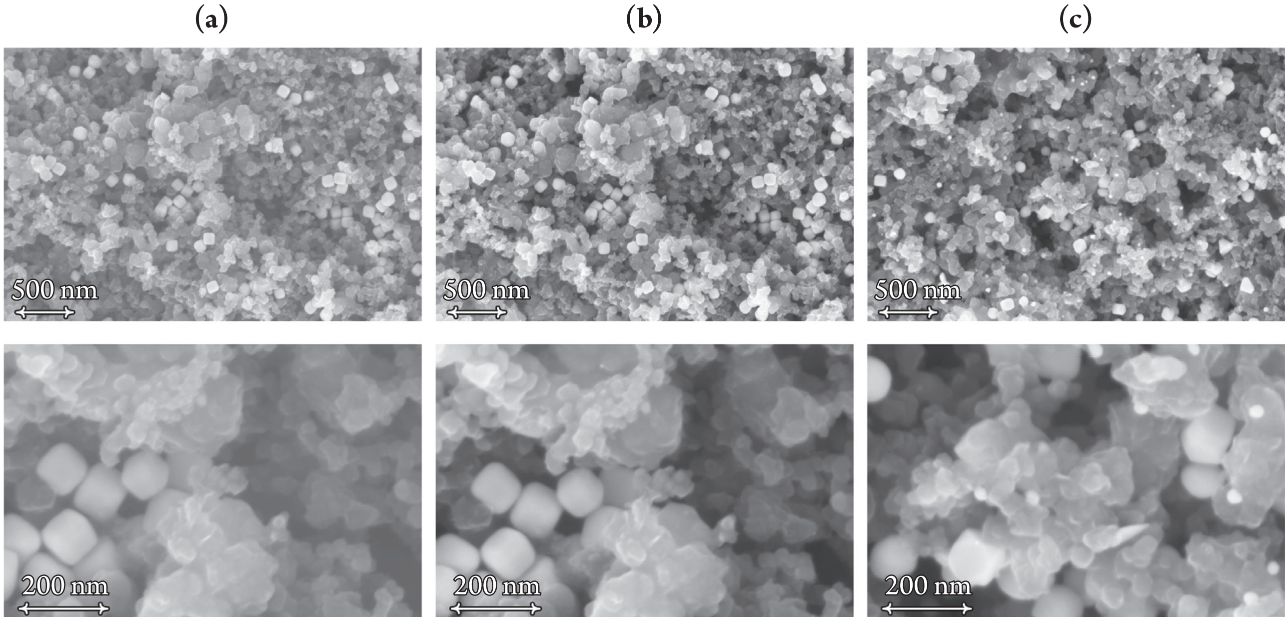

Fig. 8. SEM micrographs of different magnification of a GDE modified by Ag NCs. Identical locations are shown prior to **(a)** and after **(b)** a potentiostatic electrolysis at −2.0 V *vs.* an Ag | AgCl | 3 mol dm^{-3} KCl(aq) reference electrode consuming 1600 C cm^{-2}. A different location is shown after the electrolysis in **(c)**.

ing pre-electrolysis EM scanning can prove significant when the sample is used for electrolysis and scanned afterwards.

To demonstrate the irradiation effect in itself, we carried out prolonged SEM scans on one of our catalyst samples. As revealed by Fig. 6, the effect of contamination (as visualized by the growth and even the apparent merging of the nanocubes) is more pronounced when larger magnifications are applied (*i.e.*, when the beam is more focused) or when the sample is scanned for longer times.

At first glance, the growing and subsequently merging nanocubes shown in Fig. 6 may resemble the coalescence of Pt nanoparticles observed by Chorkendorff et al. under *in situ* TEM conditions [22]. Note, however, that under TEM conditions, the accelerating voltage and the electron dose are both much higher than in SEM. Accordingly, the main feature that Chorkendorff et al. described in their study was a shrinkage (and not a growth) of most nanoparticles, with only a few of these displaying actual coalescence [22]. Shrinkage in this study was shown to be an effect of both the high electron dose and the oxidizing atmosphere. None of these are characteristic of our SEM measurements; thus in our case, it seems more straightforward to presume that the beam has little effect on the nanocubes themselves, and it is rather the under-beam formation of a carbonaceous passive layer what is seen in Fig. 6.

Although the SEM images recorded at an accelerating voltage of 1.5 kV may not allow a clear distinction between the core of the nanoparticles and the contamination layer formed around them (Figs. 6 and 7a), the contamination layer can be visualized by EM scans at higher (20 kV) accelerating voltage (Fig. 7b). That under the formed carbonaceous contamination layer the Ag nanocubes preserve their original shape can be confirmed by the HAADF–STEM and the TEM bright field images shown in Figs. 7c and d, respectively.

It is of worth noting that the contamination layer is most probably formed by the PVP capping agent, remnants of which remain adsorbed on the Ag nanocubes despite the applied UV–ozone treatment, and then get polymerized and pinned to the electrode surface by the electron beam [28]. Based on the electrocatalytic degradation pattern shown by Fig. 5, we can assume that some PVP may also remain on the substrate, forming there a carbonaceous shell that is however presumed to be not as thick as on the surfaces of the nanocubes, where PVP is primarily adsorbed.

The under-beam formation of the passive layer on the surface of nanoparticulate catalysts seems to block the pre-scanned surface even if entirely different settings, and much harsher electrolysis conditions, compared to what was described before, are applied. This is demonstrated by Fig. 8, where we modified a gas diffusion electrode (GDE) with carbon-supported Ag NCs (this time, without the application of UV-ozone treatment), and performed electrolysis by applying a potential of −1.4 V *vs.* RHE, thus passing through a total charge amount of 1600 C cm^{-2}. While the identical location SEM images of Fig. 8a and b show no trace of degradation, particle deformation and the appearance of newly formed, small particles is clearly shown by the SEM micrograph of Fig. 8c, recorded at a random spot after the electrolysis. Although as pointed out in [40], in fact any organic contaminations of a catalyst sample may act as source of material for the formation of passive carbonaceous crust layers, the prominent role of PVP in this process is further supported by our numerous IL–SEM studies on PVP-free catalysts, where no such contamination effects were ever seen [11–20].

4. Concluding remarks

No effort has so far been made to demonstrate the effect of capping-agent related under-beam passive layer formation on the catalytic behaviour of nanoparticle type electrocatalysts. This is considered worrying, particularly because of the emerging popularity of IL–SEM-based stability studies where the pre-electrolysis scanning can contaminate (and consequently disable) the catalyst sample in a way that the post-electrolysis scan would deceivingly show no degradation.

Using PVP-functionalised Ag nanocubes as model catalysts of CO_2 reduction, we demonstrated how under-beam contamination (a carbonaceous, passive crust formed over the catalyst particles) might account for artefacts in IL–SEM studies in such a way that the experimenter is provided with false comfort with regard to the stability of the catalyst. This paper was written with the aim to direct attention to this possible pitfall of IL–SEM studies, which may especially emerge when IL–SEM is applied on electrocatalysts prepared by a synthesis route involving capping agents.

Apart from the issues that PVP remnants can cause in the interpretation of IL–SEM experiments, it should also be emphasized that shape-forming surfactants may exert further unwanted effects also on the essential catalytic properties. *E.g.*, in case of the system studied here we have to note that if no action (in our case, UV-ozone treatment) is taken to remove (at least most of) the adhering PVP remnants, this will negatively affect both the selectivity and the stability of the catalyst. In our case omission of the UV-ozone treatment resulted, for example, in the overall Faradaic efficiency (toward CO production) dropping from $\sim 80\%$ to $\sim 65\%$, and a further dropping to below 50% over 2 hours of electrolysis (under conditions similar to those applying for Fig. 2b). The removal of capping agents may be based on plasma/thermal annealing [41] (note that the UV-ozone treatment we applied here proved to be far from ideal), or it may even rely on mere electrochemical methods. Namely, it was recently shown in two independent studies (by our group [42] and by Pankhurst et al. [43]) that capping agent remnants may effectively be removed by the harsh cathodic potentials applied during CO_2 electrolysis. Needless to say, the latter "*operando* activation" method [42] does not work for capping agents baked to the catalyst surface by the electron beam in an IL–SEM scenario.

Declaration of Competing Interest

The authors declare that they have no known competing financial interests or personal relationships that could have appeared to influence the work reported in this paper.

Acknowledgement

Support by the CTI Swiss Competence Center for Energy Research (SCCER Heat and Electricity Storage) is gratefully acknowledged. P. B. acknowledges financial support from the Swiss National Foundation (grant 200020–172507). S. V. acknowledges support from the National Research, Development and Innovation Office of Hungary (NKFIH grant FK135375). N. K. and M. de J. G.-V. acknowledge the financial support by the Swiss Government Excellence Scholarships for Foreign Scholars (ESKAS).

References

[1] D.R. Feldman, W.D. Collins, P.J. Gero, M.S. Torn, E.J. Mlawer, T.R. Shippert, Observational determination of surface radiative forcing by CO2 from 2000 to 2010, Nature 519 (7543) (2015) 339–343, https://doi.org/10.1038/nature14240.

[2] S. Nitopi, E. Bertheussen, S.B. Scott, X. Liu, A.K. Engstfeld, S. Horch, B. Seger, I.E. L. Stephens, K. Chan, C. Hahn, J.K. Nørskov, T.F. Jaramillo, I. Chorkendorff, Progress and perspectives of electrochemical CO2 reduction on copper in aqueous electrolyte, Chem. Rev. 119 (12) (2019) 7610–7672, https://doi.org/10.1021/acs.chemrev.8b00705.

[3] E. Royer, Réduction de l'acide carbonique en acide formique, Compt. Rend. Hebd. Séances Acad. Sci. 70 (1870) 731–732.

[4] H.-R.M. Jhong, S. Ma, P.J.A. Kenis, Electrochemical conversion of CO2 to useful chemicals: Current status, remaining challenges, and future opportunities, Curr. Opin. Chem. Eng. 2 (2) (2013) 191–199, https://doi.org/10.1016/j.coche.2013.03.005.

[5] A.D. Handoko, F. Wei, Jenndy, B.S. Yeo, Z.W. Seh, Understanding heterogeneous electrocatalytic carbon dioxide reduction through operando techniques, Nature Catal. 1 (12) (2018) 922–934, https://doi.org/10.1038/s41929-018-0182-6.

[6] A. Bergmann, B. Roldán Cuenya, Operando insights into nanoparticle transformations during catalysis, ACS Catal. 9 (11) (2019) 10020–10043, https://doi.org/10.1021/acscatal.9b01831.

[7] K.J.J. Mayrhofer, J.C. Meier, S.J. Ashton, G.K.H. Wiberg, F. Kraus, M. Hanzlik, M. Arenz, Fuel cell catalyst degradation on the nanoscale, Electrochem. Commun. 10 (8) (2008) 1144–1147, https://doi.org/10.1016/j.elecom.2008.05.032.

[8] N. Hodnik, M. Zorko, M. Bele, S. Hočevar, M. Gaberšček, Identical location scanning electron microscopy: A case study of electrochemical degradation of PtNi nanoparticles using a new nondestructive method, J. Phys. Chem. C 116 (40) (2012) 21326–21333, https://doi.org/10.1021/jp303831c.

[9] N. Hodnik, S. Cherevko, Spot the difference at the nanoscale: Identical location electron microscopy in electrocatalysis, Curr. Opin. Electrochem. 15 (2019) 73–82, https://doi.org/10.1016/j.coelec.2019.03.007.

[10] J.C. Meier, I. Katsounaros, C. Galeano, H.J. Bongard, A.A. Topalov, A. Kostka, A. Karschin, F. Schüth, K.J.J. Mayrhofer, Stability investigations of electrocatalysts on the nanoscale, Energy Environ. Sci. 5 (11) (2012) 9319, https://doi.org/10.1039/c2ee22550f.

[11] M. Rahaman, A. Dutta, A. Zanetti, P. Broekmann, Electrochemical reduction of CO2 into multicarbon alcohols on activated Cu mesh catalysts: An identical location (IL) study, ACS Catal. 7 (11) (2017) 7946–7956, https://doi.org/10.1021/acscatal.7b02234.

[12] A. Dutta, M. Rahaman, M. Mohos, A. Zanetti, P. Broekmann, Electrochemical CO2 conversion using skeleton (sponge) type of Cu catalysts, ACS Catal. 7 (8) (2017) 5431–5437, https://doi.org/10.1021/acscatal.7b01548.

[13] P. Moreno-García, N. Schlegel, A. Zanetti, A. Cedeño López, M.deJ. Gálvez-Vázquez, A. Dutta, M. Rahaman, P. Broekmann, Selective electrochemical reduction of CO2 to CO on Zn-based foams produced by Cu^{2+} and template-assisted electrodeposition, ACS Appl. Mater. Interfaces 10 (37) (2018) 31355–31365, https://doi.org/10.1021/acsami.8b0989.

[14] A. Dutta, C.E. Morstein, M. Rahaman, A. Cedeño López, P. Broekmann, Beyond copper in CO_2 electrolysis: Effective hydrocarbon production on silver-nanofoam catalysts, ACS Catal. 8 (9) (2018) 8357–8368, https://doi.org/10.1021/acscatal.8b01738.

[15] M.deJ. Gálvez-Vázquez, S. Alinejad, H. Hu, Y. Hou, P. Moreno-García, A. Zana, G. K.H. Wiberg, P. Broekmann, M. Arenz, Testing a silver nanowire catalyst for the selective CO2 reduction in a gas diffusion electrode half-cell setup enabling high mass transport conditions, CHIMIA Int. J. Chem. 73 (11) (2019) 922–927, https://doi.org/10.2533/chimia.2019.92.

[16] Y. Hou, S. Bolat, A. Bornet, Y.E. Romanyuk, H. Guo, P. Moreno-García, I.Z. Montiel, Z. Lai, U. Müller, V. Grozovski, P. Broekmann, Photonic curing: Activation and stabilization of metal membrane catalysts (MMCs) for the electrochemical reduction of CO2, ACS Catal. 9 (10) (2019) 9518–9529, https://doi.org/10.1021/acscatal.9b03664.

[17] Y. Hou, R. Erni, R. Widmer, M. Rahaman, H. Guo, R. Fasel, P. Moreno-García, Y. Zhang, P. Broekmann, Synthesis and characterization of degradation-resistant Cu@CuPd nanowire catalysts for the efficient production of formate and CO from CO2, ChemElectroChem 6 (12) (2019) 3189–3198, https://doi.org/10.1002/celc.201900752.

[18] M.deJ. Gálvez-Vázquez, P. Moreno-García, H. Guo, Y. Hou, A. Dutta, S.R. Waldvogel, P. Broekmann, Leaded bronze alloy as a catalyst for the electroreduction of CO2, ChemElectroChem 6 (8) (2019) 2324–2330, https://doi.org/10.1002/celc.201900537.

[19] A.V. Rudnev, K. Kiran, A. Cedeño López, A. Dutta, I. Gjuroski, J. Furrer, P. Broekmann, Enhanced electrocatalytic CO formation from CO_2 on nanostructured silver foam electrodes in ionic liquid/water mixtures, Electrochim. Acta 306 (2019) 245–253, https://doi.org/10.1016/j.electacta.2019.03.102.

[20] A. Dutta, I.Z. Montiel, R. Erni, K. Kiran, M. Rahaman, J. Drnec, P. Broekmann, Activation of bimetallic AgCu foam electrocatalysts for ethanol formation from CO2 by selective Cu oxidation/reduction, Nano Energy 68 (2020) 104331, https://doi.org/10.1016/j.nanoen.2019.104331.

[21] W.T. Osowiecki, J.J. Nussbaum, G.A. Kamat, G. Katsoukis, M. Ledendecker, H. Frei, A.T. Bell, A.P. Alivisatos, Factors and dynamics of Cu nanocrystal reconstruction under CO2 reduction, ACS Appl. Energy Mater. 2 (11) (2019) 7744–7749, https://doi.org/10.1021/acsaem.9b01714.

[22] S.B. Simonsen, I. Chorkendorff, S. Dahl, M. Skoglundh, J. Sehested, S. Helveg, Direct observations of oxygen-induced platinum nanoparticle ripening studied by in situ TEM, J. Am. Chem. Soc. 132 (23) (2010) 7968–7975, https://doi.org/10.1021/ja910094r.

[23] M. Arenz, A. Zana, Fuel cell catalyst degradation: Identical location electron microscopy and related methods, Nano Energy 29 (2016) 299–313, https://doi.org/10.1016/j.nanoen.2016.04.027.

[24] R. Lariviere Stewart, Insulating films formed under electron and ion bombardment, Phys. Rev. 45 (7) (1934) 488–490, https://doi.org/10.1103/physrev.45.488.

[25] M. von Ardenne, Das elektronen-rastermikroskop, Z. Phys. 109 (9–10) (1938) 553–572, https://doi.org/10.1007/bf01341584.

[26] L. Marton, N.N. Das Gupta, C. Marton, Modifications of specimens in electron microscopy, Science 104 (2689) (1946) 35–36, https://doi.org/10.1126/science.104.2689.35.

[27] M.T. Postek, A.E. Vladár, Does your SEM really tell the truth?—How would you know? Part 1, Scanning 35 (6) (2013) 355–361, https://doi.org/10.1002/sca.21075.

[28] M.T. Postek, A.E. Vladár, K.P. Purushotham, Does your SEM really tell the truth?—How would you know? Part 2, Scanning 36 (3) (2013) 347–355, https://doi.org/10.1002/sca.21124.

[29] B. Luo, Y. Fang, J. Li, Z. Huang, B. Hu, J. Zhou, Improved stability of metal nanowires via electron beam irradiation induced surface passivation, ACS Appl. Mater. Interfaces 11 (13) (2019) 12195–12201, https://doi.org/10.1021/acsami.9b00875.

[30] S.F. Tan, M. Bosman, C.A. Nijhuis, Molecular coatings for stabilizing silver and gold nanocubes under electron beam irradiation, Langmuir 33 (5) (2017) 1189–1196, https://doi.org/10.1021/acs.langmuir.6b03721.

[31] S.H. Im, Y.T. Lee, B. Wiley, Y. Xia, Large-scale synthesis of silver nanocubes: The role of HCl in promoting cube perfection and monodispersity, Angew. Chem. 117 (14) (2005) 2192–2195, https://doi.org/10.1002/ange.200462208.

[32] A.V. Rudnev, Online chromatographic detection, in: K. Wandelt (Ed.), Encyclopedia of Interfacial Chemistry, Elsevier, Amsterdam, 2018, pp. 321–325, https://doi.org/10.1016/b978-0-12-409547-2.13564-4.

[33] J. Zhang, Q. Wang, X. Zhang, J. Wang, M. Guo, B.J. Wiley, C. Li, C. Hu, Carbamide promoted polyol synthesis and transmittance properties of silver nanocubes, Inorg. Chem. Front. 3 (4) (2016) 547–555, https://doi.org/10.1039/c5qi00256g.

[34] K.M. Koczkur, S. Mourdikoudis, L. Polavarapu, S.E. Skrabalak, Polyvinylpyrrolidone (PVP) in nanoparticle synthesis, Dalton Trans. 44 (41) (2015) 17883–17905, https://doi.org/10.1039/c5dt02964c.

[35] N. Naresh, F.G.S. Wasim, B.P. Ladewig, M. Neergat, Removal of surfactant and capping agent from Pd nanocubes (Pd-NCs) using tert-butylamine: Its effect on electrochemical characteristics, J. Mater. Chem. A 1 (30) (2013) 8553, https://doi.org/10.1039/c3ta11183k.

[36] D. Ung, B.M. Cossairt, Effect of surface ligands on CoP for the hydrogen evolution reaction, ACS Appl. Energy Mater. 2 (3) (2019) 1642–1645, https://doi.org/10.1021/acsaem.9b00240.

[37] Y. Hori, Electrochemical CO_2 reduction on metal electrodes, in: C.G. Vayenas, R.E. White, M.E. Gamboa-Aldeco (Eds.), Modern Aspects of Electrochemistry, Vol. 42, Springer, New York, 2008, pp. 89–189, https://doi.org/10.1007/978-0-387-49489-0.

[38] D. Sun, X. Xu, Y. Qin, S.P. Jiang, Z. Shao, Rational design of Ag-based catalysts for the electrochemical CO2 reduction to CO: A review, ChemSusChem 13 (2019) 39–58, https://doi.org/10.1002/cssc.201902061.

[39] A. Moysiadou, X. Hu, Stability profiles of transition metal oxides in the oxygen evolution reaction in alkaline medium, J. Mater. Chem. A 7 (45) (2019) 25865–25877, https://doi.org/10.1039/c9ta10308b.

[40] M. Zorko, B. Jozinović, M. Bele, N. Hodnik, M. Gaberšček, SEM method for direct visual tracking of nanoscale morphological changes of platinum based electrocatalysts on fixed locations upon electrochemical or thermal treatments, Ultramicroscopy 140 (2014) 44–50, https://doi.org/10.1016/j.ultramic.2014.02.006.

[41] I. Puspitasari, E. Skupien, F. Kapteijn, P. Kooyman, Au capping agent removal using plasma at mild temperature, Catalysts 6 (2016) 179, https://doi.org/10.3390/catal6110179.

[42] H. Hu, M. Liu, Y. Kong, N. Mysuru, C. Sun, M. d. J. Gálvez-Vázquez, U. Müller, R. Erni, V. Grozovski, Y. Hou, P. Broekmann, Activation matters: Hysteresis effects during electrochemical looping of colloidal Ag nanowire catalysts, ACS Catal. 10 (2020) 8503–8514. https://doi.org/10.1021/acscatal.0c02026.

[43] J.R. Pankhurst, P. Iyengar, A. Loiudice, M. Mensi, R. Buonsanti, Metal–ligand bond strength determines the fate of organic ligands on the catalyst surface during the electrochemical CO2 reduction reaction, Chem. Sci. 11 (2020) 9296–9302, https://doi.org/10.1039/d0sc03061a.

1.4 Environment Matters: CO_2RR Electrocatalyst Performance Testing in a Gas-Fed Zero-Gap Electrolyzer

Authors: María de Jesús Gálvez-Vázquez, Pavel Moreno-García, Heng Xu, Yuhui Hou, Huifang Hu, Iván Zelocualtecatl Montiel, Alexander V. Rudnev, Shima Alinejad, Vitali Grozovski, Benjamin J. Wiley, Matthias Arenz, and Peter Broekmann

ACS Catal. **10**, 13096–13108 (2020), DOI: 10.1021/acscatal.0c03609

Highlights: This study investigates the structural deterioration of silver nanocubes in a gas-fed zero-gap electrolyzer as a possible source of device durability. There are no morphological changes in the catalyst, and the device performance remains stable at potentials more positive than –1.8 V vs. Ag/AgCl. At harsher cathodic potentials, smaller Ag nanoparticles begin to appear on formerly catalyst-free regions, and the device failure commences within minutes. Salt precipitation and flooding of the gas diffusion electrode were identified as higher impact sources in the system failure than the structural changes of the catalyst. The system exhibited remarkable partial current densities and faradaic efficiencies towards CO formation (~625 mA cm^{-2} and ~85%, respectively). Moreover, it is shown that the reaction environment affects the product selectivity of the reaction. It is suggested that CO_2RR investigations should increasingly be performed using technical approaches because the knowledge acquired from H-cell experiments might not be directly extended to flow cell studies.

Contributions: I was the main responsible for preparing the gas diffusion electrodes and performing the electrochemical CO_2RR experiments in the gas-fed zero-gap electrolyzer and the H-cell. Moreover, I carried out the SEM characterization of the gas diffusion electrodes. I contributed with Dr. Pavel Moreno-García in the results analysis, preparation of the figures, and redaction of the manuscript.

ACS Catalysis

pubs.acs.org/acscatalysis Research Article

Environment Matters: CO_2RR Electrocatalyst Performance Testing in a Gas-Fed Zero-Gap Electrolyzer

María de Jesus Gálvez-Vázquez,[⊥] Pavel Moreno-García,[*,⊥] Heng Xu, Yuhui Hou, Huifang Hu, Iván Zelocualtecatl Montiel, Alexander V. Rudnev, Shima Alinejad, Vitali Grozovski, Benjamin J. Wiley, Matthias Arenz, and Peter Broekmann*

Cite This: *ACS Catal.* 2020, 10, 13096−13108

Read Online

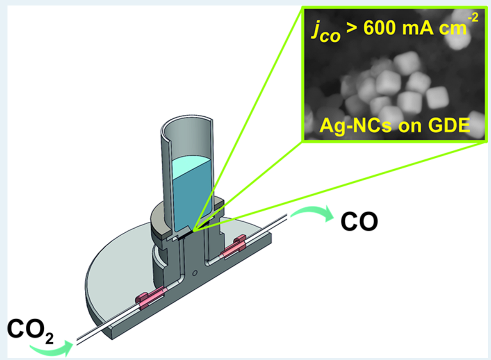

ABSTRACT: Among the electrolyzers under development for CO_2 electroreduction at practical reaction rates, gas-fed approaches that use gas diffusion electrodes (GDEs) as cathodes are the most promising. However, the insufficient long-term stability of these technologies precludes their commercial deployment. The structural deterioration of the catalyst material is one possible source of device durability issues. Unfortunately, this issue has been insufficiently studied in systems using actual technical electrodes. Herein, we make use of a morphologically tailored Ag-based model nanocatalyst [Ag nanocubes (NCs)] assembled on a zero-gap GDE electrolyzer to establish correlations between catalyst structures, experimental environments, electrocatalytic performances, and morphological degradation mechanisms in highly alkaline media. The morphological evolution of the Ag−NCs on the GDEs induced by the CO_2 electrochemical reduction reaction (CO_2RR), as well as the direct mechanical contact between the catalyst layer and anion-exchange membrane, is analyzed by identical location and post-electrolysis scanning electron microscopy investigations. We find that at low and mild potentials positive of −1.8 V versus Ag/AgCl, the Ag−NCs undergo no apparent morphological alteration induced by the CO_2RR, and the device performance remains stable. At more stringent cathodic conditions, device failure commences within minutes, and catalyst corrosion leads to slightly truncated cube morphologies and the appearance of smaller Ag nanoparticles. However, comparison with complementary CO_2RR experiments performed in H-cell configurations in a neutral environment clearly proves that the system failure typically encountered in the gas-fed approaches does not stem solely from the catalyst morphological degradation. Instead, the observed CO_2RR performance deterioration is mainly due to the local high alkalinity that inevitably develops at high current densities in the zero-gap approach and leads to the massive precipitation of carbonates which is not observed in the aqueous environment (H-cell configuration).

KEYWORDS: *CO_2 electroreduction, gas diffusion electrodes, zero-gap electrolyzer, carbon monoxide, exchange membrane electrode assembly*

■ INTRODUCTION

Powering the electrochemical reduction reaction of carbon dioxide (CO_2RR) with renewable energy sources has emerged as a compelling alternative to other approaches to CO_2 valorization,[1,2] toward meeting the increasing demand for commodity/platform chemicals and thereby contributing to efforts to close the anthropogenic carbon cycle.[3,4] In recent decades, significant progress has been made to understand the reaction mechanisms of this process through the development of cutting-edge catalyst materials that increase the activity [partial current density (PCD) of generated products] and selectivity (faradaic efficiency, FE) of the process. Strong cases of commercial viability have been made for formate ($HCOO^-$) and CO production, which require the transfer of only two electrons from the electrocatalyst to the CO_2 reactant molecule.[5,6] Formate is efficiently formed on Sn-, Bi-, In-, and Pb-based catalysts, whereas CO forms preferably on Ag-, Au-, and Zn-based catalysts.[7] CO is a particularly appealing product because it can be used as a stockpile for subsequent transformation either in the Fischer−Tropsch process[8] or in sequential electrochemical[9] and fermentation methods.[10]

Using catalyst screening methods based on H-cell experiments in which reactant CO_2 gas is usually dissolved in an aqueous bicarbonate-based electrolyte, a significant number of works have reported that Ag-,[11−13] Au-,[14,15] and Zn-based[16−18] cathode materials provide excellent CO selectivity and

Received: August 18, 2020
Revised: October 15, 2020
Published: October 27, 2020

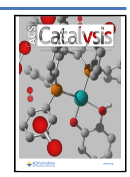

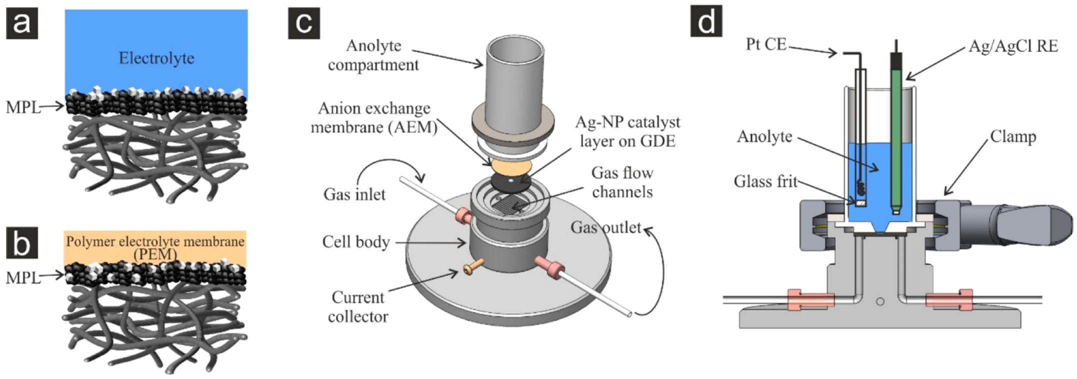

Figure 1. Schematics of the reaction interfaces in (a) liquid flow-cell electrolyzer and (b) exchange membrane electrode assembly (MEA) or zero-gap assembly. (c) Depiction and assembly of the zero-gap flow cell used in this work for the CO_2RR. (d) Cross-sectional view of the assembled cell with reference and counter electrodes (CE and RE, respectively) immersed in the anolyte compartment. MPL in panels (a,b) stands for the MPL on which the catalyst material (Ag–NCs) is embedded.

operational stability. Many works have also reported insightful correlations between the use of a tailored catalyst nanostructure and electrocatalytic performance.[19,20] In addition, diverging from the bicarbonate-based electrolyte that was once used almost ubiquitously, it has been found that highly concentrated (potassium) hydroxide-based catholyte solutions suppress the parasitic hydrogen evolution reaction (HER) and improve the CO_2RR performance because OH^- ions exhibit excellent ionic conductivity and reduce the activation energy barriers for CO_2 electroreduction.[9,21−24] Through these and other improvements, the field has reached a significant level of maturity so that currently, the associated research is driven by more ambitious endeavors, namely, scaling up the CO_2RR process to practical realization.[10,25] Toward this end, experimental platforms have been developed to circumvent or attenuate the mass transport limitations that are intrinsic to traditional H-type cell measurements[26−28] and arise from the low solubility of the dissolved CO_2 reactant in aqueous electrolytes. This pursuit opens a new avenue to the CO_2RR and related fields because the insights extracted from H-cell measurements with either stationary or rotating disk electrodes do not necessarily hold for their gas-fed homologues and both approaches bear fundamental kinetic differences that must be addressed to approach process commercialization.[29−31]

Among the various types of CO_2 electrolyzers under development, gas-fed approaches that use gas diffusion electrodes (GDEs) as cathodes and that are inspired by polymer electrolyte fuel cell technologies are considered to be the most promising.[1,21,30,32−36] Consequently, studies on Ag–GDEs in contact with flowing alkaline electrolytes (Figure 1a) have grown in popularity to achieve higher PCD_{CO} and FE_{CO} values as well as lower CO_2RR onset potentials and to explore possible enhancements to performance longevity.[37−41] However, electrolyzer designs that rely on this cell configuration are not without shortcomings that affect device performance and stability, thereby overshadowing their intrinsic electrocatalytic activity. These issues stem from (i) high ohmic losses owing to the electrolyte layer separating the electrodes,[30] (ii) electrolyte percolation through the microporous layer (MPL) of GDEs and concomitant carbonate salt precipitation,[42,43] and (iii) CO_2 crossover from the cathodic to the anodic compartment upon CO_2 neutralization by OH^- ions to HCO_3^-/CO_3^{2-}.[32,44,45]

Motivated by this, a few recent works on alternative cell designs with only an aqueous anolyte between the membrane and anode and no liquid electrolyte layer between the catalyst layer and (an)ion-exchange membrane [indistinctively called exchange membrane electrode assemblies (MEAs) or catholyte-free or zero-gap membrane assemblies, see Figure 1b][1,32,46] have been reported, enabling comparably reduced ohmic overpotentials, enhanced stability, and excellent CO selectivity.[25,47,48] This zero-gap configuration not only affords reduced ohmic losses but also attenuates complications that arise from poor membrane hydration and electrode flooding at high current densities, which are otherwise problematic to fully gas-fed electrolyzers[46,49] (note that exchange MEA electrolyzers may still suffer from the parasitic uptake of CO_2 at the interface of the cathode and anion-exchange membrane, thus facilitating the undesirable CO_2 discharge on the anode surface).[43,44,50] Nonetheless, one persistent hurdle that precludes the commercial deployment of these technologies is insufficient long-term device stability, which continues to fall short of the minimum target value of 8×10^4 h.[5] Efforts to identify the factors that lead to process failure have been undertaken, and strategies to alleviate such failures have been proposed (e.g., appropriate selection of the reactor design, electrode production method and hydrodynamics,[1] management of electrolyte percolation through the GDE,[39,51] and carbonation tolerance of the electrodes[43,44]).

In this context, another aspect that may also be a source of device durability issues and that has been minimally investigated using actual technical electrodes on which very large current densities (>300 mA cm^{-2}) are enforced is the structural deterioration of the catalyst material.[31,40] In particular, studies of the catalyst morphological evolution of Ag-based exchange MEAs induced by the CO_2RR reaction itself are lacking, as well as studies of the effect of direct mechanical contact between the catalyst layer and anion-exchange membrane (Figure 1b). To shed light on this unexplored aspect of CO_2RR on Ag–GDEs, we make use of morphologically tailored Ag-based model nanocatalysts [Ag nanocubes (Ag–NCs)] assembled on zero-gap GDEs to establish correlations between structure, environment, electrocatalytic performance, and degradation mechanisms under the abovementioned most favorable CO_2RR conditions (i.e., a highly alkaline membrane adjacent to the catalyst layer). Submonolayer surface coverages are purposely employed to unambiguously address possible structure degradation at the level of a single Ag–NC. Besides investigation of the catalyst activity and selectivity, we devote particular attention to the

https://dx.doi.org/10.1021/acscatal.0c03609
ACS Catal. 2020, 10, 13096−13108

time evolution of both the electrochemical performance of the process and the material's nanostructure induced upon CO_2 electrolysis at large current densities, as enforced on the model exchange Ag−MEAs. We find that our testbed enables among the highest CO partial current densities and competitive FE_{CO} values (−625 mA cm^{-2} and 85%, respectively) even at the applied sub-monolayer catalyst coverages. Two distinct electrode potential regimes were observed, each exhibiting significantly different behaviors. At low and mild applied potentials ($E \geq -1.8$ V vs Ag/AgCl), stability prevails across the PCD_{CO} and FE_{CO}, electrolyzer performance, and catalyst structure. Conversely, at greater cathodic potentials, the process selectivity and activity severely degrade, leading to performance failure even though the catalyst morphology undergoes significantly less deterioration. Thus, this work enables the deconvolution of catalyst structural stability from system performance stability. Finally, a comparison with standard H-type reference measurements reveals that CO_2RR product selectivity is influenced by electrolyzer design and, therefore, that the knowledge developed using such batch-type approaches should not be regarded as directly transferable to gas-fed platforms. Overall, the results underscore that more effort must be devoted to the understanding and optimization of system design parameters (e.g., water management, prevention of salt precipitation, CO_2 flow rate, and electrolyte flow rate) that have a more significant impact on the product spectrum and longevity of the exchange MEA electrolyzers than that of the structural degradation of the catalyst, which is shown to be mild.

EXPERIMENTAL SECTION

Synthesis of Ag−NCs. Silver NCs were synthesized using a previously reported method with minor modification.[52] 5 mL of ethylene glycol (EG, J. T. Baker) was added to a 250 mL two-neck flask preheated to 160 °C. A light N_2 flow was introduced just above the EG for the first 10 min, followed by heating the solvent for another 50 min. Next, 3 mL EG solution of $AgNO_3$ (94 mM) and 3 mL EG solution containing polyvinylpyrrolidone (PVP, M_w = 55,000, 144 mM) and NaCl (0.22 mM) were simultaneously injected into the flask at a rate of 45 mL/h, with the solution observed to turn yellow during this process. Under continuous stirring at 160 °C, the solution exhibited a color transition series from yellow to clear yellow, brown, greenish, and finally ochre and opaque. The whole process required 16 h to 24 h for completion. After the solution had turned opaque, the reaction was quenched by adding 22 mL of acetone to the hot solution, followed by cooling in an ice-water bath. To purify the NCs, the solution was first centrifuged at 2000*g* for 30 min, and then, the precipitate was dispersed and centrifuged 3× in 10 mL of deionized water at 9000*g* for 10 min per run.[53] The product was finally dispersed in 5 mL of deionized water for future use.

Preparation of Ag−NC Catalyst Ink. To prepare the carbon-supported Ag−NC ink, 1.5 mg of the prepared Ag−NCs and 0.26 mg of carbon black (Vulcan XC 72R, Cabot) were separately dispersed in 10 mL of isopropanol (VLSI Selectipur, BASF SE, Ludwigshafen, Germany) by 1 h of sonication. Both suspensions were intermixed, sonicated for 1 h, and dried using a Rotary evaporator (Buchi R210, 45 °C, 85 mbar). The obtained carbon-supported Ag−NCs (85 wt % Ag−NC and 15 wt % C black) were then redispersed in 1 mL of isopropanol containing 50 μL of Nafion (5 wt %, 15−20% water, Sigma-Aldrich). The resulting suspension was subjected to sonication for 1 h yielding a homogeneous catalyst ink. For the sake of reproducibility and comparison, catalyst inks were also prepared with commercial Ag−NCs (NanoXact, nanoComposix) and used for complementary CO_2RR experiments.

Preparation of the Ag−NC−GDEs. The model catalyst material in this work consists of cubic Ag nanoparticles (Ag−NCs) with an average edge length of (113.1 ± 10.6) nm. The Ag−NC−GDEs for all electrochemical and characterization experiments were prepared as follows: a defined circular area of 7.07×10^{-2} cm^2 on the GDEs' hydrophobic surface (diameter of 2 cm, Sigracet 39 BC, Fuel Cell Store) was modified by dropcasting 50 μL of carbon-supported Ag−NC ink onto its top surface. This catalyst solution was percolated through the porous body of the GDEs by a vacuum filtration system placed on the backside of the electrode, and subsequent drying at ambient conditions was allowed for at least 30 min. Analysis by inductively coupled plasma−mass spectrometry (ICP−MS) of freshly prepared samples was used to determine the catalyst mass loading, which amounted to $\sim 7.1 \times 10^{-2}$ mg_{Ag} cm^{-2}.

Assembly of the Gas Flow Cell. The assembly and main components of the zero-gap gas-flow cell employed in this work to investigate correlations between the catalyst structure and process performance of CO_2RR to CO on Ag−NC−GDEs are schematically depicted in Figure 1c,d. This assembly consists of a stainless-steel cell body with the gas flow channels used to feed the CO_2 from the backside of the prepared Ag−NC−GDEs mounted on the outermost location of the central portion. Other components incorporated into the cell include a current collector and a gas inlet and outlet to control the supply of the CO_2 reactant (99.999%, Carbagas, Switzerland) and analysis of the gaseous products, respectively. All CO_2RR experiments were set up by placing a freshly prepared Ag−NC−GDE on top of the gas flow channels, with its catalyst-modified surface facing upward. Subsequently, a clean hydroxide-functionalized Sustainion alkaline membrane (X37-50 RT, Dioxide materials) and a poly(tetrafluoroethylene) (PTFE) anolyte compartment were carefully placed on top of the Ag−NC−GDE. A clamp was then used to ensure cell tightness and mechanical stability. KOH electrolyte-supporting solution (10 mL, 2 M; pH: 14.3, Sigma-Aldrich) was added to the anolyte compartment, and a Ag/AgCl (3 M KCl, double junction design, Metrohm) electrode and a Pt mesh (99.99%, MaTeck) separated by a glass frit served as the reference and counter electrodes, respectively. Note that the PTFE anolyte compartment has a central orifice (7.07×10^{-2} cm^2) in its bottom part that provides direct contact between the electrolyte and the underlying anion-exchange membrane, while the Ag−NC−GDE is prevented from establishing physical contact with the supporting anolyte. During electrolysis, a humidified CO_2 stream (16 mL min^{-1}) was continuously fed through the gas flow channels of the stainless-steel cell body adjacent to the prepared Ag−NC−GDEs.

Electrochemical Reduction of CO_2 (CO_2RR) Using Ag−NC−GDEs. All electrolytes were prepared using chemicals of at least ACS reagent grade and deionized water (Millipore, 18.2 MΩ cm, 3 ppb toc). Both ECi-200 (Nordic electrochemistry) and Autolab PGSTAT128 N (Metrohm) potentiostats were used to perform all electrochemical experiments. Electrochemical impedance spectroscopy measurements were conducted before and after every CO_2 electrolysis experiment, and the results were considered to build the potential-dependent product distributions and partial current densities displayed and mentioned throughout the text. Potentiostatic

https://dx.doi.org/10.1021/acscatal.0c03609
ACS Catal. 2020, 10, 13096−13108

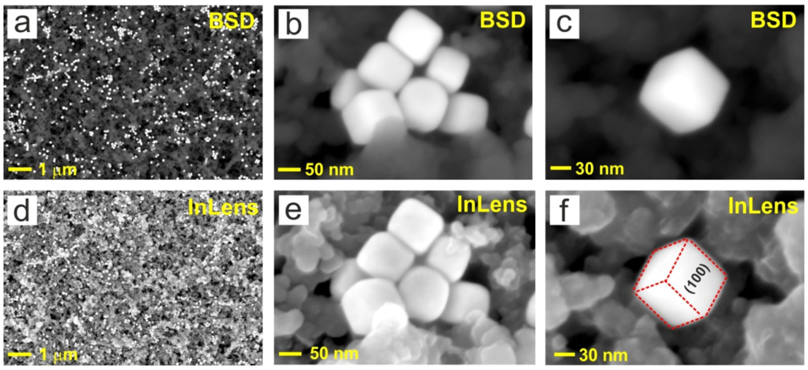

Figure 2. Representative SEM images at different magnifications showing the surface of an as-prepared Ag−NC−GDE cathode for CO_2RR. (a,d) Ag−NC catalyst sub-monolayer coverage on the MPL of the GDE. (b,c) and (e,f) reveal the well-defined cubic morphology of the Ag−NCs. Images (a−c) were acquired using the BSD detector of the scanning electron microscope. (d−f) Correspond to the same sample surface areas shown in the upper panels but were recorded with the InLens SE detector.

CO_2 electrolysis experiments were carried out at selected applied electrode potentials for 1 h, during which time the electrogenerated gaseous products were analyzed by online gas chromatography (SRI Instruments) in sequential intervals of 10 min. The electrolyte was analyzed after the applied electrolysis condition (post reaction) to quantify the produced formate by means of ion-exchange chromatography (Metrohm Ltd., Switzerland). For comparison, the performance of the Ag−NC−GDEs was also tested by dedicated reference measurements using 2 M $KHCO_3$ as the electrolyte in both the gas-flow cell and the conventional H-cell configurations. For the H-cell measurements, a proton-exchange membrane (Nafion 117, Sigma-Aldrich) separated the catholyte from the anolyte, and the working electrode consisted of a rectangular piece of carbon paper (0.8 × 3 cm) prepared in the same way as the Ag−NC−GDEs for zero-gap measurements. The back side and the edges of these electrodes were masked with the PTFE tape, thus leaving an uncovered geometric surface area of 0.2 cm^2. A single junction Ag/AgCl electrode (saturated KCl, Pine Research) and a Pt foil (2.5 × 0.8 cm, 99.99%, MaTeck) were used as the reference and counter electrodes, respectively. All electrode potential values in this work are in reference to the standard $Ag/AgCl_{3M}$ reference electrode. The data corresponding to the product selectivity and partial current densities of all experiments are displayed in Tables S2−S6. A thorough description of complementary experimental details is presented in a previous publication.[36]

Scanning Electron Microscopy and Energy-Dispersive X-ray Spectroscopy Characterization. Morphological characterization of the prepared Ag−NC−GDEs and assessment of the spatial distribution of the Ag−NCs over the samples was carried out with scanning electron microscopy (SEM) imaging experiments. Imaging was performed before (for the as-prepared electrodes) and after having sustained defined CO_2RR time intervals at selected applied electrode potentials. The analysis was conducted sequentially with a Zeiss Gemini 450 scanning electron microscope with both InLens secondary electron and backscattered electron detectors (Inlens SE and BSD detectors, respectively). An accelerating voltage of 5 kV and a current of 200 pA were applied at a working distance of 6.6−6.8 mm. The BSD detector enables clear identification of the Ag−NCs along the surface of the GDE's MPL because this technique is highly sensitive to the atomic number of the elements being imaged. However, the images acquired with the InLens SE detector provide better morphological resolution of the Ag−NCs. The use of both imaging operational modes coupled to energy-dispersive X-ray analysis (EDX) analysis made it possible to track morphological catalyst changes induced by CO_2 electrolysis and/or physical contact between the catalyst material and anion-exchange membrane on the Ag−NC−GDEs used. Complementary identical location (IL−SEM) experiments were conducted on Ag−NC−GDEs for which selected sample positions were imaged by the SEM instrument before and after CO_2RR experiments.

AZtec 4.2 software (Oxford Instruments) was used to acquire EDX spectra and surface mappings of selected Ag−NC−GDEs. An acceleration voltage of 10 kV and a current of 1.2 nA were applied at a working distance of 8.5 mm.

Catalyst Loading and Post-electrolysis Electrolyte and Ag−NC−GDE Analysis by ICP−MS. Freshly prepared Ag−NC−GDEs were immersed in 3 mL HNO_3 (BASF SE, Ludwigshafen, Germany) for 24 h to dissolve the Ag−NCs embedded on their surfaces. The resulting solutions were diluted with 3% HNO_3 solution by a factor of 500 and were then fed into a NExION 2000 ICP−MS instrument (PerkinElmer) to obtain the Ag mass loading of the electrodes. To identify possible Pt dissolution from the employed Pt counter electrode during CO_2 electrolysis, the following ICP−MS and EDX control experiments were conducted. First, 10 μL of post-reaction anolyte (after CO_2RR at −2.0 V for 60 min in 2 M KOH) was diluted with 10 mL of 3% HNO_3 solution for ICP−MS analysis. No Pt dissolution was detected in two independent measurements. Additionally, two post-electrolysis Ag−NC−GDEs were immersed in 3 mL aqua regia for 24 h and the solutions were diluted by factor 100 with 3% HNO_3. The corresponding ICP−MS spectra showed no signal other than the background further confirming the absence of Pt on the catalyst surface and supporting GDE. Finally, EDX analysis of a Ag−NC−GDE sample after being subjected to similar CO_2RR conditions also excluded the presence of any Pt deposited on the employed cathodes (see Figure S8).

X-ray Diffraction Catalyst Characterization. The crystallinity of the Ag−NCs was determined by means of X-ray diffraction (XRD) techniques (Bruker D8) using Cu Kα radiation (λ = 0.1540 nm, 40 mA) generated at 40 keV. Scans were recorded at 1° min^{-1} for 2θ values between 20 and 100°. The samples were prepared by dropcasting Ag−NCs dispersed in isopropanol on a graphite foil (0.13 mm, 99.8%, Alfa Aesar) and then allowing the solution to dry under ambient

https://dx.doi.org/10.1021/acscatal.0c03609
ACS Catal. 2020, 10, 13096−13108

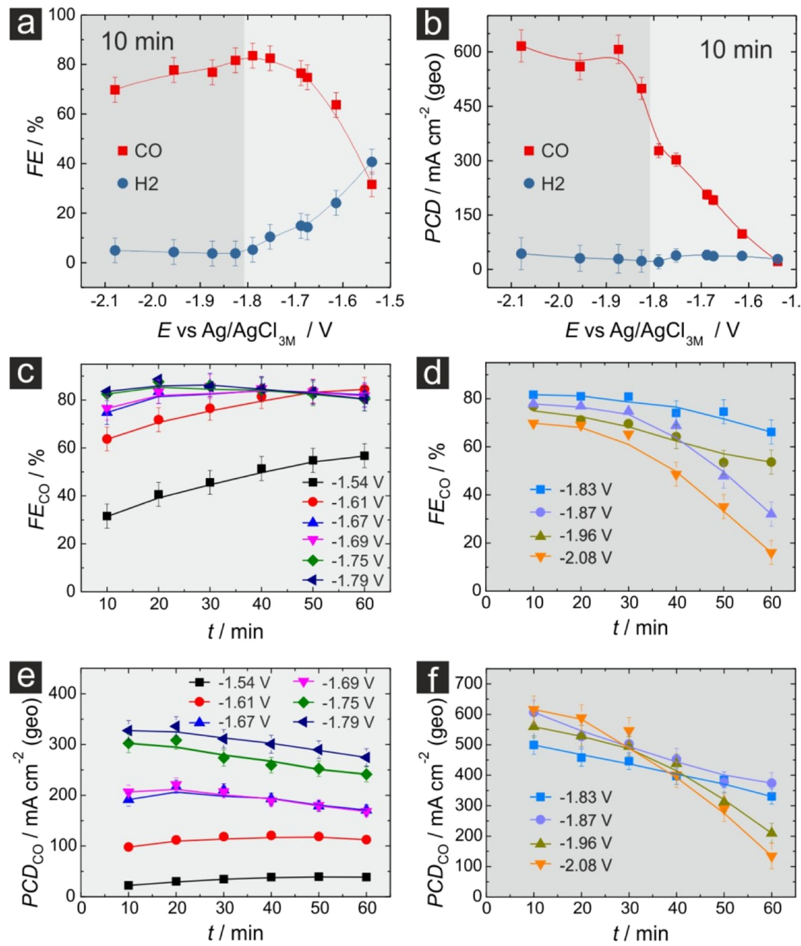

Figure 3. Potential-dependent FEs (a) and PCDs (b) of the gaseous products obtained from CO_2RR on the gas-fed Ag−NC−GDEs 10 min after beginning CO_2 electrolysis. Time evolution of the FE_{CO} at (c) mild (-1.5 V > E > -1.8 V) and (d) high applied potentials (-1.83 V > E > -2.1 V). Corresponding time evolution of the PCD_{CO} at mild (e) and high (f) applied potentials. All experiments were carried out using 2 M KOH in the anolyte compartment. The solid lines in all panels are guides to the eye to better observe the trends. The experimental error was accounted for using ±5% error bars.

conditions. The obtained XRD patterns were analyzed and compared with JCPD (Joint Committee on Powder Diffraction) for peak assignment.

RESULTS AND DISCUSSION

Characterization of Ag−NC−GDEs by SEM. Figure 2 shows representative SEM images of an as-prepared Ag−NC−GDE. We present data acquired sequentially at the same position with both the BSD and InLens SE detectors of the scanning electron microscope. Clear distinction between the Ag−NCs (bright) and the supporting GDE (dark) is provided by the BSD detector, which is sensitive to the atomic number of the analyzed material (Figure 2a−c). We observe a highly dispersed sub-monolayer of Ag−NC surface coverage built up by both single Ag−NCs and sparse groups of the particles (Figure 2b,c). This observation implies that the electrochemical performance of the Ag−NC−GDEs will be partially determined by parasitic side reactions (e.g., HER) taking place also on catalyst-free regions. This is supported by the combined SEM−EDX analysis of an as-prepared Ag−NC−GDE sample displayed in Figure S1a−d. The images acquired using the InLens SE detector (Figure 2d−f) offer improved morphological resolution of single Ag−NCs and their cubic shape, which is more easily observed at large magnifications (Figure 2e−f). Statistical analysis of more than 400 Ag−NCs provided an average edge length of 113.1 ± 10.6 nm, while XRD characterization confirmed the high crystallinity of the assembled Ag−NCs (Figure S1e,f). Recent theoretical and experimental studies in H-cell configurations have reported the superior and stable catalytic performance of cubic Ag nanoparticles compared to their octahedral and spherical counterparts.[19,20]

Electrocatalytic Performance of Ag−NC−GDEs for CO_2RR in Zero-Gap Electrolyzer. Potentiostatic CO_2RR experiments at selected applied potentials ranging between -1.55 and -2.1 V versus Ag/AgCl were conducted for 1 h using a dedicated Ag−NC−GDE as the cathode in a zero-gap gas flow-cell configuration (Figure 1b−d) for every potential. A favorable alkaline reacting environment was provided by the 2 M KOH electrolyte used in the anolyte compartment.[42] Figure 3a displays the potential-dependent product distribution of the gaseous products obtained after 10 min of CO_2 electrolysis. Besides the modest FE_{CO} observed at E ~ -1.55 V, all obtained FE_{CO} values at potentials more negative than -1.6 V surpassed 65%, reaching a maximum value of approximately 85% at -1.8 V. Diverging from previous reports in which an abrupt decay of FE_{CO} was observed with progressively higher potentials/current densities, only a slight decrease of CO

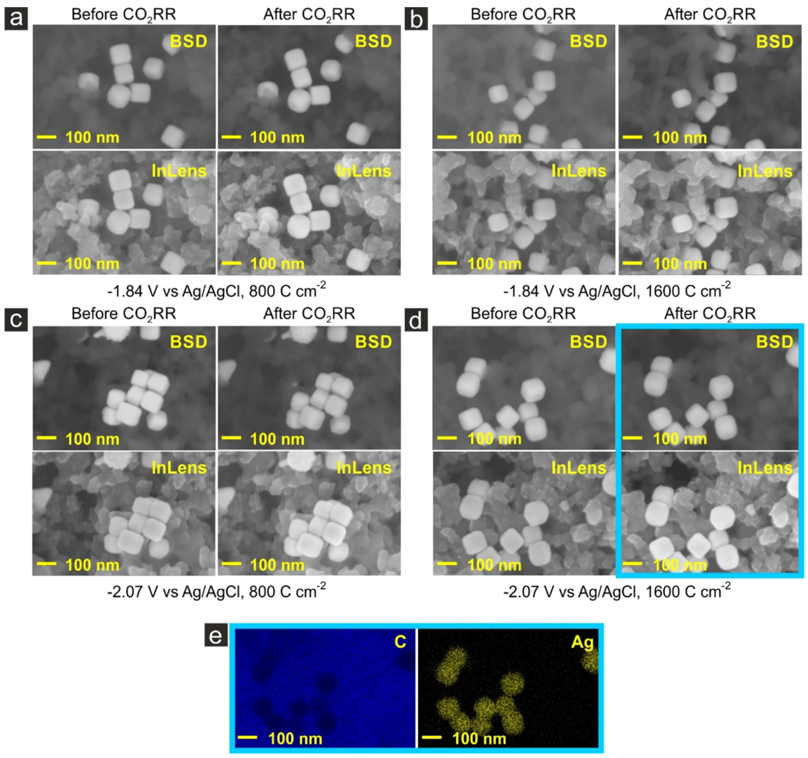

Figure 4. Representative IL−SEM images of Ag−NC−GDE cathode surfaces before and after having conducted dedicated gas-fed CO_2RR experiments at −1.84 V for (a) 30 min (800 C cm^{-2}) and (b) 60 min (1600 C cm^{-2}) and at −2.07 V for (c) 13 min (800 C cm^{-2}) and (d) 32 min (1600 C cm^{-2}) captured using both BSD and InLens SE detectors. (e) Elemental EDX mappings showing the spatial distribution of C (dark blue) and Ag (yellow) corresponding to the sample location highlighted by the blue rectangle in (d). All CO_2RR experiments were carried out using 2 M KOH in the anolyte compartment.

selectivity was detected at the harshest applied cathodic conditions due to an emerging formate contribution. However, it should be noted that in those previous reports either a bipolar membrane or a 0.5 M $KHCO_3$ buffer layer was used between the cathode and proton-exchange membrane.[32,54,55] The efficiency of parasitic H_2 stayed at FE_{H2} levels ≤10% for potentials more negative than −1.75 V. The corresponding dependence of the partial current densities PCD_{CO} and PCD_{H2} on the enforced potentials is shown in Figure 3b. The PCD_{CO} increases steeply as the cathodic potential increases from −1.54 to −1.87 V reaching highly competitive levels at approximately −600 mA cm^{-2} (see Table S1). Further cathodic polarization to approximately −2.1 V leads to a slightly increased PCD_{CO} reaching approximately −625 mA cm^{-2}. The PCD_{H2} did not exceed −50 mA cm^{-2} at all applied potentials. These CO selectivities and partial current densities stand out considering that for the as-prepared Ag−NC−GDEs, a significant portion of the three-phase boundary layer where the fed CO_2, polymer electrolyte, and catalyst material meet is constituted by the unmodified MPL of the support GDEs (Figure 2a). Clearly, an increase of the catalyst loading would lead to even better CO efficiencies and activities.[31] However, it is important to remember that a low catalyst surface coverage on the GDEs was deliberately applied to successfully monitor the morphological evolution of the Ag−NC catalyst at the single nanoparticle level (see below).

Distinct temporal evolution of both FE_{CO}s and PCD_{CO}s was found to depend on the magnitude of the applied potentials. Based on the temporal stability that these values promoted, two apparent potential regimes were identified for FE_{CO} and PCD_{CO}. These regimes are highlighted by different color codes in Figure 3. The panels corresponding to applied potentials that sustained the above-described performance throughout the duration of the experiments are highlighted by light gray rectangles (−1.5 V > E > −1.8 V). The panels highlighted in darker gray stand for results derived from applied potentials that led to the decay of FE_{CO} and PCD_{CO} values from their initial levels. Figure 3 panels c and e show that both CO selectivity and activity either improve or stay fairly stable across the lifespan of the experiments, provided that the applied potential was always less negative than −1.8 V. Conversely, when the potential surpassed this value, both CO production figures decreased over time. This decline was initially mild but intensified abruptly after 30 min with an increase of the applied potential (Figure 3 panels d and f).

Morphology Evolution of Ag−NC-Based Catalyst Induced by CO_2RR in Zero-Gap Flow Cell and H-Type Cell. To determine whether the observed decay in device performance during CO_2RR at the specific time intervals and applied potentials observed in Figure 3 panels d and f arises from morphological transformations of the cathodes (through morphological changes of the Ag−NCs or through their local rearrangement along the GDE surface), we analyzed Ag−NC−GDEs that were used for CO_2RR under those same conditions using *ex situ* SEM imaging experiments. Note that in the present study, our Ag−NC catalyst was subjected to significantly harsher cathodic conditions as compared to those reported in ref 61 reaching over two orders higher current densities and ∼400 mV more cathodic potentials.

In the first attempt, we employed the so-called IL−SEM-based technique.[56,57] This analysis is meant to provide the structural evolution of electrocatalyst materials by comparing

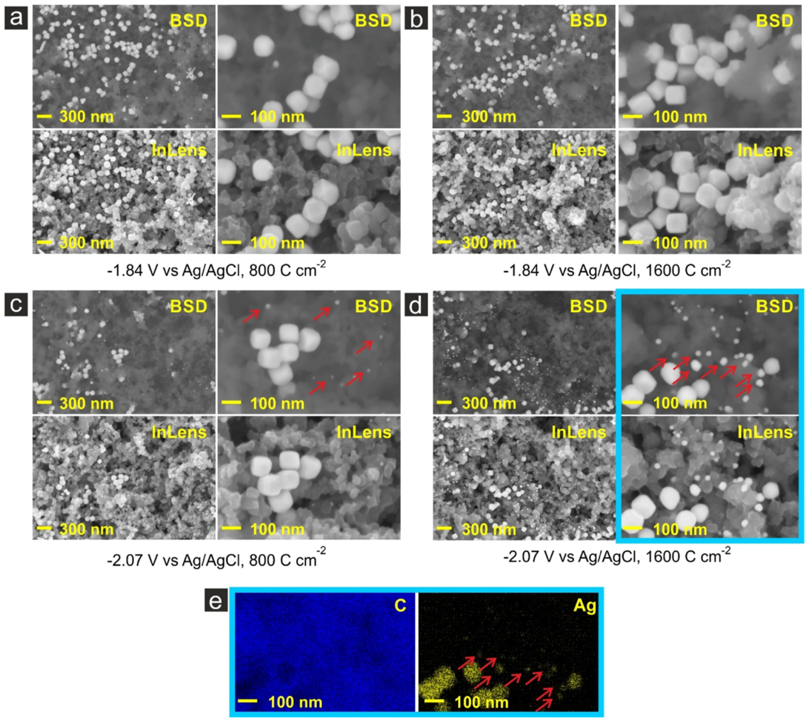

Figure 5. Representative SEM images of Ag−NC−GDE cathode surfaces after having conducted dedicated gas-fed CO_2RR experiments at −1.84 V for (a) 30 min (800 C cm^{-2}) and (b) 60 min (1600 C cm^{-2}) and at −2.07 V for (c) 13 min (800 C cm^{-2}) and (d) 32 min (1600 C cm^{-2}) captured using both BSD and InLens SE detectors. (e) Elemental EDX mappings showing the spatial distribution of C (dark blue) and Ag (yellow) of the sample location highlighted by the blue rectangle in (d). Red arrows identify Ag nanoparticles formed upon cathodic corrosion of the Ag−NC catalyst. All CO_2RR experiments were carried out using 2 M KOH in the anolyte compartment.

their morphology at the same sample location before and after being subjected to electrolysis.[56,57] We have previously employed this strategy to successfully assess structure−activity correlations caused by CO_2RR on bare porous metal electrocatalysts.[17,58] Herein, we monitored the structural evolution of Ag−NC−GDEs by IL−SEM for samples that were subjected to high cathodic potential values at which CO partial current densities reached −500 mA cm^{-2} and −620 mA cm^{-2} (−1.84 and −2.07 V, respectively). For each applied potential, the electrolysis was carried out until charge densities of 800 and 1600 C cm^{-2} were passed on dedicated Ag−NC−GDEs. These selected conditions are key for enabling insightful correlation between the SEM-based post-electrolysis studies and the data presented in Figure 3c−f.

Figure 4a−d presents representative IL−SEM images corresponding to Ag−NC−GDEs that were subjected to such CO_2RR conditions. Surprisingly, comparison of SEM images acquired before and after CO_2 electrolysis show that neither detachment nor degradation of the Ag−NCs seem to arise regardless of the specific applied potential, passed charge, or electrolysis duration. Post-electrolysis EDX mappings on sample regions that were scrutinized by IL−SEM also hint at the absence of cathodic corrosion and redeposition phenomena (compare Figures 4e and S1b,d). Furthermore, complementary IL−SEM experiments in which five sequential CO_2RR cycles were applied to a Ag−NC−GDE sample at the most stringent cathodic conditions are displayed in Figure S2. Although this sample was electrochemically stressed more severely (total cumulated Q = 13306 C cm^{-2} and $t \sim 4.5$ h), the combined IL−SEM−EDX analysis showed again no apparent sample degradation. These results alone would imply, at first sight, that the developed Ag−NC−GDEs tested in the proposed zero-gap flow cell do not undergo morphological degradation upon CO_2RR at all and that the undermined catalytic performance observed in Figure 3 at harsh cathodic conditions should originate from another failure source. However, an important aspect that did not need consideration in our previously reported IL−SEM structural CO_2RR studies and that can be the source of SEM imaging misinterpretation when studying colloidal nanocatalysts is the influence of surfactants that are left behind on their surfaces following their synthesis. Indeed, it has been shown that electron beam irradiation on nanomaterials synthesized by additive-assisted colloidal methods can lead to their improved structural stability through transformation of the adsorbed surfactants into dense carbonaceous shells.[59] Moreover, local surface passivation induced by SEM imaging has been identified on PVP-capped Ag NCs that hinders diffusion of Ag surface atoms.[60] This suggests that IL−SEM experiments might not accurately reveal the morphological evolution of colloidal catalyst materials as the initial electron irradiation conducted before the electrolysis step stabilizes and deactivates the scrutinized locations. Therefore, a second series of SEM imaging experiments were performed on the surface of Ag−NC−GDEs that were subjected to the same CO_2RR conditions as shown in Figure 4 but whose surfaces were not exposed to the electron beam of the SEM prior to the electrolysis.

Figure 5a−b displays representative images of Ag−NC−GDEs after having been subjected to −1.84 V. The Ag−NCs in panels a and b have undergone insignificant morphological changes after either 30 or 60 min of electrolysis (800 C cm^{-2} and 1600 C cm^{-2}, respectively). Furthermore, the images acquired with the BSD detector revealed the absence of

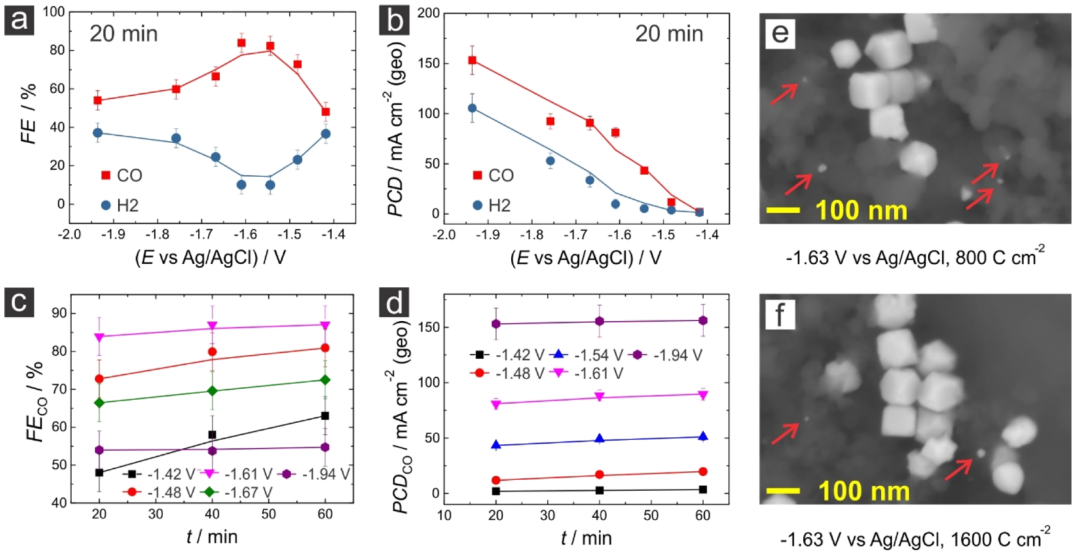

Figure 6. Potential-dependent FEs (a) and PCDs (b) obtained on the Ag−NC−GDE in the H-cell configuration. Both variables were recorded 20 min after the CO_2 electrolysis experiment was initialized. Time evolution of the FE_{CO} (c) and PCD_{CO} (d) at (-1.42 V $\geq E \geq -1.94$ V). Representative SEM images of cathode surfaces after having conducted dedicated CO_2RR experiments at -1.63 V for (e) 196 min (800 C cm^{-2}) and (f) 304 min (1600 C cm^{-2}). Complementary SEM images of cathode surfaces subjected to -1.92 V are shown in Figure S6. These CO_2RR experiments were carried out with an H-type cell using 2 M $KHCO_3$ as the electrolyte. The solid lines in panels (a−d) are guides to the eye to better observe the trends. The experimental error was accounted for using ±5% error bars.

material removal from the Ag−NCs that would be redeposited in the form of smaller nanoparticles along the electrode surface under the applied cathodic conditions.[61] Importantly, excellent electrochemical performance figures ($PCD_{CO} \geq 300$ mA cm^{-2} and FE_{CO} ∼80%) are attained and sustained if the potential remains just positive of this applied value (-1.8 V vs Ag/AgCl, see Figure 3 panels c and e). Because of the morphological integrity of the actual catalyst observed under these conditions, it is reasonable to think that the purely electrochemical performance of the Ag−NCs−GDEs should be sustained over long electrolysis periods if the other system parameters do not lead to failure (e.g., salt precipitation, electrolyte penetration into the adjacent GDE, etc). However, diverging from what was observed in IL−SEM analysis, the electrodes exposed to more demanding cathodic conditions revealed alteration of the Ag−NC structure that may be linked to the deterioration of PCD_{CO}s and FE_{CO}s observed in Figure 3 panels d and f. Figure 5c shows representative images of a Ag−NC−GDE cathode that underwent CO_2RR at -2.07 V for 13 min (800 C cm^{-2}). Although the Ag−NCs maintained their overall cubic appearance, the BSD−SEM images reveal smaller, randomly distributed Ag nanoparticles (<5 nm) that arise from these more stringent CO_2 electrolysis conditions. The red arrows in the upper right image of Figure 5c indicate the appearance of particles adsorbed on regions of the GDE that were not covered by the Ag−NC catalyst material prior to CO_2RR. This phenomenon was more evident on cathodes subjected to 32 min (1600 C cm^{-2}) of electrolysis. Figure 5d demonstrates that the particles formed near the Ag−NCs when treated with these longer reaction times increased not only in size (∼10 nm) but also in population along the formerly catalyst-free substrate regions. This is also supported by the EDX mapping shown in Figure 5e acquired on the sample location highlighted by the blue rectangle in Figure 5d. Additionally, analysis of single Ag−NCs indicated that the material source for these electrochemically formed particles stems mainly from the cube's vertices, eventually leading to the appearance of small (111) planes of truncated cube-like particles (Figure S3). Thus, it is clear that monitoring of the electrochemically induced morphological evolution of the colloidal catalyst is accurately described provided that the nanoparticles are not passivated by electron beam irradiation prior to electrolysis (as is the case in IL−SEM investigations). We suggest, however, that the observed mild morphological alteration of the Ag−NC catalyst on the GDE surfaces alone cannot be the physical origin for the significantly affected PCD_{CO}s and FE_{CO}s, as shown in Figure 3 panels d and f, at potentials more negative than -1.8 V.

To elucidate whether this decay in performance originates instead from the high bulk pH value (∼14) of the electrolyte used, reference CO_2RR electrochemical and SEM experiments similar to those shown in Figures 3 and 5 were carried out on Ag−NC−GDEs, employing a significantly less basic 2 M $KHCO_3$ electrolyte (pH ∼8). These results are displayed in Figures S4 and S5 following the same color code and image representation as of Figures 3 and 5. Figure S4a,b shows the corresponding FEs and PCDs of the electrogenerated gaseous products. Besides a slightly lower PCD_{CO} at most cathodic applied potentials (-1.86 V $\geq E \geq -2.14$ V), all other displayed quantities (PCD_{H2}, FE_{CO}, and FE_{H2}) exhibited the same qualitative potential- and time-dependent behaviors after 10 min CO_2 electrolysis, as discussed above, when the 2 M KOH electrolyte was used (compare Figure 3c−f with Figure S4c−f). The reduction in PCD_{CO} at high applied potentials might be related to the lower ionic conductivity of the HCO_3^- ion in comparison to that of OH^- and its relative deficiency to lower the CO_2 activation energy barrier.[42] Interestingly, suppression of the parasitic HER was equally effective when using both supporting electrolytes. The fact that the temporal dependence of FE_{CO} and PCD_{CO} as the electrolysis proceeded revealed again a stability bifurcation that depended on the potential window examined (Figure S4c−f) but not on the specific bulk pH is not surprising. Indeed, it has been predicted that the local pH adjacent to the three-phase boundary layer of

https://dx.doi.org/10.1021/acscatal.0c03609
ACS Catal. 2020, 10, 13096−13108

a gas-fed GDE at CO_2RR reaction rates above 50 mA cm^{-2} becomes rather similar for both neutral and highly alkaline electrolytes due to the driven cathode half reactions (both CO_2 and water reduction generate OH^- as a byproduct).[30] The difference in the local pH at the cathode between both electrolyte solutions under CO_2RR reacting conditions at targeted $j_s \geq 200$ mA cm^{-2} might actually be negligible.[30] Similar to the experiments conducted in the 2 M KOH electrolyte, as shown in Figure 5, SEM analysis of a Ag−NC−GDE after 60 min CO_2RR at mild applied potential (E = −1.84 V, 1600 C cm^{-2}) in 2 M $KHCO_3$ showed minor structural degradation of the Ag−NCs (Figure S5). This finding suggests that the performance decay in our gas-fed zero-gap flow cell at large CO_2RR rates might be more significantly influenced by the increased local alkalinity rather than the relatively minor structural degradation of the Ag−NCs and the original bulk pH. Furthermore, an increasingly high alkalinity at the three-boundary layer in GDEs has been found to lead to issues related to electrolyte carbonation, electrolyte penetration through the GDE body (electrode flooding), and salt precipitation.[39,43,44,49,51] Electrolyte intrusion beyond the MPL of the Ag−NC−GDEs at high cathodic potentials also contributes to the decay in FE_{CO} and PCD_{CO}, as observed in Figure 3d,f and S4d,f, due to an increase of the CO_2 diffusion length. This is in agreement with recently reported work by Leonard et al.[43] who observed a clear increase of flooding propensity and loss of the nominal MPL hydrophobicity under stringent CO_2RR reductive conditions.

To further support this argument, we resorted to investigations performed in conventional H-cell configurations in which none of these detrimental aspects would influence the supply of dissolved CO_2 to the cathode through the liquid electrolyte. Figure 6a,b summarizes these experimental results. In comparison to the gas-fed experiments, significantly lower PCD_{CO}s are observed in all of the inspected potential window due to the dominant effect of the mass transport limitations of CO_2 dissolved in the used 2 M $KHCO_3$ electrolyte. In addition, the use of this non-optimal,[9,21−24] almost neutral electrolyte leads to larger PCD_{H2}s (as great as PCD_{H2} ∼ 100mA cm^{-2}) at high cathodic potentials relative to the values observed in the zero-gap experiments. The potential-dependent product selectivity shows an increase of FE_{CO} as the potential varied from low to mild applied values (-1.4 V $\geq E \geq -1.6$ V), although in contrast to the observed trends for the more technical approach, the CO efficiency significantly decreases as the competing HER benefits at more negative values. Moreover, in contrast to the results from the zero-gap experiments, neither FE_{CO} nor PCD_{CO} decays from its initial value as the electrolysis reaction proceeds, regardless of the applied potential (Figure 6c,d). Considering that the Ag−NCs used in these H-cell experiments seem to have undergone a similar degree of degradation and associated mechanism at mild and high applied potentials relative to that of the zero-gap counterparts (Figures 6e−f and S6), it seems evident that the system stability issues acting at high potentials and longer electrolysis times in the gas-fed configuration stem mainly from a sub-optimal reactor design and the high local alkalinity at high current densities. Indeed, we found a clear correlation between the decaying FE_{CO} and PCD_{CO} and occurrence of GDE flooding and salt precipitation, which cause device performance failure at high cathodic potentials in the gas-fed approach. Figure S7a,b shows typical contact angle images for water droplets on Ag−NC−GDEs before and after being submitted to CO_2RR at −2.07 V for 32 min. The decrease of contact angle indicates that the barrier properties of the MPL are to some extent undermined upon electrolysis. The corresponding EDX spectra additionally show a clear decay of the F signal due to degradation of the hydrophobic PTFE coating of the MPL (Figure S7c). Moreover, Figure S8a presents optical images showing the typical appearance of the employed GDEs at different experimental stages (as-received GDE, as-prepared Ag−NC−GDE and Ag−NC−GDE after having sustained CO_2RR at −2.07 V for 32 min and 1600 C cm^{-2}). The EDX spectra and mapping displayed in Figure S8b,c further support that, under these drastic cathodic conditions, carbonate/bicarbonate precipitation on the catalyst-modified GDE surface and its periphery takes place. Additionally, Figures S9 and S10 show that these undesired events (flooding and precipitation) can even be observed on the backside of such electrodes, irrespectively of the employed electrolyte. We would like to emphasize that this kind of massive salt precipitation is only observed in the GDE approach, irrespective of the used electrolyte, but not in the H-type cell configuration where the partial current densities of CO formation are mass transport limited and remain stable during electrolysis.

Comparison of CO_2RR Product Distribution in Zero-Gap Flow Cell and H-Type Cell. Finally, another important aspect that requires attention is the spectrum of products yielded from CO_2RR processes, which might also be affected by the specificities of the experimental approach employed (cell design and environment).[62] Along these lines, fundamental differences regarding the product selectivity were observed between the gas-fed- and H-cell-based approaches. As illustrated in Figure S11, formate was detected as a CO_2 electrolysis product over a large potential window using alkaline as well as almost basic electrolytes when the zero-gap testbed was used. This finding is in agreement with reports by Sargent, Sinton et al. on increased formate production on Ag−GDEs in highly alkaline aqueous environments (Figure 1a).[40] These authors proposed that the enhanced formate production when using highly alkaline environments adjacent to the Ag−GDE might be due to the limited ability of a temporary H_3O^+ molecule that is believed to assist the first protonation step of the adsorbed *COOH intermediate on the CO reaction pathway.[63] Accordingly, Figure S11 shows that both FE_{HCOO^-} and PCD_{HCOO^-} were more prominent when the hydroxide-based solution was employed and peaked at $E \sim -1.87$ V, amounting to non-negligible values of FE_{HCOO^-} ∼20.1% and PCD_{HCOO^-} ∼148 mA cm^{-2}, respectively. This result agrees with a recent report by Seger et al. who identified formate as a significant CO_2RR side reaction using a zero-gap electrolyzer combined with a basic anolyte at high current densities ≥200 mA cm^{-2}.[46] Conversely, our experiments in the H-cell yielded only a minor formate contribution at the highest applied potential (FE_{HCOO^-} ∼2.6% and PCD_{HCOO^-} ∼7.5 mA cm^{-2}). This result underlines the fact that the vast knowledge developed through batch-type CO_2RR experiments does not necessarily translate to more practical approaches aimed at industrial CO_2 reduction. Therefore, more effort must be devoted to understanding the particularities inherent to gas-fed CO_2RR platforms by going beyond a purely catalyst development-oriented approach and focusing more on rational electrolyzer design, engineering solutions, and process optimization to provide more robust and stable gas−liquid

https://dx.doi.org/10.1021/acscatal.0c03609
ACS Catal. 2020, 10, 13096−13108

interfaces. Precipitation and flooding phenomena might, for instance, be prevented through incorporation of application-tailored microstructures and wettability into novel GDE designs.[43] Encouraging efforts in this direction are being made, for instance, by Schmid et al.[64] who have recently addressed the importance of optimized operating modes, electrolyzer design, and materials selection that enable nearly practical scale electrochemical CO_2-to-CO conversion. One key finding of these investigations that enables stable and long-term CO_2RR operation at −200 mA cm^{-2} is the attenuation of salt precipitation, GDE flooding, and CO_2 crossover to the anode compartment by utilizing a carbonate-free, sulfate-based neutral electrolyte in a liquid flow-cell electrolyzer.

CONCLUSIONS

We studied the performance of a model Ag−NC catalyst for CO_2RR to carbon monoxide on technical GDE in a zero-gap configuration and highly alkaline environments. The system exhibited remarkable CO_2 to CO conversion figures in terms of FE and PCD (FE_{CO} ∼ 625 mA cm^{-2} and PCD_{CO} ∼ 85%) even at sub-monolayer Ag−NC catalyst coverages on the GDEs. Based on the temporal system stability that they promoted, two apparent potential regimes were identified for FE_{CO} and PCD_{CO}. At mild applied potentials (−1.5 V > E vs Ag/AgCl > −1.8 V), the CO_2RR process improved or remained stable over time reaching PCD_{CO}s > 300 mA cm^{-2} and FE ∼ 85%. However, at greater cathodic potentials, both CO production figures were initially more prominent but then weakened over time. This decline was initially mild but intensified abruptly after ∼30 min with increasing applied potential. The morphological evolution of the Ag−NCs on the GDEs induced by the CO_2RR as well as the direct mechanical contact between the catalyst layer and anion-exchange membrane was analyzed by IL−SEM and post-electrolysis SEM investigations. The former approach turned out to be unsuitable for structural characterization of electrolysis-induced changes on colloidal catalysts that bear a surfactant shell on their surface left behind from the synthesis method. On the other hand, post-electrolysis SEM studies enabled the true morphological evolution of the catalyst that strongly depended on the applied electrolysis conditions. Regardless of the applied experimental conditions, no detachment of Ag−NC particles from the GDEs was detected. It was found that at low and mild potentials, the Ag−NCs undergo insignificant morphological alteration. However, at harsher cathodic conditions, smaller Ag nanoparticles begin to appear, adsorbed on formerly catalyst-free substrate regions. The material source of these electrochemically generated nanoparticles seems to come from the corners of the Ag−NCs. The observed mild cathodic corrosion of the catalyst leads to slightly truncated cube morphologies. However, complementary CO_2RR experiments in a neutral environment on Ag−NC−GDEs conducted in both zero-gap and conventional H-type cell configurations suggest that system failure is rooted in more factors than the observed morphological degradation of the catalyst. That is, the high alkalinity level at the three-phase boundary layer where the fed CO_2, catalyst material, and polymer electrolyte meet leads, to a significant degree, to the observed CO_2RR performance decline. The high alkalinity level inevitably develops at the reaction interface in the zero-gap electrolyzers at high cathodic reaction rates >300 mA cm^{-2} even when the starting bulk electrolyte is neutral, thereby causing electrolyte percolation through the GDEs, electrode flooding, and salt precipitation. Thus, this work enables the deconvolution of catalyst structural stability from system performance stability. Although the application of higher catalyst loadings on the GDEs would probably alleviate these issues, a more robust, long-lasting solution to the intrinsic challenges posed by gas-fed approaches must be proposed to near industrial CO_2RR deployment. Finally, as stated by some other recent works, we suggest that CO_2RR studies should increasingly be performed using technical approaches because the conclusions extracted from H-type cell experiments might not be directly translatable to electrolyzer-based studies.

ASSOCIATED CONTENT

Supporting Information

The Supporting Information is available free of charge at https://pubs.acs.org/doi/10.1021/acscatal.0c03609.

SEM, EDX, XRD, and edge size distribution of Ag−NCs; literature survey on CO_2RR to CO on Ag−GDEs; IL−SEM of Ag−NC−GDEs subjected to zero-gap CO_2RR in 2 M KOH; SEM image of single Ag−NCs after zero-gap CO_2RR in 2 M KOH at high cathodic potentials; potential-dependent FEs and PCDs from zero-gap CO_2RR in 2 M $KHCO_3$; SEM imaging of Ag−NCs−GDEs after zero-gap CO_2RR in 2 M $KHCO_3$; SEM imaging of Ag−NCs−GDEs after CO_2RR in H-type cell; optical micrographs of employed GDEs at different experimental stages and EDX characterization of a Ag−NC−GDE after CO_2RR in 2 M KOH at stringent cathodic conditions; potential-dependent FE_{HCOO^-} and PCD_{HCOO^-} from zero-gap CO_2RR in 2 M KOH and 2 M $KHCO_3$; and complete database of all experiments (PDF)

AUTHOR INFORMATION

Corresponding Authors

Pavel Moreno-García − *Department of Chemistry and Biochemistry, University of Bern, Bern 3012, Switzerland;* orcid.org/0000-0002-6827-787X; Email: pavel.moreno@dcb.unibe.ch

Peter Broekmann − *Department of Chemistry and Biochemistry, University of Bern, Bern 3012, Switzerland;* orcid.org/0000-0002-6287-1042; Email: peter.broekmann@dcb.unibe.ch

Authors

María de Jesus Gálvez-Vázquez − *Department of Chemistry and Biochemistry, University of Bern, Bern 3012, Switzerland*

Heng Xu − *Department of Chemistry, Duke University, Durham, North Carolina 27708-0354, United States*

Yuhui Hou − *Department of Chemistry and Biochemistry, University of Bern, Bern 3012, Switzerland;* orcid.org/0000-0003-1616-562X

Huifang Hu − *Department of Chemistry and Biochemistry, University of Bern, Bern 3012, Switzerland*

Iván Zelocualtecatl Montiel − *Department of Chemistry and Biochemistry, University of Bern, Bern 3012, Switzerland*

Alexander V. Rudnev − *Department of Chemistry and Biochemistry, University of Bern, Bern 3012, Switzerland; A.N. Frumkin Institute of Physical Chemistry and Electrochemistry Russian Academy of Sciences, Moscow 119071, Russia*

https://dx.doi.org/10.1021/acscatal.0c03609
ACS Catal. 2020, 10, 13096−13108

Shima Alinejad − *Department of Chemistry and Biochemistry, University of Bern, Bern 3012, Switzerland*; orcid.org/0000-0002-1151-3333
Vitali Grozovski − *Department of Chemistry and Biochemistry, University of Bern, Bern 3012, Switzerland*
Benjamin J. Wiley − *Department of Chemistry, Duke University, Durham, North Carolina 27708-0354, United States*; orcid.org/0000-0002-1314-6223
Matthias Arenz − *Department of Chemistry and Biochemistry, University of Bern, Bern 3012, Switzerland*; orcid.org/0000-0001-9765-4315

Complete contact information is available at:
https://pubs.acs.org/10.1021/acscatal.0c03609

Author Contributions

[⊥]M.J.G.-V. and P.M.G. contributed equally. The manuscript was written through contributions of all authors. All authors have given approval to the final version of the manuscript.

Notes

The authors declare no competing financial interest.

■ ACKNOWLEDGMENTS

Support by the CTI Swiss Competence Center for Energy Research (SCCER Heat and Electricity Storage) is gratefully acknowledged. P.B. acknowledges financial support from the Swiss National Foundation (grant 200020-172507). M.d.J.G.-V. acknowledges the financial support by the Swiss Government Excellence Scholarships for Foreign Scholars (ESKAS) and thanks Antonio Calderon I. for the preparation of the cell's schematic drawings. A. R. acknowledges financial support from the Ministry of Science and Higher Education of the Russian Federation. M.A. acknowledges funding from the Swiss National Science Foundation (SNSF) via the project No. 200021_184742.

■ REFERENCES

(1) Vennekoetter, J.-B.; Sengpiel, R.; Wessling, M. Beyond the catalyst: How electrode and reactor design determine the product spectrum during electrochemical CO_2 reduction. *Chem. Eng. J.* **2019**, *364*, 89−101.
(2) Wang, Y.; Xia, Q.; Bai, X.; Ge, Z.; Yang, Q.; Yin, C.; Kang, S.; Dong, M.; Li, X. Carbothermal activation synthesis of 3D porous g-C_3N_4/carbon nanosheets composite with superior performance for CO_2 photoreduction. *Appl. Catal., B* **2018**, *239*, 196−203.
(3) Jhong, H.-R. M.; Ma, S.; Kenis, P. J. Electrochemical conversion of CO_2 to useful chemicals: current status, remaining challenges, and future opportunities. *Curr. Opin. Chem. Eng.* **2013**, *2*, 191−199.
(4) Seh, Z. W.; Kibsgaard, J.; Dickens, C. F.; Chorkendorff, I.; Nørskov, J. K.; Jaramillo, T. F. Combining theory and experiment in electrocatalysis: Insights into materials design. *Science* **2017**, *355*, No. eaad4998.
(5) Kibria, M. G.; Edwards, J. P.; Gabardo, C. M.; Dinh, C. T.; Seifitokaldani, A.; Sinton, D.; Sargent, E. H. Electrochemical CO_2 Reduction into Chemical Feedstocks: From Mechanistic Electrocatalysis Models to System Design. *Adv. Mater.* **2019**, *31*, 1807166.
(6) Fan, M.; Prabhudev, S.; Garbarino, S.; Qiao, J.; Botton, G. A.; Harrington, D. A.; Tavares, A. C.; Guay, D. Uncovering the Nature of Electroactive Sites in Nano Architectured Dendritic Bi for Highly Efficient CO_2 Electroreduction to Formate. *Appl. Catal., B* **2020**, *274*, 119031.
(7) Hori, Y. *Electrochemical CO2 Reduction on Metal Electrodes in Modern Aspects of Electrochemistry*; Springer: NY, 2008; p 89−189.
(8) Bushuyev, O. S.; De Luna, P.; Dinh, C. T.; Tao, L.; Saur, G.; van de Lagemaat, J.; Kelley, S. O.; Sargent, E. H. What Should We Make with CO_2 and How Can We Make It? *Joule* **2018**, *2*, 825−832.
(9) Jouny, M.; Luc, W.; Jiao, F. High-rate electroreduction of carbon monoxide to multi-carbon products. *Nat. Catal.* **2018**, *1*, 748−755.
(10) Haas, T.; Krause, R.; Weber, R.; Demler, M.; Schmid, G. Technical photosynthesis involving CO_2 electrolysis and fermentation. *Nat. Catal.* **2018**, *1*, 32−39.
(11) Ma, S.; Liu, J.; Sasaki, K.; Lyth, S. M.; Kenis, P. J. A. Carbon Foam Decorated with Silver Nanoparticles for Electrochemical CO_2 Conversion. *Energy Technol.* **2017**, *5*, 861−863.
(12) Dutta, A.; Morstein, C. E.; Rahaman, M.; Cedeño López, A.; Broekmann, P. Beyond Copper in CO_2 Electrolysis: Effective Hydrocarbon Production on Silver-Nanofoam Catalysts. *ACS Catal.* **2018**, *8*, 8357−8368.
(13) Hatsukade, T.; Kuhl, K. P.; Cave, E. R.; Abram, D. N.; Jaramillo, T. F. Insights into the electrocatalytic reduction of CO_2 on metallic silver surfaces. *Phys. Chem. Chem. Phys.* **2014**, *16*, 13814−13819.
(14) Chen, Y.; Li, C. W.; Kanan, M. W. Aqueous CO_2 Reduction at Very Low Overpotential on Oxide-Derived Au Nanoparticles. *J. Am. Chem. Soc.* **2012**, *134*, 19969−19972.
(15) Nursanto, E. B.; Jeon, H. S.; Kim, C.; Jee, M. S.; Koh, J. H.; Hwang, Y. J.; Min, B. K. Gold catalyst reactivity for CO_2 electroreduction: From nano particle to layer. *Catal. Today* **2016**, *260*, 107−111.
(16) Won, D. H.; Shin, H.; Koh, J.; Chung, J.; Lee, H. S.; Kim, H.; Woo, S. I. Highly Efficient, Selective, and Stable CO_2 Electroreduction on a Hexagonal Zn Catalyst. *Angew. Chem., Int. Ed.* **2016**, *55*, 9297−9300.
(17) Moreno-García, P.; Schlegel, N.; Zanetti, A.; Cedeño López, A.; Gálvez-Vázquez, M. d. J.; Dutta, A.; Rahaman, M.; Broekmann, P. Selective Electrochemical Reduction of CO_2 to CO on Zn-Based Foams Produced by Cu^{2+} and Template-Assisted Electrodeposition. *ACS Appl. Mater. Interfaces* **2018**, *10*, 31355−31365.
(18) Luo, W.; Zhang, Q.; Zhang, J.; Moioli, E.; Zhao, K.; Züttel, A. Electrochemical reconstruction of ZnO for selective reduction of CO_2 to CO. *Appl. Catal., B* **2020**, *273*, 119060.
(19) Yang, M.; Zhang, J.; Cao, Y.; Wu, M.; Qian, K.; Zhang, Z.; Liu, H.; Wang, J.; Chen, W.; Huang, W. Facet Sensitivity of Capping Ligand-Free Ag Crystals in CO_2 Electrochemical Reduction to CO. *ChemCatChem* **2018**, *10*, 5128−5134.
(20) Liu, S.; Tao, H.; Zeng, L.; Liu, Q.; Xu, Z.; Liu, Q.; Luo, J.-L. Shape-Dependent Electrocatalytic Reduction of CO_2 to CO on Triangular Silver Nanoplates. *J. Am. Chem. Soc.* **2017**, *139*, 2160−2163.
(21) Dinh, C.-T.; Burdyny, T.; Kibria, M. G.; Seifitokaldani, A.; Gabardo, C. M.; García de Arquer, F. P.; Kiani, A.; Edwards, J. P.; De Luna, P.; Bushuyev, O. S.; Zou, C.; Quintero-Bermudez, R.; Pang, Y.; Sinton, D.; Sargent, E. H. CO_2 electroreduction to ethylene via hydroxide-mediated copper catalysis at an abrupt interface. *Science* **2018**, *360*, 783−787.
(22) Hoang, T. T. H.; Verma, S.; Ma, S.; Fister, T. T.; Timoshenko, J.; Frenkel, A. I.; Kenis, P. J. A.; Gewirth, A. A. Nanoporous Copper−Silver Alloys by Additive-Controlled Electrodeposition for the Selective Electroreduction of CO_2 to Ethylene and Ethanol. *J. Am. Chem. Soc.* **2018**, *140*, 5791−5797.
(23) Kim, B.; Hillman, F.; Ariyoshi, M.; Fujikawa, S.; Kenis, P. J. A. Effects of composition of the micro porous layer and the substrate on performance in the electrochemical reduction of CO_2 to CO. *J. Power Sources* **2016**, *312*, 192−198.
(24) Liu, M.; Pang, Y.; Zhang, B.; De Luna, P.; Voznyy, O.; Xu, J.; Zheng, X.; Dinh, C. T.; Fan, F.; Cao, C.; de Arquer, F. P. G.; Safaei, T. S.; Mepham, A.; Klinkova, A.; Kumacheva, E.; Filleter, T.; Sinton, D.; Kelley, S. O.; Sargent, E. H. Enhanced electrocatalytic CO_2 reduction via field-induced reagent concentration. *Nature* **2016**, *537*, 382−386.
(25) Liu, Z.; Yang, H.; Kutz, R.; Masel, R. I. CO_2 Electrolysis to CO and O_2 at High Selectivity, Stability and Efficiency Using Sustainion Membranes. *J. Electrochem. Soc.* **2018**, *165*, J3371−J3377.
(26) Kas, R.; Hummadi, K. K.; Kortlever, R.; de Wit, P.; Milbrat, A.; Luiten-Olieman, M. W. J.; Benes, N. E.; Koper, M. T. M.; Mul, G. Three-dimensional porous hollow fibre copper electrodes for efficient

and high-rate electrochemical carbon dioxide reduction. *Nat. Commun.* **2016**, *7*, 10748.

(27) Ma, S.; Sadakiyo, M.; Luo, R.; Heima, M.; Yamauchi, M.; Kenis, P. J. A. One-step electrosynthesis of ethylene and ethanol from CO_2 in an alkaline electrolyzer. *J. Power Sources* **2016**, *301*, 219−228.

(28) Moreno-García, P.; Kovács, N.; Grozovski, V.; Gálvez-Vázquez, M. d. J.; Vesztergom, S.; Broekmann, P. Toward CO_2 Electroreduction under Controlled Mass Flow Conditions: A Combined Inverted RDE and Gas Chromatography Approach. *Anal. Chem.* **2020**, *92*, 4301−4308.

(29) Kim, C.; Dionigi, F.; Beermann, V.; Wang, X.; Möller, T.; Strasser, P. Alloy Nanocatalysts for the Electrochemical Oxygen Reduction (ORR) and the Direct Electrochemical Carbon Dioxide Reduction Reaction (CO_2RR). *Adv. Mater.* **2019**, *31*, 1805617.

(30) Burdyny, T.; Smith, W. A. CO_2 reduction on gas-diffusion electrodes and why catalytic performance must be assessed at commercially-relevant conditions. *Energy Environ. Sci.* **2019**, *12*, 1442−1453.

(31) De Gregorio, G. L.; Burdyny, T.; Loiudice, A.; Iyengar, P.; Smith, W. A.; Buonsanti, R. Facet-dependent selectivity of Cu catalysts in electrochemical CO_2 reduction at commercially viable current densities. *ACS Catal.* **2020**, *10*, 4854−4862.

(32) Delacourt, C.; Ridgway, P. L.; Kerr, J. B.; Newman, J. Design of an Electrochemical Cell Making Syngas ($CO+H_2$) from CO_2 and H_2 Reduction at Room Temperature. *J. Electrochem. Soc.* **2008**, *155*, B42.

(33) Dufek, E. J.; Lister, T. E.; McIlwain, M. E. Bench-scale electrochemical system for generation of CO and syn-gas. *J. Appl. Electrochem.* **2011**, *41*, 623−631.

(34) Higgins, D.; Hahn, C.; Xiang, C.; Jaramillo, T. F.; Weber, A. Z. Gas-Diffusion Electrodes for Carbon Dioxide Reduction: A New Paradigm. *ACS Energy Lett.* **2019**, *4*, 317−324.

(35) Weekes, D. M.; Salvatore, D. A.; Reyes, A.; Huang, A.; Berlinguette, C. P. Electrolytic CO_2 Reduction in a Flow Cell. *Acc. Chem. Res.* **2018**, *51*, 910−918.

(36) Gálvez-Vázquez, M. d. J.; Alinejad, S.; Hu, H.; Hou, Y.; Moreno-García, P.; Zana, A.; Wiberg, G. K. H.; Broekmann, P.; Arenz, M. Testing a Silver Nanowire Catalyst for the Selective CO_2 Reduction in a Gas Diffusion Electrode Half-cell Setup Enabling High Mass Transport Conditions. *Chimia* **2019**, *73*, 922−927.

(37) Verma, S.; Lu, X.; Ma, S.; Masel, R. I.; Kenis, P. J. A. The effect of electrolyte composition on the electroreduction of CO_2 to CO on Ag based gas diffusion electrodes. *Phys. Chem. Chem. Phys.* **2016**, *18*, 7075−7084.

(38) Verma, S.; Hamasaki, Y.; Kim, C.; Huang, W.; Lu, S.; Jhong, H.-R. M.; Gewirth, A. A.; Fujigaya, T.; Nakashima, N.; Kenis, P. J. A. Insights into the Low Overpotential Electroreduction of CO_2 to CO on a Supported Gold Catalyst in an Alkaline Flow Electrolyzer. *ACS Energy Lett.* **2018**, *3*, 193−198.

(39) Dinh, C.-T.; García de Arquer, F. P.; Sinton, D.; Sargent, E. H. High Rate, Selective, and Stable Electroreduction of CO_2 to CO in Basic and Neutral Media. *ACS Energy Lett.* **2018**, *3*, 2835−2840.

(40) Gabardo, C. M.; Seifitokaldani, A.; Edwards, J. P.; Dinh, C.-T.; Burdyny, T.; Kibria, M. G.; O'Brien, C. P.; Sargent, E. H.; Sinton, D. Combined high alkalinity and pressurization enable efficient CO_2 electroreduction to CO. *Energy Environ. Sci.* **2018**, *11*, 2531−2539.

(41) Dufek, E. J.; Lister, T. E.; McIlwain, M. E. Influence of Electrolytes and Membranes on Cell Operation for Syn-Gas Production. *Electrochem. Solid-State Lett.* **2012**, *15*, B48.

(42) Bhargava, S. S.; Proietto, F.; Azmoodeh, D.; Cofell, E. R.; Henckel, D. A.; Verma, S.; Brooks, C. J.; Gewirth, A. A.; Kenis, P. J. A. System Design Rules for Intensifying the Electrochemical Reduction of CO_2 to CO on Ag Nanoparticles. *ChemElectroChem* **2020**, *7*, 2001−2011.

(43) Leonard, M. E.; Clarke, L. E.; Forner-Cuenca, A.; Brown, S. M.; Brushett, F. R. Investigating Electrode Flooding in a Flowing Electrolyte, Gas-Fed Carbon Dioxide Electrolyzer. *ChemSusChem* **2020**, *13*, 400−411.

(44) Pătru, A.; Binninger, T.; Pribyl, B.; Schmidt, T. J. Design Principles of Bipolar Electrochemical Co-Electrolysis Cells for Efficient Reduction of Carbon Dioxide from Gas Phase at Low Temperature. *J. Electrochem. Soc.* **2019**, *166*, F34−F43.

(45) Ma, M.; Clark, E. L.; Therkildsen, K. T.; Dalsgaard, S.; Chorkendorff, I.; Seger, B. Insights into the carbon balance for CO_2 electroreduction on Cu using gas diffusion electrode reactor designs. *Energy Environ. Sci.* **2020**, *13*, 977−985.

(46) Larrazábal, G. O.; Strøm-Hansen, P.; Heli, J. P.; Zeiter, K.; Therkildsen, K. T.; Chorkendorff, I.; Seger, B. Analysis of Mass Flows and Membrane Cross-over in CO_2 Reduction at High Current Densities in an MEA-Type Electrolyzer. *ACS Appl. Mater. Interfaces* **2019**, *11*, 41281−41288.

(47) Liu, Z.; Masel, R. I.; Chen, Q.; Kutz, R.; Yang, H.; Lewinski, K.; Kaplun, M.; Luopa, S.; Lutz, D. R. Electrochemical generation of syngas from water and carbon dioxide at industrially important rates. *J. CO2 Util.* **2016**, *15*, 50−56.

(48) Kutz, R. B.; Chen, Q.; Yang, H.; Sajjad, S. D.; Liu, Z.; Masel, I. R. Sustainion Imidazolium-Functionalized Polymers for Carbon Dioxide Electrolysis. *Energy Technol.* **2017**, *5*, 929−936.

(49) Weng, L.-C.; Bell, A. T.; Weber, A. Z. Towards membrane-electrode assembly systems f or CO_2 reduction: a modeling study. *Energy Environ. Sci.* **2019**, *12*, 1950−1968.

(50) Yin, Z.; Peng, H.; Wei, X.; Zhou, H.; Gong, J.; Huai, M.; Xiao, L.; Wang, G.; Lu, J.; Zhuang, L. An alkaline polymer electrolyte CO_2 electrolyzer operated with pure water. *Energy Environ. Sci.* **2019**, *12*, 2455−2462.

(51) Jeanty, P.; Scherer, C.; Magori, E.; Wiesner-Fleischer, K.; Hinrichsen, O.; Fleischer, M. Upscaling and continuous operation of electrochemical CO_2 to CO conversion in aqueous solutions on silver gas diffusion electrodes. *J. CO2 Util.* **2018**, *24*, 454−462.

(52) Wiley, B.; Sun, Y.; Xia, Y. Polyol Synthesis of Silver Nanostructures: Control of Product Morphology with Fe(II) or Fe(III) Species. *Langmuir* **2005**, *21*, 8077−8080.

(53) Skrabalak, S. E.; Au, L.; Li, X.; Xia, Y. Facile synthesis of Ag nanocubes and Au nanocages. *Nat. Protoc.* **2007**, *2*, 2182−2190.

(54) Li, Y. C.; Zhou, D.; Yan, Z.; Gonçalves, R. H.; Salvatore, D. A.; Berlinguette, C. P.; Mallouk, T. E. Electrolysis of CO2 to Syngas in Bipolar Membrane-Based Electrochemical Cells. *ACS Energy Lett.* **2016**, *1*, 1149−1153.

(55) Salvatore, D. A.; Weekes, D. M.; He, J.; Dettelbach, K. E.; Li, Y. C.; Mallouk, T. E.; Berlinguette, C. P. Electrolysis of Gaseous CO_2 to CO in a Flow Cell with a Bipolar Membrane. *ACS Energy Lett.* **2018**, *3*, 149−154.

(56) Mayrhofer, K. J. J.; Meier, J. C.; Ashton, S. J.; Wiberg, G. K. H.; Kraus, F.; Hanzlik, M.; Arenz, M. Fuel cell catalyst degradation on the nanoscale. *Electrochem. Commun.* **2008**, *10*, 1144−1147.

(57) Hodnik, N.; Zorko, M.; Bele, M.; Hočevar, S.; Gaberšček, M. Identical Location Scanning Electron Microscopy: A Case Study of Electrochemical Degradation of PtNi Nanoparticles Using a New Nondestructive Method. *J. Phys. Chem. C* **2012**, *116*, 21326−21333.

(58) Rahaman, M.; Dutta, A.; Zanetti, A.; Broekmann, P. Electrochemical Reduction of CO_2 into Multicarbon Alcohols on Activated Cu Mesh Catalysts: An Identical Location (IL) Study. *ACS Catal.* **2017**, *7*, 7946−7956.

(59) Luo, B.; Fang, Y.; Li, J.; Huang, Z.; Hu, B.; Zhou, J. Improved Stability of Metal Nanowires via Electron Beam Irradiation Induced Surface Passivation. *ACS Appl. Mater. Interfaces* **2019**, *11*, 12195−12201.

(60) Tan, S. F.; Bosman, M.; Nijhuis, C. A. Molecular Coatings for Stabilizing Silver and Gold Nanocubes under Electron Beam Irradiation. *Langmuir* **2017**, *33*, 1189−1196.

(61) Huang, J.; Hörmann, N.; Oveisi, E.; Loiudice, A.; De Gregorio, G. L.; Andreussi, O.; Marzari, N.; Buonsanti, R. Potential-induced nanoclustering of metallic catalysts during electrochemical CO_2 reduction. *Nat. Commun.* **2018**, *9*, 3117.

(62) Wang, G.; Pan, J.; Jiang, S. P.; Yang, H. Gas phase electrochemical conversion of humidified CO_2 to CO and H_2 on proton-exchange and alkaline anion-exchange membrane fuel cell reactors. *J. CO2 Util.* **2018**, *23*, 152−158.

(63) Seifitokaldani, A.; Gabardo, C. M.; Burdyny, T.; Dinh, C.-T.; Edwards, J. P.; Kibria, M. G.; Bushuyev, O. S.; Kelley, S. O.; Sinton, D.; Sargent, E. H. Hydronium-Induced Switching between CO_2 Electroreduction Pathways. *J. Am. Chem. Soc.* **2018**, *140*, 3833−3837.
(64) Reinisch, D.; Schmid, B.; Martić, N.; Krause, R.; Landes, H.; Hanebuth, M.; Mayrhofer, K. J. J.; Schmid, G. Various CO_2-to-CO Electrolyzer Cell and Operation Mode Designs to avoid CO_2-Crossover from Cathode to Anode. *Z. Phys. Chem.* **2020**, *234*, 1115−1131.

NOTE ADDED AFTER ASAP PUBLICATION

This paper was published on October 27, 2020, before all final corrections were made. The corrected version was reposted on November 6, 2020.

Supporting Information

The Environment Matters: CO_2RR Electrocatalyst Performance Testing in a Gas-Fed Zero-Gap Electrolyzer

María de Jesus Gálvez-Vázquez,[a,‡] Pavel Moreno-García,[a,‡,] Heng Xu,[b] Yuhui Hou,[a] Huifang Hu,[a] Iván Zelocualtecatl Montiel,[a] Alexander V. Rudnev,[a,c] Shima Alinejad,[a] Vitali Grozovski,[a] Benjamin J. Wiley,[b] Matthias Arenz,[a] Peter Broekmann[a]*

[a]University of Bern, Department of Chemistry and Biochemistry, Freiestrasse 3, 3012 Bern, Switzerland

[b]Duke University, Department of Chemistry, Durham, North Carolina, USA

[c]A.N. Frumkin Institute of Physical Chemistry and Electrochemistry Russian Academy of Sciences, Leninskii pr. 31,119071 Moscow, Russia

Corresponding Authors

*E-mails: pavel.moreno@dcb.unibe.ch (P.M.-G.); peter.broekmann@dcb.unibe.ch (P.B.)

Contents **page**

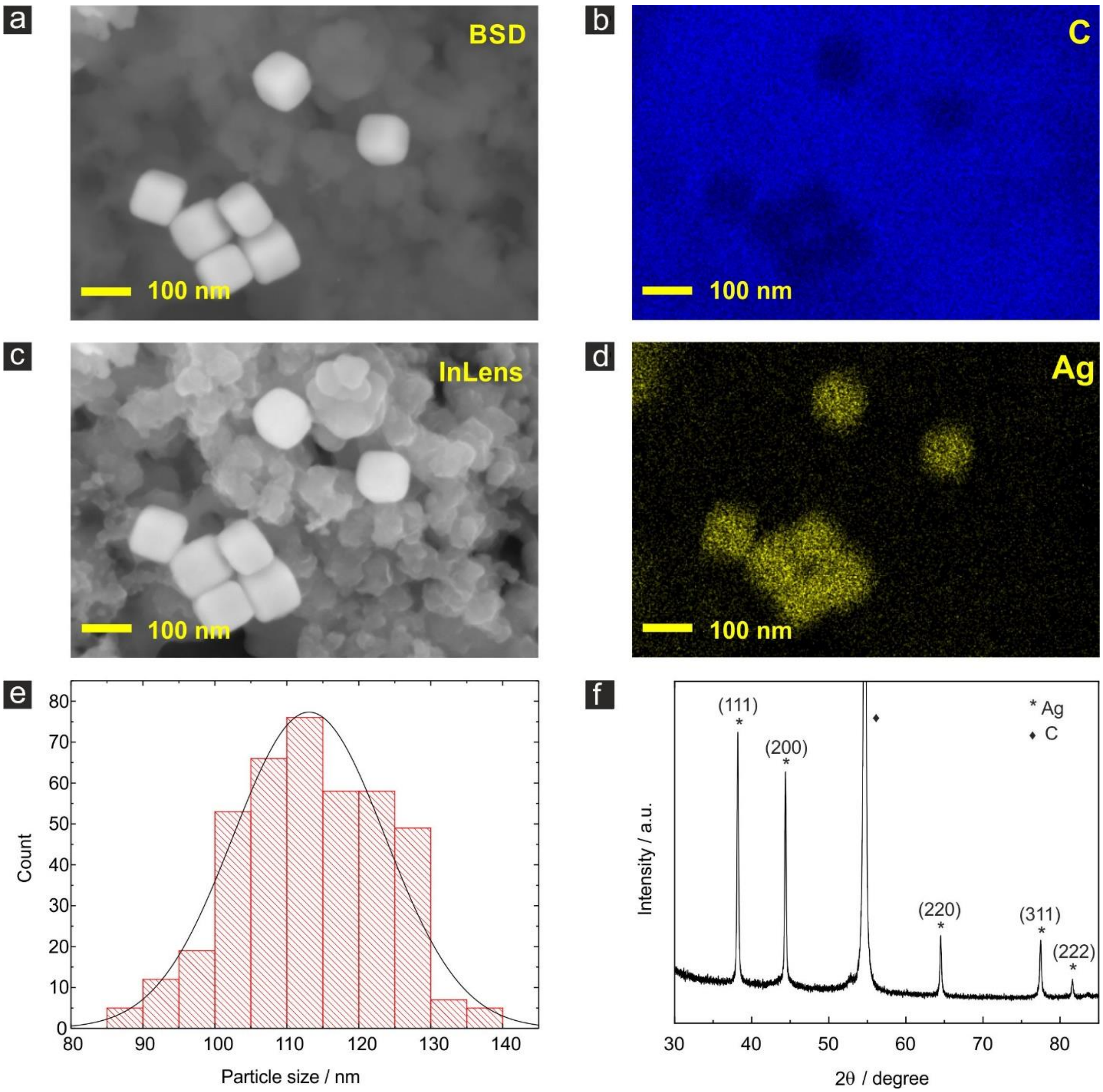

Figure S1. Representative SEM (a and c) and EDX (b and d) characterization of as-prepared Ag-NCs-GDEs. The local C and Ag distributions are indicated in dark blue (b) and yellow (d), respectively. (e) Edge size distribution of the Ag-NP catalyst employed in this work (analysis of more than 400 single particles). (f) XRD spectrum of the nanocrystalline catalyst after dropcasting on a graphite foil support.

Table S1. Contributions on CO_2 electroreduction on Ag catalyts for production of CO. Only works reporting PCD_{CO}s above 100 mA cm^{-2} are listed.

Electrolyzer type	GDE type	Catalyst nanostructure	Electrolyte	Catalyst loading	Membrane	Electrode size	FE_{CO} / %	PCD_{CO} / mA cm^{-2}	Operational stability/time	Ref.
Zero-gap	GDE (Sigracet 39 BC)	Nanocubes (113.1 ± 10.6 nm)	2 M KOH	~7.1 x 10^{-2} mg cm^{-2}	AEM (Sustainion X37-50 RT)	0.071 cm^2	85	~625	1 h	This work
Flowing catholyte	GDE	20-40 nm AgNPs (Alfa Aesar, 45509,06)	KOH/KCO_3, pH 13.6	0.2-0.35 mg cm^{-2}	none	(1.5 x 1.7) cm^2	~100	196	~ 1 h	[1]
Zero-gap	Porous Ag filtration membrane as GDE	Well-connected pore openings (2–5 µm)	AEM (Sustainion X37-50 grade 60), (anolyte 0.1 M $KHCO_3$)		AEM (Sustainion X37-50 grade 60)	4 cm^2	> 90	~200	1 h	[2]
Flowing catholyte	Sprayed Ag (Sigracet 35 BC GDLs)	Ag NPs < 100 nm (576832, Sigma Aldrich)	3 M CsOH	2 mg cm^{-2}	Without	1 cm^2	98	866	Longer than 210 s	[3]
Flowing catholyte	Sputtered Ag on PTFE membranes, and carbonate-derived Ag	Conformal Ag on PTFE membranes (250-750 nm thick)	1 M KOH		AEM	1 cm^2	92	~170	100 h	[4]
Flowing catholyte	Ag-NPs GDE	Evaporated 100 nm thick Ag	1 M KOH	2 mg cm^{-2}	AEM	1 cm^2	~100 at 7 atm	~300	10 h	[5]
Zero-gap	Carbon GDL (Sigracet 35 BC GDL, Ion Power)	Spray-coated Ag NPs 20 nm, US Nano)	AEM (Sustainion X37-50 grade 60), (anolyte: water or 0.01 M $KHCO_3$)	2 mg cm^{-2}	AEM (Sustainion X24)	6.25 cm^2	~95/ 98	570/ 196	4 h/ 4000 h	[6]
Flowing catholyte	Sigracet 39 BC carbon paper as GDL	Air brushed < 100 nm Ag powder (Sigma Aldrich)	2 M $KHCO_3$	0.75 mg cm^{-2}	Nafion 117	~10 cm^2	90	198	1 h	[7]
Solid supported catholyte (thin layer)	Carbon cloth (Fuel Cell Store, GDL-CT)	Air brushed Ag nanopowder (Sigma)	1 M $NaHCO_3$	1.5 mg cm^{-2}	bipolar	4 cm^2	50	100	~27 h	[8]
Flowing catholyte	Ag-GDE (Covestro)		0.1 M K_2SO_4/1.5 M $KHCO_3$, pH 7		ZrO_2 diaphragm	10 cm^2	~70	~210	1200 h	[9]
Flowing catholyte	Sprayed Ag on GDL (Freudenberg, H2315 I2 C6)	Ag powder (50-60 nm, 99.9%, Iolitec)	0.5 M K_2SO_4	5 mg cm^{-2}	CEM (Fumapem F14100, Fumatech)	4.5 cm^2	56 (30°C)	168 (30°C)	47 min	[10]
Flowing catholyte	Ag-GDE (Covestro)	Ag NPs	0.4 M K_2SO_4		Nafion	7.67 cm^2	~65	~100	>800 h	[11]
Flowing catholyte	Ag-GDE (Silflon, Gaskatel)		0.5 M K_2SO_4		Nafion 115	8.4 cm^2	92 (60°C, 24.7 atm)	322 (60°C, 24.7 atm)	~1 h	[12]
PEM	GDE (Sigracet 35	Ag NPs	AEM Sustainion	1 mg cm^{-2}	AEM Sustainion	6.25 cm^2	90	180	1000 h	[13]

	BC)									
Flowing catholyte	Toray paper with MPL (20% PTFE)	Ag-NPs (<100 nm, Sigma-Aldrich)	1 M KOH	0.8 mg cm^{-2}	Without	2 cm^2	~90	280	380 s	[14]
Flowing catholyte	GDE (Sigracet 35 BC)	Ag-NPs (<100 nm, Sigma-Aldrich)	3 M KOH	2 mg cm^{-2}	Without	10 cm^2	91.3	440	420 s	[15]
Zero-gap	Ag-GDE	µm-sized Ag particles	0.1 M K_2SO_4 / 0.5 M $KHCO_3$ (pH ~7)		ZrO_2 diaphragm	10 cm^2	> 90	~270	1500 h	[16]
Flowing catholyte	Ag-GDE	Ag-NPs	0.5 M K_2SO_4/1 M $KHCO_3$		ZrO_2 diaphragm	10 cm^2	> 90	~180	1 h	[17]

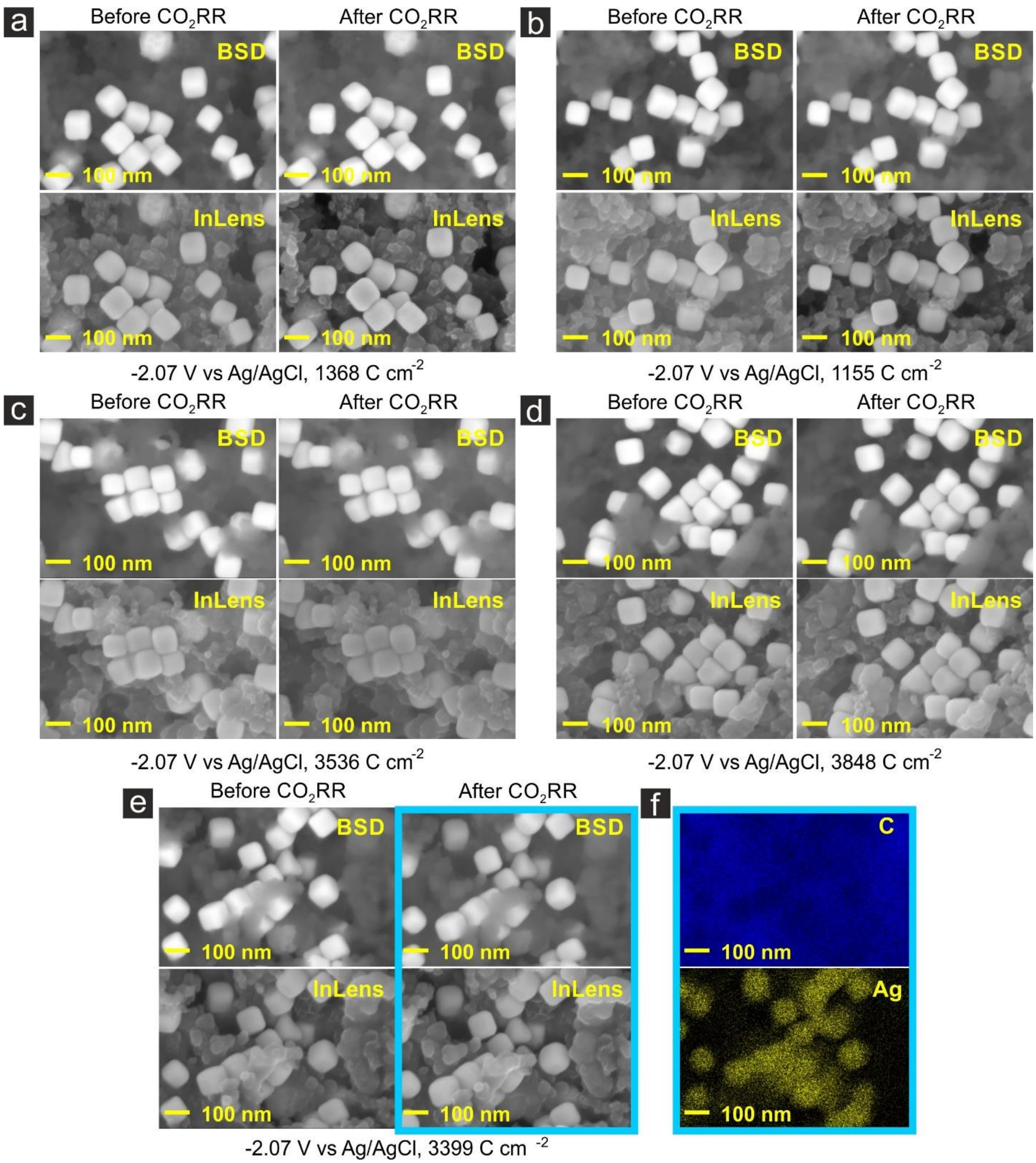

Figure S2. IL-SEM images of Ag-NC-GDE cathode surfaces before and after having conducted sequential gas-fed CO_2RR experiments at -2.07 V for (a) 30 min (1368 C cm^{-2}), (b) 27 min (1155 C cm^{-2}), (c) 90 min (3536 C cm^{-2}), (d) 120 min (3848C cm^{-2}) and (e) 120 min (3399 C cm^{-2}). The SEM images were captured using both BSD and InLens SE detectors. (f) Elemental EDX mappings showing the spatial distribution of C (dark blue) and Ag (yellow) of the sample location highlighted by the blue rectangle in (e). All CO_2RR experiments were carried out using 2 M KOH in the anolyte compartment.

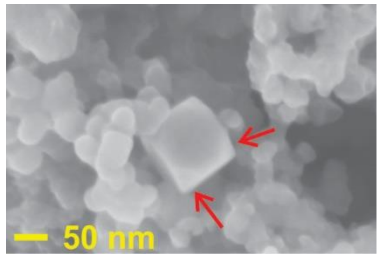

Figure S3. InLens SE image of a Ag-NC-GDE cathode surface after conducting a gas-fed CO_2RR experiment at -2.07 V for ~13 min (800 C cm^{-2}). The red arrows identify eroded corners of a single Ag-NC following cathodic catalyst corrosion. This CO_2RR experiment was carried out using 2 M KOH in the anolyte compartment.

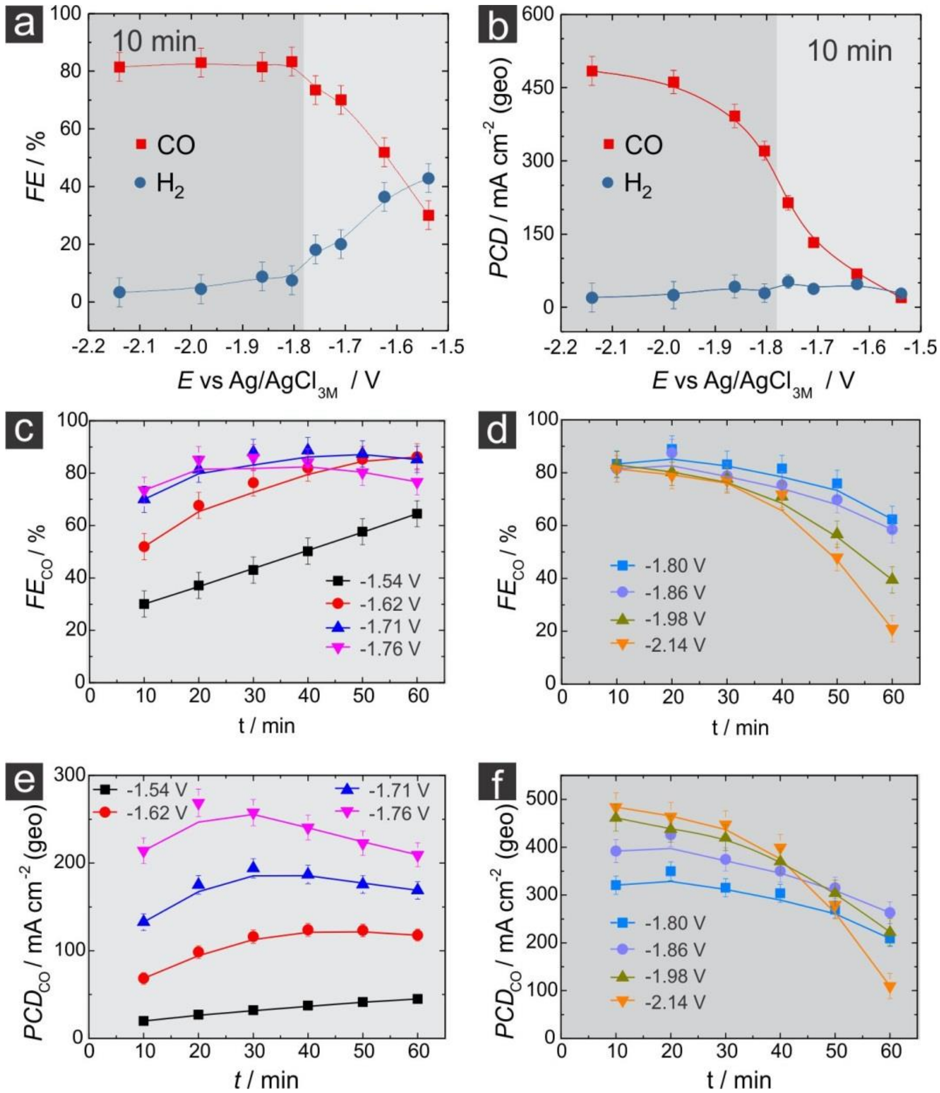

Figure S4. Potential-dependent *FE*s (a) and *PCD*s (b) obtained on the gas-fed Ag-NC-GDEs and recorded 10 min after having started the CO_2 electrolysis. Time evolution of the FE_{CO} at mild (c) and high (d) applied potentials. Time evolution of the PCD_{CO} at mild (e) and high (f) applied potentials. All experiments were carried out using 2 M $KHCO_3$ in the anolyte compartment. The solid lines in all panels are guides to the eye to better observe the trends. The experimental error was accounted for using ± 5% error bars.

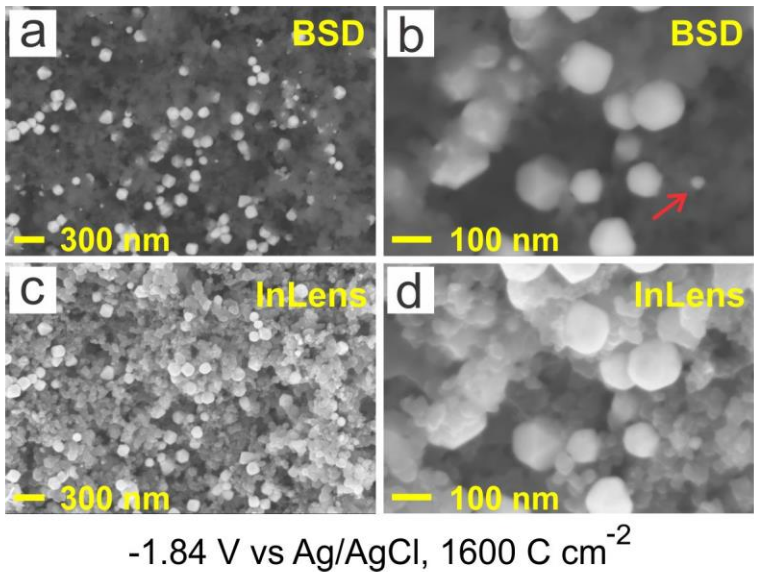

Figure S5. Representative SEM images of cathode surfaces after conducting dedicated gas-fed CO_2RR experiments at (a) -1.84 V for 60 min (1600 C cm^{-2}) using both BSD (a and b) and InLens SE (c and d) detectors. The red arrow in (b) indicates a new Ag nanoparticle that formed following cathodic catalyst corrosion. These CO_2RR experiments were carried out using 2 M $KHCO_3$ in the anolyte compartment.

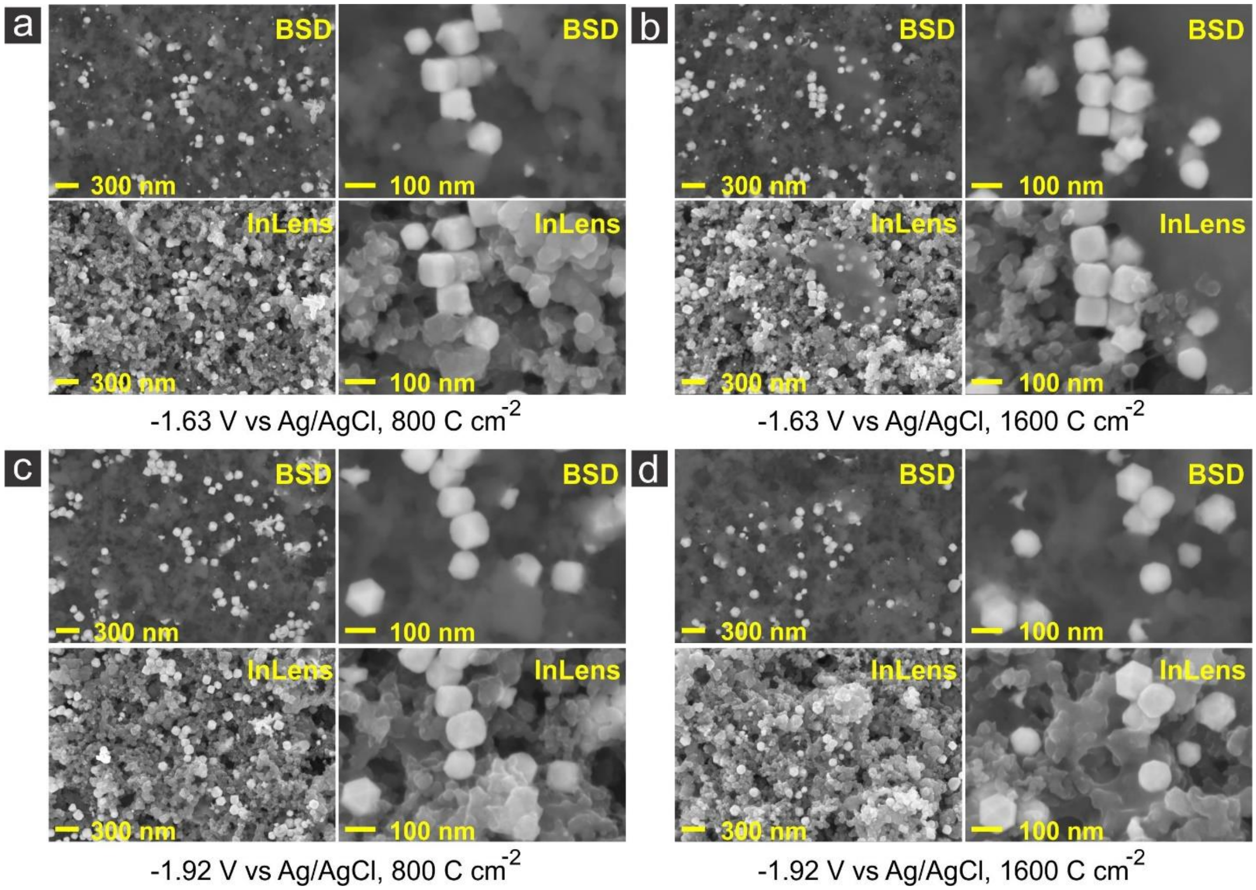

Figure S6. Representative SEM images of cathode surfaces after conducting dedicated CO_2RR experiments in an H-type cell configuration at -1.63 V for (a) 196 min (800 C cm^{-2}) and (b) 304 min (1600 C cm^{-2}), and at -1.92 V for (c) 39 min (800 C cm^{-2}) and (d) 61 min (1600 C cm^{-2}). These CO_2RR experiments were carried out using 2 M $KHCO_3$ as the electrolyte.

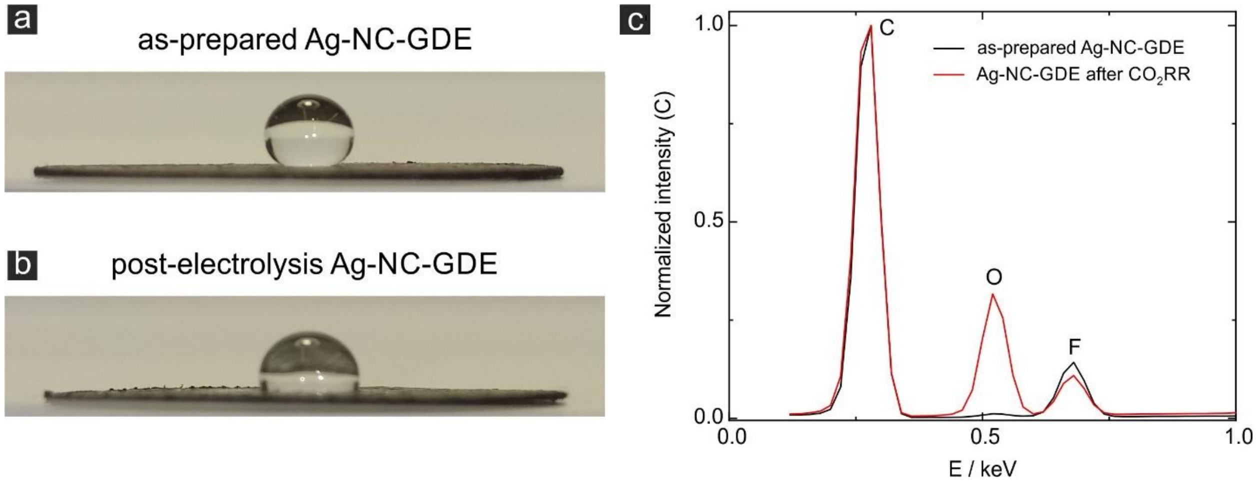

Figure S7. Contact angle images for water droplets on Ag-NC-GDEs (a) before and (b) after having sustained CO_2RR electrolysis at –2.07 V for 32 min (1600 C cm^{-2}). (c) EDX spectra acquired on the front side of the Ag-NC-GDEs before and after the applied CO_2 electrolysis. The spectra were normalized with respect to the C signal. The F signal is used as marker of the PTFE hydrophobic MPL layer that undergoes degradation as a result of the CO_2RR and/or the physical contact with the AEM.

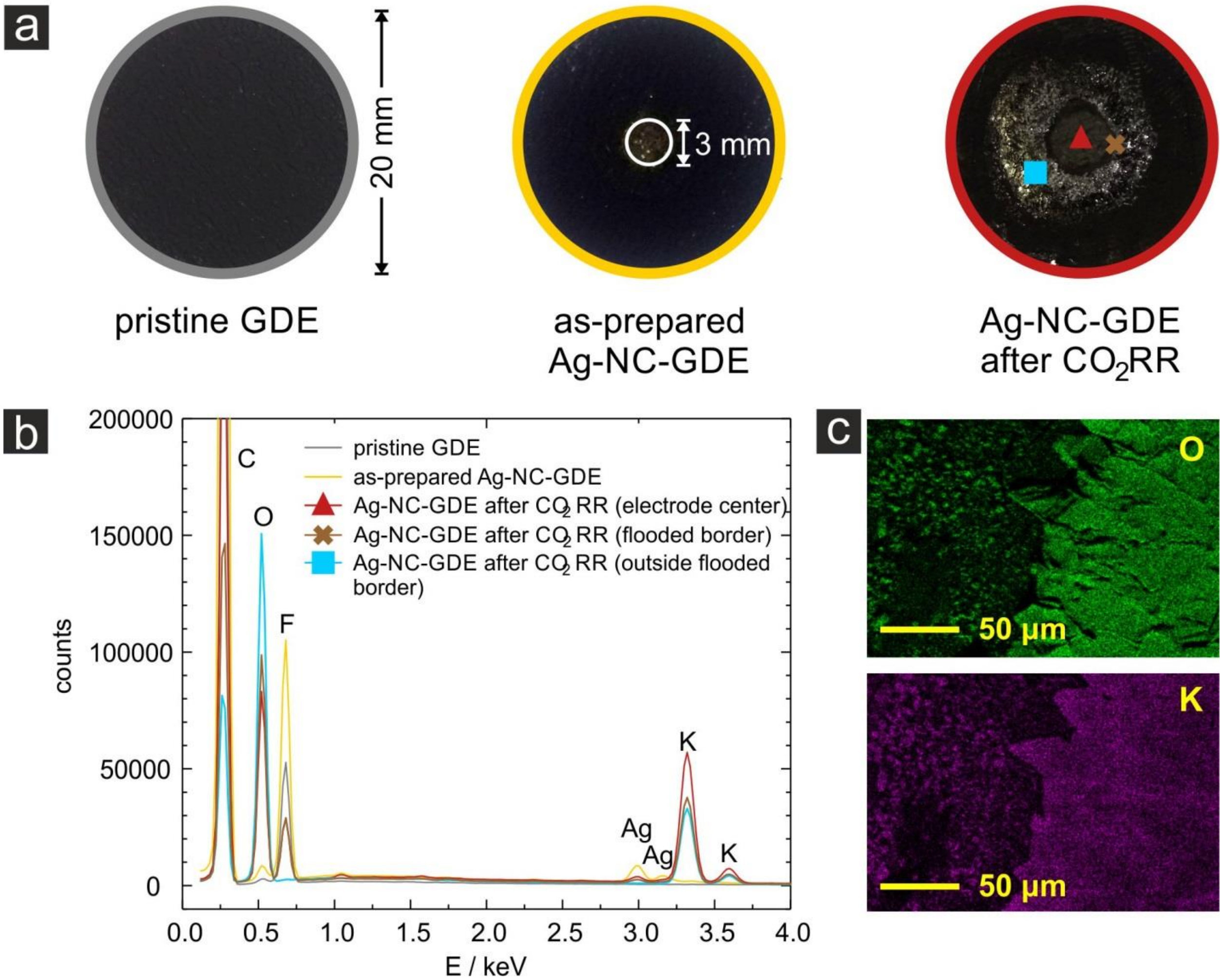

Figure S8. (a) Representative optical micrographs of GDEs at different experimental stages. The white circle in the central part of the as-prepared Ag-NC-GDE shows the catalyst-modified area of the GDE that is in direct contact with the anion exchange membrane. The Ag-NC-GDE on the right was subjected to gas-fed CO_2RR at -2.07 V for 32 min (1600 C cm^{-2}) with 2 M KOH in the anolyte compartment. (b) EDX spectra acquired on indicated locations along the sample surface of the Ag-NC-GDE after having been subjected to CO_2 electrolysis. (c) EDX mapping of the flooded border region showing O and K intensities in green and magenta, respectively.

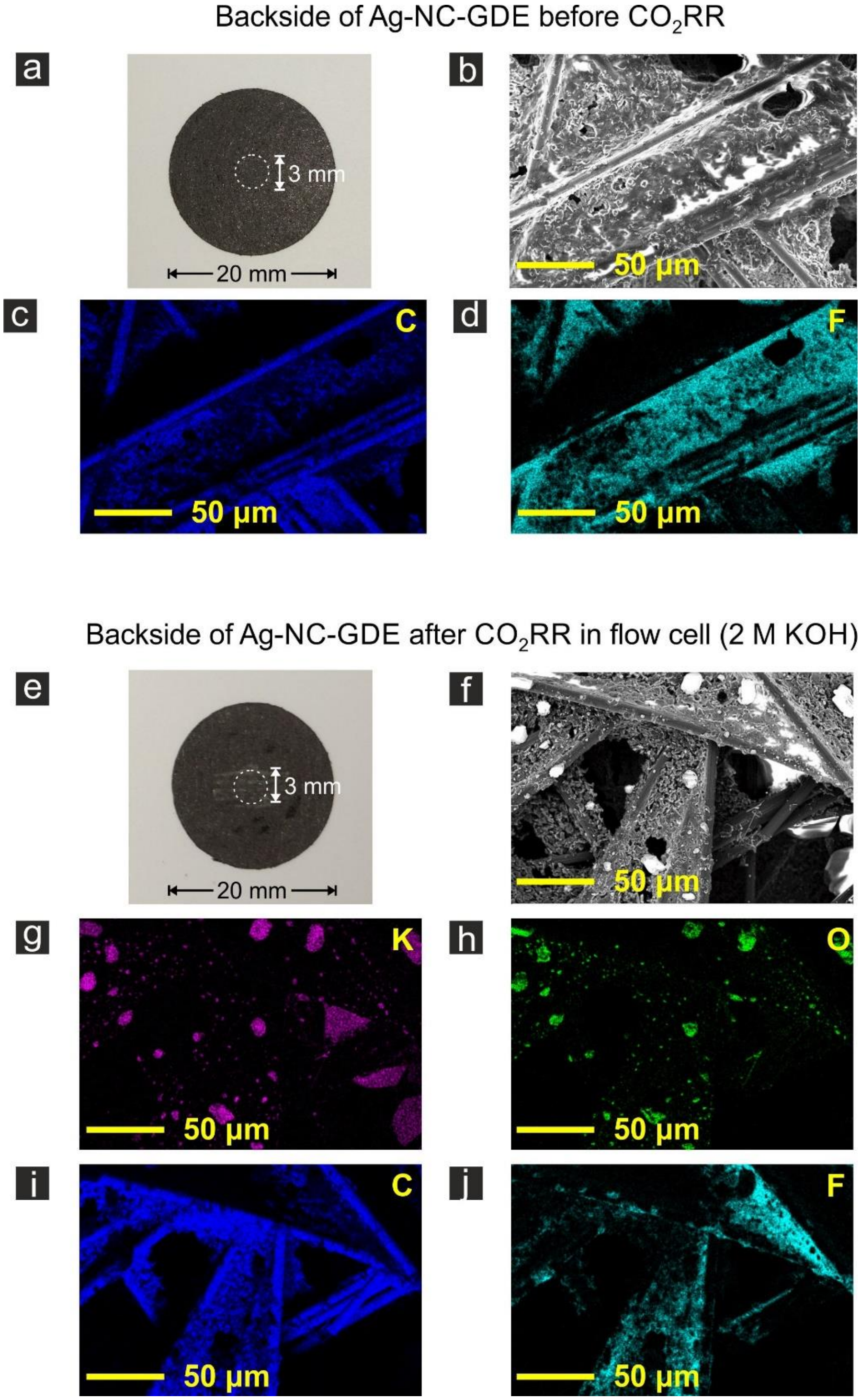

Figure S9. Representative optical micrographs of the backside of GDEs at different experimental stages: (a) before and (e) after having been subjected to gas-fed CO_2RR at -2.07 V for 32 min (1600 C cm^{-2}) with 2 M KOH in the anolyte compartment. Corresponding SEM and EDX mapping acquired on the backside's central parts of Ag-NC-GDEs before (b-d) and after the applied CO_2 electrolysis (f-j). The C, F, K and O EDX intensities are indicated in dark blue, cyan, magenta and green respectively. The white circle in the central part of the Ag-NC-GDEs (a and e) show the backside of the catalyst-modified electrode that was in contact with the anion exchange membrane.

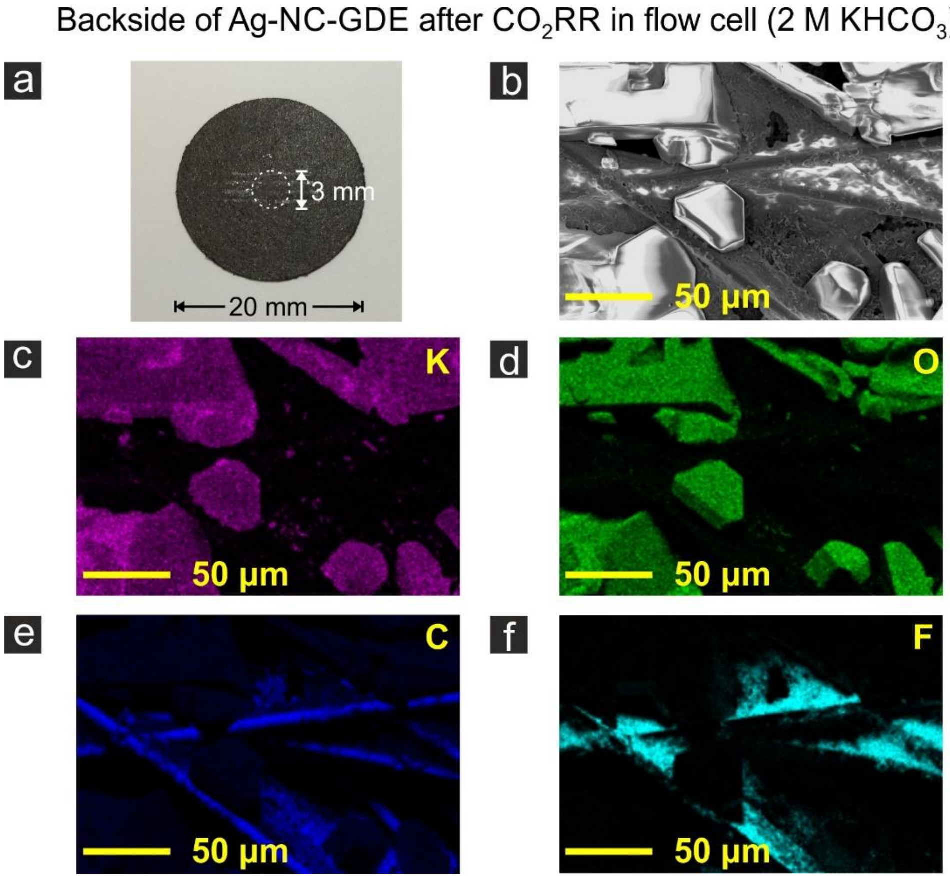

Figure S10. (a) Representative optical micrograph of the backside of a GDEs after having been subjected to gas-fed CO_2RR at -2.07 V for 32 min (1600 C cm^{-2}) with 2 M $KHCO_3$ in the anolyte compartment. (b-f) Corresponding SEM and EDX mapping acquired on the backside's central part of the Ag-NC-GDEs. The C, F, K and O EDX intensities are indicated in dark blue, cyan, magenta and green respectively. The white circle in the central part of (a) shows the backside of the catalyst-modified GDE that was in contact with the anion exchange membrane.

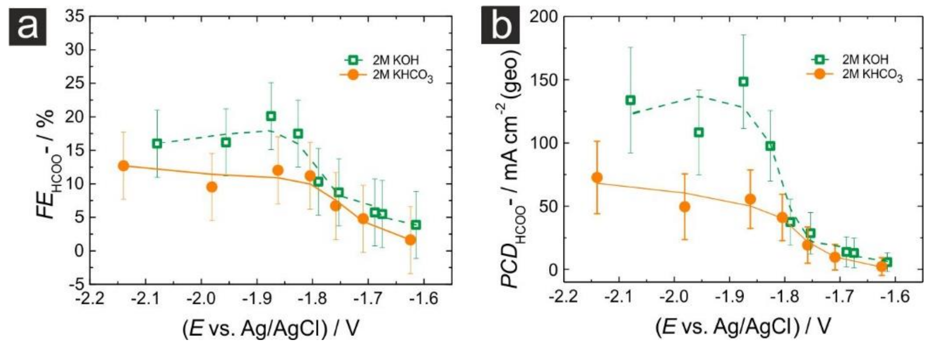

Figure S11. Potential dependence of FE_{HCOO^-} (a) and PCD_{HCOO^-} (b) on the gas-fed Ag-NC-GDEs after 60 min CO_2RR in highly (green) and weakly alkaline (yellow) anolytes, obtained by post-electrolysis ion chromatography analysis. The solid lines in all panels are guides to the eye to better observe the trends. The experimental error was accounted for using ± 5% error bars.

E vs Ag/AgCl	10 min		20 min		30 min		40 min		50 min		60 min		
/ V	FE_{CO} / %	FE_{H2} / %	FE_{CO} / %	FE_{H2} / %	FE_{CO} / %	FE_{H2} / %	FE_{CO} / %	FE_{H2} / %	FE_{CO} / %	FE_{H2} / %	FE_{CO} / %	FE_{H2} / %	FE_{HCOO^-} / %
-1.54	31.57 ± 5	40.73 ± 5	40.65 ± 5	35.51 ± 5	45.60 ± 5	30.71 ± 5	51.41 ± 5	26.93 ± 5	54.81 ± 5	23.46 ± 5	56.75 ± 5	21.88 ± 5	
-1.61	63.73 ± 5	24.17 ± 5	71.81 ± 5	16.89 ± 5	76.54 ± 5	12.13 ± 5	81.53 ± 5	9.43 ± 5	83.74 ± 5	7.75 ± 5	84.48 ± 5	6.91 ± 5	3.87 ± 5
-1.67	74.81 ± 5	14.32 ± 5	83.53 ± 5	8.66 ± 5	86.22 ± 5	6.16 ± 5	84.62 ± 5	5.20 ± 5	83.32 ± 5	4.98 ± 5	82.19 ± 5	5.54 ± 5	5.48 ± 5
-1.69	76.53 ± 5	14.87 ± 5	83.42 ± 5	9.64 ± 5	85.65 ± 5	7.73 ± 5	84.77 ± 5	7.38 ± 5	83.49 ± 5	8.07 ± 5	81.78 ± 5	10.92 ± 5	5.73 ± 5
-1.75	82.53 ± 5	10.44 ± 5	87.62 ± 5	6.05 ± 5	85.96 ± 5	5.39 ± 5	84.14 ± 5	6.15 ± 5	82.60 ± 5	8.98 ± 5	80.43 ± 5	10.82 ± 5	8.70 ± 5
-1.79	83.59 ± 5	5.26 ± 5	88.63 ± 5	3.79 ± 5	85.57 ± 5	4.29 ± 5	84.70 ± 5	4.87 ± 5	83.30 ± 5	5.61 ± 5	80.54 ± 5	7.41 ± 5	10.31 ± 5
-1.83	81.66 ± 5	3.77 ± 5	80.97 ± 5	3.04 ± 5	80.89 ± 5	4.38 ± 5	74.11 ± 5	4.23 ± 5	74.59 ± 5	7.35 ± 5	66.15 ± 5	14.24 ± 5	17.49 ± 5
-1.87	76.87 ± 5	3.71 ± 5	71.13 ± 5	6.34 ± 5	69.57 ± 5	9.13 ± 5	64.20 ± 5	13.81 ± 5	53.46 ± 5	25.69 ± 5	53.63 ± 5	27.67 ± 5	20.09 ± 5
-1.96	77.83 ± 5	4.29 ± 5	76.93 ± 5	4.96 ± 5	74.75 ± 5	7.08 ± 5	68.83 ± 5	13.36 ± 5	47.79 ± 5	36.17 ± 5	32.00 ± 5	56.45 ± 5	16.18 ± 5
-2.08	69.81 ± 5	4.95 ± 5	69.02 ± 5	7.66 ± 5	65.34 ± 5	11.66 ± 5	48.60 ± 5	34.17 ± 5	35.16 ± 5	49.36 ± 5	16.05 ± 5	72.12 ± 5	16.00 ± 5

Table S2. Potential and time dependence of product selectivity for zero-gap CO_2RR experiments on Ag-NC-GDEs in 2 M KOH.

***E* vs Ag/AgCl**	**10 min**		**20 min**		**30 min**		**40 min**		**50 min**		**60 min**		
/ V	***PCD*$_{CO}$ / mA cm^{-2}**	***PCD*$_{H2}$ / mA cm^{-2}**	***PCD*$_{CO}$ / mA cm^{-2}**	***PCD*$_{H2}$ / mA cm^{-2}**	***PCD*$_{CO}$ / mA cm^{-2}**	***PCD*$_{H2}$ / mA cm^{-2}**	***PCD*$_{CO}$ / mA cm^{-2}**	***PCD*$_{H2}$ / mA cm^{-2}**	***PCD*$_{CO}$ / mA cm^{-2}**	***PCD*$_{H2}$ / mA cm^{-2}**	***PCD*$_{CO}$ / mA cm^{-2}**	***PCD*$_{H2}$ / mA cm^{-2}**	***PCD*$_{HCOO^-}$ / mA cm^{-2}**
-1.54	22.33 ± 3.54	28.81 ± 3.54	30.37 ± 3.73	26.53 ± 3.73	34.77 ± 3.81	23.42 ± 3.81	38.76 ± 3.77	20.31 ± 3.77	39.63 ± 3.61	16.96 ± 3.61	38.70 ± 3.41	14.92 ± 3.41	
-1.61	98.09 ± 7.70	37.20 ± 7.70	111.85 ± 7.79	26.30 ± 3.73	118.69± 7.75	18.80 ± 7.75	120.99 ± 7.42	13.99 ± 7.42	118.82 ± 7.09	11.00 ± 7.09	112.58 ± 6.66	9.21 ± 6.66	5.69 ± 7.34
-1.67	191.55 ± 12.80	36.66 ± 12.80	216.95 ± 12.99	22.48 ± 3.73	210.54 ± 12.21	15.03 ± 12.21	192.75 ± 11.39	11.85 ± 11.39	178.81 ± 10.73	10.68 ± 10.73	170.81 ± 10.39	11.51 ± 10.39	12.91 ± 11.78
-1.69	206.47 ± 13.49	40.11 ± 13.49	221.05 ± 13.25	25.53 ± 3.73	207.07 ± 12.09	18.69 ± 12.09	189.13 ± 11.16	16.47 ± 11.16	179.89 ± 10.77	17.40 ± 10.77	168.22 ± 10.29	22.47 ± 10.29	13.77 ± 12.01
-1.75	302.42 ± 18.32	38.26 ± 18.32	308.64 ± 17.61	21.32 ± 3.73	273.62 ± 15.92	17.17 ± 15.92	259.50 ± 15.42	18.96 ± 15.42	252.42 ± 15.28	27.44 ± 15.28	241.23 ± 15.00	32.45 ± 15.00	28.61 ± 16.44
-1.79	327.58 ± 19.59	20.63 ± 19.59	336.04 ± 18.96	14.35 ± 3.73	311.12 ± 18.18	15.62 ± 18.18	300.78 ± 17.75	17.28 ± 17.75	289.91 ± 17.40	19.53 ± 17.40	274.60 ± 17.05	25.27 ± 17.05	37.46 ± 18.17
-1.83	499.06 ± 30.56	23.07 ± 30.56	458.19 ± 28.29	17.18 ± 3.73	446.29 ± 27.59	24.19 ± 27.59	397.36 ± 26.81	22.66 ± 26.81	385.16 ± 25.82	37.93 ± 25.82	330.36 ± 24.97	71.11 ± 24.97	97.66 ± 27.92
-1.87	606.82 ± 39.47	29.28 ± 39.47	527.27 ± 37.07	47.03 ± 3.73	502.96 ± 36.15	66.02 ± 36.15	452.28 ± 35.23	97.31 ± 35.23	376.61 ± 35.23	180.99 ± 35.23	374.08 ± 34.87	192.97 ± 34.87	148.50 ± 36.97
-1.96	559.37 ± 35.93	30.85 ± 35.93	528.94 ± 34.38	34.13 ± 3.73	494.88 ± 33.10	46.90 ± 33.10	438.17 ± 31.83	85.06 ± 31.83	311.67 ± 32.61	235.87 ± 32.61	209.58 ± 32.75	369.77 ± 32.75	108.36 ± 33.49
-2.08	616.26 ± 44.14	43.69 ± 44.14	588.82 ± 42.65	65.39 ± 3.73	547.24 ± 41.88	97.61 ± 41.88	401.53 ± 41.31	282.32 ± 41.31	289.97 ± 41.24	407.13 ± 41.24	134.86 ± 42.02	606.05 ±42.02	133.91 ± 41.83

Table S3. Potential and time dependence of product partial current density (*PCD*) for zero-gap CO_2RR experiments on Ag-NC-GDEs in 2 M KOH.

E vs Ag/AgCl	10 min		20 min		30 min		40 min		50 min		60 min		
/ V	FE_{CO} / %	FE_{H2} / %	FE_{CO} / %	FE_{H2} / %	FE_{CO} / %	FE_{H2} / %	FE_{CO} / %	FE_{H2} / %	FE_{CO} / %	FE_{H2} / %	FE_{CO} / %	FE_{H2} / %	FE_{HCOO^-} / %
-1.54	30.05 ± 5	42.91 ± 5	37.14 ± 5	38.06 ± 5	43.02 ± 5	34.51 ± 5	50.19 ± 5	29.13 ± 5	57.67 ± 5	23.47 ± 5	64.52 ± 5	17.25 ± 5	
-1.62	51.91 ± 5	36.42 ± 5	67.71 ± 5	23.16 ± 5	76.33 ± 5	15.73 ± 5	81.96 ± 5	10.69 ± 5	85.29 ± 5	7.89 ± 5	86.26 ± 5	6.80 ± 5	1.63 ± 5
-1.71	70.05 ± 5	20.04 ± 5	81.46 ± 5	11.48 ± 5	87.97 ± 5	7.09 ± 5	88.70 ± 5	5.90 ± 5	87.41 ± 5	5.92 ± 5	85.27 ± 5	7.31 ± 5	4.78 ± 5
-1.76	73.49 ± 5	18.14 ± 5	85.17 ± 5	9.67 ± 5	85.90 ± 5	7.42 ± 5	84.20 ± 5	7.68 ± 5	80.34 ± 5	9.33 ± 5	76.70 ± 5	12.91 ± 5	6.70 ± 5
-1.80	83.32 ± 5	7.50 ± 5	88.94 ± 5	4.58 ± 5	83.15 ± 5	5.13 ± 5	81.57 ± 5	6.58 ± 5	75.92 ± 5	10.43 ± 5	62.35 ± 5	19.00 ± 5	11.19 ± 5
-1.86	81.49 ± 5	8.84 ± 5	87.54 ± 5	4.88 ± 5	78.77 ± 5	6.19 ± 5	75.42 ± 5	8.49 ± 5	69.78 ± 5	13.85 ± 5	58.48 ± 5	26.43 ± 5	12.01 ± 5
-1.98	82.98 ± 5	4.44 ± 5	80.18 ± 5	3.78 ± 5	77.67 ± 5	5.11 ± 5	70.93 ± 5	10.37 ± 5	56.70 ± 5	24.09 ± 5	39.43 ± 5	46.66 ± 5	9.53 ± 5
-2.14	81.46 ± 5	3.34 ± 5	79.02 ± 5	3.16 ± 5	77.18 ± 5	4.24 ± 5	71.80 ± 5	8.71 ± 5	47.94 ± 5	33.13 ± 5	20.94 ± 5	77.90 ± 5	12.69 ± 5

Table S4. Potential and time dependence of product selectivity for zero-gap CO_2RR experiments on Ag-NC-GDEs in 2 M $KHCO_3$.

E vs Ag/AgCl	10 min		20 min		30 min		40 min		50 min		60 min		
/ V	PCD_{CO} / mA cm^{-2}	PCD_{H2} / mA cm^{-2}	PCD_{CO} / mA cm^{-2}	PCD_{H2} / mA cm^{-2}	PCD_{CO} / mA cm^{-2}	PCD_{H2} / mA cm^{-2}	PCD_{CO} / mA cm^{-2}	PCD_{H2} / mA cm^{-2}	PCD_{CO} / mA cm^{-2}	PCD_{H2} / mA cm^{-2}	PCD_{CO} / mA cm^{-2}	PCD_{H2} / mA cm^{-2}	PCD_{HCOO^-} / mA cm^{-2}
-1.54	19.77 ± 3.29	28.23 ± 3.29	27.01 ± 3.64	27.67 ± 3.64	32.07 ± 3.73	25.73 ± 3.73	37.49 ± 3.73	21.76 ± 3.73	41.53 ± 3.60	16.90 ± 3.60	44.91 ± 3.48	12.01 ± 3.48	
-1.62	68.44 ± 6.59	48.03 ± 6.59	98.47 ± 7.27	33.68 ± 7.27	116.08 ± 7.60	23.92 ± 7.60	123.83 ± 7.55	16.16 ± 7.55	123.07 ± 7.22	11.38 ± 7.22	117.77 ± 6.83	9.28 ± 6.83	2.29 ± 7.04
-1.71	132.80 ± 9.48	37.98 ± 9.48	175.16 ± 10.75	24.68 ± 10.75	194.15 ± 11.03	15.65 ± 11.03	186.97 ± 10.54	12.44 ± 10.54	175.60 ± 10.04	11.89 ± 10.04	168.88 ± 9.90	14.47 ± 9.90	9.62 ± 10.07
-1.76	214.16 ± 14.57	52.88 ± 14.57	268.70 ± 15.77	30.50 ± 15.77	257.62 ± 15.00	22.27 ± 15.00	240.62 ± 14.29	21.94 ± 14.29	222.76 ± 13.86	25.88 ± 13.86	209.42 ± 13.65	35.24 ± 13.65	19.19 ± 14.32
-1.80	320.61 ± 19.24	28.88 ± 19.24	349.81 ± 19.66	18.01 ± 19.66	315.26 ± 18.96	19.47 ± 18.96	303.50 ± 18.60	24.49 ± 18.60	269.61 ± 17.75	37.04 ± 17.75	209.06 ± 16.76	63.72 ± 16.76	41.05 ± 18.35
-1.86	391.95 ± 24.05	42.51 ± 24.05	426.01 ± 24.33	23.77 ± 24.33	374.41 ± 23.77	29.41 ± 23.77	349.97 ± 23.20	39.40 ± 23.20	314.93 ± 22.56	62.50 ± 22.56	263.10 ± 22.49	118.93 ± 22.49	55.50 ± 23.12
-1.98	461.36 ± 27.80	24.69 ± 27.80	437.85 ± 27.30	20.62 ± 27.30	419.74 ± 27.02	27.59 ± 27.02	370.29 ± 26.10	54.16 ± 26.10	304.00 ± 26.81	129.19 ± 26.81	222.59 ± 28.22	263.39 ± 28.22	49.52 ± 25.98
-2.14	484.02 ± 29.71	19.87 ± 29.71	463.96 ± 29.36	18.54 ± 29.36	447.65 ± 29.00	24.59 ± 29.00	399.20 ± 27.80	48.41 ± 27.80	279.45 ± 29.14	193.10 ± 29.14	109.59 ± 26.17	407.75 ± 26.17	72.71 ± 28.65

Table S5. Potential and time dependence of product partial current density (*PCD*) for zero-gap CO_2RR experiments on Ag-NC-GDEs in 2 M $KHCO_3$.

E vs Ag/AgCl	20 min				40 min				60 min					
/ V	FE_{CO} / %	FE_{H2} / %	PCD_{CO} / mA cm^{-2}	PCD_{H2} / mA cm^{-2}	FE_{CO} / %	FE_{H2} / %	PCD_{CO} / mA cm^{-2}	PCD_{H2} / mA cm^{-2}	FE_{CO} / %	FE_{H2} / %	FE_{HCOO^-} / %	PCD_{CO} / mA cm^{-2}	PCD_{H2} / mA cm^{-2}	PCD_{HCOO^-} / mA cm^{-2}
-1.42	48.00 ± 5	36.63 ± 5	1.87 ± 0.20	1.43 ± 0.20	57.99 ± 5	32.10 ± 5	2.71 ± 0.23	1.50 ± 0.23	63.04 ± 5	28.15 ± 5		3.50 ± 0.28	1.56 ± 0.28	
-1.48	72.75 ± 5	22.94 ± 5	11.78 ± 0.81	3.72 ± 0.81	79.90 ± 5	17.43 ± 5	17.02 ± 1.07	3.71 ± 1.07	80.90 ± 5	17.11 ± 5		19.66 ± 1.22	4.16 ± 1.22	
-1.54	82.38 ± 5	9.97 ± 5	43.25 ± 2.63	5.23 ± 2.63	84.07 ± 5	10.62 ± 5	49.05 ± 2.92	6.20 ± 2.92	83.61 ± 5	11.51 ± 5		51.13 ± 3.06	7.04 ± 3.06	
-1.61	83.92 ± 5	10.12 ± 5	80.99 ± 4.83	9.77 ± 4.83	87.05 ± 5	10.11 ± 5	88.35 ± 5.08	10.26 ± 5.08	87.03 ± 5	11.00 ± 5		89.65 ± 5.15	11.33 ± 5.15	
-1.67	66.44 ± 5	24.53 ± 5	90.69 ± 6.83	33.48 ± 6.83	69.61 ± 5	22.63 ± 5	95.36 ± 6.85	31.00 ± 6.85	72.50 ± 5	22.29 ± 5		99.33 ± 6.85	30.54 ± 6.85	
-1.76	59.82 ± 5	34.33 ± 5	92.35 ± 7.72	52.99 ± 7.72	60.99 ± 5	32.46 ± 5	95.30 ± 7.81	50.72 ± 7.81	59.07 ± 5	32.32 ± 5		92.67 ± 7.84	50.71 ± 7.84	
-1.94	53.96 ± 5	37.17 ± 5	153.11 ± 14.19	105.47 ± 14.19	53.76 ± 5	38.02 ± 5	155.56 ± 14.47	110.01 ± 14.47	54.70 ± 5	38.74 ± 5	2.65 ± 5	156.24 ± 14.28	110.65 ± 14.28	7.51 ± 14.17

Table S6. Potential and time dependence of product selectivity (*FE*) and partial current density (*PCD*) for H-type cell CO_2RR experiments on Ag-NC-GDEs in 2 M $KHCO_3$.

References

1. Leonard, M. E.; Clarke, L. E.; Forner-Cuenca, A.; Brown, S. M.; Brushett, F. R., Investigating Electrode Flooding in a Flowing Electrolyte, Gas-Fed Carbon Dioxide Electrolyzer. *ChemSusChem* **2020,** *13* (2), 400-411.
2. Larrazábal, G. O.; Strøm-Hansen, P.; Heli, J. P.; Zeiter, K.; Therkildsen, K. T.; Chorkendorff, I.; Seger, B., Analysis of Mass Flows and Membrane Cross-over in CO_2 Reduction at High Current Densities in an MEA-Type Electrolyzer. *ACS Appl. Mater. Interfaces* **2019,** *11* (44), 41281-41288.
3. Bhargava, S. S.; Proietto, F.; Azmoodeh, D.; Cofell, E. R.; Henckel, D. A.; Verma, S.; Brooks, C. J.; Gewirth, A. A.; Kenis, P. J. A., System Design Rules for Intensifying the Electrochemical Reduction of CO_2 to CO on Ag Nanoparticles. *ChemElectroChem* **2020,** *7* (n/a), 2001-2011.
4. Dinh, C.-T.; García de Arquer, F. P.; Sinton, D.; Sargent, E. H., High Rate, Selective, and Stable Electroreduction of CO_2 to CO in Basic and Neutral Media. *ACS Energy Lett.* **2018,** *3* (11), 2835-2840.
5. Gabardo, C. M.; Seifitokaldani, A.; Edwards, J. P.; Dinh, C.-T.; Burdyny, T.; Kibria, M. G.; O'Brien, C. P.; Sargent, E. H.; Sinton, D., Combined High Alkalinity and Pressurization Enable Efficient CO_2 Electroreduction to CO. *Energy Environ. Sci.* **2018,** *11* (9), 2531-2539.
6. Liu, Z.; Yang, H.; Kutz, R.; Masel, R. I., CO_2 Electrolysis to CO and O2 at High Selectivity, Stability and Efficiency Using Sustainion Membranes. *J. Electrochem. Soc.* **2018,** *165* (15), J3371-J3377.
7. Duarte, M.; De Mot, B.; Hereijgers, J.; Breugelmans, T., Electrochemical Reduction of CO_2: Effect of Convective CO_2 Supply in Gas Diffusion Electrodes. *ChemElectroChem* **2019,** *6* (22), 5596-5602.
8. Salvatore, D. A.; Weekes, D. M.; He, J.; Dettelbach, K. E.; Li, Y. C.; Mallouk, T. E.; Berlinguette, C. P., Electrolysis of Gaseous CO_2 to CO in a Flow Cell with a Bipolar Membrane. *ACS Energy Lett.* **2018,** *3* (1), 149-154.
9. Haas, T.; Krause, R.; Weber, R.; Demler, M.; Schmid, G., Technical Photosynthesis Involving CO_2 Electrolysis and Fermentation. *Nat. Catal.* **2018,** *1* (1), 32-39.
10. Vennekoetter, J.-B.; Sengpiel, R.; Wessling, M., Beyond the catalyst: How Electrode and Reactor Design Determine the Product Spectrum During Electrochemical CO_2 Reduction. *Chem. Eng. J.* **2019,** *364*, 89-101.
11. Jeanty, P.; Scherer, C.; Magori, E.; Wiesner-Fleischer, K.; Hinrichsen, O.; Fleischer, M., Upscaling and Continuous Operation of Electrochemical CO_2 to CO Conversion in Aqueous Solutions on Silver Gas Diffusion Electrodes. *J. CO_2 Util.* **2018,** *24*, 454-462.
12. Dufek, E. J.; Lister, T. E.; Stone, S. G.; McIlwain, M. E., Operation of a Pressurized System for Continuous Reduction of CO_2. *J. Electrochem. Soc.* **2012,** *159* (9), F514-F517.
13. Kutz, R. B.; Chen, Q.; Yang, H.; Sajjad, S. D.; Liu, Z.; Masel, I. R., Sustainion Imidazolium-Functionalized Polymers for Carbon Dioxide Electrolysis. *Energy Technol.* **2017,** *5* (6), 929-936.
14. Kim, B.; Hillman, F.; Ariyoshi, M.; Fujikawa, S.; Kenis, P. J. A., Effects of Composition of the Micro Porous Layer and the Substrate on Performance in the Electrochemical Reduction of CO_2 to CO. *J. Power Sources* **2016,** *312*, 192-198.
15. Verma, S.; Lu, X.; Ma, S.; Masel, R. I.; Kenis, P. J. A., The effect of Electrolyte Composition on the Electroreduction of CO_2 to CO on Ag Based Gas Diffusion Electrodes. *Phys. Chem. Chem. Phys.* **2016,** *18* (10), 7075-7084.
16. Krause, R.; Reinisch, D.; Reller, C.; Eckert, H.; Hartmann, D.; Taroata, D.; Wiesner-Fleischer, K.; Bulan, A.; Lueken, A.; Schmid, G., Industrial Application Aspects of the Electrochemical Reduction of CO_2 to CO in Aqueous Electrolyte. *Chem. Ing. Tech.* **2020,** *92* (1-2), 53-61.
17. Reinisch, D.; Schmid, B.; Martić, N.; Krause, R.; Landes, H.; Hanebuth, M.; Mayrhofer, K. J. J.; Schmid, G., Various CO_2-to-CO Electrolyzer Cell and Operation Mode Designs to avoid CO_2-Crossover from Cathode to Anode. *Z. Phys. Chem.* **2020,** *234* (6), 1115-1131.

1.5 Testing a Silver Nanowire Catalyst for the Selective CO_2 Reduction in a Gas Diffusion Electrode Half-cell Setup Enabling High Mass Transport Conditions

Authors: María de Jesús Gálvez-Vázquez, Shima Alinejad, Huifang Hu, Yuhui Hou, Pavel Moreno-García, Alessandro Zana, Gustav K. H. Wiberg, Peter Broekmann, and Matthias Arenz

CHIMIA International Journal for Chemistry **73** (11), 922-927 (2019), DOI: 10.2533/chimia.2019.922

Highlights: This work presents the comparison of the performance of silver nanowires as a catalyst material for CO_2RR in a zero-gap flow cell electrolyzer and a traditional H-cell. Current densities >100 mA cm^{-2} are reached with a faradaic efficiency for CO up to 70% in the flow cell device, depending on the applied electrode potential. The partial current densities reached in the H-cell resulted in one order of magnitude less than in the flow cell. It is highlighted that the CO_2RR catalysts must be tested in flow cell devices, where there are no mass transport limitations.

Contributions: I carried out all the electrochemical CO_2 reduction experiments and the analysis of the results. I also prepared most of the figures and wrote some sections of the manuscript.

doi:10.2533/chimia.2019.922 Chimia 73 (2019) 922–927 © Swiss Chemical Society

Testing a Silver Nanowire Catalyst for the Selective CO_2 Reduction in a Gas Diffusion Electrode Half-cell Setup Enabling High Mass Transport Conditions

María de Jesús Gálvez-Vázquez[a§], Shima Alinejad[a§], Huifang Hu[a§], Yuhui Hou[a], Pavel Moreno-García[a], Alessandro Zana[a], Gustav K. H. Wiberg[b], Peter Broekmann*[a], and Matthias Arenz*[a]

Abstract: In this work, we discuss the application of a gas diffusion electrode (GDE) setup for benchmarking electrocatalysts for the reductive conversion of CO_2 (CO_2RR: CO_2 reduction reaction). Applying a silver nanowire (Ag-NW) based catalyst, it is demonstrated that in the GDE setup conditions can be reached, which are relevant for the industrial conversion of CO_2 to CO. This reaction is part of the so-called 'Rheticus' process that uses the CO for the subsequent production of butanol and hexanol based on a fermentation approach. In contrast to conventional half-cell measurements using a liquid electrolyte, in the GDE setup CO_2RR current densities comparable to technical cells (>100 mA cm^{-2}) are reached without suffering from mass transport limitations of the CO_2 reactant gas. The results are of particular importance for designing CO_2RR catalysts exhibiting high faradaic efficiencies towards CO at technological reaction rates.

Keywords: CO_2 reduction · Gas diffusion electrode · Silver nanowire catalyst

María de Jesús Gálvez-Vázquez studied chemistry and received her MSc Specialization in Materials Science at the Benemérita Universidad Autónoma de Puebla (Mexico). In 2017 she started her PhD project in the group of Prof. Peter Broekmann at the University of Bern (Switzerland). Her main focus is the study of different catalyst materials applied to the electrochemical reduction of carbon dioxide under controlled mass transport conditions.

Shima Alinejad obtained her MSc in materials engineering from the University of Tehran (Iran). In 2018, she joined NanoElectroCatalysis group of Matthias Arenz at the University of Bern (Switzerland) as a researcher assistant, and in 2019 she started her PhD in the same group. Her PhD project focuses on developing new measuring platform for the electrocatalysts.

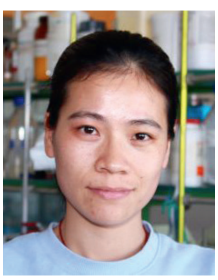

Huifang Hu obtained her MSc in Materials Science and Engineering from Fuzhou University (China). After a short experience in technical college, she joined the Interfacial Electrochemistry Group of Prof. Peter Broekmann as a PhD student in 2019. Her PhD project focuses on the electrochemical conversion of CO_2 into value-added products.

Dr. Yuhui Hou received her PhD degree in physical chemistry from Xiamen University, China in 2015. Before joining Prof. Peter Broekmann's group at University of Bern, Switzerland, she worked as a postdoctoral fellow in Hokkaido University in Japan, where she mainly focused on methane conversion. Her current research interest is to develop electrocatalysts *via* colloidal synthesis approach for electrochemical CO_2 reduction. She is also interested in investigation of material degradation under electrochemical CO_2 reduction conditions by identical-location electronic microscopy.

Dr. Pavel Moreno-García carried out his PhD degree in science of chemistry and molecular science at the University of Bern under the supervision of Prof. Thomas Wandlowski from 2009 to 2013. During this period, his work was devoted to the study of electronic transport characteristics through nano objects at electrified solid-liquid interfaces by *in situ* STM techniques. In 2013 he joined the group of Prof. Peter Broekmann where he has been involved in electrocatalytic topics related to the direct electrochemical conversion of carbon dioxide into more valuable products and instrumental development and studies using laser ablation/ionization mass spectrometry.

*Correspondence: Prof. P. Broekmann[a], E-mail: peter.broekmann@dcb.unibe.ch; Prof. M. Arenz[a], E-mail: matthias.arenz@dcb.unibe.ch
[a]Department of Chemistry and Biochemistry, University of Bern, Freiestrasse 3, Bern CH-3012, [b]Department of Physical Science, Harold Washington College, City colleges of Chicago, 30 E Lake St, Chicago, IL 60601 USA
[§]Equally contributing first authors

Dr. Alessandro Zana has worked in the group of Professor Arenz, first at the University of Copenhagen (2011–2016) then at the University of Bern, after receiving his PhD. He is currently working in the field of electrochemistry/electrocatalysis, interfaces and collective properties of nanoparticles. He is interested in studying electronic properties of nano systems and developing new solutions for renewable energy sources.

Dr. Gustav K. H. Wiberg received his PhD in electrochemistry from the Technical University of Munich, Germany (2010) and an MSc in engineering physics from Chalmers University of Technology, Sweden (2006). He has worked as a post-doctoral fellow at Argonne National Laboratory (ANL), USA (2010–2013), at the University of Copenhagen, Denmark (2013–2014), and at the University of Bern, Switzerland (2016). Currently, he is a lecturer of chemistry and physics at Harold Washington College – one of the City Colleges of Chicago, USA (2017–present). His current research focuses on electrocatalysis for energy conversion, as well as instrumentation and experimentation method development.

Prof. Peter Broekmann obtained his MSc in chemistry (1998) and a PhD (2000) from the University of Bonn. After a post-doctoral stay in 2001 at the University of Twente, he became project leader at the Institute of Physical Chemistry in Bonn. Since 2008 Prof. Broekmann holds a lecturer position for electrochemistry at the University of Bern (Switzerland). His research focuses on metal deposition processes for semiconductor and electrocatalysis applications.

Prof. Matthias Arenz studied physics with chemistry minor in Bonn (Germany) and received his diploma (Physical Chemistry) in 1999 and in 2002 his PhD on model electrodes for electrocatalysis with Prof. K. Wandelt. Already during his PhD studies he spent seven months in the group of Dr. P. N. Ross and Dr. N. M. Markovic at the Lawrence Berkeley National Laboratory (USA) and returned to the group in 2002 with a Feodor Lynen Fellowship (A.v. Humboldt Foundation) for two years of post-doctoral work. Back in Germany, in 2004, he joined the group of Prof. U. Heiz in Ulm and Munich, before establishing in Munich (2006) an independent Emmy Noether Group of the German Science Foundation (DFG). In 2010 he became tenured Associate Professor at the University of Copenhagen (Denmark) and in 2016 Full Professor at the University of Bern (Switzerland). His group focusses on electrocatalytic reactions related to energy conversion and storage.

1. Introduction

The mitigation of the increase of the greenhouse gas CO_2 in our atmosphere is one of the major societal challenges we are currently facing. The large-scale conversion of CO_2 captured from the atmosphere, into high-value products is considered a technologically feasible approach to address this goal. If combined with renewables (hydro, wind, and solar) that provide 'clean' electric power, the electrochemical CO_2 reduction (CO_2RR: CO_2 reduction reaction) is particularly interesting and significant R&D efforts are addressed to develop selective electrocatalysts.[1] A prime example of such a CO_2RR process is the so-called 'Rheticus' process which combines an electrochemical conversion of CO_2 into CO, an essential reactant for the subsequent production of butanol and hexanol based on a fermentation approach.[2] Thus the CO_2RR might become not only sustainable but also economically feasible.

In the search for cheap, abundant and selective electrocatalysts for the CO_2RR many academic studies apply so-called H-type electrochemical cells with liquid electrolyte. The cells are designed as electrochemical half-cells containing the working electrode (WE) and the reference electrode (RE) in one compartment, and the counter electrode (CE) in another one. These two compartments are separated by a membrane to avoid product crossover,[3] (Fig. 1). The reactant (CO_2 gas) is physically dissolved into the liquid electrolyte where it reaches the active catalyst *via* convection and diffusion. The advantage of such a setup is its straightforward use in screening different electrode materials under defined conditions. However, the product formation can easily be affected by mass transport limitations due to the low gas solubility in the electrolyte, which is limited to about 35 mM, as well as relative slow gas diffusion in liquids. Therefore, in liquid electrolytes the limited availability of CO_2 reactant influences the overall reaction rate as well as the product selectivity. While the CO_2 concentration at the catalyst surface is limited, water, (or protons depending on the electrolyte pH) the reactant to form H_2 gas, is readily available. As a consequence, in more applied studies often electrochemical reactors with a two (or three) electrode setup are used.[4] Such setups are technologically relevant as they allow realistic reaction rates. However, the different factors that determine such rates are often complex and

a)

b)

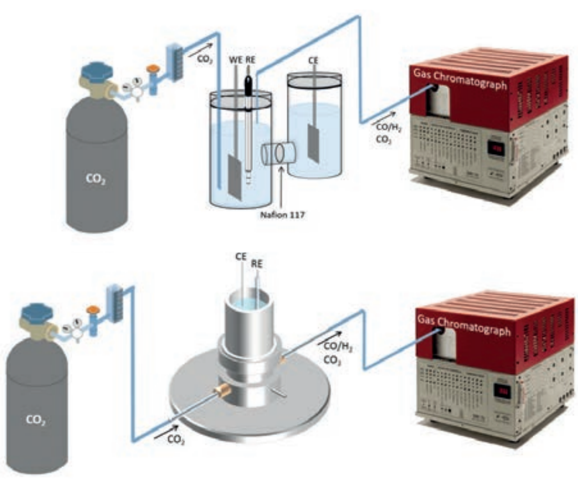

Fig. 1. Schematic drawings of a) typical measurement configuration using an H-type cell in a three-electrode configuration; the CO_2 reactant is dissolved in the liquid electrolyte b) measurement configuration using the GDE setup; the CO_2 reactant is led to the catalyst layer through the GDL and does not need to pass through liquid electrolyte; at the same time a three-electrode configuration is maintained.

difficult to distinguish. Furthermore, cathode (CO_2RR) and anode processes (oxygen evolution reaction; OER) might influence each other and often no information of the individual electrode potentials is obtained.[5]

In the present work, we demonstrate an 'intermediate' setup that bridges measurements in H-type cells and electrochemical reactors, *i.e.* a gas diffusion electrode (GDE) setup with a three-electrode configuration. The GDE setup has originally been developed to benchmark oxygen reduction reaction (ORR) electrocatalysts under realistic mass transport conditions.[6] Similar to a real fuel cell, in the GDE setup the gaseous reactant is guided to the catalyst layer through a gas diffusion layer (GDL) avoiding mass transport limitations typically experienced when working with liquid electrolyte. The catalyst layer is not in contact with any liquid electrolyte, but instead a membrane electrolyte separates the working electrode (catalyst layer) compartment from an electrochemical cell housing the liquid electrolyte, the CE and the RE. Thus a realistic condition for the WE environment is combined with the advantages offered by a three electrode setup.[6] To investigate CO_2RR catalysts the setup has been slightly adapted, as described below. Applying a silver nanowire (Ag-NW) based catalyst that has been previously tested in an H-type cell,[7] it is demonstrated that high currents (reaction rates) can be reached without mass transport limitation of the CO_2 reactant.

2. Experimental

2.1 *Synthesis of Silver Nanowires (Ag-NWs)*

Ag-NWs were synthesized according to a modified protocol introduced by Liu *et. al*.[7] 125 mg of polyvinylpyrrolidone (M = 1,300,000 g/mol, Acros Organic) were dissolved in 20 mL of ethylene glycol (Sigma-Aldrich, 99.8%) and heated to 160 °C for 1 h in an oil bath. The solution was thoroughly agitated (320 rpm). Subsequently, 250 µL of 50 mM sodium bromide (Alfa Aesar, 99.0%) was added to the previous solution. After 15 min, 7.5 mL of 100 mM silver nitrate (Alfa Aesar, 99%) was dropwise injected within 65 min. After the complete addition of the $AgNO_3$ solution, the reaction bath was kept at 160 °C for 35 min, followed by immersion in an ice-water bath. The formed Ag-NWs were washed 3 times with acetone (Honeywell) followed by centrifugation. Finally, the Ag-NWs were thoroughly washed (3 times) with H_2O.

2.2 *Preparation of the Ag-NWs Ink*

For the preparation of the carbon-supported Ag-NW ink, 5 mg of the Ag NWs and 0.9 mg of carbon black (Vulcan XC 72R, Cabot) were separately dispersed in 10 mL of isopropanol (VLSI Selectipur, BASF) by 1 h sonication. Both suspensions were intermixed, sonicated for 1 h and dried using a Rotavapor. Thus, the obtained carbon-supported Ag-NWs were re-dispersed in 1 mL of isopropanol containing 50 µL of Nafion (5 wt.%, 15–20% water, Sigma-Aldrich). This suspension was subjected to sonication for 1 h yielding a homogeneous catalyst ink (85% Ag-NW and 15% C black).

2.3 *Electrochemical Reduction of CO_2 (CO_2RR) Using Ag-NWs as Electrocatalyst*

Gas diffusion electrodes were prepared using Sigracet 39 BC carbon paper as the GDL substrate. The Sigracet 39 BC carbon paper is covered by a microporous layer (MPL) treated with 5% of PTFE (Fuel Cell Store). The carbon paper was cut into circular pieces (2 cm in diameter) and subsequently placed onto a nylon membrane filter (pore size 0.22 µm, Fischerbrand) on top of the funnel of a vacuum filtrating system. This assembly was then covered with a paper mask bearing a central hole of 3 mm in diameter. Subsequently, 40 µL of the as-prepared carbon-supported Ag-NW ink was drop-cast on the carbon paper, thus resulting in a GDE exposed geometric surface area of 7.07×10^{-2} cm^2. The obtained GDEs were dried at ambient conditions for at least 30 min. The employed flow-cell was assembled by placing the prepared GDE on the lower cell body, and a Sustainion X37-50 RT alkaline membrane (Dioxide materials) on top of it. 10 mL of 2 M KOH (solution pH: 14.3, ≥85%, Merck) were used as supporting electrolyte placed above the membrane. The Ag-NW catalyst had no direct contact with the supporting electrolyte. A Ag/AgCl electrode (3 M KCl, Metrohm, double junction design) and Pt wire served as reference and counter electrode, respectively. Both ECi-200 (Nordic electrochemistry) and Autolab PGSTAT128 N (Metrohm) potentiostats were used to perform the CO_2RR electrolysis experiments.

During electrolysis, a humidified CO_2 stream (16 ml min^{-1}, 99.999% Carbagas, Switzerland) was continuously fed through the channels of the stainless-steel cell body adjacent to the prepared GDEs. Potentiostatic CO_2 electrolysis experiments were carried out for 1 h at selected applied electrode potentials. To avoid a possible influence of catalyst layer degradation on the product distribution, a newly prepared GDE was used for each CO_2 electrolysis experiment. Analysis of the gaseous products was carried out every 10 min by online gas chromatography (GC) triggered by the potentiostat.

The continuous flow of humidified CO_2 was used to transport the gaseous products from the GDE flow-cell to the sample loop of the gas chromatograph (Model 8610C, SRI Instruments) equipped with a thermal conductivity detector (TCD) and a flame ionization detector (FID) coupled to a methanizer to detect hydrogen and carbon monoxide, respectively. To avoid damage the column of the GC, the outlet gas of the CO_2RR was passed by a drying tube to remove the excess of water (Cole-Parmer Drierite, Fisher Scientific) before reaching the sample loop of the GC. Eqn (1) was used to determine the faradaic efficiency (FE) for a given gaseous product *i:*

$$FE_i = \frac{I_i}{I_{total}} = \frac{c_i \cdot v \cdot F \cdot z}{10^6 \cdot V_m \cdot I_{total}} \qquad (1)$$

where I_i represents the partial current for the conversion of CO_2 into product *i*, c_i its concentration in ppm measured by online GC using an independent calibration standard gas (Carbagas, Switzerland), ν the gas flow rate (measured by a universal flowmeter 7,000 GC by Ellutia), *F* represents Faraday's constant, *z* the number of electrons involved in the formation of the particular product, V_m the molar volume and I_{total} the total current at the time of the measurement.

Electrochemical impedance spectroscopy measurement was conducted to determine the solution resistance between RE and WE (iR drop).

The electrolyte was analyzed after the electrolysis (*post reaction*) to quantify the formate content by means of ion exchange chromatography (Metrohm Ltd., Switzerland). This chromatograph was coupled to a L-7100 pump, a separation and an ion exclusion column (Metrosep A Supp 7-250, columns) and a conductivity detector.

For comparison, the performance of the catalyst was also tested in a conventional half-cell configuration using a custom-built gas-tight H-type glass cell with a proton exchange membrane (Nafion 117, Sigma Aldrich) separating the catholyte and the anolyte. The working electrode consisted of a rectangular piece (0.8 cm × 3 cm) of a carbon paper prepared in a similar way as the electrodes for the GDE measurements. The back side and the edges of the electrode were masked with Teflon tape thus leading to a geometric surface area of 0.2 cm^{-2}. A single junction Ag/AgCl (saturated KCl, Pine Research) and a Pt foil (0.25 cm × 0.8 cm) were used as reference and counter electrode, respectively. Prior to the CO_2 electrolysis, the cathodic and anodic compartments were both filled with 30 mL of 0.5 M $KHCO_3$ (ACS grade, Sigma-Aldrich) electrolyte solution and saturated with CO_2 for 30 min, achieving a final pH value of 7.2. The CO_2 flow was kept constant throughout the potentiostatic CO_2 electrolysis and enabled the transport of gaseous products from the headspace of the catholyte to the sample loop of the GC. The CO_2 electrolysis experiments in the half-cell configuration were performed in an analogous way as the ones carried out in the GDE set up. The analysis of gaseous products was carried out in intervals of 20 min. The total electrolysis time per applied potential was 1 hour

The catalyst layers were characterized before and after CO_2 electroreduction by means of scanning electron microscopy (Zeiss Gemini 450 SEM equipped with an Inlens SE detector). An accelerating voltage of 1.5 kV was applied at a working distance of 2–3 mm.

3. Results and Discussion

Potentiostatic CO_2 electroreduction experiments on carbon-supported Ag-NWs (85 wt.% Ag-NWs and 15 wt.% of C black) were carried out in the GDE setup to investigate their activity and selectivity as a function of the applied electrolysis potential. Fig. 2 displays the resulting potential-dependent product distribution in terms of faradaic efficiencies (FEs, panel a) and partial current densities (PCDs, panel b). CO and H_2 were the only gaseous products detected by GC analysis. As a third product formate could be detected and quantified *post reaction* in the (liquid) electrolyte compartment of the cell (see Fig. 1) by means of ionic exchange chromatography. Note that in our experiments, the FE of formate is substantially higher than the typically reported values on polycrystalline Ag electrocatalysts (commonly ~ 8% at -1.4 V vs RHE).[8]

The FE vs E plot (Fig. 2a) can be subdivided into three characteristic sections. Hydrogen is the predominant electrolysis product in the first potential regime (> –1.55 V vs Ag/AgCl) with FE_{H2} values never dropping below to 40%, while FE_{CO} does not exceed 35%. In the second characteristic potential section ranging from –1.55 to –1.9 V vs Ag/AgCl FE_{H2} starts to decrease and the CO efficiency passes a maximum of about 70% at –1.75 V vs Ag/AgCl. From Fig. 2a it becomes evident that the FE values for CO and H_2 are strongly anti-correlated to each other, similar to what is known from polycrystalline Ag catalysts tested in a liquid electrolysis environment.[8c] Formate appears as a by-product of the CO_2 electrolysis at applied potentials of < –1.6 V vs Ag/AgCl and reaches a maximum of about 25% at –1.9 V vs Ag/AgCl. In the third characteristic section of the FE vs E plot, at E < –1.9 V vs Ag/AgCl, the parasitic HER becomes the dominant electrolysis process on the expense of the CO_2RR.

The corresponding potential-dependent PCDs for CO, H_2 and formate production are displayed in Fig. 2b. It is seen that by using gas diffusion electrodes, CO_2RR current densities can be achieved which are ~1 order of magnitude higher than the ones typically observed in classical half-cell electrolysis measurements carried out in unstirred aqueous electrolytes.[9] In the present case, a PCD_{CO} of ~130 mA cm^{-2} (normalized to the geometric surface area) at FE_{CO} = 70% was determined at a potential of ~ –1.78 V vs Ag/AgCl. Pre-screening experiments on the same catalyst, carried out in classical H-type half-cell arrangements, resulted in a higher selectivity of the Ag-NWs reaching CO faradaic efficiencies of >95% (Fig. 3), those results are comparable to the previously reported results by Liu *et. al.* However, the PCD for CO production was substantially higher in this present study. Liu *et. al.* reported a maximum PCD for CO of –3 mAcm^{-2} at ~ –1.2 V vs RHE[7] whereas in our pre-screening experiments a maximum PCD of ~16 mA cm^{-2} was achieved at a potential of –1.73 V vs Ag/AgCl.

As discussed above, the significantly lower CO_2RR current densities in the conventional H-type cells using aqueous electrolyte environment as compared to the GDE setup can be explained by transport limitations. In the liquid electrolyte the CO_2 solubility is limited and diffusion significantly inhibited as compared to the gas phase. A direct comparison of the overpotentials in both setups is less straightforward. The thermodynamic CO_2 reduction potentials are pH and product dependent. At pH 7 the reduction potential of CO_2 to CO with respect to NHE (recall that at pH 7 and 1 atm of H_2, the H_2/H^+ couple is –0.420 V) is:[10]

$$CO_2\,(g) + 2\,H^+ + 2\,e^- \rightarrow CO\,(g) + H_2O,\ E^\circ_{redox} = -0.520\ V$$

Thus in both setups significant overpotentials are observed. To refer to the pH-independent RHE scale one needs to establish the pH of the reaction environment. In the conventional H-type cell this is straightforward and all measured electrode potentials can be easily plotted on an RHE scale. In the GDE setup the pH at the RE might be different from the one the catalyst experiences. Thus a referral to RHE with regard of the pH in the liquid electrolyte enclosing the RE might lead to misleading shifts in the reduction potentials.

It should be further noted that it is expected that both the partial CO_2RR current densities and the corresponding faradaic efficiencies observed for the Ag-NW catalyst in the GDE setup can be further improved. In the GDE setup the overall GDE performance

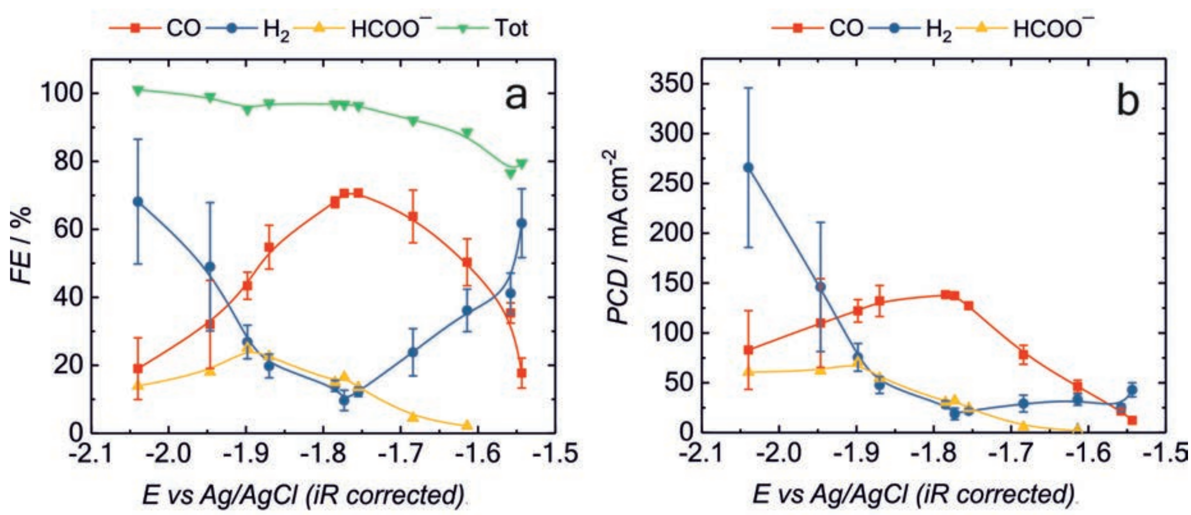

Fig. 2. a) Product distribution of the CO_2RR carried out in the new GDE cell set-up over Ag-NW based electrocatalysts (85% wt.% Ag NW and 15% wt.% of C) at different applied potentials (2 M KOH electrolyte); each value for FE_{CO} and FE_{H2} is the average from six measurements taken every 10 min for in total 1 h of electrolysis; the error bars indicate the standard deviation; b) corresponding partial current densities (PCDs).

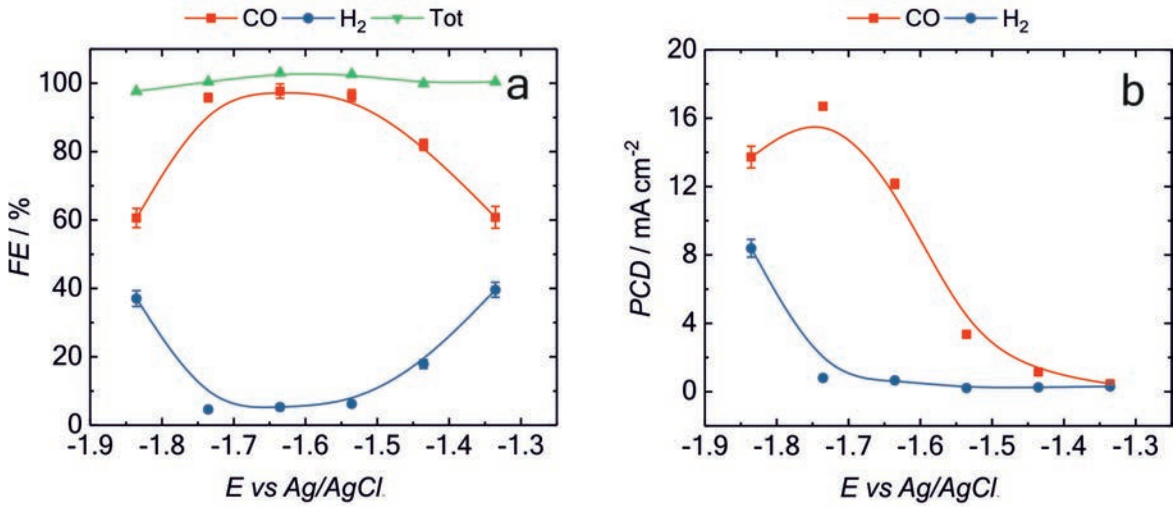

Fig. 3. a) Product distribution of the CO_2RR carried out in an H-type cell over Ag-NW based electrocatalysts (85% wt.% Ag NW and 15% wt.% C) at different applied potentials (0.5 M $KHCO_3$ electrolyte); b) corresponding partial current densities (PCDs).

depends not only on the intrinsic electrocatalytic properties of the Ag-NWs but also on their particular mass loading, their spatial distribution inside the GDE, the local pH as well as the pore distribution. For example, in initial tests of the GDE setup with the same Ag-NW catalyst, a Nafion membrane and/or acidic electrolyte in the upper compartment were used. This led to a significant increase in hydrogen production (FE_{H2}) and almost no CO could be detected (not shown). We addressed this behavior to the acidic pH of Nafion and a simple exchange of the membrane and electrolyte in the CE and RE compartment led to a drastic improvement in CO formation.

Not only are the activity and selectivity of importance for the evaluation of the overall catalyst performance but also its stability. Particularly the higher current densities at higher applied overpotentials might lead to an undesired detachment of the active NWs from the carbon support or might cause other structural degradation processes. Therefore, in an effort to shed light into this issue, identical location (IL) scanning electron microscopy was applied to the Ag-NWs catalyst before (Fig. 4a,b) and after (Fig. 4c,d) the CO_2 electrolysis. The carbon-supported Ag-NW/C catalyst was stressed for 133 min at –0.83 V vs RHE (total charge density 2,453C cm^{-2}). Clearly, there are no severe morphological changes visible in the IL-SEM inspection by comparing the catalyst morphology at the same location before and after CO_2 electrolysis, suggesting that the Ag-NW/C catalyst exhibits superior structural stability, at least under the given experimental conditions.

4. Conclusions

Herein we present a study of a Ag-NW catalyst for the selective CO_2RR to CO. The catalyst performance has been tested in a GDE setup allowing high CO_2 reactant mass transport as well as in a classic H-type cell using liquid electrolyte. In the GDE setup current densities sufficient for technological applications (>100 mA cm^{-2}) are reached with FE_{CO} up to 70%, depending on the applied electrode potential. Comparison to the same catalyst in liquid electrolyte environment suggests that the FE towards CO can be further improved by optimizing the catalyst layer with respect to mass loading, spatial distribution, pore distribution, local pH, *etc*. Our results highlight that for technical applications, catalyst testing in H-type cells and aqueous electrolyte environment is not sufficient, and GDE setups such as the one presented in this work can bridge basic and applied catalyst development.

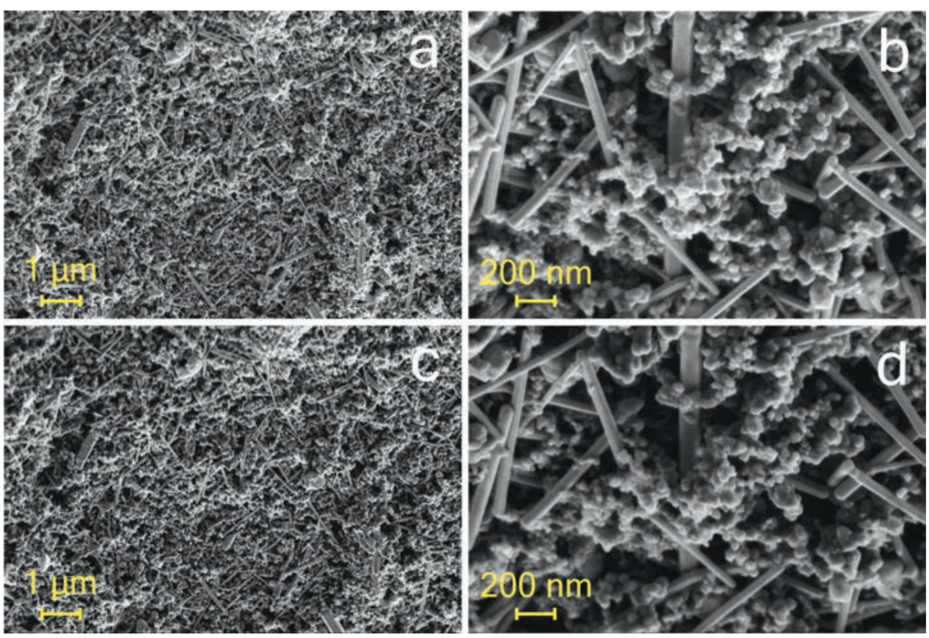

Fig. 4. Identical location (IL) analysis of the Ag NW before (a,b) and after (c,d) performing the CO_2 electrolysis at –0.83 V vs RHE for 133 min (total charge density applied = 2,453C cm^{-2}).

Notes

The authors declare no competing financial interests.

Acknowledgements

The financial support by the Swiss Competence Center for Energy Research (Innoswiss, SCCER Heat and Electricity Storage) is gratefully acknowledged. P.B. and M.A. acknowledge the financial support by the Swiss National Science Foundation (SNSF) *via* the project No. 200020_172507 (P.B.) and 200021_184742 (M.A.). This study was performed with the support of the interfaculty Microscopy Imaging Centre (MIC) of the University of Bern. M. J. G.-V. gratefully acknowledges the financial support by Swiss Government Excellence Scholarships for Foreign Scholars (ESKAS). H. H. thankfully acknowledges the China Scholarship Council (CSC) for the scholarship support.

Received: September 25, 2019

[1] a) S. Nitopi, E. Bertheussen, S. B. Scott, X. Y. Liu, A. K. Engstfeld, S. Horch, B. Seger, I. E. L. Stephens, K. Chan, C. Hahn, J. K. Norskov, T. F. Jaramillo, I. Chorkendorff, *Chem. Rev.* **2019**, *119*, 7610, DOI: 10.1021/acs.chemrev.8b00705; b) M. Rahaman, A. Dutta, A. Zanetti, P. Broekmann, *Acs Catal.* **2017**, *7*, 7946, DOI: 10.1021/acscatal.7b02234; c) J. Durst, A. Rudnev, A. Dutta, Y. C. Fu, J. Herranz, V. Kaliginedi, A. Kuzume, A. A. Permyakova, Y. Paratcha, P. Broekmann, T. J. Schmidt, *Chimia* **2015**, *69*, 769, DOI: 10.2533/chimia.2015.769.

[2] T. Haas, R. Krause, R. Weber, M. Demler, G. Schmid, *Nat. Catal.* **2018**, *1*, 32, DOI: 10.1038/s41929-017-0005-1.

[3] A. V. Rudnev, in 'Encyclopedia of Interfacial Chemistry', Ed. K. Wandelt, Elsevier, Oxford, **2018**, p. 321, DOI: https://doi.org/10.1016/B978-0-12-409547-2.13564-4.

[4] J. B. Vennekoetter, R. Sengpiel, M. Wessling, *Chem. Eng. J.* **2019**, *364*, 89, DOI: 10.1016/j.cej.2019.01.045.

[5] O. G. Sánchez, Y. Y. Birdja, M. Bulut, J. Vaes, T. Breugelmans, D. Pant, *Curr. Opin. Green Sust. Chem.* **2019**, *16*, 47, DOI: https://doi.org/10.1016/j.cogsc.2019.01.005.

[6] a) M. Inaba, A. W. Jensen, G. W. Sievers, M. Escudero-Escribano, A. Zana, M. Arenz, *Energ. Environ. Sci*. **2018**, *11*, 988, DOI: 10.1039/c8ee00019k; b) G. K. H. Wiberg, M. Fleige, M. Arenz, *Rev. Sci. Instrum.* **2015**, *86*, DOI: Artn 02410210.1063/1.4908169; c) G. W. Sievers, A. W. Jensen, V. Brüser, M. Arenz, M. Escudero-Escribano, *Surfaces* **2019**, *2*, 336.

[7] S. Liu, X.-Z. Wang, H. Tao, T. Li, Q. Liu, Z. Xu, X.-Z. Fu, J.-L. Luo, N*ano Energy* **2018**, *45*, 456, DOI: https://doi.org/10.1016/j.nanoen.2018.01.016.

[8] a) Y. Hori, H. Wakebe, T. Tsukamoto, O. Koga, *Electrochim. Acta* **1994**, *39*, 1833, DOI: https://doi.org/10.1016/0013-4686(94)85172-7; b) N. Hoshi, M. Kato, Y. Hori, *J. Electroanal. Chem.* **1997**, *440*, 283, DOI: https://doi.org/10.1016/S0022-0728(97)00447-6; c) T. Hatsukade, K. P. Kuhl, E. R. Cave, D. N. Abram, T. F. Jaramillo, *Phys. Chem. Chem. Phys.* **2014**, *16*, 13814, DOI: 10.1039/c4cp00692e; d) Y.-C. Hsieh, S. D. Senanayake, Y. Zhang, W. Xu, D. E. Polyansky, *Acs Catal.* **2015**, *5*, 5349, DOI: 10.1021/acscatal.5b01235; e) S. Kaneco, K. Iiba, K. Ohta, T. Mizuno, A. Saji, *Electrochim. Acta* **1998**, *44*, 573, DOI: https://doi.org/10.1016/S0013-4686(98)00178-9; f) F. Quan, M. Xiong, F. Jia, L. Zhang, *Appl. Surf. Sci.* **2017**, *399*, 48, DOI: https://doi.org/10.1016/j.apsusc.2016.12.069.

[9] a) H.-R. M. Jhong, S. Ma, P. J. A. Kenis, *Curr. Opin. Chem. Engin.* **2013**, *2*, 191, DOI: https://doi.org/10.1016/j.coche.2013.03.005; b) D. M. Weekes, D. A. Salvatore, A. Reyes, A. Huang, C. P. Berlinguette, *Acc. Chem. Res.* **2018**, *51*, 910, DOI: 10.1021/acs.accounts.8b00010; c) B. Endrödi, G. Bencsik, F. Darvas, R. Jones, K. Rajeshwar, C. Janáky, *Progr. Ener. Comb. Sci.* **2017**, *62*, 133, DOI: https://doi.org/10.1016/j.pecs.2017.05.005.

[10] A. M. Appel, J. E. Bercaw, A. B. Bocarsly, H. Dobbek, D. L. DuBois, M. Dupuis, J. G. Ferry, E. Fujita, R. Hille, P. J. A. Kenis, C. A. Kerfeld, R. H. Morris, C. H. F. Peden, A. R. Portis, S. W. Ragsdale, T. B. Rauchfuss, J. N. H. Reek, L. C. Seefeldt, R. K. Thauer, G. L. Waldrop, *Chem. Rev*. **2013**, *113*, 6621, DOI: 10.1021/cr300463y.

1.6 Leaded Bronze Alloy as a Catalyst for the Electroreduction of CO_2

Authors: María de Jesús Gálvez-Vázquez, Pavel Moreno-García, Huizhang Guo, Yuhui Hou, Abhijit Dutta, Siegfried R. Waldvogel, and Peter Broekmann

ChemElectroChem, **6** (8), 2324-2330 (2019), DOI: 10.1002/celc.201900537

Highlights: This study investigates the electrochemical performance of a leaded bronze, $CuSn_7Pb_{15}$, as a catalyst for CO_2RR. It was found that $CuSn_7Pb_{15}$ is a competitive electrocatalyst for formate production. The catalytic properties of the leaded bronze are mainly determined by elemental lead, which forms clusters embedded in the Cu/Sn matrix that are removed and dispersed on the cathode surface during the polishing electrode pre-treatment (confirmed by scanning Auger microscopy). IL-SEM and EDX characterization of the electrode before and after CO_2RR suggest that lead is redistributed under operando conditions, provided sufficiently high potentials are applied.

Contribution: I conducted all the electrochemical measurements and results analysis. Also, I prepared the figures and wrote the draft of the manuscript together with Dr. Pavel Moreno-García.

JOHN WILEY AND SONS LICENSE
TERMS AND CONDITIONS

Nov 06, 2021

This Agreement between University of Bern -- María de Jesús Gálvez-Vázquez ("You") and John Wiley and Sons ("John Wiley and Sons") consists of your license details and the terms and conditions provided by John Wiley and Sons and Copyright Clearance Center.

License Number	5183131185982
License date	Nov 06, 2021
Licensed Content Publisher	John Wiley and Sons
Licensed Content Publication	ChemElectroChem
Licensed Content Title	Leaded Bronze Alloy as a Catalyst for the Electroreduction of CO2
Licensed Content Author	Peter Broekmann, Siegfried R. Waldvogel, Abhijit Dutta, et al
Licensed Content Date	Apr 29, 2019
Licensed Content Volume	6
Licensed Content Issue	8
Licensed Content Pages	7
Type of use	Dissertation/Thesis
Requestor type	Author of this Wiley article
Format	Print and electronic
Portion	Full article

Will you be translating?	No
Title	Dr.
Institution name	University of Bern
Expected presentation date	Nov 2021
Requestor Location	University of Bern Freiestrasse 3 Bern, 3012 Switzerland Attn: University of Bern
Publisher Tax ID	EU826007151
Total	0.00 CHF

Terms and Conditions

TERMS AND CONDITIONS

This copyrighted material is owned by or exclusively licensed to John Wiley & Sons, Inc. or one of its group companies (each a"Wiley Company") or handled on behalf of a society with which a Wiley Company has exclusive publishing rights in relation to a particular work (collectively "WILEY"). By clicking "accept" in connection with completing this licensing transaction, you agree that the following terms and conditions apply to this transaction (along with the billing and payment terms and conditions established by the Copyright Clearance Center Inc., ("CCC's Billing and Payment terms and conditions"), at the time that you opened your RightsLink account (these are available at any time at http://myaccount.copyright.com).

Terms and Conditions

- The materials you have requested permission to reproduce or reuse (the "Wiley Materials") are protected by copyright.

- You are hereby granted a personal, non-exclusive, non-sub licensable (on a stand-alone basis), non-transferable, worldwide, limited license to reproduce the Wiley Materials for the purpose specified in the licensing process. This license, **and any CONTENT (PDF or image file) purchased as part of your order,** is for a one-time use only and limited to any maximum distribution number specified in the license. The first instance of republication or reuse granted by this license must be completed within two years of the date of the grant of this license (although copies prepared before the end date may be distributed thereafter). The Wiley Materials shall not be used in any other manner or for any other purpose, beyond what is granted in the license. Permission is granted subject to an appropriate acknowledgement given to the author, title of the material/book/journal and the publisher. You shall also duplicate the copyright notice that appears in the Wiley publication in your use of the Wiley

Material. Permission is also granted on the understanding that nowhere in the text is a previously published source acknowledged for all or part of this Wiley Material. Any third party content is expressly excluded from this permission.

- With respect to the Wiley Materials, all rights are reserved. Except as expressly granted by the terms of the license, no part of the Wiley Materials may be copied, modified, adapted (except for minor reformatting required by the new Publication), translated, reproduced, transferred or distributed, in any form or by any means, and no derivative works may be made based on the Wiley Materials without the prior permission of the respective copyright owner.**For STM Signatory Publishers clearing permission under the terms of the STM Permissions Guidelines only, the terms of the license are extended to include subsequent editions and for editions in other languages, provided such editions are for the work as a whole in situ and does not involve the separate exploitation of the permitted figures or extracts,** You may not alter, remove or suppress in any manner any copyright, trademark or other notices displayed by the Wiley Materials. You may not license, rent, sell, loan, lease, pledge, offer as security, transfer or assign the Wiley Materials on a stand-alone basis, or any of the rights granted to you hereunder to any other person.

- The Wiley Materials and all of the intellectual property rights therein shall at all times remain the exclusive property of John Wiley & Sons Inc, the Wiley Companies, or their respective licensors, and your interest therein is only that of having possession of and the right to reproduce the Wiley Materials pursuant to Section 2 herein during the continuance of this Agreement. You agree that you own no right, title or interest in or to the Wiley Materials or any of the intellectual property rights therein. You shall have no rights hereunder other than the license as provided for above in Section 2. No right, license or interest to any trademark, trade name, service mark or other branding ("Marks") of WILEY or its licensors is granted hereunder, and you agree that you shall not assert any such right, license or interest with respect thereto

- NEITHER WILEY NOR ITS LICENSORS MAKES ANY WARRANTY OR REPRESENTATION OF ANY KIND TO YOU OR ANY THIRD PARTY, EXPRESS, IMPLIED OR STATUTORY, WITH RESPECT TO THE MATERIALS OR THE ACCURACY OF ANY INFORMATION CONTAINED IN THE MATERIALS, INCLUDING, WITHOUT LIMITATION, ANY IMPLIED WARRANTY OF MERCHANTABILITY, ACCURACY, SATISFACTORY QUALITY, FITNESS FOR A PARTICULAR PURPOSE, USABILITY, INTEGRATION OR NON-INFRINGEMENT AND ALL SUCH WARRANTIES ARE HEREBY EXCLUDED BY WILEY AND ITS LICENSORS AND WAIVED BY YOU.

- WILEY shall have the right to terminate this Agreement immediately upon breach of this Agreement by you.

- You shall indemnify, defend and hold harmless WILEY, its Licensors and their respective directors, officers, agents and employees, from and against any actual or threatened claims, demands, causes of action or proceedings arising from any breach of this Agreement by you.

- IN NO EVENT SHALL WILEY OR ITS LICENSORS BE LIABLE TO YOU OR ANY OTHER PARTY OR ANY OTHER PERSON OR ENTITY FOR ANY SPECIAL, CONSEQUENTIAL, INCIDENTAL, INDIRECT, EXEMPLARY OR PUNITIVE DAMAGES, HOWEVER CAUSED, ARISING OUT OF OR IN CONNECTION WITH THE DOWNLOADING, PROVISIONING, VIEWING OR USE OF THE MATERIALS REGARDLESS OF THE FORM OF ACTION, WHETHER FOR BREACH OF CONTRACT, BREACH OF WARRANTY, TORT, NEGLIGENCE, INFRINGEMENT OR OTHERWISE (INCLUDING, WITHOUT LIMITATION, DAMAGES BASED ON LOSS OF PROFITS, DATA, FILES, USE, BUSINESS OPPORTUNITY OR CLAIMS OF THIRD PARTIES), AND WHETHER OR NOT THE PARTY HAS BEEN ADVISED OF THE POSSIBILITY OF SUCH

DAMAGES. THIS LIMITATION SHALL APPLY NOTWITHSTANDING ANY FAILURE OF ESSENTIAL PURPOSE OF ANY LIMITED REMEDY PROVIDED HEREIN.

- Should any provision of this Agreement be held by a court of competent jurisdiction to be illegal, invalid, or unenforceable, that provision shall be deemed amended to achieve as nearly as possible the same economic effect as the original provision, and the legality, validity and enforceability of the remaining provisions of this Agreement shall not be affected or impaired thereby.

- The failure of either party to enforce any term or condition of this Agreement shall not constitute a waiver of either party's right to enforce each and every term and condition of this Agreement. No breach under this agreement shall be deemed waived or excused by either party unless such waiver or consent is in writing signed by the party granting such waiver or consent. The waiver by or consent of a party to a breach of any provision of this Agreement shall not operate or be construed as a waiver of or consent to any other or subsequent breach by such other party.

- This Agreement may not be assigned (including by operation of law or otherwise) by you without WILEY's prior written consent.

- Any fee required for this permission shall be non-refundable after thirty (30) days from receipt by the CCC.

- These terms and conditions together with CCC's Billing and Payment terms and conditions (which are incorporated herein) form the entire agreement between you and WILEY concerning this licensing transaction and (in the absence of fraud) supersedes all prior agreements and representations of the parties, oral or written. This Agreement may not be amended except in writing signed by both parties. This Agreement shall be binding upon and inure to the benefit of the parties' successors, legal representatives, and authorized assigns.

- In the event of any conflict between your obligations established by these terms and conditions and those established by CCC's Billing and Payment terms and conditions, these terms and conditions shall prevail.

- WILEY expressly reserves all rights not specifically granted in the combination of (i) the license details provided by you and accepted in the course of this licensing transaction, (ii) these terms and conditions and (iii) CCC's Billing and Payment terms and conditions.

- This Agreement will be void if the Type of Use, Format, Circulation, or Requestor Type was misrepresented during the licensing process.

- This Agreement shall be governed by and construed in accordance with the laws of the State of New York, USA, without regards to such state's conflict of law rules. Any legal action, suit or proceeding arising out of or relating to these Terms and Conditions or the breach thereof shall be instituted in a court of competent jurisdiction in New York County in the State of New York in the United States of America and each party hereby consents and submits to the personal jurisdiction of such court, waives any objection to venue in such court and consents to service of process by registered or certified mail, return receipt requested, at the last known address of such party.

WILEY OPEN ACCESS TERMS AND CONDITIONS

Wiley Publishes Open Access Articles in fully Open Access Journals and in Subscription journals offering Online Open. Although most of the fully Open Access journals publish open access articles under the terms of the Creative Commons Attribution (CC BY) License only, the subscription journals and a few of the Open Access Journals offer a choice of Creative Commons Licenses. The license type is clearly identified on the article.

The Creative Commons Attribution License

The Creative Commons Attribution License (CC-BY) allows users to copy, distribute and transmit an article, adapt the article and make commercial use of the article. The CC-BY license permits commercial and non-

Creative Commons Attribution Non-Commercial License

The Creative Commons Attribution Non-Commercial (CC-BY-NC)License permits use, distribution and reproduction in any medium, provided the original work is properly cited and is not used for commercial purposes.(see below)

Creative Commons Attribution-Non-Commercial-NoDerivs License

The Creative Commons Attribution Non-Commercial-NoDerivs License (CC-BY-NC-ND) permits use, distribution and reproduction in any medium, provided the original work is properly cited, is not used for commercial purposes and no modifications or adaptations are made. (see below)

Use by commercial "for-profit" organizations

Use of Wiley Open Access articles for commercial, promotional, or marketing purposes requires further explicit permission from Wiley and will be subject to a fee.

Further details can be found on Wiley Online Library
http://olabout.wiley.com/WileyCDA/Section/id-410895.html

Other Terms and Conditions:

v1.10 Last updated September 2015

Questions? customercare@copyright.com or +1-855-239-3415 (toll free in the US) or +1-978-646-2777.

DOI: 10.1002/celc.201900537

Leaded Bronze Alloy as a Catalyst for the Electroreduction of CO_2

María de Jesús Gálvez-Vázquez+,[a] Pavel Moreno-García+,*[a] Huizhang Guo,[b] Yuhui Hou,[a] Abhijit Dutta,[a] Siegfried R. Waldvogel,[c] and Peter Broekmann[a]

The performance of a leaded bronze alloy with $CuSn_7Pb_{15}$ (wt%) chemical composition is studied as a cathode material for CO_2 electroreduction (CO_2RR) in aqueous 0.5 M $KHCO_3$ electrolyte. It was found that the catalytic characteristics of the proposed CO_2RR electrocatalyst are dominated by elemental lead. Surface characterization by means of digital 3D optical microscopy, white light interferometry, scanning electron microscopy (SEM), energy dispersive X-ray spectroscopy (EDX) and scanning auger microscopy (SAM) revealed that segregated Pb clusters embedded in a Cu-rich Cu/Sn matrix are, to a large extent, dispersed on the cathode surface upon sample preparation through mechanical polishing. Identical location SEM-EDX studies before and after CO_2 electrolysis revealed that further Pb surface redistribution takes place under operando CO_2RR conditions, provided sufficiently high potentials are applied. The as-prepared electrocatalyst proved to be a suitable and powerful alternative for the selective and efficient production of formate (maximum achieved faradaic efficiency and partial current density for formate are 58.6% and $-11.08\ mA\,cm^{-2}$ at -1.07 V and -1.17 V vs. RHE, respectively). Moreover, in comparison to neat lead, this material can be handled with less precaution.

The electrochemical reduction of carbon dioxide (denoted as CO_2RR hereinafter) to valuable chemicals by employing the excess of intermittent electric power from renewal energy sources is a promising approach to mitigate global warming caused by anthropogenic CO_2 emissions.[1] Additionally, its electrosynthesis to value-added chemical products seems to be key for the future transition of the entire chemical sector going along with the energy transition.[2] Essential for the CO_2RR process is the development of catalyst materials able to provide increasing reaction rates and control over the product distribution. Furthermore, such catalysts should be based on abundant and inexpensive raw materials to approach industrial scale CO_2 electrolysis. In particular, electroreduction of CO_2 to formate ($HCOO^-$) appears to have best chances for the development of technically and economically viable processes.[3] To date, its demand keeps rising in pharmaceutical and biotechnological synthesis and in paper and pulp production as well as in its traditional uses for textile finishing and as additive for animal feeds.[4] Moreover, formate has also been proposed as an energy carrier for fuel cells and hydrogen storage.[5] Among the post transition metals (Hg, Cd, Pb, Tl, In, Sn, and Bi) with high hydrogen overpotential and negligible CO adsorption to reduce selectively CO_2 to formate in aqueous medium,[6] lead appears to be the most straightforward and suitable cathode material for technical applications, since it combines the high-overpotential for the parasitic hydrogen evolution reaction (HER) with lower toxicity than cadmium and mercury.[4,7] Bimetallic metal alloys have also been applied to CO_2RR aiming at boosting formate production due to synergistic interactions between two transition metals[3b,8] or a transition metal and copper.[9] Recently, we investigated leaded bronze as a novel cathode material for a variety of electro-organic reactions that features the catalytic performance of lead but exhibits a higher mechanical and chemical stability.[10] In particular, the cathodic corrosion by organic intermediates could be suppressed. It was found that the employed alloys are rather inhomogeneous and composed of two distinct domains, a copper/tin rich and a lead-enriched phases,[11] which make them a promising cathode alternative when pristine copper does not support side reactions or substrate decomposition.[10c]

In this contribution we extend these previous studies by investigating the catalytic performance of such leaded bronze alloys for CO_2RR focusing on the alloy that has exhibited best cathodic electrosynthesis performance, e.g., $CuSn_7Pb_{15}$ (nominal bulk composition given in weight percent, wt%). The electrochemical investigations show that the material exhibits high faradaic efficiency (46 to 60%) and partial current densities (3 to 11 $mA\,cm^{-2}$) for formate production at moderate applied potentials (-0.95 to -1.15 V) vs. RHE (reversible hydrogen electrode). Surface analysis of the cathode materials by optical and Scanning Electron Microscopy (SEM), Energy Dispersive X-ray Spectroscopy (EDX) and Scanning Auger Microscopy (SAM) revealed that the Pb amount at the surface of the cathode material significantly exceeds the corresponding nominal con-

[a] M. d. J. Gálvez-Vázquez,+ Dr. P. Moreno-García,+ Dr. Y. Hou, Dr. A. Dutta, Prof. Dr. P. Broekmann
Department of Chemistry and Biochemistry
University of Bern
Freiestrasse 3, 3012, Bern, Switzerland
E-mail: pavel.moreno@dcb.unibe.ch
[b] Dr. H. Guo
Wood Materials Science, Institute for Building Materials
ETH Zürich
Stefano-Franscini-Platz 3, 8093 Zürich, Switzerland
[c] Prof. Dr. S. R. Waldvogel
Institute of Organic Chemistry
Johannes Gutenberg University
Duesbergweg 10-14, 55128 Mainz, Germany
[+] M. J. Gálvez-Vázquez and P. Moreno-García contributed equally to this work.

Supporting information for this article is available on the WWW under https://doi.org/10.1002/celc.201900537

tent of the alloy. This is due to the fine dispersion of Pb clusters (up to 500 μm²) that are present not only in the Cu-rich Cu/Sn matrix phase but also on the surface of the $CuSn_7Pb_{15}$ electrode material. Such dispersion of the soft Pb is the result of the mechanical polishing treatment of the sample surface prior to the CO_2 electrolysis.

The employed bronze alloy is commonly used for bearings and is therefore commercially available and inexpensive (in the range of 10 € Kg^{-1}). While neat lead should be handled with gloves, leaded bronze can be directly touched by unprotected hands. It requires very simple preparation to be applied as a cathode in electrochemical studies. After having been downsized from ingots by mechanical cutting to dimensions suitable for experiments in a half-cell reaction configuration, the surface of the samples is mechanically polished with a diamond suspension on a nylon cloth to remove the outermost oxide layers and impurities (see Experimental Section). They are subsequently masked by Teflon tape to leave an area of 1 cm² exposed to the electrolyte during electrolysis. Figure 1 displays

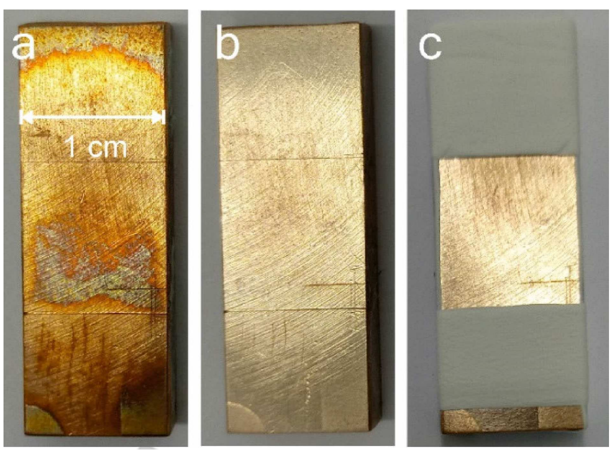

Figure 1. Optical micrographs of the $CuSn_7Pb_{15}$ sample a) before and b) after mechanical polishing and c) after masking with Teflon tape.

a typical sample before and after being treated by mechanical polishing and subsequent masking. The figure shows that surface features originating from the initial cutting such as scratches and grooves on the surface of the sample are not removed upon the polishing step. The morphological characteristics of the cathodes were studied by means of digital 3D optical microscopy and white light interferometry. Figures 2a and b display representative topographies of a freshly polished sample. Both microscopy techniques reveal the presence of three distinct features, e.g., randomly oriented scratches, grooves with preferential direction and pseudo round depressions. The cross-section of all these features ranges from a few up to several tenths of micrometers. We ascribe the grooves with preferential directionality to the initial cutting of the material whereas the randomly oriented scratches are induced by the mechanical polishing step. The images also show that both types of stripes are generally shallower than the randomly distributed depressions, which may reach depths close to the

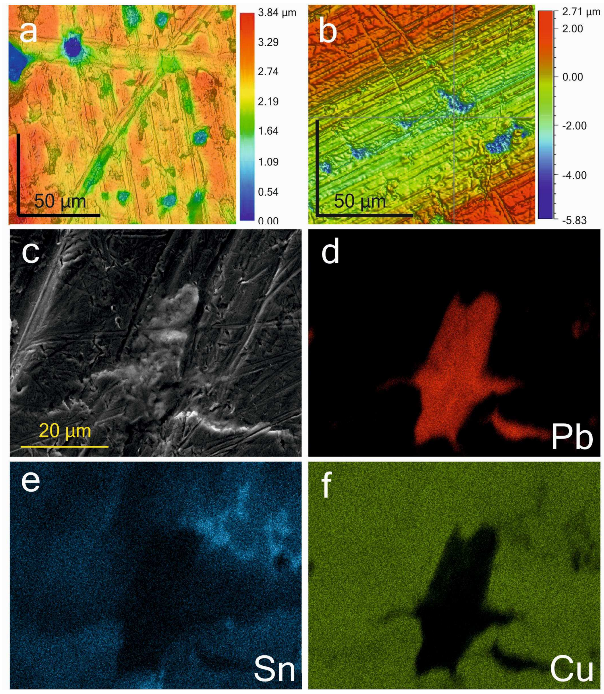

Figure 2. Surface analysis of the polished $CuSn_7Pb_{15}$ sample by a) digital 3D optical microscopy, b) white light interferometry, c) SEM imaging and d) Pb, e) Sn and f) Cu EDX mapping of the $CuSn_7Pb_{15}$ alloy.

tenth of micrometers. These cavities might result from the mechanical polishing procedure that selectively removes and redistributes the softer Pb from the sample surface. To support this and shed further light on the origin of the observed depressions, we present a combined SEM-EDX analysis displayed in Figure 2c–f. Panel c depicts a representative SEM image of such an isolated feature. Correlation of the SEM results with the EDX maps in panels d-f demonstrates that the observed depressions are, to a large extent, composed of a Pb-rich phase and that the surrounding matrix is constituted by a Cu-rich (essentially Pb-free) Cu/Sn phase. This is supported by previous spatial chemical analysis based on Laser Ionization Mass Spectrometry (LIMS) studies that revealed that the leaded bronze alloys of similar composition are quite inhomogeneous materials with mostly two distinct phases, a Cu/Sn-rich and a Pb/Sn-rich phases.[11] We note also that some of the depressions were completely depleted of Pb. However, from the EDX results alone it does not become clear whether the Pb originally forming segregated Pb-rich domains is quantitatively removed from the sample or redistributed along its surface. This has important implications since it is only the outermost sample surface which is relevant for the catalytic performance of the cathodes. Therefore surface-sensitive Scanning Auger Microscopy (SAM) studies were carried out (few nanometers depth resolution and ~0.5 at% detection limit) to address the laterally resolved quantitative element distribution on a freshly polished $CuSn_7Pb_{15}$ sample. Three representative sample positions comprising both completely and partially depleted Pb clusters embedded in the Cu/Sn matrix were analyzed by area mappings and the surface stoichiometry was determined using

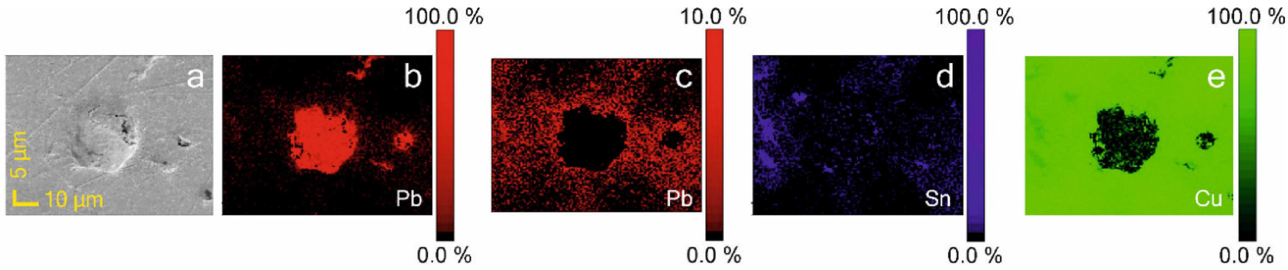

Figure 3. a) Representative SEM image of a polished $CuSn_7Pb_{15}$ sample location. SAM element mappings for b) Pb, c) Pb cut off at 10 at%, d) Sn and e) Cu signals. The color scale bar in the images is expressed in atomic percent.

selected analysis points. One such analyzed region is displayed in Figure 3. It was found that the sample is composed of partially eroded Pb-rich clusters (> 91 wt% Pb) surrounded by a Cu/Sn matrix over which a thin Pb layer is present. This layer exhibits a lateral concentration gradient with higher Pb accumulation at closest proximity with the clusters-matrix interface (see Figure 3b–c). We assume that this thin Pb film results from lead uptake from the clusters and subsequent lateral dispersion by the polishing preparation step on the surrounding Cu/Sn domains. Based on these SAM experiments the composition of the surface matrix, which occupies ~87% of the total surface,[10c] was determined to be $Cu_{71}Sn_9Pb_{20}$ (expressed in wt%). This means that the overall Pb surface content significantly exceeds the alloy nominal composition once it has been polished. This might explain why in our previous studies, the electrocatalytic efficiency of this leaded alloy was as high as that of bulk Pb provided the remaining host Cu/Sn matrix does not support side reactions.[10c] It is then expected that the CO_2RR capabilities of the $CuSn_7Pb_{15}$ cathode might be determined to a large extent by lead.

To probe the effect of the polishing treatment on the catalytic activity of the $CuSn_7Pb_{15}$ towards CO_2RR, linear sweep voltammograms (LSVs) were recorded in the potential range between −0.20 and −1.50 V vs. RHE in both Ar- and CO_2-saturated 0.5 M $KHCO_3$ electrolytes for dedicated non-polished and polished samples. Figure 4 shows the respective steady state LSVs for polished and non-polished specimens in black and red, respectively. Reduction processes beyond −0.85 V vs. RHE in the Ar-saturated electrolytes (dashed lines) are dominated solely by the hydrogen evolution reaction (HER). Clearly the unpolished sample exhibits preferential activity for the undesired HER while the treated sample suppresses its production. In contrast, the LSVs obtained in CO_2-saturated electrolytes (solid lines) show a higher activity at lower applied potentials for the polished sample than for the untreated one. This is due to superposition of the parasitic HER and CO_2 electrolysis, the latter being more favored on the polished sample having increased Pb surface content.

Potentiostatic electroreduction experiments in H-type cell arrangement were carried out in CO_2-saturated 0.5 M $KHCO_3$ electrolyte to investigate the catalyst activity and product selectivity expressed in terms of partial current densities (PCDs), respectively faradaic efficiencies (FEs) at different applied sample potentials. The corresponding current transients are

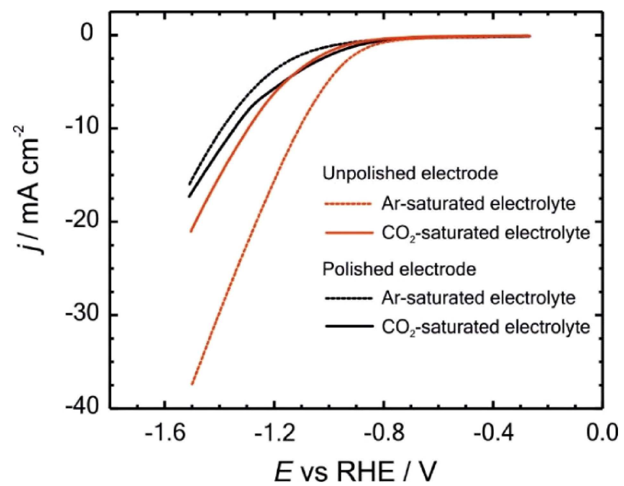

Figure 4. Linear sweep voltammograms of the polished (black) and unpolished (red) $CuSn_7Pb_{15}$ cathodes in Ar-saturated (dashed lines) and CO_2-saturated (solid lines) 0.5 M $KHCO_3$ electrolyte. Scan rate 20 mV s^{-1}.

shown in Figure S1. The liquid and gaseous products were quantified by *post mortem* ion exchange chromatography and online gas chromatography in intervals of 20 min (3 h total duration for each experiment). Figure 5a shows the product distribution of the CO_2RR on the investigated polished $CuSn_7Pb_{15}$ cathode as a function of the applied potential. At low applied potentials (−0.6 to −0.75 V) the main process is generation of the parasitic hydrogen, which is accompanied by a minimum amount of CO. The respective efficiencies are FE_{H2} ~ 60% and FE_{CO} < 5%. Note that the missing contribution to reach 100% total efficiency might be ascribed to the sluggish reduction of metastable tin and/or lead oxides at such low potentials.[6b,8,12] Upon increase of the applied cathodic potentials, the overall efficiency of the HER decreases to a quasi-steady value around 40%, that one of CO slightly increases and remains relatively constant without exceeding 10% and the one of formate increases steeply and remains in the 50-60% range in the potential window from −1.0 to −1.2 V. A very minor selectivity for methane is found at highest applied potentials (max FE_{CH4} = 2.6% at −1.17 V). The corresponding PCDs as a function of the applied potentials are displayed in Figure 5b. The maximum FE_{HCOO^-} and PCD_{HCOO^-} are 58.6% and −11.08 mA cm^{-2} achieved at −1.07 V and −1.17 V vs. RHE,

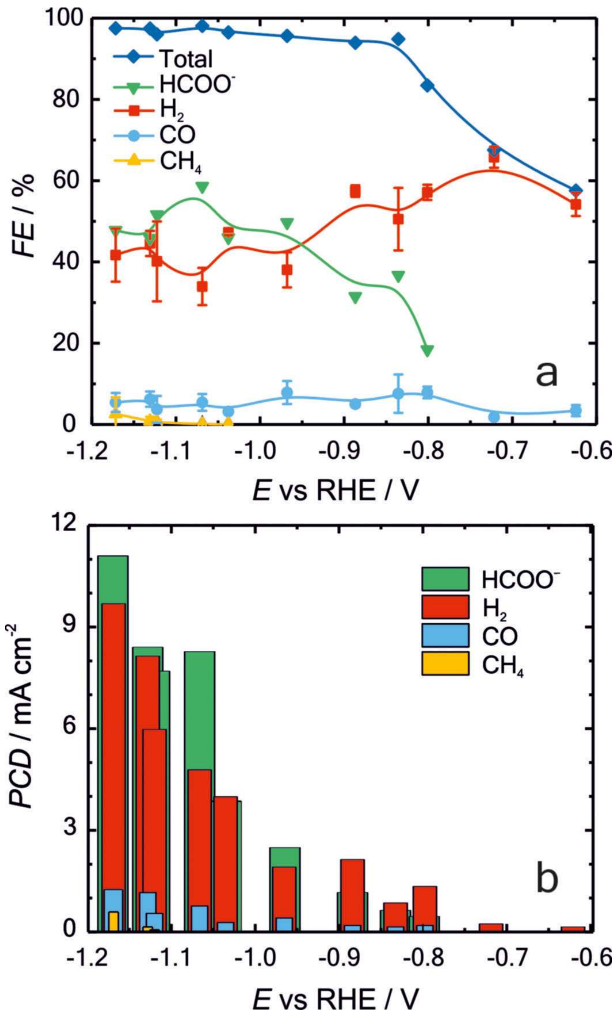

Figure 5. a) Product distribution of CO_2RR on polished $CuSn_7Pb_{15}$ at different applied potentials in CO_2-saturated 0.5 M $KHCO_3$ electrolyte. The error bar is the standard deviation from the measurements done to quantify the gas products every 20 min. b) Corresponding partial current densities.

respectively. Control experiments in Ar-saturated electrolyte only rendered H_2 in significant amount as electrolysis product.

We rationalize the product selectivity of mechanically polished $CuSn_7Pb_{15}$ electrocatalyst for CO_2RR as follows: considering that the active surface is constituted by two well distinct phases (a Pb-rich almost Cu-free Pb/Sn phase and a Cu-rich Cu/Sn phase) and that the typical products formed on them do not decompose on each other, we expect a cathode product selectivity composed of a mixture of their typical product distributions. The main chemical produced by either pristine Pb or PbSn alloys upon CO_2RR in aqueous medium is $HCOO^-$ usually exceeding the amount of evolved H_2 from the parasitic HER in a wide potential range.[3b,4,6a,7c,f,8] On the other hand, the catalytic properties of the Cu-rich Cu/Sn phase could be dominated either by its major component, by the overall alloy ensemble or by a combination of both. The typical products when utilizing CuSn alloys for CO_2 electrolysis, based on their importance, follow the sequence $HCOO^-$, H_2 and CO.[9a,b,d] Finally, it is well known that the most abundant products on untreated polycrystalline Cu at potentials positive of −0.9 V vs. RHE are H_2, $HCOO^-$ and CO whereas in the range [−1.0 to −1.2] V H_2 and CH_4 (max $FE_{CH4}>40\%$) dominate.[13] Assuming that sluggish reduction of native tin and lead oxides on the surface of the cathode material takes place when lower potentials in the range [−0.6 to −0.8] V vs. RHE are applied,[6b] convolution of all these characteristics explains the product selectivity dependence on the applied potentials during potentiostatic CO_2RR experiments using $CuSn_7Pb_{15}$ (Figure 5a). Moreover, the minor CH_4 yield at most negative applied potentials indicates that the catalytic effect of the Cu from the Cu/Sn matrix of the used leaded bronze is significantly minimized compared to that of unalloyed polycrystalline Cu.[13] The relatively low amount of Sn in the Cu/Sn matrix might also suppress significantly the catalytic characteristics of bulk Cu. Therefore, the overall catalytic properties of the polished $CuSn_7Pb_{15}$ seem to be mainly determined by elemental Pb from the segregated Pb clusters and the Pb redistributed on the sample surface by the polishing sample preparation. Analogue potentiostatic CO_2RR investigations at selected low, mild and high potentials were conducted for unpolished $CuSn_7Pb_{15}$ cathodes. The FE and PCD data of these experiments is displayed in Figure S2 showing preferential selectivity for HER due to the relatively low amount of Pb on the surface of the untreated samples. Additionally, the CO_2RR performance of two alternative polished leaded alloy cathodes ($CuSn_{10}Pb_{10}$ and $CuSn_5Pb_{20}$) was also tested. Although their FEs_{HCOO^-} are not far from those attained with the $CuSn_7Pb_{15}$ cathode, the achieved $PCDs_{HCOO^-}$ shown in Figure S3 are, however, much lower. These observations match qualitatively previous activity trends obtained using these three alloys as cathode materials for electro-organic synthesis.[10c] This is due to the fact that it is the $CuSn_7Pb_{15}$ bronze which is the most inhomogeneous alloy with superior amount of Pb-rich domains (the actual active sites to generate formate).

Another aspect investigated in this work that is, to some extent overlooked in CO_2 electrocatalysis, was the surface morphological transformation of the cathode resulting from the CO_2 conversion itself. Studies based on heat maps from micro X-ray fluorescence spectroscopy have demonstrated that these ternary alloy samples undergo structural changes when used as electrocatalysts for organic synthesis.[10c] Those macroscopic studies revealed increasing element inhomogeneities induced by the high applied potentials during the electroreductions. Herein we present identical location SEM-EDX studies shedding light on the microscopic transformations the catalyst surface undergoes as a result of the competing HER and CO_2RR at high and low enforced potentials. Figure 6a is an SEM image of a polished $CuSn_7Pb_{15}$ sample before electrolysis that shows, based on the EDX mappings in panels b-d, a partially eroded Pb cluster embedded in the Cu/Sn matrix. Figure 6e-h shows similar analysis at the very same sample location after having sustained 3 h CO_2 potentiostatic electrolysis at −1.12 V. Potential-induced lead redistribution from the central cluster along the surface in the form of Pb particles is clearly seen that further increases the initial inhomogeneity of the cathode surface. This suggests that additional activation of the material for CO_2RR might be achieved under *operando* conditions. Consideration of

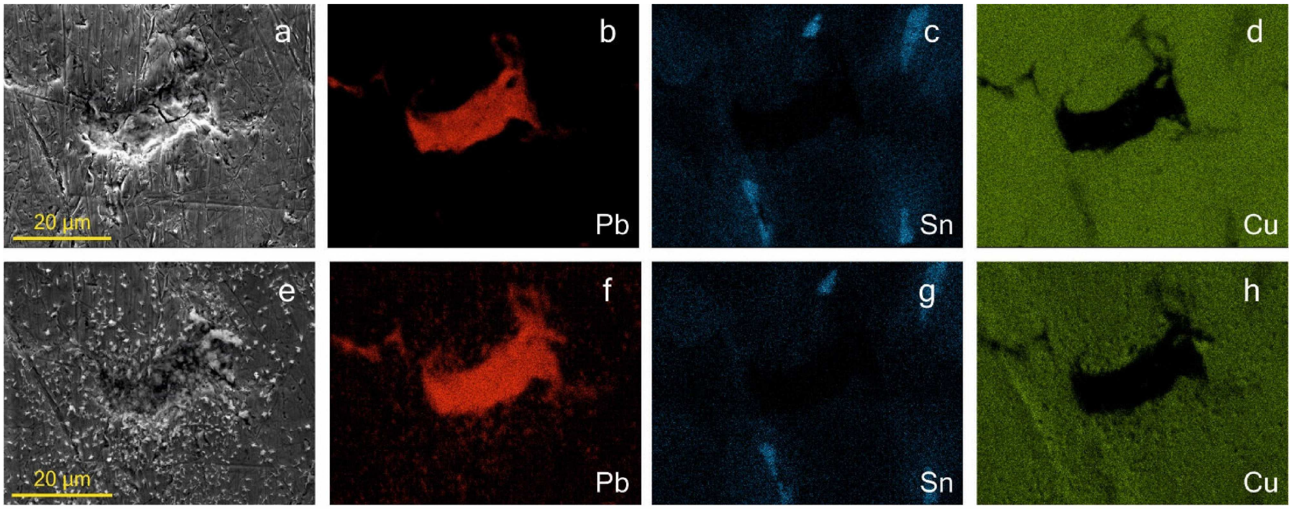

Figure 6. Representative IL-SEM images of a polished $CuSn_7Pb_{15}$ sample location a) before and b) after 3 h electrolysis at −1.12 V in CO_2-saturated 0.5 M $KHCO_3$ electrolyte. Corresponding EDX element mappings b–d) before and f-h) after application of the electrolysis for Pb, Sn and Cu signals.

Table 1. CO_2RR data at pristine Pb and Pb-based alloyed electrodes at different applied potentials.

Catalyst	Electrolyte	Electrolysis potential [V vs. RHE]	PCD_{HCOO^-} [mA cm^{-2}]	FE_{HCOO^-} [%]	Ref.
[100] Pb dendrites on porous Pb	1 M $KHCO_3$	−0.99	−7.5	97	[7f]
Oxide-derived Pb	0.5 M $NaHCO_3$	−0.75	~−0.1 (at −1.0 V)	~100	[7c]
Pb plate	0.5 M NaOH	−0.89	−2.5	65	[4]
Pb granules	0.5 M $KHCO_3$	−0.82	−0.79 (total)	30-90	[7b]
Pb from melt	0.5 M $KHCO_3$	−1.18	−5.5 (total)	72-89	[14]
Roughened Pb plate	1 M $KHCO_3$	−0.96	~−1.5	88	[7d]
$Sn_{42.5}Pb_{57.5}$ (wt%)	0.5 M $KHCO_3$	−1.36	−45.7	79.8	[3b]
$Cu_{20.8}Pb_{79.2}$ (wt%)	0.05 M $KHCO_3$	~−0.79	−1.45	50	[9a]
Electrodeposited $Sn_{63.2}Pb_{36.8}$ (wt%)	0.5 M $KHCO_3$	−1.36		90-95	[8]
Pb clusters on Cu-NWs	0.5 M $KHCO_3$	−0.93	~−2.1	22	[9c]
Sn-rich CuSn alloy NPs	0.1 M $KHCO_3$	−1.17	~2.5	73	[9e]
$CuSn_6Pb_6$ (wt%)	1.5 M HCl + 0.08 M $AlCl_3$	−0.65 V (vs. Ag/AgCl)	0.12	28	[15]
Leaded bronze alloy $CuSn_7Pb_{15}$ (wt%)	0.5 M $KHCO_3$	−1.07	−11.1 (at −1.17 V)	~60	this work

the gradual current density increase over time at such high potentials observed in the corresponding chronoamperograms supports this idea (chronoamperograms at potentials negative of −1.07 V, see Figure S1). Similar experiments at milder reaction conditions (−0.83 V) were performed for the polished sample shown in Figure 2c–f. The post-electrolysis SEM-EDX data is presented in Figure S4. The morphological changes induced at this lower potential are significantly lesser. Smaller electrolysis-induced protruding Pb particles are almost exclusively located on top of the original Pb clusters. Their size, abundance and delocalization along the surface are, nonetheless, much less pronounced than when larger potentials were applied (compare Figure 2, 6 and S4). The effect of the Pb redistribution induced by low applied potentials during electrolysis on the catalyst activity seems to be minor. Note also that at this low applied potentials the presence of metastable oxides on the material surface might retard its morphological alteration.

Finally, Table 1 displays previous and most notable results of pristine Pb and Pb-based bimetallic electrocatalysts applied to CO_2RR for formate production. Compared to those performances, our $CuSn_7Pb_{15}$ electrocatalyst exhibits average FE_{HCOO^-} and very competitive reaction rates (PCD_{HCOO^-}). We suggest that rational design of alternative leaded bronze alloys coupled to similar sample preparation treatment prior to CO_2RR could further optimize their selectivity and activity towards formate production.

In summary, we investigated the performance of a leaded bronze alloy with $CuSn_7Pb_{15}$ chemical composition (wt%) as cathode material for CO_2 electroreduction in aqueous 0.5 M $KHCO_3$ electrolyte. This is motivated by the need to divert from pristine Pb cathode materials that are excellent for formate electrosynthesis but are significantly more toxic and possess lower mechanical and chemical stability. It was found that the catalytic characteristics of the proposed CO_2RR electrocatalyst are dominated by elemental lead. Characterization by optical microscopy with focus variation, white light interferometry, SEM, EDX, surface sensitive Scanning Auger Microscopy and electrochemical investigations revealed that immiscible Pb clusters embedded in a Cu-rich Cu/Sn matrix are to a large extent redistributed on the cathode surface upon sample preparation by mechanical polishing. This Pb thin film together with the segregated Pb-rich clusters occupy an extended surface area that exceeds the expected one from the material's nominal composition. Identical location SEM-EDX studies revealed that further Pb surface redistribution takes place under operando CO_2RR conditions provided that sufficiently high potentials are applied. The electrocatalyst proved to be a suitable option for selective and efficient formate production (max FE_{HCOO^-} and PCD_{HCOO^-} are 58.6% and −11.08 mA cm^{-2} at −1.07 V and −1.17 V vs. RHE).

Experimental Section

The employed $CuSn_7Pb_{15}$ cathodes consisted of alloy slabs with dimensions of $1\times0.45\times2.8$ cm^3. To remove native metal oxides and impurities from the surface, selected leaded bronze alloy electrodes were polished manually for 3 min with a polycrystalline diamond suspension (MetaDi Supreme) with a particle size of 9 μm on a nylon polishing cloth (both from Buehler). They were then thoroughly rinsed with Milli-Q water (Millipore, 18.2 MΩ cm, 3 ppb toc) and masked with Teflon tape leaving an uncovered surface area of 1 cm^2.

The surface morphology of the $CuSn_7Pb_{15}$ sample was analyzed after mechanical polishing and prior to CO_2RR by means of a white light interferometer (Contour GT, Bruker) and a digital optical microscope with focus variation capabilities (VHX600, Keyence). Surface component distributions were analyzed by identical location scanning electron microscope (SEM, FEI Quanta 200F, Hillsboro, USA) before and after electrochemical investigations. The TEAM™ EDX Analysis System of the SEM was used to acquire and analyze the EDX mapping results. The acceleration voltage used was 20 kV. Scanning Auger electron microscopy was used to determine the surface element composition of the sample. The Auger analysis was done using a SMART-200 Semiconductor Micro-Analysis Review Tool from Physical Electronics. The field emitter electron gun worked with a beam energy of 10 keV at a background pressure lower than 10^{-9} mbar. Atomic concentration maps were calculated by standard sensitivity factors from lateral intensity distribution maps measured for each detected element. Adsorption layers were removed, in dedicated experiments, by sputtering with a 2 keV Ar^+ ion beam, using a raster size of 4×4 mm.

The electrochemically active surface areas (ECSAs) of polished and unpolished $CuSn_7Pb_{15}$ cathodes were determined by cyclic voltammetry (CV) using di-methyl viologens (DMV^{2+}) as reversible redox-probe (Figure S5). CVs were carried out in aqueous 1 M Na_2SO_4 (decahydrate, Merck, 99.0%) solution containing 10 mM $DMVCl_2$ (Aldrich, 98%) at different sweep rates. The ECSAs were determined on the basis of the Randles-Sevcik Equation (1)

$$i_p = 2.69 \times 10^5\, n^{3/2}\, A\, c\, D^{1/2}\, \nu^{1/2} \tag{1}$$

with i_p representing the peak current of the first reduction process, n the number of transferred electrons (n = 1), c the concentration of the redox-active DMV^{2+} species, D the DMV^{2+} diffusion coefficient and ν the potential sweep rate. The DMV^{2+} diffusion coefficient was measured by ^{1}H-DOSY-NMR ($D=5.5\times10^{-10}$ m^2 s^{-1}). The ECSA was determined by linear regression of the respective i_p vs. $\nu^{1/2}$ plots where the surface area to determine was the free parameter. The ECSA of the non-polished sample was ca. 2% larger than its polished counterpart.

Linear sweep voltammetry (LSV) measurements and potentiostatic CO_2 electrolysis experiments were conducted using a potentiostat/galvanostat (Metrohm Autolab 128 N, The Netherlands) and a custom-made, airtight H-type cell with a Nafion membrane (Nafion 117, Sigma Aldrich) separating the catholyte from the anolyte. The three electrode arrangement was composed of a selected leaded bronze alloy, a leakless Ag/AgCl (3 M) and a Pt foil (0.8×2 cm) acting as working, reference and counter electrodes, respectively. Prior to CO_2 electrolysis experiments, both cell compartments were filled with 30 ml of a 0.5 M $KHCO_3$ (ACS grade, Sigma-Aldrich). The electrolyte was saturated by CO_2 gas (99.999%, Carbagas, Switzerland) for at least 30 min. CO_2 was continuously purged through the catholyte during the electrolysis experiments. The cell resistance was determined by electrochemical impedance spectroscopy at different potentials and the applied potentials during potentiostatic electrolysis were subsequently iR corrected. For the sake of comparability, the applied potentials vs. the Ag/AgCl (3 M) were converted to RHE scale using Equation (2):

$$\begin{aligned} &\mathrm{E\ vs.\ RHE\ (V)} = \\ &\mathrm{E\ vs.\ Ag/AgCl\ (3\,M)\ (V)} + 0.210\,\mathrm{V} + 0.0591\,\mathrm{V} \times \mathrm{pH} \end{aligned} \tag{2}$$

The pH value of the CO_2-saturated 0.5 M $KHCO_3$ solution was 7.2 and that of Ar-saturated solution 8.15.

Potentiostatic CO_2 electrolyses were performed for 3 h at different applied potentials. A freshly polished $CuSn_7Pb_{15}$ electrode was used for each experiment. Analysis of the gas products from the CO_2 electroreduction was carried out every 20 min by online gas chromatography (GC). The continuous flow of CO_2 was used to transport the gas products from the catholyte headspace to the sampling loop of the gas chromatograph (GC, SRI Instruments Multi-Gas Analyzer #3) equipped with a TCD and an FID detector. Equation (3) was used to calculate the partial current density of a given gaseous product:

$$j_0\ (i) = x_i\ n_i\ F\ v_m \tag{3}$$

where x_i represents the volume fraction of the products measured via online GC using an independent calibration standard gas (Carbagas, Switzerland), n_i is the number of electrons involved in the reduction reaction to form a particular product i, v_m represents the molar CO_2 gas flow rate measured by a universal flowmeter (7000 GC flowmeter by Ellutia) at the exit of the electrochemical cell and F is the Faraday constant. The partial current density for a given reaction product was normalized with respect to the total current density thus providing the faradaic efficiency (FE) for a given reaction product.

The electrolyte from the catholyte was analyzed *post-mortem* to quantify the liquid products (formate) by means of ion exchange chromatography (Metrohm Ltd., Switzerland). This chromatograph was coupled to a L-7100 pump, a separation and an ion exclusion column (Metrosep A Supp 7-250, columns) and a conductivity detector.

Acknowledgements

This work was supported by the CTI Swiss Competence Center for Energy Research (SCCER Heat and Electricity Storage). M. J. G.-V. gratefully acknowledges the financial support by Swiss Government Excellence Scholarships for Foreign Scholars (ESKAS). S. R. W. highly appreciates the financial support by the research network ELYSION (Carl Zeiss Foundation). P.B. acknowledges financial support from the Swiss National Foundation (no. 200020_172507).

Conflict of Interest

The authors declare no conflict of interest.

Keywords: leaded bronze · carbon dioxide reduction · formate production · identical location SEM · electrocatalysis

[1] a) D. T. Whipple, P. J. A. Kenis, *J. Phys. Chem. Lett.* **2010**, *1*, 3451–3458; b) J. Qiao, Y. Liu, F. Hong, J. Zhang, *Chem. Soc. Rev.* **2014**, *43*, 631–675.

[2] a) S. Möhle, M. Zirbes, E. Rodrigo, T. Gieshoff, A. Wiebe, S. R. Waldvogel, *Angew. Chem. Int. Ed.* **2018**, *57*, 6018–6041; *Angew. Chem.* **2018**, *130*, 6124–6149; b) A. Wiebe, T. Gieshoff, S. Möhle, E. Rodrigo, M. Zirbes, S. R. Waldvogel, *Angew. Chem. Int. Ed.* **2018**, *57*, 5594–5619; *Angew. Chem.* **2018**, *130*, 5694–5721.

[3] a) C. Oloman, H. Li, *ChemSusChem* **2008**, *1*, 385–391; b) S. Y. Choi, S. K. Jeong, H. J. Kim, I.-H. Baek, K. T. Park, *ACS Sustainable Chem. Eng.* **2016**, *4*, 1311–1318.

[4] B. Innocent, D. Liaigre, D. Pasquier, F. Ropital, J.-M. Léger, K. B. Kokoh, *J. Appl. Electrochem.* **2009**, *39*, 227–232.

[5] a) N. V. Rees, R. G. Compton, *J. Solid State Electrochem.* **2011**, *15*, 2095–2100; b) X. Yu, P. G. Pickup, *J. Power Sources* **2008**, *182*, 124–132; c) M. Grasemann, G. Laurenczy, *Energy Environ. Sci.* **2012**, *5*, 8171–8181.

[6] a) Y. Hori, H. Wakebe, T. Tsukamoto, O. Koga, *Electrochim. Acta* **1994**, *39*, 1833–1839; b) J. E. Pander, M. F. Baruch, A. B. Bocarsly, *ACS Catal.* **2016**, *6*, 7824–7833; c) W. Lv, R. Zhang, P. Gao, L. Lei, *J. Power Sources* **2014**, *253*, 276–281; d) Y. Wang, J. Zhou, W. Lv, H. Fang, W. Wang, *Appl. Surf. Sci.* **2016**, *362*, 394–398; e) M. Alvarez-Guerra, A. Del Castillo, A. Irabien, *Chem. Eng. Res. Des.* **2014**, *92*, 692–701.

[7] a) B. Innocent, D. Pasquier, F. Ropital, F. Hahn, J. M. Léger, K. B. Kokoh, *Appl. Catal. B* **2010**, *94*, 219–224; b) F. Köleli, T. Atilan, N. Palamut, A. M. Gizir, R. Aydin, C. H. Hamann, *J. Appl. Electrochem.* **2003**, *33*, 447–450; c) C. H. Lee, M. W. Kanan, *ACS Catal.* **2015**, *5*, 465–469; d) Z. He, J. Shen, Z. Ni, J. Tang, S. Song, J. Chen, L. Zhao, *Catal. Commun.* **2015**, *72*, 38–42; e) E. Bertin, S. Garbarino, C. Roy, S. Kazemi, D. Guay, *J. CO2 Util.* **2017**, *19*, 276–283; f) M. Fan, S. Garbarino, G. A. Botton, A. C. Tavares, D. Guay, *J. Mater. Chem. A* **2017**, *5*, 20747–20756.

[8] C. E. Moore, E. L. Gyenge, *ChemSusChem* **2017**, *10*, 3512–3519.

[9] a) M. Watanabe, M. Shibata, A. Kato, M. Azuma, T. Sakata, *J. Electrochem. Soc.* **1991**, *138*, 3382–3389; b) A. Katoh, H. Uchida, M. Shibata, M. Watanabe, *J. Electrochem. Soc.* **1994**, *141*, 2054–2058; c) Y. Wang, H. Hu, Y. Sun, Y. Tang, L. Dai, Q. Hu, A. Fisher, X. J. Yang, *Adv. Mater. Interfaces* **2019**, *6*, 1801200; d) M. Morimoto, Y. Takatsuji, R. Yamasaki, H. Hashimoto, I. Nakata, T. Sakakura, T. Haruyama, *Electrocatalysis* **2018**, *9*, 323–332; e) A. Vasileff, C. Xu, L. Ge, Y. Zheng, S.-Z. Qiao, *Chem. Commun.* **2018**, *54*, 13965–13968.

[10] a) C. Gütz, M. Selt, M. Bänziger, C. Bucher, C. Römelt, N. Hecken, F. Gallou, T. R. Galvão, S. R. Waldvogel, *Chem. Eur. J.* **2015**, *21*, 13878–13882; b) C. Gütz, M. Bänziger, C. Bucher, T. R. Galvão, S. R. Waldvogel, *Org. Process Res. Dev.* **2015**, *19*, 1428–1433; c) C. Gütz, V. Grimaudo, M. Holtkamp, M. Hartmer, J. Werra, L. Frensemeier, A. Kehl, U. Karst, P. Broekmann, S. R. Waldvogel, *ChemElectroChem* **2018**, *5*, 247–252.

[11] V. Grimaudo, P. Moreno-García, A. Riedo, S. Meyer, M. Tulej, M. B. Neuland, M. Mohos, C. Gütz, S. R. Waldvogel, P. Wurz, P. Broekmann, *Anal. Chem.* **2017**, *89*, 1632–1641.

[12] A. Dutta, A. Kuzume, V. Kaliginedi, M. Rahaman, I. Sinev, M. Ahmadi, B. Roldán Cuenya, S. Vesztergom, P. Broekmann, *Nano Energy* **2018**, *53*, 828–840.

[13] K. P. Kuhl, E. R. Cave, D. N. Abram, T. F. Jaramillo, *Energy Environ. Sci.* **2012**, *5*, 7050–7059.

[14] Y. Hori, K. Kikuchi, S. Suzuki, *Chem. Lett.* **1985**, *14*, 1695–1698.

[15] A. Schizodimou, G. Kyriacou, *Electrochim. Acta* **2012**, *78*, 171–176.

Manuscript received: March 29, 2019
Accepted manuscript online: April 11, 2019

CHEMELECTROCHEM

Supporting Information

Leaded Bronze Alloy as a Catalyst for the Electroreduction of CO_2

María de Jesús Gálvez-Vázquez[+], Pavel Moreno-García[+],* Huizhang Guo, Yuhui Hou, Abhijit Dutta, Siegfried R. Waldvogel, and Peter Broekmann

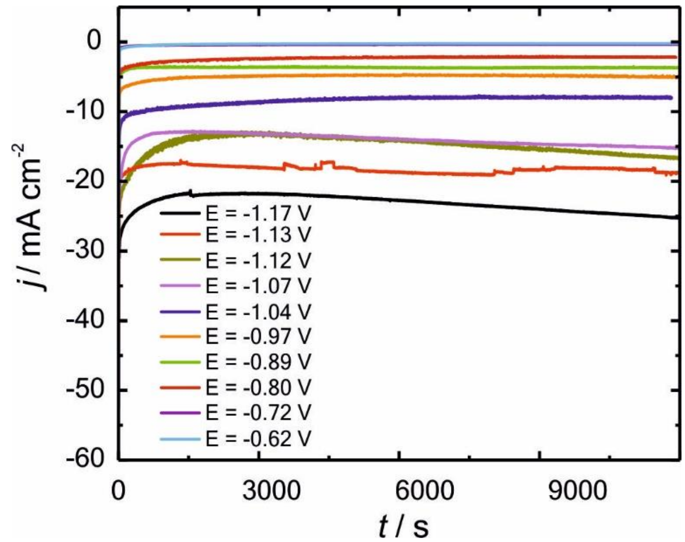

Figure S1. Sample chronoamperograms at selected applied potentials for CO_2RR in CO_2-saturated 0.1 M $KHCO_3$ electrolyte using mechanically polished CuSn7Pb15 samples.

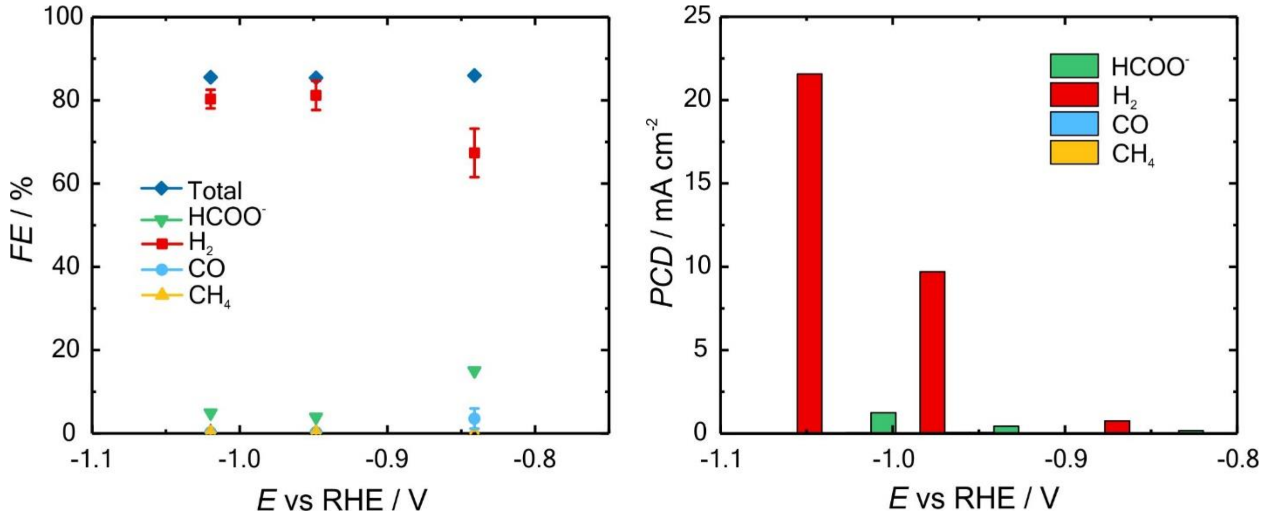

Figure S2.. a) Product distribution of CO_2RR on unpolished CuSn7Pb15 at selected applied potentials in CO_2-saturated 0.5 M $KHCO_3$ electrolyte. The error bar is the standard deviation from the measurements done to quantify the gas products every 20 min. b) Corresponding partial current densities.

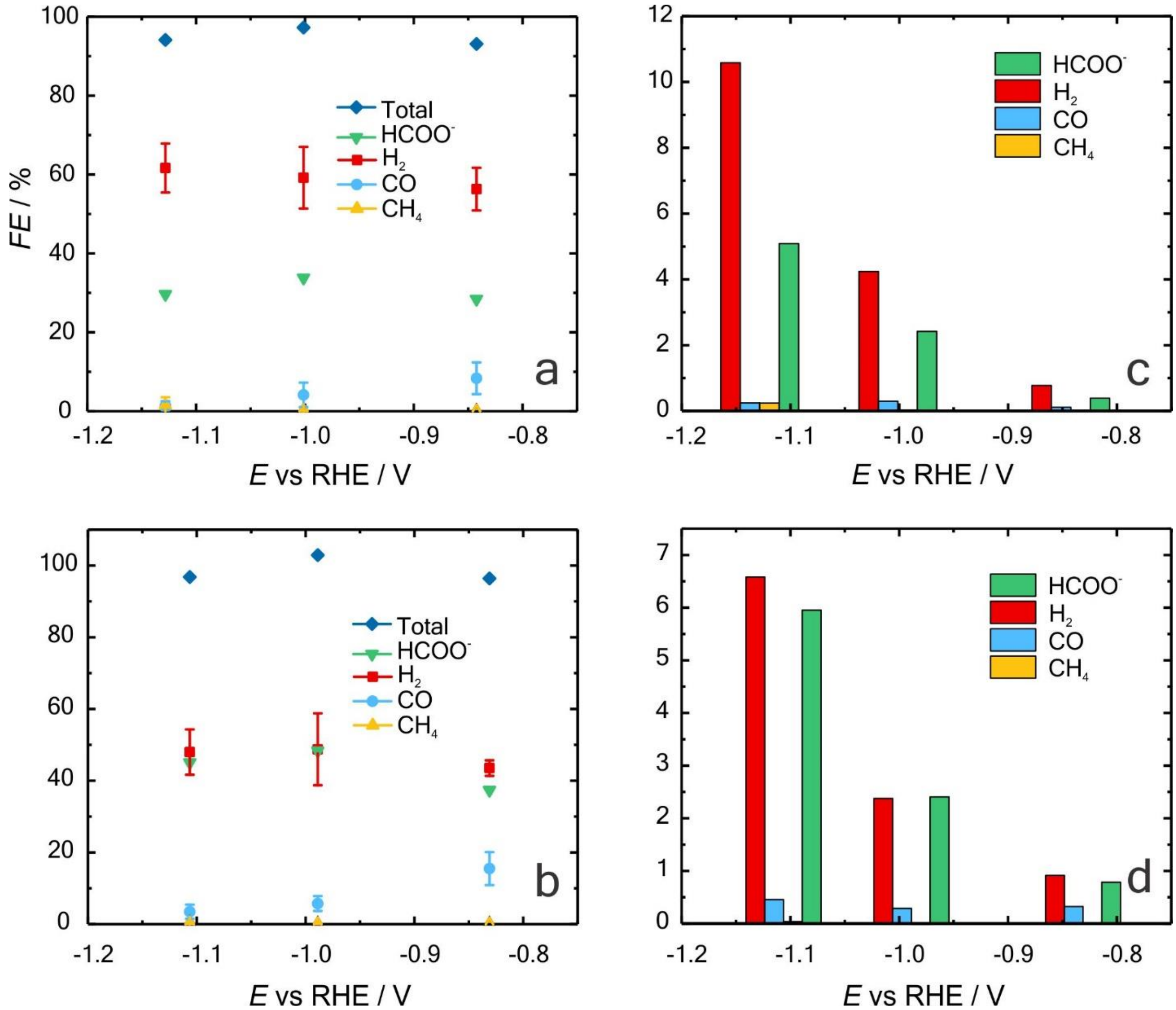

Figure S3.. a) Product distribution of CO_2RR on polished a) CuSn5Pb20 and b) CuSn10Pb10 at selected applied potentials in CO_2-saturated 0.5 M $KHCO_3$ electrolyte. The error bar is the standard deviation from the measurements done to quantify the gas products every 20 min. c) and b) Corresponding partial current densities.

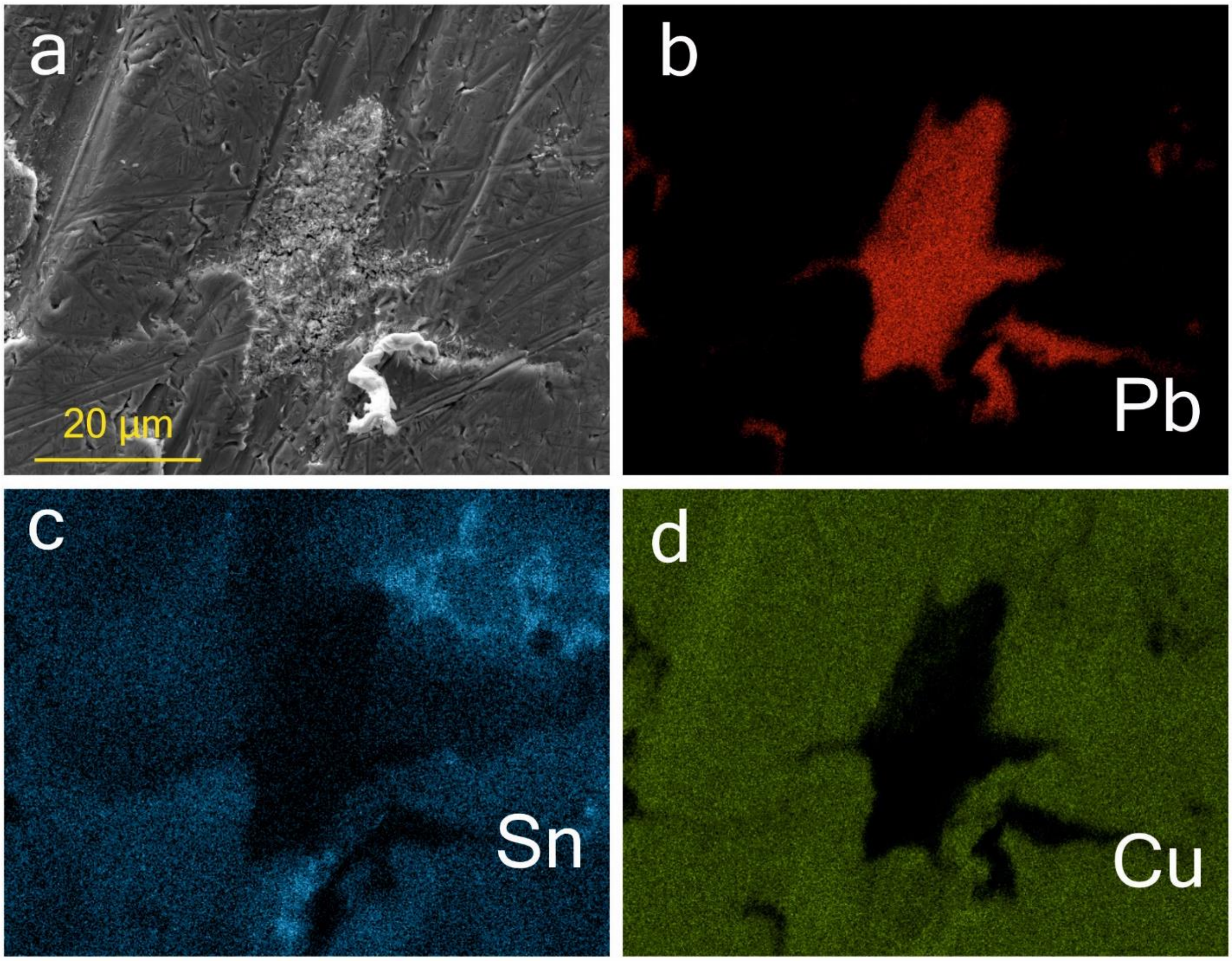

Figure S4. IL-SEM image of a polished CuSn7Pb15 sample location after 3 h electrolysis at -0.83 V in CO_2-saturated 0.5 M $KHCO_3$ electrolyte. Corresponding EDX element mappings of b) Pb, c) Sn and d) Cu signals. The SEM-EDX analysis of the same location before conduction of the CO2RR is shown in Fig. 2c-f in the main text.

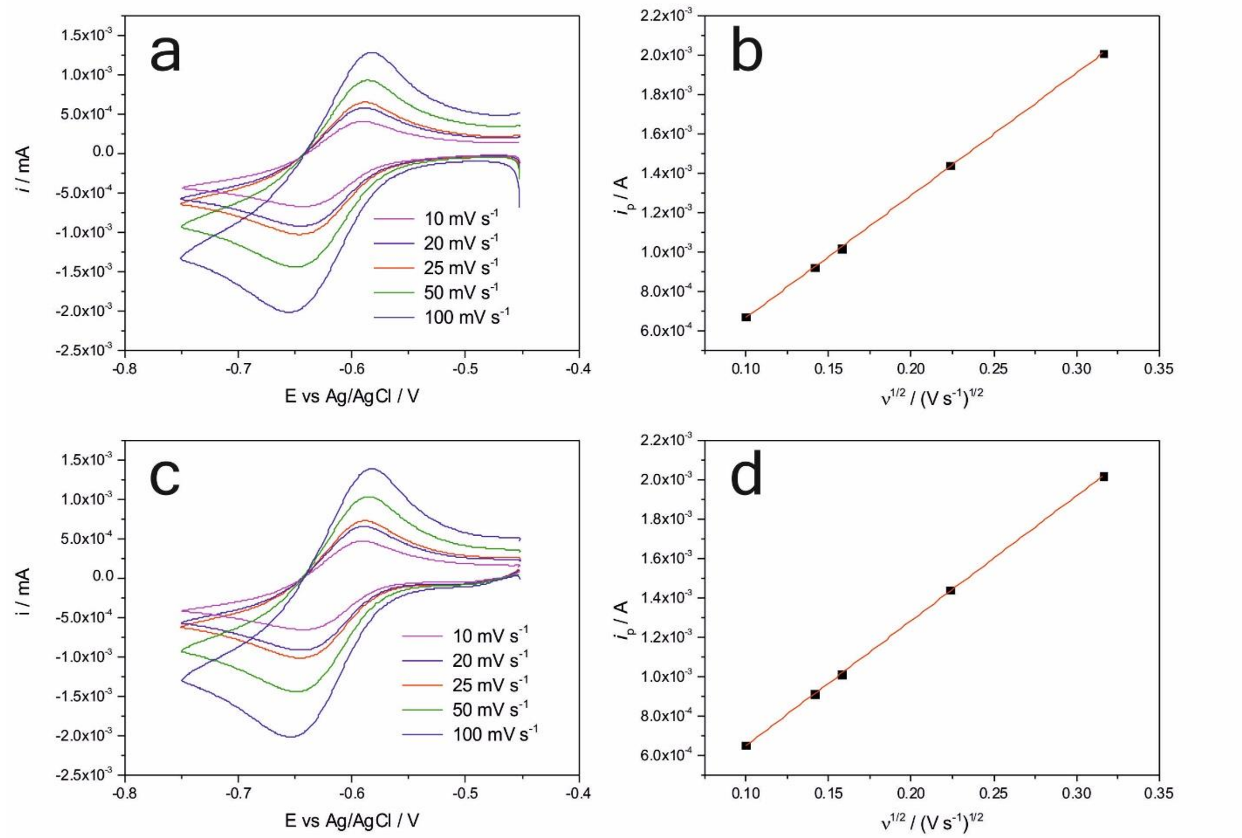

Figure S5. Cyclic voltammetry in 1 M Na_2SO_4 containing 10 mM di-methyl viologen dichloride at different potential sweep rates (ν) for a) polished and c) unpolished CuSn7Pb15 cathodes. b) and d) are the i_p (peak current) vs $\nu^{1/2}$ plots that were used to determine the electrochemically active surface areas of the polished, respectively unpolished samples. The unpolished sample exhibited a ca 2% larger ECSA than the mechanically polished sample.

1.7 Full Model for the Two-step Polarization Curves of Hydrogen Evolution, Measured on RDEs in Dilute Acid Solutions

Authors: María de Jesús Gálvez-Vázquez, Vitali Grozovski, Noémi Kovács, Peter Broekmann, and Soma Vesztergom

J. Phys. Chem. C, **124** (7), 3988–4000 (2020), DOI: 10.1021/acs.jpcc.9b11337

Highlights: An analytical model for the full polarization curves of HER on rotating disk electrodes in mildly acidic solutions was devised. It was assumed that HER proceeds according to a quasi-reversible two-electron reaction, $H^+ + H_2O + 2e^- \rightleftharpoons H_2 + OH^-$, obeying the Erdey–Grúz–Volmer–Butler equation. The model can reproduce the two-step behavior of the polarization curves and be used to fit measured currents over a broad range of pH, rotation rate, and electrode potential on both Au and Pt. A very important implication of the model is that the plateau lengths seen on RDE polarization curves are inversely related to the electrocatalytic activity. At fixed rotation rates, a linear relationship exists between the plateau length and the bulk solution pH. By analyzing this relationship, kinetic parameters k and α_c were estimated.

Contribution: I performed all the HER experiments on gold and platinum electrodes and participated in discussing the results.

THE JOURNAL OF PHYSICAL CHEMISTRY C

pubs.acs.org/JPCC Article

Full Model for the Two-Step Polarization Curves of Hydrogen Evolution, Measured on RDEs in Dilute Acid Solutions

María de Jesús Gálvez-Vázquez, Vitali Grozovski, Noémi Kovács, Peter Broekmann,* and Soma Vesztergom*

Cite This: J. Phys. Chem. C 2020, 124, 3988−4000 Read Online

ACCESS | Metrics & More | Article Recommendations

ABSTRACT: Polarization curves of the hydrogen evolution reaction (HER), recorded on rotating disk electrodes (RDEs) in mildly acidic solutions, usually show a "two step" behavior. That is, two exponentially rising segments (the first commonly assigned to H^+, the second to water reduction) are separated by a limiting current plateau. Here, we devise an analytical model for the full polarization curve by assuming that HER proceeds according to a quasireversible two-electron reaction, $H^+ + H_2O + 2e^- \rightleftharpoons H_2 + OH^-$, obeying the Erdey-Grúz−Volmer−Butler equation. Our model is able to reproduce the two step behavior of polarization curves and can also be used for the fitting of measured currents over a broad range of pH, rotation rate, and electrode potential, on both Au and on Pt. We show that the length of the limiting current plateaus measured on RDEs for HER is inversely related to the electrocatalytic activity of the electrode and that at a given rotation rate a linear relationship exists between the plateau length and the bulk solution pH. By analyzing this relationship, we can estimate kinetic parameters, even in cases where the transport performance of the RDE would otherwise not be sufficient to measure well-defined kinetic currents at low overpotentials.

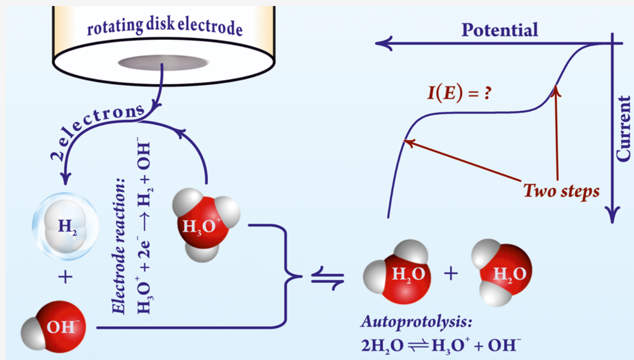

■ INTRODUCTION

The electrochemical hydrogen evolution reaction (HER) is regarded as a straightforward way of transferring electrical energy to a chemical one, enabling the storage of electricity gained from renewable sources like hydro and solar plants.[1] The development of efficient catalysts for HER has thus become a subject of intensive research. Hydrogen evolution gains, however, further importance, as HER is an almost inevitable side reaction of cathodic electrode processes occurring in aqueous environments. For example, in the electroreduction of CO_2[2,3] or the deposition of base metals,[4−6] HER often appears as a parasitic reaction.

It is usually claimed[7] that in acidic solutions the overall hydrogen evolution reaction can be described as

$$H^+ + e^- \rightarrow \frac{1}{2}H_2 \qquad \text{(R1)}$$

while in neutral or alkaline media the reaction is written as

$$H_2O + e^- \rightarrow \frac{1}{2}H_2 + OH^- \qquad \text{(R2)}$$

The exact mechanism of the above reactions, including the identification of the rate-determining step and the pH dependency, is still a matter of debate. While according to Reaction R2, HER can also occur, at a moderate rate, in solutions that are neutral or even alkaline, when hydrogen production is the primary goal of the electrode process, usually acidic conditions are applied.

Under acidic conditions, Reaction R1 is known to proceed quickly on certain transition metals (e.g., on platinum[8−14]) and less quickly on others (e.g., on gold[15−20]). The catalytic performance of these metals can be explained by Sabatier's principle;[21] that is, the catalytic rate follows a volcano trend with the binding energy of the metal and hydrogen.

To obtain meaningful kinetics in acidic solutions, it is essential to compensate for the effect of mass transport, as it can have a decisive role in the observed current/overpotential characteristics, especially for kinetically facile reactions.[21] It is usually assumed[11,20] that experimentally measured currents for HER can be described, at least at certain overpotential intervals, by the Erdey-Grúz−Volmer−Butler equation:

Received: December 6, 2019
Revised: January 17, 2020
Published: January 18, 2020

$$j = j_0\left[-\exp\left(-\frac{\alpha_c F\eta}{RT}\right) + \exp\left(\frac{(1-\alpha_c)F\eta}{RT}\right)\right] \tag{1}$$

While current/potential curves recorded at high transport rates on a gold rotating disk electrode (RDE) can be made subject to analysis based on eq 1,[20] on more facile catalysts like Pt, no kinetic currents can be determined due to the presence of severe diffusion hindrance even at vigorous stirring. As noted by Zheng et al.[14] and by the group of Gasteiger,[12,13] on a Pt surface, the rate of charge transfer becomes so fast (with respect to that of mass transfer) that essentially a thermodynamic equilibrium is established.

The pH dependency of the rate of HER is often related to a reactant switching from H^+ to water molecule (from Reaction R1 to R2).[21−27] This reactant switching can be observed, for example, on the polarization curves of HER recorded at rotating disk electrodes[28] immersed into mildly acidic solutions, exhibiting a “two step” behavior, as shown by Figure 1.

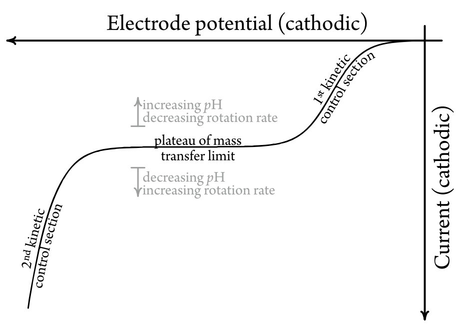

Figure 1. Polarization curve of an RDE, showing two hydrogen evolution steps with an intermittent limiting current plateau section.

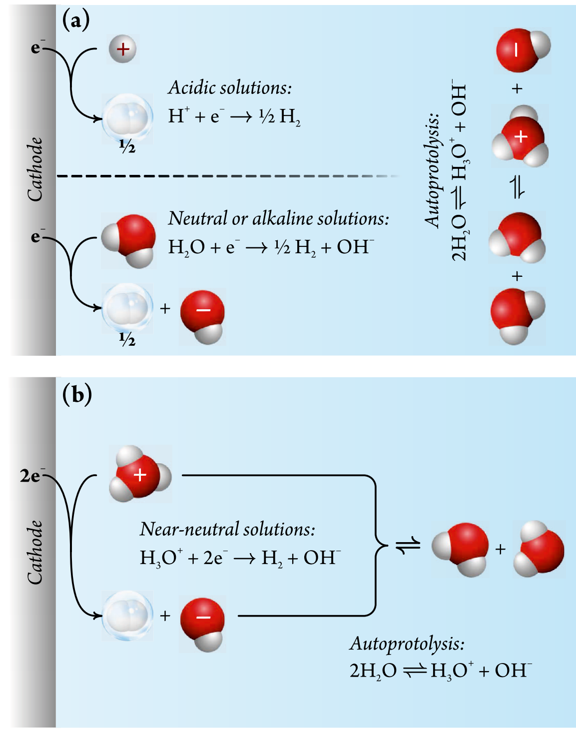

Figure 2. Reaction schemes for HER. Two separate reactions are shown in (a) for acidic and neutral to alkaline solutions. A combined scheme is shown in (b) for near-neutral solutions. The autoprotolysis of water is part of both schemes.

Figure 1 demonstrates that in mildly acidic conditions HER is kinetically controlled at low cathodic overpotentials, yielding cathodic currents that rise exponentially with the applied cathodic overpotential (“first kinetic control section”). At higher cathodic overpotentials, the mass transport of H^+ becomes rate determining and a limiting current plateau is attained. Cathodic currents higher than the limiting current of H^+ reduction can only be achieved by applying extremely negative potentials (see the “second kinetic control section” in Figure 1). At such potentials, it is usually assumed that apart from H^+ reduction (Reaction R1), also the reduction of water molecules (Reaction R2) contributes to HER; thus, a further exponential increase of the cathodic current can be seen, following the limiting plateau section.

The described two step behavior of HER polarization curves was first noticed as early as 1956 by Nagel and Wendler[29] and it was studied more recently by the groups of Tobias,[22] Mayrhofer,[23,24] Bruckenstein,[30] Arenz,[31] Pereira,[32] and the present authors.[27] Finding an adequate model to describe the shape of the two step polarization curves is, however, difficult due to complications arising from an interplay of the mass transport of the diffusing species (H^+ and OH^-) and a bulk chemical reaction, the autoprotolysis of water:

$$H_2O \rightleftharpoons H^+ + OH^- \tag{R3}$$

To write proper kinetic equations for HER, Reactions R1−R3 all have to be taken into account, in a scheme suggested by Figure 2a. This was attempted before by Hessami and Tobias,[22] who used the equidiffusivity approximation (i.e., the assumption that the diffusion coefficients of H^+ and OH^- ions are equal in the solution) to solve combined reaction−diffusion−convection equations to obtain pH profiles. The approach of Mayrhofer et al.[23,24] was based on a different, finite diffusion layer-based approximation, where the diffusion layer thickness was determined by a weighted average of the two diffusion coefficients. None of these two methods were concerned, however, about the kinetics of HER. In the work of Hessami and Tobias,[22] the pH profiles were parametrized by the current of HER (and no potential dependence of this current was analyzed), while in the works of Mayrhofer et al.,[23,24] the approximation of full reversibility was used (that is, the authors assumed that the near-surface pH depends linearly on the applied potential, as dictated by Nernst’s equation).

In a recent work of our group,[27] we attempted to model HER by taking into account two strictly irreversible reactions, the reduction of H^+ and that of water molecules, both following Erdey-Grúz−Volmer−Butler kinetics. In ref 27, we developed a digital simulation-based modeling approach to HER and we presented an approximative analytical model that could well describe polarization curves at various values of pH and rotation rates. In this model, we used an assumption that the diffusivity of OH^- ions exceeds that of H^+ and that thus at high current densities the near-surface solution layer does not turn alkaline but neutral instead. The resulting model could be used to describe HER polarization curves measured on nickel electrodes.

The model described in ref 27 followed the reaction scheme shown in Figure 2a and it thus contained altogether four variable (fittable) kinetic parameters: two reaction rate and two charge-transfer coefficients, each describing the reduction of

H^+ and that of H_2O molecules, respectively. We noticed, however, a strong correlation between the fitted parameters, which suggested that the reduction of this model would still be possible.

In this present paper, we aim to develop an analytical model that can well describe the polarization curves of HER, recorded on rotating disk electrodes immersed into mildly acidic solutions, by taking into consideration a quasireversible charge-transfer reaction, which represents the combination or Reactions R1 and R2 and that contains an inherent coupling, as a result of autoprotolysis, Reaction R3, between the concentrations of H^+ and OH^- ions. From a mathematical point of view, this model, represented by Figure 2b, is simpler than the one previously described,[27] as it contains only two variable kinetic parameters (a single reaction rate and a single charge-transfer coefficient).

In what follows, we will give a brief description of the model and then present how it can be used for the estimation of kinetic parameters of HER on two chosen model electrodes (gold and platinum). We will demonstrate that the different lengths of the limiting current plateaus observed on these metals can be used as a direct measure of electrocatalytic hindrance.

■ THEORY

Thermodynamic Considerations. Although Reactions R1 and R2 (the formation of H_2 either by the reduction of H^+ ions or by that of water molecules) are seemingly different, from a thermodynamic point of view, both processes lead to the same equilibrium conditions. The standard potentials are $E^{\ominus}_{R1} = 0$ V and $E^{\ominus}_{R2} = -0.8277$ V vs standard hydrogen electrode (SHE)[33] and assuming equilibrium conditions, we can use Nernst's equation to relate the potentials of electrode Reactions R1 and RRR2 to the a_{H^+} and a_{OH^-} activities of H^+ and OH^- ions, respectively, as well as to the Φ_{H_2} fugacity of hydrogen gas:

$$E_{R1} = E^{\ominus}_{R1} - \frac{RT}{F}\ln\left(\frac{\Phi_{H_2}^{1/2}}{a_{H^+}}\right) \tag{2}$$

and

$$E_{R2} = E^{\ominus}_{R2} - \frac{RT}{F}\ln(\Phi_{H_2}^{1/2}a_{OH^-}) \tag{3}$$

while from the equilibrium condition $E_{R1} = E_{R2}$ it follows that

$$E^{\ominus}_{R2} - E^{\ominus}_{R1} = \frac{RT}{F}\ln(a_{H^+}a_{OH^-}) \tag{4}$$

Assuming that the autoprotolysis of water, Reaction R3, exactly determines the product of H^+ and OH^- activities as the ionic product of water K_w, we get to $K_w = 1.019 \times 10^{-14}$ using the standard potential values mentioned before. It can thus be seen that Reactions R1–R3 are not independent from each other and they all have to be considered when describing the thermodynamics of hydrogen evolution. Somewhat contradicting this statement, in the formal kinetic treatment of HER, it is still common to treat Reactions R1 and R2 as separate processes, each valid in its respective pH regime. In what follows, we aim to develop a kinetic treatment that can describe hydrogen evolution on an electrode surface near which the pH shifts, depending on the applied electrode potential, from acidic to alkaline values.

Kinetic Considerations. As a first step, we have to write kinetic rate equations for HER that take both H^+ and OH^- ions into account. Probably the most straightforward possibility of doing this is to sum Reactions R1 and R2, in a manner illustrated by Figure 2b, to get

$$H^+ + H_2O + 2e^- \underset{j_a}{\overset{j_c}{\rightleftharpoons}} H_2 + OH^- \tag{R4}$$

Reaction R4 contains the H^+ (or the H_3O^+) ion as a reactant and the OH^- ion as a product. Assuming that the reaction can proceed in both directions, the current density j yielded by the reaction can be expressed as a sum of cathodic (j_c) and anodic (j_a) terms:

$$j = j_c + j_a \tag{5}$$

Assuming that Reaction R4 follows the Erdey-Grúz–Volmer–Butler equation, the cathodic and anodic current densities may be formally expressed as

$$j_c = -2Fk'c^0_{H_2O}c^0_{H^+}\exp\left[-\frac{\alpha_c F}{RT}(E - E°)\right] \tag{6a}$$

and

$$j_a = 2Fk'c^0_{H_2}c^0_{OH^-}\exp\left[\frac{\alpha_a F}{RT}(E - E°)\right] \tag{6b}$$

In eqs 6a and 6b, α_c and α_a are charge-transfer coefficients, k' is a reaction rate coefficient, and the c^0 terms stand for near-surface concentrations. The eqs 6a, 6b can be simplified by utilizing the usual assumption that $\alpha_a + \alpha_c = n = 2$ (the number of electrons involved in Reaction R4).[34] Further assuming that the near-surface concentrations of water and of H_2 molecules can be treated as unit constants—the latter, at least, in a solution saturated with H_2, assuming that the dissolved H_2 concentration shows no significant pH dependence—we can introduce another reaction rate coefficient k in place of k' as

$$k = k'c^0_{H_2O} = k'c^0_{H_2} \tag{7}$$

This turns eqs 6a and 6b into

$$j_c = -2Fkc^0_{H^+}\exp\left[-\frac{\alpha_c F}{RT}(E - E°)\right] \tag{8a}$$

and

$$j_a = 2Fkc^0_{OH^-}\exp\left[\frac{(2-\alpha_c)F}{RT}(E - E°)\right] \tag{8b}$$

In eqs 6a, 6b, 8a, and 8b, $E°$ denotes a potential value where no net current flows in the case when $c^0_{H^+} = c^0_{OH^-}$. $E°$ can thus be expressed as

$$E° = E^{\ominus}_{R1} + \frac{RT}{2F}\ln K_w \tag{9}$$

using Nernst's equation (where we again assumed a unity fugacity of H_2).

Provided that the activity coefficients of H^+ and OH^- ions can both be considered unity and that the autoprotolysis Reaction R3 is fast enough so that it always maintains the equilibrium constraint that

$$c_{H^+}c_{OH^-} = K_w c^{\ominus 2} \tag{10}$$

https://dx.doi.org/10.1021/acs.jpcc.9b11337
J. Phys. Chem. C 2020, 124, 3988–4000

Table 1. Description of Symbols Used

symbol	meaning	formula or typical value(s)
basic physicochemical parameters		
pH^∞	pH of the bulk of the solution	3
f	rotation rate of the RDE	625 min^{-1}
k	reaction rate coefficient for Reaction R4	1 $\mu\mathrm{m\ s}^{-1}$
α_c	charge-transfer coefficient for Reaction R4	1
T	temperature	298.15 K
$\mathcal{D}$	diffusion coefficient of H^+ and OH^- ions, considered equal	$10^{-4}\ \mathrm{cm^2\ s^{-1}}$
ν	kinematic viscosity of the solution	$8.917 \times 10^{-7}\ \mathrm{m^2\ s^{-1}}$
constants		
F	Faraday's constant	96 485.3 C mol^{-1}
R	Regnault's constant	8.314 J $\mathrm{mol}^{-1}\ \mathrm{K}^{-1}$
$c^\ominus$	standard concentration	1 mol dm^{-3}
a	Kármán's constant[28]	0.51023
$\Gamma(1/3)$	see eq 20	2.67894
$E^\ominus_\mathrm{R1}$	standard potential of Reaction R1	0 V vs SHE
$E^\ominus_\mathrm{R2}$	standard potential of Reaction R2	−0.8277 V vs SHE
K_w	autoprotolysis constant of water	1.019×10^{-14}
derived quantities		
$c^\infty_{\mathrm{H}^+}$	H^+ concentration in the bulk of the solution	$10^{-\mathrm{pH}}c^\ominus$
Δc^∞	difference of H^+ and OH^- concentrations in the bulk	$c^\infty_{\mathrm{H}^+} - \frac{K_\mathrm{w}{c^\ominus}^2}{c^\infty_{\mathrm{H}^+}} \approx c^\infty_{\mathrm{H}^+}$
ω	angular frequency of rotation	$2\pi f$
δ_N	generalized Nernstian diffusion layer thickness, see eq 19	$\frac{\nu^{1/6}\Gamma\left(\frac{1}{3}\right)\mathcal{D}^{1/3}}{3^{2/3}a^{1/3}\omega^{1/2}}$
$\theta(\alpha)$	combined kinetic parameter, see eq 22	$2K_\mathrm{w}^{1/2}\left[1 + 2k\frac{\delta_\mathrm{N}}{\mathcal{D}}K_\mathrm{w}^{-\alpha/2}\exp\left(\frac{FE}{RT}\alpha\right)\right]$
$c^0_{\mathrm{H}^+}$	near-surface H^+ concentration, see eq 21	$c^\ominus K_\mathrm{w}^{1/2}\left[\frac{\left(\frac{\Delta c^\infty}{c^\ominus}\right) + \sqrt{\left(\frac{\Delta c^\infty}{c^\ominus}\right)^2 + \theta(-\alpha_\mathrm{c})\theta(2-\alpha_\mathrm{c})}}{\theta(-\alpha_\mathrm{c})}\right]$
j	current density of the RDE, see eq 23	$F\frac{\mathcal{D}}{\delta_\mathrm{N}}\left[c^0_{\mathrm{H}^+} - \frac{{c^\ominus}^2K_\mathrm{w}}{c^0_{\mathrm{H}^+}} - \Delta c^\infty\right]$
$j_{\mathrm{cat,H}^+}$	catalytic current density of H^+ reduction, see eq 24	$-2Fc^\infty_{\mathrm{H}^+}kK_\mathrm{w}^{\alpha_\mathrm{c}/2}\exp\left(-\frac{\alpha_\mathrm{c}FE}{RT}\right)$
j_0	exchange current density, see eq 25	$-2Fc^\infty_{\mathrm{H}^+}kK_\mathrm{w}^{\alpha_\mathrm{c}/2}\left(\frac{c^\ominus}{c^\infty_{\mathrm{H}^+}}\right)^{\alpha_\mathrm{c}}$
j_lim	limiting current density, see eq 26	$-F\frac{\mathcal{D}}{\delta_\mathrm{N}}\Delta c^\infty$
$j_{\mathrm{cat,H_2O}}$	catalytic current density of water splitting, see eq 29	$-Fc^\ominus\sqrt{\frac{2\mathcal{D}kK_\mathrm{w}^{\alpha_\mathrm{c}/2+1}}{\delta_\mathrm{N}}}\exp\left(-\frac{\alpha_\mathrm{c}FE}{2RT}\right)$
j_rev	Nernstian (reversible) current density, see eq 31	$-F\frac{\mathcal{D}}{\delta_\mathrm{N}}\left\{\Delta c^\infty - c^\ominus\left[\exp\left(\frac{FE}{RT}\right) - K_\mathrm{w}\exp\left(-\frac{FE}{RT}\right)\right]\right\}$

independent of space and of time, eqs 8a, 8b can further be simplified to the following form:

$$j_\mathrm{c} = -2FkK_\mathrm{w}^{\alpha_\mathrm{c}/2}\exp\left(-\frac{\alpha_\mathrm{c}FE}{RT}\right)c^0_{\mathrm{H}^+} \tag{11a}$$

and

$$j_\mathrm{a} = 2FkK_\mathrm{w}^{\alpha_\mathrm{c}/2}{c^\ominus}^2\exp\left(\frac{(2-\alpha_\mathrm{c})FE}{RT}\right)\frac{1}{c^0_{\mathrm{H}^+}} \tag{11b}$$

where $c^\ominus = 1$ mol dm^{-3} is the standard concentration.

Note that to get from eqs 6a and 6b to eqs 11a and 11b, we made use of eq 9, where, by definition, $E^\ominus_\mathrm{R1} = 0$ V vs SHE. Thus, the electrode potential E, appearing in equation set 11a, 11b, is also to be referenced to SHE.

Equations 11a and 11b determine the current of the electrode reaction provided that the near-surface concentration of hydrogen ions, $c^0_{\mathrm{H}^+}$, is known. On rotating disk electrodes (RDEs), stationary currents can be measured for HER and deriving a mathematical expression for $c^0_{\mathrm{H}^+}$ becomes possible as described below.

Problem of Transport. Provided that (i) mass transfer occurs only by means of diffusion and convection and other means of transport (e.g., migration) can be ignored and (ii) that the diffusion coefficients D_{H^+} and D_{OH^-} are constants, independent of the concentrations and of spatial coordinates, the condition of stationarity can be expressed in the form of the following equation:

$$D_{\mathrm{H}^+}\frac{\mathrm{d}^2c_{\mathrm{H}^+}}{\mathrm{d}z^2} - D_{\mathrm{OH}^-}\frac{\mathrm{d}^2c_{\mathrm{OH}^-}}{\mathrm{d}z^2} - v_z\left(\frac{\mathrm{d}c_{\mathrm{H}^+}}{\mathrm{d}z} - \frac{\mathrm{d}c_{\mathrm{OH}^-}}{\mathrm{d}z}\right) = 0 \tag{12}$$

Here, v_z denotes the axial (z direction) component of the stationary fluid flow under the RDE that can be approximated[35] as

https://dx.doi.org/10.1021/acs.jpcc.9b11337
J. Phys. Chem. C 2020, 124, 3988−4000

$$v_z = -az^2\sqrt{\frac{\omega^3}{\nu}} \tag{13}$$

where $a \approx 0.51023$,[28] ω denotes the angular velocity of rotation, and ν the kinematic viscosity of the solution.

If we now express the concentration of OH^- ions from eq 10 as $c_{OH^-} = \frac{K_w c^{\ominus 2}}{c_{H^+}}$ and plug this into eq 12, we arrive to a nonlinear ordinary differential equation, describing stationary H^+ concentration profiles under the RDE. This equation has no analytical solution; assuming, however, that the diffusion coefficients of H^+ and OH^- ions are equal—and this assumption is not uncommon—[22]the differential equation can be linearized in the form:

$$\mathcal{D}\frac{d^2}{dz^2}\Delta c(z) + az^2\sqrt{\frac{\omega^3}{\nu}}\frac{d}{dz}\Delta c(z) = 0 \tag{14}$$

where $\mathcal{D} = D_{H^+} = D_{OH^-}$ is the diffusion coefficient of H^+ and OH^- ions (assumed to be equal) and the function

$$\Delta c(z) = c_{H^+}(z) - c_{OH^-}(z) = c_{H^+}(z) - \frac{K_w c^{\ominus 2}}{c_{H^+}(z)} \tag{15}$$

was introduced to describe the difference of H^+ and OH^- concentrations as a function of the z distance measured from the electrode surface. Equation 14 is a linear, second-order ordinary differential equation with a known solution:

$$\Delta c(z) = \Delta c^\infty + (\Delta c^0 - \Delta c^\infty)Q_{1/3}\left(\frac{az^3\omega^{3/2}}{3\mathcal{D}\nu^{1/2}}\right) \tag{16}$$

In eq 16, Δc^0 and Δc^∞ denote near-surface ($z = 0$) and bulk ($z \to \infty$) concentration differences (see eq 15) and $Q_s(x)$ is the regularized incomplete gamma function[36] (with $s = 1/3$) defined as

$$Q_s(x) = \frac{\int_x^\infty u^{s-1}\exp(-u)du}{\int_0^\infty u^{s-1}\exp(-u)du} \tag{17}$$

From eq 16, the current density can be expressed as

$$j = -F\mathcal{D}\lim_{z\to 0}\frac{d\Delta c(z)}{dz} = F\frac{\mathcal{D}}{\delta_N}(\Delta c^0 - \Delta c^\infty) \tag{18}$$

where

$$\delta_N = \frac{\nu^{1/6}\Gamma\left(\frac{1}{3}\right)\mathcal{D}^{1/3}}{3^{2/3}a^{1/3}\omega^{1/2}} \tag{19}$$

is the generalized Nernstian diffusion layer thickness that contains the gamma function[36] defined by the integral

$$\Gamma(x) = \int_0^\infty u^{x-1}\exp(-u)du \tag{20}$$

Modeling the Polarization Curve of an RDE. The current density expressed by eq 18 is equal to that given in eq 5, with the partial current densities defined by eqs 11a and 11b. This yields the following expression for $c^0_{H^+}$:

$$c^0_{H^+} = c^\ominus K_w^{1/2}\left[\frac{\left(\frac{\Delta c^\infty}{c^\ominus}\right) + \sqrt{\left(\frac{\Delta c^\infty}{c^\ominus}\right)^2 + \theta(-\alpha_c)\theta(2-\alpha_c)}}{\theta(-\alpha_c)}\right] \tag{21}$$

where the $\theta(\alpha)$ function (a dimensionless, potential dependent, combined kinetic parameter) is defined as

$$\theta(\alpha) = 2K_w^{1/2}\left[1 + 2k\frac{\delta_N}{\mathcal{D}}K_w^{-\alpha/2}\exp\left(\frac{FE}{RT}\alpha\right)\right] \tag{22}$$

Finally, the equation of a polarization curve recorded on an RDE can be expressed by combining eqs 18 and 21 to

$$j = F\frac{\mathcal{D}}{\delta_N}\left[c^0_{H^+} - \frac{c^{\ominus 2}K_w}{c^0_{H^+}} - \Delta c^\infty\right] \tag{23}$$

Equation 23 is the final result of this theoretical treatment. It is an analytical formula for the current density of an RDE on which hydrogen is evolved at a given pH, rotation rate (f), and electrode potential (E). The parameters of this model are listed in Table 1, where it can be seen that the model relies only on two kinetic parameters, the k reaction rate coefficient and the α_c charge-transfer coefficient of Reaction R4. Note that the presented model is very robust, as it considers only the effect of charge transfer, that of mass transport occurring by diffusion and convection, and the effect of the autoprotolysis. Although no mechanistic details (such as those of H adsorption to the surface) are considered, we will see that this robust model delivers well when used for the fitting of experimentally obtained data.

■ EXPERIMENTAL

The rotating disk electrodes used in this study were obtained from Metrohm (Herisau, Switzerland). The diameter of the disk electrodes was (3.00 ± 0.05) mm, embedded into a PEEK shaft of 10 mm outer diameter. The geometric surface area was used for calculating current densities. Prior to the experiments, the electrodes were dipped, for a few moments, into Caro's acid and were then rinsed abundantly with ultrapure water (Milli-Q by Merck Millipore, R = 18.2 MΩ cm, used for the preparation of solutions as well).

The studied solutions of different pH were prepared by diluting calculated amounts of a 0.1 mol dm^{-3} $HClO_4$ (70%, Merck, Suprapure) stock solution and solid $NaClO_4$ (99.99%, trace metals basis, Merck) with ultrapure water, by keeping the ionic strength at a fixed value of 0.1 mol dm^{-3}. The pH of the solutions was measured by a calibrated Metrohm 914 pH meter.

A lab-made three-electrode glass cell was used for the experiments. For measurements on Au, a large Au foil was used as a counter electrode, while for measurements on Pt, we applied a large surface area Pt foil. All measurements were carried out by using a $Hg|Hg_2SO_4|K_2SO_4$ (sat) reference electrode (Radiometer Analytical XR200, connected to the main chamber through a Luggin capillary). Electrode potentials in the paper are reported with reference to the standard hydrogen electrode (SHE); for the potential shift, the value of E_{Hg/Hg_2SO_4} = 650 mV was used.

Prior to measurements, the solution in the cell was deaerated with a pure Ar (5N, Alphagaz) flow for 15 min and saturated by hydrogen (5N, Alphagaz). The electrodes were submerged

https://dx.doi.org/10.1021/acs.jpcc.9b11337
J. Phys. Chem. C 2020, 124, 3988−4000

to the electrolyte solution without potential control, and the equilibrium potential E^{eq} was determined by measuring the open-circuit potential. Polarization curves presented in the paper were recorded point by point by steady-state current measurements at given electrode potentials and rotation rates, according to the following sequence (see Figure 3): the

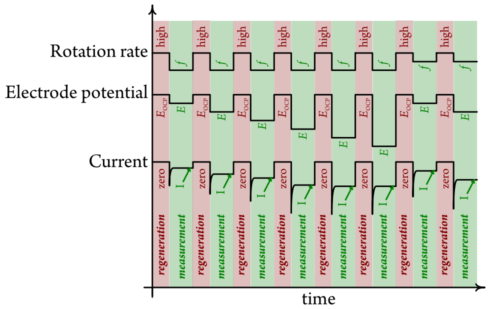

Figure 3. Experimental protocol for the measurement of HER polarization curves on RDEs. The stationary current of the RDE is measured at given electrode potential (E) and rotation rate (f) values (green periods). Between the measurements, the potential control is switched off and the RDE rotated quickly, to remove accumulated bubbles (red periods).

electrode potential and the rotation rate were set, and the current was measured until it reached a stationary value. Then, the potential was set back to E^{eq} and a rotation rate of $f = 4500$ min^{-1} was applied for some seconds to remove any accumulated H_2 from the surface. The current measurement was then repeated with other potential and rotation rate settings. The measured data were IR-corrected postexperimentally—the solution resistance was determined by means of high-frequency impedance measurements. During all measurements, the solutions were kept saturated with H_2 by continuous but slow purging (that did not interfere with the hydrodynamics of rotation).

The measurements were automated by using an Autolab PGSTAT128N potentiostat in connection with a Metrohm Autolab rotator unit and by the application of the Nova v2.1 software.

RESULTS

Experimentally obtained polarization curves are shown in Figure 4 for both the gold and the platinum RDE. These curves were recorded in mildly acidic solutions ($2.0 \lesssim \text{pH} \lesssim 3.6$) and at different rotation rates ($400 < f < 2500$). As shown by the figures, the measured polarization curves can well be fitted using eq 23. Note that during the fitting we varied only three parameters ($\mathcal{D}$, k, and α_c), while the other parameters were fixed at values listed in Table 1. Also note that the optimization was carried out by considering all data points shown either for gold or for platinum Figure 4 and not in a curve-by-curve manner. Even under such strict conditions, the calculated values (shown by the green curves) match reasonably well the measured ones (shown by the red dots).

Optimized values of α_c, k, and $\mathcal{D}$ are given in the caption of Figure 4 for Au and Pt. As can be seen, the optimized $\mathcal{D}$ values match well with the diffusion coefficient of H^+ ion known from the literature.[31] The determined values of α_c are also in good agreement with those found in the literature[37] and, as we will show later, the determined k and α values can be recombined to exchange current densities in the expected range for both gold[38] and platinum.[11]

A notable difference between the polarization curves of gold and platinum, as can be seen in Figure 4, is in the length of their limiting current plateaus, which is substantially shorter in the case of Pt. This, as we will see below, can be explained by the reaction rate coefficient k on platinum being 5 orders of magnitude higher compared with gold, and by that the determined α_c values for the two metals also differ.

DISCUSSION

General Behavior of the Model; Polarization Curve Segments. As could be seen in Figure 4, the model function given by eq 23 can describe well the two step behavior of HER polarization curves. For the parameter values listed in Table 1, a calculated polarization curve is shown in Figure 5 (thick gray curve).

First of all, it can be seen that the modeled polarization curves clearly exhibit three distinct parts: (i) a starting exponential rise, assigned to the charge-transfer-controlled reduction of H^+ ions denoted by j_{cat,H^+} and plotted by a dashed red curve in Figure 5; (ii) an almost horizontal plateau section (j_{lim}), shown by a dashed black line, where the current is limited by the rate of transport of H^+; and, finally, (iii) another exponential rise that we may assign to a charge-transfer-controlled reduction of H_2O, denoted by j_{cat,H_2O} and is shown by the green dashed curve in Figure 5.

The model is able to describe a smooth transition between the aforementioned limiting cases. Formulae for the current density for each limiting case can be derived as follows.

Catalytic Current of H^+ Reduction, j_{cat,H^+}. In this limiting case, the current is controlled by the catalytic reduction of (i.e., charge transfer to) H^+ ions. If the cathodic potential is far enough from the equilibrium potential E^{eq} (where the rate of the opposite reaction, hydrogen oxidation, is negligible) but still not very negative (so that the transport of H^+ ions still does not become rate limiting), current can be determined by assuming that $\omega \to \infty$ and that $\exp\left[\frac{FE}{RT}(2 - \alpha_c)\right] \approx 0$. This turns eq 23 into

$$j_{\text{cat},H^+} = -2Fc_{H^+}^{\infty}\, kK_w^{\alpha_c/2} \exp\left(-\frac{\alpha_c FE}{RT}\right) \tag{24}$$

The current density calculated from eq 24 is plotted by the red dashed curve in Figure 5. As shown by the Tafel representation in Figure 5b, this section of the polarization curve is characterized by a Tafel slope of $\sim\frac{59\ \text{mV}}{\alpha_c}$. Equation 24 is also useful for expressing the exchange current density j_0 by evaluation at $E = E^{eq} = \frac{RT}{F}\ln\left(\frac{c_{H^+}^{\infty}}{c^{\ominus}}\right)$

$$j_0 = -2Fc_{H^+}^{\infty}\, kK_w^{\alpha_c/2}\left(\frac{c^{\ominus}}{c_{H^+}^{\infty}}\right)^{\alpha_c} \tag{25}$$

The variation of exchange current densities on pH is shown for gold and platinum in Figure 6. These data agree well with values found in the literature.[11,38]

Limiting Current of H^+ Reduction, j_{lim}. In this limiting case, shown by the black dashed line in Figure 5, the current density is governed solely by the transport of H^+ ions from the bulk of the solution to the electrode surface. A formula for the limiting current j_l can be provided within the framework of the

https://dx.doi.org/10.1021/acs.jpcc.9b11337
J. Phys. Chem. C 2020, 124, 3988−4000

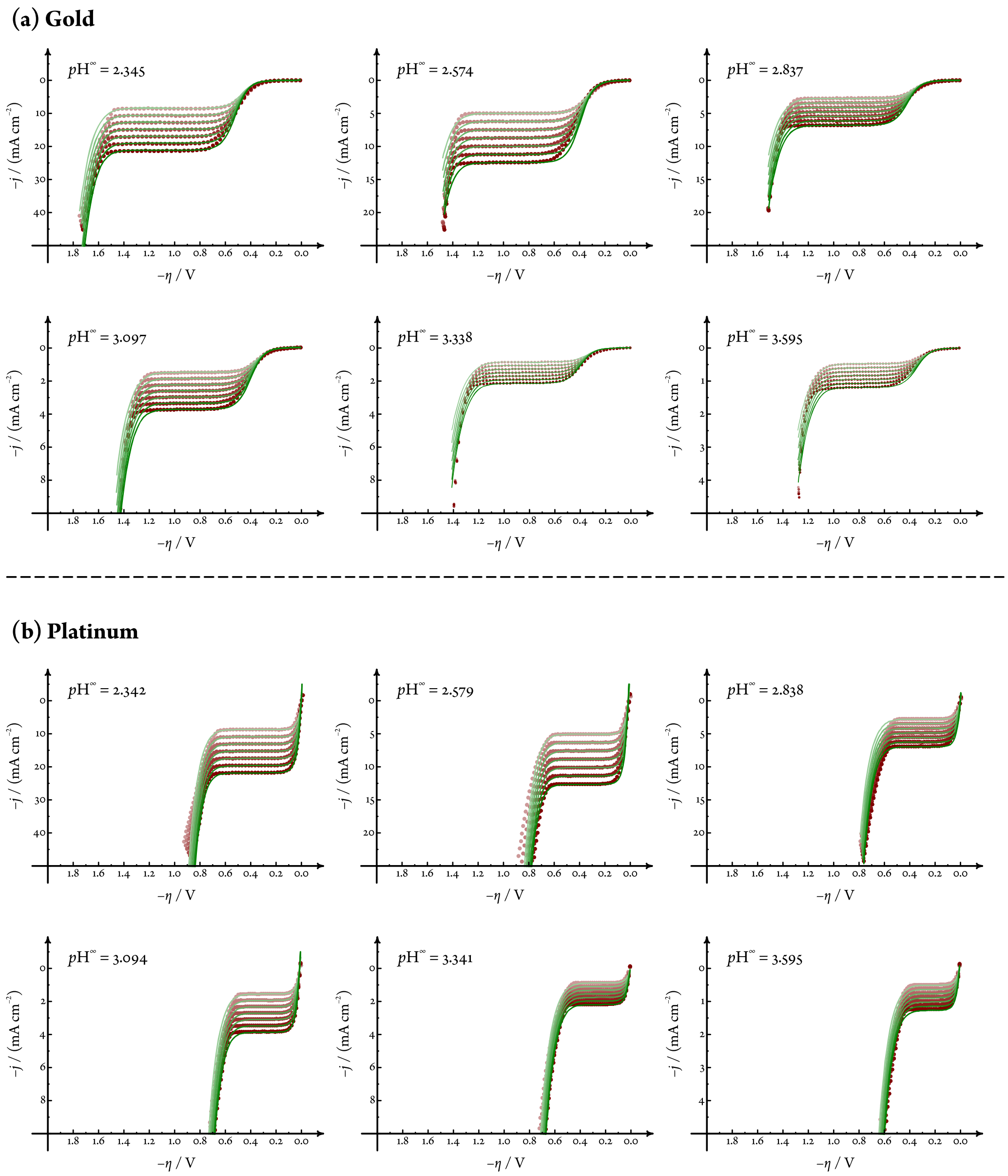

Figure 4. Experimentally obtained polarization curves (red dots) on an Au (a) and on a Pt (b) RDE, showing a two step behavior. In each panel (at different values of pH), the cathodic current density increases as the rotation rate f is set to values of 400, 625, 900, 1225, 1600, 2025, and 2500 min^{-1}. The green curves are created by fitting the model described by eq 23 globally, that is, for all pH and rotation rate values, and by optimizing only three parameters (α_c, k, and $\mathcal{D}$). Determined confidence intervals (at 95% statistical certainty) for the fitted parameters are $\alpha_c = 0.486 \pm 0.067$, $\lg\left(\frac{k}{\mathrm{m\,s^{-1}}}\right) = -5.10 \pm 0.26$ and $\mathcal{D} = (1.027 \pm 0.053) \times 10^{-4}\ \mathrm{cm^2\,s^{-1}}$ for gold and $\alpha_c = 0.643 \pm 0.037$, $\lg\left(\frac{k}{\mathrm{m\,s^{-1}}}\right) = 0.024 \pm 0.050$ and $\mathcal{D} = (1.069 \pm 0.043) \times 10^{-4}\ \mathrm{cm^2\,s^{-1}}$ for platinum. Other parameter values (not optimized) are shown in Table 1.

presented model by assuming that the near-surface concentration difference of H^+ and OH^- ions (Δc^0) equals zero in eq 18. Then

$$j_{\mathrm{lim}} = -F\frac{\mathcal{D}}{\delta_N}\Delta c^{\infty} \tag{26}$$

where for fairly acidic solutions, we can assume that $\Delta c^{\infty} \approx c^{\infty}_{\mathrm{H^+}}$ and thus

$$j_{\mathrm{lim}} \approx -F\frac{\mathcal{D}}{\delta_N}c^{\infty}_{\mathrm{H^+}} \tag{27}$$

The Tafel slope corresponding to this flat plateau is, as shown in Figure 5b, ∞.

Case of Mixed Charge-Transfer/Transport Control for H^+ Reduction. It can be shown that in this region of mixed control, where the gray curve in Figure 5 already leaves $j_{\mathrm{cat,H^+}}$ but still does not attain the limiting current plateau, our model yields current densities that fully match those calculated from the Koutecký–Levich equation[39] and thus for this "first transition" section of the polarization curve

$$\frac{1}{j_{\mathrm{trs1}}} = \frac{1}{j_{\mathrm{cat,H^+}}} + \frac{1}{j_{\mathrm{lim}}} \tag{28}$$

Charge-Transfer-Controlled H_2O Reduction. When the potential is very negative, a series expansion of the current, as

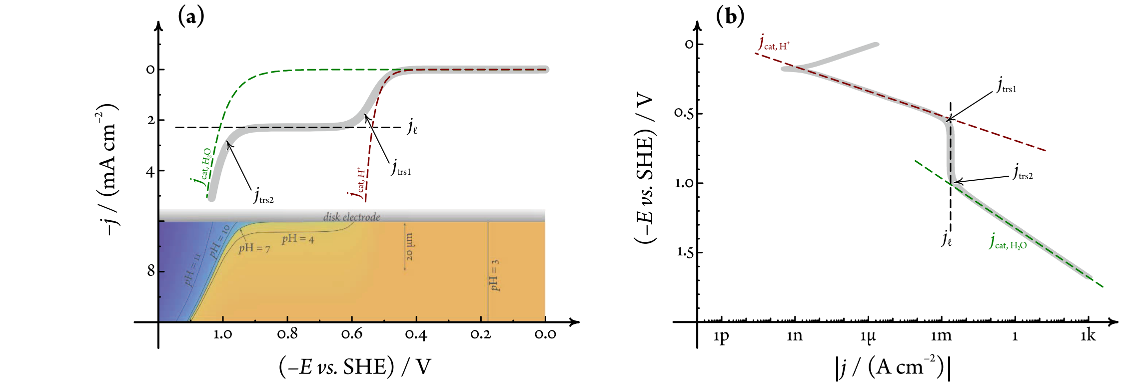

Figure 5. Polarization curve (thick gray) calculated using eq 23 and the parameter values of Table 1, shown in two different representations: with linear axis scaling in (a) and on a Tafel plot in (b). The three different segments of the curves, marked by the dashed lines, can be approximated by eqs 24−30, as discussed in the text. The contour map in the background of (a) shows the variation of pH as a function of the distance measured from the electrode surface at each disk potential. (Details of calculating pH profiles using the presented model are discussed later, cf. to Figure 9).

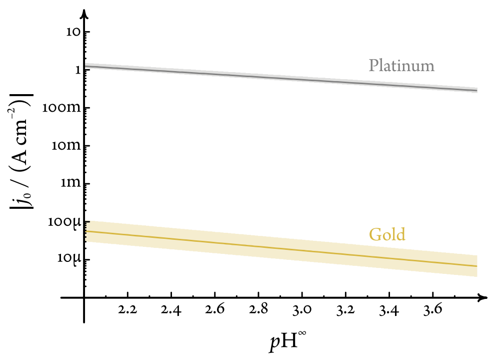

Figure 6. Exchange current densities j_0 in the studied pH range, calculated by using eq 25, based on the kinetic parameters determined by nonlinear fitting in Figure 4 for gold and platinum.

given by eq 23, around $-\infty$ for the term $\exp\left(-\frac{F\alpha_c E}{RT}\right)$ to the first order yields the following equation

$$j_{\mathrm{cat,H_2O}} = -Fc^{\ominus}\sqrt{\frac{2\mathcal{D}kK_{\mathrm{w}}^{\alpha_c/2+1}}{\delta_{\mathrm{N}}}}\exp\left(-\frac{\alpha_c FE}{2RT}\right) \quad (29)$$

Note that, as expected, this equation is independent of $c_{\mathrm{H^+}}^{\infty}$. This current is shown by the dashed green curve in Figure 5; as seen in the Tafel representation, Figure 5b, the corresponding Tafel slope is $\sim\frac{118\ \mathrm{mV}}{\alpha_c}$.

Mixed Charge-Transfer Control of H_2O Reduction and Transport Control of H^+ Reduction. It can be shown that at the potential regime between these two segments, i.e., in the "second transition section", the current can be described by the equation

$$j_{\mathrm{trs2}} = \frac{j_{\mathrm{lim}}}{2} - \sqrt{\left(\frac{j_{\mathrm{lim}}}{2}\right)^2 + j_{\mathrm{cat,H_2O}}^2} \quad (30)$$

In what follows, we will analyze the effect of varying certain parameters (α_c and k) on the calculated polarization curves.

Parameter Dependencies. *Dependence on α_c.* Polarization curves calculated based on eq 23 show a strong dependence on the value of the charge-transfer coefficient α_c, as illustrated by Figure 7a,b.

With respect to the definition of the charge-transfer coefficient α_c, we emphasize that since the presented model is built on Reaction R4, a two-electron reaction, we assumed that $\alpha_c + \alpha_a = 2$;[34] thus, based on this definition, $\alpha_c = 1$ represents symmetry.

Note in Figure 7b that the Tafel slopes of the first and second exponentially increasing segments are $\frac{59\ \mathrm{mV}}{\alpha_c}$ and $\frac{118\ \mathrm{mV}}{\alpha_c}$, in accordance with what was said earlier about these segments. Also note that as a result of the two differing Tafel slopes, the length of the transport-limited plateau is heavily influenced by the value of α_c: smaller α_c values result in longer plateaus.

Dependence on k. The dependence of the polarization curves on the reaction rate coefficient k is illustrated by Figure 7c,d. Note that as shown by the figure, the polarization curves tend toward a reversible curve (indicated in Figure 7c,d by a dashed blue line) if we increase the value of k. Indeed, in the $k \to \infty$ limit, the current of eq 23 reduces to

$$j_{\mathrm{rev}} = -F\frac{\mathcal{D}}{\delta_{\mathrm{N}}}\left\{\Delta c^{\infty} - c^{\ominus}\left[\exp\left(\frac{FE}{RT}\right) - K_{\mathrm{w}}\exp\left(-\frac{FE}{RT}\right)\right]\right\} \quad (31)$$

Note that we get to this very same expression of the reversible current if we solve eq 12 by assuming that the value of Δc_0 is determined by Nernst's equation (that is, if we utilize a Nernstian boundary condition). As expected, eq 31 contains no kinetic parameters as it is a consequence of thermodynamic and transport-related considerations.

Note in Figure 5 that the "first steps" of the polarization curves calculated for finite k values tend to achieve the reversibility limit quite easily. In the case of $\alpha_c = 1$, the first steps of the polarization curves calculated for $k \geq 10^{-2}$ m s^{-1} are practically indistinguishable from the reversible current. This agrees well with the experimental observations and the argumentation of Gasteiger et al. who have warned that in such cases no conclusions with respect to the kinetics of HER should be drawn from RDE experiments.[12] We note, however, that for the "second step" of the polarization curves, it takes far higher (in fact, unrealistically high, $k \geq 1$ m s^{-1}) rate coefficients to match the reversibility case. This finding offers a new perspective for the interpretation of RDE polarization curves, as will be discussed below.

Kinetic Parameters from Plateau Lengths. As we saw before, HER polarization curves exhibit plateaus of different lengths when measured on metals of different electrocatalytic activities (Figure 4); this behavior is reproduced by the

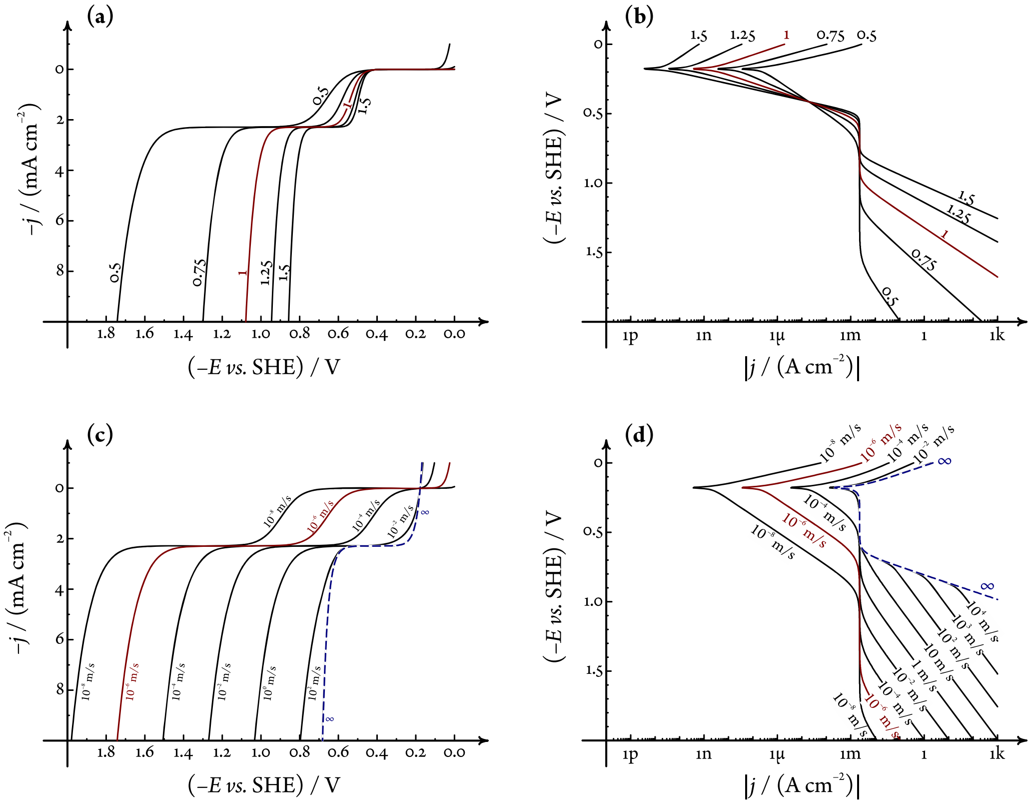

Figure 7. Effect of varying the parameters α_c (a, b) and k (c, d) on the calculated polarization curves. Values assumed are shown on the graph; other parameters are given in Table 1. Polarization curves are shown in two different representations: with linear axis scaling (a, c) and on a Tafel plot (b, d).

presented model. Although the fitting of the whole model to a set of measurements is computationally not difficult—eq 23 is, after all, an analytical expression—and fitting the full model is always favorable, it seems worthy to analyze plateau lengths and, in particular, their dependence on the pH, in the hope that this analysis will make kinetic parameters accessible more easily.

As the term plateau length is, however, not well-defined, it seems easier to introduce the concept of breakdown overpotential (η_{br}) as a quantity of similar meaning. We define η_{br}, as illustrated by Figure 8a, as the overpotential at which the measured current, following the second current step, reaches the value of $2j_{lim}$.

Keeping in mind that $E^{eq} = \frac{RT}{F}\ln\left(\frac{c^{\infty}_{H^+}}{c^{\ominus}}\right)$, we can obtain the following formula for the value of η_{br} from eq 30:

$$\frac{F\eta_{br}}{RT\ln 10} = -\left(1 + \frac{2}{\alpha_c}\right)\mathrm{pH} + \frac{1}{\alpha_c}\lg\left(\frac{\mathcal{D}}{\delta_N k K_w^{1+\alpha_c/2}}\right) \tag{32}$$

That is, following a standard Levich analysis for the determination of $\mathcal{D}$, we can plot the normalized breakdown potentials (measured at a chosen, fixed rotation rate) as a function of pH; we can then perform linear fitting to these data (shown in Figure 8b for a rotation rate of 625 min^{-1} for gold and platinum) and determine α_c and k values from the slope and intercept. As shown in Table 2, the results are acceptable but not as reliable as those of full-model fitting.

pH Profiles. The presented model may not only be found useful to fit HER polarization curves but it may also give predictions on how the local pH changes in the vicinity of a rotating electrode at which H_2 evolves. The basis of such predictions is eq 16. In it, expressing Δc^0 with the aid of the current density j by using eq 23, we arrive to the following equation describing the variation of the concentration differences of H^+ and OH^- as a function of the distance measured from the electrode surface:

$$\frac{\Delta c(z)}{\Delta c^{\infty}} = 1 - \frac{j}{j_l}Q_{1/3}\left[\left\{\frac{z}{\delta_N}\Gamma\left(\frac{4}{3}\right)\right\}^3\right] \tag{33}$$

Concentration difference profiles, calculated based on eq 33, are shown in Figure 9a. Provided that pH^{∞} is known, eq 33 permits the direct calculation of pH profiles as well; for that we need to recall the definition of Δc in eq 15. The pH(z) profile can then be calculated as

$$\mathrm{pH}(z) = -\lg\left[\frac{\Delta c(z)}{2c^{\ominus}} + \sqrt{K_w + \left(\frac{\Delta c(z)}{2c^{\ominus}}\right)^2}\right] \tag{34}$$

Some example pH profiles are shown in Figure 9b.

It follows from eqs 33 and 18 that as the cathodic current increases, pH values measured in the vicinity of the electrode will rise. Exactly at $j = j_{lim}$, the pH at the electrode surface reaches neutrality ($\mathrm{pH}^0 \approx 7$). When a cathodic current density higher than j_{lim} is forced through the electrode surface, the near-electrode solution region gets alkaline, yet at a given distance, the pH drops suddenly to acidic values (see Figure 9b).

The distance at which the aforementioned drop occurs (i.e., the distance of the neutrality point z_{neut}) depends on how

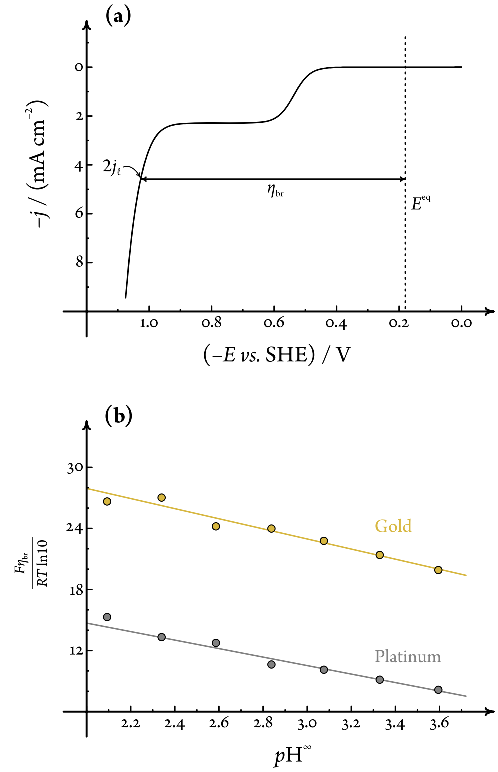

Figure 8. (a) Concept of the breakdown overpotential η_{br} illustrated on a polarization curve. (b) Dimensionless breakdown overpotentials plotted as a function of pH for gold and platinum, determined from measured data (dots). The lines were created by linear fitting to the measured data, using a pH^2 weighting. The acquired slopes and intercepts were used according to eq 32 to calculate the kinetic parameters shown in Table 2. Chosen rotation rate: 625 min^{-1}.

Table 2. Kinetic Parameters of HER on Pt and on Au, in Mildly Acidic Solutions[a]

system		$\lg\left(\frac{k}{\mathrm{m\,s^{-1}}}\right)$	α_c
Au	Figure 4	-5.10 ± 0.26	0.486 ± 0.067
	Figure 8	-5.2 ± 1.4	0.50 ± 0.11
Pt	Figure 4	0.024 ± 0.050	0.643 ± 0.037
	Figure 8	0.2 ± 1.6	0.63 ± 0.16

[a]Parameters were determined either by the fitting of the full model to all measured data, Figure 4, or by plotting limiting current plateau lengths as a function of pH, Figure 8.

much the current density exceeds the limiting current density and it can be expressed as

$$\frac{z_{\text{neut}}}{\delta_{\text{N}}} = \frac{\sqrt[3]{Q_{1/3}^{-1}\left(\frac{j_l}{j}\right)}}{\Gamma\left(\frac{4}{3}\right)} \tag{35}$$

where we denoted by $Q_s^{-1}(x)$ the inverse of the regularized incomplete gamma function $Q_s(x)$, defined by eq 17.

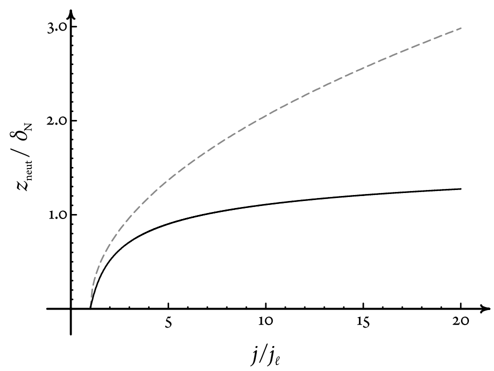

Figure 10. Full black curve: the distance of neutrality (normalized to the diffusion layer thickness δ_N) as a function of the current density normalized to j_l. Note that the function, eq 35, is not defined for $|j| < |j_l|$. Dashed gray curve: an estimate for the neutrality distance based on an analytical solution assuming that $D_{OH^-} \gg D_{H^+}$.[27]

In Figure 10, z_{neut} is plotted as a function of the normalized current density j/j_l. The z_{neut} quantity can be interpreted as a measure of how deep the near-electrode solution layer becomes alkaline, as shown by Figure 9. Note in Figure 10 that true alkalination (i.e., the appearance of a pH $\gtrsim$ 7 region) can only occur if $j/j_l > 1$ and that at high current densities, the depth of alkalination can exceed the diffusion layer thickness δ_N.

Concluding Remarks; Comparison to Other Works. The presented model seems suitable to describe polarization curves of HER measured at two electrodes of different electrocatalytic activities (Au and Pt). The extracted parameters are in agreement with some shown in the literature before,[11,20] yet at this point, we would like to emphasize

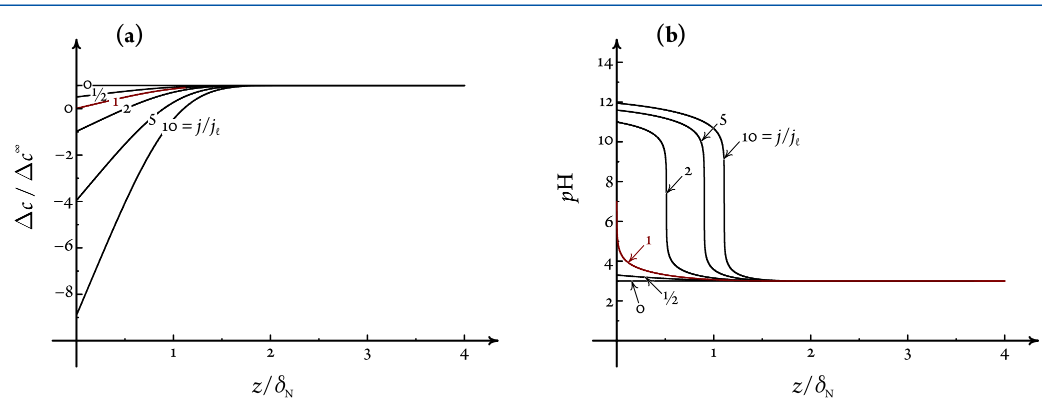

Figure 9. (a) Normalized concentration difference profiles as a function of the normalized distance, for some chosen values of the normalized current density (shown in the figure). (b) An example for pH profiles calculated for various normalized current values, assuming that pH$^\infty$ = 3.

limitations of the treatment and to make a brief comparison to earlier works on the topic of HER.

An important issue, to which we would like to direct the readers attention, is the equidiffusivity assumption that we utilized. This assumption, although not unprecedented in the literature (see the works of Tobias as an example[22]), poses some limitations to the validity of our analysis. Avoiding use of the assumption is, unfortunately, not possible, as it is required for eq 12 to be analytically solvable. The equidiffusivity assumption means that we consider the diffusion coefficients of H^+ and OH^- ions equal, appearing as a common coefficient $\mathcal{D}$ in our equations. We are aware (and the reader should also be) that this approximation is only valid on an order of magnitude level (while in reality, D_{H^+} is supposed to be about 2 times higher than D_{OH^-}). The equidiffusivity assumption, as also pointed out by Tobias,[22] renders the concentration of OH^- at and under the disk surface to be underestimated. That the model equations can still be used to obtain good apparent fits of the measured polarization curves is probably attributed to the fact that currents measured at high cathodic overpotentials show only a moderate (order of 1/3) dependence on $\mathcal{D}$ (cf. eq 29).

At this point, it seems worthy to make a comparison between the model presented here and one of our previous attempts at modeling polarization curves of HER. In ref 27, we constructed analytical approximations to an otherwise digital simulation-based model where we assumed that the diffusion coefficient of OH^- is not only equal to but actually much higher than that of H^+. This assumption also led to a fittable model function, but it predicted that the near-surface solution region, instead of getting alkaline, would get neutral up to a certain depth. Of course, under these circumstances, the "distance of neutrality" was higher than the one obtained here: instead of the formation of a thin alkaline layer, we assumed the formation of a thicker, however, neutral layer. In Figure 10, we show a comparison between the two approaches.

A further difference between the model presented here and the one we described before[27] is that while the previous one was dealing with two irreversible reactions (namely, the reduction of H^+ ions and that of water molecules), the present model is built on a combined, quasireversible, reaction (Reaction R4). The present model thus performs better compared with the previous one in two ways: (i) it provides good fits with only two (instead of four) kinetic parameters, and (ii) it is also able to model a quasiequilibrium (that is, the $k \to \infty$ case). Although within the framework of the present model it is still possible to distinguish two reactions (see our discussion of polarization curve segments assigned to H^+ reduction and to water splitting), we emphasize here that such distinctions are all but arbitrary and the treatment presented here is built on a single charge-transfer reaction, Reaction R4.

In comparison to the models of some other authors,[22−24] a clear advantage of the model presented here is that it contains kinetic parameters and does not rely on the use of the Nernstian boundary condition. This condition would predict that the near-surface pH is exactly determined by, and directly proportional to, the electrode potential. Instead of using a Dirichlet (i.e., Nernstian) boundary condition, our model utilizes a Neumann condition[40] and thus allows the calculation of kinetic currents.

Although the model seems to fit experimental data on a broad scale (Figure 4), here we would like to draw the attention of the readers to another limitation, which arises from the very fact that we assumed the validity of the Erdey-Grúz−Volmer−Butler equation for Reaction R4. We thus ignored any effects related to surface kinetics and that the parameters k and α_c can be potential dependent.[41] This simplification was, however, necessary to describe the experimentally observed two step behavior of HER, visible at high cathodic overpotentials. Consequently, the k and α_c parameters that we determined here can be considered valid primarily at high overpotential. Although some variations of these parameters may occur—and this is probably responsible for the fits of Figure 4 not being perfect at low overpotentials—the overall fits are still satisfactory.

■ CONCLUSIONS

We have developed a new model that is able to describe HER as it occurs on RDEs immersed into mildly acidic solutions, where the polarization curves show a two step behavior. The model is centered around a single reaction, Reaction R4, that contains both H^+ ions (as a reactant) and OH^- ions (as a product). We assumed that the Erdey-Grúz−Volmer−Butler equation applies for this reaction and that the diffusion coefficient of the two reacting species (H^+ and OH^-) are equal. On the basis of these assumptions, we managed to solve the differential equations governing the system; the resulting analytical model could be used for the fitting of experimentally obtained polarization curves. By varying only three model parameters, we achieved good fits over a relatively broad range of pH and rotation rates for both Au and Pt RDEs.

A very important implication of the model is that the plateau lengths seen on RDE polarization curves are (inversely) related to electrocatalytic activity. We showed that at fixed rotation rates, a linear relationship exists between the plateau length and the bulk solution pH. By analyzing this relationship, we can get a good estimate of the kinetic parameters k and α_c, even in cases where the transport performance of the RDE is not sufficient to measure well-defined kinetic currents using the standard Koutecký−Levich analysis.[12,41]

Within the presented framework, it is also possible to model the variation of pH as a function of distance measured from the electrode surface. This result may become useful if we study HER as a side reaction of, for example, metal deposition processes where local pH rises can have unwanted effects on the deposit.

■ AUTHOR INFORMATION

Corresponding Authors

Peter Broekmann − *Department of Chemistry and Biochemistry, University of Bern, CH-3012 Bern, Switzerland;* orcid.org/0000-0002-6287-1042; Phone: +41316314317; Email: peter.broekmann@dcb.unibe.ch

Soma Vesztergom − *Department of Physical Chemistry, Eötvös Loránd University of Budapest, H-1117 Budapest, Hungary;* orcid.org/0000-0001-7052-4553; Phone: +36204612429; Email: vesztergom@chem.elte.hu

Authors

María de Jesús Gálvez-Vázquez − *Department of Chemistry and Biochemistry, University of Bern, CH-3012 Bern, Switzerland*

Vitali Grozovski − *Department of Chemistry and Biochemistry, University of Bern, CH-3012 Bern, Switzerland*

Noémi Kovács − *Department of Chemistry and Biochemistry, University of Bern, CH-3012 Bern, Switzerland; Department of Physical Chemistry, Eötvös Loránd University of Budapest, H-1117 Budapest, Hungary*

Complete contact information is available at: https://pubs.acs.org/10.1021/acs.jpcc.9b11337

Notes

The authors declare no competing financial interest.

■ ACKNOWLEDGMENTS

Support by the CTI Swiss Competence Center for Energy Research (SCCER Heat and Electricity Storage) is gratefully acknowledged. P.B. acknowledges financial support from the Swiss National Foundation (grant No. 200020−172507). S.V. acknowledges support from the National Research, Development and Innovation Office of Hungary (NKFIH grant Nos. PD124079 and K129210). M.d.J.G.-V. and N.K. acknowledge the financial support by the Swiss Government Excellence Scholarships for Foreign Scholars (ESKAS).

■ REFERENCES

(1) Wang, H.; Gao, L. Recent Developments in Electrochemical Hydrogen Evolution Reaction. *Curr. Opin. Electrochem.* **2018**, *7*, 7−14.
(2) Ooka, H.; Figueiredo, M. C.; Koper, M. T. M. Competition between Hydrogen Evolution and Carbon Dioxide Reduction on Copper Electrodes in Mildly Acidic Media. *Langmuir* **2017**, *33*, 9307−9313.
(3) Cave, E. R.; Shi, C.; Kuhl, K. P.; Hatsukade, T.; Abram, D. N.; Hahn, C.; Chan, K.; Jaramillo, T. F. Trends in the Catalytic Activity of Hydrogen Evolution during CO_2 Electroreduction on Transition Metals. *ACS Catal.* **2018**, *8*, 3035−3040.
(4) Schlesinger, M.; Paunovic, M., Eds., *Modern Electroplating*, 5th ed.; Wiley: New York, 2010.
(5) Ritzert, N. L.; Moffat, T. P. Ultramicroelectrode Studies of Self-Terminated Nickel Electrodeposition and Nickel Hydroxide Formation upon Water Reduction. *J. Phys. Chem. C* **2016**, *120*, 27478−27489.
(6) Wu, J.; Wafula, F.; Branagan, S.; Suzuki, H.; van Eisden, J. Mechanism of Cobalt Bottom-Up Filling for Advanced Node Interconnect Metallization. *J. Electrochem. Soc.* **2019**, *166*, D3136−D3144.
(7) Horányi, G. *Electrochemical Dictionary*;Bard, A. J.; Scholz, F.; Inzelt, G., Eds.; Springer Verlag: Heidelberg, 2008; p 343.
(8) Bockris, J. O. M.; Ammar, I. A.; Huq, A. K. M. S. The Mechanism of the Hydrogen Evolution Reaction on Platinum, Silver and Tungsten surfaces in Acid Solutions. *J. Phys. Chem. A.* **1957**, *61*, 879−886.
(9) Bagotzky, V. S.; Osetrova, N. V. Investigations of Hydrogen Ionization on Platinum with the Help of Micro-Electrodes. *J. Electroanal. Chem. Interfacial Electrochem.* **1973**, *43*, 233−249.
(10) Tavares, M. C.; Machado, S. A. S.; Mazo, L. H. Study of Hydrogen Evolution Reaction in Acid Medium on Pt Microelectrodes. *Electrochim. Acta* **2001**, *46*, 4359−4369.
(11) Neyerlin, K. C.; Gu, W.; Jorne, J.; Gasteiger, H. A. Study of the Exchange Current Density for the Hydrogen Oxidation and Evolution Reactions. *J. Electrochem. Soc.* **2007**, *154*, B631−B635.
(12) Sheng, W.; Gasteiger, H. A.; Shao-Horn, Y. Hydrogen Oxidation and Evolution Reaction Kinetics on Platinum: Acid vs Alkaline Electrolytes. *J. Electrochem. Soc.* **2010**, *157*, B1529−B1536.
(13) Durst, J.; Siebel, A.; Simon, C.; Hasché, F.; Herranz, J.; Gasteiger, H. A. New insights into the electrochemical hydrogen oxidation and evolution reaction mechanism. *Energy Environ. Sci.* **2014**, *7*, 2255−2260.
(14) Zheng, J.; Sheng, W.; Zhuang, Z.; Xu, B.; Yan, Y. Universal Dependence of Hydrogen Oxidation and Evolution Reaction Activity of Platinum-group Metals on pH and Hydrogen Binding Energy. *Sci. Adv.* **2016**, *2*, No. e1501602.
(15) Pentland, N.; Bockris, J. O. M.; Sheldon, E. Hydrogen Evolution Reaction on Copper, Gold, Molybdenum, Palladium, Rhodium, and Iron. *J. Electrochem. Soc.* **1957**, *104*, 182.
(16) Ives, D. J. G. Some Abnormal Hydrogen Electrode Reactions. *Can. J. Chem.* **1959**, *37*, 213−221.
(17) Brug, G. J.; Sluyters-Rehbach, M.; Sluyters, J. H.; Hemelin, A. The Kinetics of the Reduction of Protons at Polycrystalline and Monocrystalline Gold Electrodes. *J. Electroanal. Chem. Interfacial Electrochem.* **1984**, *181*, 245−266.
(18) Conway, B. E.; Bai, L. State of Adsorption and Coverage by Overpotential-Deposited H in the H_2 Evolution Reaction at Au and Pt. *Electrochim. Acta* **1986**, *31*, 1013−1024.
(19) Khanova, L. A.; Krishtalik, L. I. Kinetics of the hydrogen evolution reaction on gold electrode. A new case of the barrierless discharge. *J. Electroanal. Chem.* **2011**, *660*, 224−229.
(20) Kahyarian, A.; Brown, B.; Nesić, S. Mechanism of the Hydrogen Evolution Reaction in Mildly Acidic Environments on Gold. *J. Electrochem. Soc.* **2017**, *164*, H365−H374.
(21) Obata, K.; Stegenburga, L.; Takanabe, K. Maximizing Hydrogen Evolution Performance on Pt in Buffered Solutions: Mass Transfer Constrains of H_2 and Buffer Ions. *J. Phys. Chem. C* **2019**, *123*, 21554−21563.
(22) Hessami, S.; Tobias, C. W. In-Situ Measurement of Interfacial pH Using a Rotating Ring-Disk Electrode. *AIChE J.* **1993**, *39*, 149−162.
(23) Katsounaros, I.; Meier, J. C.; Klemm, S. O.; Topalov, A. A.; Biedermann, U. P.; Auinger, M.; Mayrhofer, K. J. J. The Effective Surface pH during Reactions at the Solid-Liquid interface. *Electrochem. Commun.* **2011**, *13*, 634−637.
(24) Auinger, M.; Katsounaros, J. C.; Meier, I.; Klemm, S. O.; Biedermann, P. U.; Topalov, A. A.; Rohwerder, M.; Mayrhofer, K. J. J. Near-surface ion distribution and buffer effects during electrochemical reactions. *Phys. Chem. Chem. Phys.* **2011**, *13*, 16384−16394.
(25) Shinagawa, T.; García-Esparza, A. T.; Takanabe, K. Insight on Tafel Slopes from a Microkinetic Analysis of Aqueous Electrocatalysis for Energy Conversion. *Sci. Rep.* **2015**, *5*, No. 13801.
(26) Strmcnik, D.; Uchimura, M.; Wang, C.; Subbaraman, R.; Danilovic, N.; van der Vliet, D.; Paulikas, A. P.; Stamenkovic, V. R.; Markovic, N. M. Improving the Hydrogen Oxidation Reaction Rate by Promotion of Hydroxyl Adsorption. *Nat. Chem.* **2013**, *5*, 300−306.
(27) Grozovski, V.; Vesztergom, S.; Láng, G. G.; Broekmann, P. Electrochemical Hydrogen Evolution: H^+ or H_2O Reduction? A Rotating Disk Electrode Study. *J. Electrochem. Soc.* **2017**, *164*, E3171−E3178.
(28) Vesztergom, S. *Encyclopedia of Interfacial Chemistry: Surface Science and Electrochemistry*;Wandelt, K., Ed.; Elsevier: Amsterdam, 2018; pp 421−444.
(29) Nagel, K.; Wendler, F. Die Wasserstoffelektrode als zweifache Elektrode. *Z. Elektrochem.* **1956**, *60*, 1064−1072.
(30) Kanzaki, Y.; Tokuda, K.; Bruckenstein, S. Dissociation Rates of Weak Acids Using Sinusoidal Hydrodynamic Modulated Rotating Disk Electrode Employing Koutecky-Levich Equation. *J. Electrochem. Soc.* **2014**, *161*, H770−H779.
(31) Wiberg, G. K. H.; Arenz, M. On the Influence of Hydronium and Hydroxide Ion Diffusion on the Hydrogen and Oxygen Evolution Reactions in Aqueous Media. *Electrochim. Acta* **2015**, *159*, 66−70.
(32) Carneiro-Neto, E. B.; Lopes, M. C.; Pereira, E. C. Simulation of Interfacial pH Changes during Hydrogen Evolution Reaction. *J. Electroanal. Chem.* **2016**, *765*, 92−99.
(33) Vanýsek, P. *CRC Handbook of Chemistry and Physics*, 93rd ed.; Haynes, W. M., Ed.; Chemical Rubber Company: Boca Raton FL, 2012.
(34) Guidelli, R.; Compton, R. G.; Feliu, J. M.; Gileadi, E.; Lipkowski, J.; Schmickler, W.; Trasatti, S. Defining the Transfer

Coefficient in Electrochemistry: An Assessment (IUPAC Technical Report). *Pure Appl. Chem.* **2014**, *86*, 245−258.
(35) Bard, A. J.; Faulkner, L. R. *Electrochemical Methods. Fundamentals and Applications*; John Wiley & Sons: New York, 2001.
(36) Bronstein, I. N.; Semendjajew, K. A.; Musiol, G.; Muehlig, H. *Taschenbuch der Mathematik*; Verlag Harri Deutsch: Frankfurt am Main, 2008.
(37) Haghighat, S.; Dawlaty, J. M. pH Dependence of the Electron-Transfer Coefficient: Comparing a Model to Experiment for Hydrogen Evolution Reaction. *J. Phys. Chem. C* **2016**, *120*, 28489−28496.
(38) Nørskov, J. K.; Bligaard, T.; Logadottir, A.; Kitchin, J. R.; Chen, J. G.; Pandelov, S.; Stimming, U. Trends in the Exchange Current for Hydrogen Evolution. *J. Electrochem. Soc.* **2005**, *152*, J23−J26.
(39) Koutecky, J.; Levich, V. G. The use of a rotating disk electrode in the studies of electrochemical kinetics and electrolytic processes. *Zh. Fiz. Khim.* **1958**, *32*, 1565−1575.
(40) Cheng, A. H.-D.; Cheng, D. T. Heritage and early history of the boundary element method. *Eng. Anal. Boundary Elem.* **2005**, *29*, 268−302.
(41) Kucernak, A. R.; Zalitis, C. General Models for the Electrochemical Hydrogen Oxidation and Hydrogen Evolution Reactions: Theoretical Derivation and Experimental Results under Near Mass-Transport Free Conditions. *J. Phys. Chem. C* **2016**, *120*, 10721−10745.

https://dx.doi.org/10.1021/acs.jpcc.9b11337
J. Phys. Chem. C 2020, 124, 3988−4000

1.8 Toward CO_2 Electroreduction Under Controlled Mass Flow Conditions: A Combined Inverted RDE and Gas Chromatography Approach

Authors: Pavel Moreno-García, Noémi Kovács, Vitali Grozovski, María de Jesús Gálvez-Vázquez, Soma Vesztergom, and Peter Broekmann

Anal. Chem. **92** (6), 4301−4308 (2020), DOI: 10.1021/acs.analchem.9b04999

Highlights: A novel setup to study reactions under steady-state conditions was developed. This setup coupled an inverted rotating disc electrode device with gas chromatography detection. This hydrodynamic configuration allows a higher rate of transport due to convection compared to other quiescent systems. The developed system was successfully validated with a non-gas evolving electrochemical reaction (ferro-/ferricyanide redox couple) and with a gas-evolving reaction (hydrogen evolution). Furthermore, this setup was used to study the CO_2RR on a polycrystalline silver electrode. The results allowed resolving the voltammetric response to individual contributions of actual CO_2 reduction and hydrogen evolution.

Contributions: I helped in some of the measurements carried out with the developed setup. I also conducted the SEM and EDX characterization of the Ag rotating disc electrode after polishing it with alumina or diamond solution needed in the supporting information of this investigation.

analytical chemistry

pubs.acs.org/ac Article

Toward CO_2 Electroreduction under Controlled Mass Flow Conditions: A Combined Inverted RDE and Gas Chromatography Approach

Pavel Moreno-García,*,§ Noémi Kovács,§ Vitali Grozovski, María de Jesús Gálvez-Vázquez, Soma Vesztergom,* and Peter Broekmann

Cite This: Anal. Chem. 2020, 92, 4301−4308 Read Online

ACCESS | Metrics & More | Article Recommendations | Supporting Information

ABSTRACT: The use of rotating disk electrodes (RDEs) is probably the most convenient way of studying simple electrode reactions under well-defined transport conditions. Standard RDEs become, however, less expedient when the studied electrode process is a complex one, leading to the formation of various reaction products. In these cases, the accurate detection and quantification of the formed products are desirable. If the formed products are gaseous, then the usual way of quantifying them is the use of online gas chromatography (GC), a method that is not compatible with open RDE cells. In order to overcome these difficulties, we present here a sophisticated inverted RDE (iRDE) cell design. The design combines various advantages: it is amenable to the same mathematical treatment as standard (downward-facing) RDEs; it can be operated airtight and coupled to online GC; and due to its upward-facing design, the electrode surface is less prone to blockage by any formed gas bubbles. The iRDE&GC design is tested using simple model reactions and is demonstratively used for studying the electrochemical reduction of CO_2, accompanied by parasitic hydrogen evolution, on a silver electrode.

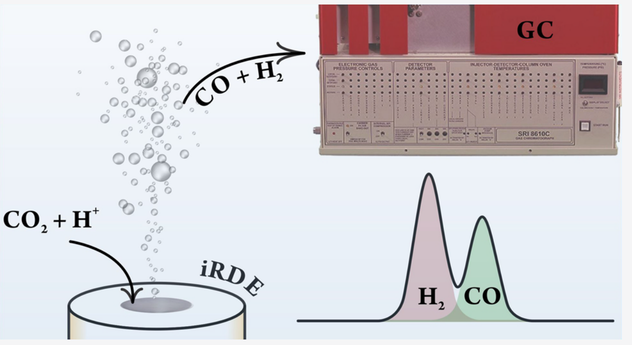

Easy to construct with a variety of electrode materials and amenable to rigorous theoretical treatment, the rotating disk electrode (RDE) is the most widely employed hydrodynamic method used for the investigation of electrode processes.[1] In an RDE system, stationary concentration profiles are attained rather quickly and steady-state current/potential characteristics can be measured. The rate of mass transfer in an RDE configuration is typically higher than that of diffusion alone in quiescent systems, which makes RDEs useful for electrocatalysis research. By using RDEs, the supply of reactants to the electrode surface can be controlled, enabling the distinction between mass transport and kinetic limitations, e.g., by means of analysis based on the Koutecký−Levich equation.[1,2]

The interpretation of RDE measurements becomes less straightforward when the studied reaction has complex kinetics (leading to the formation of more than one reaction product) or if it is accompanied by other (parasitic) side reactions. Examples include the deposition of base metals,[3,4] almost inevitably accompanied by hydrogen evolution; the chloralkali process competing with oxygen evolution;[5] and the electrochemical reduction of either carbon dioxide[6−11] or nitrogen.[12,13] These latter processes, apart from being accompanied by hydrogen evolution, can themselves lead to the formation of various products. In these cases, the accurate (quantitative) determination of the formed products is a prerequisite of any valid RDE analysis. Since many of the products are gaseous, online gas chromatographic (GC) headspace analysis[14] seems to be an obvious choice; however, applying GC in a traditional (i.e., open-to-air) RDE cell is not straightforward.

To the best of our knowledge, there exist only a few designs in the literature for hermetically closed RDE cells that could be applicable to, although they were not applied to, online GC detection.[15,16] These designs utilized magnetic coupling in order to transfer the momentum necessary to rotate an electrode through the cell wall. The approach successfully circumvents the problem of sealing between the rotating shaft and the stagnant cell wall: it may not ensure, however, a full transfer of momentum under high-friction conditions.

A possible alternative to magnetic coupling[15,16] is offered by the use of direct momentum transfer through a gland seal. While airtight seals are difficult to design, liquid-tight seals are

Received: November 2, 2019
Accepted: February 21, 2020
Published: February 21, 2020

relatively easy to manufacture, with the only requirement that the RDE is brought into contact with the electrolyte solution by insertion through the cell bottom. In this case, the headspace itself can be tightly connected to a GC instrument, and the top of the cell also allows an insertion point for a (fixed) reference electrode. As in the case of other "H-type" cell designs,[14] the counter electrode compartment must be separated, by a membrane, from the inverted RDE (iRDE) compartment so that any counter electrode products are excluded from the GC analysis.

Apart from the direct transfer of momentum, a further advantage of using an iRDE design for GC analysis arises from the fact that in iRDEs the electrode is upward-facing. This has no adverse effect on the validity of the hydrodynamic calculations necessary for the mathematical description of transport[17] (i.e., simple expressions such as the Levich and Koutecký−Levich equations remain applicable). It aids, however, in the removal of bubbles that often cause electrode surface blockage in standard (downward-facing) RDE designs.

Some iRDE designs have already been published,[18−22] and some of these were operated in airtight cells. Hermetic cells were, however, used only in order to ensure oxygen-free conditions, and so far, no GC-based product detection was carried out in an iRDE configuration. Furthermore, the previous iRDE designs were validated only for simple model reactions (namely, the ferro-/ferricyanide redox system[18−20]), and either no validation for gas-evolving reactions was used or the interpretation of these measurements was not conclusive.[21,22]

This contribution aims to fill the gap of combining an iRDE configuration with GC-based product detection. The constructed iRDE&GC design is validated by means of simple test measurements. We show that the limiting currents measured in a ferro-/ferricyanide test system and those measured for the hydrogen evolution reaction (HER) in mildly acidic solutions are in perfect agreement with the Levich equation. In the case of the latter reaction, we are also able to detect 100% of the formed hydrogen by means of GC.

Subsequently, we employ the developed iRDE&GC system, fitted with a polycrystalline Ag electrode, for a demonstrative test measurement on the electrochemical CO_2 reduction reaction (CO_2RR). The iRDE&GC system is a powerful tool in this case for a combined product distribution−reaction kinetics study. We show that by using the iRDE&GC hyphenation, partial currents of CO_2RR and HER can be distinguished and made subject, individually, to kinetic analysis.

■ EXPERIMENTAL SECTION

Cell and iRDE Design. The hermetically tight iRDE cell (Figure 1) consists of two separable compartments made of round borosilicate glass flasks (nominal volume: 80 cm^3). Necks for inserting the reference and counter electrodes and the gas inlets and outlets are mounted on the flasks and are equipped with custom-winding poly(tetrafluoroethylene) (PTFE) caps and O-ring fittings, allowing gastight operation. A Nafion ion-exchange membrane (Nafion 117, Sigma-Aldrich) connects the working and counter electrode compartments. The housing of the iRDE, machined from polyoxymethylene (POM), provides rigid connection to a standard rotator unit (AFMSRCE, Pine) and bears a cone joint to fit to the outer socket of the electrochemical cell (size 29/32, ground glass joint standard). Rotation is transferred by a modified RDE shaft that fits into the AFMSRCE rotator. It bears two ceramic sleeves, passing through radial shaft seals.

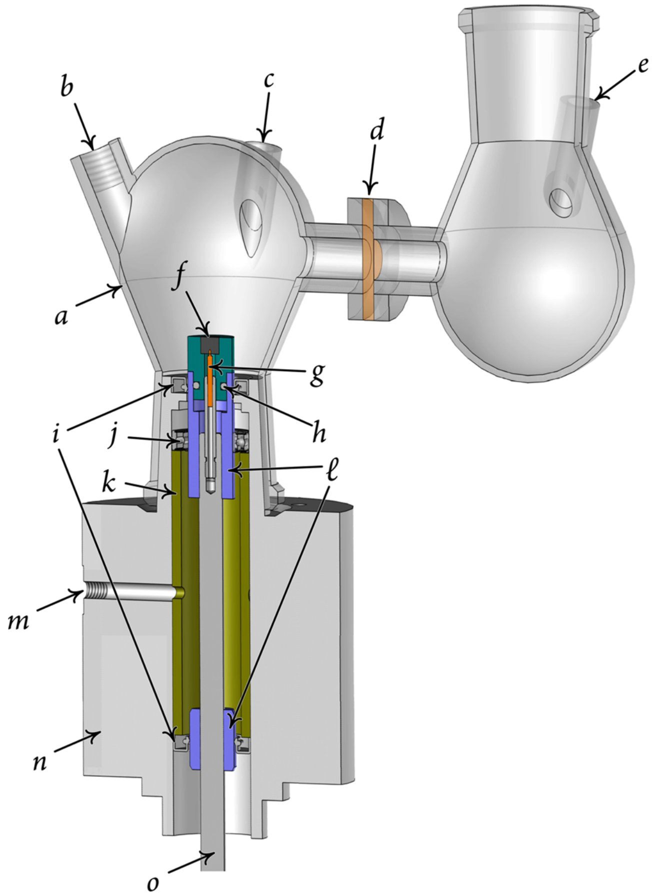

Figure 1. H-type cell equipped with an iRDE. Parts of the design: (*a*) glass cell body, (*b*) purging gas inlet (outlet not shown), (*c*) reference electrode inlet, (*d*) membrane and sealing junction, (*e*) counter electrode inlet, (*f*) PCTFE iRDE tip with an electrode embedded, (*g*) spring contact node, (*h*) PTFE tip groove for the O-ring fitting, (*i*) radial shaft seals (upper and lower), (*j*) ball bearing, (*k*) pressurized gland chamber, (*l*), ceramic fittings (upper and lower), (*m*) pressurizer gas inlet, (*n*) POM housing, and (*o*) rotating shaft (stainless steel).

As a safety component, the design also includes a pressure chamber: a single POM tube confined between the radial shaft seals, fed by N_2 or Ar (99.999%, Carbagas) through a lateral pressurizing gas inlet. Through it, a constant overpressure of 0.2−0.4 bar is maintained in the gland seal, preventing the leakage of electrolyte solution into the seal. The exact coaxial position of the rotating shaft is maintained by a ball bearing, situated in the upper part of the pressure chamber. The radial shaft seals are made of high-quality Viton rubber and operate oil- and grease-free. The upper seal comes in contact with the solution in the working electrode compartment.

The RDE working electrodes are pressed into a laboratory-made poly(chlorotrifluoroethylene) (PCTFE) holder, fitted into the upper ceramic sleeve. Tightness is maintained by an O-ring (not shown in Figure 1), placed in the groove of the PTFE holder. A spring contact in the shaft provides electrical connection to the working electrode. The whole system is easy to maintain, and the radial shaft seals can be exchanged once they are worn out.

https://dx.doi.org/10.1021/acs.analchem.9b04999
Anal. Chem. 2020, 92, 4301−4308

Gas Chromatography. Any gaseous products generated in the cell can be detected by connecting the purging gas outlet to a GC analyzer (SRI Instruments Multigas Analyzer no. 3). The continuous flow of a carrier gas (usually Ar or CO_2, both 99.999% pure, Carbagas) through the electrolysis cell carries volatile reaction products from the headspace into the sampling loops of the gas chromatograph. The partial current I_i, corresponding to the formation of a gaseous product i, can be calculated as[14]

$$I_i = x_i n_i F v_m \tag{1}$$

where x_i denotes the mole fraction of the products, determined by GC using an independent calibration standard gas (Carbagas), n_i is the number of electrons involved in the reduction reaction to form a particular product ($n = 2$ for both CO and H_2 formation), $F = 96\,485.3$ C mol^{-1} is Faraday's constant, and v_m is the molar gas flow rate measured with a universal flowmeter (7000 GC flowmeter, Ellutia) at the exit of the electrochemical cell.

The Faradaic efficiency (FE) of a given reaction product can be determined by dividing the respective partial current, determined from eq 1, by the total current, measured electrochemically. During the operation of the iRDE&GC cell, aliquots are analyzed in intervals of 7 to 20 min during steady-state electrolyses. For the measurements reported, we managed to detect, within the range of error, 100% of the products because no soluble products were formed. The latter was also checked by a postmortem analysis of the electrolyte using ion exchange chromatography (Metrohm).

Electrochemistry. Electrochemical measurements were performed at room temperature with a potentiostat/galvanostat system (Metrohm Autolab 128N) in a three-electrode configuration. A "leakless" Ag|AgCl|3 mol dm^{-3} KCl reference electrode (Pine) and a Pt foil counter electrode (0.8 cm × 2.0 cm, Goodfellow) were used. The glassy carbon, Pt, and Ag working electrodes were 5-mm-diameter disk electrodes purchased from Pine. When reporting current densities (j) instead of the current (I), we used the geometric surface area (0.196 cm^2) for normalization.

All electrodes were polished to a mirror finish with 0.05 μm alumina particles (Micropolish, Buehler) on a polishing cloth (Buehler) and thoroughly rinsed with Milli-Q water (18.2 M cm, TOC ≤ 5 ppb, Millipore) prior to electrochemical measurements.

All of the reported potentiostatic or potentiodynamic measurement results were obtained by using automatic IR compensation, following an impedance-spectroscopy-based determination of the cell resistance.

Chemicals. All solutions were prepared with as-received chemicals and Milli-Q water. Potassium ferrocyanide ($K_4[Fe(CN)_6]$, ≥99.5), potassium ferricyanide ($K_3[Fe(CN)_6]$, ≥99%), and potassium chloride (KCl, ≥99.5%) were purchased from Fluka. Potassium sulfate (K_2SO_4, ≥99%), sulfuric acid (96% H_2SO_4, suprapure), sodium perchlorate ($NaClO_4$, 99.99%), and perchloric acid (70% $HClO_4$, suprapure) were purchased from Merck.

■ RESULTS AND DISCUSSION

Validation of the iRDE Design in the Absence of Gas Evolution. In order to check the hydrodynamic performance of the iRDE design, we measured linear sweep voltammograms (LSVs, sweep rate 20 mV s^{-1}) on a glassy carbon iRDE in a 1 mol dm^{-3} KCl electrolyte solution containing the ferro-/ferricyanide redox couple in equimolar (5 mmol dm^{-3}) concentrations. The voltammograms, shown in Figure 2,

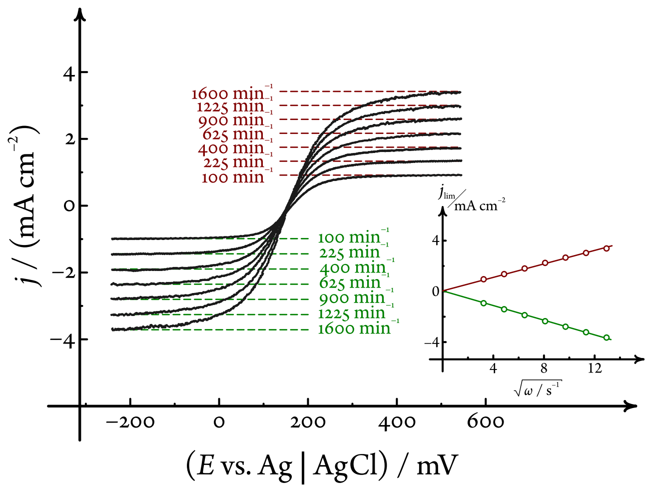

Figure 2. Validation of the hydrodynamic performance of the iRDE setup with a non-gas-evolving reaction. Limiting currents (both anodic and cathodic) measured by linear sweep voltammetry on a glassy carbon iRDE in a solution containing the $K_4[Fe(CN)_6]$/$K_3[Fe(CN)_6]$ redox couple in equimolar concentrations scale linearly with the square root of the rotation rate. Green and red dashed lines show the cathodic and anodic limiting currents, respectively, predicted by eq 2 and the diffusion coefficient values mentioned in the text, at the given rotation rates. Sweep rate 20 mV s^{-1}.

were recorded at seven different rotational rates, distributed equidistantly on a square-root scale between 100 and 1600 min^{-1}. Well-defined limiting currents were reached for both the oxidation and reduction reactions, showing an excellent linear dependence ($R^2 = 0.9996$, with a zero offset) on the square root of the rotational rate. This dependence was analyzed by using the Levich equation[1]

$$j_{\mathrm{lim}} = 0.620 nFD^{2/3}\nu^{-1/6}\omega^{1/2}c \tag{2}$$

where $n = 1$ is the number of electrons transferred, D denotes the diffusion coefficient and c denotes the bulk concentration of the reacting species, $\nu = 0.008917$ cm^2 s^{-1} is the kinematic viscosity of water at 25 °C, and ω is the angular frequency of rotation.

The analysis yielded the diffusion coefficients, (8.25 ± 0.25) × 10^{-6} and (9.42 ± 0.17) × 10^{-6} cm^2 s^{-1}, for the $[Fe(CN)_6]^{4-}$ and $[Fe(CN)_6]^{3-}$ ions, respectively. These are in good agreement with the literature data,[23] confirming that in this simple redox system (where no gas evolution is taking place) the hydrodynamic behavior of the iRDE is the same as that of normal RDEs.

Validation of the iRDE Design for a Gas-Evolving Reaction. We used the hydrogen evolution reaction (HER) as a model reaction in order to study the influence of gas formation on the hydrodynamic properties of the iRDE system.

For these measurements, a 0.1 mol dm^{-3} $NaClO_4$ electrolyte solution was prepared, the pH of which was adjusted to the value of 2.56 (checked with a pH meter) by the addition of a small amount of perchloric acid. Linear sweep voltammograms (sweep rate 50 mV s^{-1}) recorded on a Pt iRDE immersed in this solution exhibited a well-defined diffusion-limited plateau, as shown in Figure 3. Although in the case of this gas-evolving

https://dx.doi.org/10.1021/acs.analchem.9b04999
Anal. Chem. 2020, 92, 4301−4308

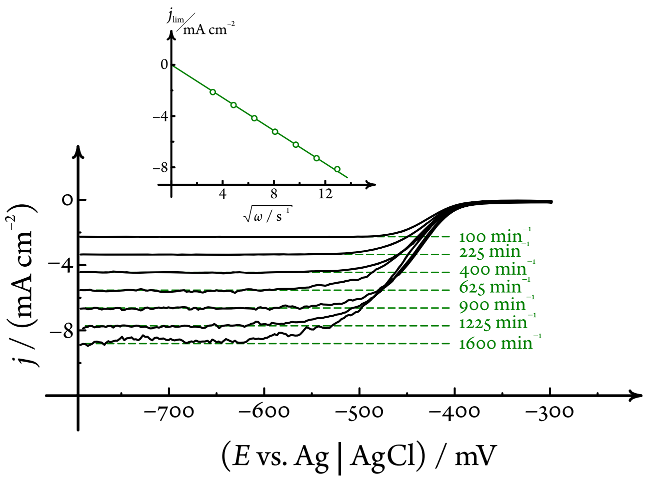

Figure 3. Validation of the hydrodynamic performance of the iRDE setup with HER, a gas-evolving reaction. Limiting currents measured by linear sweep voltammetry (sweep rate 50 mV s^{-1}) on a Pt iRDE in a pH 2.56 $HClO_4$/$NaClO_4$ solution scale linearly with the square root of the rotational rate. The dashed green lines are limiting current predictions of the Levich equation (eq 2), calculated using the diffusion coefficient value mentioned in the text at all of the given rotational rates.

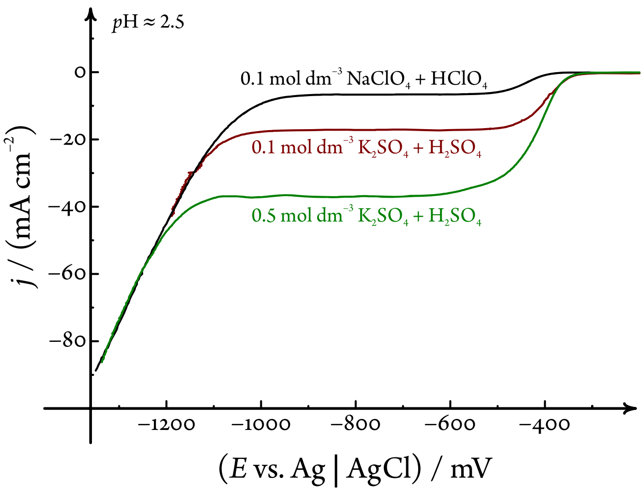

Figure 4. Although the bulk pH is about the same, LSVs obtained in different electrolyte solutions exhibit varying limiting currents for H^+ reduction. The sweep rate is 50 mV s^{-1}, the rotational rate is 900 min^{-1}, and the electrolyte compositions and the pH are shown in the graph. The given pH was set by adding a few drops of the respective concentrated acid to the electrolyte solution.

reaction the noise of the current signal was considerably higher compared to that of the previous case, the limiting currents did show a linear dependence on the square root of the rotational rate, and an analysis based on the Levich equation (eq 2) yielded a value of $(8.79 \pm 0.12) \times 10^{-5}$ cm^2 s^{-1} for the diffusion coefficient of H^+ ions, again matching previous reports well.

At this point we note that the aforementioned diffusion coefficient value was obtained by assuming that $c_{H^+} = 10^{-pH}$ mol dm^{-3} in eq 2. In other words, we considered a unity relative activity coefficient of H^+ ions, and we assumed that the limiting current is determined solely by the concentration of free H^+ in the solution.

While both of the above assumptions are fairly valid for a $HClO_4$/$NaClO_4$ electrolyte solution, they do not hold for more complex (i.e., buffered) systems. In K_2SO_4 solutions acidified with sulfuric acid, for example, we measured voltammograms that exhibited higher than expected limiting currents, confirming the previous experimental results of Nierhaus et al.[22] obtained with another iRDE design. In ref 22, this peculiar current enhancement was explained by an "extra stirring" of the electrolyte due to the produced H_2 bubbles. We believe, however, that there exists an alternative, more straightforward explanation, namely, that the current increase is due to the buffered nature of the H_2SO_4/K_2SO_4 system that contains not only H^+ but also HSO_4^- ions acting as a proton source.[10,24,25]

The above argument is supported by Figure 4, where three linear sweep voltammograms are compared. These LSVs were recorded in electrolyte (either $NaClO_4$ or K_2SO_4) solutions that were acidified to a pH value of about 2.5 by the addition of small volumes of the native, concentrated acid (either $HClO_4$ or H_2SO_4). Although the bulk pH and also other parameters (such as the sweep and rotational rates) of the recorded LSVs are essentially the same, Figure 4 reveals a pronounced difference in the limiting currents. We ascribe this 2- to 6-fold increase in the limiting current (depending on the sulfate concentration) to the buffering capacity of HSO_4^- ions.

Validation of the iRDE&GC Hyphenation. The hydrogen evolution reaction, leading to the formation of a single reaction product (H_2), is an ideal platform for validating the hyphenation of the iRDE design with GC detection. In order to achieve this, we applied a continuous Ar flow to the cell and led the gas in the headspace to the sampling loop of a gas chromatograph. After some 30 min of electrolysis, practically independent of the applied rotational rate, we were able to detect 100 ± 5% of the formed hydrogen gas. The latency can be explained by the gaseous product requiring a certain time to reach and fill up the sampling loop.

Figure 5a shows electrochemically measured and, based on eq 1, chromatographically determined currents of HER measured in a pH 3.75 $HClO_4$/ $NaClO_4$ solution at potentials in the limiting current region. Note that both currents, although matching each other relatively well, decay significantly and drop by about 28% of their initial values over the approximately 80 min time frame of the electrolysis.

This current drop, seen only in H-type iRDE cells equipped with a membrane, can be explained by a permanent pH change (also in the bulk of the solution), caused by the long-lasting electrolysis becoming partially exhaustive. Indeed, as shown by Figure 5b, the linear sweep voltammograms measured before and after electrolysis exhibit different limiting current values, and a corresponding pH change can also be measured directly with a meter. For the experiment shown in Figure 5b, the pH increased from a value of 3.76 to 3.93. This change scales well with the decrease in the limiting current (measured before and after the electrolysis) and is also in agreement with the H^+ concentration change that the charge of the electrolysis is expected to cause in the total electrolyte volume of the working compartment (about 87 cm^3 for this experiment).

It should further be noted with respect to the iRDE&GC hyphenation that for this system to deliver correct "chromatographic currents" it is crucial to make sure that all of the gas bubbles formed during the electrolysis reach the headspace and do not remain adhered to the tip surface. This can be assured by directing the purging gas inlet tube as close as possible to the tip (however, not directly to the electrode) surface.

https://dx.doi.org/10.1021/acs.analchem.9b04999
Anal. Chem. 2020, 92, 4301−4308

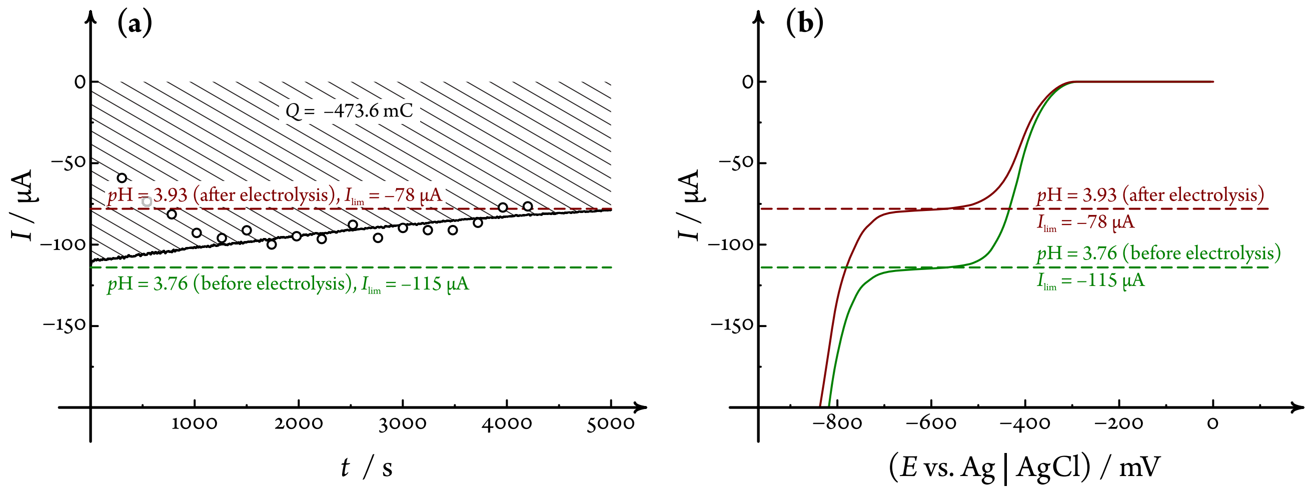

Figure 5. Results of long-term electrolysis (hydrogen evolution from a $HClO_4/NaClO_4$ electrolyte solution) measured by iRDE&GC. Currents measured electrochemically (full black curve) and chromatographically (calculated using eq 1, dots) at $E = -625$ mV vs Ag|AgCl are shown in (a). A slow drift (decay) over time can be observed as a result of the electrolysis becoming exhaustive. Values of pH measured before and after the electrolysis, along with limiting currents estimated using the respective H^+ concentrations and the diffusion coefficient of 8.79×10^{-5} cm^2 s^{-1} are shown by the dashed horizontal lines. This pH change is in alignment with the shifting of the LSV plateaus shown in (b) and also corresponds to the estimated H^+ concentration change calculated by taking into account the charge of the electrolysis, shown as the hatched area in (a), and a cell volume of 87 cm^3. The applied rotational rate was 1600 min^{-1}, and the linear sweep voltammograms were recorded at a sweep rate of 50 mV s^{-1}.

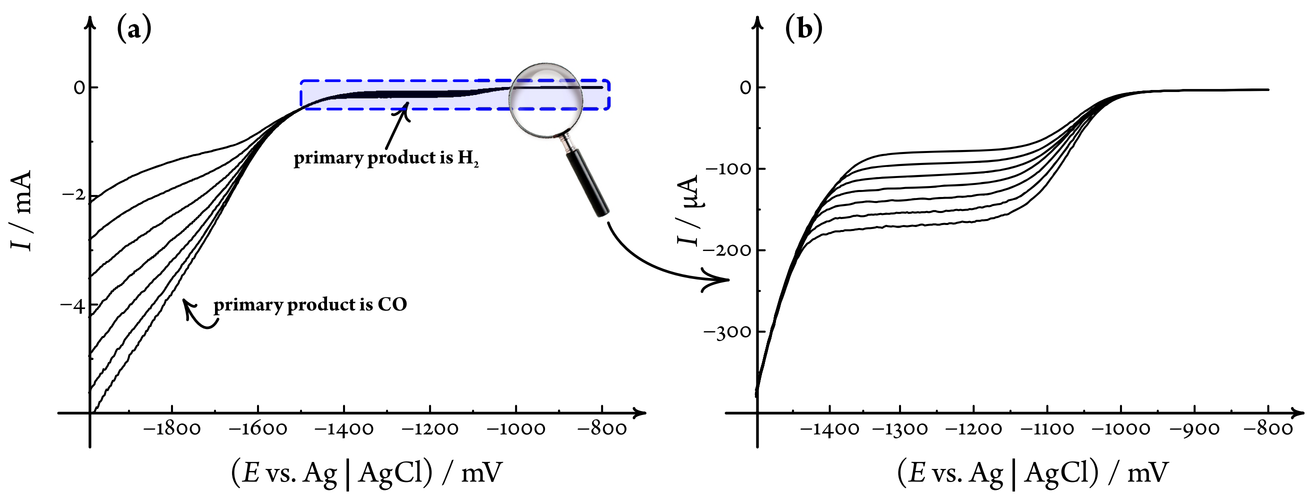

Figure 6. (a) Survey voltammograms recorded at a sweep rate of 50 mV s^{-1} on a Ag iRDE in a 0.1 mol dm^{-3} K_2SO_4 solution saturated with CO_2 (pH ~4.17). Cathodic currents increase with increasing rotational rates (100, 225, 400, 625, 900, 1225, and 1600 min^{-1}). (b) Hydrogen evolution attains a limiting current at lower overpotentials. At higher cathodic overpotentials, the electroreduction of CO_2 competes with the reduction of water. In this potential range, CO is the primary product of electrolysis.

Although the approach results in an elevated noise level of the electrochemical measurement, it has only a small effect on the hydrodynamics (cf. Figure 3, where this configuration was already used; the measured limiting currents, however, did remain well-defined).

Using the iRDE&GC System to Investigate the CO_2RR. In a further demonstrative experiment, we attempt to use the developed iRDE&GC system to study the electroreduction of carbon dioxide as it occurs on a silver iRDE in a 0.1 mol dm^{-3} K_2SO_4 solution saturated with CO_2 (pH ~4.17). We chose this specific electrolyte composition in order to get well-defined potential ranges where the predominant reduction product is either H_2 or CO.

Linear sweep surveys, shown in Figure 6a, revealed that HER goes on and becomes diffusion-limited in the potential range between −1.2 and −1.4 V vs Ag|AgCl: this range is displayed in detail in Figure 6b. It can be assumed that in this potential range the sole electrode reaction taking place is that described by eq 3,

$$2H^+ + 2e^- \rightarrow H_2 \tag{3}$$

where the reactant H^+ ions are present either in the form of free H^+ or in the form of HSO_4^-.

At potentials more cathodic than −1.6 V vs Ag|AgCl, we see the onset of another process: the electroreduction of CO_2 that yields CO as the primary product

$$CO_2 + 2H^+ + 2e^- \rightarrow CO + H_2O \tag{4}$$

Although the voltammograms in Figure 6a exhibit no clear plateaus for this process, they do confirm the limiting role of transport because the currents measured below −1.6 V clearly depend, more or less linearly, on the square root of the applied

https://dx.doi.org/10.1021/acs.analchem.9b04999
Anal. Chem. 2020, 92, 4301−4308

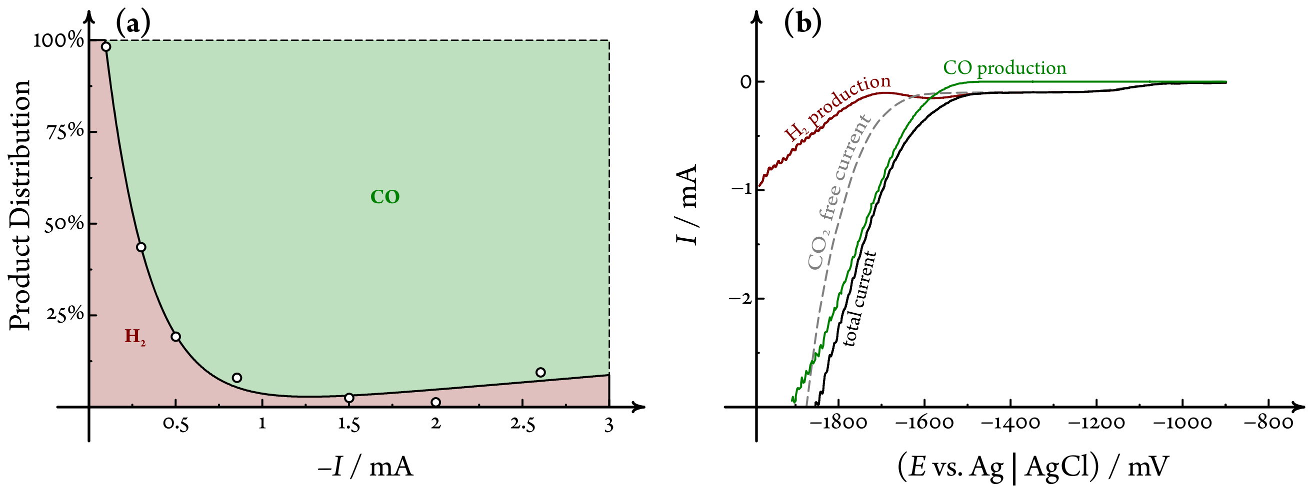

Figure 7. IRDE&GC system applied to the study of the electrolysis of a 0.1 mol dm^{-3} K_2SO_4 solution saturated with CO_2 (pH ~4.17). Applied rotational rate 625 min^{-1}. (a) Faradaic efficiencies of H_2 and CO formation are determined chromatographically (dots) and are interpolated using an arbitrary function (exponential decay superimposed on a straight line, black curve). (b) This interpolation allows the separation of the recorded LSVs: the total current and the partial currents of H_2 and CO production are shown as black, red, and green curves, respectively. An LSV measured in a CO_2-free (Ar-saturated) K_2SO_4 solution, the pH of which was set to 4.15 by direct H_2SO_4 addition, is shown as a reference (dashed gray curve).

rotational rate. This could be caused by a concentration limitation of either CO_2 or H^+ or both in the system under study: note that H^+ also appears as a reactant in eq 4.

It is very probable that at extremely cathodic potentials ($E < -1.8$ V vs Ag|AgCl) a third process, namely, the electrolysis of water molecules, should also occur

$$2H_2O + 2e^- \rightarrow H_2 + 2OH^- \quad (5)$$

again favoring the production of H_2 over that of CO. With respect to this process, it is important to note that its exact onset potential can be heavily affected by effects such as the buffer (HSO_4^-) concentration of the solution[25] and even the choice of the polishing material. Polishing with alumina particles, for example, was recently shown to shift the onset of water reduction to less cathodic potentials.[26] (More about the effect of alumina polishing can be read in the Supporting Information.)

The above-described scenario can be confirmed and even quantified by applying iRDE&GC hyphenation. By carrying out galvanostatic electrolyses of CO_2-saturated K_2SO_4 solutions at a fixed rotational rate (625 min^{-1}), we applied GC detection in order to determine the product distribution of the cathode process. In agreement with literature data,[27,28] the only detectable products were H_2 and CO, and within the first 40 min of the electrolyses, a 100% detection efficiency was practically achieved. After each electrolysis, the current was switched off and the electrolyte solution was replaced in order to avoid the accumulation of the exhaustion effects described in the previous section.

The recorded Faradaic efficiency vs current data were subjected to a numerical interpolation in order to determine the product distribution shown in Figure 7a. This figure allows a distinction among three current density regions with remarkably different product yields.

First, at currents not exceeding the limiting current of HER from acidic media (i.e., the maximal current that can be supplied by the reaction in eq 3), it seems that H_2 is the primary product of electrolysis, and there is very little, if any, detectable CO. At current densities exceeding this limiting current (about 0.1 mA for the system shown in Figure 7), there is a marked increase in CO productivity due to the onset of CO_2RR, as described by eq 4. The growing CO productivity trend continues up to the point where the current becomes approximately an order of magnitude higher than the limiting current of (acidic) HER, at which point the Faradaic efficiency of H_2 evolution will again increase. This is due to the onset of the direct reduction of water molecules according to eq 5.

The two aforementioned processes (CO_2RR and the reduction of water molecules) occur concomitantly, and the LSV recorded in the system (black curve in Figure 7b) exhibits no clear limiting current plateau for CO_2RR. Nevertheless, the interpolation shown in Figure 7a does create some means to separate the individual contributions of CO production (electroreduction) and H_2 formation (H^+ or water reduction) to the total current.

At each and every point on the LSV shown by the black curve in Figure 7b, we can calculate, using the interpolation of Figure 7a, the partial currents that correspond to CO and to H_2 formation. These partial currents are plotted as green and red curves, respectively, in Figure 7b. The sum of the partial currents, by definition, equals the total current shown by the black curve.

Identifying the two partial currents, as shown in Figure 7b, allows for a better understanding of the kinetics of CO_2RR: a reaction that is inevitably coupled to hydrogen evolution. The figure reveals that at potentials less cathodic than the onset potential of CO_2RR, all measured currents can be attributed to hydrogen evolution, and this section of the LSV is identical to that measured in a CO_2-free electrolyte solution of the same pH (dashed gray curve shown as a reference in Figure 7b).

The onset of CO_2 reduction allows the cathodic current to increase beyond the limiting current of (acidic) hydrogen evolution at $E < -1.5$ V vs Ag|AgCl. This current increase, at least initially, can be fully ascribed to CO_2 electroreduction: the reduction of water molecules only seems to commence at more negative potentials, $E < -1.75$ V. Note that the apparent onset potential of water reduction is about 150 mV more negative in the CO_2-saturated solution than in the CO_2-free

https://dx.doi.org/10.1021/acs.analchem.9b04999
Anal. Chem. 2020, 92, 4301−4308

reference system and that the partial current of H_2 production does not rise monotonically with the applied potential. It seems more than plausible to assume that this peculiar feature, revealed by the iRDE&GC hyphenation, can be explained by the H^+ consumption of CO_2RR, as described by eq 4. Due to the autoprotolysis equilibrium of water, the H^+ consumption of CO_2RR leads to an increase in near-surface OH^- concentrations, and as OH^- ions appear as a product in eq 5, this shifts the onset of water reduction toward more cathodic values.

CONCLUSIONS

We presented the design of a custom-made, hermetically sealed inverted rotating disk electrode coupled to a gas chromatographic detection system. The developed iRDE&GC system is suitable for electrochemical kinetic studies with the simultaneous analysis of the formed (gaseous) reaction products. The performance of the iRDE&GC hyphenation was evaluated using the ferro-/ferricyanide redox system and the hydrogen evolution reaction as test settings.

Apart from having conducted a successful validation of the iRDE&GC system, we pointed out two major caveats of the design. Probably the most important condition of using the iRDE&GC hyphenation is related to an inherent property of any GC-based headspace analyses in electrochemistry, namely, that the electrolyses must hold long enough that the reaction products can accumulate in the sampling loop in a sufficient amount in order to facilitate 100% detection. Even in the case of an upward-facing iRDE system it seems unavoidable to carefully orient the purging gas flow to remove any formed gas bubbles that could otherwise remain adhered to the electrode tip, resulting in detection deficiencies. Special care must be taken in this situation so that the purging gas flow does not interfere with the convective transport of the rotating disk.

Another important point that deserves emphasis is related to the transport conditions of the iRDE cell. In this hydrodynamic configuration, convection allows for a much higher rate of transport, compared to that in other quiescent systems. Although it is usually assumed that on rotating electrodes stationary current/potential characteristics can be attained, this condition may not hold for long-lasting experiments during which the electrolysis becomes at least partially exhaustive. This second limitation may, however, be overcome if the electrolyte solution is replaced from time to time or when a continuous flow of electrolyte guarantees that no permanent bulk concentration changes can be caused by the electrolysis.

We have further shown, by means of one demonstrative experiment, that the developed iRDE&GC hyphenation can have great potential in understanding the kinetics of technologically relevant electrochemical processes. We demonstrated that in the case of carbon dioxide reduction on silver electrodes the iRDE&GC setup allows for a resolution of the voltammetric response to individual contributions of actual reduction and hydrogen evolution.

ASSOCIATED CONTENT

Supporting Information

The Supporting Information is available free of charge at https://pubs.acs.org/doi/10.1021/acs.analchem.9b04999.

Scanning electron micrographs and energy-dispersive X-ray spectra of alumina and diamond-polished silver RDE surfaces (PDF)

AUTHOR INFORMATION

Corresponding Authors

Pavel Moreno-García – *Department of Chemistry and Biochemistry, University of Bern, CH–3012 Bern, Switzerland*; orcid.org/0000-0002-6827-787X; Email: pavel.moreno@dcb.unibe.ch

Soma Vesztergom – *Department of Physical Chemistry, Eötvös Loránd University of Budapest, H–1117 Budapest, Hungary*; orcid.org/0000-0001-7052-4553; Email: vesztergom@chem.elte.hu

Authors

Noémi Kovács – *Department of Chemistry and Biochemistry, University of Bern, CH–3012 Bern, Switzerland; Department of Physical Chemistry, Eötvös Loránd University of Budapest, H–1117 Budapest, Hungary*

Vitali Grozovski – *Department of Chemistry and Biochemistry, University of Bern, CH–3012 Bern, Switzerland*

María de Jesús Gálvez-Vázquez – *Department of Chemistry and Biochemistry, University of Bern, CH–3012 Bern, Switzerland*

Peter Broekmann – *Department of Chemistry and Biochemistry, University of Bern, CH–3012 Bern, Switzerland*; orcid.org/0000-0002-6287-1042

Complete contact information is available at: https://pubs.acs.org/10.1021/acs.analchem.9b04999

Author Contributions

[§]These authors contributed equally.

Notes

The authors declare no competing financial interest.

ACKNOWLEDGMENTS

We kindly acknowledge the efforts dedicated to this project by Mr. Thomas Hübscher and Mr. René Schraner of the mechanical and electronics workshops of the University of Bern. Support by the CTI Swiss Competence Center for Energy Research (SCCER Heat and Electricity Storage) is gratefully acknowledged. P.B. acknowledges financial support from the Swiss National Foundation (grant 200020-172507). S.V. acknowledges support from the National Research, Development and Innovation Office of Hungary (NKFIH grant PD124079). M.d.J.G.-V. and N.K. acknowledge the financial support of the Swiss Government Excellence Scholarships for Foreign Scholars (ESKAS).

REFERENCES

(1) Vesztergom, S. In *Encyclopedia of Interfacial Chemistry: Surface Science and Electrochemistry*; Wandelt, K., Ed.; Elsevier: Amsterdam, 2018; pp 421–444.

(2) Levich, B. *Discuss. Faraday Soc.* **1947**, *1*, 37–49.

(3) Kuhn, A. T.; Chan, C. Y. *J. Appl. Electrochem.* **1983**, *13*, 189–207.

(4) Ying, R. Y. *J. Electrochem. Soc.* **1988**, *135*, 2964–2971.

(5) Vos, J. G.; Koper, M. T. M. *J. Electroanal. Chem.* **2018**, *819*, 260–268.

(6) Hall, A. S.; Yoon, Y.; Wuttig, A.; Surendranath, Y. *J. Am. Chem. Soc.* **2015**, *137*, 14834–14837.

(7) Bandi, A. *J. Electrochem. Soc.* **1990**, *137*, 2157–2160.

(8) Aoki, A.; Nogami, G. *J. Electrochem. Soc.* **1995**, *142*, 423–427.

(9) Bandi, A.; Kühne, H.-M. *J. Electrochem. Soc.* **1992**, *139*, 1605–1610.

(10) Ooka, H.; Figueiredo, M. C.; Koper, M. T. M. *Langmuir* **2017**, *33*, 9307–9313.

(11) Dutta, A.; Kuzume, A.; Kaliginedi, V.; Rahaman, M.; Sinev, I.; Ahmadi, M.; Roldán Cuenya, B.; Vesztergom, S.; Broekmann, P. *Nano Energy* **2018**, *53*, 828−840.
(12) Murakami, T.; Nishikiori, T.; Nohira, T.; Ito, Y. *J. Am. Chem. Soc.* **2003**, *125*, 334−335.
(13) Zhou, F.; Azofra, L. M.; Ali, M.; Kar, M.; Simonov, A. N.; McDonnell- Worth, C.; Sun, C.; Zhang, X.; MacFarlane, D. R. *Energy Environ. Sci.* **2017**, *10*, 2516−2520.
(14) Rudnev, A. V. In *Encyclopedia of Interfacial Chemistry: Surface Science and Electrochemistry*; Wandelt, K., Ed.; Elsevier: Amsterdam, 2018; pp 321−325.
(15) Fleige, M. J.; Wiberg, G. K. H.; Arenz, M. *Rev. Sci. Instrum.* **2015**, *86*, No. 064101.
(16) Jung, S.; Kortlever, R.; Jones, R. J. R.; Lichterman, M. F.; Agapie, T.; McCrory, C. C. L.; Peters, J. C. *Anal. Chem.* **2017**, *89*, 581−585.
(17) Riddiford, A. C. In *Advances in Electrochemistry and Electrochemical Engineering*; Delahay, P., Ed.; Interscience: New York, 1966; pp 47−116.
(18) Zdunek, A. D. *J. Electrochem. Soc.* **1992**, *139*, 2549−2551.
(19) Bressers, P. M. M. C.; Kelly, J. J. *J. Electrochem. Soc.* **1995**, *142*, L114−L115.
(20) Bradley, P. E.; Landolt, D. *J. Electrochem. Soc.* **1997**, *144*, L145−L148.
(21) Parys, H. V.; Tourwé, E.; Breugelmans, T.; Depauw, M.; Deconinck, J.; Hubin, A. *J. Electroanal. Chem.* **2008**, *622*, 44−50.
(22) Nierhaus, T.; Parys, H. V.; Dehaeck, S.; van Beeck, J.; Deconinck, H.; Deconinck, J.; Hubin, A. *J. Electrochem. Soc.* **2009**, *156*, P139−P148.
(23) Konopka, S. J.; McDuffie, B. *Anal. Chem.* **1970**, *42*, 1741−1746.
(24) Grozovski, V.; Vesztergom, S.; Láng, G. G.; Broekmann, P. *J. Electrochem. Soc.* **2017**, *164*, E3171−E3178.
(25) Auinger, M.; Katsounaros, I.; Meier, J. C.; Klemm, S. O.; Biedermann, P. U.; Topalov, A. A.; Rohwerder, M.; Mayrhofer, K. J. J. *Phys. Chem. Chem. Phys.* **2011**, *13*, 16384−16394.
(26) Monteiro, M. C.; Koper, M. T. *Electrochim. Acta* **2019**, *325*, 134915.
(27) Hori, Y.; Wakebe, H.; Tsukamoto, T.; Koga, O. *Electrochim. Acta* **1994**, *39*, 1833−1839.
(28) Dutta, A.; Morstein, C. E.; Rahaman, M.; Cedeño López, A.; Broekmann, P. *ACS Catal.* **2018**, *8*, 8357−8368.

https://dx.doi.org/10.1021/acs.analchem.9b04999
Anal. Chem. 2020, 92, 4301−4308

SUPPORTING INFORMATION

for the paper

Towards CO_2 Electroreduction under Controlled Mass Flow Conditions: A Combined Inverted RDE & Gas Chromatrography Approach

Pavel Moreno-García[a,1,*], Noémi Kovács[a,b,1], Vitali Grozovski[a], María de Jesús Gálvez-Vázquez[a], Soma Vesztergom[b,*], Peter Broekmann

[a] *University of Bern, Department of Chemistry and Biochemistry*
Freiestraße 3, CH–3012 Bern, SWITZERLAND

[b] *Eötvös Loránd University, Department of Physical Chemistry*
Pázmány Péter sétány 1/A, H–1117 Budapest, HUNGARY

Contents

*Corresponding authors.
Email addresses: pavel.moreno@dcb.unibe.ch (Pavel Moreno-García), vesztergom@chem.elte.hu (Soma Vesztergom)

[1] These authors contributed equally.

1. SEM and EDX Mapping of Alumina and Diamond Polished Silver RDEs

In a recent work (cited as Ref. 26 of the paper), Monteiro and Koper described an interesting phenomenon; namely, that the contamination of gold electrodes with alumina particles by electrode polishing leads to an enhancement in activity for hydrogen evolution (HER). In order to see whether alumina particles also exert an effect on the results of CO_2 electroreduction on silver RDEs (studied in our paper by the iRDE&GC hyphenation), we used both alumina and diamond suspensions (both of 50 nm particle size) for the polishing of an Ag RDE.

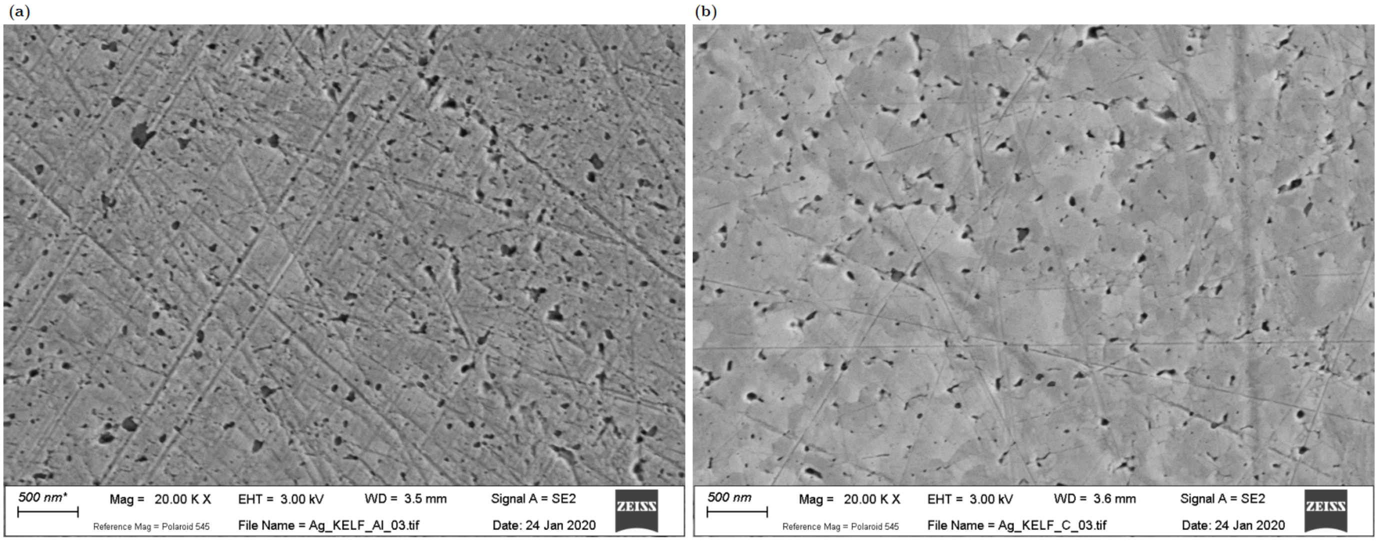

Figure S1: SEM micrographs of the surface of an Ag RDE polished by 50 nm alumina (a) and diamond (b) particles. (Zeiss Gemini 450 SEM, Germany; accelerating voltage: 3 kV, working distance: 3.5–3.6 mm.)

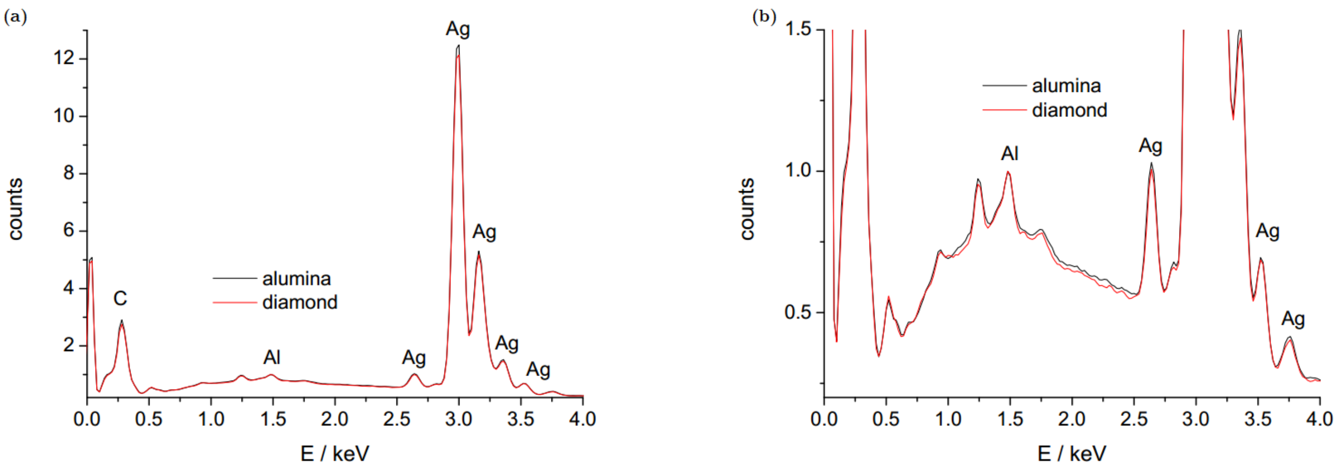

Figure S2: EDX spectra of an alumina and a diamond polished Ag RDE surface, overlapped in one plot, shown at different scaling in (a) and (b). The spectra were normalized to the Ka line of aluminum (1.48 keV). The main peaks are labelled (Ag, C and Al). An accelerating voltage of 10 kV and a working distance of 8.5 mm was applied.

SEM micrographs of the surfaces, shown in Figure S1, revealed no major differences between the two surfaces polished by different materials. The EDX spectra of the two surfaces, Figure S2, also showed minor if any differences. EDX revealed that the diamond-polished surface contains ~ 0.4 wt% Al, while the one polished by alumina (and then rinsed abundantly with MilliQ water) showed only a ~ 0.3 wt% (that is, even less) Al content.

We are aware that EDX may not be sensitive enough to indicate small Al contaminations that can already have a significant effect on the electrochemical measurements, thus we also repeated an iRDE&GC experiment under the same conditions that we applied for Figure 7 of the paper. By applying a current density of -2.6 mA and a rotation rate of 625 min^{-1} we detected a $93.8\% \pm 4.5\%$ Faradaic efficiency for the production of CO on an Ag iRDE polished by a diamond suspension; for the alumina-polished electrode, this value was $90.5\% \pm 4.3\%$. Although there are some minor differences, pointing in the direction suggested by Ref. 26, it seems that the iRDE&GC hyphenation is not sensitive enough to point these out.

1.9 Inverted RDE (iRDE) as Novel Test Bed for Studies on Additive-Assisted Metal Deposition under Gas-Evolution Conditions

Authors: Pavel Moreno-García, Vitali Grozovski, María de Jesús Gálvez Vázquez, Nisarga Mysuru, Kiran, Noémi Kovács, Yuhui Hou, Soma Vesztergom, and Peter Broekmann

J. Electrochem. Soc., **167** (4), 042503 (2020), DOI: 10.1149/1945-7111/ab7984

Highlights: A custom-made hermetically sealed inverted rotating disc electrode (iRDE) instrument coupled to gas chromatography for quantitative analysis of gas evolving processes was implemented to investigate the influence of a model redox-active suppressor additive on the electrochemical deposition of cobalt using linear sweep voltammetry and galvanostatic electrolysis. It was found that the addition of minor amounts of the additive to the standard cobalt-based virgin make-up solution significantly decreases the rate and efficiency of Co deposition and favors the competing hydrogen evolution under specific experimental conditions. It was possible to deconvolve the overall process into its three individual components: metal ion reduction, HER, and the additive activation process.

Contribution: I was responsible for the ex situ SEM and EDX characterization of the iRDE working electrode after the different electrodeposition conditions were applied.

Journal of The Electrochemical Society

Inverted RDE (iRDE) as Novel Test Bed for Studies on Additive-Assisted Metal Deposition under Gas-Evolution Conditions

Journal of The Electrochemical Society, 2020 **167** 042503
1945-7111/2020/167(4)/042503/6/$40.00 © 2020 The Electrochemical Society ("ECS"). Published on behalf of ECS by IOP Publishing Limited

Inverted RDE (iRDE) as Novel Test Bed for Studies on Additive-Assisted Metal Deposition under Gas-Evolution Conditions

Pavel Moreno-García,[1,z] Vitali Grozovski,[1] María de Jesús Gálvez Vázquez,[1] Nisarga Mysuru,[1] Kiran Kiran,[1] Noémi Kovács,[1,2] Yuhui Hou,[1] Soma Vesztergom,[1,2] and Peter Broekmann[1,*,z]

[1]*Department of Chemistry and Biochemistry, University of Bern, Switzerland*
[2]*Department of Physical Chemistry, Eötvös Loránd University, Budapest 1117, Hungary*

The development of Co interconnects by electrochemical means is more challenging than that of Cu interconnects not only due to the ever decreasing critical feature dimensions but also to intrinsic complications of the water/Co system, as Co electrodeposition processes are inevitably plagued by the competing hydrogen evolution reaction (HER). We present herein a novel custom-made inverted RDE instrument, particularly suitable for studying additive-assisted metal deposition processes that are accompanied by HER or any other gas evolving side reactions. We investigate the influence of a model redox-active suppressor additive on the electrochemical deposition of cobalt by means of linear sweep voltammetry and galvanostatic electrolysis coupled to online gas chromatography analysis. We find that under specific experimental conditions, addition of minor amounts of the additive to the standard Co-based virgin make-up solution significantly decreases the rate and efficiency of Co deposition, and favours instead the competing HER. Moreover, we identify and quantify the reductive conversion of the additive that accompanies the primary metal deposition process. Importantly, our approach complements standard screening Co plating studies as it succeeds to directly deconvolve the overall process into its three individual components, namely the metal ion reduction, the HER and the additive activation process.
 [DOI: 10.1149/1945-7111/ab7984]

Manuscript submitted January 18, 2020; revised manuscript received February 13, 2020. Published March 4, 2020.

Supplementary material for this article is available online

For the last two decades, the manufacture of state-of-the-art back-end-of-line (BEOL) interconnect structures has been based on Cu electrodeposition processes.[1,2] However, the critical dimension of such structures has currently approached the electron mean free path (MFP) of copper, introducing new challenges to the continuous scaling of interconnects for the 7 nm technology node and beyond.[3–5] Reports on shorter MFP metals (e.g., Ni, Co, Mo, and Ru) that are less prone to resistance scaling effects keep promise to continue downsizing device dimensions.[3,6–12] Similarly to what was done for copper, the electrochemical screening of additive-assisted cobalt plating processes for cutting-edge interconnects is based on rotating disc electrode (RDE) approaches.[13–17] Nonetheless, the manufacture of Co interconnects by wet methods is found to be more challenging than it was in the case of Cu, not only due to the ever decreasing critical feature dimensions but also due to the intrinsic complications of the water/Co system. Co electrodeposition processes, carried out from aqueous plating baths, are unavoidably accompained by the hydrogen evolution reaction (HER). The standard reduction potential of Co^{2+} to metallic Co lies 280 mV more negative than that of H^+ to H_2.[16,18,19] This implies that, unlike Cu, a complete description of the Co electroplating process requires quantification of the parasitic gas evolving process. Obviously, the realization of gas analysis coupled to RDE experiments is challenging, since it requires a hermetic sealing of the cell around rotating elements and the implementation of gas analysis techniques, e.g., gas chromatography (GC). Additionally, a fraction of the electrochemically generated gas bubbles typically adheres to the surface of both the RDE working electrode and its embedding shaft, preventing them from reaching the solution-gas interface. This partial shielding of active electrode sites by bubble retention at the RDE tip undermines the accuracy of the electrochemical measurements and hinders quantitative analysis of the gaseous products collected from the headspace of an electrochemical reactor. Therefore, we present here an inverted RDE (*i*RDE) cell design, coupled to GC for the first time, that helps overcoming these technical limitations.[20] Note that although alternative *i*RDE-based investigations have been previously reported demonstrating that the analytical equations of mass and charge transfer valid for the conventional RDE also comply with the proposed *i*RDEs, no quantitative analysis of electrochemically generated gaseous products was carried out in these cells.[21–27] Our home-developed instrument features important assets: *i*) it is amenable to the same mathematical treatment as standard (downward facing) RDEs; *ii*) it can be operated air-tight and coupled to online GC; and *iii*) due to its upward facing design, the electrode surface is less prone to blockage by any formed gas bubbles.

In this paper we investigate the influence of a model redox-active suppressor additive on the electrochemical deposition of cobalt by means of linear sweep voltammetry and galvanostatic electrolysis, coupled to an online detection of gaseous products by gas chromatography. We find that the addition of minor amounts (60 ppm) of the model suppressor additive to the standard Co-based virgin make-up solution (VMS) significantly decreases the efficiency of Co deposition and favours the competing hydrogen evolution reaction instead, when lower current densities than those corresponding to the limiting current density value of H^+ reduction are applied. In addition, we are able to identify and quantify a reductive conversion of the additive that comes along with the deposition process. Importantly, as schematically depicted in Fig. 1, our approach complements standard screening Co plating studies because it succeeds to deconvolve the overall process into its individual components, e.g., Co^{2+} reduction to metallic Co, HER and reductive additive activation.

Experimental

$CoSO_4 \cdot 7H_2O$ (ReagentPlus, ⩾ 99%) and H_3BO_3 (ReagentPlus, 99.97%) were purchased from Sigma-Aldrich. H_2SO_4 (96% Suprapure) was purchased from Merck. The VMS cobalt plating solution (50 mM $CoSO_4 \cdot 7H_2O$, 0.5 M H_3BO_3, adjusted to pH 2.5 by H_2SO_4 addition) was prepared with as-received chemicals and Milli-Q water (18.2 MΩ cm, TOC ⩽ 5 ppb, Millipore).[15,18] The electrolyte was deoxygenated by Ar bubbling (99.9999%, Carbagas, Switzerland) through the solution for 20 min prior to the measurements. All electrochemical measurements were performed at room temperature by a potentiostat/galvanostat system (Metrohm Autolab

*Electrochemical Society Member.
[z]E-mail: pavel.moreno@dcb.unibe.ch; peter.broekmann@dcb.unibe.ch

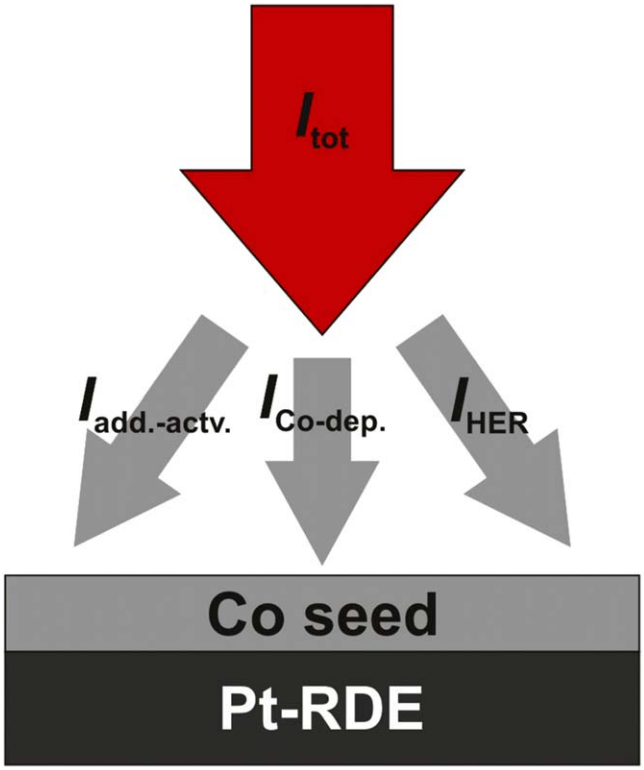

Figure 1. Scheme representing the deconvolution of the overall cathodic process into its individual components by the *i*RDE&GC approach.

128 N, The Netherlands) in a three electrode configuration using a custom-made H-type glass cell fitted on top of the *i*RDE. Ionic conductivity between the two cell compartments was achieved via a proton exchange membrane (Nafion 117, Sigma-Aldrich). A leakless $Ag/AgCl_{3M}$ electrode (Metrohm, Switzerland) and a Pt wire (99.99% MaTeck) were used as reference and counter electrode, respectively. The support working electrode for Co deposition was a 5 mm diameter, 4 mm thick Pt disk purchased from MaTeck. The electrode was pressed and embedded into the home-made polytetrafluoroethylene (PTFE) shaft of the *i*RDE setup. Prior to the electrochemical measurements, the electrode was first polished on a polishing cloth (Buehler) to a mirror finish with 0.05 μm alumina particles (Micropolish, Buehler) and thoroughly rinsed by Milli-Q water. The Pt surface was then covered for 1 min by a drop of fresh piranha solution followed by rinsing with Milli-Q water. Finally the surface was electrochemically polished in 1 M H_2SO_4 by sequential oxidation/reduction at ±4 V, respectively, for 30 s each, and the surface was then rinsed and protected by a droplet of Milli-Q water.

All electrochemical investigations were carried out on Co-seeded Pt electrodes. The seed was deposited at -10 mA cm^{-2} and 100 rpm for 25 s.

The ohmic resistance of the solution was determined by means of electrochemical impedance spectroscopy (EIS) at various applied sample potentials where no electrochemical reactions take place. The applied potentials for linear sweep voltammetry and galvanostatic Co electrodeposition accounted for the *IR* drop accordingly.

The Co current efficiencies (FE_{Co}) in galvanostatic electrodeposition measurements were determined by integrating the current of anodic dissolution experiments of the respective Co layers at $E =$ 0.5 V vs $Ag|AgCl_{3M}$. The Co seed contribution was taken into account (subtracted) for the efficiency determination. Gaseous products generated during Co deposition from the HER (or any other side reaction) were analyzed by online gas chromatography (GC, SRI Instruments Multi-Gas Analyzer #3) hermetically connected to the *i*RDE. The continuous flow of Ar through the electrolysis cell during Co deposition carried the volatile reaction products from the headspace of the *i*RDE cell ensemble into the sampling loops of the gas chromatograph. The partial current density j_i of any gaseous product is calculated using Eq. 1:

$$j_i = x_i n_i F \cdot \nu_m \quad [1]$$

where x_i represents the volume fraction of product *i* measured via online GC using an independent calibration standard gas (Carbagas, Switzerland), n_i the number of electrons involved in the electrochemical reaction to form it (here 2 for H_2 evolution), *F* the Faraday constant (96485.3 C mol^{-1}) and ν_m the molar Ar gas flow rate measured by a universal flowmeter (7000 GC flowmeter by Ellutia) at the exit of the electrochemical cell. The partial current density for the produced H_2 was normalized to the total current density thus providing the faradaic efficiency of H_2 production (FE_{H2}).

To demonstrate the usefulness of our *i*RDE&GC approach for additive-assisted metal deposition screening investigations, dedicated linear sweep voltammetric and galvanostatic deposition experiments employing VMS plating baths containing 60 ppm of a model suppressing additive were also carried out. The additive-carrying VMS solution is denoted as VMS-ADD hereafter.

Ex situ SEM-EDS analyses of the *i*RDE working electrodes at different stages of the Co electrodeposition were performed using a Zeiss instrument (Gemini 450 SEM, Germany). The recorded SEM images were acquired at 3 kV, 3.4–3.6 mm and 100 pA as accelerating voltage, working distance and current. The corresponding applied values for the EDS investigations were 18 kV, 8.5 mm and 300 pA. These results are shown in Fig. S1 (available online at stacks.iop.org/JES/167/042503/mmedia) of the Supplementary Information file.

Results and Discussion

iRDE and cell assembly.—In this section we provide a brief description of the custom-made *i*RDE&GC setup. Detailed description of the instrument can be found in Ref. 20. The hermetically tight *i*RDE cell consists of two separable compartments made of modified 80 ml round borosilicate glass flasks (see upper part in Fig. 2A). Reference electrode, counter electrode and gas input and outlet necks with custom winding are attached hermetically to the flasks by custom-made polytetrafluoroethylene (PTFE) caps and O-ring fittings. Physical connection between compartments is provided by a Nafion proton exchange membrane separating catholyte from anolyte. Both compartments are provided with gas inputs and outlets via PTFE caps to feed Ar gas to the cell and chromatograph, respectively. The main features of the *i*RDE setup are shown in Fig. 2. The contacting part (*b*, *b*') of the *i*RDE with the glass cell is machined of polyoxymethylene polymer (POM). It provides rigid connection to the RDE rotator (AFMSRCE from Pine, not shown) and bears a cone joint to fit the outer socket of the *i*RDE cell (size 29/32, ground glass joint standard). The rotation momentum is transferred by a modified RDE shaft (*a*, *a*') that fits the MSR rotator. It bears two ceramic sleeves (*q*) that pass through radial shaft seals (*k*). A pressure chamber (*l*) confined between the radial shaft seals is fed by N_2 or Ar gas (99.999% Carbagas Switzerland) through a lateral pressuring gas inlet (*j*) to enforce a constant pressure of 0.2–0.4 bar above the ambient pressure. Note that the enforced pressure inside the gland chamber (*l*) has no influence on the inner part of the electrochemical cell. It simply ensures that the electrolyte contained by the working cell compartment (*c*) does not leak through the seal surrounding the upper rotating ceramic fitting (*q*). The pressurized chamber is a single POM tube fixed in the main housing. The latter also holds both radial shaft seals in place. The shaft exact coaxial position is maintained by a ball bearing (*m*) situated in the upper part of the pressure chamber. The radial shaft seals are made of high quality Vitton rubber and operate oil/grease-free. Note that the upper seal (*k*) comes in contact with the solution in the *i*RDE cell compartment. The RDE working electrode is pressed into a lab made PTFE holder (*n*), which is fitted into the upper ceramic sleeve.

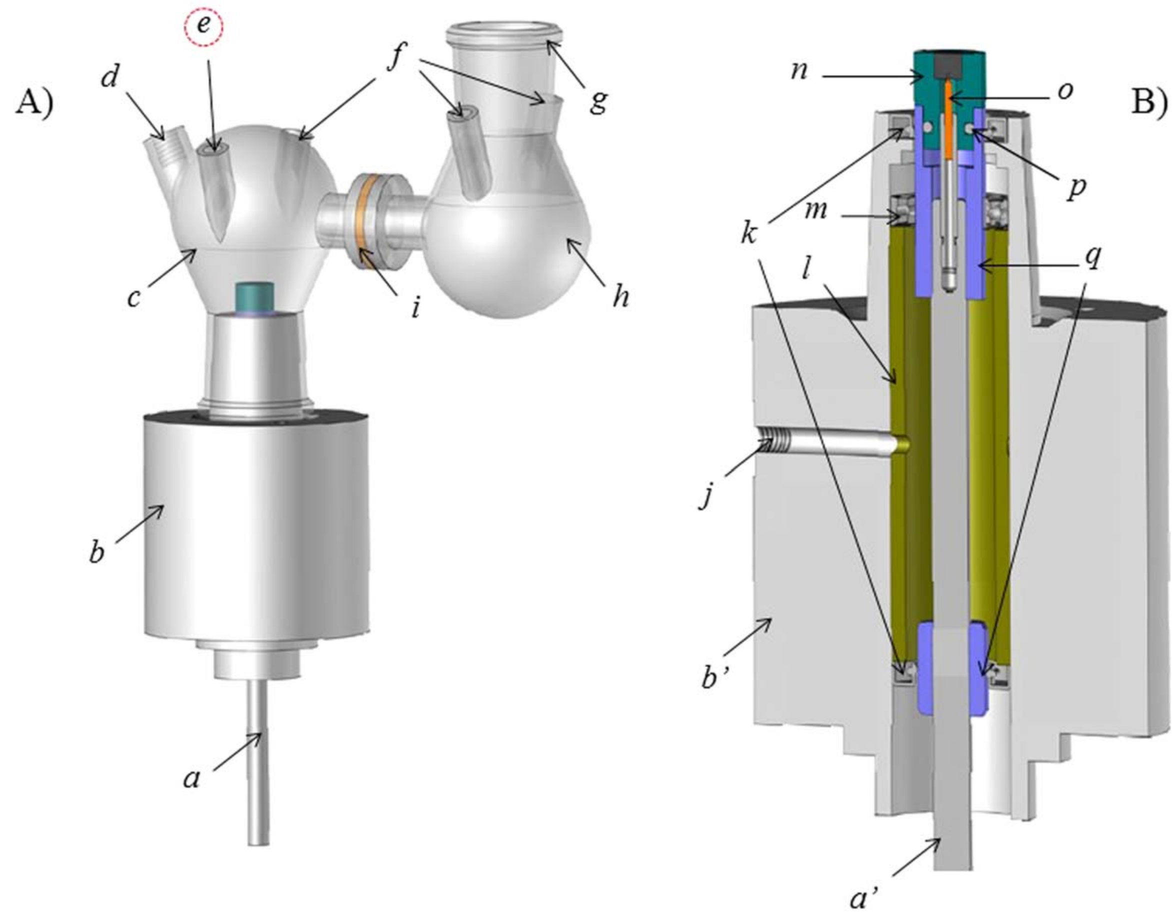

Figure 2. Schematic representation of the (A) H-type cell mounted on the *i*RDE assembly and (B) cross-section of the *i*RDE setup. Components of the design are *a*/*a'*: rotating shaft; *b*/*b'*: *i*RDE housing; *c*: working cell compartment; *d*: reference electrode inlet; *e*: purging gas outlet for GC analysis; *f*: purging gas inlet/outlet; *g*: counter electrode inlet; *h*: counter cell compartment; *i*: H^+ exchange membrane; *j*: pressurized gas inlet; *k*: radial shaft seals; *l*: pressurized gland chamber; *m*: ball bearing; *n*: PTFE *i*RDE tip with embedded electrode; *o*: spring contact node; *p*: PTFE tip groove for O-ring fitting; *q*: ceramic fittings.

Tightness between the RDE holder and the upper ceramic sleeve is maintained by an O-ring placed in the groove of the PTFE holder (*p*). The spring contact from the shaft (*o*) provides the electrical contact for the working electrode. The whole system is maintenance friendly and the radial shaft sealings can be straightforwardly exchanged once they are worn out.

Quantification of Co and H_2 current efficiencies by iRDE&GC during galvanostatic deposition.—Figure 3 displays an overview of the *i*RDE&GC-based metal deposition approach that we introduce to quantitatively describe the overall electrochemical process. Similarly to superconformal Co deposition on patterned wafers, the plating studies are performed on Co-seeded supports to match the experimental conditions of metal interconnect manufacture as closely as possible.[13–15,17] Prior to Co layer deposition, a thin Co seed was deposited from the additive-free VMS solution at –10 mA cm^{-2} and 100 rpm for 25 s. This condition ensures high Co deposition efficiencies necessary to yield a compact, homogeneous Co seed layer on the Pt-RDE support without the interference of generated bubbles. Figures S1A–S1B show typical SEM characterization of a Pt-*i*RDE working electrode before and after Co seed deposition. The corresponding EDS spectra displayed in Figs. S1F–S1G reveal the presence of the thin Co layer on top of the underlying Pt support that forms upon electrochemical deposition. This seed layer was then anodically dissolved back into the plating bath at 0.5 V vs $Ag/AgCl_{3M}$. This seed deposition/dissolution procedure was applied three times to estimate the average Co seed current efficiency from the respective Q_{diss}/Q_{dep} ratios before every Co bulk deposition experiment was carried out (Figs. 3A–3B). A typical example of such calculation is displayed in Fig. S2. Based on a significant

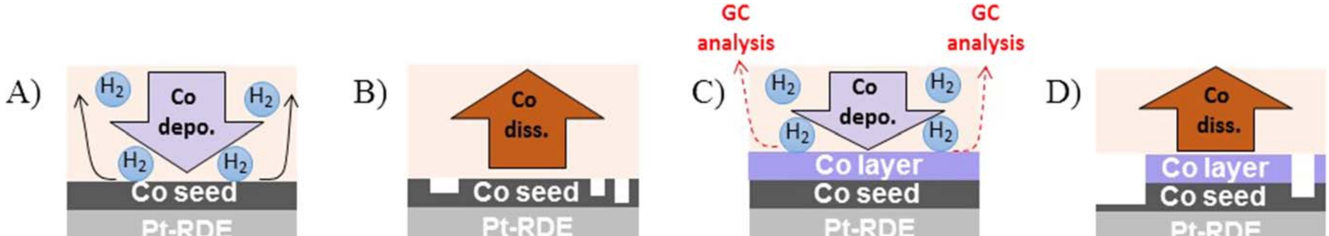

Figure 3. Schematic representation of the iRDE&GC approach for quantification of the galvanostatic Co deposition and accompanying HER efficiencies: (A) galvanostatic Co seed deposition on rotating Pt disk support; (B) anodic Co seed dissolution; (C) galvanostatic Co layer deposition on Co-seeded Pt – *i*RDE and simultaneous analysis of gaseous products by online gas chromatography; (D) Anodic dissolution of the whole Co deposit.

amount of iterations, the Co seed deposition efficiency was found to be (72.6 ± 4.8) %. The high current efficiency and morphological homogeneity of the deposited seed layer are due to the applied current density being higher than the expected mass transport limiting current for proton reduction under the applied conditions. Additionally, the electrogenerated bubbles do not interfere with the metal deposition and straightforwardly detach from the solid liquid interface due to the upward facing configuration of the iRDE and the applied rotation. Next, galvanostatic Co layer deposition was performed on a freshly seeded support at selected current density, angular frequency and deposition time. Simultaneously, electrogenerated gaseous products (here H_2) were analyzed at selected time intervals by the coupled gas chromatograph as soon as the layer deposition set in (Fig. 3C). Once the desired layer was achieved, the electrodeposited Co was anodically dissolved back into the VMS solution (Fig. 3D). Finally, the Co layer current efficiency was determined analogously to the case of the seed, this time by subtracting the charge corresponding to the seed dissolution. Addition of FE_{Co} and FE_{H2} thus renders quantitative description of the whole process (additive-free case). Note that direct assessment of the parasitic HER contribution by a dedicated method is usually missing, and its introduction to metal deposition studies enables unequivocal confirmation of the electrochemical data.

We exemplarily demonstrate the above-mentioned strategy for Co deposition through galvanostatic experiments conducted at a rotation rate of 900 rpm and lasting for different times at current density values of either –5 or –10 mA cm^{-2}. These values lie close but at opposite sides of the expected mass transport limited current density (ca.—8.1 mA cm^{-2}, based on the Levich equation) for H^+ reduction at a pH of 2.5 and a rotation rate of 900 rpm.[28] They lie, however, considerably below the corresponding limiting current for Co^{2+} reduction (ca. –42 mA cm^{-2}).[29] Note that the selection of higher applied rotational frequencies for Co bulk deposition obeys to the fact that the FE_{H2} increases with ω. The increased partial current density of proton reduction enabled accurate quantification of electrogenerated hydrogen by online GC analysis at shorter times. An upcoming publication will address the effect of pH, applied current densities and rotation rates on the overall Co deposition process in more detail. Figures 4A and 4D show the corresponding measured Co current efficiencies (FE_{Co}) as a function of the applied deposition time. For the experiments performed with $j = -5$ mA cm^{-2}, at deposition times shorter than 5 min, the FE_{Co} amounted to ~30%. When longer electrolysis (5 min $\leqslant t \leqslant$ 60 min) were carried out the FE_{Co} values rose up to 39.8% ± 1.3% and stayed rather constant, regardless of the specific duration. The experiments at $j =$ –10 mA cm^{-2} show significantly larger FE_{Co} values clustering at 64.7 ± 2.6%. Corresponding analysis of the electrogenerated hydrogen accompanying the deposition was carried out at times just before the single depositions were stopped. Additionally, FE_{H2} values were also determined for the longer electrolysis ($t \geqslant$ 16.5 min) in sequential intervals of 7 min starting at 9.5 min. This dwell time corresponds to the shortest period a whole GC run for H_2 detection takes. Figures 4B and 4E summarize the GC results. The displayed FE_{H2} vs t dependencies show that an initiation period of about 15 min is required to achieve quantitative determination of the HER contribution to the whole process: the reason for this latitude is that the electrogenerated hydrogen needs a certain time to fill the cell headspace and the GC loops. This is an intrinsic limitation of the *i*RDE&GC approach that may not be fully circumvented but can to some extent be improved by, e.g., increasing the surface area of the working electrode and/or decreasing the volume of the electrochemical cell. The plot clearly shows that once this conditioning period is elapsed, the actual FE_{H2} values reach a constant value of 58.5% ± 1.4% or 35.5 ± 1.9% for the current densities of –5 or –10 mA cm^{-2}, respectively. The experimental summary displayed in panels C and F fully describe the overall electrochemical process and enable the deconvolution of the current density into two components: one corresponding to the primary Co deposition, the other to the parasitic HER. The total faradaic efficiencies reach 99.6 ± 1.2% and 99.8 ± 1.1% for both experiments with applied current densities of –5 and –10 mA cm^{-2}, respectively, within (15 $\leqslant t \leqslant$ 60) min. It is noteworthy that our approach enables direct insight into the gas evolution component of the electrochemical process, which is typically inferred from the electrochemical data. In the following section we demonstrate that this feature proves particularly useful for additive-assisted Co electrodeposition studies where a third

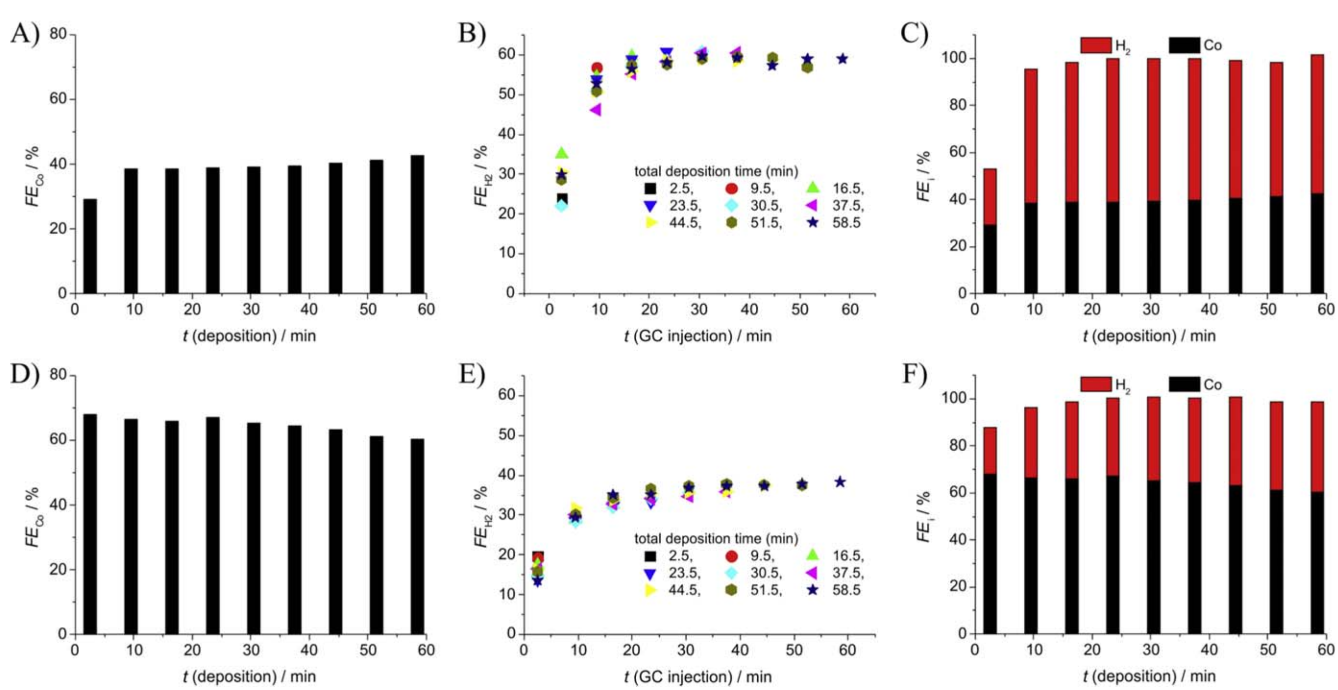

Figure 4. (A) and (D) Co current efficiencies of galvanostatic Co plating from additive-free VMS electrolyte on Co-seeded Pt - *i*RDEs at a rotation rate of 900 rpm, as a function of the total deposition time, at current densities of –5 mA cm^{-2} (A) and –10 mA cm^{-2} (D). Corresponding FE_{H2} values calculated from coupled online GC measurements at all applied GC injection times are shown in (B) and (E). Panels (C) and (F) summarize the FE survey at $j = -5$ mA cm^{-2} (C) and $j = -10$ mA cm^{-2} (F).

constituent (additive activation) needs to be taken into account for the complete description of the process.

Influence of a model suppressing additive on Co electrodeposition.—In this section we demonstrate how the *i*RDE&GC hyphenation can be used for advanced screening studies on additive-assisted Co plating. Figure 5A shows a comparison of linear sweep voltammograms (LSVs) recorded in a bare VMS plating bath and in a bath where the model suppressing additive was added to the VMS in a 60 ppm final concentration. Both LSVs were independently acquired with *IR* drop compensation on Co-seeded Pt *i*RDE electrodes at a sweep rate of 10 mV s^{-1} and a rotation rate of 900 rpm. From the data it is obvious that the action of the model additive at the Co surface significantly slows down the kinetics of the electrochemical process as compared to the additive-free experiment (e.g., the potential required to reach j = –5 mA cm^{-2} is shifted by ∼250 mV in the cathodic direction when the additive is present). Further support for the inhibiting characteristics of the test additive on the Co deposition is exemplarily provided by the potential transients displayed in Fig. 5B. These were recorded during galvanostatic deposition experiments lasting 60 min at a current density of −10 mA cm^{-2} and a rotation rate of 900 rpm in VMS (green) and VMS-ADD (blue) plating baths. Besides a slight instability of the potential in the early stage of the deposition (first 5 min), both potential transients attain steady-state during the time span of the experiment. However, the attained potential values are about 350 mV more negative in the additive-containing electrolyte, which qualitatively correlates with the LSV results.

To discern the effect of the additive on the kinetics of both Co deposition and HER, similar analysis as shown for the additive-free experiment in Fig. 4 was performed with a VMS-ADD plating bath at –5 and –10 mA cm^{-2} current densities; these results are shown in Figs. 5C and 5D. Note that for this experiment the FE_{Co} values were determined via anodic dissolution only at the end of the deposition. The plots are built assuming that the Co current efficiency is independent of the deposition time at ($5 \leqslant t \leqslant 60$) min as it was found in the case of the experiments where no additive was used (Figs. 4A and 4D). It is clearly noticeable for the experiment carried out at j = –5 mA cm^{-2} that the Faradaic efficiencies of both Co deposition and HER are severely affected by the action of the test additive under reactive conditions. Compared to the experiment in pristine VMS, the FE_{Co} is significantly diminished by roughly a factor 8 (see Figs. 4A and 5C). The opposite trend is observed for FE_{H2} which rises to values about 74.2%. The situation is somewhat different when instead of –5 mA cm^{-2}, we apply a current density of –10 mA cm^{-2}. In this case, although both FE_{Co} and FE_{H2} are diminished, compared to their respective values measured in additive-free VMS, their intrinsic ratios remain much closer to the additive-free case (compare Figs. 4F and 5D). The observed difference between the j = –5 mA cm^{-2} and j = –10 mA cm^{-2} case can be explained by taking into consideration the limiting current value of HER expected in the pH = 2.5 solution (ca. –8.1 mA cm^{-2}). It seems that in case of applied current densities higher than this value, the additive—in the absence of free H^+ ions in the boundary layer—exerts a much smaller "boosting effect" on H^+ reduction.

Interestingly, regardless of the applied current density, summation of the FE_{Co} and FE_{H2} values measured in VMS-ADD solutions falls short of the 100% Faradaic efficiency, which was not the case in the additive-free case (see Figs. 4C and 4F). In general, the Faradaic efficiencies obtained from VMS-ADD solutions lack 14%–22% (Figs. 5C–5D). This deficit hints that a reductive conversion of the

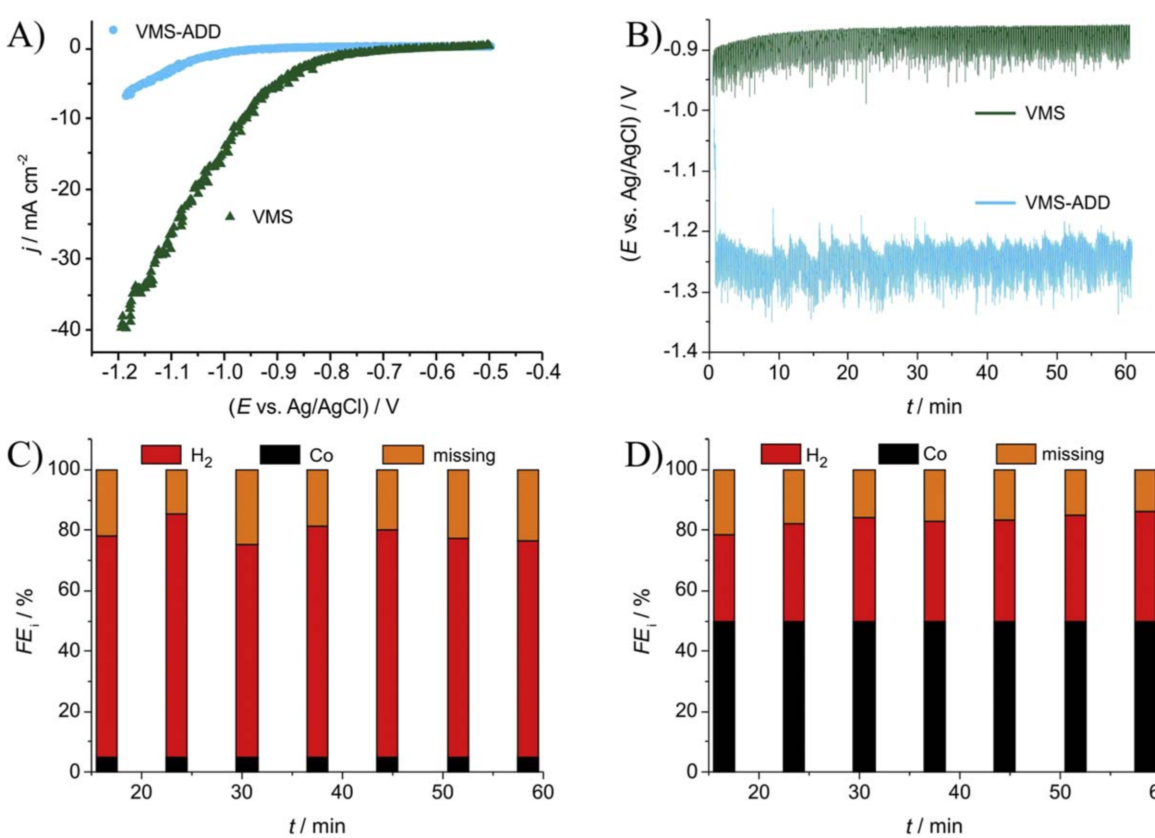

Figure 5. (A) Linear sweep voltammograms recorded on a Co-seeded Pt - *i*RDEs in VMS (green) and VMS-ADD (blue) solutions at a sweep rate of 10 mV s^{-1} and a rotation rate of 900 rpm. Automatic *IR* compensation was applied. (B) Potential transients corresponding to galvanostatic Co depositions at j = –10 mA cm^{-2} in VMS (green) and VMS-ADD (60 ppm, blue) solutions. (C) and (D) Faradaic efficiencies of Co deposition (black) and H_2 generation (red) from 1 h galvanostatic deposition experiments at current densities of –5, respectively –10 m A cm^{-2} from a VMS-ADD electrolyte. The FE_{H2} values are calculated from coupled online GC measurements.

suppressor additive, concomitant with the metal deposition and HER, may take place under the applied experimental conditions. This demonstrates that the relatively minor concentration of the additive in the plating bath further decreases in the bath as the Co^{2+} reduction and HER proceed. Table S1 displays the calculated amount of Co^{2+} and precursor additive consumed upon 1 h electrolysis at –5 and –10 mA cm^{-2} and 900 rpm based on Faraday's law of electrolysis and the partial Faraday efficiencies displayed in Figs. 5C–5D. These data show that after 1 h electrolysis the concentration of the precursor additive diminishes by less than 10% relative to the initial value. Note that the *i*RDE&GC approach is required to account for this extra *FE* deficit that standard electrochemical methods often fail to recognize, ascribing Co Faradaic efficiency losses to H_2 generation alone.[16] In this respect it is interesting to note, for example, that the blue LSV in Fig. 5A shows no hint of reductive conversion of the suppressor additive.

We suggest that the unique capability of our approach to break down the overall process into its individual components, e.g., metal deposition, HER and possible additive conversion should be exploited in future screening of additive-assisted superconformal filling investigations.

Conclusions

We present the design and operation of a custom-made hermetically sealed inverted RDE (*i*RDE) instrument coupled to gas chromatography for quantitative analysis of gas evolving processes. We demonstrate that the setup is a useful test bed particularly suitable for additive-assisted metal deposition studies that are plagued by the HER or any other gas evolving side process. Particularly, we investigate the influence of a model redox-active suppressor additive on the electrochemical deposition of cobalt by means of linear sweep voltammetry and galvanostatic electrolysis coupled to simultaneous online gas analysis by GC. We find that addition of minor amounts (60 ppm) of the additive to the standard Co-based virgin make up solution significantly decreases the rate and efficiency of Co deposition and favours those of the competing hydrogen evolution under specific experimental conditions. Importantly, we are able to identify and quantify reductive conversion of the additive that comes along with the metal deposition process. We suggest that more attention should be devoted to this aspect, which is usually neglected or scarcely studied. Investigations providing such information could add useful insights into plating bath stability. Finally, we propose that the developed *i*RDE&GC approach builds on existing additive-assisted electroplating approaches because it enables unambiguous dissection of the overall process into its individual components, e.g., M^{n+} reduction to elemental M^0, HER and potential additive conversion.

Acknowledgments

We kindly acknowledge the efforts dedicated to this project by Thomas Hübscher and René Schraner, of the mechanical and electronics workshops of the University of Bern. Support by the CTI Swiss Competence Center for Energy Research (SCCER Heat and Electricity Storage) is gratefully acknowledged. P.B. acknowledges financial support from the Swiss National Foundation (grant 200020–172507). S.V. acknowledges support from the National Research, Development and Innovation Office of Hungary (NKFIH grants PD124079). M.d.J. G.-V., N.K. and K.K. acknowledge the financial support by the Swiss Government Excellence Scholarships for Foreign Scholars (ESKAS).

ORCID

Pavel Moreno-García https://orcid.org/0000-0002-6827-787X
María de Jesús Gálvez Vázquez https://orcid.org/0000-0002-0416-6556
Noémi Kovács https://orcid.org/0000-0002-7112-3396
Soma Vesztergom https://orcid.org/0000-0001-7052-4553
Peter Broekmann https://orcid.org/0000-0002-6287-1042

References

1. P. C. Andricacos, *The Electrochemical Society Interface*, **7**, 23 (1998).
2. P. C. Andricacos, *The Electrochemical Society Interface*, **8**, 32 (1988).
3. Q. Huang, T. W. Lyons, and W. D. Sides, *J. Electrochem. Soc.*, **163**, D715 (2016).
4. K. Barmak, A. Darbal, K. J. Ganesh, P. J. Ferreira, J. M. Rickman, T. Sun, B. Yao, A. P. Warren, and K. R. Coffey, *J. Vac. Sci. Technol. A*, **32**, 061503 (2014).
5. D. Josell, S. H. Brongersma, and Z. Tőkei, *Annu. Rev. Mater. Res.*, **39**, 231 (2009).
6. D. Gall, *J. Appl. Phys.*, **119**, 085101 (2016).
7. K. Sankaran, S. Clima, M. Mees, and G. Pourtois, *ECS J. Solid State Sci. Technol.*, **4**, N3127 (2015).
8. C. H. Lee, J. E. Bonevich, J. E. Davies, and T. P. Moffat, *J. Electrochem. Soc.*, **156**, D301 (2009).
9. R. N. Akolkar, F. Gstrein, and D. J. Zierath, Pat.US2012/0153483 A1 (2012).
10. J. S. Chawla et al., *Proc. IEEE IITC/AMC*, p. 63 (2016).
11. J. Kelly et al., "Experimental study of nanoscale Co damascene BEOL interconnect structures." *IEEE/AMC*, San Jose, California, p. 40 (2016).
12. C. Auth et al., "A 10 nm high performance and low-power CMOS technology featuring 3rd generation FinFET transistors, Self-Aligned Quad Patterning, contact over active gate and cobalt local interconnects." *IEEE/IEDM*, San Francisco, California, p. 1 (2017).
13. D. Josell, M. Silva, and T. P. Moffat, *J. Electrochem. Soc.*, **163**, D809 (2016).
14. M. A. Rigsby, L. J. Brogan, N. V. Doubina, Y. Liu, E. C. Opocensky, T. A. Spurlin, J. Zhou, and J. D. Reid, *ECS Trans.*, **80**, 767 (2017).
15. J. Wu, F. Wafula, S. Branagan, H. Suzuki, and J. van Eisden, *J. Electrochem. Soc.*, **166**, D3136 (2019).
16. O. E. Kongstein, G. M. Haarberg, and J. Thonstad, *J. Electrochem. Soc.*, **157**, D335 (2010).
17. F. Wafula, J. Wu, S. Branagan, H. Suzuki, A. Gracias, and J. V. Eisden, *IEEE IITC*, 123 (2018).
18. M. A. Rigsby, L. J. Brogan, N. V. Doubina, Y. Liu, E. C. Opocensky, T. A. Spurlin, J. Zhou, and J. D. Reid, *J. Electrochem. Soc.*, **166**, D3167 (2018).
19. O. E. Kongstein, G. M. Haarberg, and J. Thonstad, *J. Appl. Electrochem.*, **37**, 669 (2007).
20. P. Moreno-García, N. Kovács, V. Grozovski, M. D. J. Gálvez-Vázquez, S. Vesztergom, and P. Broekmann, *Anal. Chem.* (2020).
21. A. D. Zdunek and J. R. Selman, *J. Electrochem. Soc.*, **139**, 2549 (1992).
22. P. E. Bradley and D. Landolt, *J. Electrochem. Soc.*, **144**, L145 (1997).
23. P. M. M. C. Bressers and J. J. Kelly, *J. Electrochem. Soc.*, **142**, L114 (1995).
24. E. J. Podlaha, A. Bögli, C. Bonhôte, and D. Landolt, *J. Appl. Electrochem.*, **27**, 805 (1997).
25. H. Van Parys, E. Tourwé, T. Breugelmans, M. Depauw, J. Deconinck, and A. Hubin, *J. Electroanal. Chem.*, **622**, 44 (2008).
26. T. Nierhaus, H. Van Parys, S. Dehaeck, J. van Beeck, H. Deconinck, J. Deconinck, and A. Hubin, *J. Electrochem. Soc.*, **156**, P139 (2009).
27. H. Van Parys, E. Tourwé, M. Depauw, T. Breugelmans, J. Deconinck, and A. Hubin, *WIT Trans. Eng. Sci.*, **54**, 183 (2007).
28. G. K. H. Wiberg and M. Arenz, *Electrochim. Acta*, **158**, 13 (2015).
29. C. Q. Cui, S. P. Jiang, and A. C. C. Tseung, *J. Electrochem. Soc.*, **137**, 3418 (1990).

Supplementary Information for

Inverted RDE (*i*RDE) as Novel Test Bed for Studies on Additive-Assisted Metal Deposition under Gas-Evolution Conditions

Pavel Moreno-García,[1,z] Vitali Grozovski,[1] María de Jesús Gálvez-Vázquez,[1] Nisarga Mysuru,[1] Kiran Kiran,[1] Noémi Kovács,[1,2] Yuhui Hou,[1] Soma Vesztergom,[1,2] Peter Broekmann[1,z]

[1]*Department of Chemistry and Biochemistry, University of Bern, 3008, Switzerland*

[2]*Department of Physical Chemistry, Eötvös Loránd University, Budapest, 1117, Hungary*

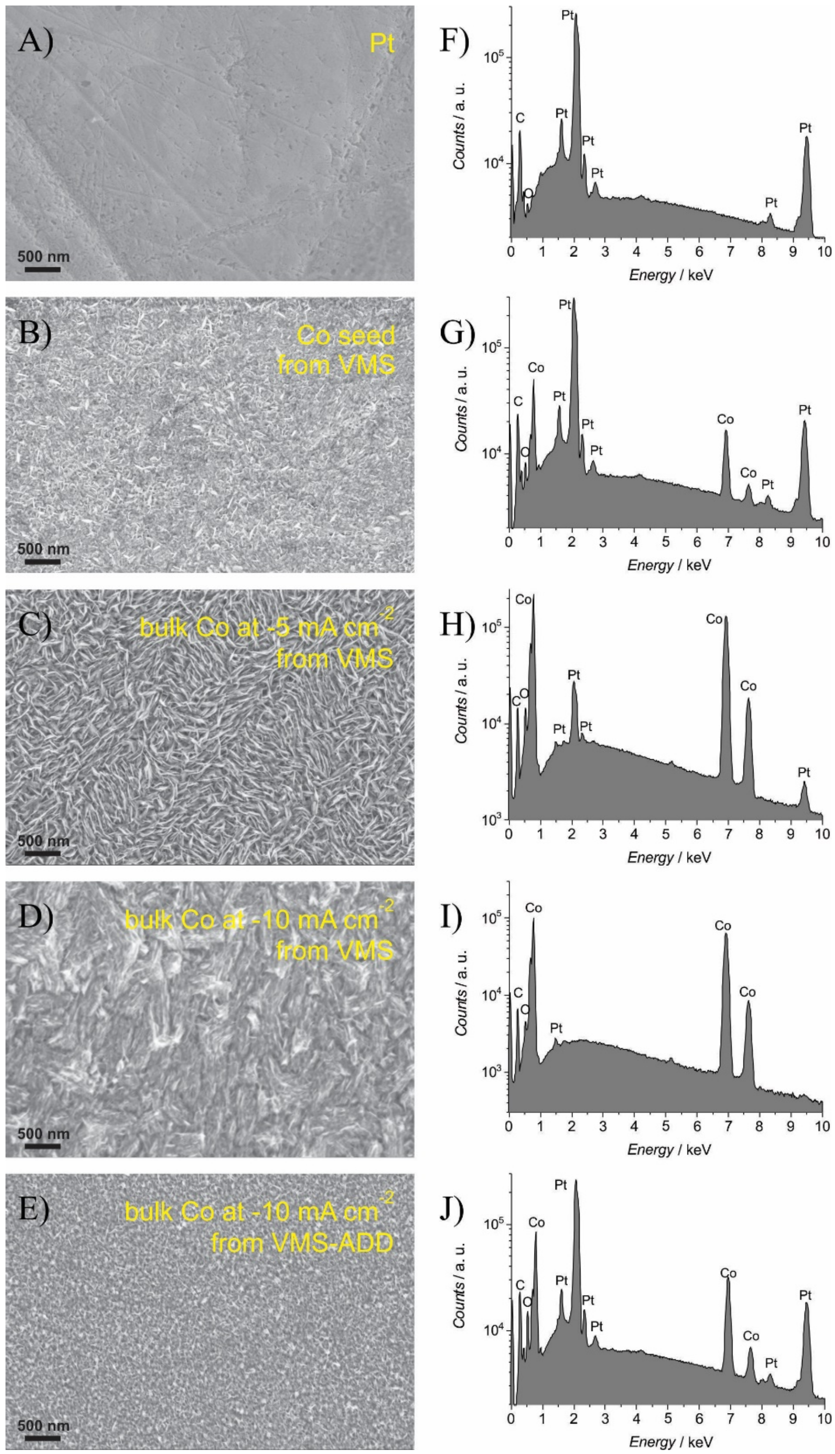

Figure S1. (A-E) *Ex situ* SEM characterization of the *i*RDE working electrode at sequential stages and different applied deposition conditions that are described in detail in the main text. (F-J) Corresponding EDS chemical analysis enabling qualitative characterization of the electrodeposited metal layers. The most intense characteristic EDS lines are L_{α} at 9.441 keV and M at 2.048 keV and K_{α} at 6.924, K_{β} at 7.649 keV and L_{α} at 0.776 keV for Pt and Co, respectively.

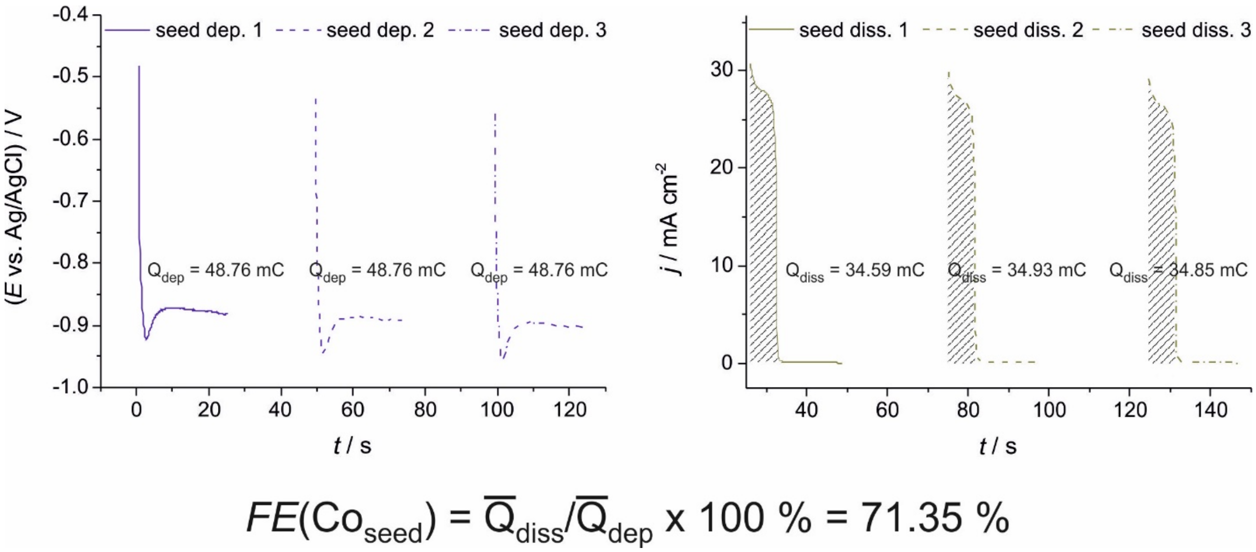

Figure S2. Typical data set for the calculation of the FE_{Co} of the Co seed layer galvanostatically deposited prior to bulk Co deposition studies. The seed deposition was always carried out at - 10 mA cm^{-2} and 100 rpm for 25 s (the electrode area was 0.196 cm^2 and the transferred charge at the interface Q was ~ 49 mC). The subsequent dissolution took place at 0.5 V vs. Ag/AgCl$_{3M}$. For the sake of representativeness, three deposition/dissolution cycles were applied before performing bulk Co deposition experiments on a freshly Co-seeded Pt-*i*RDE support. Calculation of the efficiency of the bulk Co deposition considered subtraction of the statistically determined seed contribution. (A) Potential transients recorded during galvanostatic Co seed deposition cycles. (B) Chronopotentiograms corresponding to the Co seed dissolution steps.

Table S1. Consumption of Co^{2+} ions and amount of electrochemically activated additive from the VMS-ADD plating bath calculated based on Faraday's law of electrolysis and the partial Faraday efficiencies displayed in Fig. 5C-D of the main text.

Applied current density	Amount of species electrochemically consumed after 1 h electrolysis at 900 rpm / %	
	Co^{2+}	additive[a]
-5 mA cm^{-2}	0.02	3.6
-10 mA cm^{-2}	0.52	6.5

[a]Two main products of the additive's electrochemical conversion were detected in practically the same amounts. Their electrochemical conversion required 2, respectively 4 electrons per molecule.

1.10 Selective Electrochemical Reduction of CO_2 to CO on Zn-based Foams Produced by Cu^{2+} and Template-Assisted Electrodeposition

Authors: Pavel Moreno-García, Nicolas Schlegel, Alberto Zanetti, Alena Cedeño López, María de Jesús Gálvez-Vázquez, Abhijit Dutta, Motiar Rahaman, and Peter Broekmann

ACS Appl. Mater. Interfaces, **10** (37), 31355–31365 (2018), DOI: 10.1021/acsami.8b09894

Highlights: A highly porous Zn-based foam was prepared using copper ions as a foaming agent through the dynamic hydrogen bubble template approach. The optimized $Zn_{95}Cu_6$ alloy was the most selective Zn-based CO_2 electrocatalyst toward CO formation, and a FE_{CO} = 90% at −0.95 V vs. RHE was reached. Intentional stressing by oxidation at room conditions proved to be beneficial for further activation of the catalyst. IL-SEM imaging before and after CO_2 electrolysis and long-term electrolysis experiments also showed that the developed $Zn_{94}Cu_6$ foam catalyst is both structurally and chemically stable at reductive conditions.

Contribution: I assisted in the performance of some of the electrochemical measurements and discussion of the results.

ACS APPLIED MATERIALS & INTERFACES

Research Article

Cite This: ACS Appl. Mater. Interfaces 2018, 10, 31355−31365

www.acsami.org

Selective Electrochemical Reduction of CO_2 to CO on Zn-Based Foams Produced by Cu^{2+} and Template-Assisted Electrodeposition

Pavel Moreno-García,*[,†] Nicolas Schlegel,[†] Alberto Zanetti, Alena Cedeño López, María de Jesús Gálvez-Vázquez, Abhijit Dutta, Motiar Rahaman, and Peter Broekmann*

Department of Chemistry and Biochemistry, University of Bern, Freiestrasse 3, Bern 3012, Switzerland

Supporting Information

ABSTRACT: In this work, we aim to develop a Zn-based metal foam catalyst with very large specific area suitable for efficient CO production. Its manufacture is based on the dynamic hydrogen bubble template method that consists of the superposition of metal deposition and hydrogen evolution at the solid−liquid interface. We employed Cu ions in the Zn^{2+}-rich electroplating bath as foaming agent. The concentration of Cu as foaming agent was systematically studied and an optimized $Zn_{94}Cu_6$ foam alloy was developed, which, to the best of our knowledge, is the most selective Zn-based CO_2 electrocatalyst toward CO in aqueous bicarbonate solution (FE_{CO} = 90% at −0.95 V vs reversible hydrogen electrode). This high efficiency is ascribed to the combination of high density of low-coordinated active sites and preferential Zn(101) over Zn(002) texturing. X-ray photoelectron spectroscopy investigations demonstrate that the actual catalyst material is shaped upon reduction of an oxide/hydroxide-terminating surface under CO_2 electrolysis conditions. Moreover, intentional stressing by oxidation at room conditions proved to be beneficial for further activation of the catalyst. Identical location scanning electron microscopy imaging before and after CO_2 electrolysis and long-term electrolysis experiments also showed that the developed $Zn_{94}Cu_6$ foam catalyst is both structurally and chemically stable at reductive conditions.

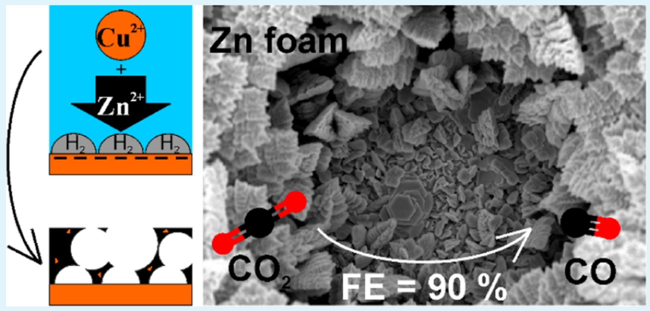

KEYWORDS: *CO_2 reduction, zinc foam catalyst, Zn−Cu alloys, metal foams, dynamic hydrogen bubble template*

■ INTRODUCTION

Electrochemical reduction of carbon dioxide (denoted as CO_2RR hereinafter) to valuable chemicals by utilizing a surplus of renewable energy is a promising approach to mitigate the greenhouse effect caused by anthropogenic CO_2 emissions.[1,2] Key to the CO_2RR process is the use of specific catalyst materials that control both the overall CO_2RR rate and the resulting product distribution. This is why, the rational design of electrocatalysts showing high efficiency and selectivity along with a high durability during CO_2 electrolysis is currently pursued by many research groups worldwide.[3−6] One of the most desired target products of the electrochemical CO_2 reduction reaction is CO, a relevant feedstock precursor for further chemical synthesis of hydrocarbons, and liquid fuels such as alcohols.[7] Pioneering work by Hori et al.[4] and more recent investigations[8−12] have already shown that, in particular, Au and Ag are excellent catalyst materials for the selective electrosynthesis of CO by CO_2RR. Although these achievements are encouraging per se, further efforts are required to develop efficient CO_2RR catalysts based on more abundant and cost-effective materials to approach industrial-scale CO_2 electrolysis. In this context, recent investigations have demonstrated that Zn can be considered as a promising alternative to the aforementioned noble metals with comparably high activity and selectivity toward CO.[13−17] We summarize the achievements reported in the literature so far as follows: particular crystal orientations (e.g., (101) faceting) and the nanostructuring of (dendritic) Zn catalysts have been found to play an eminent role in the CO efficiency.[14] The catalyst surface oxidation prior to CO_2RR was also reported to be beneficial for achieving high CO faradic efficiencies (FEs).[17] Finally, the reduction environment was found to impact the performance of the catalyst. Enhanced activity of Zn cathodes toward CO_2RR was achieved when the commonly employed bicarbonate solution was replaced by halide-containing electrolytes (particularly $Cl^−$).[13]

To further improve the catalytic properties of Zn-based catalysts for CO_2 electrolysis, we address herein the preparation and performance of a foam-type Zn catalyst. Highly porous metal foams are increasingly being used in CO_2RR studies due to their much larger specific surface area that embodies a higher density of low-coordinated active sites than catalysts with reduced surface topography.[12,18,19] An efficient and inexpensive strategy to prepare such functional porous materials is based on metal electrodeposition assisted by the dynamic hydrogen bubble template (denoted herein-

Received: June 13, 2018
Accepted: August 23, 2018
Published: August 23, 2018

DOI: 10.1021/acsami.8b09894
ACS Appl. Mater. Interfaces 2018, 10, 31355−31365

after as DHBT) method (see Figure 1).[20,21] This strategy has been used to prepare, among others, Cu-,[21,22] Ag-,[23,24] and Au-

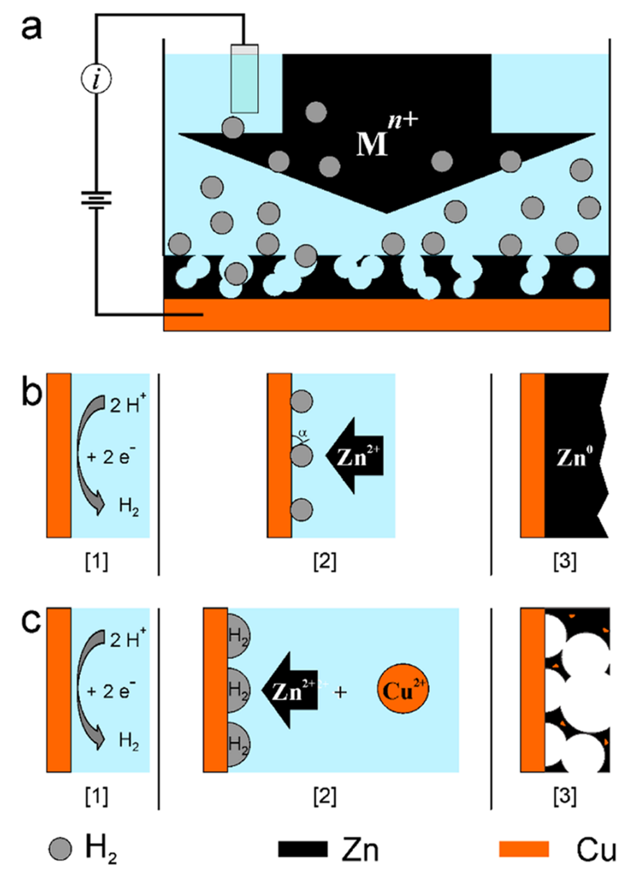

Figure 1. (a) Sketch representing the principle of metal electrodeposition assisted by the DHBT method. Representation of (b) pure Zn and (c) Zn−Cu alloy fabrication by DHBT.

based[25,26] metallic foams that have been tested for diverse applications, e.g., sensing[27,28] and (electro)catalysis.[29] Recent works report on binary Zn alloy foams serving as platforms for ammonia synthesis from nitrate,[30] Li-ion batteries,[31] and hydrogen evolution reaction (HER).[32] However, to the best of our knowledge, no Zn foam has been prepared and successfully applied to the CO_2RR.

The particular challenge tackled in this work is that Zn per se does not form porous foams, at least under standard deposition conditions of the DHBT approach. We circumvented this limitation by the controlled addition of a foaming agent. It will be demonstrated hereinafter that the presence of minor amounts of Cu^{2+} ions in the Zn plating bath is sufficient to significantly change the general deposition behavior and to induce a foaming process, which yields Zn-rich cathode materials with improved active surface area and roughness factors that are higher by a factor of ~1000 compared to bare Zn foil. Crucial for the development of such a Zn foaming process is that those trace amounts of Cu that get embedded into the Zn deposit during the electrodeposition do not alter the electrocatalytic properties of the surrounding Zn matrix with its high selectivity toward CO. The so-called identical location (IL) scanning electron microscopy (SEM) investigations were applied to investigate to which extent the catalyst morphology is altered upon massive CO_2RR.[33,34]

EXPERIMENTAL SECTION

Catalyst Preparation. Cu foil (Goodfellow, 99.9%) substrates were cut (~0.8 × 20 mm^2) and electropolished in 50% H_3PO_4 (Grogg Chemie AG, Switzerland) for 2 min at +2.1 V to generate clean surfaces. The samples were then thoroughly rinsed in Milli-Q water and sonicated for 15 min in high-purity ethanol (VWR Reag., France). They were subsequently masked by Teflon tape, leaving an exposed area of 1 cm^2. The substrates were then used as working electrodes for the DHBT-assisted galvanostatic deposition (e.g., at constant current density $j = -3$ A cm^{-2} for 20 s) of three main classes of samples, namely, pure Zn, pure Cu, and Zn−Cu alloys. In all three cases (and for all subsequent electrochemical experiments), a potentiostat/galvanostat (Metrohm Autolab 128N, the Netherlands) was used in a three-electrode cell arrangement. A double-junction Ag/$AgCl_{3M}$ electrode (Metrohm, Switzerland) was employed as the reference electrode, and bare Cu and Zn foils acted as counter electrodes for pure Cu and Zn−Cu alloy and pure Zn samples, respectively. The supporting electrolyte was in all cases 1.5 M H_2SO_4 (Selectipur, BASF SE, Ludwigshafen, Germany), and the metal-ion source was 0.2 M $ZnSO_4$ (ReagentPlus, Sigma-Aldrich) and 0.2 M $CuSO_4$ (Honeywell Fluka Puriss, Germany) for pure Zn and pure Cu samples, respectively. In the case of Zn−Cu alloy samples, eight different plating bath compositions were used, which are summarized in Table S1 of the Supporting Information. Potential transients and optical micrographs of the surface samples during metal deposition were taken, which show the simultaneous generation of hydrogen bubbles at the sample−electrolyte interface (see Figures S1 and S2). The samples were thoroughly rinsed by Milli-Q water after deposition, dried in a gentle Ar flux, and stored for a few hours before starting the CO_2RR experiments.

The electrochemical surface area (denoted hereafter ECSA) of pure Zn and optimized $Zn_{94}Cu_6$ alloy (see Table S1) samples was determined by comparing their capacitance values to those of reference flat Zn and Cu foils (99.9%, and 99.95%, Goodfellow). For this, cyclic voltammetry for selected electrodes in 0.1 M KCl at various scan rates was conducted (see Figure S3). The accessible potential window in the case of Zn samples ranged from −1.275 to −1.075 V versus reversible hydrogen electrode (RHE), where no redox peak appears. For the copper foil, the applied potential range was −0.80 to −0.50 V versus RHE. The current densities were calculated on the basis of roughness factors derived from double-layer charge/discharge curves at the middle applied potential.

Characterization Methods. The electrodeposited catalyst samples were subjected to scanning electron microscopy (SEM) analysis using a Hitachi S-3000N scanning electron microscope for surface morphology and sample thickness determination. For lateral analysis, dedicated samples scrutinized by this technique were deposited on Si(100)-supported Cu wafer coupons (100 nm Cu seed, BASF), which are suited for cross-sectioning, followed by SEM inspection (see Figure S4). The morphological properties (e.g., roughness, pore dimension and density) of the $Zn_{94}Cu_6$ foam and the pure Cu samples were additionally studied by means of a digital optical microscope with focus variation capabilities (VHX-600, Keyence).

X-ray Diffraction (XRD). The crystallinity of the $Zn_{94}Cu_6$ samples was studied by powder XRD techniques (Bruker D8) with Cu Kα radiation (λ = 0.1540 nm, 40 mA) generated at 40 keV. Scans were recorded at 1° min^{-1} for 2θ values between 20 and 100°. For these studies, the samples were galvanostatically deposited on as-received carbon paper. The obtained XRD patterns were analyzed and compared to Joint Committee on Powder Diffraction standards (JCPDS) for Zn and Cu_4Zn phases. In dedicated experiments, two more specimens were analyzed, one before and the other after a 3 h CO_2RR cycle.

Energy-Dispersive X-ray (EDX) Spectroscopy and Inductively Coupled Plasma Mass Spectrometry (ICP-MS). Element composition analyses of $Zn_{94}Cu_6$ were carried out with a Noran SIX NSS200 energy-dispersive X-ray spectrometer and a 7700x Agilent system for ICP-MS studies. For both ICP-MS and EDX character-

DOI: 10.1021/acsami.8b09894
ACS Appl. Mater. Interfaces 2018, 10, 31355−31365

izations, the $Zn_{94}Cu_6$ samples were deposited on Cu-seeded Si(100) wafer coupons.

X-ray Photoelectron Spectroscopy (XPS). XPS investigations were performed to analyze the surface elemental composition of the $Zn_{94}Cu_6$ sample. These experiments were conducted with an Omicron Multiprobe (Omicron NanoTechnology) spectrometer coupled to an EA 125 (Omicron) hemispherical analyzer. Monochromatic Al Kα radiation (1486.4 eV anode operating at 150 W and 15 kV) was used. Binding energies were calibrated using the C 1s peak of graphite at 284.5 eV or the Au 4f peak at 84.0 eV as a reference. Samples for XPS inspection were dried under an Ar stream after the electrochemical deposition and used for XPS characterization without any further modification.

Electrochemical CO_2 Reduction Reaction (CO_2RR). A custom-built gastight glass cell (H-type) was used for CO_2 electrolysis experiments. The three-electrode arrangement consisted of a leakless $Ag/AgCl_{3M}$ reference electrode (EDAQ), a Pt foil (20 mm × 8 mm) serving as counter electrode, and the electrodeposited pure Zn, $Zn_{94}Cu_6$, and bare Zn foil samples serving as working electrodes. Catholyte and anolyte were separated by a proton exchange membrane (Nafion 117, Sigma-Aldrich). Prior to CO_2 electrolysis, the cathodic and anodic compartments were both filled with 35 mL of 0.5 M $KHCO_3$ (ACS grade, Sigma-Aldrich) electrolyte solution and saturated with CO_2 gas (99.999%, Carbagas, Switzerland) for 30 min, achieving a final pH value of 7.2. The CO_2 flow was kept constant throughout the potentiostatic CO_2 electrolysis. A distinct freshly prepared sample was measured for each applied potential in the case of $Zn_{94}Cu_6$, pure Zn, and Zn foil. For all other Zn−Cu alloy foams, one sample was used for the whole potential range investigated (−0.6 to −1.1 V vs RHE in intervals of 100 mV).

The cell resistance was determined by means of electrochemical impedance spectroscopy at various applied sample potentials. For the sake of comparability, the applied potentials during CO_2RR were then compensated for *iR* drop and converted to the RHE scale by using eq 1. All potentials hereafter are referred to the RHE scale.

$$E_{\mathrm{RHE}}\ (\mathrm{V}) = E_{\mathrm{Ag/AgCl(3M)}}\ (\mathrm{V}) + 0.210\ \mathrm{V} + (0.059\ \mathrm{V} \times \mathrm{pH}) \quad (1)$$

Gas Chromatography (GC). The continuous flow of CO_2 through the electrolysis cell during CO_2RR carried the volatile reaction products from the headspace into the sampling loops of the gas chromatograph (GC, SRI Instruments Multiple Gas Analyzer #3). The partial current density of a given gaseous product was calculated using eq 2

$$I_0(i) = x_i\ n_i F \cdot \nu_m \quad (2)$$

where x_i represents the volume fraction of the products measured via online GC using an independent calibration standard gas (Carbagas, Switzerland), n_i is the number of electrons involved in the reduction reaction to form a particular product, ν_m represents the molar CO_2 gas flow rate measured by a universal flowmeter (7000 GC flowmeter by Ellutia) at the exit of the electrochemical cell, and F is the Faraday constant. The partial current density for a given reaction product was normalized with respect to the total current density, thus providing the FE for a given reaction product. Gas aliquots were analyzed in intervals of 20 min during steady-state CO_2 electrolysis in terms of an online measurement. The electrolysis experiments typically lasted 3 h. Analogous experiments were carried out with Ar-saturated electrolytes for comparison (see Figure S5).

Ion-Exchange Chromatography (IC). Liquid products were analyzed by postmortem ion-exchange chromatography (Metrohm Ltd., Switzerland). The chromatograph was coupled to an L-7100 pump, a separation column, an ion-exclusion column (Metrosep A Supp 7-250), and a conductivity detector used for formate quantification.

Catalyst Degradation Studies. For dedicated experiments, the performance stability of the $Zn_{94}Cu_6$ catalyst was explored by extending the electrolysis to 36 h at certain potentials. The time evolution of the current density *j* and FEs were monitored every 30 min. A further stability test of the cathode aimed at finding out whether its activity and selectivity are preserved upon intentional oxidation of the catalyst surface. In this experiment, 6 h electrolysis was conducted at a given potential with a freshly prepared cathode. The sample was then cleaned by thorough rinsing with Milli-Q water and left to oxidize under ambient conditions for ∼8 h. A second electrolysis experiment was then conducted under the same experimental conditions for further 6 h using the aged electrode while monitoring again *j* and FEs.

Identical Location (IL) SEM Imaging for Morphological Stability Survey. For morphological survey of the $Zn_{94}Cu_6$ catalyst and high-resolution identical location (IL) SEM imaging experiments before and after 3 h electrolysis, a Zeiss DSM 982 instrument was used, which allowed inspection of the structural integrity of the material upon CO_2RR.

■ RESULTS AND DISCUSSION

Catalyst Preparation and Characterization. Figure 1a shows a schematic representation of the DHBT-based metal electrodeposition approach that has been developed to produce a variety of porous materials for diverse applications (e.g., catalysis, sensing, Li-ion batteries, among many others).[20,21,35] This method is based on metal deposition in highly acidic aqueous electrolytes at large applied cathodic current densities (in the ampere range), where the metal electrodeposition is superimposed on the reduction of H^+ ions to H_2 bubbling off the growing deposit. H_2 bubbles act as a temporary dynamic template during the electrodeposition process. This method has been used to prepare materials exhibiting remarkably large surface active areas that combine a microporous framework (primary porosity) with nanoporous side walls (secondary porosity). Among all investigated elements, Cu is certainly the by far most employed material.[22,36,37] Inspired by recent studies that have shown promising catalytic properties of porous Cu foams toward CO_2RR,[18,19,38] herein, we applied this synthesis route to prepare analogous Zn-based catalysts for CO_2RR applications.

In the first stage, we attempted to prepare pure Zn foams by employing identical experimental conditions that are typically applied for other metal foams, particularly Cu.[22,39,40] Figure 2a,b displays topview SEM images of a typical pure Zn sample that was electrochemically deposited by the standard DHBT approach on a Cu foil substrate. Differing from the pure Cu sample (Figure 2c,d), the synthesized pure Zn deposit does not

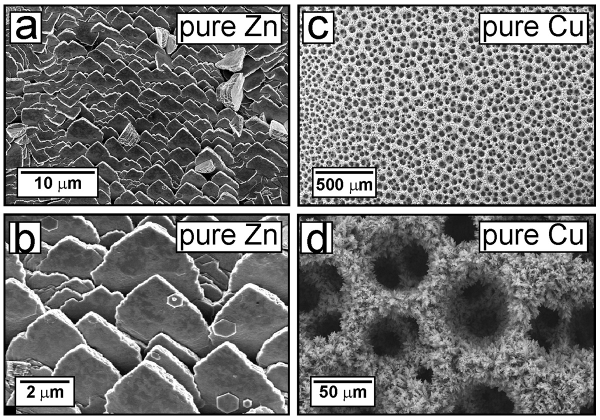

Figure 2. SEM images of DHBT-based electrodeposited pure Zn (a, b) and pure Cu (c, d) samples. The galvanostatic deposition was performed at −3 A cm^{-2} for 20 s from 0.2 M metal ion in 1.5 M H_2SO_4 supporting electrolyte.

DOI: 10.1021/acsami.8b09894
ACS Appl. Mater. Interfaces 2018, 10, 31355−31365

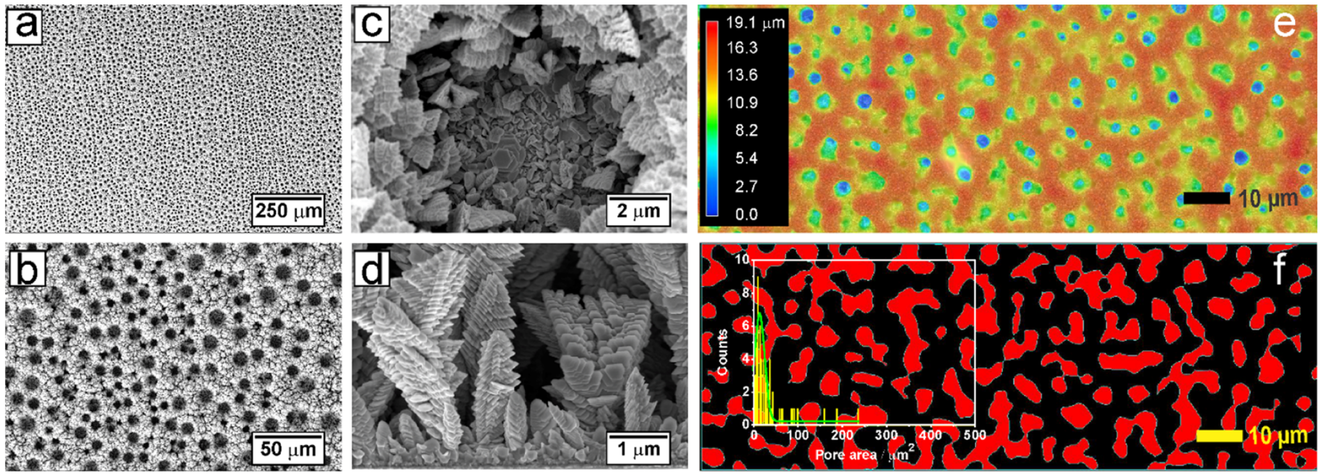

Figure 3. Morphological and roughness characterization of $Zn_{94}Cu_6$ catalyst. (a−c) Topview SEM images of the prepared catalyst at different magnifications. (d) Cross-sectional SEM image of $Zn_{94}Cu_6$ catalyst. (e) Topography analysis by digital optical microscope with focus variation of selected sample location. (f) Analysis of pore dimensions at depths ≥6 μm from the outermost sample surface.

exhibit microporosity, but is instead composed of micrometer-sized platelets, thus causing a stepped scalelike surface appearance. A close inspection of the hexagonal ad-islands on top of the platelets (Figure 2b) reveals a preferential growth of the Zn deposit along the [0001] direction. We note that the edges of individual Zn platelets are slightly roughened, most probably due to minor Zn dissolution occurring during emersion of the sample from the plating bath after deposition (∼1 s). From the morphological point of view, the pure Zn deposit is similar to the recently reported hierarchical hexagonal CO_2RR Zn catalyst (h-Zn) that demonstrated, besides a high efficiency and selectivity toward CO in CO_2RR, an extraordinarily high robustness as cathode material.[14] The absence of microporosity in the pure Zn deposit (Figure 2a,b) can be rationalized by the superposition of two major effects: First, the HER rate strongly depends on the chemical nature of the employed metal substrate. Trends in the catalytic HER activity are commonly represented in the so-called volcano plots interrelating the experimentally determined exchange current densities, j_0, as a function of the hydrogen adsorption energy (E_{M-H});[41,42] j_0 is by orders of magnitude higher for Cu (∼10^{-5} A cm^{-2}) than for Zn (∼10^{-8} A cm^{-2}), thus being indicative for a significantly slower HER kinetics on Zn. Also the metal−hydrogen bond strength is higher in the case of Cu (E_{Cu-H} ∼ 45 kcal mol^{-1}) than for Zn (E_{Zn-H} ∼ 35 kcal mol^{-1}).[43] It can be assumed that, despite having used Cu foil as substrate, both the metal deposition and the HER become governed by the growing Zn matrix and therefore by j_0(Zn) and E_{Zn-H} shortly after having started the Zn deposition. As a consequence, the partial HER current density contributing to the overall (nominal) current density of −3 A cm^{-2} is substantially reduced in the case of Zn.

Second, it is also known that the hexagonal Zn(0001) surface plane that is preferentially exposed to the electrolyte (Figure 2b) is highly hydrophilic.[44,45] As a consequence, the contact angle at the gas−liquid−solid interface is relatively small. Accordingly, the mean residence time of H_2 bubbles at the dynamic solid−liquid interface and the so-called bubble break-off diameter, d_0, are reduced in the case of Zn. These kinetic and morphological effects act synergistically to inhibit the formation of porous Zn foams, at least under the applied experimental conditions (Figure 1b).

One promising strategy to overcome these limitations of pure Zn plating is based on the addition of particular foaming agents. Combined DHBT- and additive-assisted deposition approaches have been applied to synthesize Zn foams. A number of binary Zn−Cu alloy foams have been reported in the literature for catalytic nitrate reduction,[30] Li-ion battery anode,[31] and HER applications.[32] These studies have demonstrated that Cu ions alone[32] or in combination with chelating additives like citrate[31] act as foaming agents to produce porous Zn−Cu skeletons of tunable elemental composition (Zn/Cu ratio).

Table S1 summarizes plating bath compositions used for the production of a series of Zn−Cu alloy foams as basis for a further catalyst optimization. All alloy samples exhibited the desired porous foam structure, as depicted in Figure 1c. Selected SEM images of the alloy specimens are presented in Figure S6, indicating differences in their pore characteristics (size, distribution, and density). The obtained set of binary Zn−Cu alloy catalysts was subjected to an initial fast screening, which revealed that CO and H_2 are the only products irrespective of the applied electrolysis potential and the particular elemental composition of the Zn−Cu foam catalyst used (see Table S1 and Figure S7a). Faradic efficiencies (FEs) for H_2 and CO are strongly anticorrelated. No formate and hydrocarbons were detected as typical CO_2RR products on Cu catalysts at lower and higher electrolysis potentials, respectively. From this observation, it can safely be concluded that the electrocatalytic characteristics of the co-alloyed Cu are fully suppressed when diluted in a surrounding Zn matrix. The resulting ratio of CO and H_2 efficiencies in the CO_2RR strongly depends on the Cu content in the alloy and therefore on the bath composition. H_2 is the favored electrolysis product with efficiencies ranging from 80 to 97% when Cu-rich Zn−Cu alloys were used as catalysts obtained from plating baths with metal-ion ratios of $c(Zn^{2+})/c(Cu^{2+}) \leq 10$. CO is, by contrast, the dominant electrolysis product with efficiencies ranging from 54 to 75% when Zn-rich alloys were used as catalysts obtained from electroplating baths with metal-ion ratios of $20 \leq c(Zn^{2+})/c(Cu^{2+}) \leq 100$.

Also note that the relative abundances of Zn and Cu in the formed alloy foam catalysts significantly differ from the ratio of metal ions in the corresponding plating bath. This is illustrated

DOI: 10.1021/acsami.8b09894
ACS Appl. Mater. Interfaces 2018, 10, 31355−31365

on the basis of the best-performing Zn−Cu alloy foam produced using a metal-ion ratio in the plating bath of $c(Zn^{2+})/c(Cu^{2+})$ = 30. ICP-MS and EDX analyses reveal an elemental "bulk" composition of 90.8 atom % Zn/9.2 atom % Cu and 88.6 atom % Zn/11.4 atom % Cu, respectively. Complementary surface-sensitive XPS analysis of the alloy catalyst yielded a slightly lower amount of Cu of 5.8 and 94.2 atom % Zn. The catalyst denotation is based on the XPS analysis since it is the surface elemental composition, which is decisive for the electrocatalytic properties and not the bulk composition. We therefore denote this catalyst hereinafter as $Zn_{94}Cu_6$.

Figure 3a,b displays representative SEM images of this $Zn_{94}Cu_6$ catalyst exhibiting a uniform microporosity even on a larger millimeter length scale. Cu foams deposited under similar conditions typically reveal a complex three-dimensional (3D) network of interconnected pores whose diameters gradually increase from the support to the outermost catalyst surface (see morphology of pure Cu in Figure 2d and Cu-rich Zn−Cu alloys in Figure S6).[39] Instead, we observe on the $Zn_{94}Cu_6$ foam funnel-like pores that reach from the outermost catalyst surface down to the support height level (Figure 3c). Pore side walls are composed of stacks of Zn−Cu platelets that have a similar appearance to that observed for the pure Zn deposit (see Figures 3d and 2a). The $Zn_{94}Cu_6$ sample actually combines advantageous morphological characteristics of the high-performance hexagonal h-Zn CO_2RR catalyst reported by Won et al.[14] with an intrinsically high surface area of the porous foam material. On the basis of capacity measurements, we determine a roughness factor of 1267 with reference to the planar Zn foil (Figure S3). Digital optical microscopy with focus variation provides additional depth resolution to the morphological catalyst characterization. On the basis of that, a total catalyst film thickness of ~19 μm is estimated. Figure 3e presents a 3D topographical map of the $Zn_{94}Cu_6$ catalyst. The mean pore depth lies in the 6−16 μm range, which is at least about half of the sample thickness (see Figure S4a). Taking the topmost plane of the sample as reference, all pores (depressions) deeper than 6 μm were taken into account to build two-dimensional pore maps. Depicted by red features in Figure 3f, an example of such analysis is shown. The inset is a pore-size distribution showing that the average pore area at depths ≥6 μm lies in the 5 μm^2 ≤ area ≤ 40 μm^2 range. For the sake of comparison, Figure S8 shows analogous examination for pure Cu specimen. The much larger area covered by pores relative to the outermost sample plane originates from the significantly larger amount and coalescence of produced H_2 along with their longer residence time on Cu during deposition than on Zn-based catalyst.

The crystallinity of the $Zn_{94}Cu_6$ sample was probed by X-ray diffraction (Figure 4). $Zn_{94}Cu_6$-related diffraction pattern matches well with diffraction peaks of metallic Zn (Figure 4a,c, respectively), whereas no characteristic pattern from phase-segregated Cu was detected. Only minor contributions from a Cu_4Zn phase (Figure 4b) are visible in the respective XRD spectrum of the $Zn_{94}Cu_6$ catalyst. These observations point to co-alloyed Cu that is largely diluted within the Zn matrix without disturbing substantially the crystal structure of the Zn matrix. This conclusion becomes further substantiated by EDX mapping, showing a homogeneous distribution of Cu in the Zn foam (Figure S9). A notable difference to the polycrystalline Zn reference concerns, however, the relative intensities of the (101), (102) and (002), (100) diffraction peaks (Figure 4a). More prominent (101) and (102) diffraction peaks relative to the (002) and (100) peaks might be indicative of a preferential surface faceting of the catalyst in accordance with the observations from the corresponding SEM inspection (Figure 2a,b). We note that the CO_2RR and the parasitic hydrogen evolution reaction (HER) are both surface-sensitive reactions. According to the recent experimental and theoretical studies, it is the Zn(002) facet that favors HER, whereas the CO formation kinetics gets substantially enhanced on the Zn(101) facet.[14]

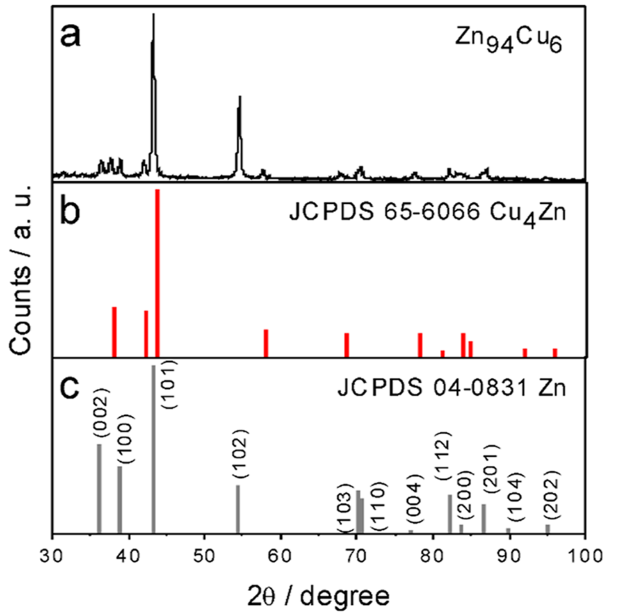

Figure 4. (a) XRD analysis of the $Zn_{94}Cu_6$-electrodeposited catalyst. (b, c) JCPDS reference XRD patterns for Cu_4Zn and Zn, respectively.

Exposure of the as-prepared $Zn_{94}Cu_6$ catalyst to the ambient atmosphere inevitably leads to substantial surface oxidation (note that there is typically a time delay of a couple of hours between catalyst preparation and application to CO_2RR). High-resolution ex situ XPS surface analysis of the $Zn_{94}Cu_6$ catalyst particularly focusing on the Zn $2p_{3/2}$ region (Figure 5a) confirms the presence of both metallic and oxidic Zn surface species. The Zn $2p_{3/2}$ photoemission peak can be deconvoluted by assuming two components with binding energies at BE = 1022.4 and 1022.6 eV, which are ascribed to metallic zinc (Zn^0)[46] and oxidized zinc (Zn^{II}),[44,45] respectively.

Further, the O 1s photoemission peak (Figure 5b) can be deconvoluted into three individual peaks. The peak centered at BE = 530.8 eV can be assigned to O^{2-} ions in metal−O bondings,[47] whereas the second, dominating peak at BE = 532.4 eV is attributed to adsorbed hydroxyl (OH) species.[48,49] A minor component at BE = 533.0 eV is due to the oxygen of adsorbed water molecules. The XPS results are indicative of a terminating surface layer on the as-synthesized $Zn_{94}Cu_6$ catalyst that is composed of mixed oxide/hydroxide phases. These are most likely Zn-related since Zn is more prone toward oxidation. Also the low abundance of Cu in the near-surface region (Figure 5c) points to a Zn-dominated oxide/hydroxide-terminating surface layer. We note that the spin−orbit split peaks at BE(Cu $2p_{3/2}$) = 933.0 eV and BE(Cu $2p_{1/2}$) = 953.0 eV are indicative of either pure Cu^0 or cuprous oxide (Cu_2O), which are indistinguishable in the XPS analysis.[50,51] The presence of CuO can, however, clearly be excluded

DOI: 10.1021/acsami.8b09894
ACS Appl. Mater. Interfaces 2018, 10, 31355−31365

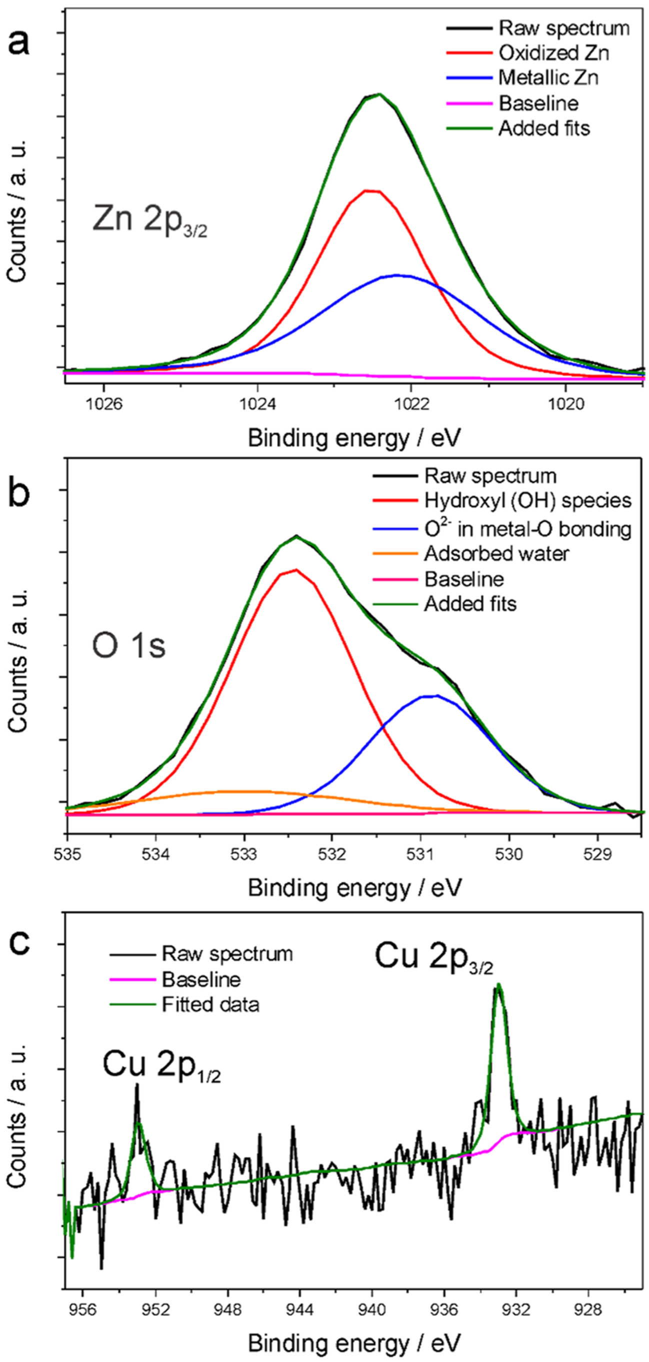

Figure 5. XPS images of (a) Zn $2p_{3/2}$, (b) O 1s, and (c) Cu 2p photoemission regions prior to CO_2RR.

(absence of shake-up satellite peaks). In addition to this, we note also that weak, yet discernible features in the $30° < 2\theta < 35°$ range of the XRD diffractogram (Figure 4a) might be assigned to ZnO-related species (PDF 21-1486 reference file).

On the basis of the reasoning above, we can consider the as-prepared $Zn_{94}Cu_6$ catalyst as oxide/hydroxide-derived even without extra thermal or plasma treatment. On the basis of our XPS analysis, we determine an elemental abundance of 28.95 atom % Zn, 2.72 atom % Cu, and 68.33 atom % O in the surface-terminating layer of the as-prepared $Zn_{94}Cu_6$ sample. The reduction of the mixed oxide/hydroxide layer under harsh cathodic conditions typically applied during CO_2RR is believed[17] to play an eminent role in the actual catalyst activation under operando conditions in analogy to other CO_2RR catalysts, e.g., Cu.[38] In accordance with this reasoning, previous in situ X-ray absorption spectroscopy studies have shown that oxidized Zn gets fully reduced at potentials applied during CO_2RR (≤ -0.7 V vs RHE).[16]

CO_2 Electrolysis: Catalytic Activity. To probe the catalytic activity of the $Zn_{94}Cu_6$ foam toward CO_2RR, linear sweep voltammograms (LSVs) were recorded in the potential range of −0.40 to −1.30 V versus RHE in both Ar- and CO_2-saturated 0.5 M $KHCO_3$ electrolytes. For the sake of comparison, analogue experiments were conducted for pure Zn catalyst and a Zn foil serving as benchmark catalysts. Figure 6a shows the respective first forward potential scans. We note that the reduction of the surface-terminating metal oxide/hydroxide layer is always superimposed on the CO_2RR and HER as origin of the non-steady-state behavior during the first LSV measurements in the potential range ($-0.5 \leq E \leq -0.8$) V versus RHE. Reductive processes in the Ar-saturated electrolyte (dashed lines in Figure 6a) are dominated mainly by the HER beyond −0.8 V. Current densities increase in the order $|j_{HER}|$ (pure Zn) < $|j_{HER}|$ (foil) < $|j_{HER}|$ ($Zn_{94}Cu_6$ foam) at potentials between −0.80 and −1.25 V and $|j_{HER}|$ (pure Zn) < $|j_{HER}|$ ($Zn_{94}Cu_6$ foam) < $|j_{HER}|$ (foil) at more negative applied potentials. We assume that this is due to the lower Zn(002) faceting relative to Zn(101) orientation of the pure Zn and

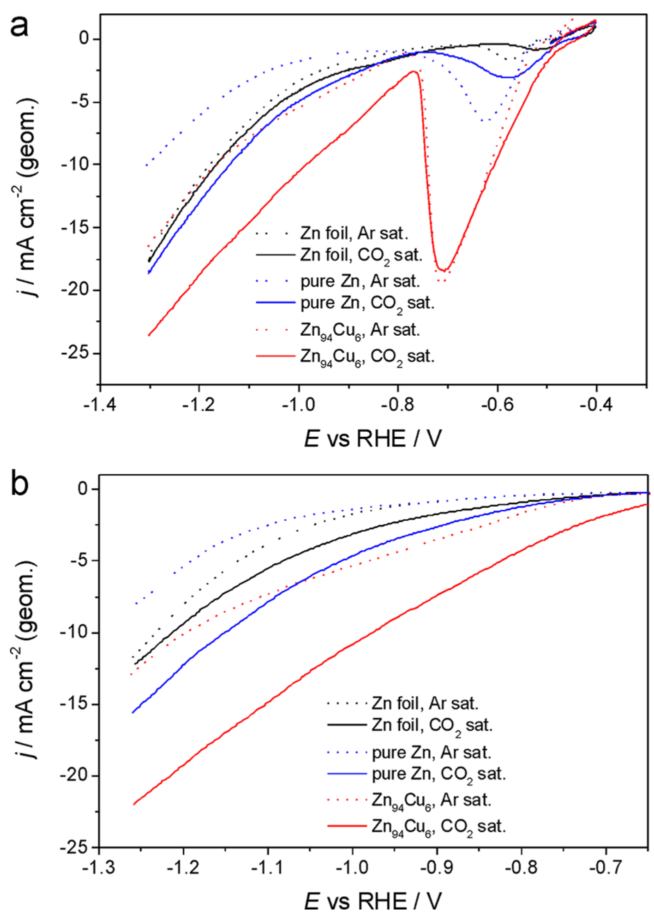

Figure 6. Linear sweep voltammograms (LSVs) of Zn foil (black), pure Zn (blue), and $Zn_{94}Cu_6$ (red) samples immersed in Ar- (dashed lines) and CO_2-saturated (solid lines) 0.5 M $KHCO_3$ electrolytes solutions. (a) First potential excursion; (b) steady-state LSVs. The applied potential scan rate was 10 mV s^{-1}.

DOI: 10.1021/acsami.8b09894
ACS Appl. Mater. Interfaces 2018, 10, 31355−31365

$Zn_{94}Cu_6$ catalysts, which has been found to be more active for H_2 production. This preference for H_2 production of the reference Zn foil surprisingly overcomes the increased electrochemical active surface area (ECSA) of our two prepared pure Zn and particularly $Zn_{94}Cu_6$ catalysts at these large applied potentials.

The trend $|j|$ (foil) < $|j|$ (pure Zn) ≪ $|j|$ ($Zn_{94}Cu_6$) is observed for the CO_2-saturated solution (solid lines in Figure 6a), thus confirming a substantial activity of the $Zn_{94}Cu_6$ catalysts toward CO_2RR, which is superimposed in the CO_2-saturated electrolytes to the (parasitic) HER. Figure 6b displays the subsequent steady-state LSVs (second potential excursion) evidencing the removal of the oxide/hydroxide-terminating surface layer that leads to the activation of the catalyst materials. A transition from the first, non-steady-state LSV to the steady-state voltammogram for $Zn_{94}Cu_6$ in Ar-saturated electrolyte is displayed in Figure S10.

Potentiostatic CO_2 electrolysis reactions were conducted for 3 h in CO_2-saturated 0.5 M $KHCO_3$ electrolyte at applied constant potentials ranging from −0.60 to −1.05 V versus RHE. The corresponding potential/time transient curves show stable steady-state reduction processes after passing an initial transient catalyst activation phase due to the oxide/hydroxide reduction (Figure S11a).

Online GC analysis of the electrolyte headspace revealed that CO and H_2 are the only gaseous products of the CO_2RR when using $Zn_{94}Cu_6$ foams as catalysts. Further nonvolatile CO_2RR products were excluded by postmortem ion-exchange chromatography (IC, sensitive to formate, acetate, oxalate, etc.) and gas chromatography (sensitive toward liquid alcohols, e.g., methanol and ethanol). In Figure 7, the CO_2RR product distribution is presented in terms of faradic efficiencies (FEs) and further referred to the total steady-state current densities derived from the current/time traces of the respective potentiostatic electrolyses (Figure S11b). The FE versus E plot can be subdivided into three characteristic domains. At lowest applied potentials ($E \geq -0.75$ V vs RHE), the total current densities are low and the CO_2RR/HER are superimposed on the (comparably slow) structural/compositional transformations in the terminating oxide/hydroxide layer. A clear indication for that is the total FE_{tot} value at −0.6 and −0.7 V, which clearly remains below 100% when considering only the gaseous products of the CO_2RR. It is therefore likely that the CO_2RR with a remarkable FE_{CO} of 56% at ca. −0.7 V takes place in the presence of the hydroxide/oxide layer, whose sluggish reduction to metallic Zn at these low applied overpotentials is superimposed on the CO_2RR.

The onset of the CO production on the hydroxide/oxide-terminated $Zn_{94}Cu_6$ catalyst is remarkably low compared to other Zn-based catalysts, thus pointing to a beneficial role of the hydroxide/oxide for the catalytic activity. In the second, more cathodic potential domain in the range of $-0.95\text{ V} \leq E \leq -0.75$ V, the reduction of the terminating oxide/hydroxide layer is readily accomplished so that we can assume that the CO_2RR takes place on a purely metallic, oxide/hydroxide-derived catalyst. The CO efficiency reaches a quasi-plateau on a high level with FE_{CO} values ranging from 80% (E = −0.8 V vs RHE) to 90% (E = −0.95 V vs RHE). To the best of our knowledge, this high selectivity toward CO production is superior to the ones of existing CO_2RR studies performed with a variety of Zn-based catalysts in bicarbonate electrolytes.[4,6,13,14,16,17] We assign the observed superior performance of the $Zn_{94}Cu_6$ catalyst to the synergy of three beneficial effects: (i) preferential Zn(101) over Zn(002) texturing,[14] (ii) catalyst activation through oxide/hydroxide reduction,[17] and (iii) increased surface step density and texture due to the concave arrangement of the porous framework (surface area effect).

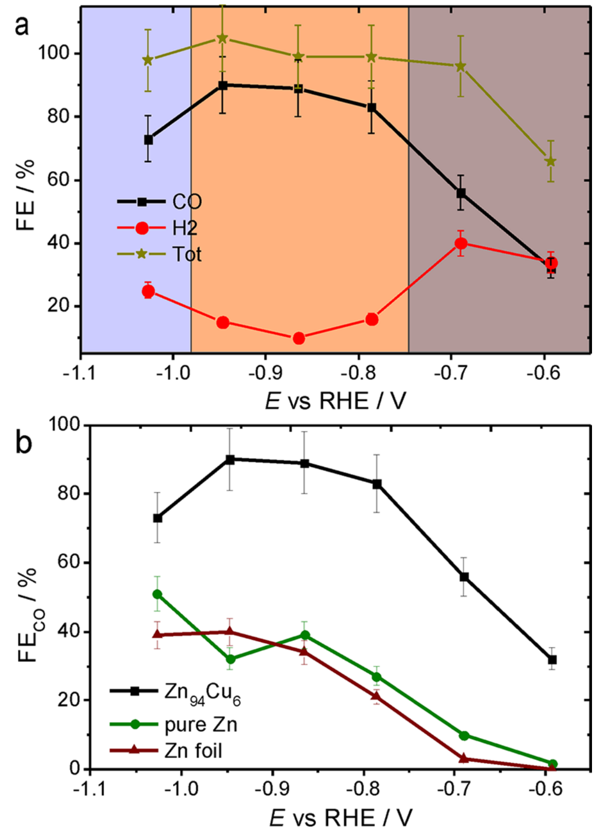

Figure 7. (a) Potential-dependent product analysis of CO_2RR on $Zn_{94}Cu_6$. (b) Comparison of CO production efficiency at applied sample potentials for $Zn_{94}Cu_6$, pure Zn, and reference Zn foil. The error bar is the standard deviation from at least three measurements carried out with a dedicated sample each.

The third potential domain in the FE vs E plot ($E \leq -0.95$ V) is characterized by a drop-down of FE_{CO} that is anticorrelated to the rise in the respective FE_{H_2} values. We do not assign this effect to a loss in electrocatalytic performance of the novel $Zn_{94}Cu_6$ catalyst, but instead to the onset of CO_2 mass transfer limitations at elevated reaction rates at higher overpotentials on the high-surface-area catalyst. We note that the HER (water splitting) does not become mass-transfer-limited, thus rationalizing its dominance at high overpotentials, particularly on the high-surface-area catalyst. This conclusion becomes more substantiated when comparing the FE results of the high-surface-area $Zn_{94}Cu_6$ catalyst to those for the pure Zn and the Zn foil references. Figure 7b shows that both reference samples follow the same qualitative trend of continuously increasing FE_{CO} values with applied potentials, which, however, remain substantially below those FE_{CO} values of the $Zn_{94}Cu_6$ catalyst presumably due to their lower availability of undercoordinated reactive sites. At highest applied electrolysis potentials of −1.0 V versus RHE, mass transfer limitation of CO_2 is obviously not yet reached for both reference catalysts. This is due to the lower total reaction rates, which are observed for both reference systems due to their lower electrochemically active surface areas.

DOI: 10.1021/acsami.8b09894
ACS Appl. Mater. Interfaces 2018, 10, 31355−31365

CO_2 Electrolysis: Catalyst Degradation. For future industrial applications of the $Zn_{94}Cu_6$ catalysts at larger scale, its improved catalytic performance relative to other Zn-based cathodes needs to be coupled to chemical and structural robustness of the catalyst.

To demonstrate the superior durability of the $Zn_{94}Cu_6$ catalysts, extended 36 h CO_2RR was carried out at E = −0.865 V versus RHE (Figure 8a). The corresponding current/time transient curve starts at large cathodic current densities assigned to the reduction of the terminating oxide/hydroxide layer. However, already within seconds, a quasi-steady-state current is reached that mainly represents the CO_2RR superimposed on a minor parasitic HER. We note that, by the end of the stressing measurement, the total current density has decreased only by ∼8% with regard to the initial quasi-steady-state value. Of equal importance is that the FE_{CO} remained on a high level close to 80% throughout the whole stressing experiment.

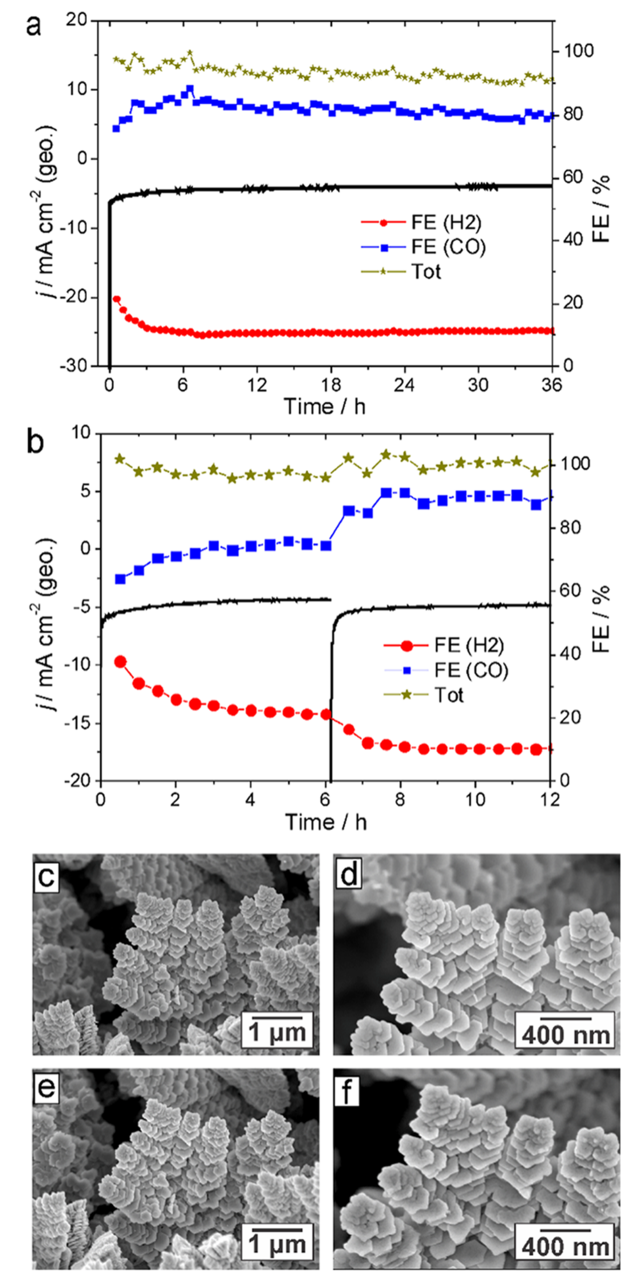

Figure 8. (a) Chronoamperogram corresponding to the chemical stability test of $Zn_{94}Cu_6$ (black line) and faradic efficiencies of products collected in intervals of 30 min by online GC during CO_2RR at −0.865 V vs RHE (solid symbols). (b) Sequential chronoamperograms (black lines) with an intermediate 8 h ambient oxidation step and faradic efficiency of obtained products (solid symbols, conditions: E = −0.865 V vs RHE). IL-SEM images of selected sample location at different magnifications before (c, d) and after (e, f) conduction of a 3 h CO_2RR cycle at −0.865 V vs RHE.

In a further extended electrolysis experiment, a 12 h CO_2RR was subdivided into two single intervals separated by a break of 8 h, where the $Zn_{94}Cu_6$ catalyst was emersed from the electrolyte and kept under ambient conditions, thereby allowing reoxidation of the already used and conditioned catalyst surface. The reduction of the freshly formed oxide/hydroxide layer at the onset of the second electrolysis interval becomes obvious from the steep decrease of the high cathodic current (Figure 8b). Instead of degradation, we observed a further improvement of the catalyst performance. The FE_{CO} increased by ∼10% with respect to the initial 6 h electrolysis interval. These results indicate that catalyst conditioning by repetitive oxidation/reduction cycles is beneficial for further activation of passive surface sites left behind by the first surface treatment, leading to improvements of the catalyst performance.

Complementary identical location (IL) SEM investigations were carried out before and after the CO_2RR to monitor possible structural/morphological alterations of the $Zn_{94}Cu_6$ catalyst.[33,34] Comparison of catalyst morphologies at the same location of the catalyst before and after electrolysis shows neither long-range nor local modifications on its surface (compare Figure 8c−f). This observation is particularly noteworthy since the actual catalyst surface undergoes chemical modifications in the course of the oxide/hydroxide reduction process. It demonstrates, however, that the reduction of the terminating oxide/hydroxide layer on the as-prepared $Zn_{94}Cu_6$ catalyst is a surface process rather than a bulk process taking place on the atomic/nanometer length scale, which is beyond the spatial resolution of the SEM instrument used. Finally, analogous XRD experiments were performed and the results are displayed in Figure S12. Both diffractograms (before and after 3 h CO_2 electrolysis) do not show appreciable alterations as a result of the electrochemical process, which further supports the structural integrity of the developed catalyst. We note, however, that the surface sensitivity of this technique is rather poor and therefore does not enable chemical characterization of the actual catalyst surface.

Transfer of the $Zn_{94}Cu_6$ Catalyst onto Technical Supports. Our catalyst screening experiments carried out from a liquid aqueous electrolyte in a classical half-cell configuration already indicate that CO_2RR faces CO_2 mass transport limitations at high overpotentials, in particular, when high-surface-area catalysts are used. For industrial applications, however, current densities are targeted in the range of hundreds of mA cm^{-2}, which is higher by at least 1 order of magnitude than what is presented herein.[52]

For technical applications, the CO_2 mass transfer limitations are circumvented by forced convection and the use of gaseous reactants.[53] The most common approach employs gas diffusion electrodes (GDEs), whose front side, containing the active catalyst (e.g., metal nanoparticles), is in contact with the liquid electrolyte, while the reactant is transported to the solid−liquid interface from its permeable back side.[54,55]

DOI: 10.1021/acsami.8b09894
ACS Appl. Mater. Interfaces 2018, 10, 31355−31365

An alternative approach utilizes catalyst materials supported on technical substrates with open-cell porosity, which enable controlled flow through the catalyst framework of liquid electrolytes, where the CO_2 reactant is dissolved. Among these, 3D hollow-fiber structures,[56] metallic 3D skeletons,[38] and technical meshes[57] have recently been applied for CO_2RR.

Motivated by these advances, the $Zn_{94}Cu_6$ catalyst was transferred onto technical Cu mesh (M) supports (Figure 9)

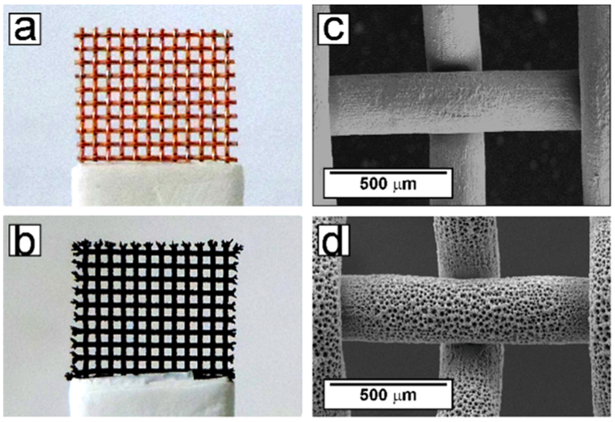

Figure 9. Optical micrographs of Cu mesh used as technical support (a) before and (b) after deposition of $Zn_{94}Cu_6$ at -3 A cm^{-2} for 20 s. SEM images of the technical substrate (c) before and (d) after catalyst deposition.

and its electrocatalytic performance was evaluated similarly to the planar foil-supported material. Figure 10a shows the dependence of FE_{CO} and FE_{H_2} on applied potentials for the mesh-supported $Zn_{94}Cu_6$ catalyst (M-$Zn_{94}Cu_6$). Qualitatively, the same behavior is observed for both $Zn_{94}Cu_6$ and M-$Zn_{94}Cu_6$. However, the complete mass transport limiting regime of dissolved CO_2 is reached at lower overpotentials for the mesh-supported catalyst (compare FE_{CO} in Figures 7a and 10a). This supports the intrinsic high activity of the $Zn_{94}Cu_6$ foam that does not lose activity at high overpotentials but whose CO yield becomes limited by poor CO_2 solubility in the used aqueous electrolyte.

Further, 8 h chemical stability tests at -0.89 V with a short interruption (30 min) after 4 h of having started the electrolysis to intentionally oxidize the surface catalyst were applied, and no apparent activity degradation or improvement was observed (see Figure 10b).

One important aspect that still needs to be addressed is the unfulfilled exploitation of the extremely large surface area of the $Zn_{94}Cu_6$ catalyst synthesized by the DHBT method. However, to overcome the low solubility of the CO_2 reactant in aqueous electrolyte that might be lowering the reaction rates via mass transport limitations, testing of $Zn_{94}Cu_6$ in, for instance, GDE configuration or electrolysis in ionic liquid-based solutions are two promising platforms that might maximize its performance. Efforts in these directions are been pursued currently by our group.

■ CONCLUSIONS

We have developed a highly porous Zn-based cathode for electrochemical reduction of CO_2 with high selectivity toward CO production. The cathode material was synthesized by the dynamic hydrogen bubble template approach. Contrary to the case of other metals (e.g., Cu, Pt, Ag), galvanostatic deposition

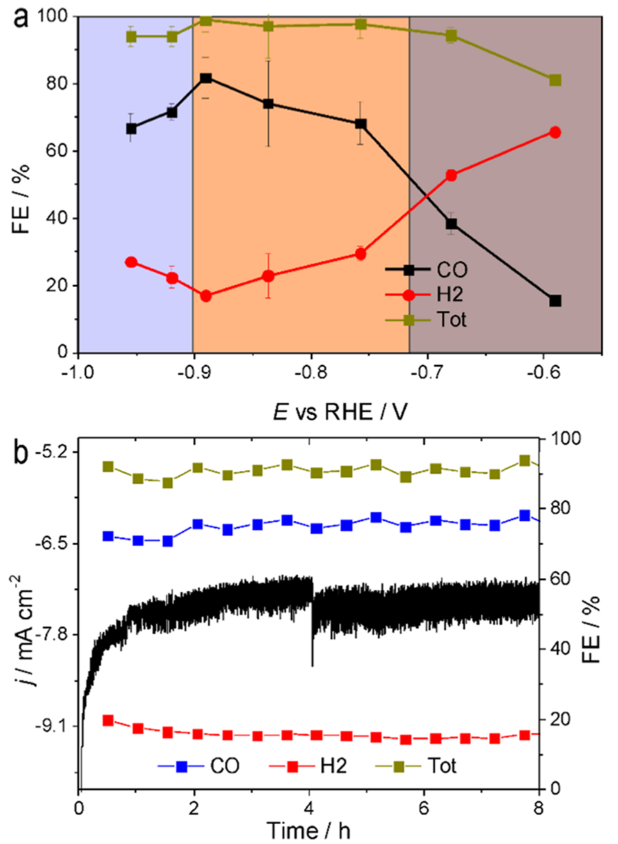

Figure 10. (a) Potential-dependent product analysis of CO_2RR on M-$Zn_{94}Cu_6$. (b) Chronoamperogram corresponding to the chemical stability test of M-$Zn_{94}Cu_6$ (black line) and faradic efficiencies of products collected in intervals of 30 min by online GC during CO_2RR (solid symbols, $E = -0.89$ V).

conducted with electroplating baths solely containing the target metal ion did not form the expected porous structure but a stepped fish scalelike surface that preferentially exhibits the (0001) plane. To circumvent this difficulty, we employed Cu ions in the Zn^{2+}-rich electroplating bath as foaming agent. The concentration of Cu as foaming agent was systematically studied and an optimized $Zn_{94}Cu_6$ foam alloy was developed, which, to the best of our knowledge, is the most selective Zn-based CO_2 electrocatalyst toward CO in aqueous bicarbonate solution (FE_{CO} = 90% at -0.95 V vs RHE). Additionally, the chemical stability of the synthesized cathode was tested and proved to be preserved for at least 36 h. This stability was found to also be immune to intentional oxidation of its surface at ambient conditions for 8 h. Moreover, this additional intermediate oxidation−reduction activation further improved the FE_{CO} by at least 10%. Ex situ identical location (IL)-SEM investigations before and after a 3 h CO_2 electrolysis cycle further confirmed the structural stability of the cathode. Finally, in an attempt to upscale the $Zn_{94}Cu_6$ catalyst, similar preparation and analysis strategies were successfully implemented for $Zn_{94}Cu_6$ samples supported by technical Cu mesh.

■ ASSOCIATED CONTENT

Supporting Information

The Supporting Information is available free of charge on the ACS Publications website at DOI: 10.1021/acsami.8b09894.

Characteristics of all prepared Zn−Cu alloys; electrochemical characterizations (galvanostatic metal deposi-

DOI: 10.1021/acsami.8b09894
ACS Appl. Mater. Interfaces 2018, 10, 31355−31365

tion and CO_2RR chronoamperograms); SEM imaging of selected Zn−Cu alloys as well as their CO_2RR performance and pore analysis of pure Cu foam; pictures of sample preparation by electrodeposition; capacitance measurements; cross-sectional SEM image of $Zn_{94}Cu_6$ and pure Cu; EDX analysis of $Zn_{94}Cu_6$ catalyst; FEs of $Zn_{94}Cu_6$ in Ar-saturated solution; and XRD analysis before and after CO_2RR (PDF)

AUTHOR INFORMATION

Corresponding Authors

*E-mail: pavel.moreno@dcb.unibe.ch (P.M.-G.).
*E-mail: peter.broekman@dcb.unibe.ch (P.B.).

ORCID

Pavel Moreno-García: 0000-0002-6827-787X
Alena Cedeño López: 0000-0002-4917-7355
Abhijit Dutta: 0000-0002-3054-0492
Motiar Rahaman: 0000-0002-8422-0566
Peter Broekmann: 0000-0002-6287-1042

Author Contributions

The manuscript was written through contributions of all authors. All authors have given approval to the final version of the manuscript.

Author Contributions

†P.M.-G. and N.S. contributed equally to this work.

Notes

The authors declare no competing financial interest.

ACKNOWLEDGMENTS

Financial support by the CTI Swiss Competence Center for Energy Research (SCCER Heat and Electricity Storage) is gratefully acknowledged. M.d.J.G.-V. acknowledges the financial support by Swiss Government Excellence Scholarships for Foreign Scholars (ESKAS). P.B. acknowledges the financial support from the Swiss National Foundation (No. 200020_172507). This study was supported by the interfaculty Microscopy Imaging Centre (MIC) of the University of Bern.

REFERENCES

(1) Whipple, D. T.; Kenis, P. J. A. Prospects of CO_2 Utilization via Direct Heterogeneous Electrochemical Reduction. *J. Phys. Chem. Lett.* **2010**, *1*, 3451−3458.

(2) Qiao, J.; Liu, Y.; Hong, F.; Zhang, J. A Review of Catalysts for the Electroreduction of Carbon Dioxide to Produce Low-Carbon Fuels. *Chem. Soc. Rev.* **2014**, *43*, 631−675.

(3) Hara, K.; Kudo, A.; Sakata, T. Electrochemical Reduction of Carbon Dioxide under High Pressure on Various Electrodes in an Aqueous Electrolyte. *J. Electroanal. Chem.* **1995**, *391*, 141−147.

(4) Hori, Y.; Wakebe, H.; Tsukamoto, T.; Koga, O. Electrocatalytic Process of CO Selectivity in Electrochemical Reduction of CO_2 at Metal Electrodes in Aqueous Media. *Electrochim. Acta* **1994**, *39*, 1833−1839.

(5) Azuma, M.; Hashimoto, K.; Hiramoto, M.; Watanabe, M.; Sakata, T. Electrochemical Reduction of Carbon Dioxide on Various Metal Electrodes in Low-Temperature Aqueous $KHCO_3$ Media. *J. Electrochem. Soc.* **1990**, *137*, 1772−1778.

(6) Kuhl, K. P.; Hatsukade, T.; Cave, E. R.; Abram, D. N.; Kibsgaard, J.; Jaramillo, T. F. Electrocatalytic Conversion of Carbon Dioxide to Methane and Methanol on Transition Metal Surfaces. *J. Am. Chem. Soc.* **2014**, *136*, 14107−14113.

(7) Li, C. W.; Ciston, J.; Kanan, M. W. Electroreduction of Carbon Monoxide to Liquid Fuel on Oxide-Derived Nanocrystalline Copper. *Nature* **2014**, *508*, 504.

(8) Chen, Y.; Li, C. W.; Kanan, M. W. Aqueous CO_2 Reduction at Very Low Overpotential on Oxide-Derived Au Nanoparticles. *J. Am. Chem. Soc.* **2012**, *134*, 19969−19972.

(9) Rosen, J.; Hutchings, G. S.; Lu, Q.; Rivera, S.; Zhou, Y.; Vlachos, D. G.; Jiao, F. Mechanistic Insights into the Electrochemical Reduction of CO_2 to CO on Nanostructured Ag Surfaces. *ACS Catal.* **2015**, *5*, 4293−4299.

(10) Nursanto, E. B.; Jeon, H. S.; Kim, C.; Jee, M. S.; Koh, J. H.; Hwang, Y. J.; Min, B. K. Gold Catalyst Reactivity for CO_2 Electro-Reduction: From Nano Particle to Layer. *Catal. Today* **2016**, *260*, 107−111.

(11) Jee, M. S.; Jeon, H. S.; Kim, C.; Lee, H.; Koh, J. H.; Cho, J.; Min, B. K.; Hwang, Y. J. Enhancement in Carbon Dioxide Activity and Stability on Nanostructured Silver Electrode and the Role of Oxygen. *Appl. Catal., B* **2016**, *180*, 372−378.

(12) Lee, H.; Kim, H.; Park, H.; Kim, J.; Kim, H.; Hwang, E.; Kim, S.-K.; Ahn, S. H. *Electrochemical Fabrication of Ag and Au Foams for Electrochemical Conversion of CO_2*, ECS Meeting Abstracts, MA2016-02, 2016; Vol. 38, p 2741.

(13) Quan, F.; Zhong, D.; Song, H.; Jia, F.; Zhang, L. A Highly Efficient Zinc Catalyst for Selective Electroreduction of Carbon Dioxide in Aqueous NaCl Solution. *J. Mater. Chem. A* **2015**, *3*, 16409−16413.

(14) Won, D. H.; Shin, H.; Koh, J.; Chung, J.; Lee, H. S.; Kim, H.; Woo, S. I. Highly Efficient, Selective, and Stable CO_2 Electro-reduction on a Hexagonal Zn Catalyst. *Angew. Chem., Int. Ed.* **2016**, *55*, 9297−9300.

(15) Keerthiga, G.; Chetty, R. Electrochemical Reduction of Carbon Dioxide on Zinc-Modified Copper Electrodes. *J. Electrochem. Soc.* **2017**, *164*, H164−H169.

(16) Rosen, J.; Hutchings, G. S.; Lu, Q.; Forest, R. V.; Moore, A.; Jiao, F. Electrodeposited Zn Dendrites with Enhanced CO Selectivity for Electrocatalytic CO_2 Reduction. *ACS Catal.* **2015**, *5*, 4586−4591.

(17) Nguyen, D. L. T.; Jee, M. S.; Won, D. H.; Jung, H.; Oh, H.-S.; Min, B. K.; Hwang, Y. J. Selective CO_2 Reduction on Zinc Electrocatalyst: The Effect of Zinc Oxidation State Induced by Pretreatment Environment. *ACS Sustainable Chem. Eng.* **2017**, *5*, 11377−11386.

(18) Dutta, A.; Rahaman, M.; Luedi, N. C.; Mohos, M.; Broekmann, P. Morphology Matters: Tuning the Product Distribution of CO_2 Electroreduction on Oxide-Derived Cu Foam Catalysts. *ACS Catal.* **2016**, *6*, 3804−3814.

(19) Sen, S.; Liu, D.; Palmore, G. T. R. Electrochemical Reduction of CO_2 at Copper Nanofoams. *ACS Catal.* **2014**, *4*, 3091−3095.

(20) Wang, M.; Yu, X.; Wang, Z.; Gong, X.; Guo, Z.; Dai, L. Hierarchically 3D Porous Films Electrochemically Constructed on Gas-Liquid-Solid Three-Phase Interface for Energy Application. *J. Mater. Chem. A* **2017**, *5*, 9488−9513.

(21) Plowman, B. J.; Jones, L. A.; Bhargava, S. K. Building with Bubbles: the Formation of High Surface Area Honeycomb-like Films via Hydrogen Bubble Templated Electrodeposition. *Chem. Commun.* **2015**, *51*, 4331−4346.

(22) Shin, H.-C.; Liu, M. Copper Foam Structures with Highly Porous Nanostructured Walls. *Chem. Mater.* **2004**, *16*, 5460−5464.

(23) Cherevko, S.; Chung, C.-H. Impact of Key Deposition Parameters on the Morphology of Silver Foams Prepared by Dynamic Hydrogen Template Deposition. *Electrochim. Acta* **2010**, *55*, 6383−6390.

(24) Cherevko, S.; Xing, X.; Chung, C.-H. Electrodeposition of Three-Dimensional Porous Silver Foams. *Electrochem. Commun.* **2010**, *12*, 467−470.

(25) Plowman, B. J.; O'Mullane, A. P.; Selvakannan, P. R.; Bhargava, S. K. Honeycomb Nanogold Networks with Highly Active Sites. *Chem. Commun.* **2010**, *46*, 9182−9184.

(26) Cherevko, S.; Chung, C.-H. Direct Electrodeposition of Nanoporous Gold with Controlled Multimodal Pore Size Distribution. *Electrochem. Commun.* **2011**, *13*, 16−19.

(27) Huan, T. N.; Ganesh, T.; Kim, K. S.; Kim, S.; Han, S.-H.; Chung, H. A Three-Dimensional Gold Nanodendrite Network

DOI: 10.1021/acsami.8b09894
ACS Appl. Mater. Interfaces 2018, 10, 31355−31365

Porous Structure and its Application for an Electrochemical Sensing. *Biosens. Bioelectron.* **2011**, *27*, 183−186.
(28) Sanzó, G.; Taurino, I.; Antiochia, R.; Gorton, L.; Favero, G.; Mazzei, F.; De Micheli, G.; Carrara, S. Bubble Electrodeposition of Gold Porous Nanocorals for the Enzymatic and non-Enzymatic Detection of Glucose. *Bioelectrochemistry* **2016**, *112*, 125−131.
(29) du Toit, H.; Di Lorenzo, M. Electrodeposited Highly Porous Gold Microelectrodes for the Direct Electrocatalytic Oxidation of Aqueous Glucose. *Sens. Actuators, B* **2014**, *192*, 725−729.
(30) Mattarozzi, L.; Cattarin, S.; Comisso, N.; Gerbasi, R.; Guerriero, P.; Musiani, M.; Vázquez-Gómez, L.; Verlato, E. Electrodeposition of Compact and Porous Cu-Zn Alloy Electrodes and Their Use in the Cathodic Reduction of Nitrate. *J. Electrochem. Soc.* **2015**, *162*, D236−D241.
(31) Varzi, A.; Mattarozzi, L.; Cattarin, S.; Guerriero, P.; Passerini, S. 3D Porous Cu−Zn Alloys as Alternative Anode Materials for Li-Ion Batteries with Superior Low T Performance. *Adv. Energy Mater.* **2018**, *8*, No. 1701706.
(32) Ashassi-Sorkhabi, H.; Abolghasemi-Fakhri, S.; Rezaei Moghadam, B.; Javan, H. One Step Electrochemical Route to the Fabrication of Highly Ordered Array of Cylindrical Nano Porous Structure and its Electrocatalytic Performance toward Efficient Hydrogen Evolution. *J. Colloid Interface Sci.* **2018**, *515*, 189−197.
(33) Mayrhofer, K. J. J.; Meier, J. C.; Ashton, S. J.; Wiberg, G. K. H.; Kraus, F.; Hanzlik, M.; Arenz, M. Fuel Cell Catalyst Degradation on the Nanoscale. *Electrochem. Commun.* **2008**, *10*, 1144−1147.
(34) Hodnik, N.; Zorko, M.; Bele, M.; Hočevar, S.; Gaberšček, M. Identical Location Scanning Electron Microscopy: A Case Study of Electrochemical Degradation of PtNi Nanoparticles Using a New Nondestructive Method. *J. Phys. Chem. C* **2012**, *116*, 21326−21333.
(35) Tsai, W. L.; Hsu, P. C.; Hwu, Y.; Chen, C. H.; Chang, L. W.; Je, J. H.; Lin, H. M.; Groso, A.; Margaritondo, G. Building on Bubbles in Metal Electrodeposition. *Nature* **2002**, *417*, 139.
(36) Nikolić, N. D.; Popov, K. I.; Pavlović, L. J.; Pavlović, M. G. Morphologies of Copper Deposits Obtained by the Electrodeposition at High Overpotentials. *Surf. Coat. Technol.* **2006**, *201*, 560−566.
(37) Nikolić, N. D.; Popov, K. I.; Pavlović, L. J.; Pavlović, M. G. The Effect of Hydrogen Codeposition on the Morphology of Copper Electrodeposits. I. The Concept of Effective Overpotential. *J. Electroanal. Chem.* **2006**, *588*, 88−98.
(38) Dutta, A.; Rahaman, M.; Mohos, M.; Zanetti, A.; Broekmann, P. Electrochemical CO_2 Conversion Using Skeleton (Sponge) Type of Cu Catalysts. *ACS Catal.* **2017**, *7*, 5431−5437.
(39) Zhang, H.; Ye, Y.; Shen, R.; Ru, C.; Hu, Y. Effect of Bubble Behavior on the Morphology of Foamed Porous Copper Prepared via Electrodeposition. *J. Electrochem. Soc.* **2013**, *160*, D441−D445.
(40) Nikolić, N. D.; Branković, G. Comparison of Open Porous Copper Structures Obtained by the Different Current Regimes of Electrolysis. *Mater. Lett.* **2012**, *70*, 11−15.
(41) Trasatti, S. Work Function, Electronegativity, and Electrochemical Behaviour of Metals: III. Electrolytic Hydrogen Evolution in Acid Solutions. *J. Electroanal. Chem. Interfacial Electrochem.* **1972**, *39*, 163−184.
(42) Nørskov, J. K.; Bligaard, T.; Logadottir, A.; Kitchin, J. R.; Chen, J. G.; Pandelov, S.; Stimming, U. Trends in the Exchange Current for Hydrogen Evolution. *J. Electrochem. Soc.* **2005**, *152*, J23−J26.
(43) Quaino, P.; Juarez, F.; Santos, E.; Schmickler, W. Volcano Plots in Hydrogen Electrocatalysis − Uses and Abuses. *Beilstein J. Nanotechnol.* **2014**, *5*, 846−854.
(44) Afanas'ev, B. N.; Akulova, Y. P. A Correlation between the Hydrophilicity of a Metal and its Surface Tension. Calculation of the Bond Energy of Water Molecules Adsorbed on an Uncharged Metal Surface. *Prot. Met.* **2000**, *36*, 25−30.
(45) Lust, E.; Jänes, A.; Lust, K.; Pullerits, R. Adsorption of Organic Compounds and Hydrophilicity of Bismuth, Cadmium and Antimony Electrodes. *J. Electroanal. Chem.* **1997**, *431*, 183−201.
(46) Gaarenstroom, S. W.; Winograd, N. Initial and Final State Effects in the ESCA Spectra of Cadmium and Silver Oxides. *J. Chem. Phys.* **1977**, *67*, 3500−3506.
(47) Pradhan, D.; Leung, K. T. Controlled Growth of Two-Dimensional and One-Dimensional ZnO Nanostructures on Indium Tin Oxide Coated Glass by Direct Electrodeposition. *Langmuir* **2008**, *24*, 9707−9716.
(48) Deng, X.; Verdaguer, A.; Herranz, T.; Weis, C.; Bluhm, H.; Salmeron, M. Surface Chemistry of Cu in the Presence of CO_2 and H_2O. *Langmuir* **2008**, *24*, 9474−9478.
(49) Bang, S.; Lee, S.; Ko, Y.; Park, J.; Shin, S.; Seo, H.; Jeon, H. Photocurrent Detection of Chemically Tuned Hierarchical ZnO Nanostructures Grown on Seed Layers Formed by Atomic Layer Deposition. *Nanoscale Res. Lett.* **2012**, *7*, 290.
(50) McIntyre, N. S.; Cook, M. G. X-ray Photoelectron Studies on some Oxides and Hydroxides of Cobalt, Nickel, and Copper. *Anal. Chem.* **1975**, *47*, 2208−2213.
(51) Biesinger, M. C.; Lau, L. W. M.; Gerson, A. R.; Smart, R. S. C. Resolving Surface Chemical States in XPS Analysis of First Row Transition Metals, Oxides and Hydroxides: Sc, Ti, V, Cu and Zn. *Appl. Surf. Sci.* **2010**, *257*, 887−898.
(52) Cook, R. L.; MacDuff, R. C.; Sammells, A. F. High Rate Gas Phase CO_2 Reduction to Ethylene and Methane Using Gas Diffusion Electrodes. *J. Electrochem. Soc.* **1990**, *137*, 607−608.
(53) Jhong, H.-R. M.; Ma, S.; Kenis, P. J. A. Electrochemical Conversion of CO_2 to Useful Chemicals: Current Status, Remaining Challenges, and Future Opportunities. *Curr. Opin. Chem. Eng.* **2013**, *2*, 191−199.
(54) Ma, S.; Sadakiyo, M.; Luo, R.; Heima, M.; Yamauchi, M.; Kenis, P. J. A. One-Step Electrosynthesis of Ethylene and Ethanol from CO_2 in an Alkaline Electrolyzer. *J. Power Sources* **2016**, *301*, 219−228.
(55) Jhong, H.-R. M.; Brushett, F. R.; Kenis, P. J. A. The Effects of Catalyst Layer Deposition Methodology on Electrode Performance. *Adv. Energy Mater.* **2013**, *3*, 589−599.
(56) Kas, R.; Hummadi, K. K.; Kortlever, R.; de Wit, P.; Milbrat, A.; Luiten-Olieman, M. W. J.; Benes, N. E.; Koper, M. T. M.; Mul, G. Three-Dimensional Porous Hollow Fibre Copper Electrodes for Efficient and High-Rate Electrochemical Carbon Dioxide Reduction. *Nat. Commun.* **2016**, *7*, No. 10748.
(57) Rahaman, M.; Dutta, A.; Zanetti, A.; Broekmann, P. Electrochemical Reduction of CO_2 into Multicarbon Alcohols on Activated Cu Mesh Catalysts: An Identical Location (IL) Study. *ACS Catal.* **2017**, *7*, 7946−7956.

DOI: 10.1021/acsami.8b09894
ACS Appl. Mater. Interfaces 2018, 10, 31355−31365

Supporting Information

Selective Electrochemical Reduction of CO_2 to CO on Zn-based Foams Produced by Cu^{2+} and Template-Assisted Electrodeposition

Pavel Moreno-García,‡* Nicolas Schlegel,‡ Alberto Zanetti, Alena Cedeño López, María de Jesús Gálvez-Vázquez, Abhijit Dutta, Motiar Rahaman, Peter Broekmann*

Department of Chemistry and Biochemistry, University of Bern, Freiestrasse 3, Bern 3012, Switzerland

* pavel.moreno@dcb.unibe.ch, peter.broekman@dcb.unibe.ch

Contents:

Table S1. Electrolyte composition of prepared Zn-Cu alloy foams and corresponding highest achieved faradaic efficiencies and partial current densities of produced CO upon CO_2RR. Galvanostatic deposition at j = -3 A cm^{-2} was conducted for 20 s with a 1.5 M H_2SO_4 electrolyte. All alloy samples were subsequently screened by potentiostatic CO_2 electrolysis in intervals of 100 mV from -1.1 to -0.6 V vs RHE and their gaseous and liquid products analyzed by GC and IC, respectively. Each potential value was applied for 40 min within which two GC analysis runs were performed before electrolysis interruption to change the potential.

Foam sample	Electrodeposition bath			FE_{CO}	j_{CO}
	$ZnSO_4$	$CuSO_4$	Zn/Cu ratio	%	mA cm^{-2} (geo.)
Zn-Cu_1	0.208 M	0.0021 M	100	70 (-0.865 V)	-5.04
Zn-Cu_2	0.207 M	0.0034 M	60	67 (-0.865 V)	-3.62
Zn-Cu_3	0.205 M	0.005 M	40	54 (-0.865V)	-4.23
$Zn_{94}Cu_6$	0.203 M	0.006 M	30	75 (-0.865V)	-5.54
Zn-Cu_4	0.2 M	0.01 M	20	69 (-0.950 V)	-6.60
Zn-Cu_5	0.2 M	0.04 M	5	20 (-0.593 V)	-0.57
Zn-Cu_6	0.15 M	0.07 M	2.1	11 (-0.593 V)	-0.30
Zn-Cu_7	0.1 M	0.1 M	1	2.8 (-1.027 V)	-1.60

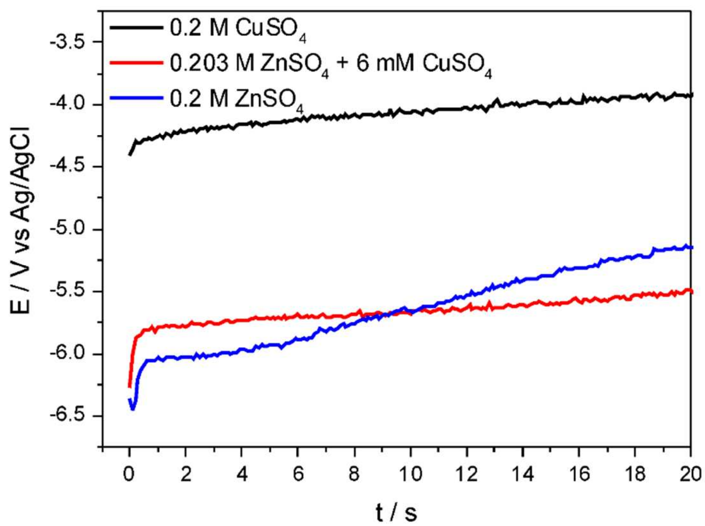

Figure S1. Potential transients corresponding to electrodeposition of pure-Cu, pure-Zn and $Zn_{94}Cu_6$ samples indicated by black, blue and red lines, respectively.

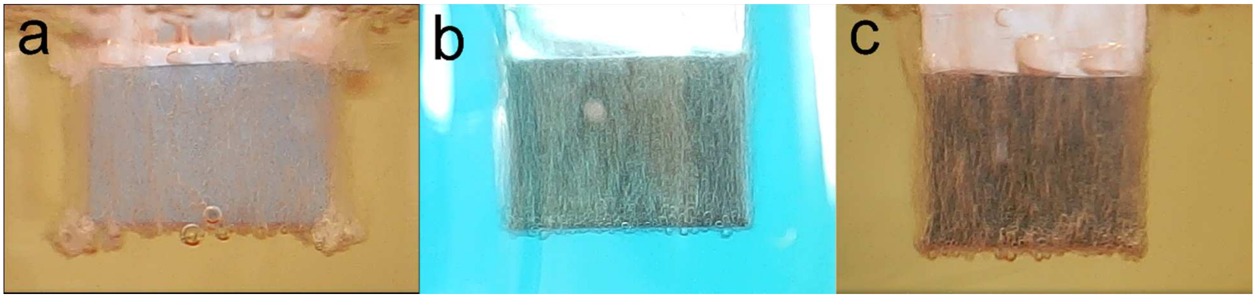

Figure S2. Optical micrographs of the electrochemical deposition by DHBT method. (a) pure-Zn, (b) pure-Cu and (c) $Zn_{94}Cu_6$ samples. The pictures were taken ~10 s after having started the galvanostatic deposition.

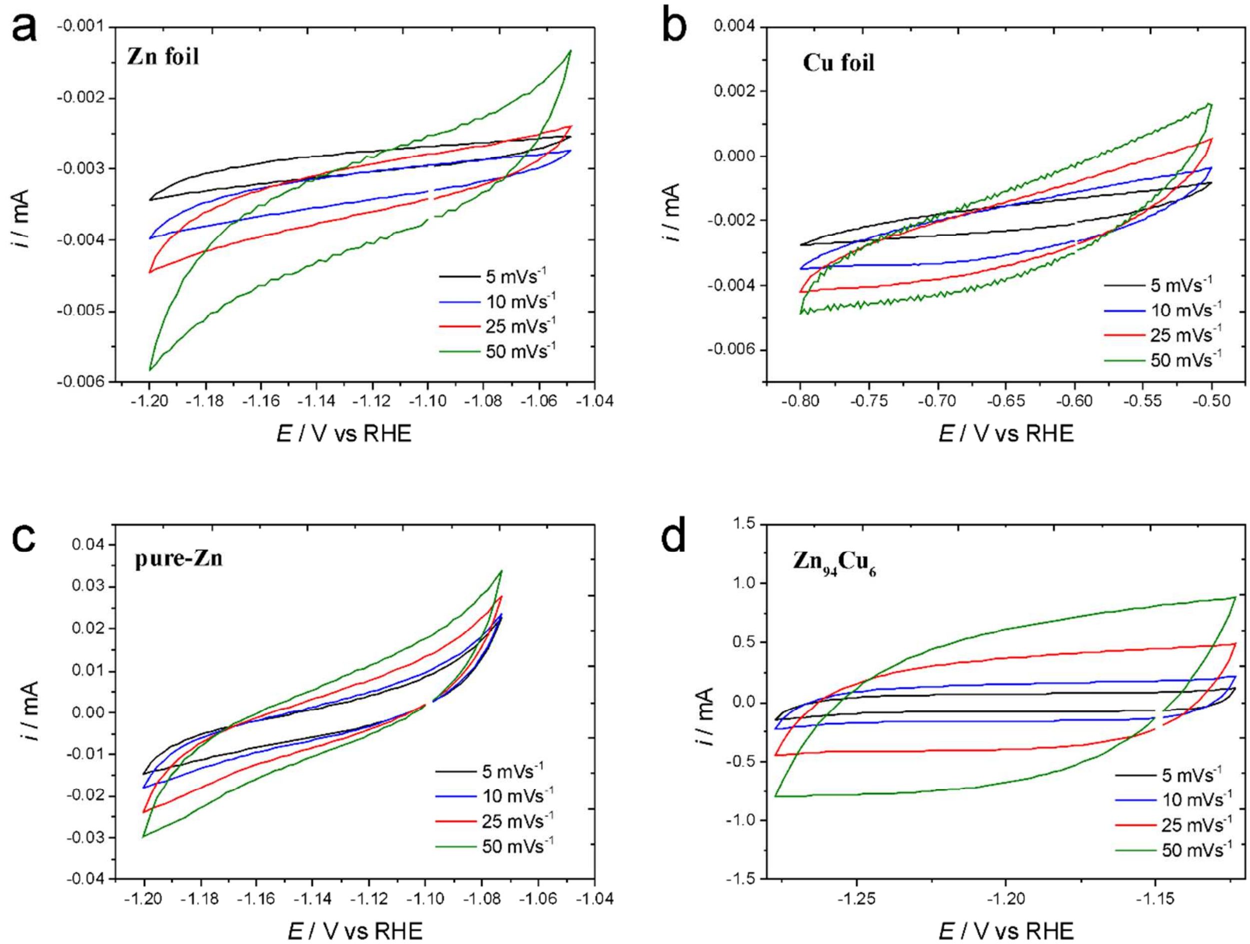

Figure S3. Cyclic voltammograms for ECSA determination of (a) Zn and (b) Cu foils as reference materials and (c) pure-Zn and (d) $Zn_{94}Cu_6$ catalyst in 0.1 M KCl as supporting electrolyte.

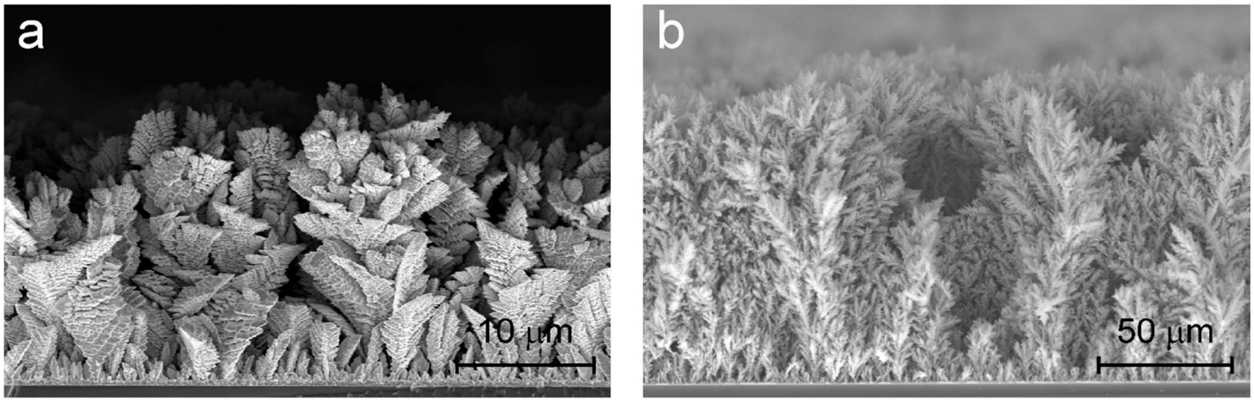

Figure S4. Cross-sectional SEM images of (a) $Zn_{94}Cu_6$ and (b) pure-Cu samples.

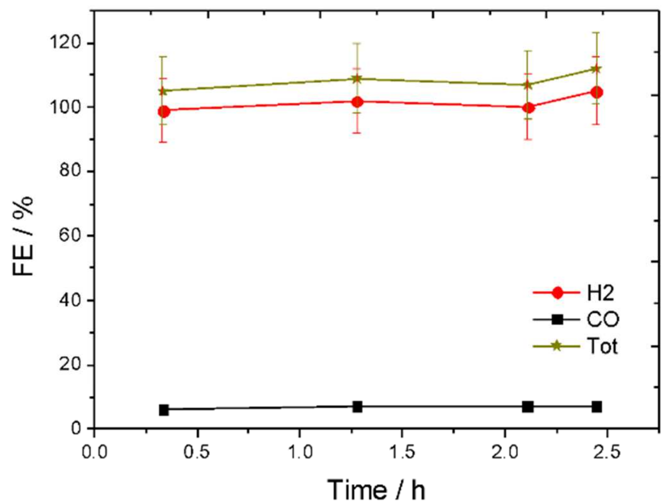

Figure S5. Faradaic efficiencies of $Zn_{94}Cu_6$ in Ar-saturated 0.5 M $KHCO_3$ solutions at -0.865 V vs RHE.

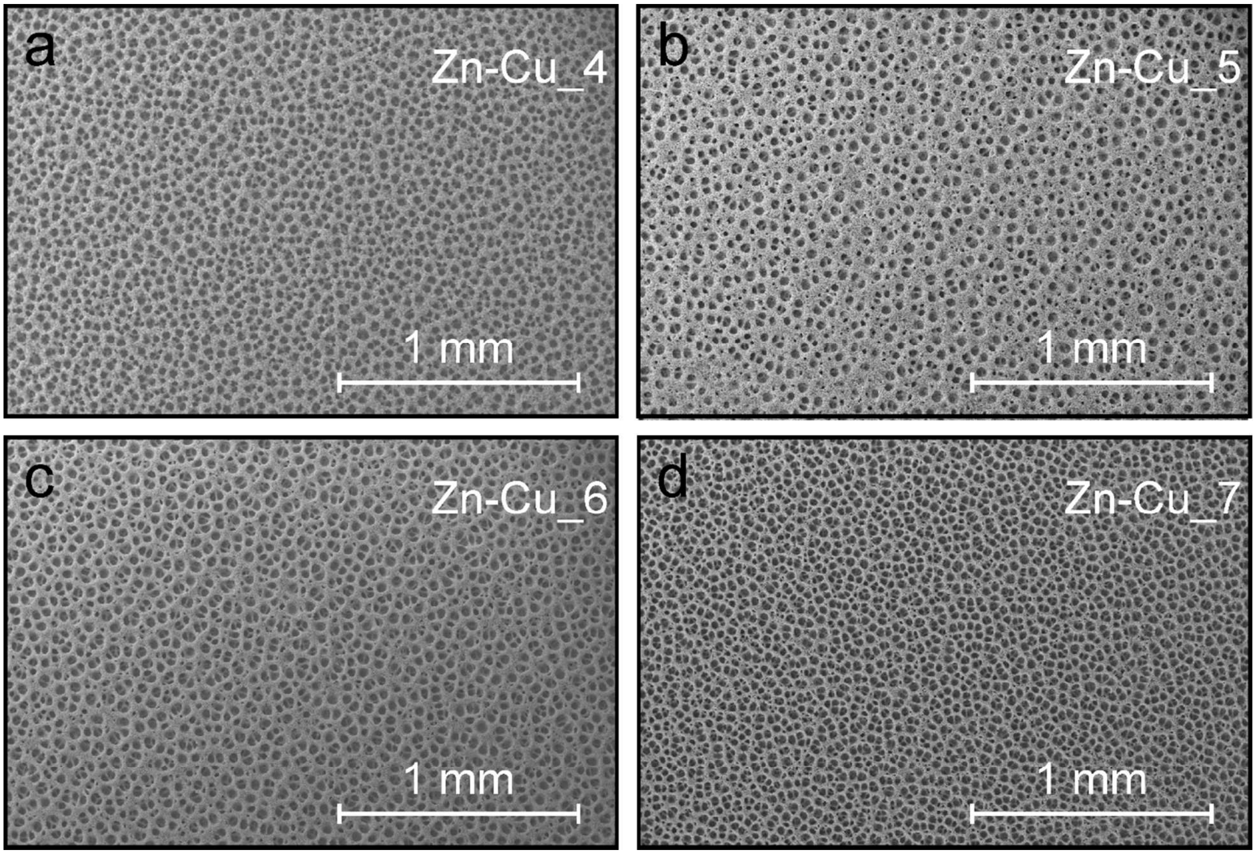

Figure S6. Top view SEM images of selected Zn-Cu alloys prepared by DHBT-assisted electroplating. The $c(Zn^{2+}/Cu^{2+})$ for (a) Zn-Cu_4, (b) Zn-Cu_5, (c) Zn-Cu_6 and (d) Zn-Cu_7 are 20, 5, 2.1 and,1 respectively.

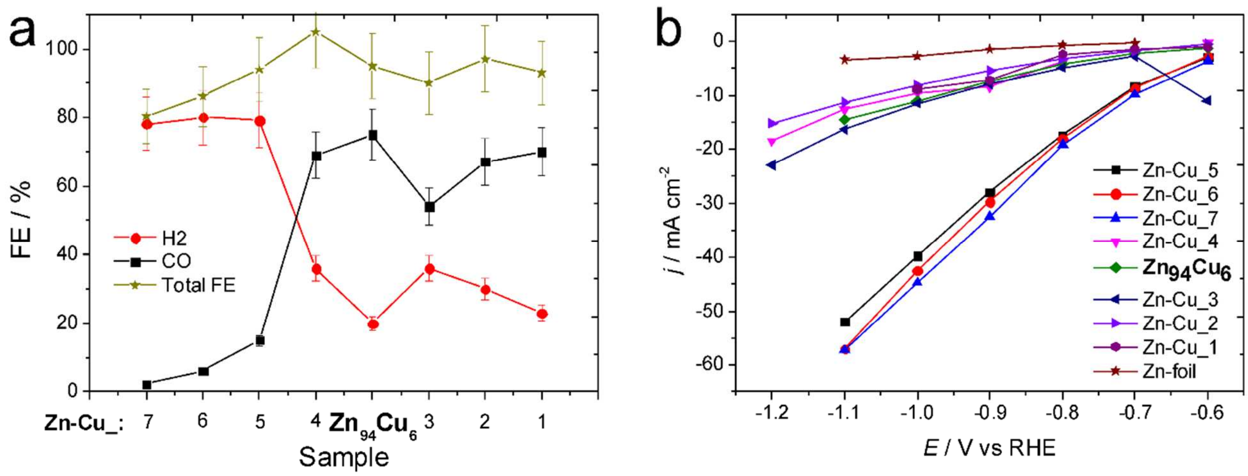

Figure S7. CO_2RR screening of all Zn-Cu alloys prepared by the DHBT method. Two groups of alloys based on their (a) H_2 and CO selectivity and (b) total current densities can be easily distinguished.

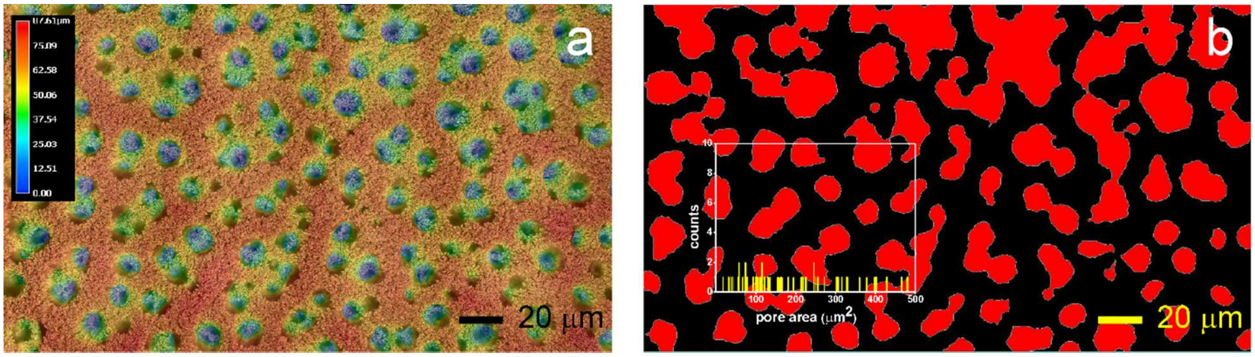

Figure S8. Pore analysis of the pure-Cu sample. (a) Topography analysis by digital optical microscope with focus variation of selected sample location. (b) Analysis of pore dimensions at depths ≥ 6 μm from the outermost sample surface.

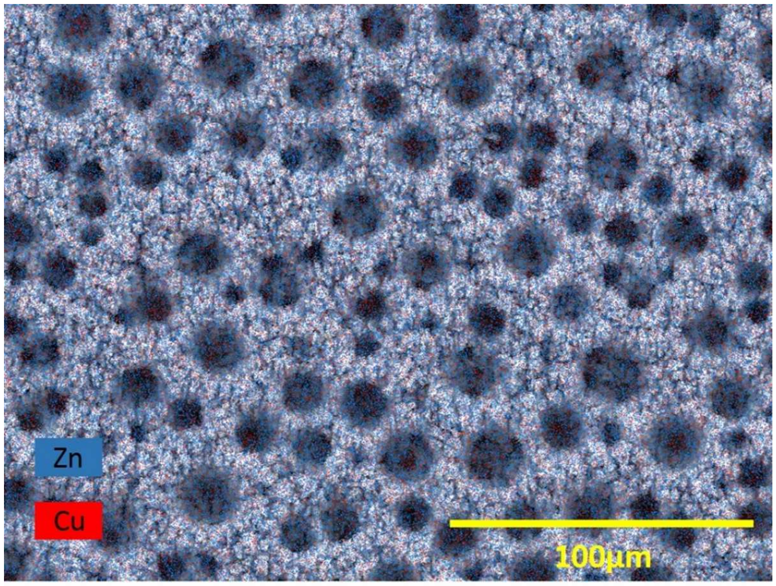

Figure S9. EDX analysis of $Zn_{94}Cu_6$ catalyst.

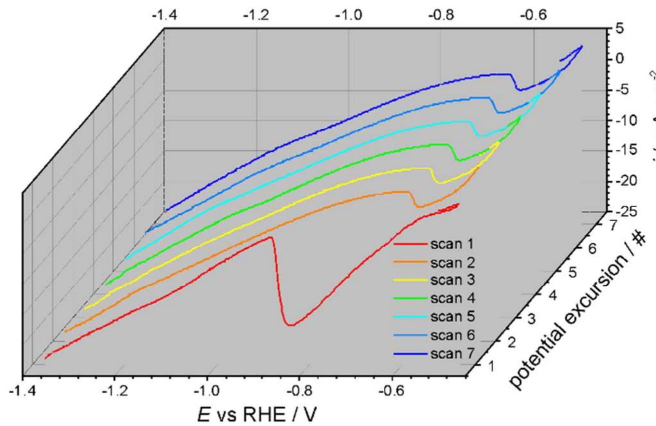

Figure S10. Linear sweep voltammetry showing the transition from non-steady state first potential scan to steady state LSV of $Zn_{94}Cu_6$ in Ar-sat. 0.5 M $KHCO_3$ solution. Scan rate ν = 10 mV s^{-1}. The starting potential value was -0.47 V vs RHE.

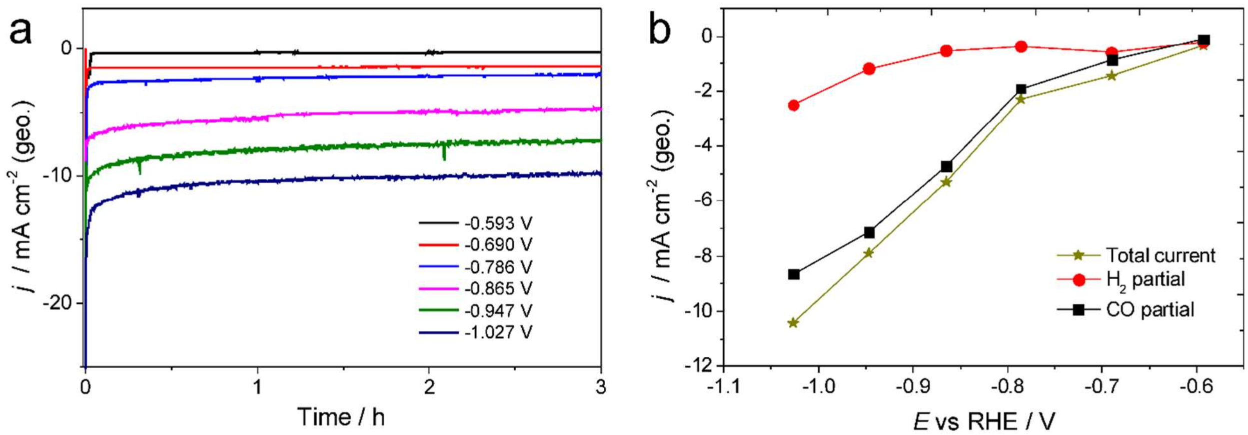

Figure S11. (a) Sample chronoamperograms at various applied potentials for CO_2RR in CO_2-saturated electrolyte using $Zn_{94}Cu_6$ deposited on Cu foil. (b) Total and partial steady state current densities recorded at various applied potentials.

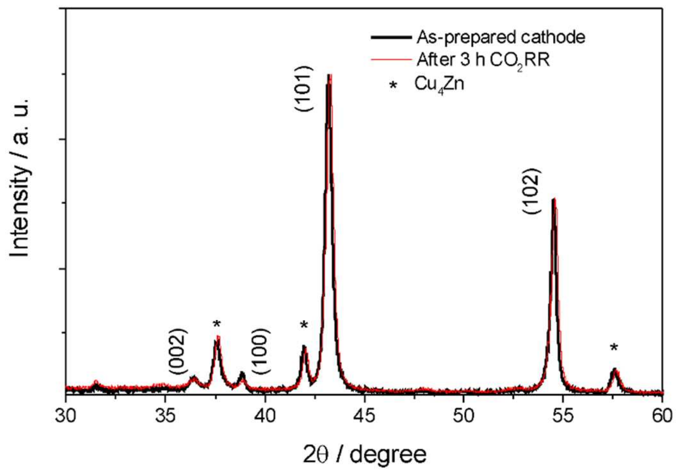

Figure S12. XRD analysis of the $Zn_{94}Cu_6$ electrodeposited catalyst before (thick black line) and after (thin red line) a 3 h CO_2RR cycle. The crystallographic planes in brackets correspond to Zn (JCPDS 04-0831). The stars correspond to Cu_4Zn phase (JCPDS65-6066).

6. Appendix

I. List of publications

1. H. Hu, M. Liu, Y. Kong, N. Mysuru, C. Sun, **M. J. Gálvez-Vázquez**, U. Müller, R. Erni, V. Grozovski, Y. Hou, and P. Broekmann, "Activation matters: hysteresis effects during electrochemical looping of colloidal Ag nanowire (Ag-NW) catalysts", *ACS Catal.*, 2020, **10** (15), 8503–8514, DOI: 10.1021/acscatal.0c02026.

2. **M. J. Gálvez-Vázquez**, H. Xu, P. Moreno-García, Y. Hou, H. Hu, B. J. Wiley, S. Vesztergom, P. Broekmann, "Unwrap Them First: Operando Potential-Induced Activation Is Required when Using PVP-Capped Ag Nanocubes as Catalysts of CO2 Electroreduction", *CHIMIA International Journal for Chemistry*, 2021, **75** (3), 163-168(6), DOI: 10.2533/chimia.2021.163.

3. Y. Hou, N. Kovács, H. Xu, C. Sun, R. Erni, **M. J. Gálvez-Vázquez**, A. Rieder, H. Hu, Y. Kong, M. Liu, B. J. Wiley, S. Vesztergom, and P. Broekmann, "Limitations of Identical Location SEM as a Method of Degradation Studies on Surfactant Capped Nanoparticle Electrocatalysts", *Journal of Catalysis*, 2021, **394**, 58-66, DOI: 10.1016/j.jcat.2020.12.006.

4. **M. J. Gálvez-Vázquez**, P. Moreno-García, H. Xu, Y. Hou, H. Hu, I. Zelocualtecatl Montiel, A. V. Rudnev, S. Alinejad, V. Grozovski, B. J. Wiley, M. Arenz, and P. Broekmann, "Environment Matters: CO_2RR Electrocatalyst Performance Testing in a Gas-Fed Zero-Gap Electrolyzer", *ACS Catal.* 2020, **10**, 13096–13108, DOI: 10.1021/acscatal.0c03609.

5. **M. J. Gálvez-Vázquez**, S. Alinejad, H. Hu, Y. Hou, P. Moreno-García, A. Zana, G. Wiberg, P. Broekmann, and M. Arenz, "Testing a Silver Nanowire Catalyst for the Selective CO_2 Reduction in a Gas Diffusion Electrode Half-cell Setup Enabling High Mass Transport Conditions", *CHIMIA International Journal for Chemistry*, 2019, **73** (11), 922-927, DOI: 10.2533/chimia.2019.922.

6. **M. J. Gálvez-Vázquez**, P. Moreno-García, H. Guo, Y. Hou, A. Dutta, S.R. Waldvogel, and P. Broekmann, "Leaded Bronze Alloy as a Catalyst for the Electroreduction of CO_2", *ChemElectroChem,* 2019, **6** (8), 2324-2330, DOI: 10.1002/celc.201900537.

7. **M. J. Gálvez-Vázquez**, V. Grozovski, N. Kovács, P. Broekmann, and S. Vesztergom, "Full model for the two-step polarization curves of hydrogen evolution, measured on RDEs in dilute acid solutions", *J. Phys. Chem. C*, 2020, **124** (7), 3988–4000, DOI: 10.1021/acs.jpcc.9b11337.

8. P. Moreno-García, N. Kovács, V. Grozovski, **M. J. Gálvez-Vázquez**, S. Vesztergom, and P. Broekmann, "Toward CO_2 Electroreduction under Controlled Mass Flow Conditions: A Combined Inverted RDE and Gas Chromatography Approach", *Anal.Chem.* 2020, **92** (6), 4301−4308, DOI: 10.1021/acs.analchem.9b04999.

9. P. Moreno-García, V. Grozovski, **M. J. Gálvez-Vázquez**, N. Mysuru, K. Kiran, N. Kovács, Yuhui Hou, S. Vesztergom, and P. Broekmann, “Inverted RDE (iRDE) as Novel Test Bed for Studies on Additive-Assisted Metal Deposition under Gas-Evolution Conditions”, *J. Electrochem. Soc*., 2020, **167** (4), 042503, DOI: 10.1149/1945-7111/ab7984.

10. P. Moreno-García, N. Schlegel, A. Zanetti, A. Cedeño López, **M. J. Gálvez-Vázquez**, A. Dutta, M. Rahaman, and P. Broekmann, “Selective Electrochemical Reduction of CO_2 to CO on Zn-based Foams Produced by Cu^{2+} and Template-Assisted Electrodeposition”, *ACS Appl. Mater. Interfaces*, 2018, **10** (37), 31355–31365, DOI: 10.1021/acsami.8b09894.

11. V. Grozovski, P. Moreno-García, E. Karst, **M. J. Gálvez-Vázquez**, A. Fluegel, S. Kitayaporn, S. Vesztergom and P. Broekmann, "Operando laser scattering: probing the evolution of local pH changes on complex electrode architectures", *J. Electrochem. Soc.*, 2021, **168,** 072504.

II. Conferences and presentations

2019

1. 8th SCCER Heat and Electricity Storage Symposium, EMPA, Dübenforf, Switzerland, November 5th. Invited talk, title: “CO_2 Electroreduction on Ag Catalysts under Controlled Mass Transport Conditions”.
2. 8th SCCER Heat and Electricity Storage Symposium, EMPA, Dübenforf, Switzerland, November 5th. Poster presentation, title: “CO_2 electroreduction on Ag catalysts from H-type to gas flow-cell experiments”.
3. Photo- and ElectroCatalysis at the Atomic Scale (PECAS2019), Donostia, San Sebastián, Spain, September 4th. Poster presentation, title: “Electrochemical conversion of CO_2 into CO using Ag nanocatalysts”.

2018

1. International Summer School “Power to X: Fundamentals and Applications of Modern Electrosynthesis”, Switzerland, September 27th – 31st. Poster presentation, title: “Hydrogen evolution reaction on metallic electrodes in acidic solutions”.
2. SCS Seminar 2018/1 “Catalysis Across Scales”, Interlaken, Switzerland, June 13th - 15th.
3. SCS Fall Meeting 2018, École Polytechnique Fédérale de Lausanne (EPFL), Switzerland, September 2nd. Poster presentation, title: “Hydrogen evolution reaction on metallic electrodes in acidic solutions”.

III. Acknowledgments

Throughout my doctoral program, I had the privilege to meet and work with amazing people. First of all, I would like to express my deepest gratitude to my supervisor, Prof. Dr. Peter Broekmann, for providing the opportunity to carry out my doctoral studies in his research group. Peter always showed his support, confidence, motivation, enthusiasm and guidance to perform this research, and I thank him immensely for the revisions of my thesis and for all the advices I got from him during my PhD. I also thank him for giving me the confidence to collaborate on one of his projects with BASF. Undoubtedly, through this adventure, I was able to learn and reinforce my theoretical and practical knowledge.

I am very grateful to Prof. Dr. Siegfried R. Waldvogel (University of Mainz) and Prof. Dr. Andreas Türler (University of Bern) for their kind acceptance of the invitation to act as referees of my PhD project. Furthermore, I acknowledge Prof. Waldvogel for providing some leaded bronzes to test their performance as CO_2RR catalysts.

Moreover, I thank Prof. Dr. Matthias Arenz for providing us with the zero-gap gas flow cell to perform the CO_2RR testing of the catalysts and giving access to his research laboratories.

Over the course of my time in Switzerland, I had the privilege to learn and work with excellent researchers and wonderful people. I deeply appreciate our postdocs: Dr. Pavel Moreno-Garcia, who has always shown unconditional support inside and outside of the lab and who is always there to help everyone or share a nice moment; Dr. Vitali Grozovski and Dr. Soma Vesztergom, who introduced me to the electrochemistry theory and experiments in our group and who always continued to support and guide my research work; Dr. Yuhui Hou who started her time in the group at the same time as me and who always found a way to solve problems in the lab, as well as introducing me to the use of the SEM; Dr. Alexander Rudnev for always sharing his knowledge, answering many questions, and providing excellent hospitality when I visited Russia; and Dr. Abhijit Dutta for his support in the lab. Mainly, I thank all of them for sharing their friendship and time.

A very special thanks go to Dr. Rocio Aguilar-Sánchez, whom I have known for more than 12 years and inspired and motivated me to do a PhD abroad. This was a wonderful experience that allowed me to open my horizons to know another kind of life and culture.

Sincere thanks go to my friends here in Bern for always motivating, supporting and being there when I need them. To my good friend Ivan, whom I have known since I was in Mexico and with whom I now work in the same lab and because of all the energy and joy that he always brings. To my dear Valentine and Aline for being the first people in Switzerland who offered their beautiful friendship. And to all the current and former group members: Noémi Kovacs, Huifang Hu, Kiran, Ying Kong, Menglong Liu, Anna Iarchuck, Changzhe Sun, Alena Cedeño-López, Motiar Rahaman, Carina Morstein, and Nicolas Schlegel, for making the working atmosphere more pleasant and cheerful.

I highly appreciate Shima Alinejad and Dr. Alessandro Zana for sharing their knowledge about GDE materials and alkaline membranes and introducing me to the use of zero-gap flow cells.

I am also very grateful to my friends in Mexico: Shunashi, Miguel Ángel, Andrea, Pablo, Carlos, Ana Luisa, Monse, Maricruz, Viry, Evelyn, Manes and Paty, who have always shown their affection and that distance is not an obstacle to continue a friendship. A very special thanks go to my friend Antonio Calderon I., whom I have known for more than 15 years in which we have shared very good times and, thanks to his design knowledge, helped prepare the schematics of the gas-flow cells. Moreover, I deeply thank my friend Chahinez in Germany, who open the doors of her house the first time when I came to Europe and for her motivation to come to experience life here.

I also thank our Technicians, René Bühler, Mike Liechti, Sven Hadorn, Denis Flury, Elea Karst, Jasmin and Rafael, because of their support and because they know and teach how the labs work. I also thank to our Engineer, Nicola Lüdi, for teaching me how to use the ICP-MS.

I am deeply grateful to Beatrice Frey, who taught me how to use the SEM and who is always kind and accessible to support us in the SEM analysis of the samples and to the members of the DCBP Mechanical Workshop, who always have an idea to solve our technical problems.

I acknowledge the financial support from the Swiss Government Excellence Scholarships for Foreign Scholars (ESKAS). Without it, coming to Switzerland to do a PhD would have been impossible. I also acknowledge Jasmin Fallahi for providing the information to adapt easily in the city of Bern and at the University of Bern.

I am deeply and sincerely grateful to my beloved Alain Rieder for his love, support and patience in every moment and for always motivating me to surpass my fears and because he always shows how beautiful life in the mountains is. I love you!

Finally, I would like to express my deepest gratitude to my family, to my parents Oscar and Esperanza and my sisters Liliana and Alinne, because they have always been with me, both in good times and in difficult times. Without them, this would not have been possible. This achievement is also thanks to you, and I thank you with all my heart for your love, unconditional support, advice and so on. I love you very much! *Por último, quisiera expresar mi más profundo agradecimiento a mi familia, a mis padres Oscar y Esperanza y a mis hermanas Liliana y Alinne, porque siempre han estado conmigo, tanto en los momentos buenos como en los momentos difíciles. Sin ellos, no hubiera sido posible esto. Este logro también es gracias a ustedes y les agradezco con todo mi corazón su amor, apoyo incondicional, consejos y demás. ¡Los quiero muchísimo!*

IV. Declaration of consent

Declaration of consent

on the basis of Article 18 of the PromR Phil.-nat. 19

Name/First Name: Gálvez-Vázquez, María de Jesús

Registration Number: 17-133-299

Study program: Chemistry and Molecular Sciences

Bachelor ☐ Master ☐ Dissertation ☑

Title of the thesis: CO2 Electroreduction on Silver Catalysts Under Controlled Mass Transport Conditions

Supervisor: Prof. Dr. Peter Broekmann

I declare herewith that this thesis is my own work and that I have not used any sources other than those stated. I have indicated the adoption of quotations as well as thoughts taken from other authors as such in the thesis. I am aware that the Senate pursuant to Article 36 paragraph 1 litera r of the University Act of September 5th, 1996 and Article 69 of the University Statute of June 7th, 2011 is authorized to revoke the doctoral degree awarded on the basis of this thesis.
For the purposes of evaluation and verification of compliance with the declaration of originality and the regulations governing plagiarism, I hereby grant the University of Bern the right to process my personal data and to perform the acts of use this requires, in particular, to reproduce the written thesis and to store it permanently in a database, and to use said database, or to make said database available, to enable comparison with theses submitted by others.

Bern, June 25th, 2021

Place/Date

Signature